



McFadzean, Ross George Bell (2023) *Polaris-SMC in-situ microwave reactor: a new technique for real time neutron diffraction of rapid microwave-induced syntheses*. PhD thesis.

<http://theses.gla.ac.uk/83705/>

Copyright and moral rights for this work are retained by the author

A copy can be downloaded for personal non-commercial research or study, without prior permission or charge

This work cannot be reproduced or quoted extensively from without first obtaining permission in writing from the author

The content must not be changed in any way or sold commercially in any format or medium without the formal permission of the author

When referring to this work, full bibliographic details including the author, title, awarding institution and date of the thesis must be given

Enlighten: Theses

<https://theses.gla.ac.uk/>
research-enlighten@glasgow.ac.uk



University
of Glasgow | School of
Chemistry

**Polaris-SMC *in-situ* microwave reactor: a new
technique for real time neutron diffraction of rapid
microwave-induced syntheses**

Ross George Bell M^cFadzean, BSc (Hons)

Submitted in the fulfilment of the requirements
for the Degree of Doctor of Philosophy

School of Chemistry
College of Science and Engineering
University of Glasgow

June 2023

“There are only four rules you need to remember. Make the plan. Execute the plan. Expect the plan to go off the rails. Throw away the plan.”[1]

Thesis abstract

Direct microwave heating holds much promise in revolutionising the synthesis of solid state materials due to the clear benefits from greatly reduced reaction times and lower energy requirements compared to conventional methods. For the modern laboratory the principles of green chemistry to reduce energy usage and actions with a detrimental impact to the environment are increasingly taking prominence, and microwave reactors work well within this framework. The rapidity of microwave heating however, makes following a reaction progression and identification of unusual synthesis pathways a difficult process. The bespoke single mode cavity reactor designed to operate within the Polaris neutron diffractometer allows for neutron data to be collected over the short time scale of a microwave reaction. The neutron data is recorded with respect to time which can then be split into smaller sections to investigate the reaction pathways in increasingly granular detail.

Throughout this project, several binary metal chalcogenide chemical systems known to be thermoelectric materials of interest were investigated. Thermoelectric generators make use of the Seebeck effect to generate useable currents from an applied temperature gradient, allowing waste heat to be converted back into valuable electricity. For each system a range of samples were prepared in which the selenium component was partially substituted with either tellurium or sulfur in order to hopefully tune the thermoelectric properties. The substitution subprojects enabled a large list of samples to be prepared for synthesis in the Polaris-SMC microwave reactor under well understood reaction conditions. Many of these materials have not been produced previously using a direct microwave heating method in the solid state, and so the insights gained from the *in-situ* neutron data should help optimisation their synthesis conditions in the future.

Acknowledgements

I would like to thank my supervisors Prof Duncan Gregory and Dr Alexey Ganin along with all the members, past and present, of the Gregory Research Group. My co-supervisor on this project was Dr Ron Smith at the ISIS Neutron and Muon Source at the STFC Rutherford Appleton Laboratory. The bespoke microwave reactor was designed by Prof Tim Drysdale who provided invaluable advice regarding the reactor operation. The technicians and facilities support staff of the University of Glasgow have been indispensable throughout the research period; Claire Wilson provided training and advice on both powder and single crystal X-ray diffraction and James Gallagher supervised operation of the scanning electron microscopy data collection. John Marshall and Andrew Hood of the physics department workshop who manufactured a replacement Perspex box to my specifications. Jonathan Walker and Fiona Gray of the disability service provided regular support in the wake of the massive disruption due to the Covid-19 pandemic.

Colin Offer at the ISIS design division and manufacturing facilities group implemented essential sample applicator component redesigns that were manufactured in the onsite workshop. Jamie Nutter at ISIS instrument and user support created an important bespoke cable on request to enable data acquisition from the reactor control panel. Jamie Nutter along with safety supervisor James Taylor provided the electronic short circuit controls and helped develop and sign off on safe operating procedures for the equipment.

Project students supervised during the course of this PhD project Audrey Lorin, Felipe Tontini, Kateřina Kadlecová and Alasdair MacLeod provided various insights into the different chemical systems that inspired further work in the subprojects. Thermoelectric properties of selected samples were measured with the help of Dr Jan-Willem Bos' research group, in particular Blair Kennedy, Stephen Wark and Robert Quinn who supervised sample preparation and carried out sample measurements on my behalf. Use of the EPSRC funded National Chemical Database Service hosted by the Royal Society of Chemistry provided access to numerous data files and literature sources necessary for sample characterisation.

Author's declaration

I certify that the thesis has been written by me. Any help I have received in my research work and the preparation of the thesis itself has been acknowledged. In addition, I certify that all information sources and literature used are indicated in the thesis.

Signature:

Table of contents

Thesis abstract	ii
Acknowledgements	iii
Author's declaration	iv
Table of contents	v
1 Introduction	1-1
1.1 Explaining the thesis to peers	1-1
1.2 Benefits and challenges of microwave synthesis	1-2
1.2.1 <i>Challenges to widespread adoption of microwave methods</i>	1-2
1.3 Scope of this project	1-3
1.3.1 <i>Chapters 2–6: background information</i>	1-4
1.3.2 <i>Chapter 7: tin chalcogenide subproject</i>	1-5
1.3.3 <i>Chapter 8: other binary metal chalcogenides</i>	1-5
1.3.4 <i>Chapter 9: in-situ neutron diffraction studies</i>	1-5
2 Basic concepts	2-6
2.1 Explaining the thesis to my inner child	2-6
2.2 Properties of electromagnetic (EM) fields and waves	2-7
2.2.1 <i>Maxwell-Ampère and Maxwell-Faraday laws</i>	2-8
2.2.2 <i>Gauss' theorem and Maxwell's equations</i>	2-8
2.2.3 <i>Permittivity, permeability and conductivity</i>	2-10
2.2.4 <i>Wave propagation in free space</i>	2-11
2.2.5 <i>Wave propagation in a waveguide</i>	2-13
2.2.6 <i>Wave propagation in matter</i>	2-16
2.2.7 <i>Single mode vs. multi mode applicators</i>	2-18
2.2.8 <i>Thermal modelling</i>	2-19
2.2.9 <i>Anisotropy, isomorphism and polymorphism</i>	2-21
2.2.10 <i>Polarisation and relaxation</i>	2-22
2.3 A brief history of commercial microwave development	2-23
2.4 Mechanisms of microwave-induced heating processes	2-25
2.4.1 <i>Conduction, magnetic and dielectric loss heating</i>	2-26
2.4.2 <i>Dipolar polarisation and ionic conduction</i>	2-27
2.4.3 <i>Interfacial polarisation</i>	2-28
2.4.4 <i>Microwave power and loss tangent</i>	2-29
2.4.5 <i>Skin depth and penetration depth</i>	2-31
2.4.6 <i>Plasma formation in microwave applicators</i>	2-33
2.4.7 <i>Temperature effects on dielectric properties</i>	2-34
2.5 Semiconductors and thermoelectric generators (TEGs)	2-36
2.5.1 <i>Defect chemistry and structural effects on EM properties</i>	2-38

2.5.2	<i>Reclaiming waste energy with thermoelectric generators (TEGs)</i>	2-41
2.5.3	<i>Measuring TEM efficiency with figure of merit</i>	2-42
2.5.4	<i>The Seebeck coefficient</i>	2-42
2.5.5	<i>Electronic, lattice and bipolar thermal conductivity</i>	2-43
2.5.6	<i>Electron-phonon coupling (EPC) and phonon-phonon interactions</i>	2-45
2.5.7	<i>Improving thermoelectric performance</i>	2-46
3	Literature review of thermoelectric materials	3-48
3.1	Explaining the thesis to a grant committee	3-48
3.2	Common thermoelectric materials (TEMs)	3-49
3.2.1	<i>Half-Heusler compounds</i>	3-50
3.2.2	<i>Skutterudites</i>	3-50
3.2.3	<i>Zintl phases</i>	3-51
3.2.4	<i>Clathrates</i>	3-51
3.2.5	<i>Metal silicides</i>	3-52
3.2.6	<i>Metal oxides</i>	3-52
3.2.7	<i>Complex ternary chalcogenides</i>	3-53
3.3	Binary metal chalcogenides	3-53
3.3.1	<i>Tin(II) and tin(IV) selenides: SnSe and SnSe₂</i>	3-54
3.3.2	<i>Review of high performing SnSe synthesis methods</i>	3-55
3.3.3	<i>Reported enhancement of SnSe performance through doping</i>	3-57
3.3.4	<i>Other tin(II) chalcogenides: SnTe and SnS</i>	3-58
3.3.5	<i>Bismuth(III) chalcogenides: Bi₂Se₃ and Bi₂Te₃</i>	3-59
3.3.6	<i>Common bismuth(III) chalcogenide synthesis methods</i>	3-60
3.3.7	<i>Bismuth(III) chalcogenide solid solutions</i>	3-61
3.3.8	<i>Antimony(III) chalcogenides: Sb₂Se₃ and Sb₂Te₃</i>	3-63
3.3.9	<i>Review of synthesis methods for enhancing Sb₂Se₃ and Sb₂Te₃</i>	3-64
3.3.10	<i>Non-stoichiometric copper chalcogenides: Cu_xSe, Cu_xTe and Cu_xS</i>	3-66
3.3.11	<i>Review of best reported copper chalcogenide synthesis methods</i>	3-67
3.4	Accounting for element abundance and toxicity	3-71
3.5	Summary	3-74
4	Experimental design and procedures	4-75
4.1	Explaining the thesis to friends	4-75
4.2	Experimental design for benchtop microwave reactions	4-76
4.2.1	<i>Sample preparation</i>	4-76
4.2.2	<i>Sample heating in modified domestic microwave oven (DMO)</i>	4-78
4.2.3	<i>Sample heating in a bespoke single mode cavity (SMC) reactor</i>	4-79
4.2.4	<i>Sample collection from benchtop experiments</i>	4-81
4.3	Experimental design for in-situ neutron reactions	4-82
4.3.1	<i>Maximising sample volume for Polaris neutron beam dimensions</i>	4-82
4.3.2	<i>Collecting pre reaction, in-situ and post reaction neutron data</i>	4-83
4.4	Data acquisition for reaction optimisation	4-84
4.4.1	<i>Measuring the temperature of microwave reactions</i>	4-84

4.4.2	<i>Impedance matching in a waveguide applicator</i>	4-86
4.5	Safety issues and risk assessment	4-92
4.5.1	<i>Preventing microwave leakage and mitigating hazards</i>	4-92
4.5.2	<i>Working in environments utilising ionising radiation</i>	4-94
4.5.3	<i>Transferring experiment samples to the sample applicator</i>	4-95
4.5.4	<i>Removing experiment samples and testing sample activity levels</i>	4-96
5	Characterisation methods	5-98
5.1	Explaining the thesis from the bottom up	5-98
5.2	Crystal structures	5-99
5.2.1	<i>Lattice parameters and unit mesh</i>	5-99
5.2.2	<i>Symmetry operations</i>	5-99
5.2.3	<i>Bravais lattices</i>	5-100
5.2.4	<i>Crystallographic space groups</i>	5-101
5.3	X-ray and neutron diffractometry techniques	5-102
5.3.1	<i>Laue method, Braggs' law and Ewald's spheres</i>	5-104
5.3.2	<i>Generation and scattering of X-rays</i>	5-105
5.3.3	<i>Crystal structure effects on X-ray diffraction (XRD) patterns</i>	5-106
5.3.4	<i>Capillary/transmission vs flat plate/Bragg-Brentano geometry</i>	5-107
5.3.5	<i>X-ray diffraction instruments used in this project</i>	5-108
5.3.6	<i>Powder neutron diffraction (PND) and time-of-flight (TOF)</i>	5-109
5.3.7	<i>Time-resolved powder neutron diffraction (PND) at ISIS</i>	5-111
5.3.8	<i>Polaris event mode data processing using Mantid Workbench</i>	5-112
5.4	Rietveld refinement	5-113
5.4.1	<i>Data collection and background correction</i>	5-113
5.4.2	<i>Peak-shape and intensity functions</i>	5-115
5.4.3	<i>Profile and structural parameters</i>	5-116
5.4.4	<i>Least-squares refinement and Fourier analysis</i>	5-117
5.4.5	<i>Geometric restraints</i>	5-117
5.4.6	<i>Estimated standard deviation (ESD) calculations</i>	5-118
5.4.7	<i>R-factor interpretation</i>	5-118
5.5	Structural analysis techniques	5-119
5.5.1	<i>Diffuse reflectance measurement using UV-vis spectroscopy</i>	5-119
5.5.2	<i>Calculating optical band gap (E_g) from Kubelka-Munk function</i>	5-121
5.5.3	<i>Sample imaging using scanning electron microscopy (SEM)</i>	5-122
5.5.4	<i>Energy dispersive X-ray spectroscopy (EDX)</i>	5-123
5.6	Determination of thermoelectric properties	5-124
5.6.1	<i>Calculating total thermal conductivity (κ_T)</i>	5-124
5.6.2	<i>Seebeck coefficient (S) and electrical conductivity (σ)</i>	5-126
5.6.3	<i>Error propagation in thermoelectric measurements</i>	5-128
6	Polaris-SMC microwave reactor components	6-130
6.1	Explaining the thesis badly	6-130
6.2	Neutron diffraction at the Diamond Light Source	6-131

6.2.1	<i>Polaris neutron diffractometer</i>	6-131
6.3	Bespoke SMC microwave reactor components	6-133
6.3.1	<i>Gerling GA4015 1.2 kW laboratory magnetron head</i>	6-133
6.3.2	<i>Gerling GA1107 2-port isolator</i>	6-134
6.3.3	<i>Gerling GA3106 directional waveguide coupler</i>	6-135
6.3.4	<i>Gerling GA3301 coupler power interface (CPI) modules</i>	6-136
6.3.5	<i>Gerling GA1022 STHT V 1.5 Auto Tuner</i>	6-137
6.3.6	<i>Gerling GA2605 pressure/vacuum quartz window</i>	6-138
6.3.7	<i>Gerling GA6004A universal waveguide applicator (UWA)</i>	6-139
6.3.8	<i>Gerling GA1206A precision sliding short circuit (SSC)</i>	6-139
6.3.9	<i>Calibrating the electronic sliding short circuit</i>	6-140
6.3.10	<i>Gerling GA4104A 1.2 kW magnetron power supply</i>	6-141
6.3.11	<i>Gerling GA3210 dual digital microwave power meter</i>	6-141
6.3.12	<i>Dataq Instruments DI-1100 data acquisition (DAQ) module</i>	6-143
6.4	Adjusting the SMC reactor configuration and peripherals	6-144
6.4.1	<i>Redesigning the protective Perspex® box</i>	6-144
6.4.2	<i>Redesigning the quick release sample stick and ampoule block</i>	6-144
6.4.3	<i>Polaris-SMC microwave reactor design considerations</i>	6-146
7	Tuning tin selenide thermoelectric efficiency	7-153
7.1	Explaining the thesis to my mum	7-153
7.2	Introduction	7-154
7.3	Sample preparation and experimental design	7-154
7.3.1	<i>Stoichiometric calculations</i>	7-154
7.3.2	<i>Synthesis parameters</i>	7-155
7.4	Effect of synthesis duration on samples in a modified DMO	7-155
7.4.1	<i>Scanning electron microscopy (SEM) analysis of early samples</i>	7-157
7.4.2	<i>Gram-scale synthesis and single crystal X-ray diffraction</i>	7-161
7.4.3	<i>Rapid synthesis of single phase SnSe₂ using a modified DMO</i>	7-164
7.5	Practice syntheses using benchtop SMC reactor	7-165
7.5.1	<i>Synthesis duration calculated from power absorption profiles</i>	7-165
7.5.2	<i>Improvement of SnSe phase fraction with excess Sn</i>	7-168
7.5.3	<i>Solid state microwave synthesis under various atmospheres</i>	7-169
7.6	Partial substitution of chalcogen site (SnSe _{1-y} X _y)	7-170
7.6.1	<i>Direct microwave-heating synthesis parameters for SnSe_{1-x}Te_x</i>	7-171
7.6.2	<i>Direct microwave-heating synthesis parameters for SnSe_{1-x}S_x</i>	7-173
7.7	Thermoelectric properties	7-177
7.7.1	<i>Optical band gap calculated from UV-vis spectroscopy</i>	7-177
7.7.2	<i>Sample densification using hot pressing</i>	7-180
7.7.3	<i>Thermal conductivity measurements</i>	7-181
7.7.4	<i>Seebeck coefficient and electrical conductivity measurements</i>	7-182
7.7.5	<i>Thermoelectric properties analysis of SnSe_{1-y}X_y samples</i>	7-183
7.8	Summary	7-189

8	Bismuth, antimony and copper chalcogenides	8-190
8.1	Explaining the thesis to a judge	8-190
8.2	Microwave synthesis of bismuth chalcogenides ($\text{Bi}_2\text{Se}_{3-x}\text{Te}_x$)	8-191
8.2.1	<i>Stoichiometric calculations and experimental design</i>	8-191
8.3	Optimisation of reaction parameters	8-192
8.3.1	<i>Adjusting experimental design to eliminate oxide formation</i>	8-192
8.3.2	<i>Bismuth chalcogenide solid solution ($\text{Bi}_2\text{Se}_{3-x}\text{Te}_x$) syntheses</i>	8-195
8.4	Antimony chalcogenide solid solutions ($\text{Sb}_2\text{Se}_{3-x}\text{Te}_x$)	8-198
8.4.1	<i>Stoichiometric calculations and experimental design</i>	8-199
8.5	Optimisation of reaction parameters	8-199
8.5.1	<i>Initial antimony selenide (Sb_2Se_3) synthesis experiments</i>	8-199
8.5.2	<i>Initial antimony telluride (Sb_2Te_3) synthesis experiments</i>	8-200
8.6	The effect of synthesis duration on $\text{Sb}_2\text{Se}_{3-x}\text{Te}_x$ solid solutions	8-201
8.6.1	<i>Ex-situ neutron diffraction of $\text{Sb}_2\text{Se}_{3-x}\text{Te}_x$ solid solution samples</i>	8-204
8.6.2	<i>Investigation of $\text{Sb}_2\text{Se}_{3-x}\text{Te}_x$ solid solution between $0 \leq x \leq 1$</i>	8-205
8.6.3	<i>$\text{Sb}_2\text{Se}_{3-x}\text{Te}_x$ multi phase transition between $0.4 \leq x \leq 0.8$</i>	8-207
8.6.4	<i>Scaling-up 5 g $\text{Sb}_2\text{Se}_{3-x}\text{Te}_x$ syntheses (between $0 \leq x \leq 1$)</i>	8-208
8.7	Microwave synthesis of copper chalcogenides	8-211
8.7.1	<i>Stoichiometric calculations and experimental design</i>	8-211
8.8	Optimisation of $\text{Cu}_{1-x}\text{Se}_{1-y}\text{Z}_y$ synthesis parameters	8-212
8.8.1	<i>Initial Cu_{1-x}Se synthesis experiments</i>	8-212
8.8.2	<i>Initial Cu_{2-x}Se synthesis experiments</i>	8-215
8.8.3	<i>Copper chalcogenide solid solution ($\text{Cu}_{1-x}\text{Se}_{1-y}\text{Te}_y$) syntheses</i>	8-218
8.8.4	<i>Rapid reaction of $\text{Cu}_{1-x}\text{Se}_{1-y}\text{S}_y$ at low pressure</i>	8-221
8.8.5	<i>Copper chalcogenide ($\text{Cu}_{1-x}\text{Se}_{1-y}\text{S}_y$) syntheses from pellets</i>	8-222
8.9	Summary	8-225
9	Polaris-SMC in-situ neutron experiments	9-227
9.1	Explaining the thesis in iambic pentameter	9-227
9.2	Introduction	9-228
9.3	Impedance measurements of reactant mixtures	9-228
9.3.1	<i>$\text{SnSe}_{1-x}\text{Te}_x$ impedance measurements</i>	9-229
9.3.2	<i>$\text{SnSe}_{1-x}\text{S}_x$ impedance measurements</i>	9-230
9.3.3	<i>$\text{Bi}_2\text{Se}_{3-x}\text{Te}_x$ impedance measurements</i>	9-231
9.3.4	<i>$\text{Sb}_2\text{Se}_{3-x}\text{Te}_x$ impedance measurements</i>	9-233
9.3.5	<i>$\text{Cu}_{1-x}\text{Se}_{1-y}\text{Te}_y$ impedance measurements</i>	9-234
9.3.6	<i>$\text{Cu}_{1-x}\text{Se}_{1-y}\text{S}_y$ impedance measurements</i>	9-234
9.4	Polaris-SMC reactor operation and performance	9-236
9.5	Tin chalcogenide <i>in-situ</i> neutron diffraction studies	9-237

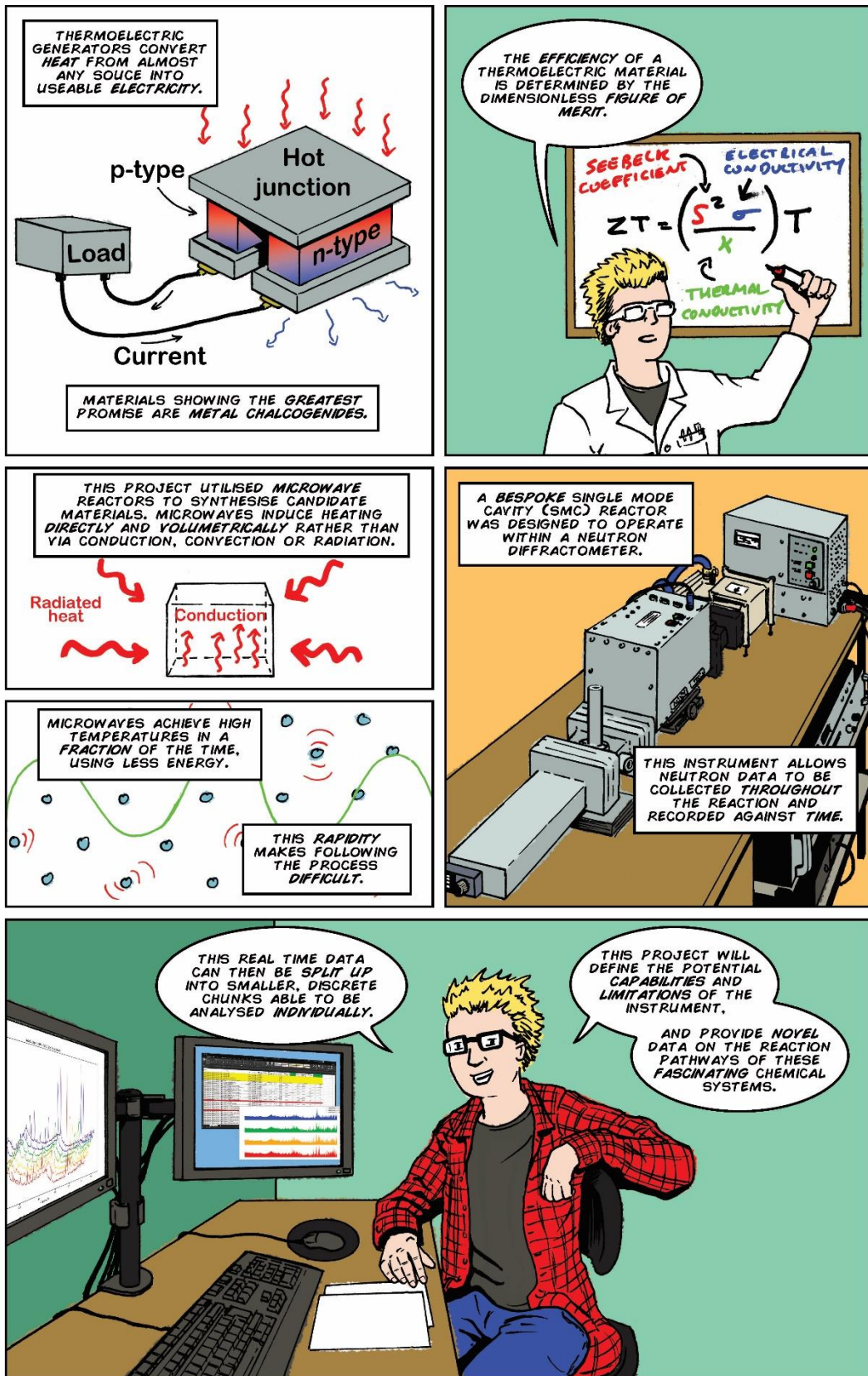
9.5.1	<i>SnSe (10 % excess Sn) in-situ TOF data</i>	9-238
9.5.2	<i>SnSe_{1-x}Te_x in-situ TOF data</i>	9-241
9.5.3	<i>SnSe_{1-x}S_x in-situ TOF data</i>	9-244
9.6	Bismuth chalcogenide <i>in-situ</i> neutron diffraction studies	9-248
9.6.1	<i>Bi₂Se_{3-x}Te_x in-situ TOF data (60 s syntheses)</i>	9-249
9.6.2	<i>Analysis of elemental powders during second ISIS beamtime</i>	9-253
9.6.3	<i>Extending Bi₂Se_{3-x}Te_x heating duration (120 s syntheses)</i>	9-254
9.7	Antimony chalcogenide <i>in-situ</i> neutron diffraction studies	9-257
9.7.1	<i>Effect of synthesis duration on Sb₂Se_{3-x}Te_x solid solutions</i>	9-257
9.7.2	<i>Comparing Sb₂Se_{3-x}Te_x (60 s and 120 s) in-situ TOF data</i>	9-259
9.8	Copper chalcogenide <i>in-situ</i> neutron diffraction studies	9-262
9.8.1	<i>Cu_{1-x}Se_{1-y}Te_y in-situ TOF data</i>	9-263
9.8.2	<i>Cu_{1-x}Se_{1-y}S_y in-situ TOF data</i>	9-267
9.9	Summary	9-270
10	Summary and suggested future work	10-271
10.1	Explaining the thesis with interpretative dance	10-271
10.2	Summary of novel project outcomes	10-272
10.2.1	<i>Chapter 7: tin chalcogenide subproject</i>	10-272
10.2.2	<i>Chapter 8: other binary metal chalcogenides</i>	10-273
10.2.3	<i>Chapter 9: in-situ neutron diffraction studies</i>	10-274
10.3	Suggested future work	10-275
Appendix		277
A-1	Managing disruption as a result of the Covid-19 pandemic	277
A-1.1	<i>Equipment breakdowns and supply chain delays</i>	277
A-1.2	<i>ISIS shutdown and user cycle postponement</i>	278
A-1.3	<i>Managing the effects of the Covid-19 pandemic on mental health</i>	279
A-1.4	<i>Financial burdens and request for funded extension to project</i>	280
A-4	Chapter 4 supplementary material	281
A-4.1	<i>Sample heating using a bespoke single mode cavity (SMC) reactor</i>	281
A-4.2	<i>Collecting pre reaction, in-situ and post reaction neutron data</i>	281
A-4.3	<i>Calibration of a vector network analyser (VNA) for a waveguide</i>	283
A-4.4	<i>Covid-19 precautions at Rutherford Appleton Laboratories (RAL)</i>	283
A-5	Chapter 5 supplementary material	284
A-5.1	<i>Unit mesh tessellation</i>	284
A-5.2	<i>Compound symmetry operations</i>	284
A-5.3	<i>Unit cells and Bravais lattices</i>	285
A-5.4	<i>Miller indices</i>	286
A-5.5	<i>Kα and Kβ electron transitions in X-ray tubes</i>	287
A-5.6	<i>Polaris event mode data processing using Mantid Workbench</i>	288
A-5.7	<i>Rietveld refinement functions</i>	291
A-5.8	<i>Diffuse reflectance and UV-vis spectroscopy</i>	292

A-5.9	<i>Preparing pellets for thermoelectric properties measurement</i>	293
A-6	Chapter 6 supplementary material	294
A-6.1	<i>How magnetrons generate microwaves</i>	294
A-6.2	<i>Redesign of quick release sample stick and ampoule block</i>	295
A-7	Chapter 7 supplementary material	298
A-7.1	<i>Effect of synthesis duration on SnSe using a modified DMO</i>	298
A-7.2	<i>Gram-scale samples prepared using modified DMO</i>	299
A-7.3	<i>Rapid synthesis of single phase SnSe₂ using a modified DMO</i>	299
A-7.4	<i>Implementation of power and temperature data acquisition devices</i>	300
A-7.5	<i>Improving SnSe phase fraction with excess Sn</i>	300
A-7.6	<i>Solid state MW synthesis under varied atmospheric conditions</i>	301
A-7.7	<i>Direct MW-heating parameters for SnSe_{1-x}Te_x</i>	302
A-7.8	<i>Direct MW-heating parameters for SnSe_{1-x}S_x</i>	303
A-7.9	<i>Sample densification by cold pressing and sintering</i>	304
A-8	Chapter 8 supplementary material	305
A-8.1	<i>Initial bismuth selenide (Bi₂Se₃) synthesis experiments</i>	305
A-8.2	<i>Initial bismuth telluride (Bi₂Te₃) synthesis experiments</i>	306
A-8.3	<i>Adjusting experimental design to eliminate oxide formation</i>	307
A-8.4	<i>Initial antimony selenide (Sb₂Se₃) synthesis experiments</i>	308
A-8.5	<i>Initial antimony telluride (Sb₂Te₃) synthesis experiments</i>	309
A-8.6	<i>The effect of synthesis duration on Sb₂Se_{3-x}Te_x solid solutions</i>	309
A-8.7	<i>Investigation of Sb₂Se_{3-x}Te_x phase transition between 0 ≤ x ≤ 1</i>	312
A-8.8	<i>Sb₂Se_{3-x}Te_x multi phase transition between 0.4 ≤ x ≤ 0.8</i>	313
A-8.9	<i>Scaling-up 5 g Sb₂Se_{3-x}Te_x syntheses (between 0 ≤ x ≤ 1)</i>	314
A-8.10	<i>Initial Cu_{1-x}Se synthesis experiments</i>	316
A-8.11	<i>Initial Cu_{2-x}Se synthesis experiments</i>	316
A-8.12	<i>Copper chalcogenide solid solution (Cu_{1-x}Se_{1-y}Te_y) syntheses</i>	317
A-8.13	<i>Rapid reaction of Cu_{1-x}Se_{1-y}S_y at low pressure</i>	318
A-8.14	<i>Copper chalcogenide (Cu_{1-x}Se_{1-y}S_y) syntheses from pellets</i>	319
A-9	Chapter 9 supplementary material	320
A-9.1	<i>SnSe (10 % excess Sn) in-situ TOF data</i>	320
A-9.2	<i>SnSe_{1-x}Te_x in-situ TOF data</i>	322
A-9.3	<i>SnSe_{1-x}S_x in-situ TOF data</i>	323
A-9.4	<i>Bi₂Se_{3-x}Te_x in-situ TOF data (60 s syntheses)</i>	324
A-9.5	<i>Interruption of neutron beam during first batch of experiments</i>	325
A-9.6	<i>Elemental reactant powders' event mode TOF data</i>	326
A-9.7	<i>Extending Bi₂Se_{3-x}Te_x heating duration (120 s syntheses)</i>	328
A-9.8	<i>Effect of synthesis duration on Sb₂Se_{3-x}Te_x solid solutions</i>	329
A-9.9	<i>Cu_{1-x}Se_{1-y}Te_y in-situ TOF data</i>	334
A-9.10	<i>Cu_{1-x}Se_{1-y}Te_y post reaction TOF histogram data</i>	334
A-9.11	<i>Cu_{1-x}Se_{1-y}S_y post reaction TOF histogram data</i>	335
A-9.12	<i>SnSe_{1-x}Te_x (stoichiometric) event mode TOF data</i>	336
A-9.13	<i>SnSe_{1-x}Te_x (10 % excess Sn) event mode TOF data</i>	337
A-9.14	<i>SnSe_{1-x}S_x (stoichiometric) event mode TOF data</i>	339
A-9.15	<i>SnSe_{1-x}S_x (10 % excess Sn) event mode TOF data</i>	340
A-9.16	<i>Bi₂Se_{3-x}Te_x event mode TOF data (60 s syntheses)</i>	342
A-9.17	<i>Bi₂Se_{3-x}Te_x event mode TOF data (120 s syntheses)</i>	343
A-9.18	<i>Comparing Sb₂Se_{3-x}Te_x (60 s and 120 s) event mode TOF data</i>	344

<i>A-9.19 $Cu_{1-x}Se_{1-y}Te_y$ event mode TOF data</i>	345
<i>A-9.20 $Cu_{1-x}Se_{1-y}S_y$ event mode TOF data</i>	346
References	347

1 Introduction

1.1 Explaining the thesis to peers



1.2 Benefits and challenges of microwave synthesis

Most chemical reactions are limited by the b.p. of a solvent in reflux systems or, for solid state reactions, conventional heating methods using high temperature furnaces. Typically, induction periods and reaction times are reduced only in accordance with Arrhenius' law which states that generally the speed of a process can be doubled with every 10 °C increase in absolute temperature. Unlike traditional high temperature furnaces which operate through a combination of conduction, convection and radiation to raise the T of the entire cavity and transfer heat to the material, microwaves (MWs) induce heating directly and volumetrically within the load, and so require significantly less energy to achieve the same level of heating. The heating effect occurs instantaneously and can be ceased just as quickly, meaning both heating and cooling times are greatly decreased. This reduced synthesis duration allows experiments to be conducted more efficiently while minimising the energy requirements per reaction cycle. The shorter time has the knock on effect of increasing overall throughput for batch and continuous operations; a valuable attribute for commercial applications such as chemical synthesis or drying[2].

Microwaves have been used to successfully synthesise many chemical systems however, the field of solid state synthesis has been largely underrepresented in the literature by comparison. Solid state reactions eliminate the need for solvent waste disposal which are a concern with both MW-induced or traditionally heated solvothermal syntheses. The varying effect of MWs depending on the material properties means that reactions can be designed to be selective, where heating can be induced faster in some materials than in others. Microwave synthesis of binary chalcogenides like the systems investigated in this thesis have garnered some interest although, the relative lack of experimentation with solid state materials leaves a corresponding ignorance regarding unique reaction pathways or control parameters. It is known that some materials synthesised using MWs can exhibit structures and morphologies that differ greatly from more traditional synthesis methods[3].

1.2.1 Challenges to widespread adoption of microwave methods

The observed benefits of rapid synthesis, increased yields and greater product purities resulting from MW-induced synthesis reactions do not have clear underlying mechanisms that are agreed upon in the scientific community.

Conventionally, MW frequencies are considered too low to meet the energy requirements necessary to break bonds such as with X-rays however, specific MW effects have been proposed. Non-thermal effects such as the increased rate of chemical reactions could be explained purely by the impact of volumetric heating over conventional heat transfer on the thermodynamics[4].

Obermayer et al reported in 2009 that by using SiC reaction vessels, solvents with significantly different dielectric properties were able to be heated at comparable rates[5]. By comparing the rates with solvents in transparent Pyrex® vessels, it was possible to separate the effects of purely thermal mechanisms resulting from specific non-thermal MW effects. The comparison showed that the SiC shielded the solvents from direct interaction with the MWs, instead heating with conventional heat transfer mechanisms. Other observations of MW-heated reactions have included improved diffusion through solids, densification of material at lower temperatures than conventional methods as well as unique morphologies or crystallographic structures[4]. The development of various *in-situ* analysis techniques such as neutron diffraction, has been used by Harrison et al to demonstrate that single crystal aspirin showed comparable parameters when heated to 100 K with MWs as those of a sample heated conventionally to 300 K[6].

For most applications, the capital cost of industrial equipment tends to be in the region of multiple thousands of pounds per kW of power generation, with additional costs associated with specific variables along with control and automation systems. With the overall efficiency from mains power to the dissipation of MWs in the target material still in the range of 50–70 %, there is incentive to make improvements to the cost/benefit calculation[7].

1.3 Scope of this project

For chemical syntheses, the rapidity of the direct MW-heating method makes following reaction progress and identification of phase changes difficult. This PhD project was proposed to demonstrate the potential of a new *in-situ* method for collecting neutron data from such fast reactions as they occur. This new technique allows researchers to map neutron diffraction data against time to identify temporary intermediates and phase changes as well as correlate such events with absorption of MWs by the sample. Better understanding of the

reaction pathways for materials produced through direct MW-heating allows them to be optimally tuned for desirable properties or compositions.

A bespoke single mode cavity (SMC) MW reactor was built from modular components to the specifications of Dr Timothy Drysdale prior to the beginning of this project. The SMC reactor was built in duplicate, with one configured to be compatible with the Polaris instrument on the ISIS neutron beamline in the Rutherford Appleton Laboratory (RAL) in Oxford, and the other for benchtop experiments at the University of Glasgow. The Polaris neutron diffractometer has in the past been used to rapidly characterise and study the structure of zeolites, batteries and ceramics over very short timescales and so is ideal for such MW reactor applications[8]–[10]. The commissioning experiments performed on the ISIS beamline were conducted on a variety of samples first investigated in subprojects using the benchtop SMC reactor. These subprojects attempted to produce single phase tin, bismuth, antimony and copper chalcogenides which are all materials with favourable or promising thermoelectric (TE) properties. Thermoelectric materials (TEMs) are able to generate useful electric current from a temperature gradient. Most of the systems chosen had limited or no previous reporting of synthesis using direct MW-heating in the solid state and so most are novel insights into their production.

1.3.1 Chapters 2–6: background information

The thesis begins with a basic introduction to the fundamental concepts of the methods and materials used throughout. Chapter 2 covers the physics of electromagnetic waves and the propagation of MWs in waveguides. Attention is given to the mechanisms through which solids with different dielectric properties are heated, as well as an overview of the defining properties of TEMs. Chapter 3 expands on this with a literature review of common chemical systems that have historically shown promise as TEMs. Specific attention is paid to the binary metal chalcogenides that were investigated throughout this project.

The experimental procedures of sample preparation/collection methods and differences between heating in a modified domestic MW oven (DMO) or a SMC reactor are described in chapter 4 with sufficient detail to allow experiment replication. Here also, specific information on the methods used to record the MW power in the SMC waveguide along with temperature of samples during

heating is discussed. Unique procedures implemented to maximise the *in-situ* neutron data collection are outlined, with particular attention given to safety issues around MW leakage and safe handling of active samples. A general background of characterisation techniques used is given in chapter 5, with focus on the benefits of neutron diffraction over X-rays, refinement of collected data and instruments used to measure TE properties of samples. Chapter 6 is devoted to descriptions of the Polaris-SMC reactor components and incorporation of the data acquisition (DAQ) module for recording MW power. Details of various adjustments made to the reactor components or configuration are justified here.

1.3.2 Chapter 7: tin chalcogenide subproject

As the chemical system that was investigated most thoroughly, the results and discussion of the tin chalcogenides are given their own chapter. Specifically attempts to overcome challenges in producing single phase samples and the measured TE properties for selected Te- and S-doped samples are highlighted.

1.3.3 Chapter 8: other binary metal chalcogenides

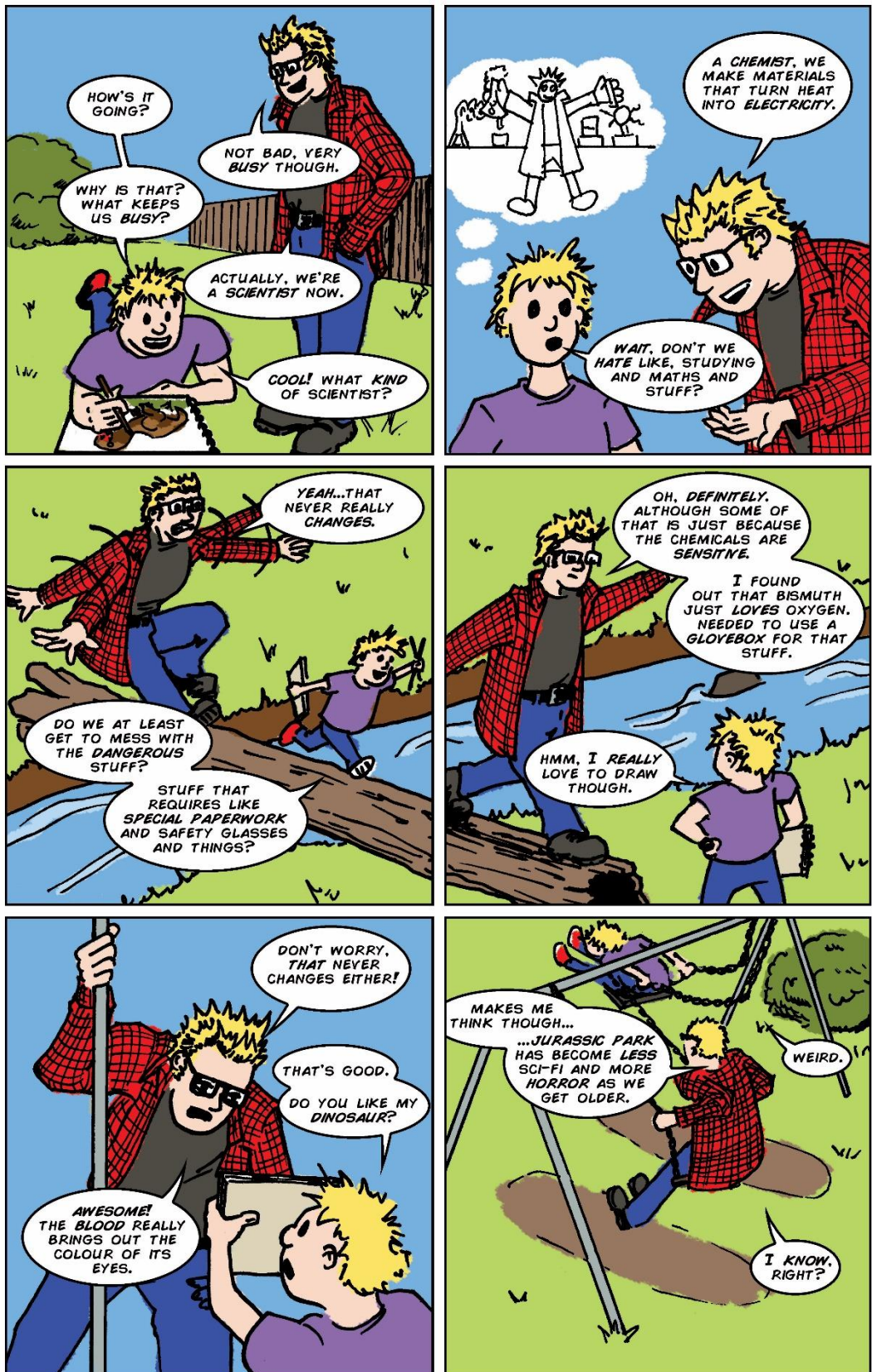
Three other binary metal chalcogenide systems were investigated with variable success due to unique challenges exacerbated the Covid-19 pandemic and so, the results are presented together. The challenges of producing uncontaminated bismuth and antimony chalcogenides are discussed along with the results of the successful synthesis of partially substituted solid solutions. Reporting on the copper chalcogenides is brief as these experiments were the most truncated by Covid-19 disruption.

1.3.4 Chapter 9: *in-situ* neutron diffraction studies

The final chapter of the thesis begins with MW impedance measurements of the various sample preparations but the main focus is on a curated selection of the recorded *in-situ* neutron data from the Polaris-SMC reactor commissioning experiments. Representative data from each of the subproject chemical systems are presented in time-resolved colourmap plots with correlated MW absorption profiles overlaid. Where possible, phase change events noted in the event mode data are more closely investigated by refinement of smaller sections (5–20 s increments) over the period of interest. Certain systems provided more intense Bragg peaks in the powder patterns than others, which were compared to offer critical appraisal of the *in-situ* technique and discuss approaches for any future work to improve upon the data quality that can be obtained.

2 Basic concepts

2.1 Explaining the thesis to my inner child



2.2 Properties of electromagnetic (EM) fields and waves

Microwave radiation covers a large range of frequencies in the sub-infrared range of the electromagnetic (EM) spectrum as shown in figure 2.1 however, most have been reserved for telecommunication and radar technologies[11].

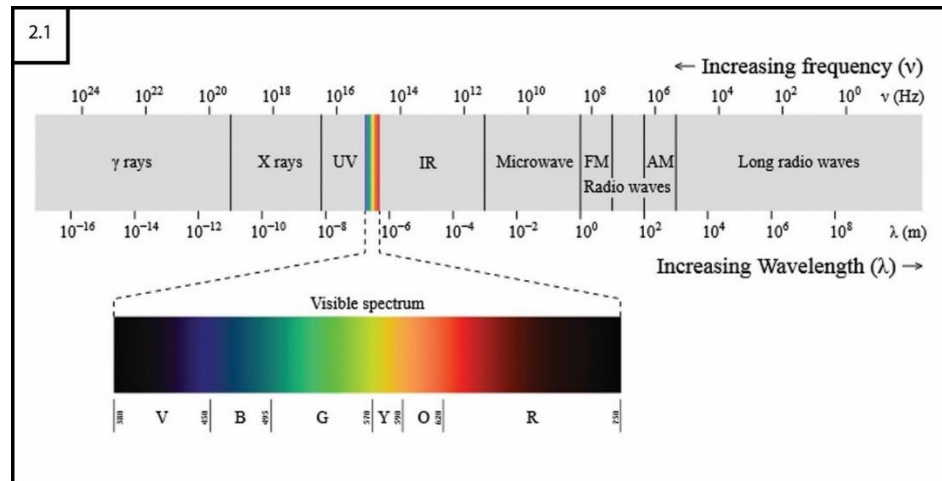


Figure 2.1: Electromagnetic spectrum diagram showing microwaves and the radio wave frequency AM to FM bands as distinct regions. Image by Philip Ronan, CC BY-SA 3.0 via Wikimedia Commons[12]

All EM waves, including the micro wavelength range, transfer energy comprised of both electric (E) and magnetic (H) field components, which are orientated orthogonal to one another in the direction of propagation and vary with time. The MW frequency range is 300 MHz to 300 GHz with the wavelength (λ) related to the frequency (f) by the speed of light (c)[13]:

$$\lambda = \frac{c}{f} \quad \text{(Equation 2-1)}$$

The speed and wavelength of light is dependent on the material through which the wave propagates, which for a vacuum: $c = 2.998 \times 10^8 \text{ ms}^{-1}$ and λ (at MW frequencies) lies in the range of 1 mm to 1. Typical commercial MW generators operate at $f = 2.45 \text{ GHz}$, with a corresponding $\lambda = 12.24 \text{ cm}$, to avoid interference with telecommunications networks and reduce the cost of magnetrons[14].

The electromotive force (EMF) along the path of a circuit is the work done by the EM fields on a unit of positive charge that is moved along said path. If a change in the current of a conductor occurs at a point, the E field resulting from the disturbance generates a H field with flux lines that encircle the electric flux lines according to the Maxwell-Ampère law[15].

2.2.1 Maxwell-Ampère and Maxwell-Faraday laws

The material properties that govern the relationship between the \mathbf{E} and \mathbf{H} fields that comprise EM waves are given by the Maxwell-Ampère law and the Maxwell-Faraday law. These laws relate the time variations of one field to the spacial variations of the other. The Maxwell-Ampère law states that the magnetomotive force around a closed path equals the total electric current over any surface bound by the path[4]:

$$\nabla \times \mathbf{H} = \sigma \mathbf{E} + \varepsilon \frac{\partial \mathbf{E}}{\partial t} \quad \text{(Equation 2-2)}$$

σ = Electrical conductivity

ε = Permittivity

These temporally changing fields continually generate each other in an expanding region, causing wave propagation away from its source. Although there is no direct interaction with physical particles, there is attenuation of the wave (a reduction of magnitude or power with continued propagation) and a time delay in its effects. The delay is due to the finite wave velocity relative to the expanding region of the wave. Electromagnetic wave propagation can result in possible ohmic loss, i.e., resistance leading to energy being dissipated as heat[15].

The Maxwell-Faraday law describes the relationship between a magnetic flux changing with respect to time and the \mathbf{E} field intensity integrated around all paths in a closed loop[4]:

$$\nabla \times \mathbf{E} = -\mu \frac{\partial \mathbf{H}}{\partial t} \quad \text{(Equation 2-3)}$$

2.2.2 Gauss' theorem and Maxwell's equations

Gauss' theorem states that integrating \mathbf{E} over any closed surface is equal to the total charge within the surface divided by the permittivity of free space (ε_0). Within dielectric materials, total charges include both free and macroscopic polarisation charges (\mathbf{P}) that gives rise to the electric displacement field (\mathbf{D})[16]:

$$\mathbf{D} = \varepsilon_0 \mathbf{E} + \mathbf{P} \quad \text{(Equation 2-4)}$$

The \mathbf{D} field is the flux through an area surrounding a charge unaltered by the presence of a dielectric medium, much like \mathbf{E} . In a simple isotropic dielectric, \mathbf{P} will be parallel to \mathbf{E} and therefore also \mathbf{D} , and so can be written in terms of ε [16]:

$$\mathbf{D} = \epsilon \mathbf{E} \quad \text{(Equation 2-5)}$$

The \mathbf{H} field strength is defined in relation to the flux density by the permeability of free space (μ_0) with no magnetisable material present[17]:

$$\mathbf{H} = \frac{\mathbf{B}}{\mu_0} \quad \text{(Equation 2-6)}$$

In magnetised materials, the magnetisation vector (\mathbf{M}) must be accounted for[17]:

$$\mathbf{H} = \frac{\mathbf{B}}{\mu_0} - \mathbf{M} \quad \text{(Equation 2-7)}$$

For paramagnetic and diamagnetic materials magnetisation is sustained by \mathbf{B} and will disappear in its absence. The \mathbf{H} field within a material fluctuates at the microscopic scale between different points and is instead considered in the macroscopic perspective, i.e., the average over regions smooths out \mathbf{M} . The \mathbf{H} field and \mathbf{M} are proportionally linked by magnetic susceptibility (χ_m)[17]:

$$\mathbf{M} = \chi_m \mathbf{H} \quad \text{(Equation 2-8)}$$

Linear media are materials in which χ_m behaves as described by equation 2-8 and where \mathbf{B} is proportional to the \mathbf{H} field strength[17]:

$$\mathbf{B} = \mu_0(\mathbf{H} + \mathbf{M}) = \mu_0(1 + \chi)\mathbf{H} \quad \text{(Equation 2-9)}$$

The permeability of a material can be substituted into equation 2-9 to show that \mathbf{B} remains proportional to \mathbf{H} [17]:

$$\mu = \mu_0(1 + \chi) \quad \text{(Equation 2-10)}$$

$$\mathbf{B} = \mu \mathbf{H} \quad \text{(Equation 2-11)}$$

In the absence of a solid medium, χ_m vanishes from the equation since a vacuum cannot be magnetised, which is what the permeability of free space (μ_0) is named for and why it is used in equation 2-6.

James Clerk Maxwell published four partial differential equations (Eqns 2-12 to 2-15) in the 1860's that mathematically describe the spacial derivatives of the four EM field vectors, showing their relationship to free charge density (ρ), current charge density (\mathbf{J}) and with respect to time during propagation[18]:

$$\nabla \cdot \mathbf{D} = \rho \quad \text{(Equation 2-12)}$$

$$\nabla \cdot \mathbf{B} = 0 \quad \text{(Equation 2-13)}$$

$$\nabla \times \mathbf{E} + \frac{\partial \mathbf{B}}{\partial t} = 0 \quad \text{(Equation 2-14)}$$

$$\nabla \times \mathbf{H} - \frac{\partial \mathbf{D}}{\partial t} = \mathbf{J} \quad \text{(Equation 2-15)}$$

The \mathbf{J} term should include both conduction and convection currents, and for conductors with free charges that obey Ohm's law it is proportional to the σ of the medium and \mathbf{E} [18]:

$$\mathbf{J} = \sigma \mathbf{E} \quad \text{(Equation 2-16)}$$

The power density (\mathbf{P}) dissipated into such a material is therefore expressed by[4]:

$$\mathbf{P} = \sigma \mathbf{E}^2 \quad \text{(Equation 2-17)}$$

2.2.3 Permittivity, permeability and conductivity

The behaviour of EM waves is characterised by effects within solid media as well as over spaces lacking physical interactions. Charles Coulomb measured the force on a small charged body near the surface of a charged conductor and found that \mathbf{E} was proportional to the surface charge density (ρ_s). This is formalised in Gauss' law which shows the divergence of the \mathbf{E} field ($\nabla \cdot \mathbf{E}$) is given by[15]:

$$\nabla \cdot \mathbf{E} = \frac{\rho_s}{\epsilon} = \frac{\rho_s}{\epsilon_0 \epsilon_r} \quad \text{(Equation 2-18)}$$

Permittivity (ϵ) is a material property which affects the force between charged particles in an applied \mathbf{E} field, and is defined by \mathbf{D} , the vector given from the product $\epsilon \mathbf{E}$ as shown in equation 2-5. It is the product of the relative permittivity (ϵ_r), a measure of the polarisability of a dielectric material, and the permittivity of free space (ϵ_0), a constant. For air $\epsilon_r = 1.0006$ and for free space $\epsilon_r = 1$, while ϵ_r for most commercial insulating materials is between 1–10. The ϵ_r of metallic conductors are difficult to measure and usually not precisely known but are considered equal to free space as the free electrons negate the permittivity[15].

The permeability (μ) of a medium is defined by \mathbf{B} as per equation 2-11 and is the sum of relative permeability (μ_r), which describes the magnetic effect of the medium, and absolute $\mu_0 = 1.257 \times 10^{-6} \text{ Hm}^{-1}$ [15]:

$$\mu = \mu_r \mu_0 \quad \text{(Equation 2-19)}$$

For most materials $\mu_r \sim 1 \text{ Hm}^{-1}$ while for ferromagnetic metals such as iron, cobalt or nickel (and their alloys) it is typically 2–6 orders of magnitude larger. In a vacuum, μ_r does not apply so \mathbf{B} is proportional to μ for a solid medium or μ_0 for a vacuum[15]:

Free charge carriers are charged particles free to move in response to an applied \mathbf{E} field. In solids, charge carriers can be “holes” of positive charge or free electrons (e), the latter of which has a negative charge of 1.602×10^{-19} C per electron. For media containing both positive and negative charge carriers, the positive holes will drift in the direction of \mathbf{E} while negative free electrons will move in the away. The electrical conductivity (σ) of a medium is defined by the product of the charge density and carrier drift velocity for both positive (ρ_p and v_p) and negative (ρ_n and v_n) charge carrier types respectively[15]:

$$\sigma = \frac{\rho_p v_p + |\rho_n| v_n}{\mathbf{E}} \quad \text{(Equation 2-20)}$$

The hole charge density and magnitude of the free electron charge density can be obtained from the carrier densities, p and n for holes and electrons respectively[15]:

$$\rho_p = pe \quad \text{(Equation 2-21)}$$

$$|\rho_n| = ne \quad \text{(Equation 2-22)}$$

The drift velocity per unit \mathbf{E} is known as mobility which for positive holes (μ_p) and negative electrons (μ_n) is given by[15]:

$$\mu_p = \frac{v_p}{\mathbf{E}} \quad \text{(Equation 2-23)}$$

$$\mu_n = \frac{v_n}{\mathbf{E}} \quad \text{(Equation 2-24)}$$

Therefore, in terms of carrier densities, the formula for σ becomes:

$$\sigma = pe\mu_p + ne\mu_e \quad \text{(Equation 2-25)}$$

Permittivity (ϵ), permeability (μ) and conductivity (σ) are intrinsic dielectric properties taken to be independent of the magnitude and orientation of the \mathbf{E} and \mathbf{H} fields. For homogeneous media the equations of force are the same throughout and the three properties are treated as constants irrespective of spacial coordinates, which would not be true for inhomogeneous and anisotropic media[15].

2.2.4 Wave propagation in free space

The behaviour of \mathbf{E} and \mathbf{H} fields that comprise EM waves are governed by the dielectric properties of the medium. The plane wavefront travels in a direction perpendicular to both sinusoidal \mathbf{E} and \mathbf{H} field vectors. The \mathbf{E} and \mathbf{H} field vectors are orientated such that their cross product, known as the Poynting vector, is

parallel to the wavefront direction. In a linear, homogenous and isotropic medium the wave propagation equations are simplified as[19]:

$$\mathbf{B} = \mu\mathbf{H} \quad \text{(Equation 2-26)}$$

$$\mathbf{J} = \sigma\mathbf{E} \quad \text{(Equation 2-27)}$$

$$\mathbf{D} = \varepsilon\mathbf{E} \quad \text{(Equation 2-28)}$$

These properties determine a medium's susceptibility to interacting with EM radiation such as MWs. The dielectric properties of non-linear media will be field dependent; for anisotropic media they will be represented as matrices rather than simple scalar functions or constants and for inhomogeneous media they will be functions of spacial coordinates[19]. The propagation of EM waves in free space sets the relative permittivity (ε_r) and relative permeability (μ_r) to 1 as well as free charge density and σ to 0; simplifying Maxwell's equations and reducing the EM field definitions to[18]:

$$\mathbf{D} = \varepsilon_0\mathbf{E} \quad \text{(Equation 2-29)}$$

$$\mathbf{B} = \mu_0\mathbf{H} \quad \text{(Equation 2-30)}$$

The EM waves propagate in a direction normal to its wavefront with a velocity (v) determined by ε and μ of the medium; which in unbounded free space will equal c [18]:

$$v = \frac{1}{\sqrt{\varepsilon_0\mu_0}} = c = 2.998 \times 10^8 \text{ ms}^{-1} \quad \text{(Equation 2-31)}$$

This relationship between three of the fundamental electromagnetism constants gives the permittivity of free space (ε_0) to be:

$$\varepsilon_0 = \frac{1}{c^2\mu_0} = 8.854 \times 10^{-12} \text{ Fm}^{-1} \quad \text{(Equation 2-32)}$$

Plane waves propagating along a z-axis will feature \mathbf{E} that is only a function of the direction of propagation (\mathbf{E}_z) and time (t) however, the divergence of \mathbf{E} reduces to[18]:

$$\nabla\mathbf{E} + \frac{\partial\mathbf{E}_z}{\partial t} = 0 \quad \text{(Equation 2-33)}$$

$\mathbf{E}_z = 0$ for EM waves, meaning it has no longitudinal component, only transverse (x and y) components with the x-axis designated parallel to the wave vector for simplicity[18]:

$$\frac{\partial \mathbf{E}_z}{\partial t} = -\frac{\partial \mathbf{B}_y}{\partial t} \quad \text{(Equation 2-34)}$$

The ratio of \mathbf{E}_z to \mathbf{B}_y gives the velocity of an EM wave in a vacuum:

$$\frac{\mathbf{E}_z}{\mathbf{B}_y} = c = 3.998 \times 10^8 \text{ ms}^{-1} \quad \text{(Equation 2-35)}$$

While the intrinsic impedance (η) of free space is given by the ratio of \mathbf{E}_z to \mathbf{H}_y [18]:

$$\eta = \frac{\mathbf{E}_z}{\mathbf{H}_y} = \sqrt{\frac{\mu_0}{\epsilon_0}} = \mu_0 c = 377 \Omega \quad \text{(Equation 2-36)}$$

Both field components lie in one plane in phase with one another with the same magnitudes at all points and at all times, propagating in a direction normal to the plane. Conventionally the \mathbf{E} field is polarised vertically while the \mathbf{H} field is polarised horizontally. The electric and magnetic energy densities are also in phase and equal since[18], [20]:

$$\frac{1/2 \epsilon_0 \mathbf{E}^2}{1/2 \mu_0 \mathbf{H}^2} = \epsilon_0 \mu_0 c^2 = 1 \quad \text{(Equation 2-37)}$$

2.2.5 Wave propagation in a waveguide

Standing waves are the result of resonance modes between forward and reflected waves from the surface of a conductive plane and which features maxima and minima of the \mathbf{E} and \mathbf{H} fields, known as nodes and nulls respectively. At the surface of the conductive plane, \mathbf{H} will be a node while \mathbf{E} will be null. At $\frac{1}{4}\lambda$ from the surface \mathbf{H} will be null and \mathbf{E} will be a node. As with all sine waves, this node/null pattern repeats with every $\frac{1}{2}\lambda$ [4].

Most waveguides are typically rectangular or circular cross-sectional hollow tubes made of conductive metal used to transmit high intensity MWs. The waveguide tends to end at or just beyond the applicator cavity with a fixed or adjustable conductive plate that reflects the MWs into a standing wave pattern. In a waveguide it is assumed that the medium of propagation is linear and homogenous with σ and charge density equal to zero (Eqns 2-29 and 2-30). The angular wavelength (λ) is the distance over which the phase of the wave changes by 1 radian, and can be calculated from the angular frequency (ω)[18]:

$$\lambda = \frac{\lambda}{2\pi} = \frac{1}{\omega \sqrt{\epsilon \mu}} \quad \text{(Equation 2-38)}$$

$$\omega = 2\pi f \quad \text{(Equation 2-39)}$$

The frequency dependence of EM radiation leads to wave dispersion which is the deformation of the waveform at the point of propagation due to the propagation velocity of the component waves being different. Dispersion is usually only an issue close to the cutoff frequency (f_c) of the waveguide but becomes more prominent with longer cavities.

The distribution of EM fields in a waveguide containing a solid dielectric material will change in response to the new boundary conditions between the air and the dielectric. The waves are spread out in transverse electric (TE) and transverse magnetic (TM) transmission modes which define the EM field distribution. These modes describe the direction of their respective EM field component with respect to the propagation direction of the wave. TE waves have the longitudinal component of $\mathbf{E}_{0,z} = 0$ while for TM waves $\mathbf{H}_{0,z} = 0$. The transverse components of the electric ($\mathbf{E}_{0,t}$) and magnetic ($\mathbf{H}_{0,t}$) fields in both wave types are mutually perpendicular at all points, with the wave impedance for TE and TM waves given in equations 2-40 and 2-41 respectively[18]:

$$\left| \frac{\mathbf{E}_{0,t}}{\mathbf{H}_{0,t}} \right| = \sqrt{\frac{\mathbf{E}_{0,z}^2 + \mathbf{E}_{0,y}^2}{\mathbf{H}_{0,z}^2 + \mathbf{H}_{0,y}^2}} = \sqrt{\frac{\mu \lambda_g}{\varepsilon \lambda}} = 377 \frac{\lambda_g}{\lambda_0} \quad \text{(Equation 2-40)}$$

$$\left| \frac{\mathbf{E}_{0,t}}{\mathbf{H}_{0,t}} \right| = \sqrt{\frac{\mathbf{E}_{0,z}^2 + \mathbf{E}_{0,y}^2}{\mathbf{H}_{0,z}^2 + \mathbf{H}_{0,y}^2}} = \sqrt{\frac{\mu \lambda}{\varepsilon \lambda_g}} = 377 \frac{\lambda_0}{\lambda_g} \quad \text{(Equation 2-41)}$$

λ_g = Angular wavelength of a guided wave

λ_0 = Angular wavelength in free space

For MWs to propagate in a waveguide then $\lambda_g \neq \lambda$; and assuming the dielectric medium in the waveguide is air then[18]:

$$\lambda = \lambda_0 = \frac{1}{\omega \sqrt{\varepsilon_0 \mu_0}} \quad \text{(Equation 2-42)}$$

The internal cross section of a rectangular waveguide, specifically the length of the broad side (b) as shown in figure 2.2, determines the minimum f_c below which wave propagation is impossible. At that point, λ_g becomes infinite and so the cutoff wavelength (λ_c) is given by[18], [20]:

$$\lambda_c = \lambda_0 = 2b$$

(Equation 2-43)

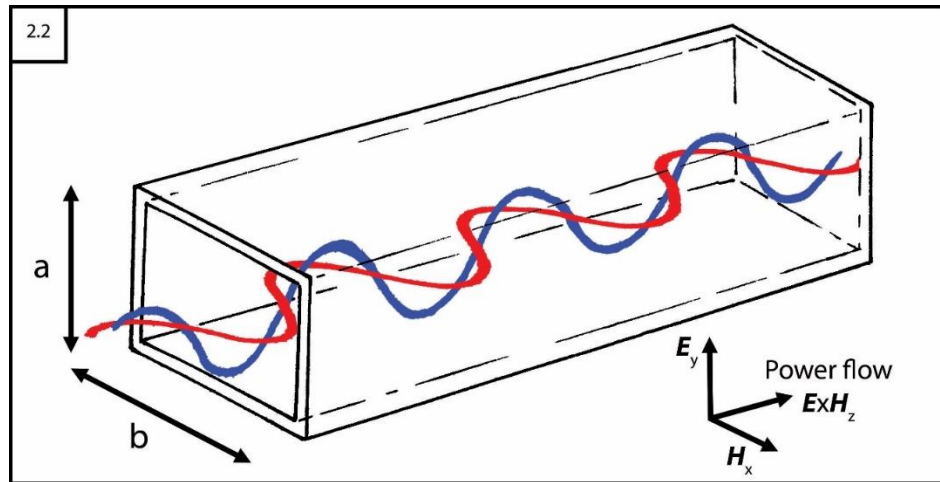


Figure 2.2: Diagram of a section of rectangular waveguide showing electric (blue) and magnetic (red) field components and direction of wave propagation

For standard 2.45 GHz MWs, λ_g lengthens from the 12.24 cm plane waves it is comprised of to 14.78 cm inside the waveguide, calculated from b [14], [18], [20]:

$$\lambda_g = \frac{\lambda_0}{\cos \theta} = \frac{\lambda_0}{\sqrt{1 + (\lambda_0/2b)^2}} \quad \text{(Equation 2-44)}$$

A wave will only be able to propagate without high attenuation if the waveguide dimensions constrain the conductive planes such that $\lambda_c < 2b$, making $\lambda_g > \lambda_0$ with a phase velocity (v_p) $> c$ [18].

The mode of propagation has the lowest f possible in a rectangular waveguide and is defined by \mathbf{E} polarised parallel to the narrow side (a) with $\frac{1}{2}$ sinusoidal variation between the faces and a maximum value at the midpoint. If the waveguide is straight then during propagation, only one field is transverse to the direction of the wavefront while the other remains perpendicular to it; e.g., \mathbf{H} will form both longitudinal ($\mathbf{H}_{0,z}$) and parallel ($\mathbf{H}_{0,x}$) components as closed loops longitudinal to the direction of propagation. The modes of TE waves are given designations of TE_{lm} where l and m indicate the number of $\frac{1}{2}$ sinusoidal variations of \mathbf{E} along the x- and y-axes respectively; $\mathbf{E} = \frac{1}{2}\lambda$ across b while $\mathbf{H} < \frac{1}{2}\lambda$. The TE_{10} mode is one of the most common single mode applicators, consisting of a rectangular waveguide where the dimensions are $a = 2b$. The \mathbf{E} field lines and closed \mathbf{H} field loops in a TE_{10} rectangular waveguide are illustrated in figure 2.3 [14], [15].

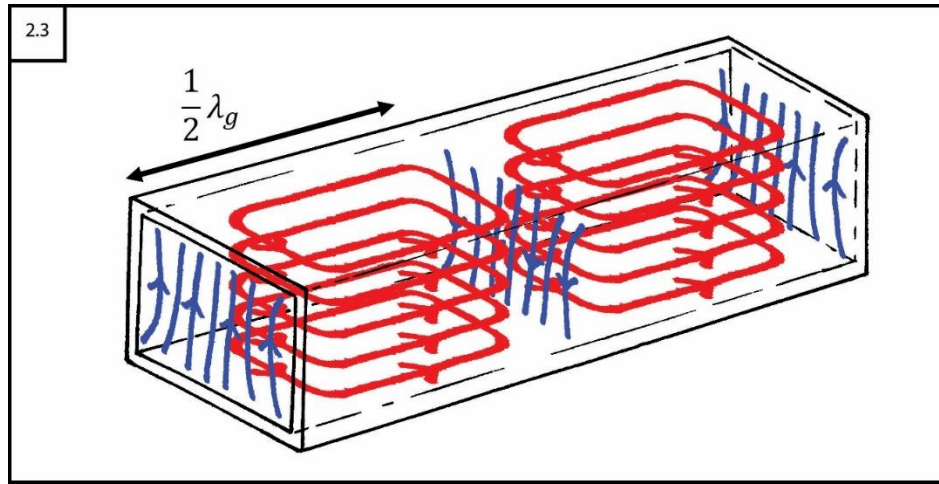


Figure 2.3: Diagram of rectangular waveguide with electric (blue) and magnetic (red) field lines depicted for the TE_{10} mode of propagation

The conductive waveguide walls define only the boundary conditions in the path of the propagating plane wave. For TM waves in a metallic waveguide the boundary conditions are simplified since \mathbf{E} must be normal to the conducting plane and $E_{0,z} = 0$ at the conductive surface; for TE waves, $E_{0,t} = 0$ at all points. Real waveguide materials are not infinitely conductive and the guided waves will induce currents to flow in their surfaces (Figure 2.4) as a result of the \mathbf{H} component grazing the walls; with part of the wave energy being dispersed as heat through simple electrical resistance, also known as Ohmic loss. There are no transverse wall currents generated through the centre line of the broad side of the waveguide [18], [20].

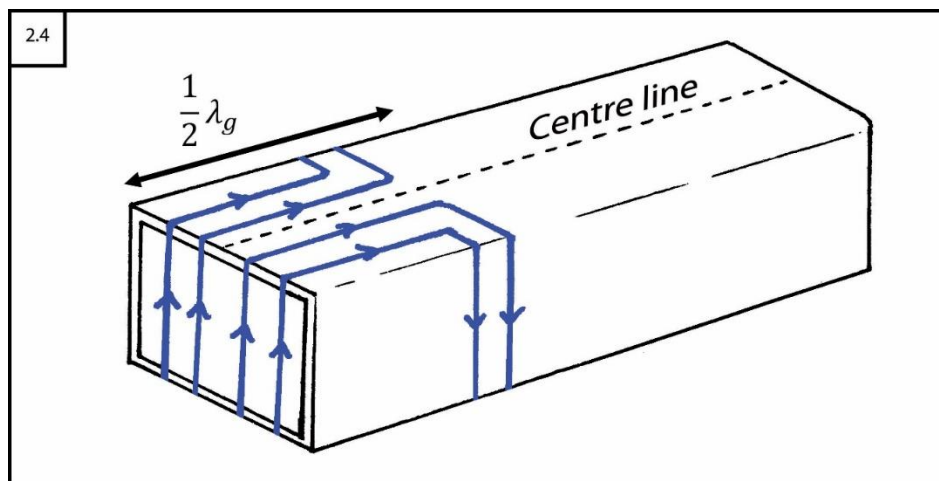


Figure 2.4: Diagram of TE_{10} waveguide with induced surface currents (blue) on the conductive walls resulting from magnetic fields grazing the waveguide

2.2.6 Wave propagation in matter

For insulators $\sigma = 0$ and loss mechanisms are dependent on the complex permittivity (ϵ'') while for a common electrical conductor, losses are due to the relatively large σ in the order of $\sim 10^7 \text{ Sm}^{-1}$. Good conductors are defined as those where the conduction current ($\sigma \mathbf{E}$) is at least $50\times$ the displacement current

$(\partial \mathbf{D} / \partial t)$. Dielectric materials are electrical insulators affected by an applied \mathbf{E} field, and with $\sigma = 0$, the wave equations reduce to[18]:

$$\nabla^2 \mathbf{E} = \varepsilon \mu \frac{\partial^2 \mathbf{E}}{\partial t^2} \quad \text{(Equation 2-45)}$$

$$\nabla^2 \mathbf{H} = \varepsilon \mu \frac{\partial^2 \mathbf{H}}{\partial t^2} \quad \text{(Equation 2-46)}$$

Ahead of the wavefront there are no fields, while at the wavefront the \mathbf{E} and \mathbf{H} field intensities propagate in phase with each other in a direction normal to its wavefront, with energy densities being equal[18]:

$$\frac{1}{2} \varepsilon \mathbf{E}^2 = \frac{1}{2} \mu \mathbf{H}^2 \quad \text{(Equation 2-47)}$$

The wavefront propagates with v_p corresponding to that of an unattenuated wave, which will be less than a wave in free space but still determined by ε and μ of the medium[18]:

$$v_p = \frac{1}{\sqrt{\varepsilon \mu}} = \frac{1}{\sqrt{\varepsilon_r \mu_r}} \frac{1}{\sqrt{\varepsilon_0 \mu_0}} = \frac{c}{\sqrt{\varepsilon_r \mu_r}} \quad \text{(Equation 2-48)}$$

Any solid material in the path of an EM wave disrupts the intrinsic impedance (η), described previously as the ratio of \mathbf{E} to \mathbf{H} field intensity. Wave impedance can be described in relation to the medium's dielectric properties, or to v by substituting the simple relationship from equation 2-31[4], [15]:

$$\eta = \frac{\mathbf{E}}{\mathbf{H}} = \frac{1}{\varepsilon v} = \mu v = \frac{\mu}{\sqrt{\varepsilon \mu}} = \sqrt{\mu / \varepsilon} \quad \text{(Equation 2-49)}$$

The standing wave heating modes in a MW reactor are precise which means that sample dimensions, location and orientation within the applicator must be taken into consideration. The \mathbf{E} and \mathbf{H} components are shifted separately by the metallic plate of a short circuit since \mathbf{E} is reflected at the centre of the plate while \mathbf{H} is reflected at the edge of the plate. Therefore, the phases in a standing wave applicator are shifted by $\frac{1}{4}\lambda$ with \mathbf{H} having the smallest intensity where \mathbf{E} is maximised and vice versa[15].

If the sample is moved away from the centre of the waveguide cavity, the \mathbf{E} distribution becomes increasingly non-uniform and heating uneven. The \mathbf{E} distribution in a TE₁₀ mode waveguide configuration produces narrow regions where the \mathbf{E} field lines are enhanced through constructive interference when forming the standing wave. When a dielectric sample is loaded in a vertical

orientation within the waveguide, the power absorption has been shown to be greater compared to a horizontal orientation as illustrated in figure 2.5, leading to enhanced chemical reactions[3], [21], [22].

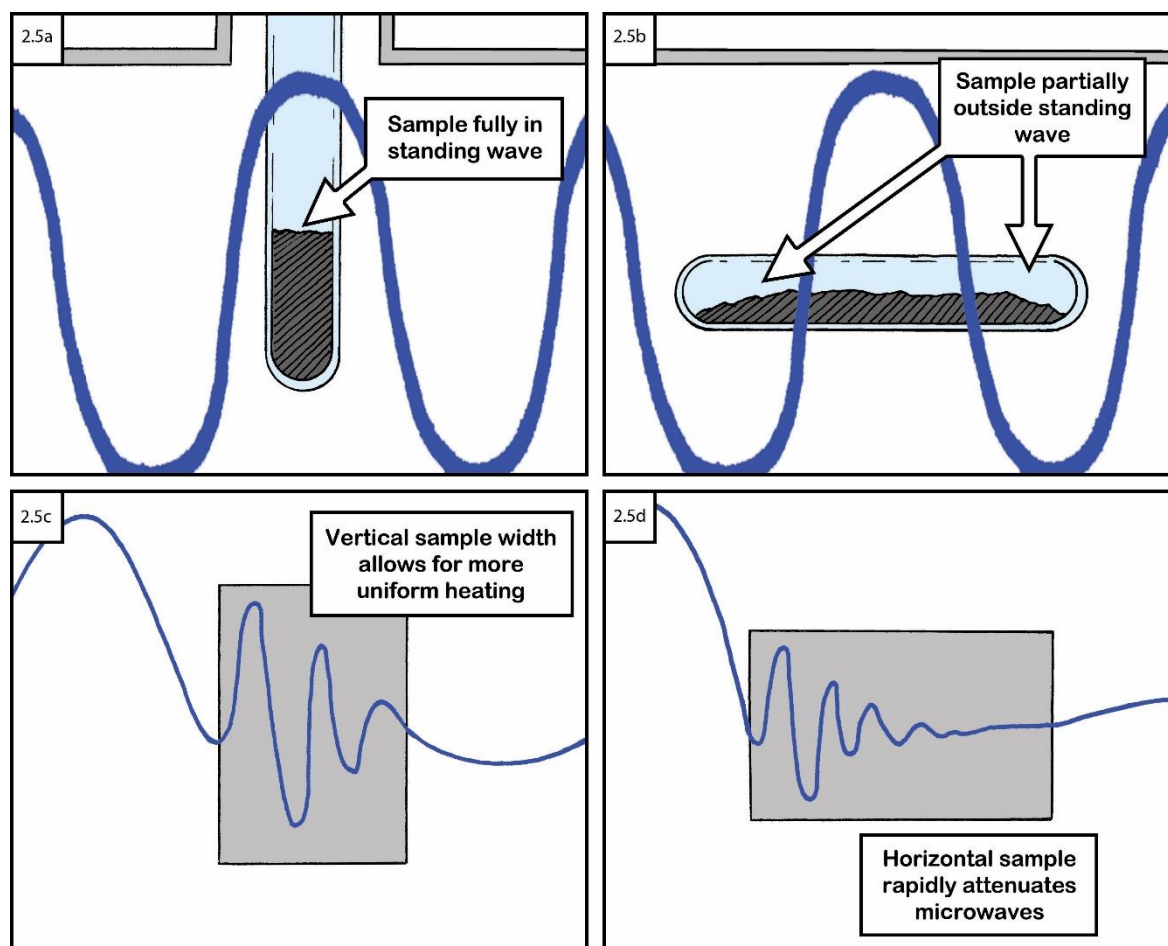


Figure 2.5: Illustrations of dielectric samples in a TE₁₀ waveguide standing wave mode a) vertical sample loading b) horizontal sample loading c) uniform heating d) uneven heating due to wave attenuation

Therefore, if a sample has particularly wide dimensions or is loaded such that portions of it lie outside the standing wave mode then heating will be unevenly applied, leading to incomplete reactions. A horizontal sample geometry will also increase the penetration depth necessary for volumetric heating (discussed further in section 2.4.5).

2.2.7 Single mode vs. multi mode applicators

Single mode cavity (SMC) applicators have dimensions that allow for the superposition of the forward and reflected MWs of a specific λ to generate a resonant standing wave pattern. A short circuit terminates the waveguide on one side of the applicator while a coupling iris is attached via flanges on the magnetron side. The predictable EM field distributions of SMC applicators are designed to generate a single resonant mode of strong constructive interference to enhance the E field, typically in the range of 1–2 kVcm⁻¹. The single standing

wave limits the sample size that can be heated however, a suitably lossy dielectric material will heat rapidly[7].

A multi mode applicator is a large metal cavity with dimensions $\gg \lambda$ of the MWs introduced through a slot, causing them to be reflected internally many times. The larger cavity allows the resulting wave pattern to contain multiple resonant heating modes as well as accommodating bigger samples or vessels. With a dielectric material inside the cavity, the f of the modes overlaps to give continuous coupling with the material. Mode stirrers can be incorporated that increase the uniformity of heating as well as multiple magnetron sources to better distribute the MW power. As the most common type of MW applicator, multi mode devices typically incorporate a conveyer belt for industrial applications or a rotating plate in DMOs to move the target material through the nonuniform field, thereby increasing homogenous heating[7], [13], [14].

Generally, SMC reactors generate greater E strength than multi modes at the same level of applied power which makes them more suitable for heating low-loss dielectrics. Single mode systems also tend to be more compact with greater power densities and are capable of incorporating only one high power magnetron source that typically have long operational lifetimes. Multi mode systems have the option of several low power magnetrons with lower mass market cost and less downtime for repair and maintenance[13], [20].

2.2.8 Thermal modelling

The heat transfer equation for the MW power dissipated in a sample of constant mass as heat (P_H) is determined by the heat capacity of the sample (C_p) and the heat transfer coefficient (k) at its surface:

$$C_p \frac{dT}{dt} + k(T - T_0) = P_H \quad \text{(Equation 2-50)}$$

T = Sample temperature

T_0 = Ambient temperature

Assuming the MW source is switched on at t_0 and the sample temperature is $T = T_0$ at $t < 0$ then the temperature change is given by:

$$T_t = T_0 + \left(1 - e^{-t/\tau}\right) \Delta T \quad \text{(Equation 2-51)}$$

$$\Delta T = T_{max} - T_0 = \frac{P_H}{k} \quad \text{(Equation 2-52)}$$

Thermal time constant (τ) = Cp/k

The initial heating rate is determined only by P_H and Cp and gives the characteristic initial slope of a MW-heating curve as shown in figure 2.6.

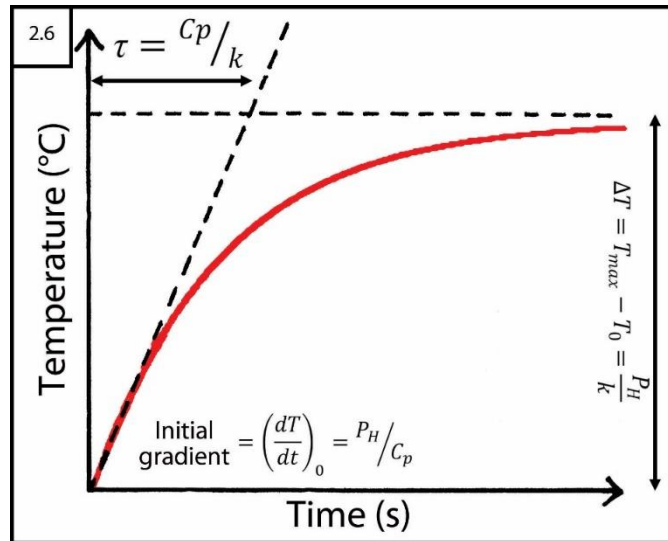


Figure 2.6: Example plot of typical microwave heating curve based on equation 2-84 neglecting radiative heat losses

Achieving temperatures approaching 1200 °C is very difficult with MW-induced heating methods since an equilibrium point will be reached where further increasing the MW power into the cavity is not enough to counteract the effects of radiative loss (P_r). The Stefan-Boltzmann law states that the total amount of radiation emitted by an object per square meter (E_r) is proportional to the Stefan-Boltzmann constant (σ_r) and the temperature of the object[4]:

$$E_r = \sigma_r T^4 \quad \text{(Equation 2-53)}$$

A term is required on the left side of equation 2-53 to include $\sigma_r = 5.67 \times 10^{-8} \text{ Wm}^{-2}\text{K}^{-4}$, the emissivity of the sample (ϵ_{em}) which is approximated to 1 as a black body radiator and the sample area (A):

$$P_r = \epsilon_{em} \sigma_r A (T^4 - T_0^4) \quad \text{(Equation 2-54)}$$

Lossy samples in contact with a vessel made from MW transparent material, such as quartz, will rapidly radiate heat away from the bulk; since unlike conventional heating, the temperature of the sample applicator cavity will be much less than that of the sample. By accounting for such radiative losses, as shown in figure 2.7, the maximum achievable temperature is considerably lower while the initial rate of heating remains governed only by P_H/Cp .

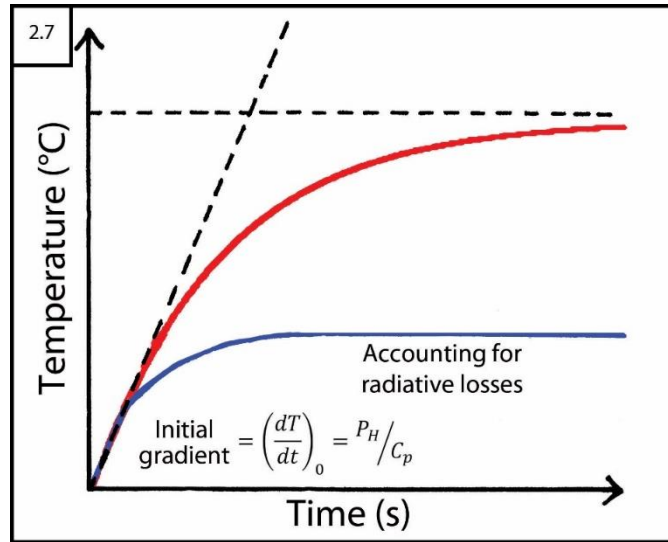


Figure 2.7: Example comparison plot of typical microwave heating curves when neglecting or including radiative heat losses

The use of MWs to heat volumetrically leads to a more rapid increase in T with larger volumes of material compared to conventional methods. Very high T can be achieved if a suitable insulating material that is non-susceptible to MWs is used to reduce radiative losses from the material.

2.2.9 Anisotropy, isomorphism and polymorphism

The properties of isotropic media are the same in all directions from a given point but crystalline media are usually anisotropic. Dielectric materials become polarised by an \mathbf{E} field, represented by the inclusion of the materials electric polarisation (\mathbf{P}) in equation 2-4[19]:

$$\mathbf{P} = \varepsilon_0 \chi \mathbf{E} \quad \text{(Equation 2-55)}$$

χ = Electrical susceptibility

And so, \mathbf{D} becomes governed only by permittivity of the material[23]:

$$\varepsilon = \varepsilon_0 \varepsilon_r = \varepsilon' - j\varepsilon'' = \varepsilon_0(1 + \chi) \quad \text{(Equation 2-56)}$$

$$\mathbf{D} = \varepsilon_0 \mathbf{E} + \mathbf{P} = \varepsilon_0(1 + \chi) \mathbf{E} = \varepsilon_0 \varepsilon_r \mathbf{E} \quad \text{(Equation 2-57)}$$

The dielectric coefficient (ε_r) always affects the ratio of \mathbf{D} to \mathbf{E} when a dielectric material is present. For linear media, the dipole moment induced by an external \mathbf{E} field will be proportional to \mathbf{E} , and if the electrical properties of the material are independent of direction, then it is considered isotropic. For anisotropic media, the polarisation resulting from an applied \mathbf{E} field will differ depending on the axis along which the field is applied[19].

Inorganic materials with the same chemical formula and comparable cation and ion sizes often crystallise with similar lattice structures, known as isomorphs,

which will also tend to demonstrate similar dielectric behaviour. Isomorphism is one basis for their classification, which includes common space group families such as spinels, garnets, skutterudites and MAX phases. Most chemical substances however, can be made to crystallise in a variety of forms known as polymorphs that are dependent on T and pressure; with each featuring different physical properties. Polymorphs of the same element or molecule will likely have different optical and electrical components, i.e., differing structures containing the same atom or ion proportions will affect its properties. Transitions between polymorphs under specific conditions of T or pressure are referred to as phase changes in the crystal structure. Enantiotropic polymorphism describes a reversible change from one crystal form to another, while an irreversible change is known as monotropic. Generally, high temperature polymorphs feature higher symmetry with an associated increase in electrical isotropy and more open lattice structures with lower density[19].

2.2.10 Polarisation and relaxation

Polar materials contain permanent dipole moments regardless of the application of an \mathbf{E} field; however, when such a field is applied, it will tend to cause the dipoles to align in the direction of the field. Material polarisation is governed by its inherent dielectric properties, in particular the electrical properties of an isotropic medium can be described by the complex dielectric constant (ϵ)[19]:

$$\epsilon_{x,y,z} = \epsilon'_{x,y,z} - j\epsilon''_{x,y,z} \quad \text{(Equation 2-58)}$$

ϵ' = Static relative permittivity of a dielectric (dielectric constant)

ϵ'' = Complex permittivity (dielectric loss)

The dielectric constant (ϵ') refers to the relative permittivity specifically of a dielectric medium with respect to the ideal permittivity; this is distinct from ϵ_r of any medium which is relative to the permittivity of a vacuum. It is time and temperature dependent as well as a function of ω ; and it represents the polarisability of molecules within an applied \mathbf{E} field. There are several possible polarising mechanisms, each with a distinct relaxation frequency which results in maximum absorption. Dielectric loss (ϵ'') actually represents all the energy losses due to dielectric loss and σ in a medium during wave propagation, i.e., the efficiency of converting EM waves to heat over time[19].

For magnetic materials, an applied \mathbf{H} field will align the magnetic dipole moments to produce an analogous magnetic polarisability (\mathbf{P}_m)[23]:

$$\mathbf{B} = \mu_0(\mathbf{H} + \mathbf{P}_m) \quad \text{(Equation 2-59)}$$

For linear magnetic material, \mathbf{P}_m is given by the product of χ_m and \mathbf{H} and so, \mathbf{B} is governed only by permeability of the material[23]:

$$\mu = \mu_0\mu_r = \mu_0(1 + \chi_m) \quad \text{(Equation 2-60)}$$

$$\mathbf{B} = \mu_0(1 + \chi_m)\mathbf{H} = \mu_0\mu_r\mathbf{H} \quad \text{(Equation 2-61)}$$

The most ubiquitous dipolar material available is water which, being present in most food items, is the molecule that is most easily affected by MWs in a DMO through dipolar polarisation as discussed further in section 2.4.2. The common MW frequencies are low enough to allow polar molecules time to rotate, resulting in dipolar polarisation being the primary phenomena; with ϵ' decreasing as individual dipoles fall out of step with \mathbf{E} . The internal friction between molecules in liquids and solids is the reason for the slowed rotation of polar molecules[19].

The alternating nature of the \mathbf{E} field causes the direction of polarisation to continuously switch. The time required for the average dipole to revert to a random distribution or to reorient in an \mathbf{E} field is known as the relaxation time (τ), which has an inverse relationship with the relaxation frequency (f_r), typically in the order of $\sim 10^{-11}$ s, and is given by[14], [24]:

$$\tau = \frac{1}{2\pi f_r} \quad \text{(Equation 2-62)}$$

2.3 A brief history of commercial microwave development

Mathematical descriptions of a device to control electron motion with a \mathbf{H} field were developed by H. Gerdien and H. Greinacher between 1910 and 1912[25]. It was Albert W. Hull who later improved Greinacher's setup and designed a magnetically controlled relay/amplifier device which he named a magnetron[25], [26]. Magnetron technology in radar applications was the initial impetus for improving the device design throughout the 1930s leading to a patent from Hollmann Hans Erich being filed in 1938 (Figure 2.8a) for the basic resonant cavity design[27]. The application of MWs as a method of food preparation was not considered until 1946 when Dr. Percy Lebaron Spencer observed that a chocolate bar in his pocket had accidentally melted while he was

working with magnetron equipment at the Raytheon company[28]. He carried out further controlled experiments, one of which resulted in a co-worker receiving an explosion of egg on their face, before he filed a patent for the use of magnetrons as a method for heating food in 1950, as shown in figure 2.8b[29].

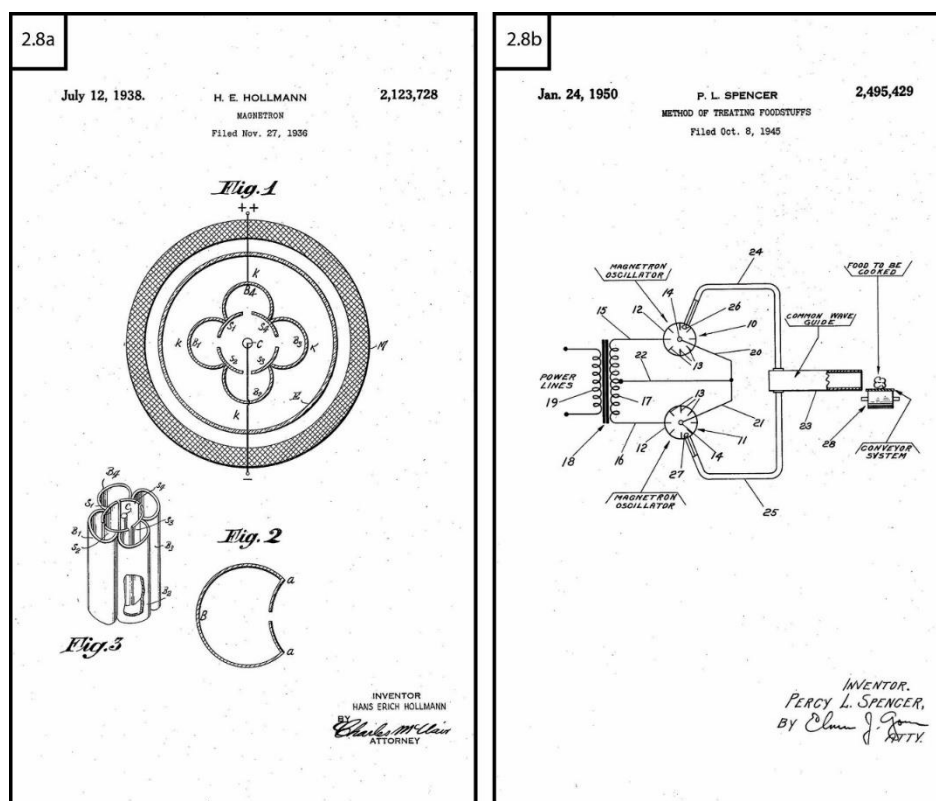


Figure 2.8: a) Magnetron patent US2123728A filed by Hollmann Hans Erich on 12th July 1938[27] b) method of treating foodstuffs patent US2495429A filed by Dr. Percy Lebaron Spencer on 24th January 1950[29]

The commercialisation of this revolutionary technology was not a simple process. The first attempt in 1947 produced by Raytheon was the Radarange, which stood at ~6 ft tall, required water cooling and specialised electrical wiring to operate and was prohibitively expensive for all but the most lucrative restaurant businesses. A more recognisably modern DMO known as the Amana Radarange was released to great success in 1967 and has since become one of the most common electrical kitchen appliances worldwide, second only to the refrigerator[28].

For chemical synthesis in industry or the laboratory, MW-induced reactions may appear novel compared to more traditional methods such as the use of high temperature furnaces. However, they have been utilised ever since the equipment became economical and widely adopted by consumers. Syntheses with MW-heating has been reported as far back as 1971 with experiments in

decomposing alcohols, ethers and ketones as well as successful organic synthesis in 1986[30], [31].

2.4 Mechanisms of microwave-induced heating processes

MW energy has been determined insufficient to directly break chemical bonds since the energy in that region of the EM spectrum is non-ionising; although catalysts that operate through an associative bond were found to perform better when heated with MWs[32].

The exact mechanisms of MW-induced chemical reactions are dependent on the properties of the reactants being heated. Good conductors such as metals and their alloys will reflect MWs rather than allow penetration however, those containing a magnetic dipole moment will interact with the **H** component which can induce surface currents that lead to heating in a process known as Joule loss. Insulators such as glass, quartz and ceramics are low-loss materials that allow complete penetration, making them mostly transparent to MWs and partially reflect as well as transmit the incident waves. Dielectric materials are high-loss and so absorb the EM energy well, dissipating it as heat through the two main loss mechanisms of dipolar polarisation and ionic conduction. Most MW-induced chemical reactions are dependent on heating lossy dielectrics where the **E** field interacts with charged particles causing dielectric loss while the **H** field will interact with any available magnetic dipoles leading to magnetic losses[14], [33], [34].

Crystalline solids containing permanent dipoles will become more lossy as ϵ' and ϵ'' vary with increasing T as discussed later in section 2.4.7. If the **E** field alternates at $f > \tau$ then the dipole orientation will also switch continuously and no longer contribute to the polarisation of the material. As MWs become attenuated into the material, the local T will gradually rise, providing more energy for dipoles to overcome the energy barriers, allowing them to rotate and follow the alternating field. The thermal energy produced per unit volume (P_T) from MW radiation is given by[14]:

$$P_T = \frac{1}{2}\sigma|\mathbf{E}|^2 + \pi f \epsilon_0 \epsilon_r'' |\mathbf{E}|^2 + \pi f \mu_0 \mu_r'' |\mathbf{H}|^2 \quad \text{(Equation 2-63)}$$

The three types of heating processes are accounted for in equation 2-63: the first term represents conduction losses, the second is dielectric losses and the third is magnetic losses. In the case of carbon in the form of graphite powder, the

conduction losses dominate, while metals are primarily heated through dielectric and magnetic losses[14].

2.4.1 Conduction, magnetic and dielectric loss heating

If a current is generated in a material, the energy is transformed into heat through a process called Joule loss, with \mathbf{E} related to the current density (i). The energy loss from per unit volume and unit time (P_T) from \mathbf{E} is given by[14]:

$$i = \sigma \mathbf{E} = \sigma \mathbf{E}_0 \sin \omega t \quad \text{(Equation 2-64)}$$

$$P_T = \frac{1}{2} \sigma \mathbf{E}_0^2 \quad \text{(Equation 2-65)}$$

Conduction losses tend to be very small at ambient T for most solids however can become significant with increasing T . Defects within the structure will reduce the energy required to produce electrons/hole pairs in the conduction and valence bands respectively, leading to greater conduction losses.

Magnetic losses are different from hysteresis or eddy current losses; they occur as a result of a phase delay in the vibration of the magnetic dipole moment, and the energy loss per unit volume and unit time (P_μ) from \mathbf{H} is given by[14]:

$$P_\mu = \pi f \mu_0 \mu_r'' \mathbf{H}_0^2 = \frac{1}{2} \omega \mu_0 \mu_r'' \mathbf{H}_0^2 \quad \text{(Equation 2-66)}$$

Different materials demonstrate significantly different heating responses to the \mathbf{E} and \mathbf{H} fields of MWs, with highly conductive materials such as metals being more efficiently heated with \mathbf{H} fields. These effects are sometimes only apparent when changing the morphology of the sample from bulk ingots to compacted powder. Bulk metals are typically reflective of MWs only absorbing to a depth of a few μm from the surface, making them ideal for the manufacture of waveguides. As the particle size of metal powders approach the skin depth (see section 2.4.5) alternative loss mechanisms that contribute to efficient MW-heating can make them good lossy absorbers. The \mathbf{H} field can induce eddy currents and magnetic resonance as well as hysteresis losses in the case of ferrous magnetic substances. Eddy currents are generated by field variations which in turn generate their own \mathbf{H} in opposition to the magnetic component of the MWs. Regardless of the method of current generation, in matter heat is produced through Joule loss[14], [35], [36].

In dielectric materials, \mathbf{D} changes with respect to the external field dependant on whether it is able to follow with or without the phase delay. The energy loss per unit volume and unit time (P_T) from \mathbf{E} is given by[14]:

$$P_T = \pi f \varepsilon_0 \varepsilon_r'' E_0^2 = \frac{1}{2} \omega \varepsilon_0 \varepsilon_r'' E_0^2 \quad \text{(Equation 2-67)}$$

2.4.2 Dipolar polarisation and ionic conduction

An applied \mathbf{E} field can induce displacement of polar molecules containing large charge distributions through either displacement of electrons with respect to the nucleus (electronic polarisation) or stretching of adjacent positive and negative ions (atomic polarisation). The \mathbf{E} field applies torque to charges bound as dipoles in a material, forcing them to continuously re-align in the direction of the oscillating \mathbf{E} field against electrostatic interactions with other charged particles. This creates a time delay between the frequency of alternating \mathbf{E} and the rotational motion of the electric dipoles. The resulting energy loss through heat due to molecular friction and ε'' is known as dipolar polarisation (P_d). The amount of heat generated is therefore directly related to the polarisability of the dipoles at MW frequencies, with no heating resulting if the dipoles reorient too slowly or too quickly. The strength of the \mathbf{E} field as well as helps determine the P_d for a material[2], [14], [19], [37]:

$$P_d = \varepsilon_0 (\varepsilon_r - 1) \mathbf{E} \quad \text{(Equation 2-68)}$$

Dipolar polarisation is more significant in liquid phase polar solvents such as water. In materials with mobile charge carriers such as electrons, the oscillating MW field generates currents that travel in phase with \mathbf{E} resulting in Ohmic resistance which is the dominant effect in solid state materials. Permanent dipoles are prevented from following rapid reversals of the field when they encounter electrostatic interactions with other dipoles. Polarisation of polar molecules tends to occur at $f < 10^{10}$ Hz, however at $f < 10^5$ Hz various types of charge polarisation known as Maxwell-Wagner mechanisms exist[19]. Figure 2.9 shows the change in the complex dielectric properties (ε' and ε'') with f along with the respective f -dependent dielectric responses; atomic (ionic) and electronic polarisation occurs at $f > \text{MW}$ range.

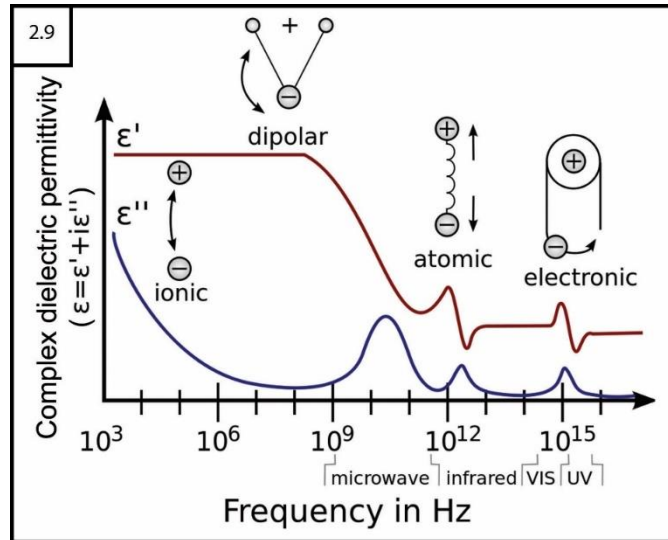


Figure 2.9: Diagram showing a plot of dielectric constant (ϵ') and dielectric loss (ϵ'') with respect to frequency along with the various dielectric mechanisms that can manifest[38]. Image adapted from Archimerged, CC via Wikimedia Commons

Ionic conduction occurs primarily at lower f and results from charged particles oscillating back and forth in the presence of the \mathbf{H} field which then collide with neighbouring particles, generating additional motion, i.e., heat. This loss mechanism is governed by the dielectric conductivity with a loss parameter given by $\sigma/\omega\epsilon_0$ and tends to generate more heat than P_d mechanisms[7], [37].

Electronic polarisation tends to occur when the electrons in an applied \mathbf{E} field undergo a net displacement with respect to the nuclei, which can also occur with charged atoms that become displaced with respect to each other. For electrical conductors such as bulk metals, it manifests as a current in phase within the material, so as per Ohm's law heat is released due to resistance. Magnetic solids will have eddy currents induced over the surface by the \mathbf{H} field, leading to Joule losses, the same phenomenon as losses due to the \mathbf{E} field[14], [19], [39].

2.4.3 Interfacial polarisation

Maxwell-Wagner mechanisms occur as a result of charges around the surface of conducting particles in a dielectric medium, much smaller than the particle size, which respond to an applied \mathbf{E} field independent of the charge on neighbouring particles. When unevenly distributed in a dielectric material, they will form conduction paths in the presence of \mathbf{E} , i.e., the charge carriers that are trapped by localised insulating regions will accumulate. These charge carriers are incapable of discharge so they become polarised such that interfaces between these areas act like combined conduction and polarisation mechanisms[19].

Charges can also accumulate at interfaces between two different materials as well as between two regions with the same substance due to the differing dielectric properties of each medium. Interfacial polarisation tends to occur most often within amorphous or polycrystalline materials where discrete regions of charge can more easily form.

2.4.4 Microwave power and loss tangent

At the boundary between free space (typically air) and a dielectric material, some of the incident power will be reflected, some will be transmitted and some attenuated within the medium. For a good dielectric where $\sigma \ll \omega \epsilon'' \epsilon_0$ the Fresnel reflection formula gives the ratio of forward power (P_F) to reflected power (P_R)[4]:

$$\frac{P_R}{P_F} = \left(\frac{\sqrt{\epsilon_r} - 1}{\sqrt{\epsilon_r} + 1} \right)^2 \quad \text{(Equation 2-69)}$$

While for a good conductor where $\sigma \gg \omega \epsilon'' \epsilon_0$, the ratio becomes[4]:

$$\frac{P_R}{P_F} = 1 - 4 \sqrt{\frac{\omega \epsilon_r \epsilon_0}{2\sigma}} \quad \text{(Equation 2-70)}$$

The average MW power (P_{av}) dissipated in a material is its ability to generate heat and is dependent on both the material properties and MW frequency[39]:

$$P_{av} = \pi f \epsilon_0 \epsilon_r'' \int_V (\mathbf{E}^2) dV \quad \text{(Equation 2-71)}$$

More power is able to be dissipated at higher f at the expense of the depth of penetration. The \mathbf{E} field strength distribution is dependent on the geometry of the sample cavity and location of the material within it, and so to achieve uniform heating these are vital factors to consider[39].

\mathbf{E} field intensity tends to decrease with distance in a conducting medium because as the wave attenuates, the energy is continuously dissipated into the material through Ohmic loss and dielectric relaxation[18]. The ability of dielectric materials to absorb MW power is known as the loss tangent ($\tan\delta$); with lossy materials having high $\tan\delta > 0.5$ being considered good MW absorbers. The propagation constant (γ) is a complex number comprised of the real attenuation constant (α) and the imaginary phase constant (β). The latter is the same as the wavenumber (k) and so contains all the necessary information about energy loss in a medium during EM wave propagation[19], [37]:

$$\gamma = \alpha + i\beta \quad \text{(Equation 2-72)}$$

$$\beta = k = \frac{2\pi}{\lambda} = \frac{\omega}{v_p} \quad \text{(Equation 2-73)}$$

For a TE₁₀ mode waveguide such as the WR430 used in this project, where a = 43.18 mm and b = 86.36 mm, β is calculated with respect to the cutoff wavenumber (k_c)[23]:

$$\beta = \sqrt{k^2 - k_c^2} = \sqrt{\left(\frac{\omega}{c}\right)^2 - \left(\frac{\pi}{b}\right)^2} \quad \text{(Equation 2-74)}$$

The MW frequency used (2.45 GHz) gives $\omega = 2\pi f = 15.39$ GHz and thus for a WR430 waveguide $\beta = 36.017$ m⁻¹. The value of E_0 applied to a sample per kW rms of MW power (P_T) in this system is given by:

$$E_0 = \sqrt{\frac{4\omega\mu_0 P_T}{ab\beta}} \approx 2400 \text{ kVm}^{-1} \quad \text{(Equation 2-75)}$$

The key electrical properties can be written as complex numbers and if magnetic properties are ignored, the complex forms of ε and σ need only be considered[19]:

$$\omega\varepsilon - j\sigma = \omega(\varepsilon' - j\varepsilon'') - j(\sigma' + j\sigma'') \quad \text{(Equation 2-76)}$$

$$\omega\varepsilon - j\sigma = (\sigma'' + \omega\varepsilon') - j(\sigma'' + \omega\varepsilon'') \quad \text{(Equation 2-77)}$$

$(\sigma'' + \omega\varepsilon'')$ = Effective permittivity

$(\sigma' + \omega\varepsilon')$ = Effective conductivity

The term $(\sigma' + j\sigma'')$ represents the carrier transport due to Ohmic and Faradaic diffusion respectively and $(\varepsilon' + j\varepsilon'')$ represents dielectric relaxation and so $\tan\delta$ is defined as[19]:

$$\tan \delta = \tan\left(\psi + \frac{\pi}{2}\right) = \frac{\sigma' + \omega\varepsilon''}{\sigma'' + \omega\varepsilon'} \quad \text{(Equation 2-78)}$$

δ = Phase lag between polarisation of material and applied E field

ψ = Phase between E field and current density (J)

If there are no dielectric losses then ε'' will tend to zero and if there are no Faradaic losses (σ'), i.e., currents generated by reduction or oxidation of a substance, then σ'' will also tend to zero. The formula simplifies to describe only losses physically due to Ohmic conductivity or more commonly in terms of loss current (ε'') to charging current (ε') ratio[19]:

$$\tan \delta = \frac{\sigma'}{\omega \varepsilon'} = \frac{\varepsilon''}{\varepsilon'} \quad \text{(Equation 2-79)}$$

Therefore, for completely lossless materials $\tan \delta = 0$.

2.4.5 Skin depth and penetration depth

A plane wave propagating through a medium that is not free space will attenuate, meaning the amplitude will decrease exponentially. Although most EM waves are reflected from a conductor, an alternating electric current becomes distributed near the surface, decreasing with greater depth through a phenomenon called the skin effect. The skin effect results from opposing eddy currents being induced by alternating \mathbf{H} . The effective resistance of the conductor increases at higher f and the current will flow between the surface and a level known as the skin depth. The attenuation distance, also known as the penetration depth (d_p) or skin depth (δ_s) is a function of wave frequency, bulk resistance/conductivity ρ (or σ) and μ that determines the extent of wave propagation in a good conductor[14], [40]:

$$\delta_s = \sqrt{\frac{2\rho}{2\pi f \mu}} = \sqrt{\frac{1}{\sigma \pi f \mu_0 \mu_r}} \quad \text{(Equation 2-80)}$$

The skin depth decreases with increasing σ , μ or f ; the relative amplitudes of \mathbf{E} and \mathbf{H} are also dependent on MW frequency[18]. Table 2.1 gives the δ_s of some selected conductors; of particular note is graphite which has δ_s an order of magnitude greater than all the others listed, meaning that it is able to be more thoroughly heated with MWs.

Table 2.1: Skin depth (δ_s) of selected conductors at a microwave frequency of 3000 MHz[18], [41]

Conductor	Electrical conductivity (Sm^{-1})	Relative permeability (Hm^{-1})	Skin depth (μm)
Aluminium	3.54×10^7	1	1.6
Brass	1.59×10^7	1	2.3
Chromium	3.8×10^7	1	1.5
Copper	6.481×10^7	1	1.2
Gold	4.5×10^7	1	1.4
Graphite	1×10^5	1	29
Magnetic iron	1×10^7	2×10^2	0.2
Nickel	1.3×10^7	1×10^2	0.26
Silver	6.15×10^7	1	1.2
Tin	8.696×10^6	1	3.12
Zinc	1.86×10^7	1	2.14

For fine metallic powders with a grain size less than the skin depth of the metal heating will not occur through Ohmic loss and only through other dielectric methods[39]. Much like σ , different materials will vary in their ability to allow MWs to propagate. As the MWs enter a medium, they are partially converted to thermal energy which reduces the MW power with distance penetrated[42]:

$$P_z = P_0 e^{(-2\alpha z)} \quad \text{(Equation 2-81)}$$

P_z = MW power at depth z

P_0 = Total MW power absorbed

The attenuation constant (α) is a measure of diminishing field amplitude with distance penetrated into a lossy dielectric and was calculated by Arthur von Hippel from the wavelength in free space (λ_0), ϵ' and $\tan\delta$ [4], [42]:

$$\alpha = \frac{2\pi}{\lambda_0} \sqrt{\frac{1}{2} \epsilon' \left(\sqrt{1 + \left(\frac{\epsilon''}{\epsilon'}\right)^2} - 1 \right)} \quad \text{(Equation 2-82)}$$

The imaginary phase constant (β), is a measure of the phase shift as the wave propagates through the material[4]:

$$\beta = \frac{2\pi}{\lambda_0} \sqrt{\frac{1}{2} \epsilon' \left(\sqrt{1 + \left(\frac{\epsilon''}{\epsilon'}\right)^2} + 1 \right)} \quad \text{(Equation 2-83)}$$

The d_p of a material is dependent on ϵ'' and defined as the distance travelled in a medium where the MW power is reduced by a factor of 1/e from the value at the point of entering the medium[42]:

$$P_{d_p} = \frac{P_0}{e} \quad \text{(Equation 2-84)}$$

Euler's number (e) = 2.718

The d_p is inversely proportional to α and therefore, can be calculated from equation 2-82[14], [42]:

$$d_p = \frac{1}{2\alpha} = \frac{\lambda_0}{2\pi \sqrt{2\epsilon' \left(\sqrt{1 + \left(\frac{\epsilon''}{\epsilon'}\right)^2} - 1 \right)}} \quad \text{(Equation 2-85)}$$

For most low-loss and some lossy materials, it is assumed that $\tan^2 \delta \ll 1$ and so in the specific instance of a plane wave in a multi mode cavity, α and thus d_p for dielectrics is reduced to[4]:

$$\alpha = \frac{f\varepsilon'}{v\sqrt{\varepsilon'}} \quad \text{(Equation 2-86)}$$

$$d_p = \frac{v\sqrt{\varepsilon'}}{2\pi f\varepsilon''} \quad \text{(Equation 2-87)}$$

For dielectric samples smaller than the d_p of the MWs, heating will be relatively uniform. The reduction in power with greater d_p though means that for certain materials, a large sample intended to produce a significant yield will prohibit heating of the bulk interior. Unless the heat from the outer layers of the sample propagates throughout the material and instigates thermal runaway (discussed further in section 2.4.7), the reaction may remain incomplete. Similarly, hotspots are inhomogeneous dissipation of MW power that typically prevent uniform heating due to material specific properties; such as the selective heating of particularly lossy components or non-uniform grain boundaries leading to interface polarisation. In solids, hotspots are discharges between materials under intense E fields and the result of large temperature gradients (∇T) formed within localised domains of the material. They can occur at the microscale on solid surfaces or in macro scale samples as selective heating. Conventional heating methods avoid hotspots as external heating generates any large ∇T far from the sample at the cavity walls. If the hotspot has a high rate of heat transfer a thermal equilibrium can be reached however, if the rate is slow then hotspots can become steady state and further enhance the rate of a chemical process or cause degradation of the material[14].

2.4.6 Plasma formation in microwave applicators

Plasma is a state of matter comprised of free electrons and positive ions typically generated from a gas phase. Plasma emits a bright glow and will manifest when MWs penetrating a load during heating supply enough energy for the electrons to become liberated from the bulk material. The ions are able to travel relatively independently and so the plasma is electrically conductive and able to interact with EM fields, with σ given by[4]:

$$\sigma = \frac{e^2 n_e}{m v_e} \quad \text{(Equation 2-88)}$$

n_e = Electron number density

v_e = Electron collision frequency

Electrical charge of an electron (e) = 1.602×10^{-19} C

Mass of an electron (m) = 9.109×10^{-31} Kg

Lower pressure plasmas typically have smaller n_e and so lower σ , and can easily be produced from MW frequencies under the right conditions. As MWs heat a material, the formation of plasma will tend to raise the T more and contribute to thermal runaway. Plasma phases are sustained by MWs through displacement currents, which will vanish once the magnetron is switched off.

2.4.7 Temperature effects on dielectric properties

Low-loss materials that contain permanent dipoles but do not dissipate MW energy well can be encouraged since ϵ' and χ factors of polarisation are dependent on temperature. The electric polarisability (P) of a medium can be related to the activation energy at a given T when an external E field is applied. The polarisation for most dielectrics is in the order of $\sim 10^{-29}$ Cm while the magnitude of an applied E field below the breakdown strength (where conducting paths through insulating material are formed) will always be $< 10^6$ Vm $^{-1}$, and so generally[19]:

$$\frac{PE}{k_B T} \ll 1 \quad \text{(Equation 2-89)}$$

Boltzmann's constant (k_B) = 1.381×10^{-23} JK $^{-1}$

As T increases, thermal fluctuations will dominate (as would be expected); while as T falls towards zero, polarisation overtake. Both the ϵ' and ϵ'' fluctuate with ΔT , although often in different ways depending on f . Berdel et al demonstrated that certain materials will have a temperature coefficient of permittivity that is overall positive or negative with respect to increasing T depending on the applied frequency. As such, the effect of T on the dielectric properties in a material are often out of sync with each other, meaning $\tan \delta$ can be made more lossy by altering f . This temperature dependence also affects the d_p , generally increasing the depth of MW attenuation with greater T [14], [43], [44].

Materials containing permanent dipoles will demonstrate a non-linear variation of ϵ' with T . In crystalline solids, only certain orientations will be allowed by the lattice configuration which require a certain energy barrier to be overcome in order for a dipole to switch between orientations. In an applied E field, the energy barrier is lower for orientations aligned with the field and higher to

switch to an orientation against the field. This reduces the time dipoles required to overcome the required energy barrier and become aligned with the field[45].

At higher f , ϵ'' is generally greater however factors such as moisture level or T have a significantly more drastic impact; with the effect so great that at a critical temperature (T_c) ϵ'' can suddenly increase very rapidly with each further degree increase in T as shown in figure 2.10. This temperature instability (known as thermal runaway) leads to a feedback of greater MW absorption and rapidly increasing T which can generate hotspots, plasma or damage the material[7].

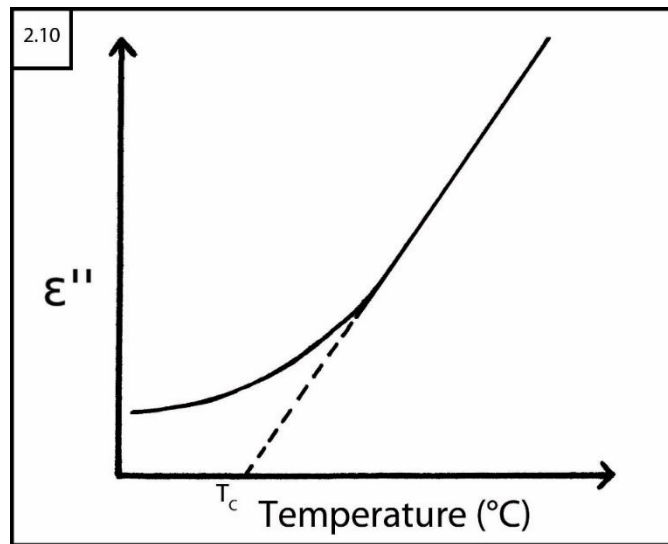


Figure 2.10: Plot of dielectric loss (ϵ'') against temperature showing the rapid positive inflection at a critical temperature (T_c)

A dielectric material with a high $\tan\delta$ that couples well with MWs can be heated efficiently and selectively over a low-loss material. Low-loss materials may eventually dissipate enough MW energy to achieve thermal runaway however the induction period will be very long, especially at low power. Low-loss materials are effectively transparent to MWs at room temperature but can be made to couple if the absolute T is increased such that its ϵ'' and therefore $\tan\delta$ value increases, reducing the induction period and overall heating time. The favourable selectivity of lossy materials means that when trying to heat a low-loss material with low d_p , the absolute T can be increased locally to encourage MW coupling by introducing an additional lossy material, known as a susceptor. A good MW susceptor with high $\tan\delta$ such as ethanol, graphite or silicon carbide will selectively absorb MWs and be rapidly heated. Graphite powder has a $\tan\delta$ reported in the range 0.36–0.67 and $d_p = 1.34$ – 2.09 cm for grain sizes 20–80 μm ; compared to MW transparent materials such as fused quartz ($\tan\delta = 0.0003$ and $d_p = 75.73$ m) or MW reflective materials such as bulk metals[2], [39], [46].

The use of a susceptor removes two major challenges to heating low-loss materials by increasing the overall energy efficiency of the process and reducing the risk of generating a potentially damaging plasma since lower power is required. Plasma formation can temporarily interrupt MW absorption by the sample and causes drastic differences in heating patterns. A susceptor is typically incorporated as an external sheath rather than doped into the target material with the exception of waste treatment processes. The susceptor sheath will raise the T in the initial heating phase through conventional heat transfer methods before the material ϵ'' is increased to the point where MW-heating takes over. This susceptor assisted method is also known as hybrid heating and results in more consistent, reproduceable and uniform heating as the MWs heat internally while the susceptor continues to heat the surface conventionally. This also reduces radiative losses from the material surface allowing greater maximum T to be reached[14].

2.5 Semiconductors and thermoelectric generators (TEGs)

Semiconductors are exclusively crystalline solids that exhibit greater σ with increasing T as the valence electrons can be mobilised without resistance to movement. This is in stark contrast to metals which are very efficient electrical conductors at low T when the electrons are able to move freely and transmit energy across the surface, constrained only by Ohm's law. At higher T , the resistance of metals increases with respect to temperature as the positive metal ions vibrate more, increasing the likelihood of collisions with the free electrons. Crystalline solids restrict electrons to allowed energy bands comprised of several energy levels and separated by forbidden band gaps. Electrons residing in the highest energy band (valance band) can be excited to jump across the band gap (E_g) to the next highest allowed band (conduction band)[15]. The energy level halfway between the valance and conduction bands is known as the fermi energy (E_f). Direct band gaps represent the minimum energy required to jump between bands of the same wavevector (Figure 2.11a) while indirect band gaps are the minimum energy required for electrons to transition between bands of differing wavevector (Figure 2.11b).

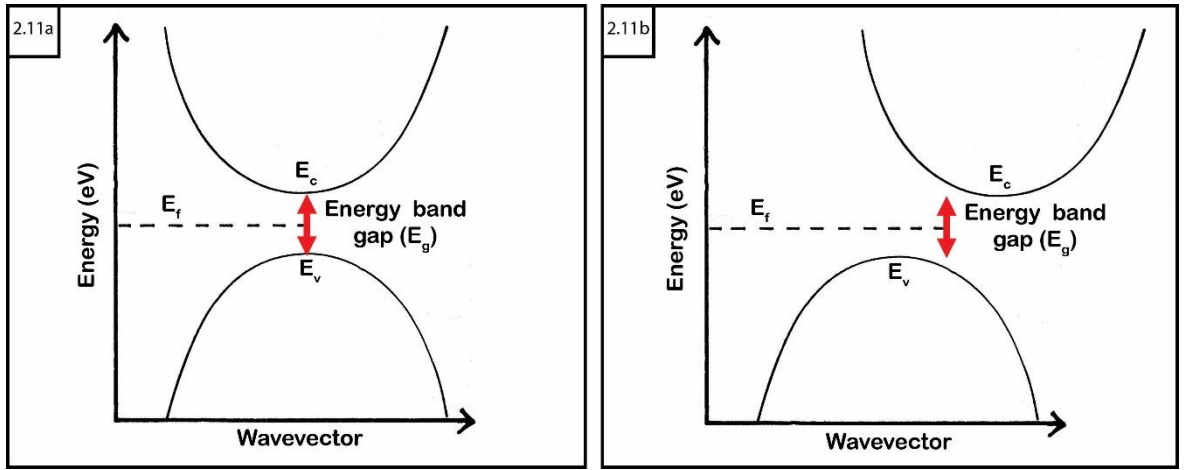


Figure 2.11: Diagram of the relationship between conduction (E_c) and valance (E_v) bands for a) direct band gap semiconductors b) indirect band gap semiconductors

The energy of E_g necessary for the electrons to jump bands to form electron-hole pairs can be calculated by subtracting the energy of the valance band (E_v) from the conduction band (E_c), or doubling the difference between the conduction band and the fermi energy:

$$E_g = E_c - E_v = 2(E_c - E_f) \quad \text{(Equation 2-90)}$$

So long as the conduction band is not completely filled, the electrons residing there are free to move and transfer energy throughout the crystal structure in response to an applied \mathbf{E} field. The empty energy level remaining when the excited electron transitions, known as a hole, represents a positive charge in the system and can also aid in the transference of energy by attracting an electron from another energy level. The relative movement of these holes due to repeated transference of electrons means that they act as charge carriers and are also affected by an applied \mathbf{E} field[15]. Lattices with E_g low enough for electrons to become excited and transfer to the conduction band at low T are known as semiconductors. These electron/hole pairs are the only available charge carriers in semiconductors so a smaller E_g means less energy is required for greater charge mobility and so larger σ .

The optical band gap is the exciton energy that determines transitions between bands, with an energy difference from the electronic band gap equal to the exciton binding energy in the range of 200–400 meV. Excitons are the bound state of electrons and holes which form when a photon is absorbed by a semiconductor and so are less than the electronic band gap.

2.5.1 Defect chemistry and structural effects on EM properties

Although crystal structures are normally presented as highly organised lattices, in reality atomic vacancies can be created and ions can migrate to interstitial spaces in response to an external influence such as temperature. When charged particles are moved within a structure, a corresponding vacancy with an associated opposite charge is left in the original site. Tuning the structure to produce defects by adjusting the stoichiometry of the reactants or the synthesis method can result in controlled atomic doping or deficiencies. The ideal structural arrangement is an infinite crystal with all components residing in their expected lattice sites, interstitial sites left empty, all electrons within valance band sites and all conduction band sites empty. Any deviations from the ideal structure are referred to as point defects[47]. Point defects can manifest in chemical systems due to ionic or electronic effects that are thermodynamically favourable, giving rise to fundamental chemical phenomena such as ionic conduction or augmented material properties[48].

There are many different types of disorder that can occur in a structure including migration of a cation and formation of a corresponding negative hole (Frenkel defects), the inverse or anti-Frenkel defect of a migrating anion, the formation of both cation and ion holes via the absence of a whole molecule (Schottky defects) which is more common in close packed alkali metal halides and anti-Schottky defects where an additional molecule is incorporated into the structure[48]. Other defects that can occur include antisite defects where cations and anions occupy the opposite positions, dislocation of structural components that disrupt the periodicity of the lattice (such as can be found at grain boundaries or surfaces that confine a crystal) or voids/inclusions resulting from aggregation of point defects into three dimensional impurities. It is possible for more complex defects to form by association of two defects such as vacancies that electrically neutralise each other[47], [48].

Generally, the introduction of an impurity or dopant (d) to a structure with an effective charge will cause an increase in the concentration (c) of opposite-charge defects and a reduction of like-charge defects. This rule applies for all native defects that exclude impurity defects that are in equilibrium and is formalised by the rule of homogeneous doping[48], [49]:

$$\frac{z_k x C_k}{z_d x C_d} < 0 \quad \text{(Equation 2-91)}$$

z_k = Effective charge of intrinsic crystal defect

z_d = Effective charge of dopant species

x = Amount of dopant, e.g., $\text{SnSe}_{1-x}\text{Te}_x$

Homogeneous doping is the result of disorder from the inclusion of aliovalent ions, i.e., those with a different valence to the target material, within the structure without changing the phase. Heterogeneous doping is the name given to an effect where the σ of an ionic conductor is increased when mixed with an insulating material due to the formations of defects on the surface of the conductor. Generally, a charged higher dimensional defect will cause an increase in the concentration of all opposite-charge defects and a reduction of all like-charge defects, provided the defect concentrations are in equilibrium; the law of heterogeneous doping is defined as[48]–[50]:

$$\frac{x(z_k C_{0,k})}{x \Sigma} < 0 \quad \text{(Equation 2-92)}$$

Σ = Charge density of interface, i.e., surface charge

The formation of vacancies involves energy expenditure to enable the relevant bonds to be broken that cannot be balanced solely by local structural changes to limit the damage or by an increase of vibrational entropy. Any crystal in thermodynamic equilibrium at a finite T will contain a finite number of point defects since their inclusion also introduces a large number of allowable crystal configurations[48]. Point defects allow for a certain level of mobility for the structural units, such as vacancies that can be filled by neighbouring atoms/ions. Structural units occupying interstitial sites also have a degree of mobility however the transition from one site to another will almost always be less energetically favourable[51].

Impurities can be introduced into a lattice structure either by direct component substitution or through incorporation into interstitial sites, depending on the relative size of the desired impurity to the host lattice ions[47]. By introducing certain impurities to semiconductor lattices the σ can be improved by introducing additional electrons or holes rather than generating them in pairs. Donor impurities provide free electrons to the conduction band if its valence

band is closer in energy level than the E_g of the rest of the structure and so does not generate corresponding holes, these result in a net majority of electrons as the energy carriers and is called an n-type semiconductor. Impurities that generate holes by accepting electrons from the valance band to an energy level below the conduction band, and so do not participate in electrical conduction, results in a net majority of positive holes as charge carriers and is called a p-type semiconductor[15].

The electrons in crystalline solids determine the electric and magnetic properties of the material. Intrinsic semiconductors are chemically pure with the number of equivalent holes and free electrons determined by the material properties. Metals are comprised of large numbers of small crystals, each of which has partially filled valence bands regardless of temperature and so all valence electrons are free electrons. At $T > 0$ K, atomic vibration in the crystal structures lead to scattering of the free electrons. The average distance between “collisions” is the mean free path of the electrons, which decreases with increasing T . This manifests when an applied \mathbf{E} field accelerates the electron motion and transfers the absorbed energy to atoms during collisions thereby increasing the thermal vibrations, i.e., greater T and resistance to electron flow. In semiconductors, additional free electrons (and corresponding holes) are generated with increasing T which increases σ until the respective charge carriers are approximately equal and the semiconductor becomes intrinsic; σ is therefore dependent on both the crystal impurity properties and T [15].

The presence of intrinsic defects such as cationic/anionic vacancies or heteroatomic substitution cause the overall structure to be more thermodynamically stable than an otherwise perfect crystal. The heating efficiency of a crystalline structure can be improved through such defects even if the material is not ideal for direct MW-heating. In some systems, doping has the effect of increasing the induction period by several minutes before sudden and dramatic increase in T is detected. Structures doping with impurities usually only requires a small concentration of dopant to produce changes orders of magnitude greater in the material properties. Larger impurity quantities can be used provided that the base structure remains approximately the same[14], [49].

2.5.2 Reclaiming waste energy with thermoelectric generators (TEGs)

Thermoelectric materials (TEMs) are defined by the correlation of heat and charge carrier transport in a conductor; of specific interest is the generation of a current in a circuit containing two conductors held at different temperatures, known as the Seebeck effect[41]. It is intuitive that the principle can be applied in reverse for cooling or heating by applying an electric current. Such devices are governed by the Peltier effect, named after French physicist Jean Charles Athenase Peltier and typically reach $\sim\frac{1}{4}$ the efficiency of a conventional heating or cooling system. Thermoelectric generators (TEGs) contain many n-type and p-type TEM segments that are connected by shunts to form an electric circuit; the shunts are typically a metal with good σ such as copper. Each TEM segment is sandwiched between hot and cold interfaces in alternating pairs as illustrated by the simplified diagram in figure 2.12, with each pair of semiconductors connected via a metal conducting plate[52], [53].

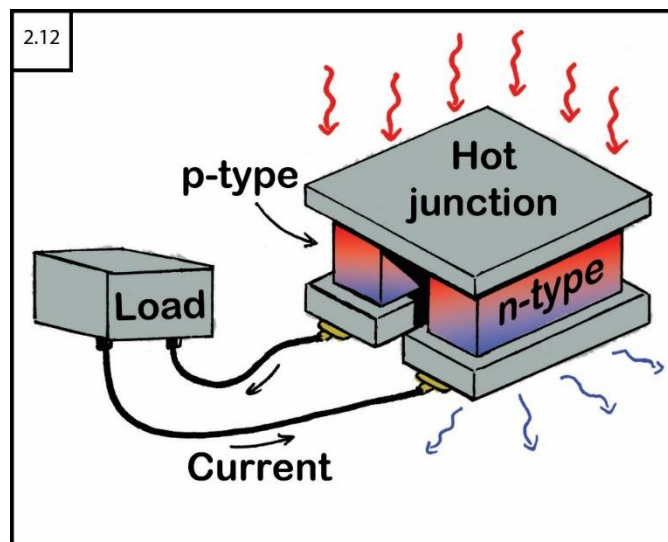


Figure 2.12: Diagram of a thermoelectric generator showing n-type and p-type semiconducting materials connected in series through a hot plate (T_H), cold plate (T_C) and a load

TEMs are of high interest for reclamation of useable electrical power from waste heat, a by-product of most modern technologies and systems. Radioisotope thermoelectric generators (RTGs) were developed in the 1950s to be capable of continuous generation of power from the thermal output of a plutonium source on the scale of hundreds of Watts. They proved essential for long-range space missions where solar panels are impractical such as Voyager 1 and 2, Cassini and New Horizons missions to the outer solar system, the Mars Science Laboratory and Viking landers as well as for long term scientific experiments left on the surface of the moon by Apollo missions 12–17[54].

The applications for such devices should be readily apparent, especially when considering that every process that involves energy transfer features losses and inefficiencies usually in the form of heat. Energy generated from the combustion of fossil fuels such as coal, oil, gas, petroleum etc is typically only ~25–34 % of the energy content of those sources, with the rest being lost as waste heat[55]. TEGs can be used to reclaim this otherwise wasted energy, with more efficient materials able to produce more useful electricity.

2.5.3 Measuring TEM efficiency with figure of merit

The Carnot efficiency (η_{max}) is the ratio of work carried out by an engine and the heat required to produce it, which has an upper limit given by the relationship between the temperature at the hot (T_H) and cold (T_C) surfaces[56], [57]:

$$\eta_{max} = \frac{T_H - T_C}{T_H} = 1 - \left(\frac{T_C}{T_H}\right) \quad \text{(Equation 2-93)}$$

Thermodynamically irreversible processes such as the cycle of power generation from TEGs, limit the value to less than the Carnot efficiency. The fraction of the Carnot efficiency of a TEG is defined by the figure of merit (ZT), which is the average of the individual figure of merit (zT) values for both n-type and p-type semiconductors used in the device. The maximum efficiency of a TEG (η) is used to determine the ZT value[52], [54], [56]:

$$\eta = \frac{\Delta T}{T_H} \frac{\sqrt{1 + ZT} - 1}{\sqrt{1 + ZT} + \frac{T_C}{T_H}} \quad \text{(Equation 2-94)}$$

It is a reasonable assumption that the electrical and thermal parameters do not vary along the length of the material, and so themselves are independent of temperature; however, the absolute T is a fundamental parameter when comparing materials over different temperatures. The figure of merit (zT) for a TEM is usually calculated from the simplified expression[52], [54], [58], [59]:

$$zT = \left(\frac{S^2\sigma}{\kappa_T}\right) T \quad \text{(Equation 2-95)}$$

2.5.4 The Seebeck coefficient

The Seebeck current created by the electromotive force (ΔU) is the sum of the EMFs generated in each conductor; it is named after Baltic-German physicist Thomas Johann Seebeck who observed that a ∇T across a circuit comprised of two different metals influenced the direction of a magnet[60]. The current is

proportional to ΔT between two electrical contact points, and are related by the coefficient of proportionality (α), also known as the Seebeck coefficient[41]:

$$\Delta U = \Delta U_1 + \Delta U_2 = \alpha_1 \Delta T + \alpha_2 \Delta T \quad \text{(Equation 2-96)}$$

A TEG circuit is constructed from n-type semiconductors containing mostly electrons as charge carriers and p-type semiconductors containing holes, which move freely when a ∇T is applied across both materials from a hot plate to a cold plate. The conducting plates will generate an \mathbf{E} field as a result of the ΔT between the plates and the thermovoltage (V_α) is generated by the Seebeck current over ∇T [52], [56], [61]:

$$V_\alpha = - \int_{T_c}^{T_H} \alpha_T dT \quad \text{(Equation 2-97)}$$

α_T = Thermal EMF (Seebeck coefficient)

The Seebeck coefficient, more often represented by S , is the entropy transported with a charge carrier divided by the carrier's charge and is given from the ratio of \mathbf{E} to ∇T [56]:

$$S = \frac{\mathbf{E}}{\nabla T} \quad \text{(Equation 2-98)}$$

The Seebeck coefficient will have a negative value for the n-type semiconductors and a positive value for the p-type semiconductors. The voltages integrated over the length of each material will accumulate and drive a current, the product of which is the electrical power of the generator[56].

2.5.5 *Electronic, lattice and bipolar thermal conductivity*

The total thermal conductivity (κ_T) is actually the sum of a few contributing factors; the first being electronic thermal conductivity (κ_e) which contributes $\sim 1/3$ of the total, since electrons will generate some heat as they meet electrical resistance. The majority of heat is transferred by phonons, i.e., vibrations of the atoms in the crystal lattice, and is known as the phonon conductivity or more commonly lattice thermal conductivity (κ_l). An additional contributor able to reduce κ_T can come from minor charge carriers able to cause bipolar thermal conductivity (κ_{bi}), a function of the E_g and T [56], [62], [63]:

$$\kappa_{bi} \propto \exp\left(\frac{-E_g}{2k_B T}\right) \quad \text{(Equation 2-99)}$$

The κ_{bi} contribution to the κ_T is usually so small as to be inconsequential in the presence of other material properties and is generally ignored.

The maximum achievable value of zT has more than doubled since the turn of the century through efforts to increase the power factor ($PF = S^2\sigma$), or reduce the κ_l by phonon engineering of the lattice through nano-structuring[56]. Usually, only materials with $zT > 0.5$ are considered to be TEMs and typically are only used in devices if $zT \geq 1$ which forms the baseline for the development of new materials.[57], [64]. Obviously, by increasing the ZT value for a given TEG with a ΔT between the hot and cold interfaces as large as possible will maximise the power generation efficiency of the device. The TEMs chosen for a particular application must be chosen with the best performance over the given ΔT they will be exposed to; which for a waste heat recovery device for a car exhaust (~350 °C range) the average ZT should be ~1.25 and for primary power generation an average $zT \geq 1.5$ at 800 °C is necessary to achieve a net efficiency of 20 %[53]. The efficiency of TEGs can be affected by factors other than the maximum zT , such as the temperature dependence other material properties that result in well performing materials such as Bi_2Te_3 (maximum $zT = 1.1$) producing a much lesser operational efficiency of $zT = 0.7$ in the constructed generator[52].

All the parameters of the figure of merit are related with respect to the charge carrier concentration (n), here represented for n-type semiconductors in which the electrons are the major carriers[63], [65]:

$$S = \frac{8\pi^2 k_B^2}{3eh^2} m^* T \left(\frac{\pi}{3n}\right)^{2/3} \quad \text{(Equation 2-100)}$$

$$\sigma = \frac{1}{\rho} = ne\mu \quad \text{(Equation 2-101)}$$

$$\kappa_T - \kappa_l = \kappa_e = L\sigma T = ne\mu LT \quad \text{(Equation 2-102)}$$

μ^* = Carrier mobility

m^* = Effective mass of the carrier

Planck's constant (h) = $6.626 \times 10^{-34} \text{ m}^2\text{kgs}^{-1}$

Lorenz number (L) $\approx 2.44 \times 10^{-8} \text{ W}\Omega\text{K}^{-2}$

From this it appears that attempts to change n will have conflicting impacts on the σ and κ_T values which are inversely proportional. Improving the materials figure of merit involves balancing the requirements of both electrical and

thermal properties, all of which are dependent on T . Maximising S requires only one type of charge carrier, as a mixed n-type and p-type semiconductor allows charge carriers to propagate in either direction relative to ∇T [52]. With increasing n , σ will also increase while S is reduced causing the PF to maximise with a $n \sim 1 \times 10^{25} \text{ cm}^{-3}$ [57]. Greater m^* leads to higher thermopower and so higher S however those benefits can be countered as larger m^* also results in slower μ^* , reducing σ . The κ_T is comprised of the electrical contribution of electrons and holes for transporting heat (κ_e) and phonon transport through the lattice (κ_l), with κ_e is inversely related to σ through the Wiedemann-Franz law[52]:

$$\frac{\kappa_e}{\sigma} = LT \quad \text{(Equation 2-103)}$$

The Lorentz number is typically given as $2.44 \times 10^{-8} \text{ W}\Omega\text{K}^{-2}$ for free electrons however it is correlated with the thermopower of the material, discussed further in section 5.6.3[52], [66]. The Wiedemann-Franz law demonstrates that for samples with very high σ or very low κ_e , the biggest determining factor for zT will be S [52].

2.5.6 Electron-phonon coupling (EPC) and phonon-phonon interactions

Electron-phonon interactions occur due to the dependence of the electronic energy levels on atomic positions in a solid, which will change as the solid undergoes thermal expansion. Electronic carriers can undergo relaxation in response to reduced atomic motion or become trapped in potential wells produced by atomic displacement[67]. Ideal TEMs will scatter phonons to reduce heat transfer through the structure with minimal resistance to σ [52]. Electron-phonon coupling (EPC) is therefore an important factor in governing the electron transport properties, while the three-phonon process is the main scattering mechanism for phonon transport in a crystal. κ_l is linked to n and has an inverse relationship to σ which is a strong indication of EPC. Fan et al demonstrated through density functional theory (DFT) analysis that κ_0 (without EPC correction) increases with n due to the increase in κ_e , while EPC causes κ_T to decrease at higher n as the rate at which κ_l decreases is faster than the rate κ_e can increase. Since electron transport coefficients are usually coupled to each other, decreasing κ_l is an effective method of achieving better TE performance through increasing n [62].

Phonon-phonon interactions (PPI) are an intrinsic process common to all crystalline solids and is the dominant factor affecting κ_l at high T . Many binary metal chalcogenides have been the focus of studies of the effect of PPI on lowering κ_l , in particular SnSe single crystals were shown to have a particularly low in-plane $\kappa_l = 0.23 \pm 0.03 \text{ Wm}^{-1}\text{K}^{-1}$ at 973 K that resulted in a maximum $zT = 2.6 \pm 0.3$ at 923 K due in part to large phonon scattering[68], [69].

2.5.7 Improving thermoelectric performance

There are several avenues through which it is possible to affect one or more of the physical parameters that contribute to a good TEM, with some general design rules that are often applied. Generally, implementing changes that increase S also tend to reduce σ (and vice versa); and according to the Wiedemann-Franz law, any effect on σ will have an opposite effect on κ_e [69]. The creation of highly distorted lattices involves at least two elements with large atomic numbers in a composition resulting in a larger unit cell, which can be achieved with doping or alloying[70]. Nanostructuring is a method intended to reduce κ_T , by designing bulk TEMs to have either induced amorphous structures or through the manifestation of nanograins[63]. Nanostructuring increases the boundaries and nanoscale lattice imperfections that aid phonon scattering and typically requires wet chemistry or high energy mechanical alloying to achieve the required nanopowders[70]. Optimisation of n through structural doping is correlated with energy level and tends to affect the band structure and S . Although n and S have an inverse relationship, increasing n tends to increase the m^* and energy band degeneration in turn having a net positive effect on the TE performance. Similarly, μ^* is affected by doping structures, where decreasing m^* tends to increase μ^* and so increase the σ , as described by the relationship with τ [71]:

$$\mu = \frac{e\tau}{m^*} \quad \text{(Equation 2-104)}$$

The carrier τ is determined by several scattering mechanisms so, manipulation of carrier scattering mechanisms can have a knock-on effect for electrical transport properties. Typically, the TEMs used for power generation have an expected operational range that makes acoustic phonon scattering the dominant contributor worth adjusting[69]. The atomic point defects that result from element substitution can strongly affect scattering of shortwave phonons, increasing the probability of collisions. This effect reduces the mean free path

(l) of the phonons as well as τ , and when the defect size is close to l the scattering effect is improved even more[71]. Electrical transport properties are also dependent on the band structure which can be improved by increasing the E_g via doping, tuning m^* or through band gap convergence[63]. Band gap convergence occurs when the energies of multiple electron bands are aligned, usually through doping, to achieve a higher degree of degeneracy and generate a higher n for a given E_F . Band gap convergence has limited benefits, with a positive influence only guaranteed in situations where a lighter band converges with a heavy band[72]. The κ_l is the primary contributing thermal transport factor in TEMs and is considered independent of any electronic parameters. Methods to lower κ_l include anharmonic bonding, introduction of crystal imperfections, formation of solid solutions and production of composite structures; but doing so also tends to reduce μ^* [69], [70]. Anharmonicity is the result of an atom being forced to deviate from its equilibrium position and so increasing anharmonicity will reduce the lifetime of a phonon, lowering κ_T [73]. In a conventional crystalline solid, changing the crystal structure can reduce the parameters that define κ_l , which are l , heat capacity at constant volume (C_v), group velocity of the phonon vibration mode (v_g) and the phonon τ [69], [71]:

$$\kappa_l = \frac{1}{3} C_v v_g l = \frac{1}{3} C_v v_g^2 \tau \quad \text{(Equation 2-105)}$$

The parameters that determine κ_l are all frequency dependent and as shown in figure 2.13, the inclusion of point defects and phonon-phonon interactions have particularly strong effects on τ at higher frequencies[69].

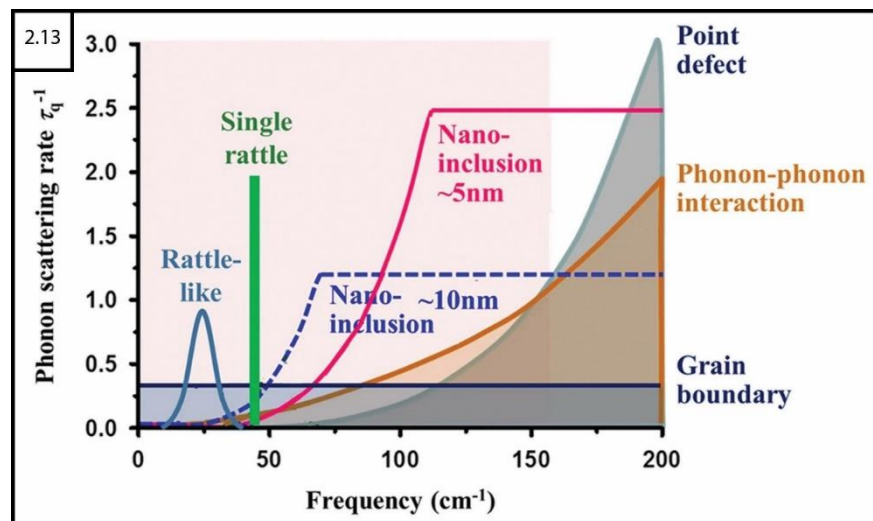
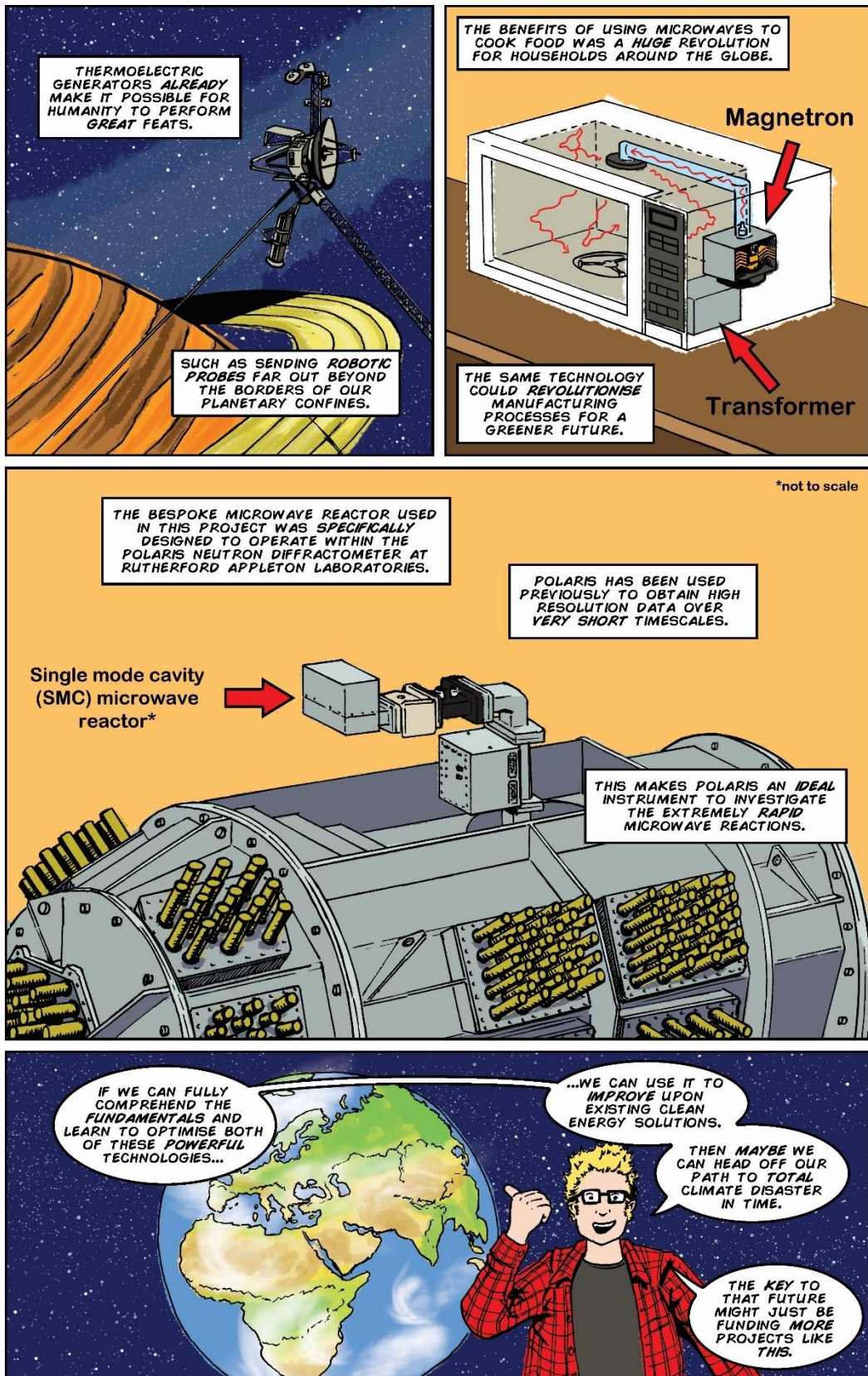


Figure 2.13: Comparison plot of various tuning mechanisms and their effect on phonon relaxation time (τ) over a range of phonon frequencies. Image by Jiong Yang et al, reproduced from ref. [69] under Creative Commons CC BY

3 Literature review of thermoelectric materials

3.1 Explaining the thesis to a grant committee



3.2 Common thermoelectric materials (TEMs)

As discussed in chapter 2, the dimensionless figure of merit (zT) is the measure of a material's efficiency at producing a voltage from an applied thermal gradient. A TEM is usually considered commercially viable when the maximum $zT \geq 1$ and research since the 2010s has mostly focussed on achieving values >2 , with several candidate materials showing promise as can be seen in figure 3.1.

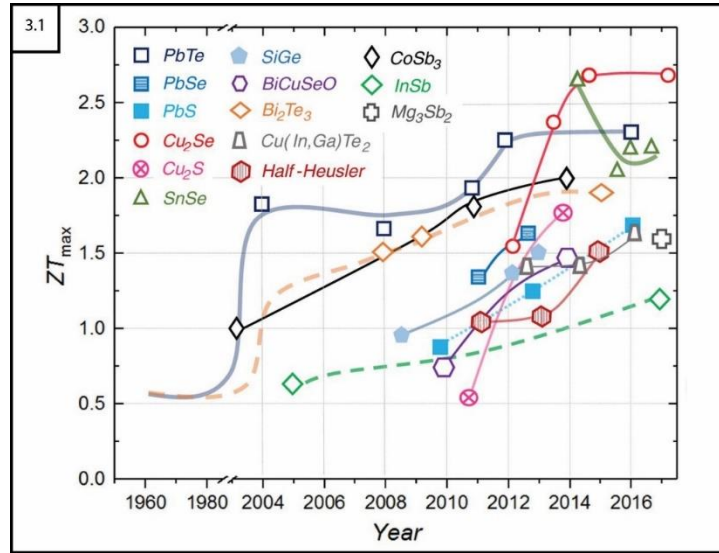


Figure 3.1: Comparison plot of maximum zT against reported year for typical high-efficiency TEMs as of 2017. From ref. [73] reprinted with permission from AAAS

The TE effect is temperature dependent meaning that although different materials may have similar reported zT values, each will be most effective under specific applicable conditions. Figure 3.2 compares the efficiency of a variety of TEMs (as per a 2017 review) over a range of temperatures. The best TEMs are doped semiconductors which can easily be assembled into TEGs; they tend to have high S and σ values, and if possible, accompanied by low κT [35].

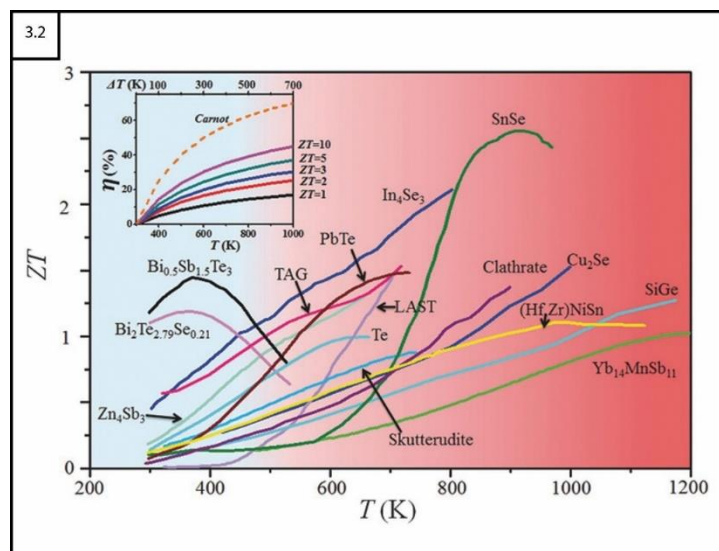


Figure 3.2: Comparison plot of maximum zT against temperature for typical high-efficiency TEMs as of 2018. Inset displays relationship between η , absolute T and ΔT of different zT values. Figure reproduced from ref. [63] with permission from John Wiley and Sons

Efforts to improve TEM performance tend to focus on decoupling the thermal and electrical properties to enhance the power factor (PF) through band engineering. Attempts are also made to reduce κ_e and κ_l , the latter of which can be altered without affecting σ . Metal chalcogenides were the only class of TEM studied as part of this project and so are discussed in greater detail in section 3.3 however, some examples of other common structure types are represented for context[35].

3.2.1 *Half-Heusler compounds*

These compounds were discovered in 1903 by Fritz Heusler with the general formula X_2YZ and due to their magnetic properties, are of great interest in the field of spintronics[54]. Half-Heuslers (HH) are mechanically and thermally stable with the general formula XYZ ; where X is a transition metal, noble metal or rare earth element, Y is a transition or noble metal and Z is a main group element[73]. The general formula indicates X atom vacancies compared to standard Heusler compounds and are comprised of three interlaced face-centred cubic ($Fm\bar{3}m$) sublattices[54]. A variety of HH systems have been studied, due to their ability to substitute different elements on each of the sublattices independently. These compounds tend to demonstrate a high PF with $S \sim 300 \mu\text{VK}^{-1}$ at room temperature, however they also often demonstrate high κT up to $10 \text{ Wm}^{-1}\text{K}^{-1}$ [54]. One of the best HH examples was reported in 2015 when p-type FeNbSb was doped with Hf through a process of levitation melting, mechanical alloying (MA) in a planetary ball and densification with spark plasma sintering (SPS). A series of FeNb $_{1-x}$ Hf $_x$ Sb alloys were produced using this method and a maximum $zT = 1.5$ at 1200 K was attributed to the FeNb $_{0.88}$ Hf $_{0.12}$ Sb sample[74].

3.2.2 *Skutterudites*

Skutterudite is another name for the mineral cobalt arsenide and is used to describe other compounds with the same general formula: TPn_3 , where T represents a transition metal and Pn represents the pnictogens (group 15 elements)[54]. Skutterudites were initially considered unsuitable for TE applications due to an intrinsically high κ_l making $zT > 1$ unlikely[75]. Skutterudites' cubic ($Im\bar{3}$) structure, comprised of eight cubes in the unit cell with six holding smaller pnictogen cube arrangements, feature two empty cubes that can be occupied by cations[54]. The cations are referred to as rattlers because they vibrate at low energies and can be used to tune the carrier

concentration and phonon scattering in the structure to improve both electronic and thermal properties[54]. A small electronegative difference between the different elements lead to high hole mobility and, through doping, n can be adjusted such that Skutterudites can act as either n-type or p-type semiconductors[75]. Skutterudites unfortunately tend to feature very high κT and so efforts are largely focussed on reducing this parameter to improve the efficiency further. Rogl et al reported in 2015 that p-type $\text{DD}_{0.59}\text{Fe}_{2.7}\text{Co}_{1.3}\text{Sb}_{11.8}\text{Sn}_{0.2}$ prepared by direct melting (DM) of stoichiometric powders and quenching in air resulted in a $zT = 1.3$ at 780 K thanks to lowered κT . Then, by applying severe plastic deformation through a high pressure torsion process, which compacts the material under high hydraulic pressure, they were able to produce $\text{DD}_{0.7}\text{Fe}_{2.7}\text{Co}_{1.3}\text{Sb}_{11.8}\text{Sn}_{0.2}$ with an improved σ and resulting $zT = 1.45$ at 850 K[76]. That same year, the same group managed to show that n-type $(\text{Sr, Ba, Yb})_{0.35}\text{Co}_4\text{Sb}_{12.3} + 9.1 \text{ wt.}\% \text{In}_{0.4}\text{Co}_4\text{Sb}_{12}$ prepared through high energy MA has an improved PF and very low κT leading to an even greater $zT = 1.8$ at 823 K[77].

3.2.3 Zintl phases

Zintl phases were described in the late 1920s as a series of intermetallic phases with salt-like crystal structures that have a lustre similar to metals[54]. They are defined by a set of rules known as the Zintl-Klemm concept which states that the number of covalent bonds formed by each anion is equal to $8 - \text{VEC}$ divided by the number of anions, where VEC is the number of valence electrons available per formula unit[54]. Zintl phases were only studied in earnest as potential TEMs from 2005. In 2006, Brown et al synthesised $\text{Yb}_{14}\text{MnSb}_{11}$ by DM and annealing at 1100 °C in a high temperature furnace and reported it as the first complex Zintl compound to meet the commercially viable threshold of $zT = 1$ at 1200 K[78]. The main obstacle to improving Zintl phase performance is the low electronic mobility that tends to manifest as a feature of the more common p-type structures. The best performing n-type material was reported in 2017; a Te-doped $\text{Mg}_3\text{Sb}_{1.48}\text{Bi}_{0.48}\text{Te}_{0.04}$ sample prepared through an arc melting process followed by SPS was shown to have a maximum $zT = 1.65$ at 520 K[79].

3.2.4 Clathrates

Clathrates are varied group of compounds, typically classified by two types of framework structure built from group 4 atoms that can encapsulate smaller

molecules or atoms[54], [80]. Type I structures have the general formula $X_2Y_6Z_{46}$ while type II structures are represented by $X_8Y_{16}Z_{136}$, in which X and Y are the “guest” atoms encapsulated by the Z framework; which is typically formed from Si, Ge or Sn[80]. Natural clathrates form from hydrogen-bonded water that can encapsulate methane molecules that become frozen in environments susceptible to the formation of permafrost however, rising global temperatures threaten these natural greenhouse gas stores. Clathrates have been proposed as potential structures of interest in the developing field of TEG design since the 1990s however, very little progress was made until 2012. A group of Japanese researchers produced n-type $Ba_8Ga_{16-x}Cu_xSn_{30}$ using the single crystal growth method developed by the American physicist Percy Williams Bridgman, in which the mixed elemental starting materials are sealed in quartz ampoules and slowly lowered out of a furnace to control crystal formation[54], [60]. They reported a very low $\kappa_T = 0.73 \text{ Wm}^{-1}\text{K}^{-1}$ leading to a competitive maximum $zT = 1.45$ at 500 K[81].

3.2.5 Metal silicides

Metal silicides, particularly systems based on Mg_2Si and $MnSi_x$, have been investigated as potential TEMs since the late 1950s although zT was consistently less than unity until the 2010s. In 2011, a solid solution of Mg_2Si - Mg_2Sn demonstrated a maximum $zT = 1.2$ in the range of 300–800 K[82]. Improvements were made in 2014 when Sb-doped $Mg_2(Si, Sn)$ was prepared using a B_2O_3 flux method in a box furnace with excess Mg, resulting in a maximum $zT = 1.5$ at 716 K being reported for $Mg_{2.08}Si_{0.364}Sn_{0.6}Sb_{0.036}$ [83].

3.2.6 Metal oxides

Metal oxides tend to show poor TE efficiency however they are often more thermally, structurally and chemically stable at high temperatures where most other TEMs would decompose, melt or oxidise. These factors, coupled with the relative abundance and inexpensiveness of common metals and the ease with which large quantities can be synthesised, makes metal oxides particularly attractive as candidates for commercial TEGs[54]. Despite being typically less efficient than other TE structures, layered oxides provide options for modifying individual constituents independently. $Na_xCo_2O_4$ is a layered metal oxide with favourable electrical properties reported in 1997 ($S = 5000 \mu\text{VK}^{-1}$ and $\sigma = 100 \text{ Sm}^{-1}$ at 300 K) leading to a favourable $PF = 50 \mu\text{Wcm}^{-1}\text{K}^{-1}$; this was greater than

for bismuth telluride, one of the best TEMs at the time[84]. High levels of Na-doping in $\text{Na}_x\text{Co}_2\text{O}_4$ where $x > 0.75$ were difficult to achieve until Lee et al described a method of growing such crystals in 2006 by heating Na in tetrahydrofuran and benzophenone and heating as-grown crystals of $\text{Na}_{0.75}\text{CoO}_2$ in the solution of Na anions for four days. They reported $S = 300\text{--}350 \mu\text{VK}^{-1}$ at ~ 80 K however, the κT measurements were also reportedly large, in the range of $8\text{--}10 \text{ Wm}^{-1}\text{K}^{-1}$, which limited the overall efficiency to $zT \sim 0.14$ [85].

3.2.7 Complex ternary chalcogenides

Various ternary chalcogenides with complex structures, large unit cells and low κT values have also been investigated, some with commercially viable TE efficiencies. Structures such as CsAg_5Te_3 prepared through a DM process and $\text{K}_2\text{Bi}_8\text{Se}_{13}$ prepared through annealing in solution were reported in 2016 with $zT \sim 1.5$ at 727 K and ~ 1.3 at 873 K respectively, while AgBi_3S_5 prepared via the Bridgman method in 2017 was reported to reach a $zT \sim 1$ at 800 K[86]–[88].

3.3 Binary metal chalcogenides

Metal chalcogenides are a class of materials that feature a diverse range of structures and chemical/physical properties. The metal atoms are bonded to at least one chalcogen atom (group 16 elements) usually referring specifically to S, Se or Te[54]. Metal chalcogenides are less ionic than metal oxides with smaller E_g which makes them ideal TEM candidates, particularly when comprised of p-block metals such as Bi or Sn[54]. Although metal tellurides such as PbTe and Bi_2Te_3 have a long-standing as effective TEMs, the push for improved metal selenides and sulfides has become more urgent as the relative scarcity and/or toxicity of elements such as lead and Te threatens future applications. Despite the toxicity, tellurides often have the best TE efficiency since Te, being the heaviest (non-radioactive) chalcogen, tends to reduce the κT in comparison with other chalcogen alternatives. The greater ionic character of tellurides also leads to greater μ^* , and thus higher σ compared to both selenides and sulfides[89]. Selenides compare favourably to the smaller/lighter chalcogens such as S and O by lowering the κT as well as having a smaller difference in electronegativity between the chalcogen and the metal. A lower electronegativity gap produces more covalent bonding with higher μ^* while the orbital overlap results in a lower E_g [90]. This trend is what makes the more massive Te further down the group such a powerful component of most TEMs. Metal selenides tend to balance the

performance requirements with the abundant, low-cost supplies necessary to manufacture at commercial scale such that even partial substitution of Te in some well performing systems could bring significant benefits. Synthesising these TEMs means a large proportion of the starting material mixture is comprised of metals which typically have very shallow δ_s . The small grain size of metal powders compared to a bulk ingot means that MW-heating through the generation of eddy currents becomes very efficient.

3.3.1 Tin(II) and tin(IV) selenides: SnSe and SnSe_2

Tin selenide (SnSe) has a quasi-2D, layered orthorhombic ($Pnma$) structure at low T in which the Sn and Se atoms are strongly bonded within the b - c plane in a corrugated formation. Each atom in a single layer is weakly bound to its three closest neighbours, stacked along the a -axis by van der Waals forces and so are easily separated. DFT calculations show that Sn vacancies in the structure lead to p-type conduction even in the presence of excess Sn or Se while n-type conduction is unlikely. The formation energy of Sn and Se vacancies in different charge states is increased with excesses of the respective elements; interstitial defects require less energy when excesses are present as expected[91], [92]. The Sn(IV) oxidation state is just as stable as Sn(II) especially in the presence of strong electrophilic ligands. Although less prominent in the literature, SnSe_2 is known as an indirect band gap, n-type semiconductor with a hexagonal close packed structure. Here, the Sn atom is octahedrally coordinated with the surrounding Se atoms which form 2D layers that sandwich the Sn ion. SnSe_2 may form alongside SnSe as a dual phase system, particularly with excess Se[92], [93]. In 2016 Li et al calculated from first principles, along with Boltzmann transport theory, the electrical and thermal transport properties of SnSe_2 monolayers as shown in figure 3.3. They reported a reasonably low minimum $\kappa T = 3.27 \text{ Wm}^{-1}\text{K}^{-1}$ at 900 K and a proposed maximum $zT = 0.94$ at 600 K[94].

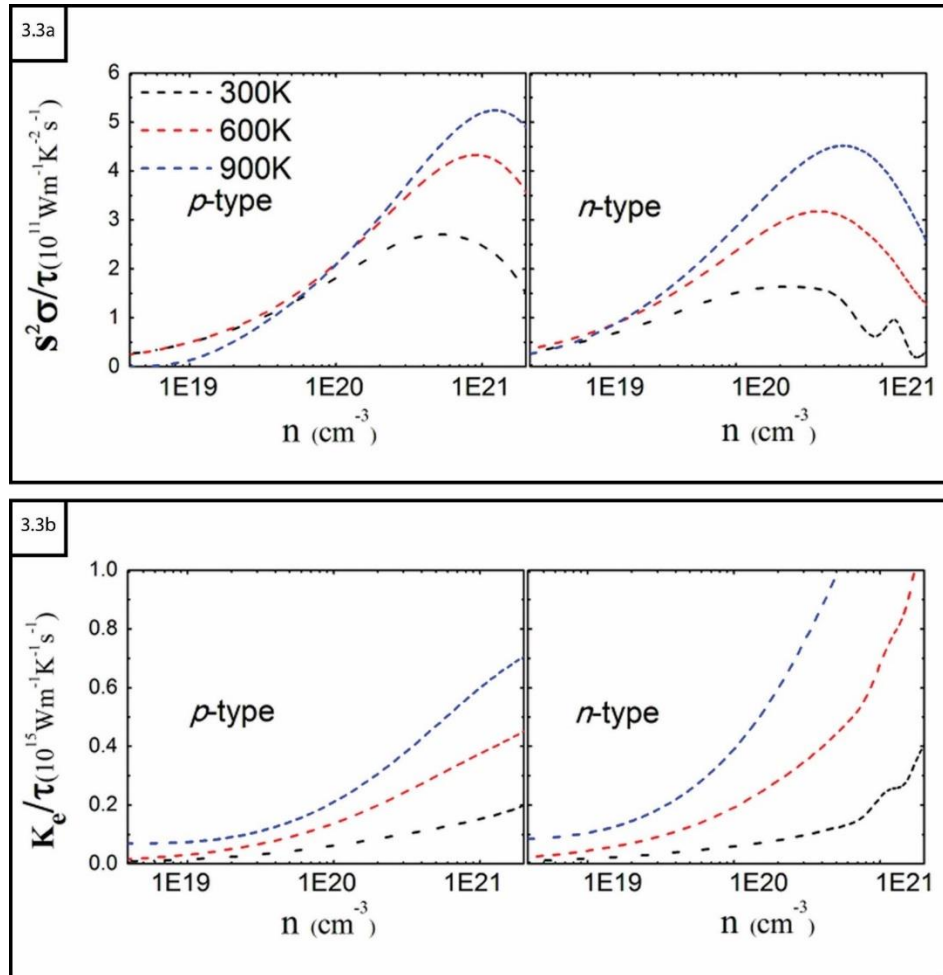


Figure 3.3: Plots of TE properties against carrier concentration for p-type and n-type monolayer SnSe₂ at 300 K, 600 K and 900 K a) power factor b) electrical thermal conductivity. Figure reproduced (adapted) from ref. [94] with permission from IOP Publishing

The SnSe structure transitions from the $Pnma$ to another orthorhombic ($Cmcm$) space group at T in the range of 750–800 K, which leads to shortening of the c -axis and compression of the corrugated layers to produce antiparallel displacement of the layers. As the structure undergoes the phase transition, the electronic properties remain unchanged while this layer compression generates phonon softening where the phonon energy is reduced, leading to decreased κT and therefore more favourable TE efficiency at high T [95].

3.3.2 Review of high performing SnSe synthesis methods

Single crystals grown by Zhao et al using the Bridgman method in April 2014 were reported with an ultralow $\kappa T = 0.23 \pm 0.03 \text{ Wm}^{-1} \text{ K}^{-1}$ at 973 K along the b -axis and a record breaking (at the time) maximum $zT = 2.6 \pm 0.3$ at 923 K as shown in figure 3.4[68].

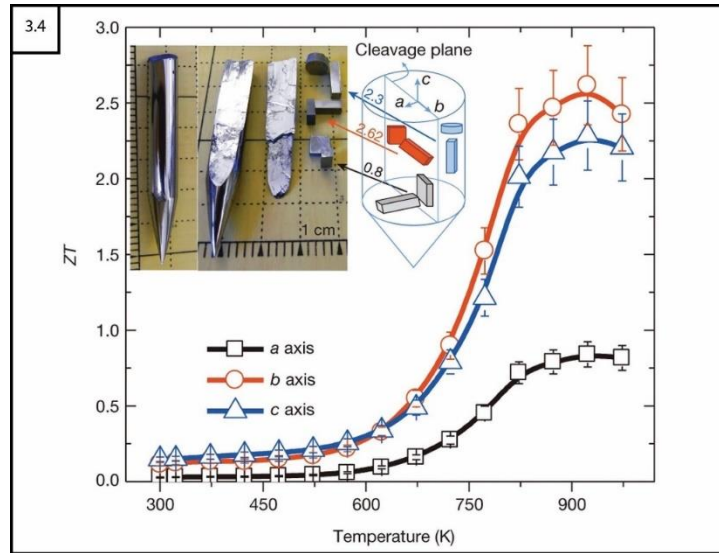


Figure 3.4: Plot of zT against temperature for SnSe samples cut along a , b and c -axes of single crystal. Figure reproduced (adapted) from ref. [68] with permission from Springer Nature

The anisotropy of the structure is the reason that the record breaking zT value occurs only along the b -axis while the low $\kappa_l = 0.36 \text{ Wm}^{-1}\text{K}^{-1}$ at 770 K was attributed to high anharmonicity of the chemical bonds. The spring constant, i.e., proportion of force an atom is subjected to compared to displacement from its equilibrium position by a passing phonon, varies with atom displacement; this enhances phonon-phonon scattering without affecting the electronic properties[56], [68]. These electrical properties define SnSe as an indirect band gap semiconductor with additional applications in photovoltaic solar cells and memory-switching devices while the anisotropic properties make the material useful in Li-intercalation batteries[93].

The requirement of the high temperature $Cmcm$ phase marks the system as a promising material for higher temperature applications, historically dominated by Pb-based TEMs which are considerably more toxic[54]. Although the single crystal form of SnSe was the first TEM reported to reach a maximum $zT = 2.6$, the benchmark encouraged greater interest in TEM research with several other materials being produced in the next few years that match or exceed this efficiency. Polycrystalline SnSe requires less complex synthesis conditions, making it a more suitable target for commercialisation however, such morphologies are often less efficient with a typical $zT < 0.6$, significantly less than single crystals. The anisotropy of polycrystalline samples favours preferred orientation parallel to the direction of a pressed pellet resulting in weakening of both σ and κ_T values[96], [97].

3.3.3 Reported enhancement of SnSe performance through doping

Li-Dong Zhao et al reported in 2016 that Na-hole-doped SnSe single crystals produced via the Bridgman method showed an increased PF over a wider T range. They measured $\sigma = 1486 \text{ Scm}^{-1}$ at 300 K, reducing to 148 Scm^{-1} at 773 K and $S \sim 160 \text{ } \mu\text{VK}^{-1}$ at 300 K, increasing to $\sim 300 \text{ } \mu\text{VK}^{-1}$ at 773 K. The resultant efficiency was calculated to be $zT = 0.7$ at 300 K, increasing to $zT = 2$ at 773 K; comparable to SnSe single crystals[98]. Using the same method in 2016, Duong et al reported that synthesising Bi-doped SnSe single crystals resulted in a maximum $zT = 2.2$ at 733 K along the b -axis[99]. Two years later, Chang et al claimed a new record with $zT \sim 2.8 \pm 0.5$ at 773 K along the out-of-plane a -axis (Figure 3.5) for Br-doped SnSe single crystals produced by carefully annealing at 1323 K for 6 hours with extremely slow heating/cooling ramp rates[100].

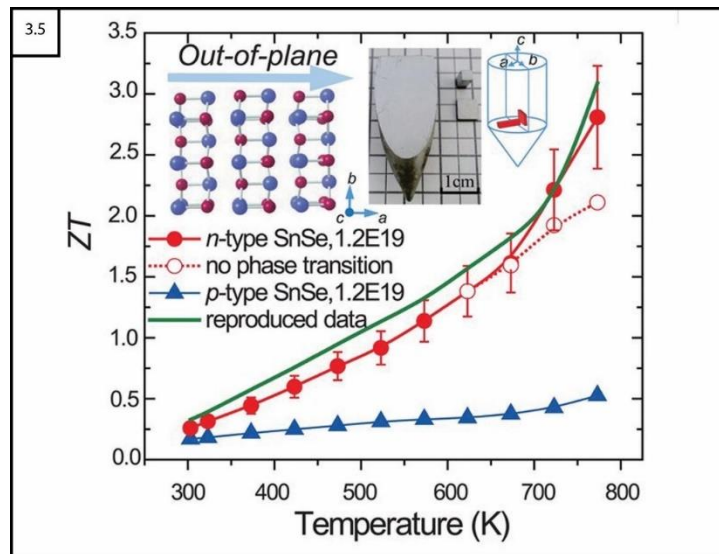


Figure 3.5: Plot of zT against temperature for Br-doped SnSe single crystals measured along the a -axis. From ref. [100] reprinted with permission from AAAS

Attempts to improve the performance of polycrystalline SnSe culminated in a recent paper by Zhou et al in 2021 for Na-doped SnSe samples with exceptional TE performance. They purified the Sn starting material before annealing stoichiometric amounts at 1223 K for 12 hours, quenched in ice water followed by annealing again at 773 K for 48 hours. The Sn purification step completely removed any oxides and reduced $\kappa_l = 0.07 \text{ Wm}^{-1}\text{K}^{-1}$ at 783 K. This led to an improved maximum $zT = 3.1$ at 783 K as shown in figure 3.6, which stands as the current record for highest TE efficiency at the time of writing[101].

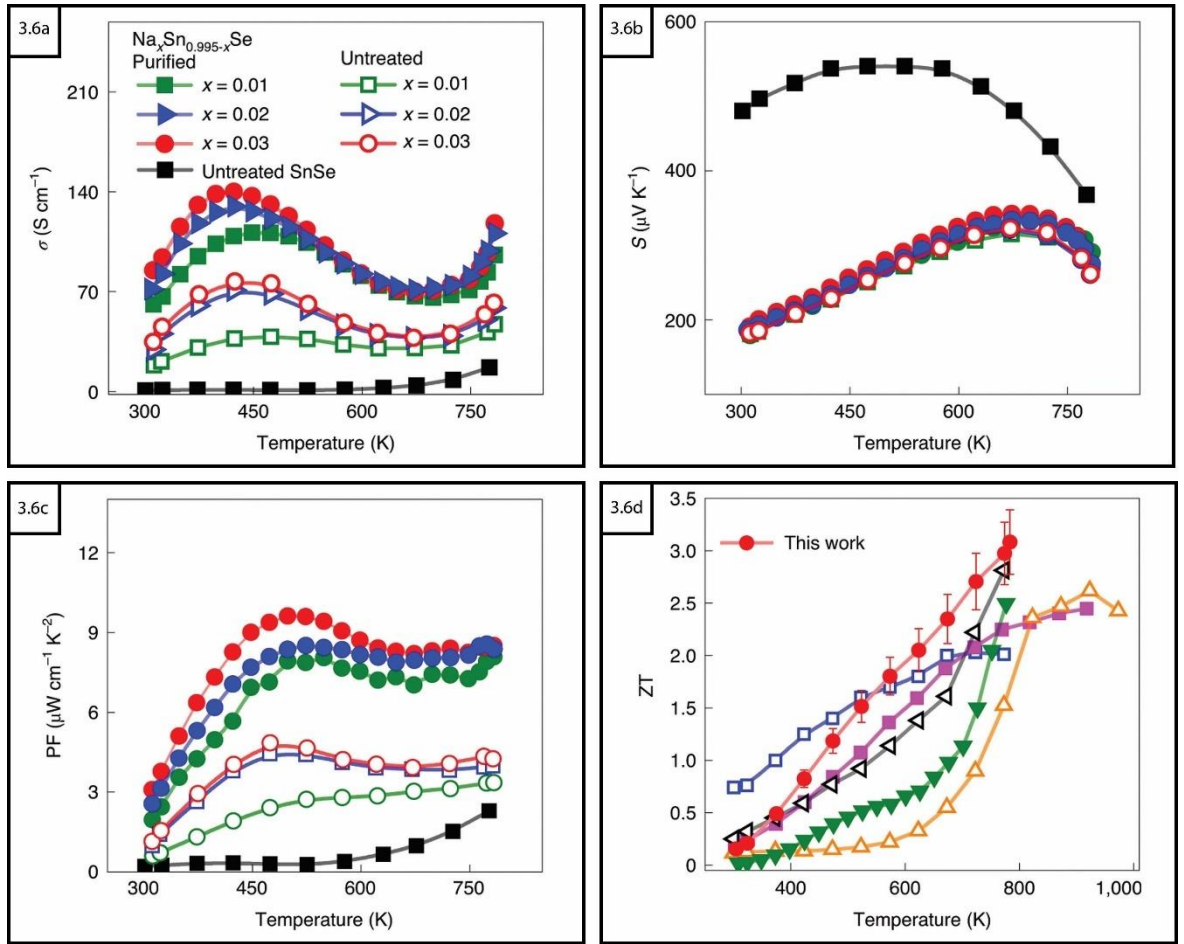


Figure 3.6: Plots of TE properties against temperature of Na doped polycrystalline $\text{Na}_x\text{Sn}_{0.995-x}\text{Se}$ samples a) electrical conductivity b) Seebeck coefficient c) power factor d) zT . Image by Chongjian Zhou et al, reproduced from ref. [101] under Creative Commons CC BY

Solvothermal (ST) synthesis (hydrothermal when water is used) is a process of crystal growth that involves heating a steel pressure vessel called an autoclave (or Teflon[®] acid digester). This method for producing both polycrystalline SnSe and SnS nanorods were both reported in 2016, with lower than ideal maximum $zT = 0.6$ at 773 K and 0.25 at 773 K respectively[102], [103]. SnSe produced through a MW-heating ST method for use as an electrode material, with 1/3 of samples being characterised as phase pure, were not prepared for TEM applications so no data is available on their TE performance[104].

3.3.4 Other tin(II) chalcogenides: SnTe and SnS

Tin telluride (SnTe) itself is non-toxic and considered eco-friendly however tends to be a poorly performing TEM with point defects of inherent Sn vacancies and high hole concentrations leading to particularly low $S = 20 \mu\text{VK}^{-1}$ and high $\kappa T = 2.88 \text{ Wm}^{-1}\text{K}^{-1}$ at room temperature[105]. Quasi crystals grown using the Bridgman method resulted in a relatively high $S = 30\text{--}40 \mu\text{VK}^{-1}$ however, only a maximum $zT = 0.55$ at 873 K was achieved[106]. The theoretical minimum $\kappa_l = 0.5 \text{ Wm}^{-1}\text{K}^{-1}$ was approached by Banik et al in 2011 through cationic Sb-doping

in a melting-annealing process to increase the hole formation in the structure, bringing zT close to unity for $\text{Sn}_{0.85}\text{Sb}_{0.15}\text{Te}$ at 800 K[107].

Tin sulfide (SnS) is a stable material comprised of non-toxic and relatively abundant components with low κ_T below 400 K however, SnS has a significantly lower TE efficiency than SnSe. The structure is similar to SnSe, with a *Pnma* lattice capable of transitioning to a *Cmcm* phase at high T with the associated phonon softening. It is also a p-type semiconductor due to intrinsic Sn vacancies, which have low formation enthalpy, favourably creating holes in the structure in the presence of excess Sn. The lighter S atoms lead to tighter interlayer spacing, longer phonon relaxation times and greater κ_l that limits TE performance[95], [108]. SnS produced through MA-SPS was reported with a maximum $zT = 0.16$ at 823 K[109].

Two 2015 studies showed that doping $\text{SnSe}_{1-x}\text{Te}_x$ and $\text{SnSe}_{1-x}\text{S}_x$ polycrystalline solid solutions by alloying n-type tin chalcogenides, and doping with I or Na respectively, improved the maximum $zT \sim 1$ at 773 K for I-doped $\text{SnS}_{0.1}\text{Se}_{0.87}\text{I}_{0.03}$ and $zT = 0.72$ at 773 K for Na-doped $\text{Sn}_{0.99}\text{Na}_{0.01}\text{Se}_{0.84}\text{Te}_{0.16}$ [110], [111]. Partial S-doping to produce $\text{SnSe}_{0.8}\text{S}_{0.2}$ resulted in a slightly better $zT = 0.82$ at 823 K[96]. In 2020, polycrystalline $\text{SnSe-SnSe}_{1-x}\text{S}_x$ solid solutions with Sn deficiencies produced through MA-SPS were reported with a maximum $zT = 1.1$ at 823 K for $\text{Sn}_{0.985}\text{Se}_{0.75}\text{S}_{0.25}$ and $zT \sim 1.75$ at 823 K for the Ag-doped $\text{Sn}_{0.978}\text{Ag}_{0.007}\text{Se}_{0.75}\text{S}_{0.25}$ [112].

At the time of writing, there are no prominent reports of any tin chalcogenides being synthesised in either single crystal or polycrystalline form through direct MW-heating of solid state material. The more recent reports of exceptional TE performance in polycrystalline SnSe samples indicates that overcoming the challenges to produce single crystals is not necessary for desirable TEMs.

3.3.5 Bismuth(III) chalcogenides: Bi_2Se_3 and Bi_2Te_3

Bismuth selenide (Bi_2Se_3) and bismuth telluride (Bi_2Te_3) both have a tetradymite structure characterised as a trigonal ($R\bar{3}m$) space group. Both complex dielectric properties (ϵ' and ϵ'') for bismuth chalcogenides increase along with the mass of the chalcogenide, meaning greater electron excitation. The difference between constants is greater for heavier atoms, and since $\tan\delta$ is the ratio of these two constants, Bi_2Te_3 should absorb MWs more easily than Bi_2Se_3

or partially substituted solid solutions for additional heating[54], [113]. Bi_2Te_3 and its alloys were some of the best performing TEMs for many years owing to intrinsically low κ_T and highly tuneable PF. Bi_2Se_3 is always an n-type semiconductor due to native point defects such as energetically stable Se vacancies at both sites; while Bi_2Te_3 can be tuned to be either n- or p-type by adjusting the Bi:Te ratio[114]. The Te_1 vacancy in Bi_2Te_3 is the most stable intrinsic defect with low formation energy in excess Bi or Te environments[115].

Bi_2Te_3 has a reported indirect $E_g = 0.15$ eV and is described as a distorted rock salt structure comprised of layers held together with van der Waals forces. The layered structure leads to anisotropy, with the best performance measured perpendicular to the c -axis [54]. The transport properties of Bi_2Te_3 are therefore also anisotropic, much like SnSe, and so are dependent on the direction of electrical and thermal propagation within the structure[89]. As shown in table 3.1, unmodified p-type Bi_2Te_3 is already considered a good TEM at low temperatures due to a commercially viable $zT = 1.11$ at 323–348 K compared to unmodified n-type Bi_2Te_3 , which is less effective with a maximum $zT = 0.68$ at 298–323 K[116].

Table 3.1: Thermoelectric properties of unmodified bismuth telluride[116]

	n-type Bi_2Te_3		p-type Bi_2Te_3	
Temperature (K)	298	323	323	348
Electrical conductivity (Sm^{-1})	38.31	42.02	83.47	98.52
Seebeck coefficient (μVK^{-1})	-209	-213	185	194
Thermal conductivity ($\text{Wm}^{-1}\text{K}^{-1}$)	0.8	0.823	0.985	0.987
Maximum zT	0.68	0.68	1.11	1.11

Although they share the same $R\bar{3}m$ crystal structure, the smaller Se atoms cause Bi_2Se_3 to exhibit stronger EPC and a lower overall S [90]. Optimising n for these systems changes the T at which the maximum zT is achieved, allowing the TEM to be tuned for multiple applications based on the environment[52]. Alloying Bi_2Te_3 tends to produce high zT materials by creating disorder of the unit cell through partial occupation of atomic sites and reducing κ_l [54].

3.3.6 Common bismuth(III) chalcogenide synthesis methods

Conventional syntheses of single crystal bismuth chalcogenides and alloys include the Bridgman method, as described in section 3.2.5, the Czochralski

method and the zone melting (ZM) method. The Czochralski method utilises a rotating heated crucible containing a stable melt composition and an orientated growth seed; the seed is slowly raised from the material melt and rotated in the opposite direction of the crucible. Single crystals grown in this way tend to have higher structural perfection with less cleavage planes oriented away from the main crystallisation direction. The equipment is expensive and has a very slow output of crystals that are more prone to splitting along the cleavage planes[117]. The starting material mixture for the ZM method are sealed inside a quartz ampoule (precoated with pyrolytic graphite) and passed through a ∇T that increases with each level. The ampoule is moved in the vertical axis such that the orientated crystals are grown from the bottom at a typical rate of 6 mmhr⁻¹ for n-type crystals, and often faster for p-type crystals. Commercial ZM apparatus produces multiple 17–25 mm diameter ingots by heating the material with an arc-melter or induction heater[117], [118].

Bi₂Se₃, Bi₂Te₃, Bi₂Se_{1.2}Te_{1.8}, p-type Bi_{0.4}Sb_{1.6}Se_{2.4}Te_{0.6} and n-type Bi₂Se_{0.6}Te_{2.4} samples were all prepared by Kadhim et al using the same direct MW-heating process used in this project (described in chapter 5). Each sample was successfully produced by heating in a vertical orientation for 600 s in an 800 W DMO with periodic shaking[119], [120]. Mastrovito et al have also reported Bi₂Se₃ and Bi₂Te₃ being prepared by heating at 1000 W for 4× 60 s cycles in a CEM MDS 2100 microwave reactor. Each of these samples were prepared in a glovebox under Ar atmosphere before heating and it was found that obtaining phase pure samples of Bi₂Se₃ required an additional 60 % excess Se[3].

3.3.7 Bismuth(III) chalcogenide solid solutions

For many years, alloying Bi₂Te₃ with Sb₂Te₃ or Bi₂Se₃ to produce p-type Bi_{2-x}Sb_xTe₃ and n-type Bi₂Se_{3-x}Te_x resulted in the best commercially viable TEMs, with efficiencies regularly reported in the region of $zT \sim 1$ at 300 K[121]. The greater chalcogen disorder of n-type Bi₂Se_{3-x}Te_x systems with the inclusion of lighter Se atoms have been shown to improve n and reduce κ_l compared to undoped Bi₂Te₃, but limited improvement in $zT = 0.8$ – 1.1 in the low T range of 273–373 K[52], [122]. Wang et al prepared n-type Bi₂Se_{3-x}Te_x from stoichiometric elemental chunks by heating at 1123 K and quenching the ingots prior to the application of melt spinning. The process involves melting the material and ejecting the molten alloy as a thin stream under pressure onto a

spinning wheel to rapidly transfer heat away. The result was a range of samples including $\text{Bi}_2\text{Se}_{0.6}\text{Te}_{2.4}$, which after SPS, achieved a maximum $zT = 1.05$ at 420 K as shown in figure 3.7[123].

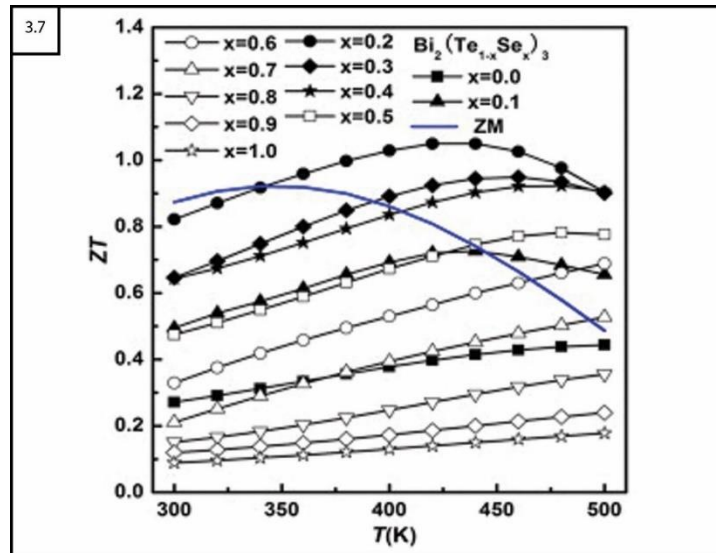


Figure 3.7: Plot of zT against temperature for a variety of $\text{Bi}_2\text{Se}_{3-x}\text{Te}_x$ samples produced through a melt spinning procedure. Figure reproduced (adapted) from ref. [123] with permission from Elsevier

Through a point-defect engineering process of melting stoichiometric ingots in a ball mill followed by either hot-pressing (HP) or hot deforming (HD) the powder product, Hu et al produced a series of promising solid solution samples that compare favourably to samples produced through more conventional methods as shown in figure 3.8. The HP $\text{Bi}_2\text{Se}_{0.7}\text{Te}_{2.3}$ sample was one of most improved with successive HD treatments, achieving a maximum $zT = 1.2$ at 445 K along with p-type Sb-doped $\text{Bi}_{0.3}\text{Sb}_{1.7}\text{Te}_3$ with a maximum $zT = 1.3$ at 380 K[124].

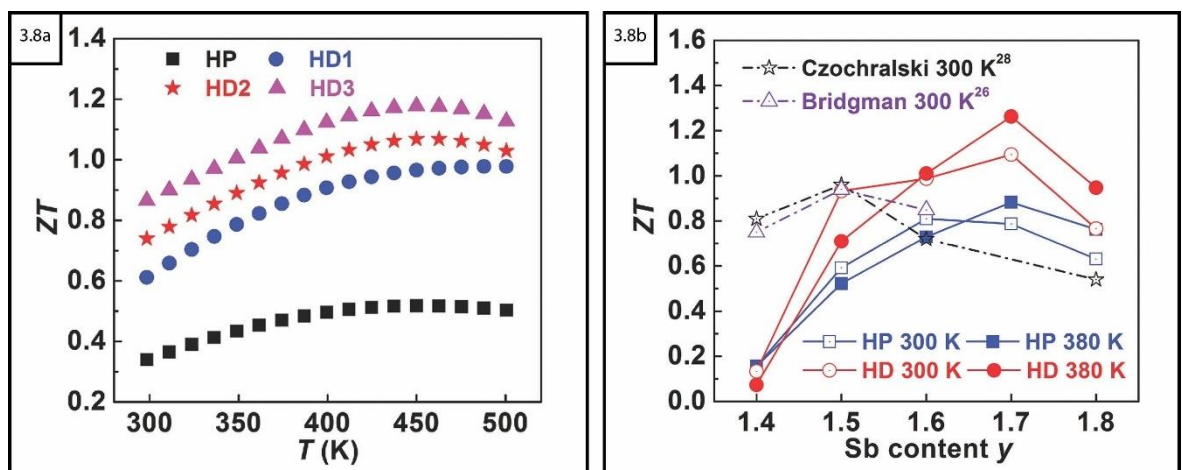


Figure 3.8: Plots of zT values a) against temperature for $\text{Bi}_2\text{Se}_{0.7}\text{Te}_{2.3}$ samples with 1, 2 or 3 hot deforming treatments b) against Sb content for hot pressed and hot deformed $\text{Bi}_{2-x}\text{Sb}_x\text{Te}_3$ samples. Figure reproduced (adapted) from ref. [124] with permission from John Wiley and Sons

ST synthesis methods have been successfully used to produce a range of $\text{Bi}_2\text{Se}_{3-x}\text{Te}_x$ samples by several research groups, using both toxic reducing agents as

well as a green method involving ascorbic acid in 2015[125]. In 2016 Hong et al used a MW-heated ST method with a CEM reactor to produce n-type $\text{Bi}_2\text{Se}_{3-x}\text{Te}_x$ nanoplates. Pellets made from $\text{Bi}_2\text{Se}_{0.3}\text{Te}_{2.7}$ reached $zT = 1.23$ at 480 K[126]. More progress has been made with p-type $\text{Bi}_{2-x}\text{Sb}_x\text{Te}_3$ alloys, with $\text{Bi}_{0.5}\text{Sb}_{1.5}\text{Te}_3$ produced in 2015 using a melt spinning-SPS process with a maximum $zT = 1.86 \pm 0.15$ at 320 K[127]. Doping $\text{Bi}_{0.5}\text{Sb}_{1.5}\text{Te}_3$, which has a maximum $zT = 0.8$ at 330 K, with either Cd, Cu or Ag was shown in a 2016 paper to achieve $zT = 1-1.4$ at ~ 450 K for $\text{Bi}_{0.5}\text{Sb}_{1.49}\text{Cd}_{0.01}\text{Te}_3$, $\text{Bi}_{0.5}\text{Sb}_{1.495}\text{Cu}_{0.005}\text{Te}_3$ and $\text{Bi}_{0.5}\text{Sb}_{1.494}\text{Ag}_{0.006}\text{Te}_3$ respectively (Figure 3.9)[128].

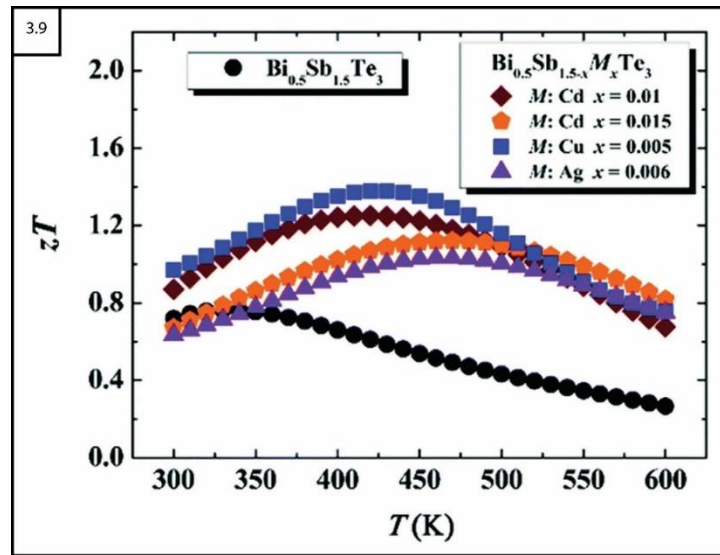


Figure 3.9: Plot of zT against temperature for cadmium, copper and silver doped $\text{Bi}_{0.5}\text{Sb}_{1.5-x}\text{M}_x\text{Te}_3$ samples. Figure reproduced (adapted) from ref. [128] with permission from the Royal Society of Chemistry

In the same year, Poudel et al confirmed that through a MA-HP process of commercial ingots it was possible to produce nano-scale crystalline powders of p-type $\text{Bi}_x\text{Sb}_{2-x}\text{Te}_3$ alloys with a maximum $zT = 1.4$ at room temperature[129].

3.3.8 Antimony(III) chalcogenides: Sb_2Se_3 and Sb_2Te_3

A_2B_3 compounds such as antimony selenide (Sb_2Se_3) tend to form layered $Pnma$ structures similar to SnSe although, $R\bar{3}m$ phases similar to bismuth chalcogenides are also common. The dielectric constants for antimony chalcogenides are relatively large and anisotropic making them resistant to charge defects and recombination, particularly in the ab -plane. Both constants increase along with the mass of the chalcogen, and so Sb_2Te_3 should absorb MWs better than either Sb_2Se_3 or partially substituted samples if extended heating is required. The TE properties can be improved with external application of pressure as well as through doping of the crystal structure. Small band gap semiconductors such as these have limited application potential at $T > 500$ K due

to the ease of excitement of minority charge carriers[130]–[133]. Sb_2Se_3 has a narrow $E_g \sim 1.2\text{--}1.3$ eV that is a valuable component when alloyed with other TEMs; it is also a valuable absorber for the sensitisation of solar cells, making them more efficient. Antisite defects within Sb_2Se_3 are favourable due to low formation energies and are only likely suppressed by controlling synthesis to be as close to stoichiometry as possible[134], [135].

Antimony telluride (Sb_2Te_3) crystallises in the $R\bar{3}m$ phase similar to Bi_2Se_3 and Bi_2Te_3 due to the heavier Te atoms and exhibits the same weak interlayer van der Waals interactions, antisite defects and large hole concentration that reduces S and enhances κ_e . Sb_2Te_3 has a much higher $\sigma = 3.8 \times 10^5 \text{ Sm}^{-1}$ compared to that of Sb_2Se_3 ($\sigma = 3 \times 10^{-5} \text{ Sm}^{-1}$), with zero band gap which gives it more metallic characteristics. This means that MWs will interact with the product largely through eddy currents generated by the \mathbf{H} field rather than the \mathbf{E} component as with most dielectrics. It has a melting point at 902 K, making it more suitable for high T applications however, single crystals tend to demonstrate a typically low $zT < 0.3$. Sb_2Te_3 always presents as a p-type semiconductor due to an intrinsically high κ_l along with the antisite defects[89], [132], [136], [137].

3.3.9 Review of synthesis methods for enhancing Sb_2Se_3 and Sb_2Te_3

Both Sb_2Se_3 and Sb_2Te_3 have been synthesised using direct MW-heating of solid state starting materials by Mastrovito et al concurrently with the bismuth chalcogenide syntheses in the 2007 study previously referenced in section 3.3.6. Successful synthesis of both Sb_2Se_3 and Sb_2Te_3 required 1 mmol of starting material to achieve favourable results; while for lesser quantities of Sb_2Se_3 (up to 0.5 mmol) no reaction was induced. In the Sb_2Te_3 syntheses, phases of unreacted Te appeared with greater prominence as the quantity deviated further from 1 mmol in either direction. Obtaining phase pure Sb_2Se_3 was found to be heavily dependent on the samples being loaded vertically within the MW reactor, with no reaction for 0.25–0.5 mmol samples loaded horizontally[3]. An increased number of heating cycles for phase pure Sb_2Te_3 was found to be necessary; while for samples loaded vertically, more intense peaks attributed to unreacted Te were present than when loaded horizontally. Reducing the amount of Te by 17 % enabled phase pure Sb_2Te_3 to be successfully produced[3]. This paper had not been read prior to the experiment design stage for this project

and so stoichiometric amounts of starting material are utilised throughout; and with the samples prepared in air rather than Ar atmosphere.

Sb_2Te_3 nanosheets produced through a MW-induced ST-SPS process was reported with relatively low $\kappa_T = 0.76 \text{ Wm}^{-1}\text{K}^{-1}$, high $\sigma = 2.49 \text{ Sm}^{-1}$ and high $S = 210 \mu\text{VK}^{-1}$ leading to a maximum $zT = 0.58$ at 420 K[138]. Efforts to improve the figure of merit through In-doping Sb_2Te_3 through a DM-MA-HP sequence was reported in 2015 with an increased $zT = 0.73$ at 615 K for $\text{Sb}_{1.85}\text{In}_{0.15}\text{Te}_3$. This was further enhanced with Ag-doping the Sb site, leading to $zT = 0.92$ at 710 K for $\text{Ag}_{0.01}\text{Sb}_{1.85}\text{In}_{0.15}\text{Te}_3$; a great improvement over the ZM method and coming closer to desirable values as shown in figure 3.10[132].

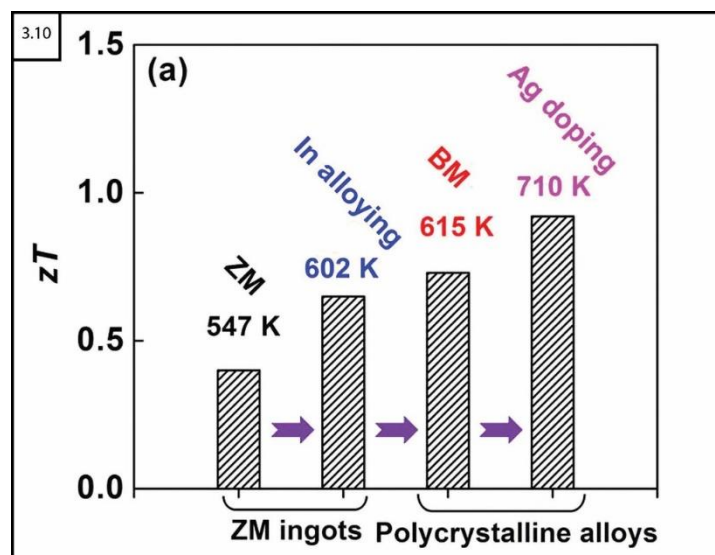


Figure 3.10: Comparison plot of maximum zT values achieved for different synthesis methods of p-type Sb_2Te_3 alloys showing $\text{Ag}_{0.01}\text{Sb}_{1.85}\text{In}_{0.15}\text{Te}_3$ approaching unity. Figure reproduced (adapted) from ref. [132] with permission from Elsevier

A maximum $zT = 1.03$ at 401 K was finally achieved in 2018 by Wang et al by alloying Sb_2Te_3 with Bi_2Te_3 to produce PN junctions using a DM-MA-annealing-SPS process, as shown in figure 3.11[139].

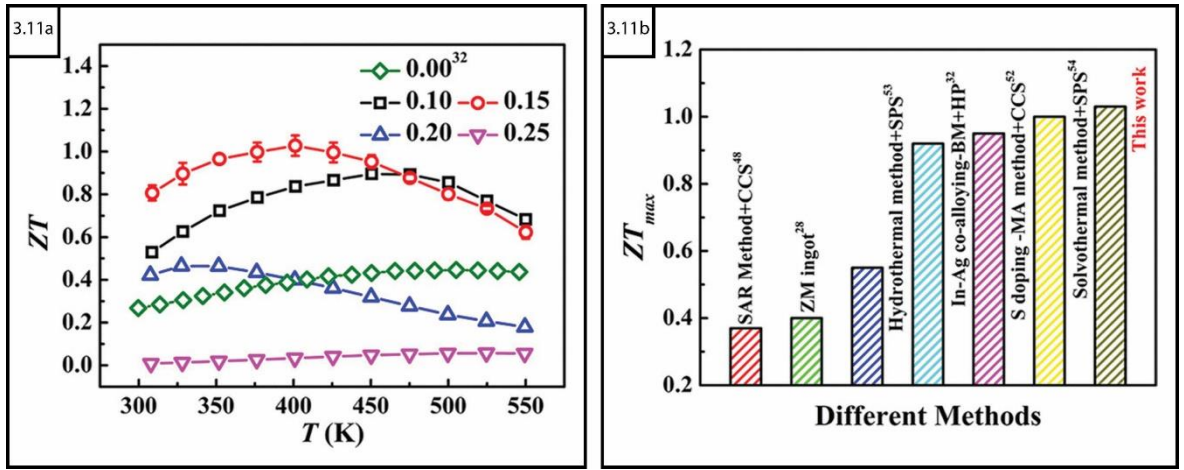


Figure 3.11: Plots of a) zT against temperature for $(\text{Bi}_2\text{Te}_3)_x-(\text{Sb}_2\text{Te}_3)_{1-x}$ PN junctions b) comparison of maximum zT for different synthesis methods. Reprinted (adapted) with permission from [139]. Copyright 2018 American Chemical Society.

3.3.10 Non-stoichiometric copper chalcogenides: Cu_xSe , Cu_xTe and Cu_xS

Copper selenide (Cu_xSe) and copper sulfide (Cu_xS) are formed from relatively abundant and non-toxic elements but have largely been overlooked as TEM candidates since studies carried out on the Cu_{2-x}Se structure in the 1960's reported mobility of the copper ions in the presence of an \mathbf{E} field resulting in decomposition during operation[54]. Interest has increased more recently due to the abundance and low cost of the starting materials, coupled with the potential for high performance if the final product can be made stable for operation. Copper chalcogenides are inherently non-stoichiometric with a tendency to generate both cation and anion vacancies and occasional Cu excesses. Stoichiometric Cu_2Se is a zero band gap material that behaves more like a metal with a relatively low $\kappa T = 0.98 \text{ Wm}^{-1}\text{K}^{-1}$ at room temperature; while Cu deficient Cu_{2-x}Se is a p-type semiconductor with reported ranges of direct $E_g = 2.1\text{--}2.3 \text{ eV}$ and indirect $E_g = 1.2\text{--}1.4 \text{ eV}$. Varying the Cu_xSe microstructure through stoichiometric manipulation produces little change in the direct band gap and the non-stoichiometric nature results in, for what other systems would be a simple chemical arrangement, a complex structure comprised of multiple Cu_xSe_y phases that become difficult to differentiate and characterise[140]–[142]. Similar to SnSe , Cu_{2-x}Se undergoes a phase transition from a highly ordered low temperature α -phase with a debated crystal structure (monoclinic, tetragonal and cubic have all been proposed) to a disordered $Fm\bar{3}m$ β -phase at $\sim 400 \text{ K}$. The greater disorder allows for increased σ , further enhanced by additional Cu vacancies; while the liquid-like nature of the Cu ions reduces κ_l , leading to overall improvement in all TE properties as shown in figure 3.12[143], [144].

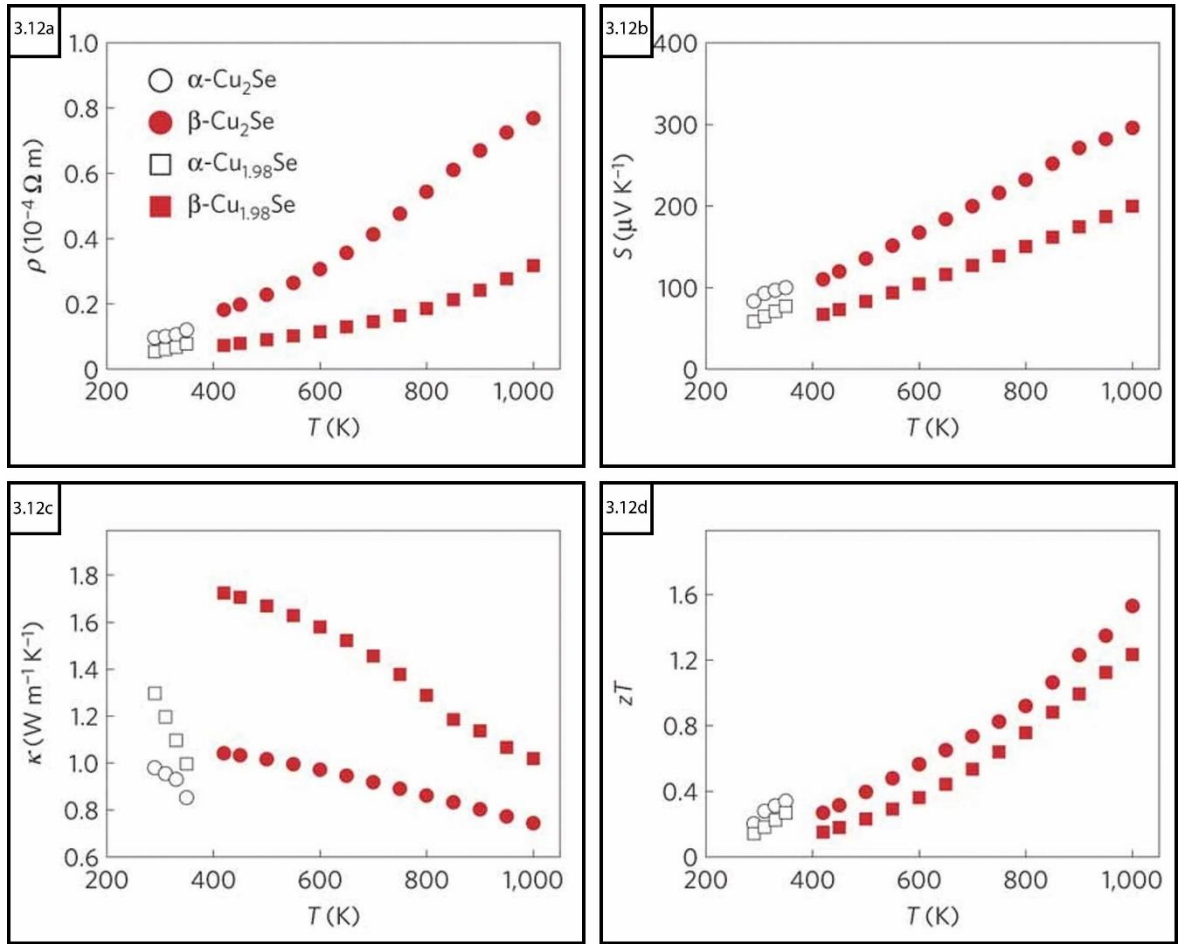


Figure 3.12: Plots of TE properties against temperature for low (α) and high (β) temperature phases of Cu_{2-x}Se a) electrical resistivity b) Seebeck coefficient c) thermal conductivity d) zT . Figure reproduced from ref. [143] with permission from Springer Nature

The structure allows Cu ions to be randomly distributed and capable of traveling between interstitial sites of the selenide planes, hence the description of liquid-like behaviour with respect restricted phonon movement in two axes rather than the usual three for most solids. This results in lower C_P and κ_T , which are correlated by the Dulong-Petit law as described in section 5.6.1[63], [65], [90].

3.3.11 Review of best reported copper chalcogenide synthesis methods

Liu et al reported a very low $\kappa_l \sim 0.5 \text{ W m}^{-1} \text{K}^{-1}$ at 1000 K and a PF of $12 \mu\text{W cm}^{-1} \text{K}^{-2}$ leading to a relatively high $zT = 1.5$ at 1000 K for the Cu_{2-x}Se β -phase prepared through DM at 1423 K for 12 hours, annealing at 1073 K for 7 days followed by SPS[143]. In 2013, the same research group synthesised polycrystalline samples of Cu₂Se_{1-x}I_x at very high T in a multi-stage heating regime lasting over 9 days followed by SPS. The samples showed that undoped polycrystalline Cu₂Se could reach $zT = 2.3$ at 400 K however the I-doped Cu₂Se_{0.96}I_{0.04} had zT closer to unity (Figure 3.13) but at lower T [145].

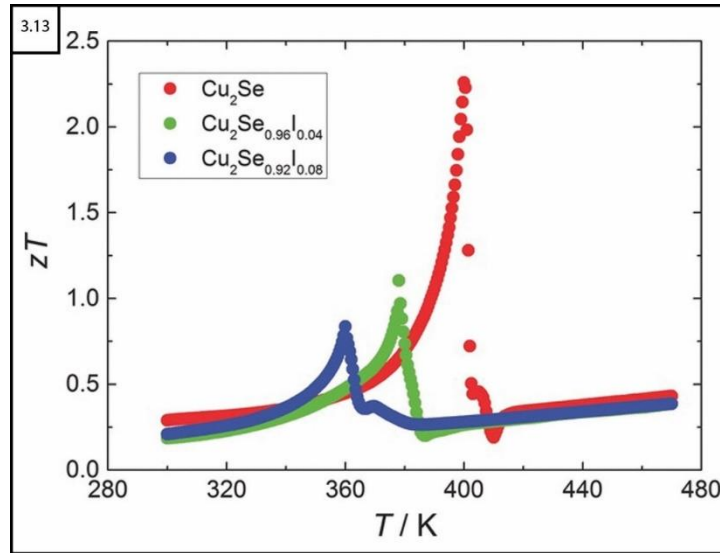


Figure 3.13: Plot of zT against temperature for undoped Cu_2Se and iodine doped $\text{Cu}_2\text{Se}_{1-x}\text{I}_x$ samples. Figure reproduced from ref. [145] with permission from John Wiley and Sons

In August 2014, Zhong et al enhanced Cu_{2-x}Se further with Al-doping in a DM-MA-HP process to reach a maximum $zT = 2.62$ at 756 K across the layer plane as shown in figure 3.14d, joining SnSe as one of the most efficient TEMs at the time[146].

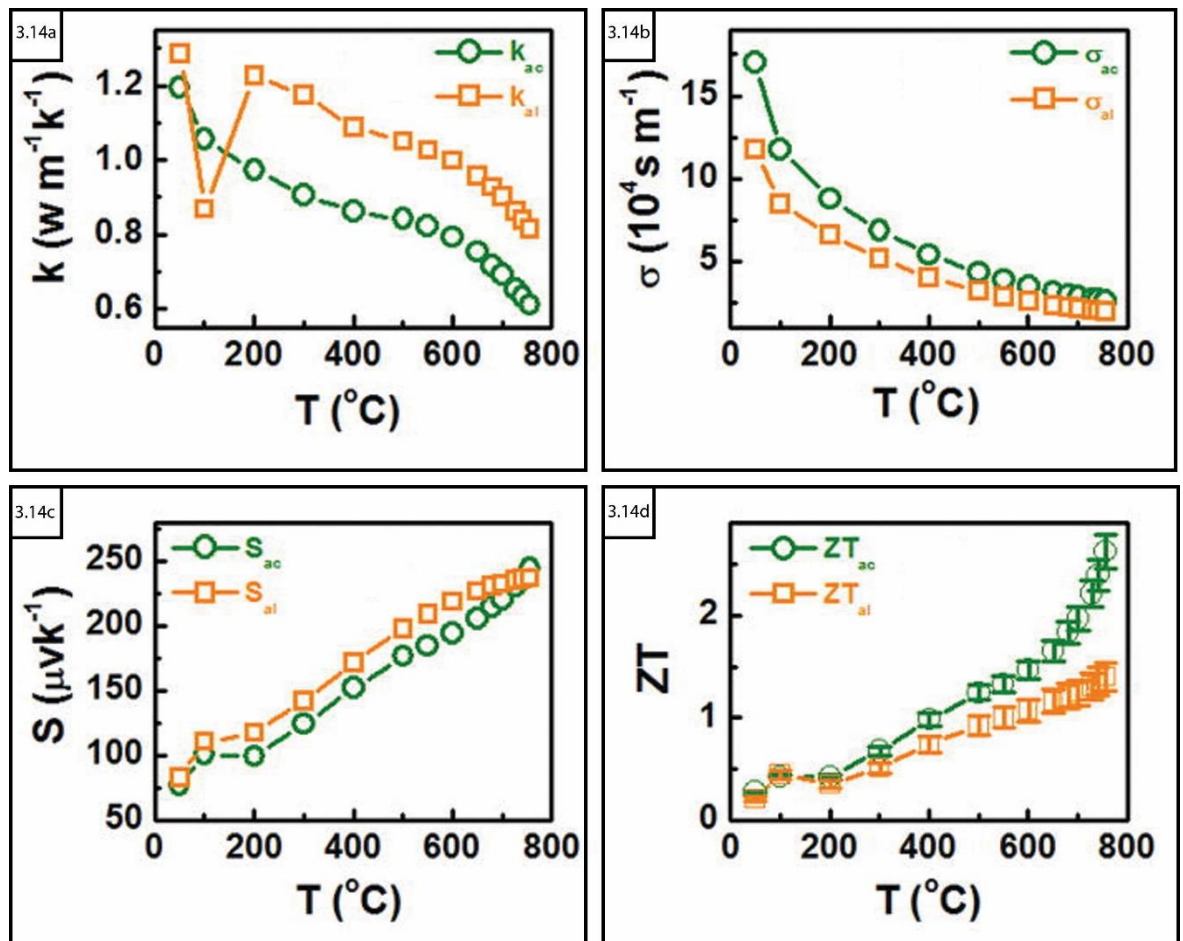


Figure 3.14: Plots of TE properties against temperature of $\text{Cu}_{1.94}\text{Al}_{0.02}\text{Se}$ measured across (ac) or along (al) the layer plane a) thermal conductivity b) electrical conductivity c) Seebeck coefficient d) zT . Figure reproduced from ref. [146] with permission from AIP Publishing

In 2017, Olvera et al achieved a comparable maximum $zT = 2.6$ at 850 K by nanocompositing Cu_{2-x}Se with In-doped CuInSe_2 using a similar DM-MA-HP process[147].

Copper telluride (Cu_{2-x}Te) has many stable phases but with weaker ionic bonding between the Cu and Te atoms compared to its selenide counterpart. It has a very high $\sigma \sim 10^8 \text{ Sm}^{-1}$. Samples synthesised through SPS have displayed a disappointingly low zT due to typically high $\kappa T = 2\text{--}4 \text{ Wm}^{-1}\text{K}^{-1}$ at room temperature. However, a direct annealing method that avoids the sintering process employed by He et al in 2015 was able to reduce n and thus κT leading to an improved $zT = 1.1$ at 1000 K[142].

Copper sulfide (Cu_{2-x}S) also known as chalcocite undergoes two phase changes with increasing T from monoclinic to hexagonal at 370 K, then to a superionic cubic phase above 700 K. In the superionic cubic phase, the structure is comprised of $Fm\bar{3}m$ S-ion sublattices with Cu ions located at various fractionally occupied positions and has been shown through multiple studies to have a very low $\kappa_l = 0.8 \text{ Wm}^{-1}\text{K}^{-1}$, with Cu_2S showing a particularly impressive $\kappa T = 0.36 \text{ Wm}^{-1}\text{K}^{-1}$ at room temperature[89], [142]. By controlling the amount of Cu in the structure through DM of stoichiometric elemental powders in a high temperature furnace at 1383 K for 18 hours followed by quenching in ice water, He et al produced $\text{Cu}_{1.97}\text{S}$ with a maximum $zT = 1.7$ at 1000 K[148]. A year later, Zhao et al enhanced the efficiency to a maximum $zT = 1.9$ at 973 K (Figure 3.15d) by using a melt-solidification technique whereby stoichiometric mixtures were pressed into pellets prior to two rounds of furnace heating (up to $\sim 1423 \text{ K}$) followed by gradual cooling to room temperature[149].

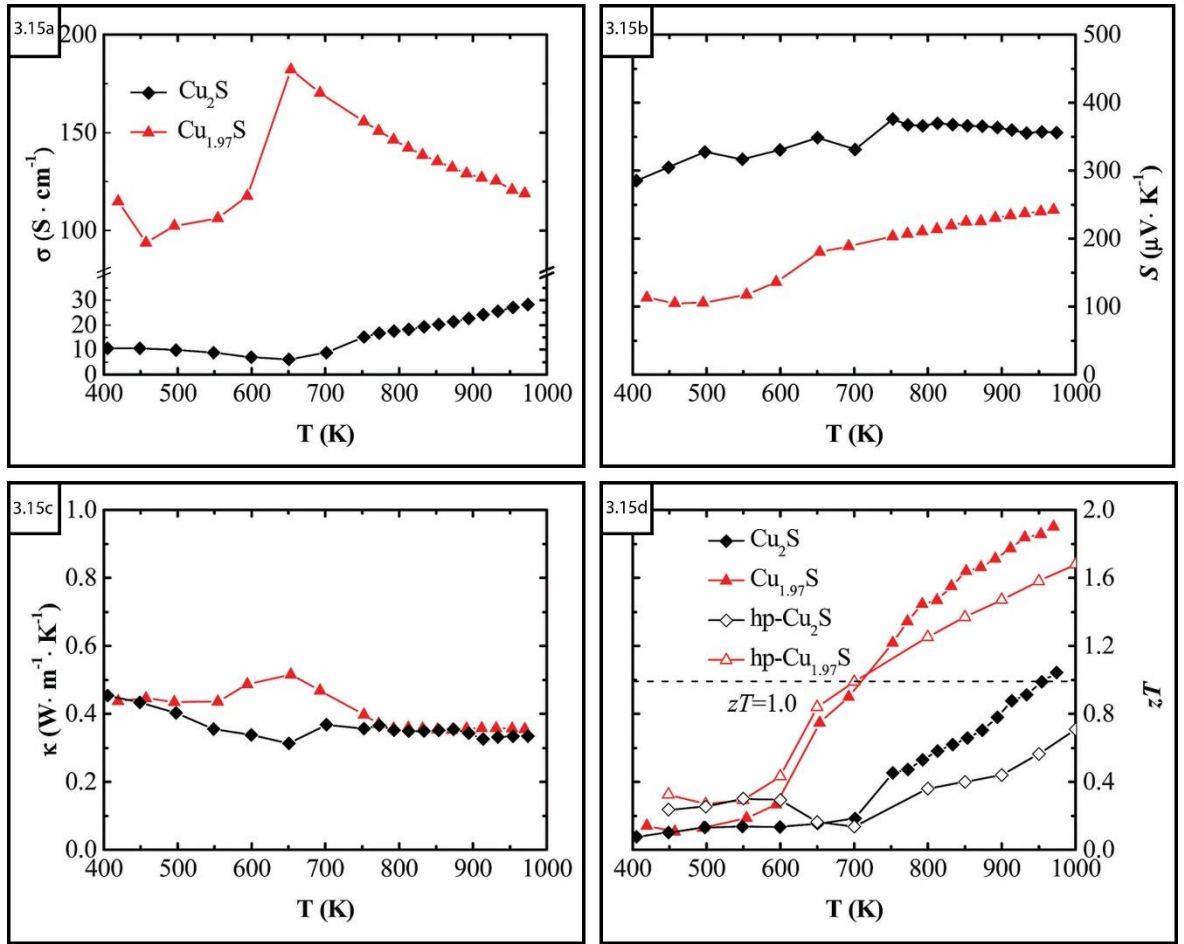


Figure 3.15: Plots of TE properties against temperature for Cu_{2-x}Se samples a) electrical resistivity b) Seebeck coefficient c) thermal conductivity d) zT . Figure reproduced from ref. [149] with permission from the Royal Society of Chemistry

S-doped Cu_{2-x}Se produced in 2017 via a DM/high T annealing process, reduced κT at high T leading to a maximum $zT = 2$ at 1000 K, an impressive 30 % increase of TE efficiency for the $\text{Cu}_{2-x}\text{Se}_{0.92}\text{S}_{0.08}$ sample compared to undoped Cu_2Se [150]. Partially substituted $\text{Cu}_{2-x}\text{Se}_{1-y}\text{Te}_y$ solid solutions have been previously synthesised in 2017 and 2018 through MA as well as by the DM/high T annealing process respectively. The series synthesised by Zhu et al in 2017 achieved a high $\text{PF} = 13.9 \mu\text{Wcm}^{-1}\text{K}^{-2}$ at 723 K for $\text{Cu}_2\text{Se}_{0.98}\text{Te}_{0.02}$ with a TE maximum $zT = 1.25$ at 773 K[151]. Similarly, from the samples produced in 2018, $\text{Cu}_2\text{Se}_{0.7}\text{Te}_{0.3}$ had the maximum $zT = 1.4$ at 1000 K which is still less than unsubstituted Cu_2Se as shown in figure 3.16[152].

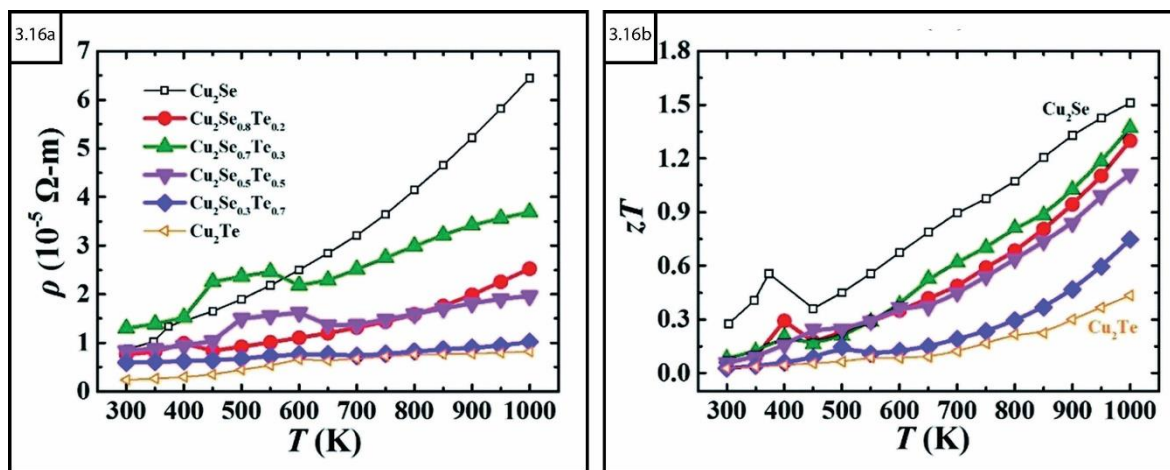


Figure 3.16: Plots of TE properties against temperature for Te-doped $\text{Cu}_2\text{Se}_{1-x}\text{Te}_x$ samples a) electrical resistivity b) zT . Figure reproduced (adapted) from ref. [152] with permission from the Royal Society of Chemistry

Although these values are less than the best performing Te- and S-doped samples mentioned previously, they are still >1 making them commercially viable and comparable to undoped Cu_{2-x}Se or Cu_{2-x}Te . At the time of writing, there are no reports of copper chalcogenides successfully synthesised using direct MW-heating of solid samples, or its effect (if any) on the non-stoichiometric phase mixture as a result. The ability to reliably prepare single phase samples of these materials is one of the main challenges to further studies of their performance and viability in useful devices.

3.4 Accounting for element abundance and toxicity

Research towards new and better TEMs considers influential factors outside the materials' performance within TEGs. Some of the best performing metal chalcogenides contain elements that are either rare or are susceptible to supply chain disruption. Figure 3.17 shows the reported median abundance of elements in the Earth's crust and seawater as reported in the CRC Handbook of Chemistry and Physics (97th Ed)[41]. Of the chalcogens, Te is much less abundant than Se while Bi metal is almost as rare as Au or Pt; and so, efforts to partially or totally replace these elements in high performance TEMs will be very beneficial. Certain elements common to high performance TEMs, such as Te, are toxic and so replacement with more benign substances will be essential for many commercial applications.

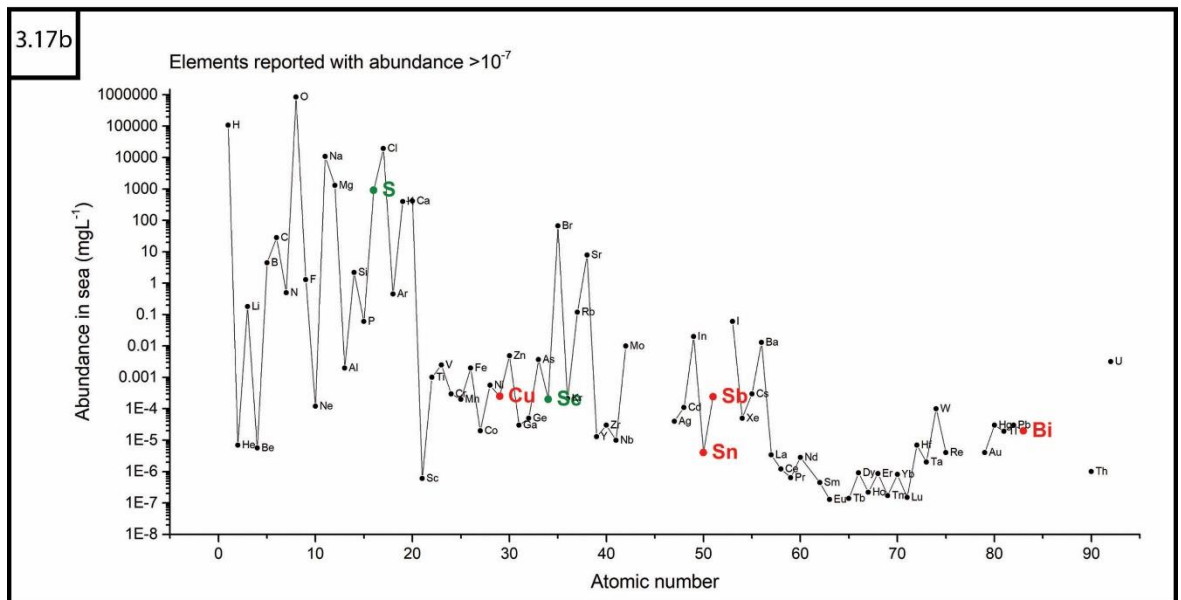
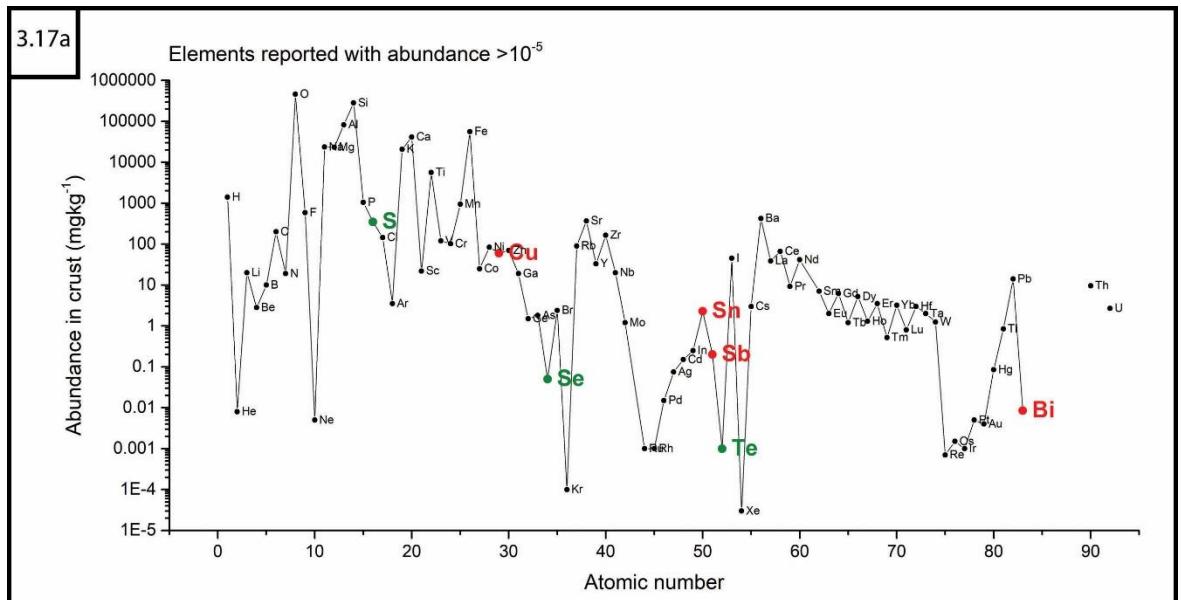


Figure 3.17: Plots of median chemical element abundance with metal elements used in this project highlighted in red and chalcogens in green. The estimated abundance a) in the crust is reported in mgkg^{-1} , equivalent to ppm by mass b) near the surface of seawater is reported in mgL^{-1} [41]

The relative supply risk is shown along with common physical parameters of the metals used throughout this project in table 3.2. The relative supply index ranges from 1 (very low risk) to 10 (very high risk) and is calculated by the Royal Society of Chemistry from abundance in crust, reserve distribution, production concentration, substitutability, recycling rate and political stability scores[153].

Despite the high performance of bismuth and antimony chalcogenides, the relative risk for both Bi and Sb is particularly high, making them less economical in the long term. Both Cu and Sn are significantly more abundant and likely to be more reliably sourced in the future.

Table 3.2: Physical properties and relative supply risk for selected metals[41], [153]–[155]

Metal	Copper	Tin	Antimony	Bismuth
Melting point (°C)	1084.62	231.928	630.628	271.406
Boiling point (°C)	2560	2586	1587	1564
Density (gcm⁻³)	8.96	7.287	6.68	9.79
Specific heat capacity (Jkg⁻¹K⁻¹)	385	227	207	122
Electrical conductivity at 273 K (Sm⁻¹)	6.481×10 ⁷	8.696×10 ⁶	2.564×10 ⁶	9.346×10 ⁵
Thermal conductivity (Wm⁻¹K⁻¹)	401	66.8	24.4	7.89
Dielectric constant	–	24	–	–
Relative supply risk	4.3	6.7	9	9

The toxicity of Se and S are < Te, making both especially attractive as partial or complete substitutions for Te in metal chalcogenides. The relative supply risk for S (Table 3.3) is very low, so endeavours to improve the synthesis procedures and TE performance of metal sulfides is an attractive avenue of investigation.

Table 3.3: Physical properties and relative supply risk for selected chalcogens[41], [153]–[155]

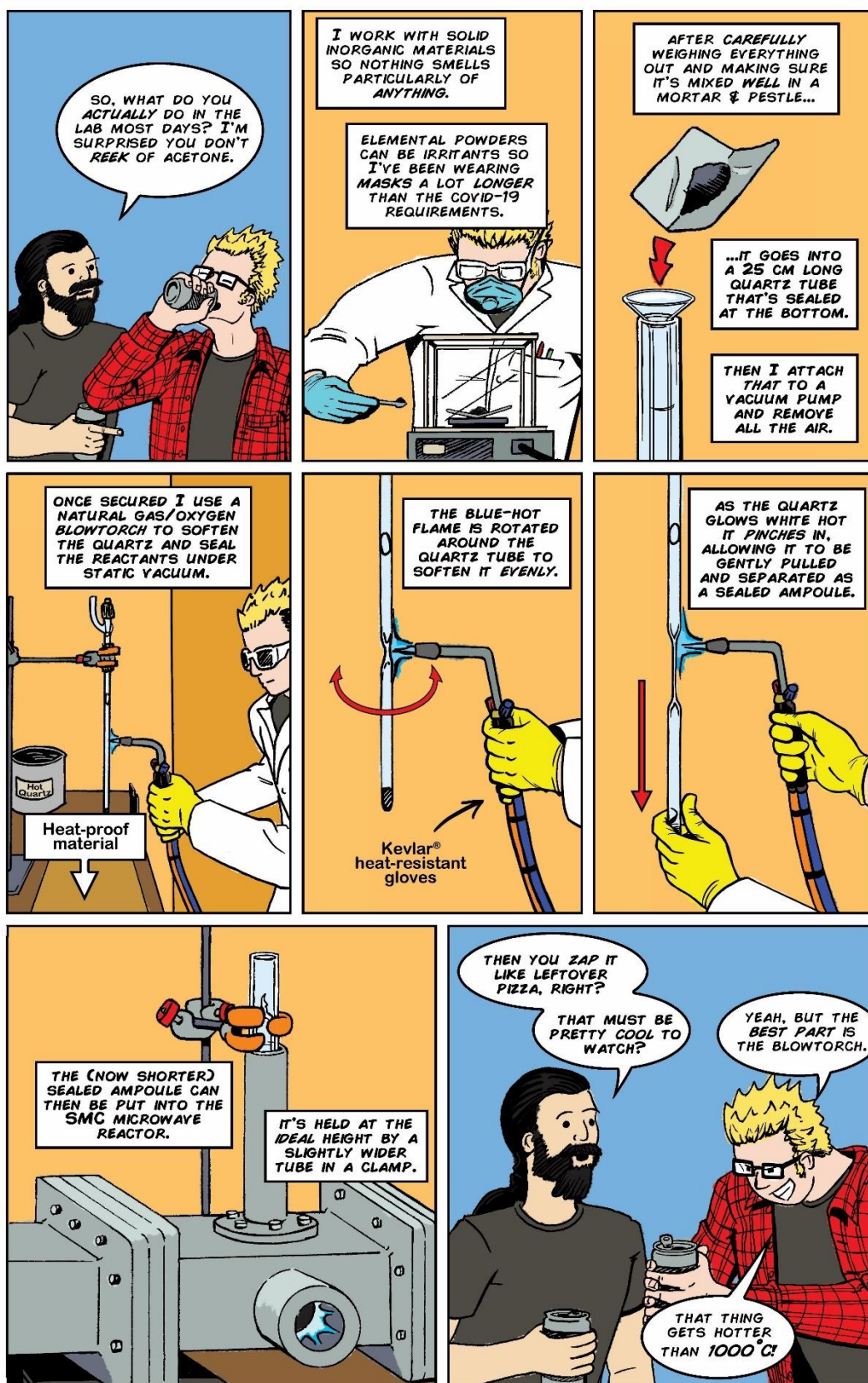
Chalcogen	Sulfur	Selenium	Tellurium
Melting point (°C)	115.21	220.8	449.51
Boiling point (°C)	444.61	685	988
Density (gcm⁻³)	2.07	4.809	6.232
Specific heat capacity (Jkg⁻¹K⁻¹)	708	321	202
Electrical conductivity (Sm⁻¹)	5×10 ⁻¹⁶	–	1×10 ⁴
Thermal conductivity (Wm⁻¹K⁻¹)	0.27	0.519	3.38 (to <i>c</i> -axis) 1.97 (⊥ to <i>c</i> -axis)
Dielectric constant	3.75 (ϵ_{11}) 3.95 (ϵ_{22}) 4.44 (ϵ_{33})	6	27.5
Relative supply risk	3.5	7.1	–

3.5 Summary

Since the early 2010s, a vast array of chemical systems that demonstrate the TE effect and show promise as potential TEMs, from skutterudites to metal oxides, have been investigated. Breakthroughs in greater efficiency of the best performing materials through doping and nanostructuring are reported yearly, and attention is being given to other important factors such as pivoting to more environmentally responsible, abundant and cost effective materials. In particular the binary metal chalcogenides like Bi_2Te_3 and its alloys have been some of the best performing TEMs available for many years. Awareness of the issues of supply chain risk and material toxicity has only grown stronger, and so efforts at reducing or replacing certain components like Te with more abundant and benign alternatives are escalating. These pursuits are not mutually exclusive to developing more efficient TEGs, exemplified by the landmark study from Zhao et al in 2014 that showed SnSe single crystals could outcompete the best performing TEMs at the time. This in fact has led to many novel materials being studied with some, like the copper selenides, now shown to be more viable than were originally assumed in the early to mid-20th century. Although the benefits of MW-induced syntheses have been known for a similar length of time as TEGs themselves, there have been few high profile examples of successful production using these methods. The rapidity of direct MW-heating should be ideal for TEM research by allowing for faster iterative design processes to be explored in developing new and better materials and devices.

4 Experimental design and procedures

4.1 Explaining the thesis to friends



4.2 Experimental design for benchtop microwave reactions

4.2.1 Sample preparation

All of the TEMs synthesised were produced from high purity elemental powders (at least 99.5 %) and mixed from a stoichiometric ratio or with an excess of a single reactant. The powders were carefully weighed out onto aluminium foil weighing boats in a Fisher Brand PS-200 analytical balance which has an associated error of ± 0.0005 g. The handmade weighing boats were easier to manipulate and reduced material loss from adhesion compared to plastic boats. Once weighed the starting materials were ground to a fine, homogenous mixture using an agate mortar and pestle then transferred into an 8 bore, 12 mm OD quartz tube (already sealed at one end) that had been cut to size using glass cutting tools as shown in figure 4.1. A long-stem funnel was used during sample loading to limit material adhesion along the length of the quartz walls.

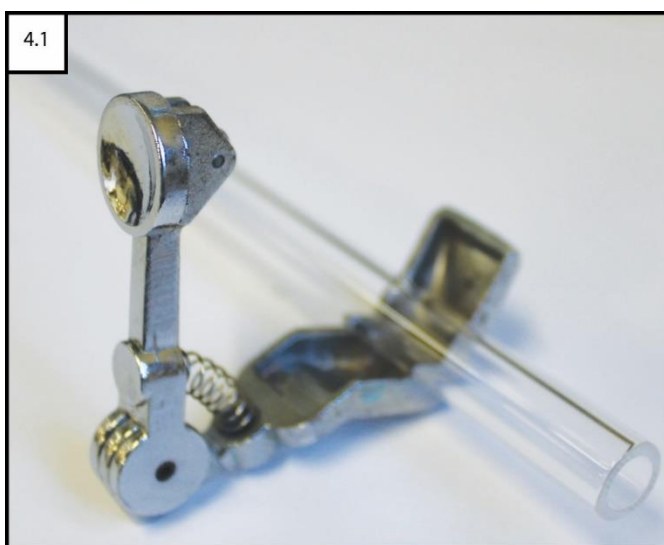


Figure 4.1: Handheld glass tubing cutter used to prepare quartz tubes of the correct length for microwave synthesis experiments

Certain samples proved to be highly reactive and so in specific cases (see chapter 8) the powder was pressed into pellets with a Specac 5 mm diameter pellet die under ~ 1 ton of pressure using a pneumatic press. Once loaded with either powder or pellet, the tube was attached using Swagelok Ultra-Torr vacuum fittings (Figure 4.2a and 4.2b) to a Young's tap (Figure 4.2c) with a glass wool plug inserted into the tube near the opening.

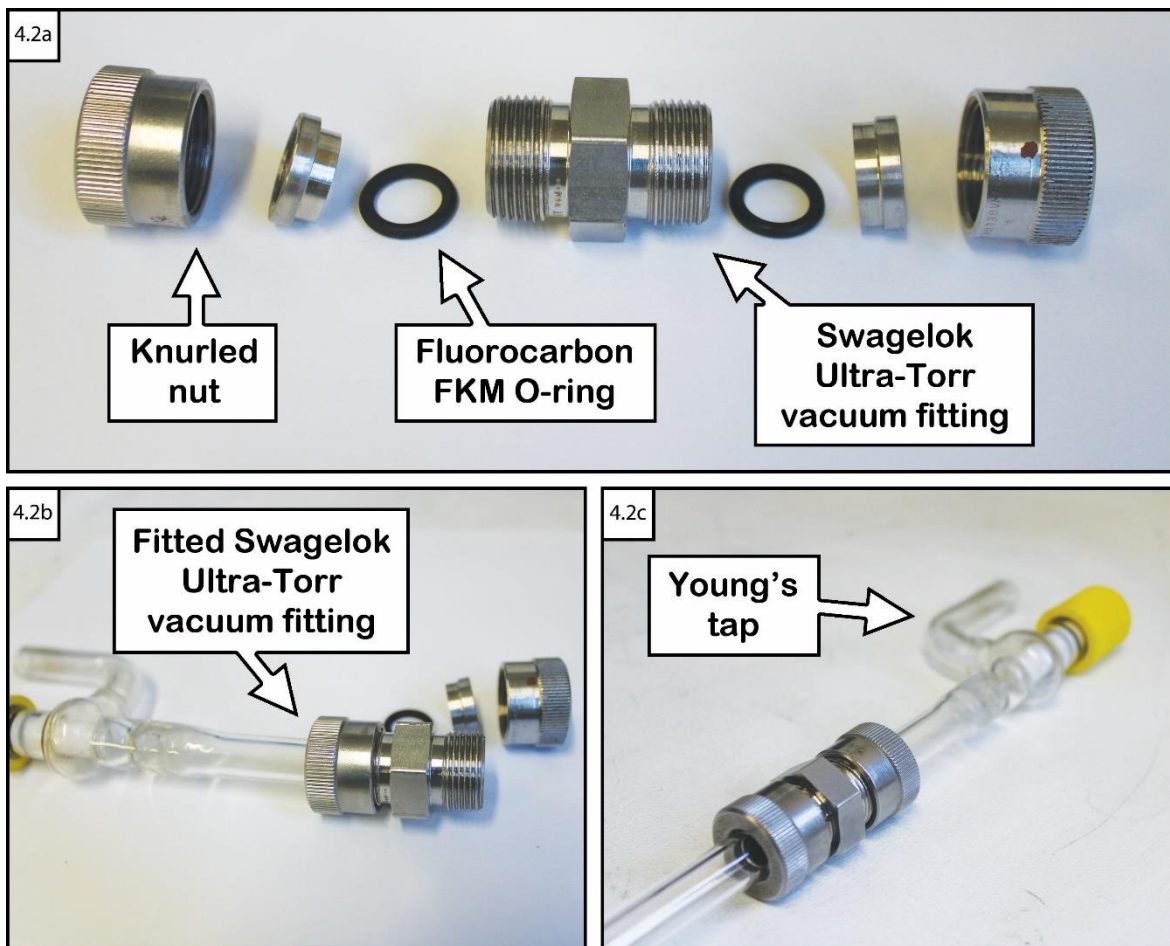


Figure 4.2: a) Swagelok Ultra-Torr vacuum fitting components b) Young's tap connected to Swagelok Ultra-Torr vacuum fitting c) complete attachment of Young's tap to quartz tube containing sample

The Young's tap is a branched quartz tube with a threaded Teflon® stopper able to be hand-tightened, and used to close off a section of quartz tube attached to the bottom. The top of the tap was connected to an Edwards oil-sealed rotary vane vacuum pump and a Balzers TPH-240 turbo pump connected in series (Figure 4.3). The pumps were used to remove the air in the sample tube down to a vacuum level of $\sim 10^{-6}$ mbar. The glass wool plug inserted into the tube acted as a safeguard against powder being accidentally drawn into the vacuum pump and causing damage.

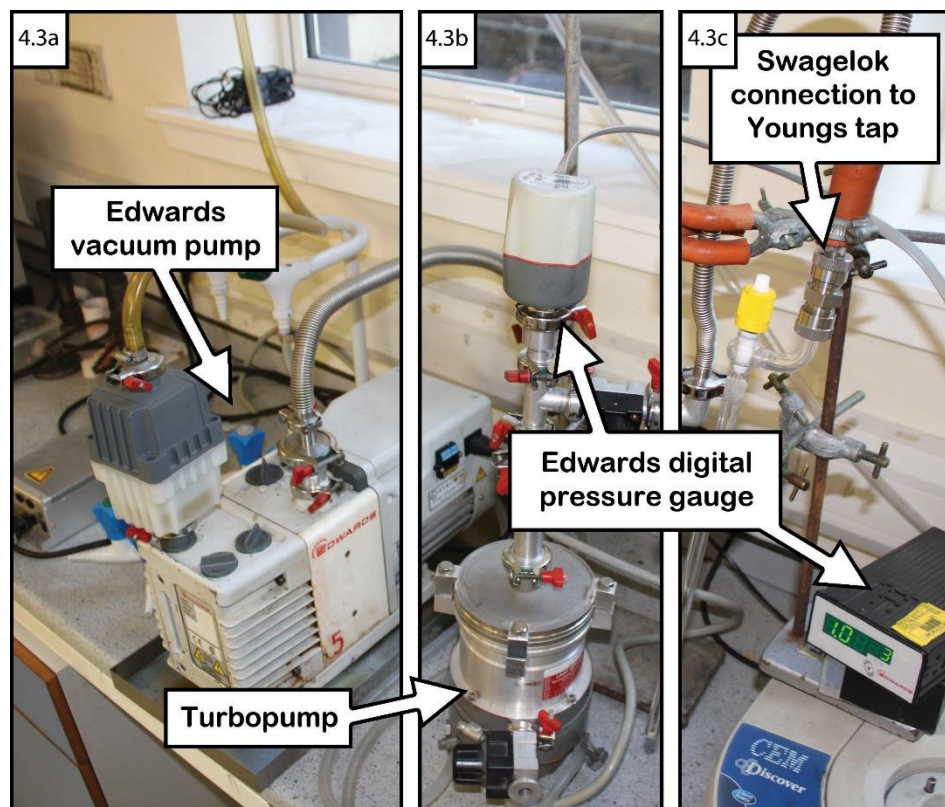


Figure 4.3: a) Edwards oil-sealed rotary vane vacuum pump b) Balzers TPH-240 turbo pump c) Edwards low pressure vacuum pressure gauge

Once the desired vacuum level was confirmed with the Edwards wide range gauge, the tap was closed to maintain a static vacuum and the quartz tube moved to the glassblowing station. A natural gas/oxygen blow torch, able to reach temperatures as high as 2770 °C, was used to evenly heat the quartz which has a softening $T \sim 1600$ °C [156]. Quartz glass emits a bright glow of radiated heat as it reaches such high T that can damage the eyes, and so protective eyewear rated to shade 6 for use with gas welding and cutting equipment was used. The quartz was carefully separated, creating a sealed ampoule holding the sample under vacuum and placed on a heat proof mat or brass sheet to cool to room temperature.

4.2.2 Sample heating in modified domestic microwave oven (DMO)

A DMO directs MW energy into the heating cavity such that the waves reflect off the cavity walls at random and create multiple modes where heating is localised. A Sharp R-272(SL)M was modified prior to the start of this project to disable and remove the turntable and drill a hole through the top of the cavity to allow samples to be introduced vertically. A MW mode was identified by systematically heating a small sample of graphite in a beaker at various points in the cavity until it was observed to glow due to efficient MW absorption. The hole drilled into the cavity from the top of the instrument was positioned above

this heating mode and was fitted with an extended metal tube to allow precise placement of experiment samples as shown in figure 4.4.

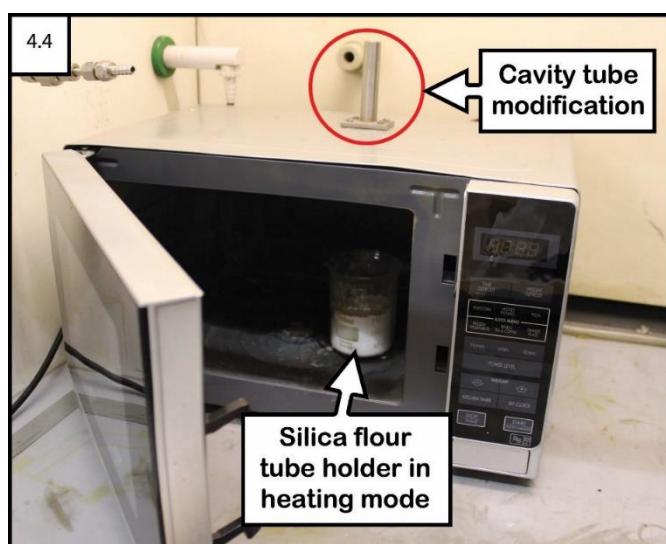


Figure 4.4: Modified Sharp R-272(SL)M domestic microwave oven with beaker of silica flour positioned under customised tube access

The tube diameter was chosen to allow a 12–14 mm OD ampoule to be introduced into a beaker containing silica flour for vertical stability while being narrow enough to prevent MW leakage. The modified DMO experiments were conducted inside a fume hood to vent any escaping gas or volatile material in the event of the quartz containment being compromised. A Perspex[®] screen was used along with the fume hood sash as a blast shield in the event of rapid, vigorous combustion of the sample. A Testmate MW-100 microwave leak detector was placed between the operator and the instrument and the modified DMO operated at full power for a predetermined duration.

4.2.3 Sample heating in a bespoke single mode cavity (SMC) reactor

DMOs do not provide a great deal of control over individual reaction parameters and can be difficult to modify to allow for *in-situ* temperature measurements. The benchtop SMC reactor is a modular system constructed from components purchased from Gerling in 2015, two years prior to the start of this project. Each component was purchased in duplicate so that the benchtop instrument would be directly analogous to the Polaris-SMC reactor at ISIS. The sample applicator on the benchtop instrument features ports with diameters $\ll \lambda_c$ on the front and rear faces that allow for ventilation and line-of-sight for an infrared (IR) thermometer as shown in figure 4.5b.

The benchtop SMC reactor was permanently set up on a table adjacent to a bank of fume hoods to provide access to a dedicated water supply for the 2-port isolator

(figure 4.5d) as well as a high voltage three phase power outlet for the 1.2 kW power supply (figure 4.5f). Both benchtop and Polaris-SMC reactors are controlled with a Gerling GA3210 dual digital microwave power meter (figure 4.5f) which allows power outputs ranging from 0 W up to a maximum of 1 kW. A warning indicator was set for power output >800 W to safeguard against damage to the magnetron from reflected power. Further details of each of the components are discussed in greater detail in section 6.3.

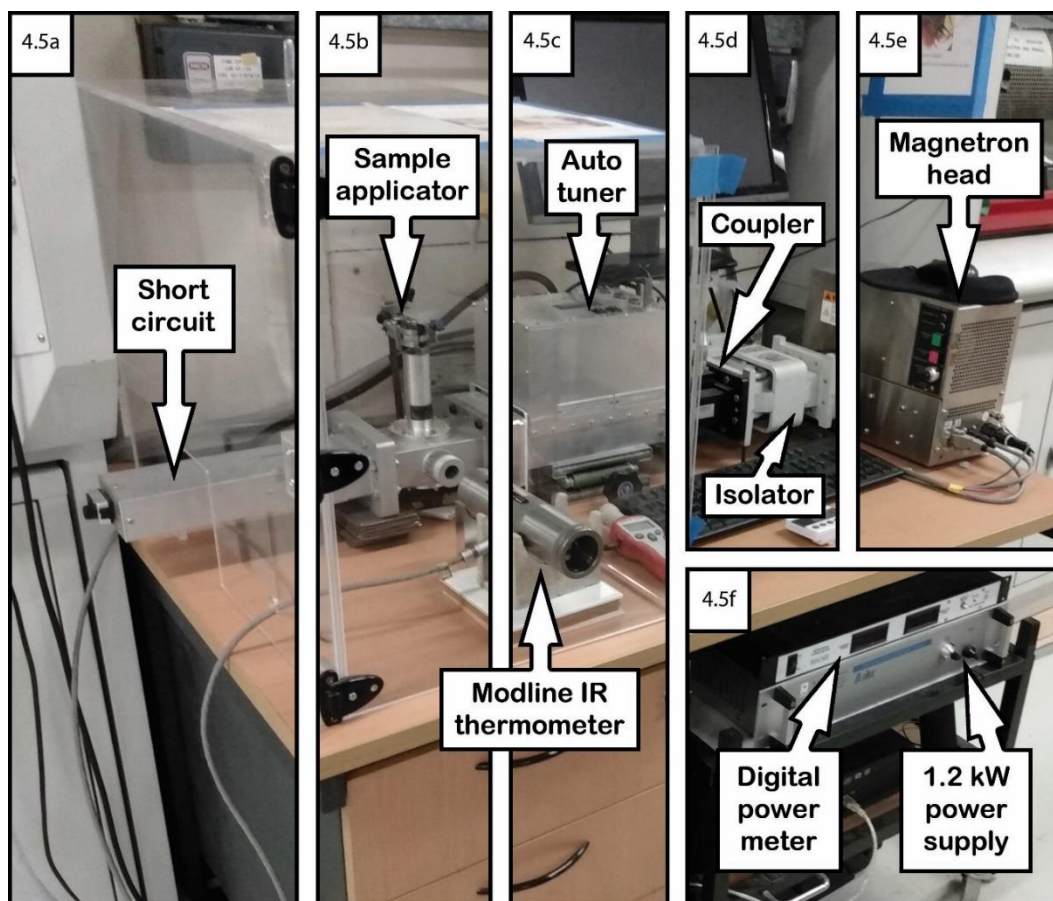


Figure 4.5: Benchtop SMC microwave reactor configuration a) manual sliding short circuit b) sample applicator c) auto tuner and Ircon Modline 5G2024 infrared thermometer d) directional waveguide coupler and 2-port isolator e) magnetron head f) digital power meter and 1.2 kW power supply

The quartz ampoule proved to be reliable containment in the modified DMO and so no additional ventilation was considered necessary when experimental work moved to the benchtop SMC reactor; a custom Perspex® box was fitted around the sample applicator as a blast shield. A 20 bore, 22 mm OD quartz tube was clamped in place through the metal tube on the top face of the sample applicator at a position that was visually confirmed to reside in the centre of the waveguide. The support tube ensured successive experiments carried out would have as little variation as possible between sample positioning in the heating mode. For experiments requiring the use of a graphite susceptor, a small quantity of graphite was transferred to a similar 20 bore, 22 mm OD quartz tube to a depth

of ~5 mm into which the sealed ampoule was allowed to rest in direct contact. A checklist for the operation of the benchtop SMC reactor is available in appendix section A–4.1. A digital lab timer was used to record the MW exposure and reaction durations, with the reaction start point typically signalled by the appearance of a bright blue glow from the sample applicator (due to arcing from the metal powder or sustained plasma formation) as shown in figure 4.6, sudden reduction in reflected power or rapid increase in T .

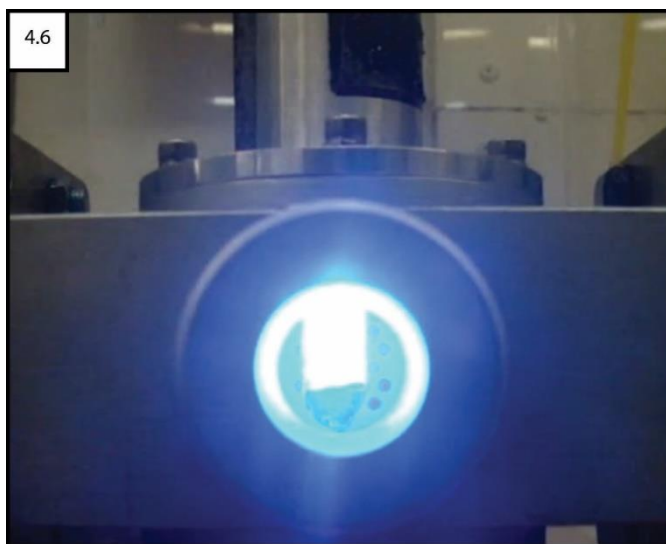


Figure 4.6: View through front face port of sample applicator in the midst of a tin selenide synthesis showing sustained plasma formation

Although each of these indicators tended to be observed simultaneously, certain chemical systems would present one more strongly than others. After the induction period, heating was allowed to progress for the pre-determined synthesis duration before the magnetron was switched off.

4.2.4 Sample collection from benchtop experiments

Once the ampoule had returned to room temperature, regardless of heating method, it was scored with a glass cutting tool while wearing rubber work gloves and carefully broken open by hand and the contents removed by scraping and tapping with a thin spatula. Samples that were tightly lodged within the tube (typically larger ingots) were removed by cracking the ampoule with the aid of a bench vice and collecting as much of the material as possible with tweezers. The products were finely ground using a mortar and pestle then weighed in the analytical balance before being transferred to a labelled sample vial for further analysis. As discussed in chapter 8, bismuth was found to be easily oxidised in air so most of those samples were prepared and collected inside an MBraun LABstar pro glovebox under a N_2 atmosphere.

4.3 Experimental design for *in-situ* neutron reactions

The Polaris-SMC reactor is comprised of identical components to the benchtop kit with some adjustments to waveguide geometry and sample handling procedures. To enable *in-situ* data collection of MW reactions the sample applicator must be inside the diffractometer sample tank with the access well of the Polaris instrument locked to users once the beam shutters have been opened. A detailed discussion on the various design considerations and how the Polaris-SMC reactor was set up at ISIS can be found in section 6.4.3.

4.3.1 Maximising sample volume for Polaris neutron beam dimensions

In total, 52 samples were prepared for *in-situ* neutron diffraction experiments with the 8 mm bore, 12 mm OD quartz ampoules loaded to a depth of ~40 mm to allow maximum cross-sectional interaction with the 40 mm neutron beam height. To achieve this depth ~5 g of material was sufficient in most cases although the Cu-Se-Te mixtures required only ~3 g of material and Cu-Se-S samples needed to be cold-pressed as $3 \times \sim 1$ g pellets. The sample height within the waveguide was visually checked with a spare sample applicator. Examples of S powder and $\text{Cu}_{1-x}\text{Se}_{0.8}\text{S}_{0.2}$ pellets are used to illustrate the ampoule positioning within the waveguide in figures 4.7a and 4.7b respectively.

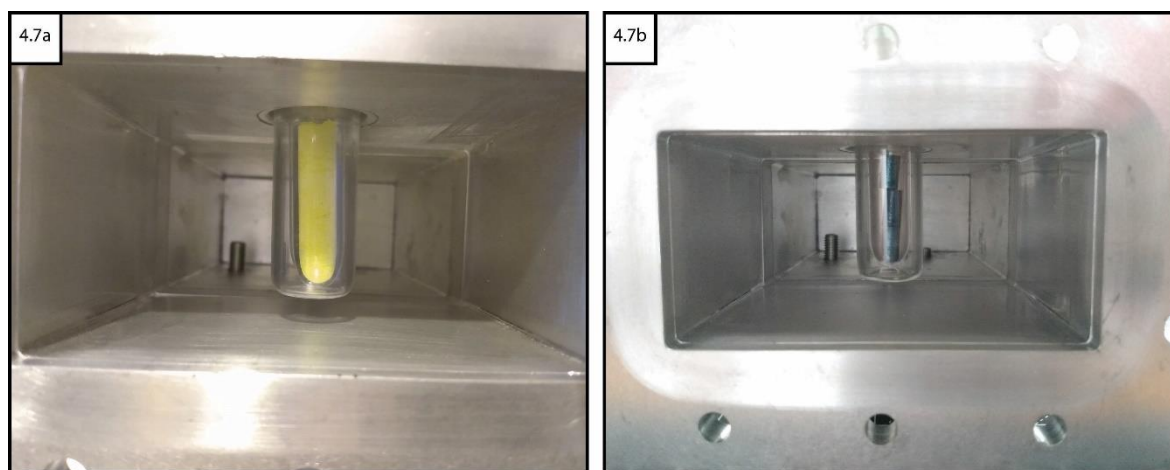


Figure 4.7: Interior view of sample applicator waveguide with a quartz support tube in position holding a sealed quartz ampoule containing a) ~40 mm depth of sulfur powder b) three 1 g pellets of $\text{Cu}_{1-x}\text{Se}_{0.8}\text{S}_{0.2}$

All ampoules were evacuated and sealed at a height of ~90 mm (Figure 4.7) due to limitations with the ampoule support block as discussed in section 6.4.2.

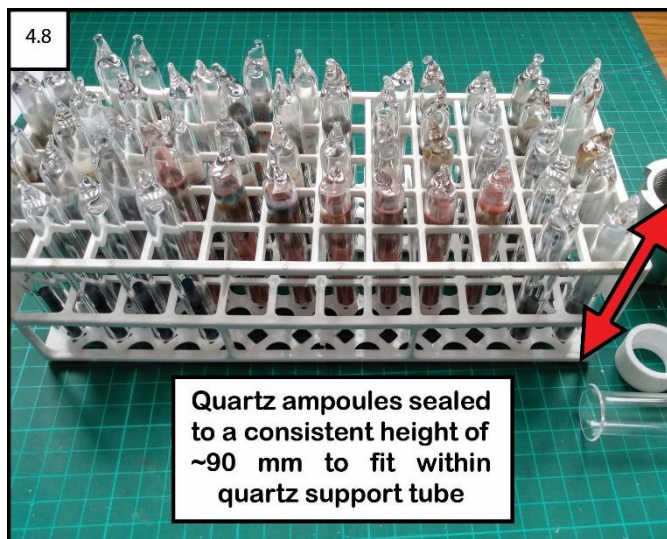


Figure 4.8: Test tube rack containing 52 starting material mixtures for $\text{SnSe}_{1-x}\text{Te}_x$, $\text{SnSe}_{1-x}\text{S}_x$, $\text{Sb}_2\text{Se}_{3-x}\text{Te}_x$, $\text{Bi}_2\text{Se}_{3-x}\text{Te}_x$, $\text{Cu}_{1-x}\text{Se}_{1-y}\text{Te}_y$ and $\text{Cu}_{1-x}\text{Se}_{1-y}\text{S}_y$

Two additional ampoules were evacuated to $\sim 1 \times 10^{-6}$ mbar and sealed, one of which was empty and the other containing ~ 40 mm depth of graphite powder, in order to generate a background histogram and calibrate the MW power meter and short circuit when on site at ISIS.

4.3.2 Collecting pre reaction, in-situ and post reaction neutron data

The Polaris-SMC reactor was operated in mostly the same manner as the benchtop counterpart, with specific operational adjustments discussed in section 6.4.3. Background datasets to be subtracted from the event mode data were created from ~ 15 μA histogram scans (corresponding to ~ 5 minutes) of the following sample environments:

- Empty waveguide
- Waveguide + empty quartz support tube
- Waveguide + quartz support tube + empty quartz ampoule
- Waveguide + quartz support tube containing ~ 5 mm graphite susceptor

Histogram mode is a method of collecting neutron data cumulatively, with longer collection periods resulting in greater resolution. Event mode enables recording of neutron data against an independent variable such as temperature, pressure or absolute time depending on the requirements of the experimental design. For this project, the event mode data was recorded against absolute time to allow the data to later be split into discrete slices of a user-defined length. The neutron data collected in event mode could also be correlated with the MW absorption profile, which was also recorded against absolute time. A checklist for the operation of the Polaris-SMC reactor is available in appendix section A–

4.2. All of the *in-situ* Polaris-SMC commissioning experiment data was recorded using the same general three-part process. For each sample a $\sim 15 \mu\text{A}$ histogram scan of the starting materials was collected prior to heating. An event mode scan was initiated prior to sample heating and the data collection recorded throughout the duration of the planned synthesis; along with an extra 1–2 mins after MW power was switched off to record the beginning of sample cooling. A second post reaction $\sim 15 \mu\text{A}$ histogram scan of the products was collected while the sample cooled to room temperature. The pre- and post-reaction histograms were able to be processed and visualised using the Mantid Workbench software as detailed in section 5.3.8[157].

4.4 Data acquisition for reaction optimisation

A Dataq Instruments DI-1100 4-channel data acquisition (DAQ) module was used to interpret the voltage signals sent to the power meter from the coupler probes connected to the waveguide. The forward and reflected power signals were displayed on a scrolling display in real time using the WinDAQ software on a nearby workstation. This method of recording *in-situ* power profile data was used with both the benchtop and Polaris-SMC reactors; the implementation of the DAQ is discussed fully in section 6.3.12.

4.4.1 *Measuring the temperature of microwave reactions*

Accurate measurement of sample T in a MW reactor is complicated by the presence of the high energy fields within the cavity as conventional thermometers and thermocouples will interact with and distort the fields to produce arcing. The metal probes could also cause interference with the thermocouple signal or act as an antenna that creates interference for other instruments. A shielded thermistor is typically used in DMOs to warn of dangerous levels of overheating however, they tend to have a maximum operational limit of $\sim 100 \text{ }^\circ\text{C}$. To operate within an EM field the thermistor must be grounded to the waveguide wall and terminate inside a MW absorber that can completely attenuate the waves within a few cm. This shielding is not usually suitable since unless the probe is fully protected by the dielectric absorber it will accumulate enough charge to produce electrical arcing. Thermocouples can have the same issues if they are likewise made of metal and not completely shielded[4], [14], [158]. Fibre optic devices can be used *in-situ* as the instrument material does not interact with MW energy, being typically made

of glass or plastic that is transparent in an EM field. Fibre optic probes have a typical operating limit of ~ 250 °C and so are most suitable for applications using pressurised acid digestion vessels, which would require a specialised closed Teflon® sleeve and tight fittings. Throughout this project, solid state samples were all sealed inside quartz ampoules, making the incorporation of an insulated wired probe or fibre optic cable during the sealing process extremely impractical. Also, MW-heating of solids typically reach temperatures in the range of hundreds to thousands °C depending on how well they couple [14], [158].

An Ircon Modline 5G2024 infrared (IR) thermometer, which has a temperature range of 350–2000 °C, was determined to be the simplest solution for this application. The IR thermometer was aligned with the front face port rather than above the sample applicator, as shown in figure 4.9, to monitor and record the surface temperature of a sample through the ampoule during heating.



Figure 4.9: Ircon Modline 5G2024 infrared thermometer aligned with front face port of sample applicator

This configuration was chosen to minimise the amount of quartz between the sensor and the sample as well as requiring fewer clamps and operational steps to safely transfer ampoules between experiments. The IR thermometer was aligned with its target by visually sighting the sample through a lens built into the body of the device. The instrument was connected to the same workstation as the DAQ module and the Modline software was run concurrently during system operation. The software displayed the temperature in a scrolling display within a user-defined window of time; the data were then saved in .csv format against absolute time once the experiment was concluded. Since only temperatures >350 °C were within the observable range of the instrument, it

was not possible to record any temperature profiles during the induction period of the syntheses. The time period of the data was typically set at 300 s to ensure the duration of a typical reaction was captured, along with an additional buffer for the duration of sample cooling. Differences in the timing between the events observed in the power and temperature data when overlaid indicated that the software clocks for each DAQ device were out of sync by a few seconds. To resolve this, the temperature data was offset to match up with a known event in the power profile, typically the cessation of MW power at the end of the experiment. Although the sample volumes being measured were relatively small, the formation of hotspots or sustained plasma means that the recorded temperature may not be representative of the bulk of the material and the heating profiles of dissimilar material mixtures undergoing a reaction tend to be more erratic than the expected steady heating profile of a typical dielectric such as graphite.

4.4.2 Impedance matching in a waveguide applicator

Characteristic impedance (Z_0) is the ratio of voltage to current for a wave travelling in one direction without interference from reflections and is determined by the properties of the medium in which it is propagating. MWs propagating in a waveguide can be analogised to the transmission of electrical power along an infinitely long line where Z_0 represents resistance in the line but is defined by the ratio between the alternating \mathbf{E} and \mathbf{H} fields of the wave; and as per Maxwell's equations, in terms of ε and μ [14], [159]:

$$Z_0 = \frac{V_{in,t}}{I_{in,t}} = \frac{\mathbf{E}}{\mathbf{H}} = \sqrt{\frac{\mu}{\varepsilon}} \quad \text{(Equation 4-1)}$$

MWs transmitted through matter will have a different impedance to that of free space ($\eta = 377 \Omega$), with some being reflected from the surface and some being absorbed and either transmitted or attenuated and dissipated as heat. For efficient heating to occur, energy must be transferred from the generator (magnetron) to the load (sample) with minimal loss, which is accomplished by matching the internal resistance of the generator (R'_G) to that of the load resistance (R'_L). Typically for MWs there are two limiting factors in minimising power loss, the first is Ohmic losses due to induced current in the conductive waveguide walls as a function of $P = I^2R$; usually a negligible percentage of the transmitted power. The second is the reflected power from the load which can be significant if optimum matching is not achieved[20]. If $R'_L < R'_G$ then the

greater current flow will result in more power being dissipated in the generator, leading to damage to the magnetron over time. If $R'_L > R'_G$ then the reduction in current due to the square law $P = I^2 R'_L$ means less power is dissipated as heat. The same principle applies to complex impedances in that the load impedance (Z_L) should be the complex conjugate of the generator impedance (Z_G) to facilitate optimum power transfer. Materials with $Z_L > Z_0$ will reflect most of the MW power, while those with $Z_L < Z_0$ will transmit the MWs without dissociating the power as heat. At higher f , such as used by MW generators, the waveguide distance between the generator and the load changes the apparent impedance of the load with respect to the generator. It becomes simpler to describe impedance matching in terms of the forward and reflected waves since the presence and magnitude of reflected power indicates loss in efficiency[20].

This relationship between impedance and EM fields is not as simple for a waveguide as that of resistance to current and voltage in a wire. EM waves are reflected by conductors; the \mathbf{E} lines must touch perpendicular to it (in the E-plane) while the \mathbf{H} lines must touch parallel to it (in the H-plane). For a rectangular TE₁₀ mode waveguide, described in section 2.2.5, the \mathbf{E} lines propagate normal to the broad wall (b) in the E-plane, while the \mathbf{H} lines propagate normal to the narrow wall (a) in the H-plane[160]. The wave impedance of a rectangular waveguide can be calculated from the following relationship between dielectric properties of the medium inside the waveguide (in this case air), f_c and f of the incident MWs[161]:

$$Z_0 = \frac{\eta}{\sqrt{1 - (f_c/f)^2}} = \frac{120\pi\sqrt{\epsilon_0\mu_0}}{\sqrt{1 - (f_c/f)^2}} = \frac{377 \Omega}{\sqrt{1 - (f_c/f)^2}} \quad \text{(Equation 4-2)}$$

f_c in WR340 waveguide = 1.74 GHz

The characteristic impedance of a WR340 waveguide at the 2.45 GHz microwave frequency is therefore 535.5 Ω .

While not precisely reflecting reality, the transmission line model is a very good approximation of waveguide impedance if the real equivalent circuit parameters are defined as analogues to the capacitance, inductance, conductance, and resistance per unit length of a conventional transmission line. The impedance is a complex value that consists of both a real (resistance) component that is

independent of f and an imaginary (reactive) component that is f -dependent. Due to the reactance component the total impedance will be f -dependent; with the general formula given by [23], [159], [162]:

$$Z_0 = \sqrt{\frac{R' + j\omega L'}{G' + j\omega C'}} \quad \text{(Equation 4-3)}$$

R' = Series resistance

L' = Series inductance

ω = Transmissibility of free space

The shunt conductance (G') and shunt capacitance (C') refer to the low resistance connection between two points in an electrical circuit; the formation of an alternate path for a current is the shunt or bypass. At a voltage node where the standing wave is at a minimum, if the cavity is detuned away from resonance, it can be represented by a shunt equivalent circuit. A voltage anti node, where the standing wave is at a maximum, is $\frac{1}{4}\lambda_g$ from the voltage node and is best represented by a series circuit. For a low loss system where $R' \ll j\omega L'$ and $G' \ll j\omega C'$, the characteristic impedance equation can be simplified to [20], [23], [159]:

$$Z_0 = \sqrt{L'/C'} \quad \text{(Equation 4-4)}$$

The series inductance in this context therefore refers to the tendency of a transmission line to oppose a change in current, and shunt capacitance is the tendency to oppose a change in voltage [159].

The parameters that determine Z_L of individual samples in this PhD project were measured using a PocketVNA portable vector network analyser. A two port matrix like the PocketVNA can collect data for four different S-parameters, each a complex value of magnitude and phase that is typically dependent on f and a measure of how much radio wave frequencies (RF) are scattered from specific input or output ports in the device:

S_{11} = Reflection coefficient (impedance match to input)

S_{12} = Reverse isolation (transmission coefficient of reverse power in a device)

S_{21} = Transmission coefficient of gain/loss between input and output ports

S_{22} = Reflection coefficient (impedance match to output)

Data was collected for the magnitude, phase (ϕ_t), resistance (R), reactance (X), complex impedance ($|Z|$), conductance (G) and voltage standing wave ratio (VSWR) across the frequency range of the magnetron head for both S_{11} and S_{22} parameters. The complex impedance is defined by the resistance and reactance and therefore means $|Z|$ is frequency dependent also:

$$|Z| = \sqrt{R^2 + X^2} \quad \text{(Equation 4-5)}$$

The measured impedances of the S_{11} parameters were plotted on Smith charts to graphically represent the extent of impedance matching. Smith charts like that shown in figure 4.10, are used to graphically represent the real and imaginary components of impedance values when plotted in a way that represents the extremes of open and short circuit conditions.

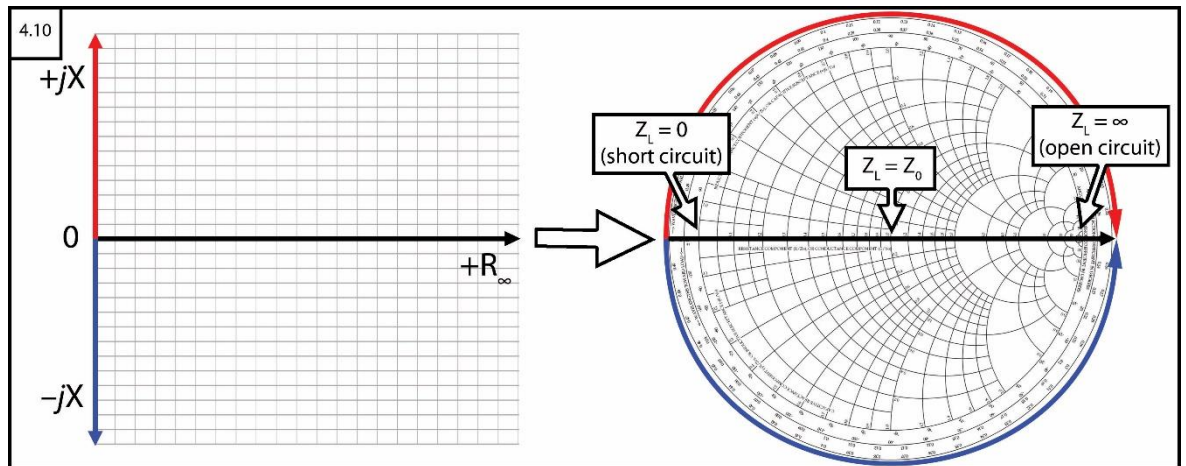


Figure 4.10: Transformation of the two-dimensional Cartesian complex plane into a circular Smith chart where positive real components are plotted inside the circle with respect to the horizontal axis. Blank Smith chart image modified from ETH Zurich, CC via Wikimedia Commons[163]

The horizontal x-axis through the middle represents the real component of the relationship; the scale is normalised with 0 (short circuit) on the far left, 1 (intrinsic load of the input device $\sim 50 \Omega$) in the centre and ∞ (open circuit) on the far right. The positive and negative imaginary components are represented by the circular y-axis that connects each end of the horizontal x-axis. As the data points tend towards Z_0 at the centre of the plot area the sample is considered to be better matched. The farther from the centre point of the Smith chart, the more reflected power will be returned to the magnetron in the functioning system which will affect the standing wave in the waveguide. Although a perfect impedance match with the generator is ideal, it is almost impossible to achieve in real systems such as this. Slight reflection of the incident power back to the

source due to physical imperfections in the RF connectors or circuit components can add constructively or destructively to cause mismatch loss.

The PocketVNA was connected to bespoke COAX-waveguide adaptors purchased from Aspen Electronics Ltd via standard SMA to COAX connector cables. The waveguide adaptors were secured to a spare sample applicator as shown in figure 4.11. The device was calibrated with the included short, open and load standards however this method is more typical for coaxial connectors rather than a hollow waveguide. Ideally, specialised adaptors are used to calibrate a VNA for a waveguide system as described in appendix section A-4.3.

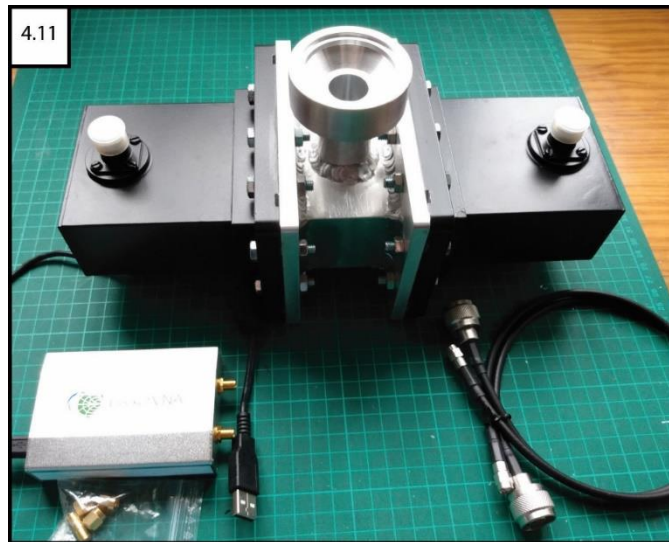


Figure 4.11: Spare sample applicator with attached COAX to waveguide adaptors shown sitting next to PocketVNA portable vector network analyser and SMA to COAX connecting cables

Each sample environment measurement was accumulated for ten repetitions to obtain average values, beginning with the empty waveguide, empty quartz tube and quartz ampoule containing graphite (Figures 4.12–4.14). The f range of the measurements was set to match the SMC magnetron output $f = 2450 \pm 30$ Hz. To begin, the empty waveguide recorded $Z_0 = 32\text{--}85 \Omega$ over the applied frequencies with 66Ω at $f = 2450$ Hz as shown in figure 4.12. This is much lower than the value for a WR340 waveguide calculated earlier as 535.5Ω and is due to the use of standard coaxial calibration of the PocketVNA rather than waveguide calibration.

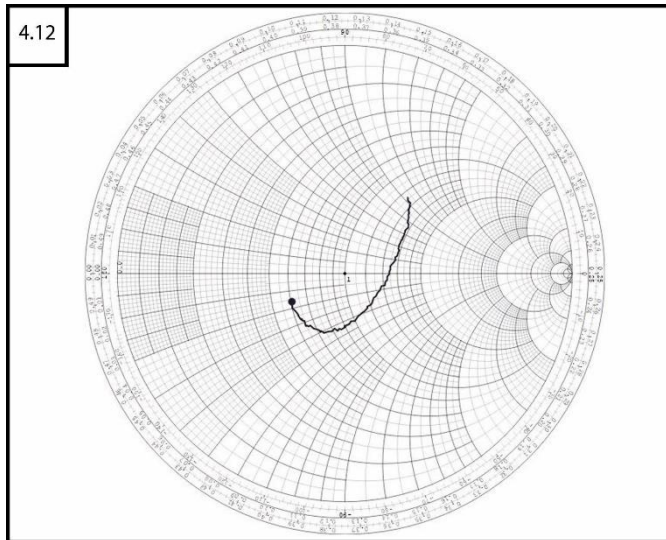


Figure 4.12: Impedance against frequency plot for an empty waveguide across the full frequency range of the SMC magnetron

The empty quartz tube within the waveguide yields a slightly larger $Z_0 = 30\text{--}90\ \Omega$ as shown in figure 4.13 with $60\ \Omega$ at $f = 2450\ \text{Hz}$ indicating most of the power is being transmitted as expected.

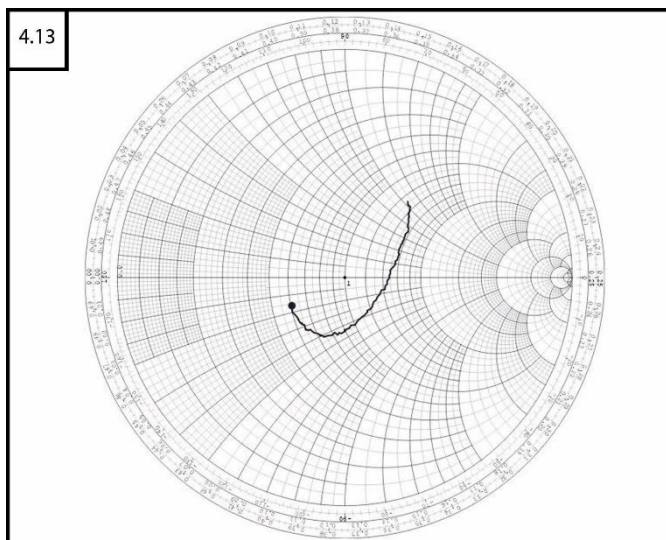


Figure 4.13: Impedance against frequency plot for an empty quartz tube across the full frequency range of the SMC magnetron

A sample of graphite featured a much larger $Z_L = 72\text{--}113\ \Omega$ as shown in figure 4.14 with $78\ \Omega$ at $f = 2450\ \text{Hz}$. The increased mismatch from Z_G at f indicates some reflection from the graphite even though the introduction of a dielectric into the waveguide would be expected to lower impedance. The increase is likely due to the non-ideal calibration procedure however, the difference is not very great which indicates a reasonable level of absorption regardless.

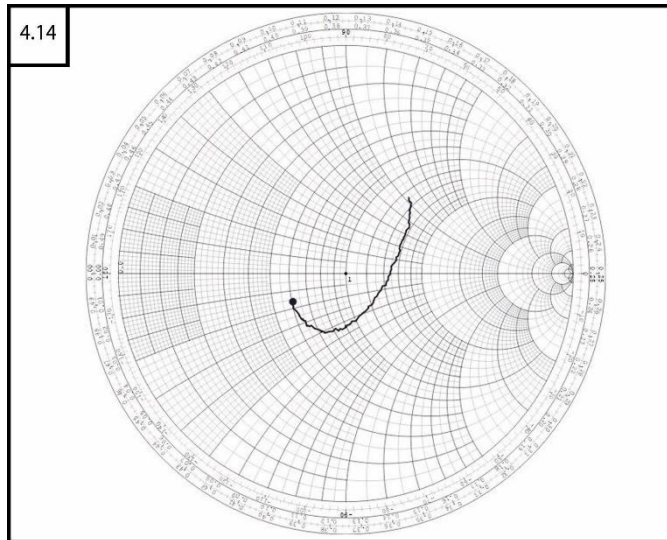


Figure 4.14: Impedance against frequency plot for a quartz tube containing a sealed quartz ampoule of graphite powder across the full frequency range of the SMC magnetron

The introduction of either a quartz tube or an ampoule containing graphite powder did not greatly affect the propagation of the MWs through the waveguide with $Z_0 = 60\text{--}78 \Omega$. The effect of performing a coaxial rather than a waveguide calibration for the empty waveguide determines that all measured impedances should be considered only with respect to the 66Ω for the unloaded sample applicator in indicating the level of potential MW absorption rather than as accurate measurement of Z_L for each material load.

4.5 Safety issues and risk assessment

Individual risk assessments and COSHH forms for the chemical and experimental hazards for all experiments conducted at the University of Glasgow and on site at RAL were adjusted appropriately in response to the Covid-19 pandemic including reduced working hours in the lab, strict social distancing, regular hand sanitisation and masks worn at all times while indoors. An account of the provisions and steps taken by RAL to enable safe on site working is provided in appendix section A-4.4.

4.5.1 Preventing microwave leakage and mitigating hazards

Human tissues contain lots of water and other MW susceptible tissues and so are extremely vulnerable to heating as well as non-thermal risks to the nervous system and genetic structures from MW radiation. The maximum MW exposure limit in most countries is 1 mWcm^{-2} and manufacturers of DMOs in the UK maintain the safety limit of MW leakage at 5 mW/cm^2 at a distance of 5 cm from the equipment as specified by British Standard BS EN 60335-2-25:2012+A2:2016 household and similar electrical appliances; particular

requirements for microwave ovens, including combination MW ovens. Although the leakage limit is greater than the exposure limit, the power density of unfocussed MWs decreases proportionally to the inverse square of distance from the source, meaning the maximum exposure of a 5 mWcm^{-2} leak falls to $<1 \text{ mWcm}^{-2}$ at a distance of 11.2 cm[13]. In industrial batch MW systems designed as oven-style cavities with the magnetron installed adjacent the applicator, the door seals typically incorporate choke traps and failsafe interlocks in the same manner as DMOs. The chokes are an array of hollow recesses that are $\frac{1}{4}\lambda$ of the MWs in width that act as virtual short circuits for the main wall currents between the door and the cavity. Leakage is reduced to safe levels (but not entirely eliminated) since the phase of incident and reflected MWs have a gap length of $\frac{1}{2}\lambda$ which causes them to destructively interfere in the choke. Wi-Fi enabled devices will struggle to connect in proximity to an operating MW reactor due to the small amount of RF interference that is present[14], [20].

Continuous flow MW systems that require an entry and exit point for the target material feature inherently more chance of leakage. These ports must contain adequate chokes capable of absorbing any residual MW power and are usually designed to be as small as the dimensions of the heating target will allow, ideally less than the λ_c for the waveguide. If both dimensions of the material do not allow this, then reducing the port in one dimension to $<\frac{1}{2}\lambda$ can at least limit leakage to a single plane of polarisation[20].

Metallic mesh is used on the doors of DMOs to allow observation of heating within the cavity while preventing leakage through the window. The necessary hole size and interval of the mesh is calculated from λ_c , with smaller hole size and greater intervals providing better protection. Each component of the benchtop SMC reactor is attached via the UG-554/U flanges of WR340 waveguides (inner dimensions = $86.36 \times 43.18 \text{ mm}$) which have recommended $f = 2.2\text{--}3.3 \text{ GHz}$ and $f_c = 1.7\text{--}3.5 \text{ GHz}$. The flanges hand tightened with 10–12 bolts at each interface when initially set up or whenever the instrument is moved to ensure good electrical connection for the MWs as well as to prevent leakage. The benchtop SMC reactor and the modified DMO both feature steel tube apertures extending vertically from the sample applicator, sited above a MW heating mode. These points of access are necessary for insertion and removal of the quartz ampoules containing the samples. The diameter of the port in both cases

was $\ll \lambda_c$, which for WR340 waveguide dimensions is $\lambda_c = 2b = 172.72$ mm, and so acted as choke points to prevent leakage while allowing ease of access when introducing experiment samples.

Being odourless and invisible, MWs cannot be detected without a leak detector such as the Testmate MW-100 shown in figure 4.15, which measures the RF of the MW radiation and displays the reading on an LCD display. The detector signals MW power flux >5 mW/cm² with a high-pitched tone and flashing red LED, visible above the LCD screen. Although this limit is the maximum standard for exposure, the MW power diminishes quickly with distance from the instrument allowing the operator to safely turn off the magnetron without harm.



Figure 4.15: Testmate MW-100 microwave leak detector with LED warning light visible above LCD screen

The modified DMO can be shut down by stopping the magnetron from the front control panel or by switching off power at the socket. The benchtop SMC reactor can be immediately shut down in one of three ways, first by stopping the magnetron with the red “stop” button on the instrument, second by removing the dummy interlock from the magnetron head or lastly by switching off the power at the socket.

4.5.2 Working in environments utilising ionising radiation

As per standard ISIS operating procedure, all staff carrying out work in the vicinity of the beamline instruments is required to wear an ionising radiation

dosimeter. The dosimeter is worn outside of clothing so as to be visible at all times and features a plastic divot that will change colour from white to black in the presence of a radiation dosage higher than the maximum safety level. The Ionising Radiations Regulations 1999 (IRR99) aim to limit exposure to ionising radiation to a level that is as low as reasonably practicable (ALARP). Ionising radiation is measured in Sieverts (Sv), with typical workplace doses measured on the scale of μSv to mSv . The average annual dose to a member of the UK population from all sources of radiation is 2.7 mSv . IRR99 specifies that a non-radiation worker must not receive >1 mSv per year as a result of work with ionising radiation.

4.5.3 Transferring experiment samples to the sample applicator

Reactant mixtures prepared and sealed ahead of time as described in section 4.3.1 were placed into a ~ 95 mm length, quartz support tube held by a Macor[®] ceramic insulator inside an aluminium support block. The insulator material is a machinable glass ceramic called Macor[®] with a low thermal conductivity ($1.46 \text{ Wm}^{-1}\text{K}^{-1}$ at 25 °C) making it an excellent thermal insulator that functions well in applications at high temperatures between 800 – 1000 °C [164], [165]. The insulator reduces excess heat transfer from the quartz support tube to the ampoule block during synthesis. A threaded brass adaptor lid allowed the complete assembly to be attached to a quick release sample stick designed to safely lower the support block assembly into the sample applicator through a cylindrical tube running from the applicator to the top of the sample tank. Once resting in the applicator with the sample inside the waveguide, the button on the top of the quick release sample stick could be pressed and the stick withdrawn leaving the sample and support block in place.

With access to the Polaris well restricted by the interlock gate, an electronic jog box is used to move the sliding short circuit of the Polaris-SMC reactor vertically up and down on a motorised track. The speed of the motor can be adjusted with a dial on the jog box. At each end of the track, a limiter switch is installed that prevents the motor moving the short circuit too far in either direction. Since there is a risk to user safety with the motorised device adjacent to the sample applicator access port, both the orange and yellow power cables must be detached from the jog box control and passed through the cabling orifice of the Polaris access well prior to entering to carry out work.

4.5.4 Removing experiment samples and testing sample activity levels

Additional care must be taken when removing the experiment samples from the sample applicator since following MW heating the sample, quartz ampoule or quartz support tube may still be hot enough to cause burns until fully cooled. Following exposure to the neutron beam the samples must be checked for excess radioactivity using a Geiger counter capable of measuring up to $1 \mu\text{Svhr}^{-1}$. Different materials will manifest different levels of activity and it is possible to estimate the activation of a sample from knowledge of the neutron spectrum, exposure duration, sample mass and isotopic composition[166]. Table 4.1 presents the expected activation, contact dose and time required for an elemental sample to return to $\leq 74 \text{ Bqg}^{-1}$ following one day of neutron beam exposure. 74 Bqg^{-1} is the typical activity limit that allows samples to be declared as non-radioactive for shipping. The prompt activation of a sample is the anticipated activation for the pure solid element 120 s after neutron exposure, while contact dose is the expected dose from a 1 g pure element sample after exposure[166], [167].

Table 4.1: Activation table for selected elements utilised in this PhD project. (–) indicates no activity, (*) indicates a stable element becomes an α emitter upon activation, (†) indicates calculations adjusted from NIST data of activation from 1 day exposure to a $1 \times 10^7 \text{ ns-cm}^{-2}$ reactor thermal beam[166], [167]

Element	Prompt activation (1 unit = 37 Bqg⁻¹)	Contact dose (1 unit = 10 $\mu\text{Svhr}^{-1}\text{g}^{-1}$)	Time for activity to decay to $\leq 74 \text{ Bqg}^{-1}$
Tin	<40	<0.1	<50 days
Antimony	800	0.7	520 days
Bismuth	*	*	*
Copper	1×10^4	8.5	7.4 days
Selenium	4900	4.2 [†]	10 hours
Tellurium	2600	2.2	96 hours
Sulfur	–	–	–
Carbon	–	–	–

The data in table 4.1 are the result of an approximate calculation for decay times from 5 cm^3 pure solid element samples at an intensity equivalent to that produced by the High Intensity Powder Diffraction (HIPD) beamline at the Los Alamos Neutron Science Center (LANSCE) when operating at $100 \mu\text{A}$ (unless otherwise indicated)[166]. Since the exposure duration of each *in-situ* Polaris-SMC experiment was $\ll 1$ day in the order of several minutes, the most useful information is the expectation that samples containing Cu should be expected to have the greatest prompt activation and contact dose of the prepared samples.

While the values presented above are useful for calculating the expected level of activity from neutron diffraction experiments and can be used to estimate the anticipated activation of different chemical systems, the best determination of the safety of a sample is from direct measurement following neutron beam exposure. A low level of activity which would allow the sample to be handled for labelling and transferred to the active samples storage cabinet is $<75 \mu\text{Svhr}^{-1}$. Samples that display activity $>75 \mu\text{Svhr}^{-1}$ should be handled as little as possible, especially with bare hands. The activity decays in most cases to the range of ~ 100 or even $\sim 10 \mu\text{Svhr}^{-1}$ within a day or so. The ampoule block assembly must be allowed to cool to room temperature before the sealed ampoule can be retrieved, labelled and transferred to the active samples storage cabinet adjacent the Polaris instrument. Once the dose rate of the sample has fallen to $<0.1 \mu\text{Svhr}^{-1}$ it may be removed from the cabinet and handled freely. The sample can then be processed for disposal or transport back to the host institution, while managing the risks associated with the specific chemical hazards.

5 Characterisation methods

5.1 Explaining the thesis from the bottom up

MOST INORGANIC SOLID STATE SUBSTANCES EXIST IN THE FORM OF CRYSTALS.

JUST NOT NECESSARILY BIG CRYSTALS.

CRYSTALS FORM BECAUSE THE ATOMS CAN BE ARRANGED IN HIGHLY ORDERED, REPEATING PATTERNS.

THE SMALLEST CRYSTAL SECTION THAT CAN REPEAT IS CALLED THE UNIT CELL.

CRYSTAL STRUCTURES ARE CLASSIFIED BASED ON THE UNIT CELL CONFIGURATION.

THE CHARACTERISTIC BOND LENGTHS AND ANGLES ARE TOO SMALL TO MEASURE WITH COMMON TOOLS.

BIG CRYSTALS DIFFRACT SUNLIGHT IN VERY PRETTY WAYS.

THE ATOMS IN THE UNIT CELL ALSO DIFFRACT LIGHT...

...BUT THEY REQUIRE MUCH LONGER WAVELENGTHS OF LIGHT.

DIFFRACTOMETERS EMIT X-RAYS WHICH DIFFRACT OFF THE ELECTRON ORBITALS OF THE ATOMS.

THE DIFFRACTED X-RAYS ARE COLLECTED BY A DETECTOR THAT ROTATES AROUND THE SAMPLE.

THE INCIDENT X-RAYS DIFFRACT AT SPECIFIC ANGLES PRODUCING CONSTRUCTIVE INTERFERENCE PATTERNS.

X-ray source

Beam window

THE REGULAR DIFFRACTION OF HIGH ENERGY LIGHT WILL ACCUMULATE AT SPECIFIC POINTS.

THE RESULTING PATTERN IS LIKE A 2D PROJECTION OF THE SPACE GROUP.

Detector

THE RAW DATA CAN BE COMPARED TO DATABASES OF PATTERNS SUCH AS THE ICSD FOR ROUGH IDENTIFICATION.

FULL CHARACTERISATION REQUIRES SOFTWARE LIKE GSAS TO RUN REFINEMENT CALCULATIONS OF A MODEL STRUCTURE.

A BETTER MODEL FITS THE DIFFRACTION PATTERN MORE, SO USEFUL UNIT CELL DATA CAN BE INTERPOLATED FROM IT.

5.2 Crystal structures

Solids form as crystals when the atoms within the structure are highly ordered, to the degree that there is a minimum configuration of the lattice points that repeat in a regular pattern known as the unit cell[168]. The lattice parameters define the dimensions of the unit cell and the symmetry operations contribute to determining the space group, a description of its overall shape.

5.2.1 Lattice parameters and unit mesh

Lattice points are defined with respect to the lattice origin by a unique vector ($\vec{r} = u\vec{a} + v\vec{b} + w\vec{c}$) where \vec{a} , \vec{b} and \vec{c} are linear vectors along the respective crystallographic axis and u , v and w are integer coordinates. Two-dimensional lattice planes are defined by the unit mesh which is obtained by taking the magnitude of vectors \vec{a} and \vec{b} along with the included angle (γ)[169]. Any possible Three-dimensional (3D) unit cell is defined by the vectors with respect to the origin point which comprise the lengths of the lattice edges ($|\vec{a}| = a_0$, $|\vec{b}| = b_0$ and $|\vec{c}| = c_0$) and the angles formed between these axes ($\vec{a} \wedge \vec{b} = \gamma$, $\vec{a} \wedge \vec{c} = \beta$ and $\vec{b} \wedge \vec{c} = \alpha$) as shown in figure 5.1[168].

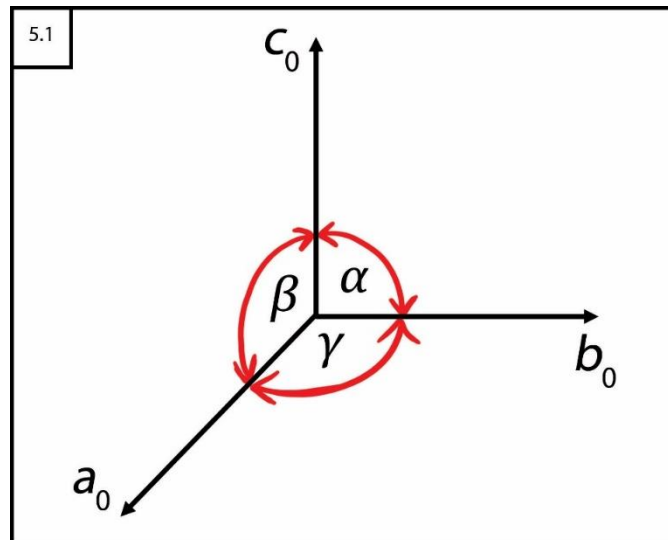


Figure 5.1: three-dimensional unit cell lattice parameters with vectors (a_0 , b_0 and c_0) and angles (α , β and γ) defined relative to an origin vertex

3D unit cells require that the unit mesh polygonal shapes are able to tessellate (see appendix section A-5.1) leading to only seven possible base shapes of unit cell which make up the 14 Bravais lattice structures[168].

5.2.2 Symmetry operations

Symmetry operations obey operational rules that must repeat as they involve movement of a point, line or plane around a unit cell (or the unit cell itself) to

create an image that is superimposable with the original position/orientation. Rotation around an axis will have an order of rotation (X) given by the ratio[169]:

$$\text{Rotation axis order } (X) = \frac{360^\circ}{\epsilon} \quad \text{(Equation 5-1)}$$

ϵ = Minimum angle required to replicate the starting point

The value of X is limited to 1-, 2-, 3-, 4- and 6-fold rotational axes since 5-fold axes and orders >6-fold do not allow parallel lines through equivalent points to maintain equal spacing. In space group notation X is presented with a subscript representing the translation along the axis as the fraction of the rotation order required for the lattice to repeat[169].

Other basic symmetry operations included: reflection around a mirror plane (m), an inversion centre ($\bar{1}$) for equidistant pairs of points on opposite sides of a central point, and translational symmetry for patterns that repeat through movement of lattice points without any rotation or reflection. The “/” notation in the point group indicates that m is operating perpendicular to the main axis of rotation. Compound symmetry occurs when two symmetry operations are performed sequentially, while combination symmetry is the result of two or more symmetry operations performed in conjunction; both types must be compatible with the space lattice[169], [170]. See appendix section A–5.2 for simple operation combinations necessary to generate compound symmetry operations. Glide planes are similar to m except the points are shifted out of alignment rather than appearing at opposite, equivalent points. a , b or c glide planes feature translation along $\frac{1}{2}$ the respective lattice vector, n glide planes are translated $\frac{1}{2}$ the diagonal component of two vectors, diamond (d) glide planes are translated $\frac{1}{4}$ the length of a diagonal vector and e glide planes are defined by glide operations along two different $\frac{1}{2}$ lattice vectors[169].

5.2.3 Bravais lattices

Lattice and symmetry elements interact to form the 3D structures of the unit cell which must tessellate to pack together, so there are only seven possible crystal systems and five primitive unit cell shapes resulting from the four basic unit mesh shapes as shown in Table 5.1[169], [171].

Table 5.1: Primitive unit cell shapes resulting from unit mesh shapes and related parameters^[169]

Unit mesh shape	Unit mesh parameters	Inter-planar spacing	Primitive unit cell shape
Parallelogram	$a_0 \neq c_0$	b_0	Monoclinic
Rectangle	$a_0 \neq b_0$	c_0	Orthorhombic
Square	$a_0 = b_0$	$a_0 = b_0 \neq c_0$	Tetragonal
Rhombus	$a_0 = b_0$	$a_0 = b_0 = c_0$	Cubic
		c_0	Hexagonal

In addition to the primitive unit cells, there are base-centred, body-centred and face-centred versions which are uniquely described by the placement of lattice points in the structure. These lattice configurations specify for 14 naturally described shapes which are collectively called Bravais lattices; shown in appendix section A–5.3^[169].

5.2.4 Crystallographic space groups

Point groups are the possible ways in which the lattice orientation can be changed without the atoms appearing to move position. The simplest point group rotations and roto-inversions are limited to the already established 1, 2, 3, 4, 6, m , $\bar{1}$, $\bar{3}$, $\bar{4}$ and $\bar{6}$ symmetry axes; with an additional 22 point groups resulting from their various combinations. The 32 total point groups are presented in table 5.2, which when combined with the 14 Bravais lattices gives a total of 230 distinct 3D space groups^{[170]–[173]}.

Table 5.2: The 32 crystallographic point groups^{[170], [173]}

Crystal system	Crystallographic point groups						
Triclinic	1	$\bar{1}$					
Orthorhombic	222	$mm2$	mmm				
Monoclinic	2	m	$2/m$				
Cubic	23	$m\bar{3}$	432	$\bar{4}3m$	$m\bar{3}m$		
Trigonal	3	$\bar{3}$	32	$3m$	$\bar{3}m$		
Tetragonal	4	$\bar{4}$	$4/m$	422	$4mm$	$\bar{4}2m$	$4/mmm$
Hexagonal	6	$\bar{6}$	$6/m$	622	$6mm$	$\bar{6}2m$	$6/mmm$

The space group of the structure is attributed first by denoting the relevant Bravais lattice symbol (P , I , F , A , B , C or R) followed by the point group notation to describe the symmetry operations. Some examples of crystal space groups that describe the materials this project include:

$Pnma$: a primitive (P) orthorhombic Bravais lattice with an n glide plane, mirror plane and a glide plane along the a -axis.

$R\bar{3}m$: a primitive-rhombohedral (R) trigonal Bravais lattice with 3-fold roto-inversion symmetry and a mirror plane.

$P3_121$: a primitive (P) trigonal Bravais lattice, a screw axis with 3-fold rotation and $1/3$ translation of the lattice vector, 2-fold and 1-fold rotational symmetry.

5.3 X-ray and neutron diffractometry techniques

Diffraction of light through crystal lattices in order to determine their structure is a broad field in which the different particles or radiation used are differentiated by unique, intrinsic properties that make each one appropriate for specific applications and interactions. The quality of a diffraction pattern is affected by the instrument resolution, the energy or λ of the radiation and the physical/chemical properties of the sample[174]. Electrons, X-rays and neutrons have overlapping but distinct λ ranges and associated f . Those that correspond with the atomic distances within the crystal structures being measured typically lie in the region of $\lambda = 0.1\text{--}10 \text{ \AA}$ while the most commonly used at laboratory scale ($\lambda = 0.5\text{--}2.5 \text{ \AA}$) correspond to the interatomic distances[174], [175].

Electron beams are generated by direct acceleration of charged particles through electric potentials in the range of 30–50 kV, producing a monochromatic source of electrons. Focussing electrons using magnetic lenses is the basis for high-resolution electron microscopy techniques such as SEM, used for direct imaging of atomic structure[175]. X-radiation produced in X-ray tubes consists of a continuous λ distribution as well as monochromatic line radiation, the latter of which produces characteristic patterns from crystalline samples. General radiation emitted by X-ray tubes are useful in Laue photography however, monochromator devices are used to eliminate it to improve scattering. The continuous background of the spectrum (also called white or bremsstrahlung radiation) results from electrons decelerating unpredictably when impacting the metal target inside the tube, and is generally less useful for diffraction analysis applications[174], [175]. X-ray diffraction is most commonly used due to the ease of X-ray production within relatively small instruments that can produce diffraction patterns of useable resolution over a course of minutes or hours. Neutron diffraction was conceptualised by German-American physicist Walter M. Elsasser 1936 and demonstrated in 1945 by Ernest O. Wollan however, it took many years until sufficiently intense neutron beams could be generated

practically from early nuclear reactors known as atomic piles. Unlike X-rays, which are scattered by the interaction with the electrons in a structure, neutrons penetrate deeper and are mostly diffracted off the much smaller atomic nuclei. For a constant λ , neutrons produce more intense diffracted beams than X-rays. Neutrons have the additional characteristic of a magnetic moment, also known as spin, and so are affected by the unbalanced electron spins in magnetic ions and can interact with unpaired electron spins to determine ordered magnetic structures. Factors that affect the extent of X-ray scattering increases progressively through the elements of the periodic table due to the continual addition of electrons to the whole. Neutron scattering is also affected by periodic increasing nuclear mass however the effect is lesser than for X-rays and largely overshadowed by resonance effects determined by absorption by a nucleus that vary in non-periodic patterns. Neutron scattering is a combination of potential scattering (dependent on the number of particles) and resonance scattering; the interference of these different scattering parameters produces variable scattering lengths when neutrons interact with different elements/isotopes[174]–[177]. Particles such as electrons or neutrons produce images of crystal structures in reciprocal space due to wave-particle duality, i.e., when in motion the particles behave as waves with λ calculated from de Broglie's equation[174]:

$$\lambda = \frac{h}{mv} \quad \text{(Equation 5-2)}$$

m = Mass of particle at rest

v = Particle velocity

There are several advantages to using neutron diffraction for *in-situ* MW experiments rather than X-rays. The first is due to the extremely short timescales of MW reactions the resolution of data obtained from a rapid neutron experiment can be easier to interpret, particularly when trying to distinguish between Bragg peaks of lighter and heavier atoms in a structure. The greater penetration of neutrons also means less compromises in equipment design such as waveguides, where the scattering of X-rays by the metal walls may require the use of less dense materials to allow for a sufficient beam flux in and out of the sample applicator.

5.3.1 Laue method, Bragg's law and Ewald's spheres

The diffraction geometry of a lattice was first described by Max von Laue as the relationship between the angles formed between the incident and diffracted beams (ψ_n and φ_n respectively) with parallel rows of atoms in the three axial directions of the unit cell lattice parameters (a , b and c)[174]:

$$h\lambda = a(\cos \psi_1 - \cos \varphi_1) \quad \text{(Equation 5-3)}$$

$$k\lambda = b(\cos \psi_2 - \cos \varphi_2) \quad \text{(Equation 5-4)}$$

$$l\lambda = c(\cos \psi_3 - \cos \varphi_3) \quad \text{(Equation 5-5)}$$

h , k and l = Miller indices (defined in appendix section A-5.4)

According to Laue, diffraction peaks are only observed where all three equations are satisfied simultaneously. Father and son physicists W. H. Bragg and W. L. Bragg determined the more useful relationship between the incident angle of radiation (also known as the Bragg angle θ), λ and interplanar lattice spacing (d -spacing) as illustrated in figure 5.2[174].

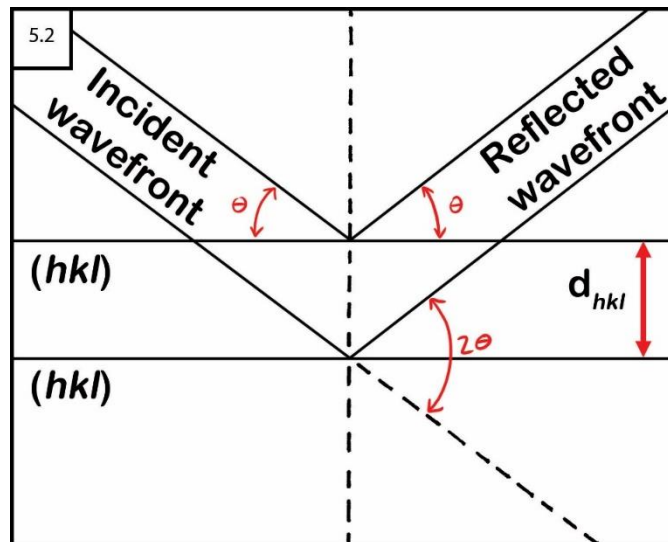


Figure 5.2: Diagram showing the geometrical relationship of identical hkl planes, interplanar d -spacing and incident angle of radiation (θ)[174]

Equally spaced parallel planes with identical triplets of Miller indices are such that each plane may be considered as a separate scattering object. Diffraction from equally spaced objects is only possible at specific angles where scattering results in patterns of constructive interference; the angles of reflection are therefore described by Bragg's Law[169], [174]:

$$n\lambda = 2d_{hkl} \sin \theta_{hkl} \quad \text{(Equation 5-6)}$$

The order of interference integer is taken to be $n = 1$ since orders >1 can be represented by first order reflections from different planes with Miller indices that are multiples of n [174]:

$$d_{hkl} = nd_{nh,nk,nl} \quad \text{(Equation 5-7)}$$

P. P. Ewald described an additional method of representing diffraction by considering an incident beam with a vector (k_0) that is selected to be the inverse of λ such that when the incident beam is scattered elastically, λ will remain constant and the scattered beam wavevector (k_1) will be the same also[174]:

$$|k_0| = \frac{1}{\lambda} = |k_1| \quad \text{(Equation 5-8)}$$

Overlapping the wavevectors in reciprocal space such that k_0 terminates at the origin of the lattice, the angle between k_0 and k_1 (which have identical lengths) is known to be 2θ from Braggs' law. So, all possible orientations of k_1 represent a sphere in 3D space, known as Ewald's sphere and will have a radius (r) = $1/\lambda$. The Ewald's sphere is necessary for visualising the 3D diffraction pattern resulting from single crystal samples[174]. As shown by Braggs' law, the significant factor affecting X-ray scattering is the relationship between angles of incidence and reflection. The atomic scattering tends to fall off with increasing 2θ due to the electron orbitals occupying $\sim 1 \text{ \AA}$ of space (comparable to λ of X-rays) resulting in scattering occurring mostly in the forward direction. Neutrons on the other hand interact in most cases only with the atomic nucleus which has a radius $\ll \lambda$ in the region of $\sim 10^{-13} \text{ cm}$, allowing the nucleus to be regarded as a point scatterer with no associated fall off with θ [176].

5.3.2 Generation and scattering of X-rays

All types of EM radiation are generated when an electric charge accelerates or decelerates; typically X-rays in the high energy range of 5–10 keV used for crystallography studies are generated through one of two methods[174]. X-ray tubes most commonly utilised in laboratory diffractometers generate X-rays by impacting a metal target anode with high-energy electrons. These X-ray sources must be continuously cooled, have low efficiency and limited brightness as a result of the anode properties. Several high intensity characteristic peaks are associated with fixed λ in patterns obtained from X-ray tubes (described in appendix section A–5.5). Synchrotrons, like the Diamond Light Source at the Rutherford Appleton Laboratories (RAL) in Oxfordshire are large, expensive,

multi-user facilities. They accelerate high-energy electrons within an enclosed storage ring; travelling along the circular path, they accelerate towards the centre emitting X-rays with extremely high brilliance and coherence as a result of the high power output compared to the capabilities of conventional X-ray tubes. The characteristic peaks associated with tube X-rays do not appear in synchrotron data due to the continuous distribution of photon energies[174]. If two or more point objects are impinged upon by X-rays, each will produce spherical waves with equal λ that constructively interfere when in phase, such that the amplitudes sum together, and destructively interfere and negate each other when out of phase. The beam energy of coherently scattered X-rays remains unchanged throughout the interaction and maintains the same λ and therefore f as the incident beam; this is known as elastic scattering. Incoherently scattered X-rays (Compton scattering) lose some energy through collisions with electrons, leading to an increase in λ and are typically ignored as a non-essential interaction. X-rays dissipated through random scattering or absorbed when photons lose energy in the process of ejecting electrons from the atom only needs to be accounted for when the absorption becomes significant[174].

5.3.3 Crystal structure effects on X-ray diffraction (XRD) patterns

X-ray diffraction of single crystals requires a single stable crystal sample between 50–250 microns, which should be selected through examination using an optical microscope to ensure they are unfractured and optically clear. The crystal is affixed to the tip of a needle-like probe using mineral oil then aligned in the instrument along the beam direction. Once mounted, the parameters for each measurement are adjusted if necessary to account for distance to the detector and the volume of the Ewald's sphere. For samples sensitive to light, air or moisture the crystal sample can be sealed in a glass capillary prior to mounting. Most solid state materials are easier to synthesis in polycrystalline form and so are analysed using powder X-ray diffraction (PXRD) which involves the detection of diffracted X-rays from powdered crystallites and measuring the scattered intensity as a function of 2θ [178]. Crystalline phases produce discrete maxima of particular intensity at specific angles in the diffraction pattern, known as Bragg reflections or Bragg peaks. Different structure features will produce unique changes in the diffraction pattern; such changes to atomic

coordinates in the unit cell or site occupancies can affect the relative peak intensities and/or positions as shown in table 5.3[174]:

Table 5.3: Effects of various crystal structure parameters and sample properties on powder diffraction patterns

Crystal structure	Sample properties	Effect on pattern
Unit cell parameters ($a, b, c, \alpha, \beta, \gamma$)	Absorption, porosity	Peak position
Atomic parameters (x, y, z etc.)	Preferred orientation, absorption, porosity	Peak intensity
Crystallinity, disorder, defects	Grain size, strain, stress	Peak shape

5.3.4 Capillary/transmission vs flat plate/Bragg-Brentano geometry

Bragg peak intensities are also affected by the diffractometer instrument parameters such as the properties of the radiation source, focussing geometry, detector properties, choice of slit, and monochromator geometry. Most laboratory powder diffractometers utilise a goniometer arm, a component that rotates the sample holder and/or the detector (and sometimes the beam source) to a precise angular position in relation to the beam source to enable detection of diffracted beams from a large range of 2θ angles. Although a horizontal goniometer axis is possible, only the vertical configuration is discussed here as it pertains to the instruments used during the course of this project. The goniometer arm features a heavy counterbalance to allow smooth rotation in the vertical plane, requiring the use of powerful stepping motors to ensure the arm rotation can be precisely controlled to an order of $\sim 1 \times 10^{-3}$ ° [174]. Transmission geometry can utilise either flat or cylindrical sample preparations with cylindrical samples typically requiring less preparation time, smaller sample quantities and less uniform density. Samples are finely ground to allow ease of loading into Mark-tubes/capillaries with a diameter ~ 0.5 – 1 mm before being sealed with a cool yellow flame. Care must be taken to mount the capillaries perpendicular to the axis of rotation of the sample stage with the use of an adjustable sample holder and optical microscope. Bragg-Brentano (reflection) geometry is defined by the diffraction vector, which bisects the angle between the incident and diffracted beam, always being normal to the plane of the sample surface as shown in figure 5.3b. This setup allows samples to be loaded into a

depression on a glass plate, then smoothed with a glass slide to provide a flat plane that takes advantage of the beam focusing. The sample preparation is therefore relatively straightforward, relying on gravity alone to hold the sample in the depression, although a binding agent such as inert oil or a wetting solvent may be used for samples that are particularly loose and liable to dislodge during analysis. Generally, this setup requires more material than transmission geometry to ensure an adequate sample thickness that is opaque to X-rays.

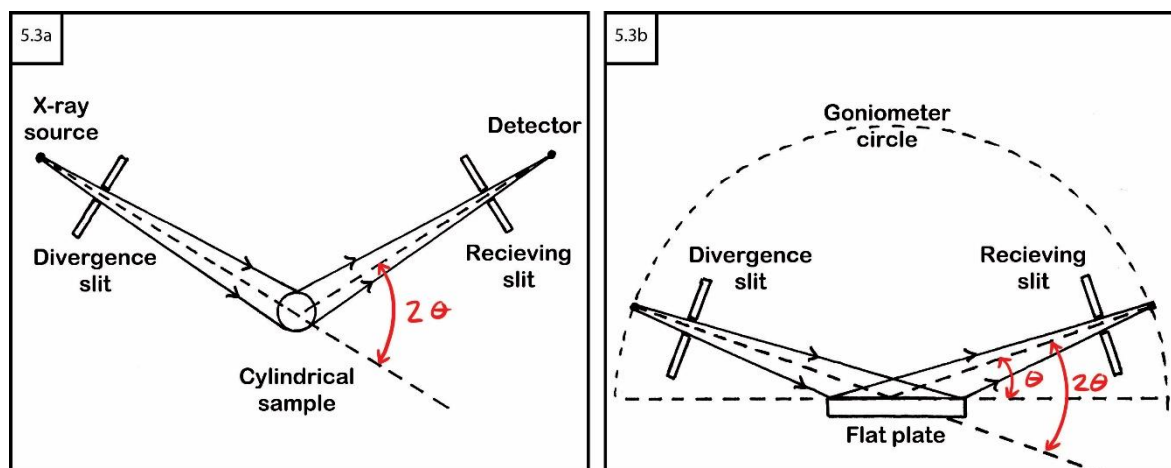


Figure 5.3: Diagrams of a) transmission geometry using a sample capillary b) Bragg-Brentano geometry for flat plate sample holders[174]

Non-random distribution, also known as preferred orientation, is an effect that manifests in powder diffraction data as greater intensity of certain Bragg peaks over others; the result of crystallites in the sample with strong cleavage or growth faces that easily pack together. Transmission geometry is less susceptible to preferred orientation than Bragg-Brentano provided the sample is constantly spinning during data collection however, the self-focusing of the diffracted beam is less precise, often resulting in lower pattern resolution[174].

5.3.5 X-ray diffraction instruments used in this project

For single crystal identification, a Bruker D8 Venture Diffractometer equipped with a Photon-II CPAD detector and dual (Cu and Mo) ImS 3.0 microfocus sources was used. When using Mo sources, the data are typically obtained over the 3–30° 2θ range and a complete data collection can take several hours[178]. As this instrument was not used for obtaining complete powder patterns, scanning was limited to ~ 30 s to identify the presence of any single crystals.

The Bruker D8 Advance DAVINCI X-ray Diffractometer enables PXRD analysis using transmission geometry and features a rotating stage with a removable sample holder, in the centre of which the capillary containing the sample was

affixed using beeswax. The X-ray detector of this instrument is mounted on a vertical goniometer arm which rotates around the spinning sample at a user-defined rate relative to the total scan time. The 0.5 mm Mark-tubes that were used required enough finely ground sample powder to fill to a depth of a ~ 5 cm, and were sealed just above the sample using a disposable cigarette lighter. The capillaries were carefully aligned with the aid of an optical microscope to ensure that the axis of rotation would remain normal to the X-ray beam. A 1 mm divergence slit was used and collection parameters were specified for a $2\theta = 5\text{--}85^\circ$ and step size between angular positions of 0.0167113° collected for a duration of 1 hour at a step rate = $0.047074^\circ\text{s}^{-1}$.

The PANalytical X'Pert Pro MPD Diffractometer features several types of sample bracket although only a fixed position bracket for Bragg-Brentano reflection geometry was used. The X-ray source remains fixed while the detector rotates independently with the aid of a goniometer arm. The finely ground sample powders were gently pressed into the circular depression of a clean glass plate using a glass slide. The slide was manually tilt tested over a sheet of foil before insertion into the bracket to ensure the sample would not spill during operation. The scan parameters used were the same as for the Bruker D8 diffractometer however the time per step was reduced to enable a collection duration of ~ 16 minutes. The collection parameters of both diffractometers were maintained for every respective analysis unless otherwise specified in the relevant section. The resulting .raw and .xrdml data files obtained from the D8 and X'Pert instruments respectively were backed up and converted to .gsas file format using PowDLL file converter[179].

5.3.6 Powder neutron diffraction (PND) and time-of-flight (TOF)

Neutrons are, as the name suggests, uncharged subatomic particles with $m = 1.675 \times 10^{-27}$ kg, only slightly heavier than a hydrogen nucleus, and a magnetic moment of -9.662×10^{-27} JT⁻¹. The scattering length of neutrons does not drop off linearly with increasing atomic mass as with X-rays and so can provide higher resolution information regarding the interior of the structure. It is therefore easier to differentiate lighter and heavier atoms that would otherwise dominate an X-ray diffraction pattern as well as distinguish between neighbouring elements with different scattering profiles. Powder neutron diffraction (PND) operates similarly to PXRD in that a neutron beam interacts with and then

scatters from the crystal structure before being recorded by the detector. Low energy neutrons are scattered isotropically, implying orbital momentum is not a factor affecting scattering since the range of interaction is $\ll \lambda$ [166]. The high energy process of generating X-rays in synchrotron facilities is also the most common method of generating neutrons for diffractometry in modern experiments. High intensity spallation (pulsed) neutron sources accelerate protons to high energies in the synchrotron ring before releasing them at a heavy metal target from which neutrons are then expelled. The resultant intense neutron beams have a nearly continuous energy spectrum, ideal for a variety of diffraction applications such as time-of-flight (TOF) measurements. As a subatomic particle, neutrons can be described by wave mechanics, with λ related to m , v and h as per de Broglie's relationship in equation 5-2. In the spallation process all the neutrons are ejected simultaneously, with higher energy neutrons traveling faster and arriving quicker at the detector. TOF techniques are therefore used to calculate the change in energy and λ of such neutrons with different v from the time-of-flight (t) taken to travel the total flight path (L) from the source to the sample and finally to the detector[174], [180]:

$$\lambda = \frac{ht}{mL} \quad \text{(Equation 5-9)}$$

When combined with Bragg's Law, given in equation 5-6, the relationship between measured d -spacing is shown to be directly proportional to t , with potential measurements as low as 0.25 Å[180]:

$$t = \frac{mL2d \sin \theta}{h} \quad \text{(Equation 5-10)}$$

When considering PND in a monochromatic instrument, Bragg's law is expressed for a fixed λ , while for TOF measurements a range of λ are available and so can be rewritten as a measure of the whole range of d -spacings at a fixed scattering angle (2θ)[180]:

$$\lambda = 2d_{hkl} \sin \theta_{hkl} \quad \text{(Equation 5-11)}$$

$$\lambda_{hkl} = 2d_{hkl} \sin \theta \quad \text{(Equation 5-12)}$$

The x-axis of neutron diffraction patterns determined from TOF experiments is typically presented in d -spacing which is λ -independent and directly proportional to t (since λ is inversely related to v). TOF diffraction patterns can

be collected simultaneously from a large angular range when using multiple detector banks. Several multi-detector bank instruments such as GEM and Polaris are installed on the ISIS beamline at RAL and feature higher count-rates by summing the patterns measured in different detector elements. The resolution of a TOF diffraction pattern ($\Delta d/d$) at a given scattering angle/detector bank is constant over the whole diffraction pattern and is defined by the uncertainties in t , L and θ ; which manifests in the data as increased peak width[174], [180], [181].

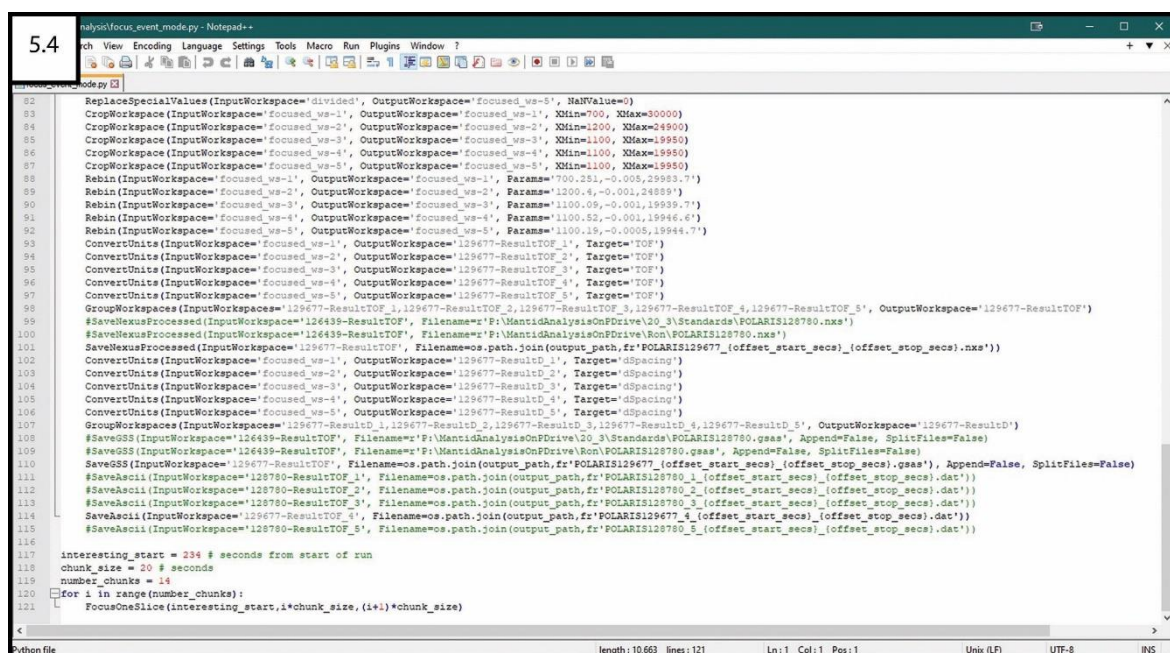
5.3.7 Time-resolved powder neutron diffraction (PND) at ISIS

The neutron beam at ISIS is generated from a pulsed beam of protons, i.e., H^+ ions, that are driven through a series of linear accelerator (Linac) injectors to impact a tantalum target. The ions are accumulated, stripped of electrons and separated into two bunches. The $\sim 2.8 \times 10^{13}$ protons are accelerated up to 800 MeV at 84 % the speed of light through $\sim 1 \times 10^4$ revolutions within the synchrotron before being deflected into the extracted proton beamline. The target station is the location of the aforementioned heavy metal Ta target which, when impinged by the proton beam, produces a burst of ~ 15 fast neutrons per proton in a spallation process. A Be reflector concentrates the resulting neutron flux towards the moderator assembly which reduces the fast neutrons spalled from the target and diverts the beam through shutters towards the 18 beamline channels[182], [183]. The Polaris diffractometer on the ISIS beamline was used to house the Polaris-SMC microwave reactor as described in chapter 6; this type of rapid, high count data collection is ideal for investigating MW synthesis reactions in real time. The Polaris sample tank is constructed with five banks of detectors arranged around its circumference. Each detector bank covers a discrete angular range and is comprised of several modules (38 total) which in turn contain multiple detector elements. To limit interference from the waveguide in the sample tank, the data collection angles were limited to those covered by bank 4 detectors, i.e., a d -spacing range of 0.2–3.7 Å[181]. Remotely controlled beam limiter jaws within the ISIS beamline are used to control the neutron beam height passing through the sample tank of the Polaris instrument. The beam dimensions were reduced to 10 mm below the beam centre, which aligned with the bottom of the quartz support tube/ampoule, and

15 mm above the beam centre to reduce interference from the top face of the waveguide.

5.3.8 Polaris event mode data processing using Mantid Workbench

The Manipulation and Analysis Toolkit for Instrument Data (Mantid Workbench) software is an advanced graphing and visualisation user interface used to manipulate and analyse neutron and muon data. The software is capable of plotting regular histogram data of neutron counts against d -spacing as well as event mode data of neutron counts against a specified independent variable such as temperature, pressure or time[157]. Dr Ron Smith, Danny Hindson (one of the Mantid developers) and I collaborated in developing the set of Python scripts that could interpret and process the *in-situ* data files generated by Polaris in an efficient and user-friendly way. The histogram and event mode data are processed by separate Python scripts; detailed information regarding their function and development can be found in appendix section A–5.6. The three key user-defined parameters of the event mode script that are unique to each experiment file are the `interesting_start` (induction period), `chunk_size` (length of data sections) and `number_chunks` (number of histograms to be output). These user adjustable lines of code (117–119) that define the number and size of output files are shown in figure 5.4 at the bottom of the Python script.



```
5.4 nrls01focus_event_mode.py - Notepad++
File View Encoding Language Settings Tools Macro Run Plugins Window ?
Python File

# Python script for processing Polaris event mode data
# User-defined parameters
interesting_start = 236 # seconds from start of run
chunk_size = 20 # seconds
number_chunks = 14

for i in range(number_chunks):
    FocusOneSlice(interesting_start,i*chunk_size,(i+1)*chunk_size)

# Data processing steps
82 ReplaceSpecialValues(InputWorkspace='divided', OutputWorkspace='focused_ws=5', HalValue=0)
83 CropWorkspace(InputWorkspace='focused_ws=1', OutputWorkspace='focused_ws=1', XMin=700, XMax=30000)
84 CropWorkspace(InputWorkspace='focused_ws=2', OutputWorkspace='focused_ws=2', XMin=1200, XMax=24900)
85 CropWorkspace(InputWorkspace='focused_ws=3', OutputWorkspace='focused_ws=3', XMin=1100, XMax=19950)
86 CropWorkspace(InputWorkspace='focused_ws=4', OutputWorkspace='focused_ws=4', XMin=1100, XMax=19950)
87 CropWorkspace(InputWorkspace='focused_ws=5', OutputWorkspace='focused_ws=5', XMin=1100, XMax=19950)
88 Rebin(InputWorkspace='focused_ws=1', OutputWorkspace='focused_ws=1', Params='700.251,-0.005,29983.7')
89 Rebin(InputWorkspace='focused_ws=2', OutputWorkspace='focused_ws=2', Params='1200.4,-0.001,24889')
90 Rebin(InputWorkspace='focused_ws=3', OutputWorkspace='focused_ws=3', Params='1100.09,-0.001,19939.7')
91 Rebin(InputWorkspace='focused_ws=4', OutputWorkspace='focused_ws=4', Params='1100.52,-0.001,19944.6')
92 Rebin(InputWorkspace='focused_ws=5', OutputWorkspace='focused_ws=5', Params='1100.15,-0.0005,19944.7')
93 ConvertUnits(InputWorkspace='focused_ws=1', OutputWorkspace='129677-ResultTOF_1', Target='TOF')
94 ConvertUnits(InputWorkspace='focused_ws=2', OutputWorkspace='129677-ResultTOF_2', Target='TOF')
95 ConvertUnits(InputWorkspace='focused_ws=3', OutputWorkspace='129677-ResultTOF_3', Target='TOF')
96 ConvertUnits(InputWorkspace='focused_ws=4', OutputWorkspace='129677-ResultTOF_4', Target='TOF')
97 ConvertUnits(InputWorkspace='focused_ws=5', OutputWorkspace='129677-ResultTOF_5', Target='TOF')
98 GroupWorkspaces(InputWorkspaces='129677-ResultTOF_1,129677-ResultTOF_2,129677-ResultTOF_3,129677-ResultTOF_4,129677-ResultTOF_5', OutputWorkspace='129677-ResultTOF')
99 #SaveNexusProcessed(InputWorkspace='126439-ResultTOF', Filename='P:\MantidAnalysisOnDrive\20_3\Standards\POLARIS128780.nxs')
100 #SaveNexusProcessed(InputWorkspace='126439-ResultTOF', Filename='P:\MantidAnalysisOnDrive\Ron\POLARIS128780.nxs')
101 #SaveNexusProcessed(InputWorkspace='129677-ResultTOF', Filename=os.path.join(output_path,fr'POLARIS129677_{offset_start_secs}_{offset_stop_secs}.nxs'))
102 ConvertUnits(InputWorkspace='focused_ws=1', OutputWorkspace='129677-ResultD_1', Target='dSpacing')
103 ConvertUnits(InputWorkspace='focused_ws=2', OutputWorkspace='129677-ResultD_2', Target='dSpacing')
104 ConvertUnits(InputWorkspace='focused_ws=3', OutputWorkspace='129677-ResultD_3', Target='dSpacing')
105 ConvertUnits(InputWorkspace='focused_ws=4', OutputWorkspace='129677-ResultD_4', Target='dSpacing')
106 ConvertUnits(InputWorkspace='focused_ws=5', OutputWorkspace='129677-ResultD_5', Target='dSpacing')
107 GroupWorkspaces(InputWorkspaces='129677-ResultD_1,129677-ResultD_2,129677-ResultD_3,129677-ResultD_4,129677-ResultD_5', OutputWorkspace='129677-ResultD')
108 #SaveGSS(InputWorkspace='126439-ResultTOF', Filename='P:\MantidAnalysisOnDrive\20_3\Standards\POLARIS128780.gsas', Append=False, SplitFiles=False)
109 #SaveGSS(InputWorkspace='129677-ResultTOF', Filename='P:\MantidAnalysisOnDrive\Ron\POLARIS128780.gsas', Append=False, SplitFiles=False)
110 SaveGSS(InputWorkspace='129677-ResultTOF', Filename=os.path.join(output_path,fr'POLARIS129677_{offset_start_secs}_{offset_stop_secs}.gsas'), Append=False, SplitFiles=False)
111 #SaveAscii(InputWorkspace='128780-ResultTOF_1', Filename=os.path.join(output_path,fr'POLARIS128780_1_{offset_start_secs}_{offset_stop_secs}.dat'))
112 #SaveAscii(InputWorkspace='128780-ResultTOF_2', Filename=os.path.join(output_path,fr'POLARIS128780_2_{offset_start_secs}_{offset_stop_secs}.dat'))
113 #SaveAscii(InputWorkspace='128780-ResultTOF_3', Filename=os.path.join(output_path,fr'POLARIS128780_3_{offset_start_secs}_{offset_stop_secs}.dat'))
114 #SaveAscii(InputWorkspace='129677-ResultTOF_4', Filename=os.path.join(output_path,fr'POLARIS129677_4_{offset_start_secs}_{offset_stop_secs}.dat'))
115 #SaveAscii(InputWorkspace='128780-ResultTOF_5', Filename=os.path.join(output_path,fr'POLARIS128780_5_{offset_start_secs}_{offset_stop_secs}.dat'))
116
117 interesting_start = 236 # seconds from start of run
118 chunk_size = 20 # seconds
119 number_chunks = 14
120 for i in range(number_chunks):
121     FocusOneSlice(interesting_start,i*chunk_size,(i+1)*chunk_size)

Python file length: 10,663 lines: 121 Ln: 1 Col: 1 Pos: 1 Unix (LF) UTF-8 INS
```

Figure 5.4: Python script used to split Polaris event mode data into user defined slices referred to in the code as `chunk size`

A final Python script was developed that could generate colourmap plots of the processed/sliced event mode data; displaying time in seconds on the x-axis, d -

spacing on the y-axis, peak intensity as a colour gradient map and an overlay of the absorbed MW power profile on the 2nd y-axis. By comparing histogram scans pre- and post-reaction with Mantid on the Polaris instrument workstation, allowed for quick verification that the diffraction pattern had changed after heating. The software enabled several post reaction histograms to be compared as waterfall plots which highlighted changes in diffraction peak position or intensity between experiment samples with increased doping.

5.4 Rietveld refinement

The least-squares Rietveld method of profile refinement is one of the most common tools for characterisation of crystal structure from a set of diffraction data; determining the associated atomic and structural parameters as well as sample phase composition. The method was developed by Hugo Rietveld during the 1960s to obtain better results from the information obscured by overlapping Bragg reflections[184], [185]. The process involves the creation of an appropriate model (\mathbf{M}_x) that can be manipulated to refine a calculated set of observable structure and profile parameters (\mathbf{y}) that is minimised as a function of diffraction parameters (\mathbf{x}) then compared to the observed diffraction data[186]:

$$Q = [\mathbf{y} - \mathbf{M}_x]^T \mathbf{W} [\mathbf{y} - \mathbf{M}_x] \quad \text{(Equation 5-13)}$$

\mathbf{W} = Weight matrix (must be positive)

The least squares refinements are carried out for the crystal structure, diffraction effects, instrument factors, lattice parameters etc. until a best fit is obtained for the calculated model against the observed pattern[184]. Further information regarding various refinement functions and correction factors is included in appendix section A–5.7. General guidelines have been published on the practical considerations when carrying out structure refinement using the Rietveld method by the Commission on Powder Diffraction (CPD) of the International Union of Crystallography (IUCr). Rietveld refinements conducted throughout this project were carried out using the General Structure Analysis System (GSAS)[187], [188].

5.4.1 Data collection and background correction

At an angular position $2\theta_i$ the detector measures a number of counts at that step i , known as the observed intensity ($Y_{o,i}$). The background is recorded at different positions and used to linearly interpolate background corrections (B_i) from

selected points between each observed intensity. Subtracting the correction from the observed intensity gives the corrected intensity which is then given a statistical weight (w_i) based on the standard deviation (σ) of each factor[185]:

$$w_i = \frac{1}{\sigma^2(Y_i) + \sigma^2(B_i)} \quad \text{(Equation 5-14)}$$

A background diffraction pattern applied to the data to smooth it out makes peak indexing and refinement simpler. The background can either be linearly interpolated before being subtracted or modelled as a function of several refinable parameters. Background subtraction must be performed several times during a refinement, which is hindered by complex patterns. Data collection factors such as diffractometer geometry, alignment, calibration and light source can have significant effects on the refinement process. For example, when using Bragg-Brentano geometry the incident beam must remain focused on the sample through all angles. If the divergence slit is wider than necessary, the beam can encounter the sample holder at low angles reducing the diffraction pattern intensities in that region. Heavily absorbing materials with high surface roughness can be detrimental to reflection geometry by reducing the intensity of low angle Bragg peaks and leading to low thermal parameters during refinement. Bragg-Brentano geometry is carried out under the assumption that X-rays are completely absorbed and diffracted by the sample with no transmission; however, samples comprised of only lighter atoms may have lower intensities at high angles, making transmission geometry a more appropriate technique. Conversely, heavily absorbing samples can be problematic for transmission geometry diffractometers by preventing the incident beam from penetrating the sample fully[189]. Preferred orientation enhances Bragg peak intensities, a difficult effect to eliminate particularly for Bragg-Brentano geometry. Many refinement programs feature a rough correction based on preferred orientation with respect to a specific hkl plane to minimise problems with pattern fitting.

Factors unique to synchrotron facilities that affect Rietveld refinement include optimisation between pattern resolution, peak intensity and signal-to-noise ratio of peak to background. The diffraction geometry and detector types may differ greatly between individual instruments on a synchrotron beamline as well as from laboratory X-ray sources. The λ of the incident light varies between

facilities depending on the energy of the synchrotron source; with third generation sources, such as at ISIS, producing light with $\lambda \sim 0.3 \text{ \AA}$. The resolution of PND data is typically lesser than PXRD with most elements having neutron absorption coefficients $\sim 10^4 \times$ lower than for X-rays. So, larger samples (5–20 mm diameter, 5–50 mm length) coupled with greater penetration of neutrons can reduce the effects of preferred orientation associated with PXRD[189]. Vanadium cans are typically used as sample holders in PND experiments since V has no coherent scattering (Bragg peaks). The raw counts of TOF patterns are strongest at the lowest d -spacing and tail off at larger d -spacing where incident intensity drops off. If the intensity is normalised against the incident intensity spectrum, the background will appear mostly flat and Bragg peaks at the higher d -spacing will appear the largest. This is a result of the Lorentz correction which enhances the scattered intensity for large d -spacing reflections[189]:

$$L = d^4 \sin \theta \quad \text{(Equation 5-15)}$$

Lorentz number (L) = $2.44 \times 10^{-8} \text{ W}\Omega\text{K}^{-2}$

5.4.2 Peak-shape and intensity functions

Bragg peaks are artifacts of both sample characteristics and instrument parameters, that by definition vary as a function of 2θ and in some cases as a function of Miller indices; a poorly fit peak shape will diminish the whole refinement. Individual diffraction peaks, despite having some Lorentzian character can be described almost exactly as a Gaussian distribution. At low scattering angles, peak asymmetry begins to become more significant and so the introduction of a correction factor can be necessary. For most PXRD data, the pseudo-Voigt approximation (pV) of the Voigt function is the most widely used symmetric analytical profile function which linearly combines both the Lorentzian (L) and Gaussian (G) functions[189], [190]:

$$pV = \eta L + (1 - \eta)G \quad \text{(Equation 5-16)}$$

η = Pseudo-Voigt mixing parameter

Although pV describes the symmetrical part of an X-ray diffraction peak, an addition function is necessary to account for asymmetry due to axial divergence of the diffracted beam at low angles. The range over which the peak contributes intensity to the diffraction pattern is established for the peak-shape function, typically at the point where the intensity is $< 0.1\text{--}1\%$ of the peak maximum[189].

With synchrotron diffraction data, the symmetric component of a peak-shape function is represented well by pV with very high resolution data showing reduced instrumental contributions to the peak shapes and highly Lorentzian peaks. In TOF data, the peak-shape functions are more complex since the neutron-pulse structure imposes asymmetric peak broadening effects[189].

5.4.3 Profile and structural parameters

A partial structural model will tend to result in calculated intensities that differ significantly from observed peaks, so a structure-free approach known as Le Bail refinement is generally advised. Ideally, a complete structural model gives relative intensities that approximate the observed peaks and the initial profile parameter refinement can be performed[189]. The profile parameters, beginning with peak width followed by peak asymmetry, can only be refined as a function of 2θ once the peak positions have been matched. Profile parameters define the position, halfwidths and symmetry of Bragg peaks in a diffraction pattern while structural parameters describe the components of the asymmetric unit cell[185]. The least-squares parameters are comprised of either profile or structural parameters as listed in table 5.4:

Table 5.4: Least-squares parameters comprised of two lists of profile or structural parameters[185], [191]

Profile parameter	Symbol	Structural parameter	Symbol
Halfwidth	U, V and W	Scale factor	$c = \frac{y_c}{y_o}$
Counter zero point	Z	Isotropic temperature	Q
Cell parameters	A, B, C, D, E and F	Fractional coordinates of i^{th} atom	x_i, y_i and z_i
Asymmetry	P	Atomic isotropic thermal parameter	B_i
Preferred orientation	G	Site occupancy multiplier	n_i
		Magnetic vector components of i^{th} atom	$K_{x,i}, K_{y,i},$ and $K_{z,i}$

Refinement of lattice parameters and zero offset in synchrotron data are rarely troublesome. These data tend to favour high Lorentzian character and so refinement of Lorentzian half-width parameters (X and Y) are usually simple while Gaussian parameters (U, V and W) can produce unrealistic results that do not relate to physical reality, or cause complete failure of the refinement[189].

5.4.4 Least-squares refinement and Fourier analysis

To minimise a function (M) with respect to the various parameters the least-squares profile refinement process is iterative; the function for a normal refinement on separate integrated intensities is given as[185]:

$$M = \sum_i w_i \left(S_{o,i}^2 - \frac{1}{c} S_{c,i}^2 \right)^2 \quad \text{(Equation 5-17)}$$

For integrated intensities of groups of overlapping reflections, the structure factors are summed over independent observations (\sum_i) and overlapping reflections (\sum_k)[185]:

$$M = \sum_i w_i \left(\sum_k S_{o,k}^2 - \frac{1}{c} \sum_k S_{c,k}^2 \right)^2 \quad \text{(Equation 5-18)}$$

Which is simplified for profile refinement to the residual[185], [190]:

$$M = \sum_i w_i \left(y_{o,i} - \frac{1}{c} y_{c,i} \right)^2 \quad \text{(Equation 5-19)}$$

Various software programs are available that can perform the refinement calculations, and all will essentially operate in the same way, by working from approximate values for all the parameters they carry out numerous refinement cycles until the function meets a specified convergence threshold. Structural parameter refinement should not begin until most (ideally all) atoms are found. Difference Fourier maps can be used to identify missing atoms for incomplete structural models and prevent incorrect description of electron density; they can be generated by subtracting the calculated electron density of the model from the calculated density from observed reflection intensities[189].

5.4.5 Geometric restraints

Powder diffraction data is a one-dimensional projection of a 3D structure and so there is always a degree of information loss. This can be compensated for by introducing geometric data such as typical bond lengths and angles from related structures as a starting point. A structure file can be used to increase the number of geometric observations allowing more parameters to be refined while maintaining a reasonable structural geometry. Structure files available from large, searchable databases such as the Inorganic Crystal Structure Database (ICSD) provide Crystallographic Information Files (.cif format) that can be imported into the refinement software[192]. Great care must be taken because

if an incorrect geometric restraint, e.g., the wrong space group is applied to the structure data, the refinement will not progress.

5.4.6 Estimated standard deviation (ESD) calculations

The estimated standard deviation (ESD) is calculated differently depending on the Rietveld refinement software used. The most often cited is the ESD in the j^{th} parameter, i.e., the minimum possible probability error arising from random errors; calculated from the number of observations (N), adjusted parameters (P) and applied constraints (C)[190]:

$$\sigma_j = \sqrt{\frac{\sum_i w_i (y_{o,i} - y_{c,i})^2}{M_{jj}(N - P + C)}} \quad \text{(Equation 5-20)}$$

$1/M_{jj}$ = Diagonal element of the inverse matrix

Statistically, each measurement is considered an independent observation and the calculated ESD makes the assumption that counting statistics are the only source of error, despite systematic errors having a significant impact. The ESD calculations are therefore only representative of the precision of a refinement parameter rather than the accuracy. A structure refinement should be guided towards convergence, where all profile and structural parameters are refined simultaneously and the ESD in the final cycle of a refinement step is ≤ 0.1 [189].

5.4.7 R-factor interpretation

R-factors are an attempt to numerically quantify the goodness-of-fit of a calculated structural model to the observed data. The profile R-factor (R_p) is calculated from the sum of all observed intensities while the weighted profile R-factor (R_{wp}) is more commonly used[185]:

$$R_p = 100 \times \sum_i \frac{|y_{o,i}^2 - \frac{1}{c} \times y_{c,i}^2|}{\sum_i y_{o,i}^2} \quad \text{(Equation 5-21)}$$

$$R_{wp} = \sqrt{\frac{\sum_i w_i (y_{o,i} - y_{c,i})^2}{\sum_i w_i (y_{o,i})^2}} \quad \text{(Equation 5-22)}$$

$$w_i = \frac{1}{\sigma^2(y_{o,i})} \quad \text{(Equation 5-23)}$$

The numerator of the R_{wp} equation is the residual minimised during Rietveld refinement, which best reflects the refinement process. R_{wp} for TOF diffraction profiles are typically small compared to those obtained from laboratory PXRD due to the background, so a good peak fit requires the R_{wp} for a background subtracted profile should ideally be calculated. An ideally fit profile should show the final R_{wp} value approach the statistically expected R_{exp} value, determined from [189], [190]:

$$R_{exp} = \sqrt{\frac{N - P + C}{\sum_i w_i (y_{O,i})^2}} \quad \text{(Equation 5-24)}$$

The ratio of these two R-factors together can be used to give the goodness-of-fit (χ^2), which if ideal, R_{wp} will be close to R_{exp} and χ^2 will be close to unity [189], [193]:

$$\chi^2 = \left(\frac{R_{wp}}{R_{exp}} \right)^2 \quad \text{(Equation 5-25)}$$

The χ^2 value will start out large when the model is poor and decrease throughout the refinement process as the model is improved, making it a relatively reliable metric for validating a model in comparison to the data. A χ^2 value that is small (approaching 1) indicates a better fit however, if $1 > \chi^2 \gg 1$ then the model can be considered incorrect or at least incomplete, requiring additional accounting for intrinsic errors within the data [193]. Visual observation of a profile fit is considered a more reliable method of monitoring the progress of a refinement. Difference plots provide greater context for the cause of a high R-factor resulting from issues with the profile parameters, e.g., where total intensity is reasonable but peak shapes do not match.

5.5 Structural analysis techniques

5.5.1 Diffuse reflectance measurement using UV-vis spectroscopy

Diffuse reflectance (DR) UV-vis spectroscopy provides a method of recording the percentage reflectance (R%) from a sample compared to a background reference as a function of λ , then calculating absolute reflectance as a function of photon energy (R_{hv}) which is used to determine the optical band gap (E_g). The measurements carried out in this project utilised the integrating sphere configuration of a Shimadzu UV-2600 UV-VIS Spectrophotometer (Figure 5.5).

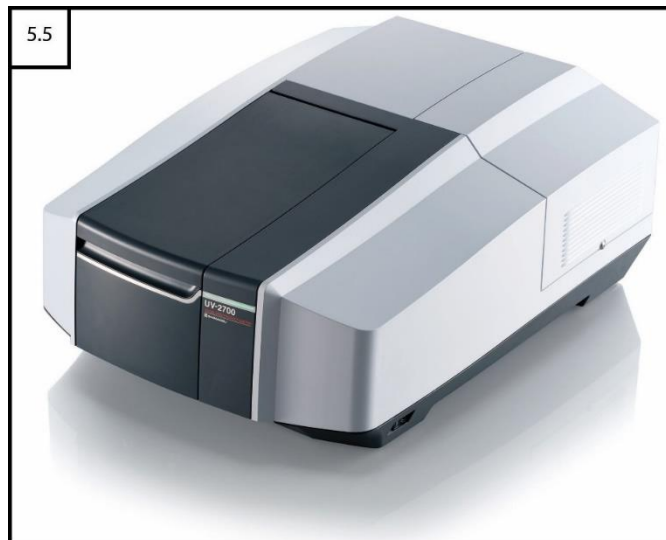


Figure 5.5: Shimadzu UV-2600 UV-VIS Spectrophotometer[194]. Image reproduced courtesy of Shimadzu Corporation

Incident light cannot penetrate opaque (solid) samples and is instead reflected symmetrically from the surface with respect to the normal line, a phenomenon referred to as specular reflection as illustrated in figure 5.6. Incident light scattered in multiple directions from rough surfaces such as paper or powder samples is called diffuse reflection.

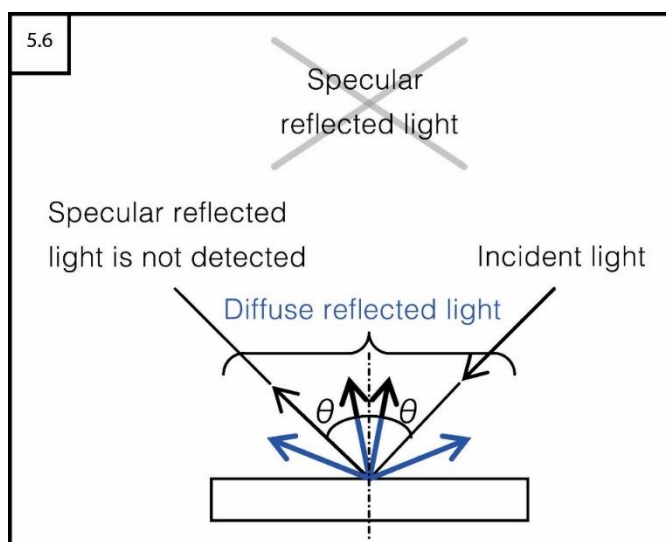


Figure 5.6: Diagram of diffuse reflected and specular reflected light reproduced courtesy of Shimadzu Corporation[194]

Relative reflectance (R%) is calculated from the proportion of reflected light measured from a sample surface relative to a reference surface with an assumed reflectance of 100 % [194]:

$$R\% = \frac{\text{Light reflected from sample}}{\text{Light reflected from reference plate}} \times 100 \quad \text{(Equation 5-26)}$$

Relative DR measurements conducted with an integrating sphere, in which BaSO₄ or some other solid surface serves as the reference, excludes specular reflected light [194]. As shown in the diagram of the ISR-2600Plus reproduced

from the Shimadzu UV-2600 brochure (Figure 5.7), the integrating sphere is a spherical chamber with apertures that directs two light beams towards the reference and sample plates with a set of fixed mirrors.

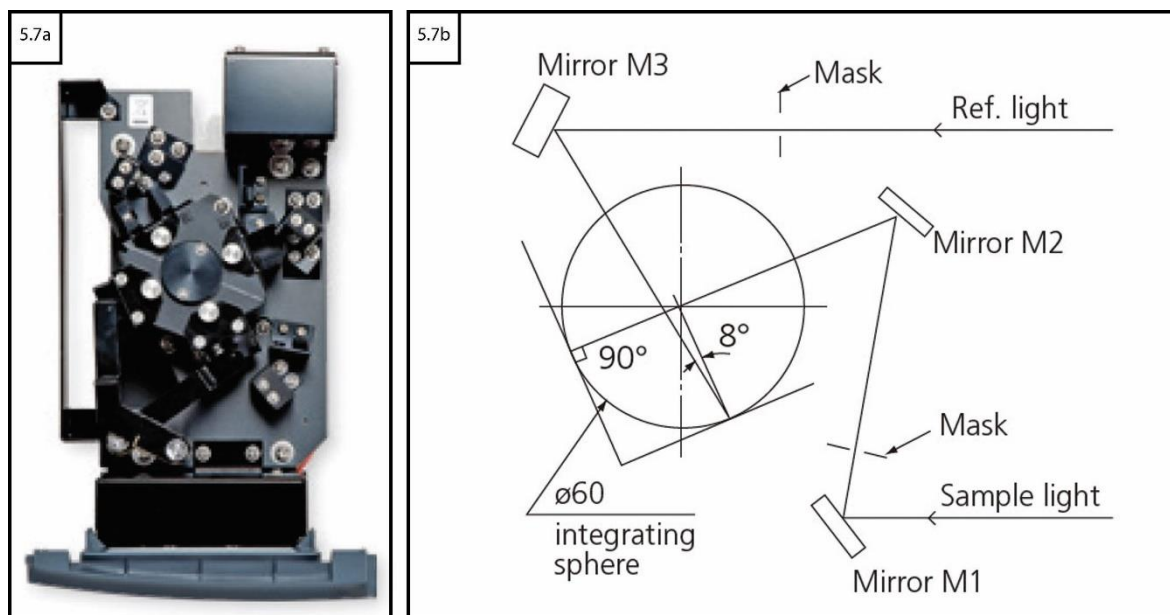


Figure 5.7: a) ISR-2600Plus integrating sphere b) integrating sphere mirror geometry[194]. Images reproduced courtesy of Shimadzu Corporation

The inner surface of the sphere is coated in a light scattering material with high reflectance which causes the beam to scatter uniformly; and with the detector located below the sphere so as to not interact directly with the incident light. All measurements were carried out with respect to a baseline scan performed over $\lambda = 190\text{--}1300$ nm using a BaSO_4 standard; further details are available in appendix section A-5.8. A small amount of finely ground sample powder was adhered to a cut rectangle of filter paper by gently spreading and pressing with a spatula, then attached to the sample stage. The instrument parameters were set with a slit width of 5 nm, accumulation time of 0.1 s, light source change $\lambda = 323$ nm, detector change $\lambda = 800$ nm and scanning speed of 0.5 nm min^{-1} . The angle of incident light was set to $0^\circ/8^\circ$ with a measurement $\lambda = 220\text{--}850$ nm.

5.5.2 Calculating optical band gap (E_g) from Kubelka-Munk function

Czech-American physicist Jan Tauc described the relationship between the absorption coefficient (α) and E_g ; the photon energy of the light beam ($h\nu$) is the kinetic energy transferred to a photon and is related to its λ [195]:

$$\alpha h\nu = \alpha_0 (h\nu - E_g)^n \quad \text{(Equation 5-27)}$$

$$h\nu = \frac{hc}{\lambda} = \frac{1239.7}{\lambda} \quad \text{(Equation 5-28)}$$

α_0 = Band tailing parameter (a constant)

ν = Photon frequency

The band gap can be determined from a Tauc plot of $(h\nu\alpha)^{1/n}$ against $h\nu$, where α can be approximated by the optical absorbance given by the Kubelka-Munk function; in which the DR (R%) is converted to absolute reflectance (R_{hv})[196]:

$$\alpha \approx F(R_{hv}) = \frac{(1 - R_{hv})^2}{2R_{hv}} \quad \text{(Equation 5-29)}$$

$$R_{hv} = \frac{R\%}{100} \quad \text{(Equation 5-30)}$$

The Tauc plots are generated using this approximation of the Kubelka-Munk function $(h\nu F(R_{hv}))^{1/n}$ against $h\nu$, where n is given a different value depending on whether direct or indirect (allowed or forbidden) E_g is applicable.

Table 5.5: Allowed and forbidden values of n for the direct and indirect band gap[195]

	Allowed E_g	Forbidden E_g
Direct	1/2	3/2
Indirect	2	3

By taking the tangent to the straight section (inflection point) of the Tauc plot curve, the x-intercept indicates the optical band gap (E_g) value for the appropriate Kubelka-Munk function that has been applied.

5.5.3 Sample imaging using scanning electron microscopy (SEM)

Scanning electron microscopes (SEM) produce images by detecting the scattered electrons and radiation resulting from interaction with an incident high-energy beam of electrons. As the electrons impact a sample, they penetrate to a depth of a few microns depending on the accelerating voltage of the beam and sample density. Secondary and backscattered electrons along with characteristic X-rays are produced as the energy propagates into the surface (Figure 5.8)[197].

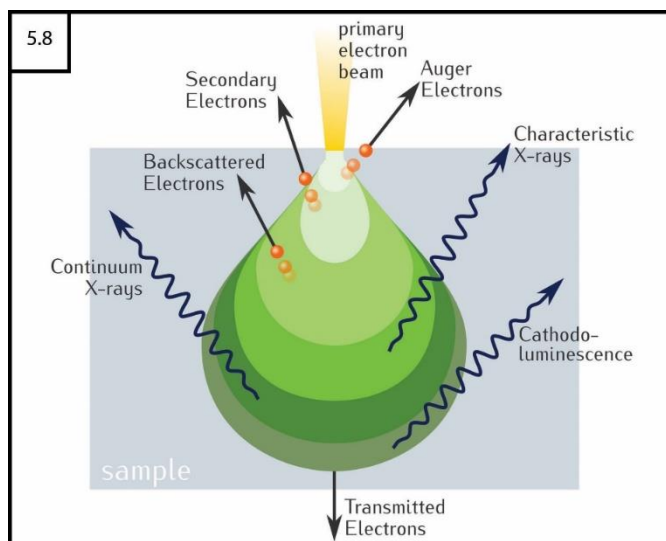


Figure 5.8: Diagram of scattering and secondarily released electrons and types of radiation from an incident high-energy electron beam[198]. Image by Ponor, CC via Wikimedia Commons

A handful of samples were prepared for imaging in a Philips/FEI XL30 ESEM Scanning Electron Microscope that features a tungsten electron gun for generating the electron beam that can be focused over small areas. They were finely ground and spread onto 12 mm diameter metal sample holders using a double-sided adhesive sticker. The samples were coated with an ultrathin layer of Au/Pd particles using a Polaron SC7640 auto/manual high-resolution sputterer to prevent non-conductive sample materials from building up an electrostatic charge. Such a charge would interfere with the electron beam, rendering the samples invisible to the ultramicroscope. Up to six samples could be loaded into the rotating sample stage located inside a vacuum chamber at any one time. The SEM collects currents leaving the sample and the measurements are translated into images using the attached Gatan X-ray Ultramicroscope, which is capable of generating images of surfaces at a resolution of 3.5 nm (at 30 kV in high vacuum mode) over a 10–40,000× magnification range. The images may not represent the visual appearance of the material surface since the electrons are scattered by any intrinsic property able to manifest a current and will also vary with the angle of incidence[199].

5.5.4 Energy dispersive X-ray spectroscopy (EDX)

Attached to the SEM is an Oxford Instruments INCA EDX microanalysis system which acquires elemental data from a sample to provide information on material composition, crystal structure, fractional distribution of elements etc. The spectrometer is capable of very high rates of data acquisition for point analysis of very small areas down to 1 μm in diameter. The elemental composition of a sample is obtained by identification of the characteristic X-ray spectra of the

material which assembles an element distribution map to visualise the spatial distribution of elements within a sample[200].

5.6 Determination of thermoelectric properties

As discussed in section 2.5.3, the efficiency of a TEM is quantified by the dimensionless figure of merit (zT), which is defined by the electrical properties (S and σ) often referred to collectively as the power factor (PF), and the total thermal conductivity (κ_T):

$$zT = \left(\frac{PF}{\kappa_T}\right)T = \left(\frac{S^2\sigma}{\kappa_l + \kappa_e}\right)T \quad \text{(Equation 5-31)}$$

The electrical contribution to thermal conductivity (κ_e) is proportional to σ with both being dependent on T , as per the Wiedemann-Franz law (Eqn 2–103). The Lorentz number (L) is usually taken as a universal factor of $2.44 \times 10^{-8} \text{ W}\Omega\text{K}^{-2}$ however, it is actually correlated with S and therefore L can be calculated more accurately from the formula proposed by Hyun-Sik Kim et al[66]:

$$L = 1.5 + \exp\left(\frac{-|S|}{116}\right) \quad \text{(Equation 5-32)}$$

Once the κ_e values are determined, they can simply be subtracted from the from the κ_T to give the lattice contribution to the thermal conductivity (κ_l).

5.6.1 Calculating total thermal conductivity (κ_T)

κ_T is not measured directly but rather calculated from the measured thermal diffusivity (α), material density ρ and specific heat capacity (C_p)[201]:

$$\kappa_T = \alpha\rho C_p \quad \text{(Equation 5-33)}$$

A Linseis LFA 1000 laser flash analysis instrument, shown in figure 5.9a, records α for a 13 mm diameter pellet sample over a range of controlled temperatures. The schematic diagram of the LFA (Figure 5.9b) shows how the pulsed laser irradiates the bottom face of a pressed sample pellet resulting in a homogenous temperature rise on the top face. The ΔT at the top face is measured with a highly sensitive high speed IR detector.

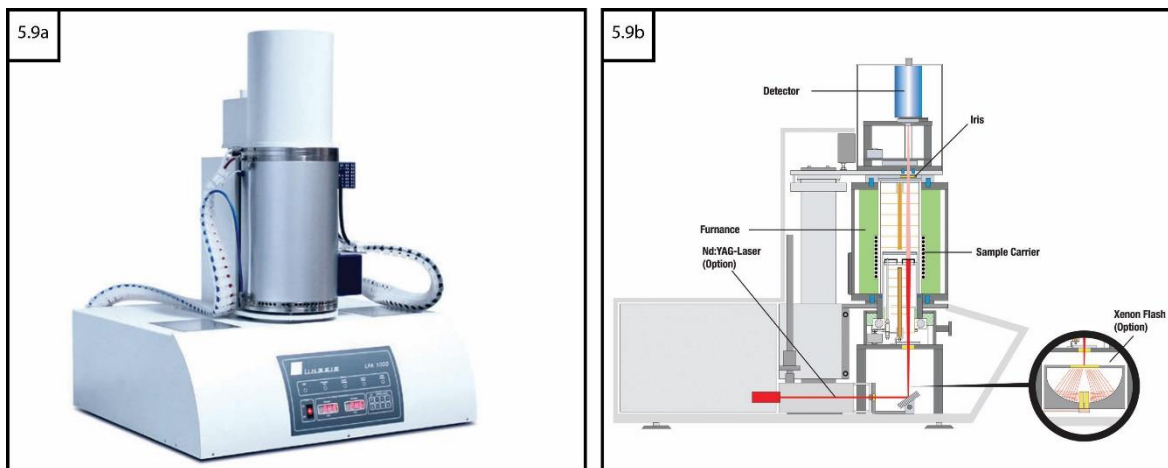


Figure 5.9: Linseis LFA 1000 laser flash analysis a) instrument b) schematic diagram[201]. Images reproduced with permission from Linseis

Pellets were produced through both cold-pressing and hot-pressing methods, the relative benefits of which are discussed in appendix section A–5.9. The material density can either be measured through calculation from the sample mass and dimensions, using an Archimedes density measurement kit or assumed from literature data if available. Different methods were compared, with the final density measurements made using an OHAUS Pioneer analytical balance and density measuring kit like that shown in figure 5.10.



Figure 5.10: a) OHAUS Pioneer analytical balance b) density measurement kit[202], [203]. Images reproduced with permission from OHAUS

Specific heat capacity (C_p) can be taken from literature, previous experiment or using the Dulong-Petit estimate. The Dulong-Petit law describes the property of solid elements that, at $T \gg 0$ K, C_p approaches a limit and does not change further for ΔT . The Dulong-Petit estimate can be expressed in terms of number of moles and the universal gas constant (R) = 8.314 JK⁻¹mol⁻¹ or in terms of the number of atoms in the sample (N) and Boltzmann's constant (k_B) = 1.381×10⁻²³ JK⁻¹:

$$C_p = 3nR = 3Nk_B \quad \text{(Equation 5-34)}$$

If the sample is not fully dense (i.e., $\rho < 95\%$) a porosity correction can be applied based on the following relationship[110]:

$$\frac{\kappa_T}{\kappa_D} = 1 - \frac{4}{3}\phi \quad \text{(Equation 5-35)}$$

$$\phi = \frac{100 - \% \rho}{100} \quad \text{(Equation 5-36)}$$

κ_D = Thermal conductivity of a fully dense sample

5.6.2 Seebeck coefficient (S) and electrical conductivity (σ)

Measurement of the electrical properties requires the sample pellets to be cut into bars with approximate dimensions of $\sim 2 \times 2 \times 12$ mm. These were prepared following analysis in the LFA using a SYJ-150 precision low speed diamond saw, like that shown in figure 5.11.

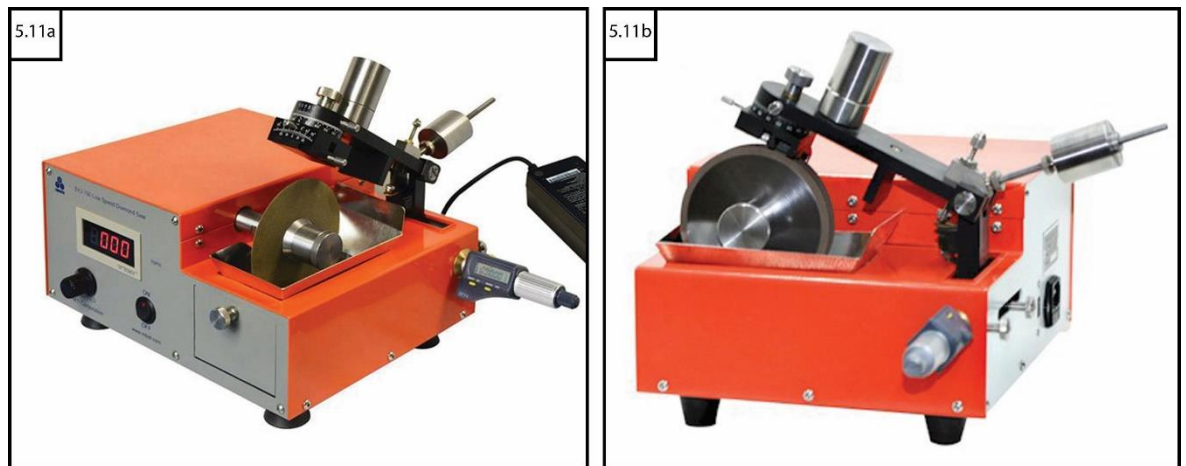


Figure 5.11: SYJ-150 precision low speed diamond saw[204]. Images courtesy of MTI Corp distributed by PI-KEM Ltd

A Linseis LSR Seebeck and electrical resistivity instrument, shown in figure 5.12, records the thermovoltage (V_{th}) and ∇T necessary to calculate S as well as the electrical resistivity (ρ) over a range of controlled temperatures with a pair of thermocouple probes.



Figure 5.12: Linseis LSR Seebeck and electrical resistivity instrument[205]. Image reproduced with permission from Linseis

The samples were secured by the heating element in the electrode clamps which generate a temperature gradient across the bar. The sample is placed in direct contact with two laterally connected thermocouple probes as shown in the schematic diagram reproduced from the instrument brochure in figure 5.13.

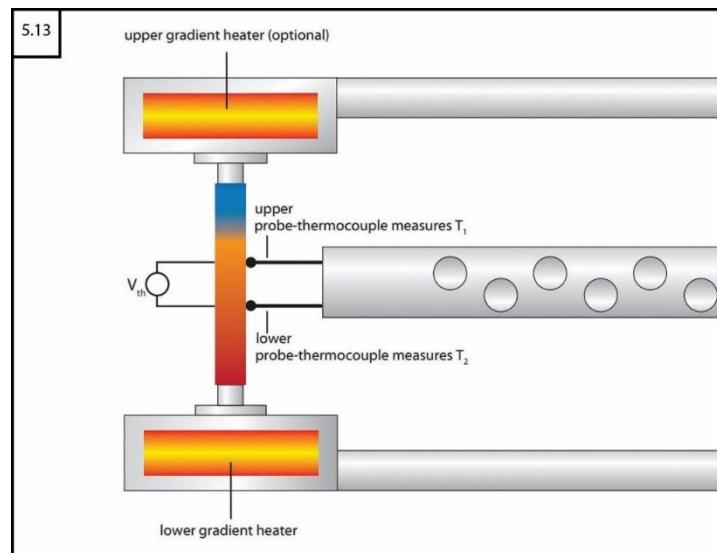


Figure 5.13: Operational mode of Linseis LSR to obtain Seebeck coefficient[205]. Image reproduced with permission from Linseis

The ΔT between probes T_1 and T_2 is recorded while one thermocouple also measures V_{th} generated from ∇T ; S is then calculated from[205]:

$$S = \frac{-V_{th}}{T_H - T_C} \quad \text{(Equation 5-37)}$$

Additionally, E_g can be estimated by rearranging the Goldschmid–Sharp equation which states that the maximum S of a semiconductor is approximate to $\frac{1}{2}E_g$ divided by the associated maximum T and elementary charge (e)[206]:

$$E_g = 2e|S|_{max}T_{max} \quad \text{(Equation 5-38)}$$

The voltage drop (V) between thermocouple probes (t) is measured from a constant direct current (I_{DC}) being applied across the sample (with cross-sectional area = A) by the two electrode clamps as shown in figure 5.14.

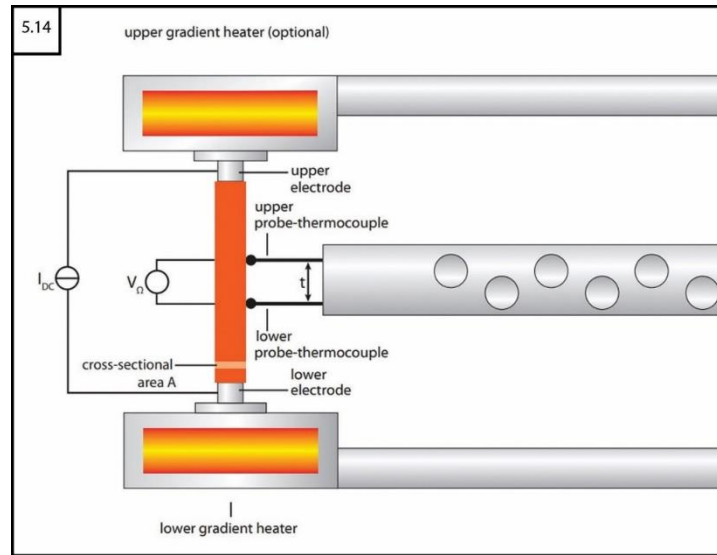


Figure 5.14: Operational mode of Linseis LSR to obtain electrical resistivity[205]. Image reproduced with permission from Linseis

The electrical resistivity (ρ) and thus σ is calculated from these values[205]:

$$\rho = \frac{V}{I_{DC}} \frac{A}{t} = \frac{1}{\sigma} \quad \text{(Equation 5-39)}$$

5.6.3 Error propagation in thermoelectric measurements

The measurement uncertainties associated with typical commercial instrument tend to be relatively small as shown in table 5.6 however, the propagation of errors quickly accumulates. Measurement of TE properties are dependent on factors such as thermal gradients which, far from ambient room temperature, add to the systematic inaccuracies.

Table 5.6: Typical uncertainty values for various measured thermoelectric properties[207]

Property	Typical uncertainty (%)
Thermal diffusivity (α)	± 3
Density (ρ)	± 1
Heat capacity (C_p)	± 5
Electrical conductivity (σ)	± 3
Seebeck coefficient (S)	± 4
Calculated figure of merit (zT)	± 15

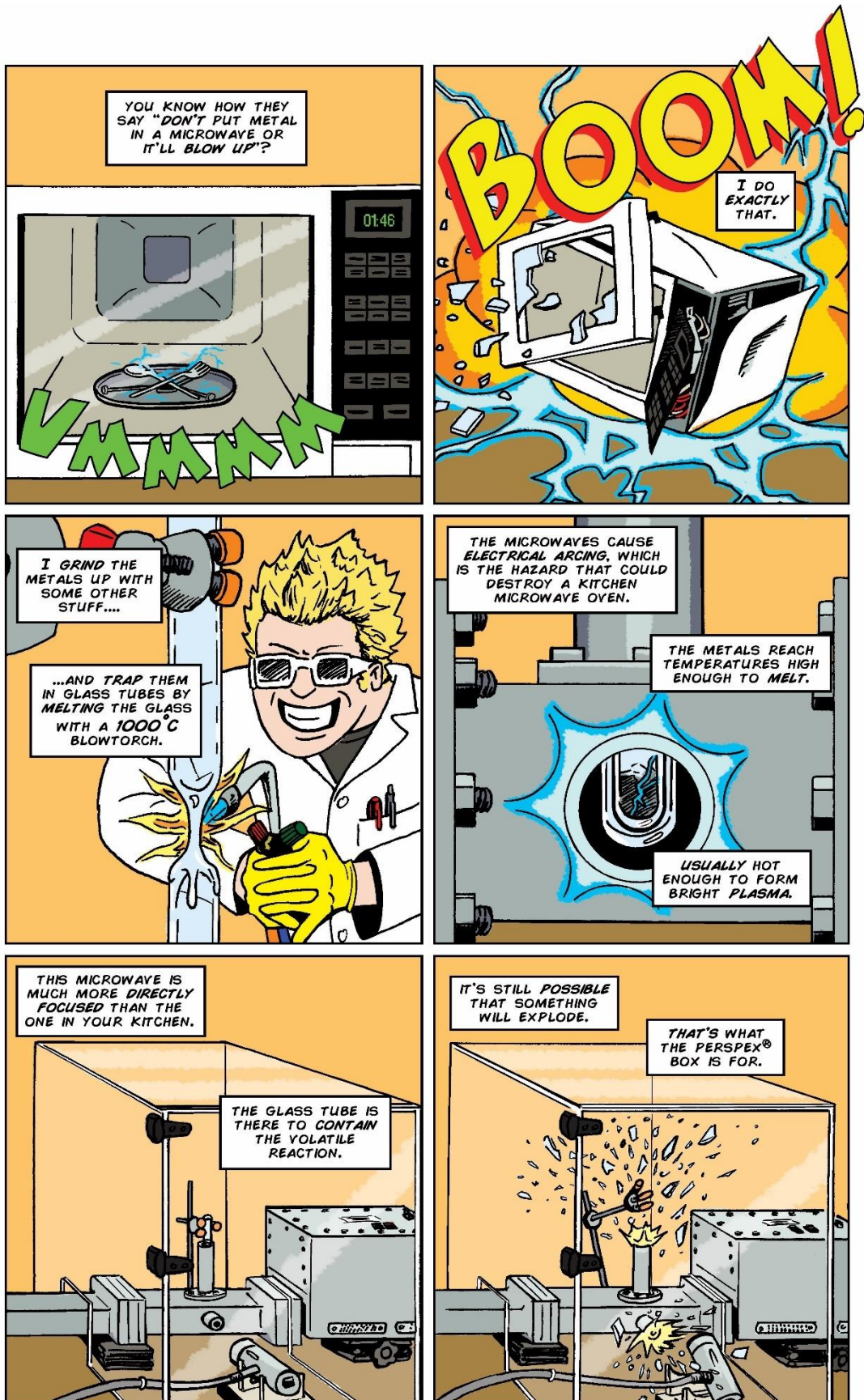
The individual uncertainties can range between 5–20 % and when multiplied, divided or squared as they are when calculating zT , the associated uncertainty for the calculated value (δzT) is given from[52]:

$$\delta zT = \sqrt{\left(2 \frac{\delta S}{S}\right)^2 + \left(\frac{\delta \sigma}{\sigma}\right)^2 + \left(\frac{\delta C_p}{C_p}\right)^2 + \left(\frac{\delta \alpha}{\alpha}\right)^2 + \left(\frac{\delta \rho}{\rho}\right)^2} \quad \text{(Equation 5-40)}$$

As samples are produced with greater amounts of doping in attempts to tune the carrier concentration, small changes greatly affect the measured properties which can be difficult to correct due to the lack of standards with which to calibrate the instruments. The complexities and cumulative errors mean that results should be viewed with a critical eye as the total uncertainty for zT values can potentially be as high as 50 %. It is therefore more pertinent to establish a close agreement between successive measurement runs under the same conditions, which will give a much more accurate appraisal of the validity of the calculated TE performance[52], [207].

6 Polaris-SMC microwave reactor components

6.1 Explaining the thesis badly



6.2 Neutron diffraction at the Diamond Light Source

The primary focus of this project was the commissioning of the bespoke SMC reactor, designed to operate within the Polaris neutron diffractometer at the ISIS Neutron and Muon Source in RAL. All the components of the SMC reactor were purchased from Gerling in 2015 in duplicate so that a benchtop instrument could be set up at the University of Glasgow as well as the on-site instrument for use with Polaris. RAL is the home of the Diamond Light Source synchrotron, the only synchrotron facility currently in operation within the UK. The RAL synchrotron is used to generate bright light beams by accelerating protons close to the speed of light before being directed towards one of the 32 attached beamlines. The ISIS Neutron and Muon Source is owned by the Science and Technology Facilities Council (STFC) and is comprised of over 30 neutron and muon instruments between the two target stations attached to Diamond. The Polaris instrument is connected to the beamline within target station 1 and is used to carry out high resolution PND studies. The high flux of neutrons used at the Diamond spallation neutron source allow measurement down to extremely low d -spacings ($\sim 0.3 \text{ \AA}$) and with very wide Q range to aid refinement of site occupancies and temperature factors in disordered materials. The basic principles of diffraction techniques including the use of neutrons are discussed in greater detail in section 5.3.6.

6.2.1 *Polaris neutron diffractometer*

The Polaris diffractometer was upgraded from 2010 to 2012 for the installation of a new detector tank and is a high intensity, medium resolution power diffractometer. Multiple detector elements are grouped into a total of 38 modules, which are separated into five banks around the circumference of the sample tank, each covering discrete angular ranges. The five detector banks are highlighted and labelled in the instrument schematic shown in figure 6.1; the circular section in the approximate centre of the schematic represents the 400 mm diameter Polaris sample tank access port into which the sample applicator section of the SMC reactor waveguide is lowered.

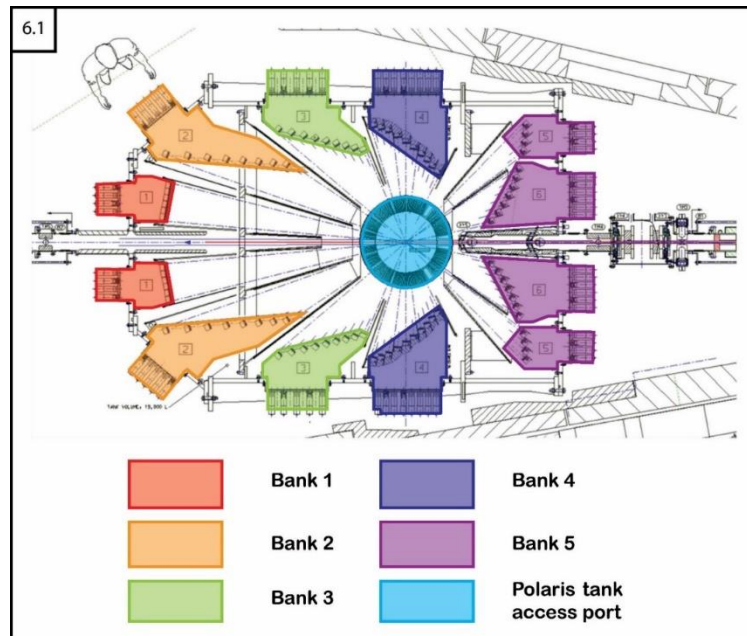


Figure 6.1: Schematic of Polaris diffractometer highlighting the five detector banks in relation to the tank access port[208]

The large number of brass-coloured, cylindrical detectors, which are more clearly seen in figure 6.2 surrounding the detector tank, allows for high resolution data to be collected in a short span of time and/or from small samples.

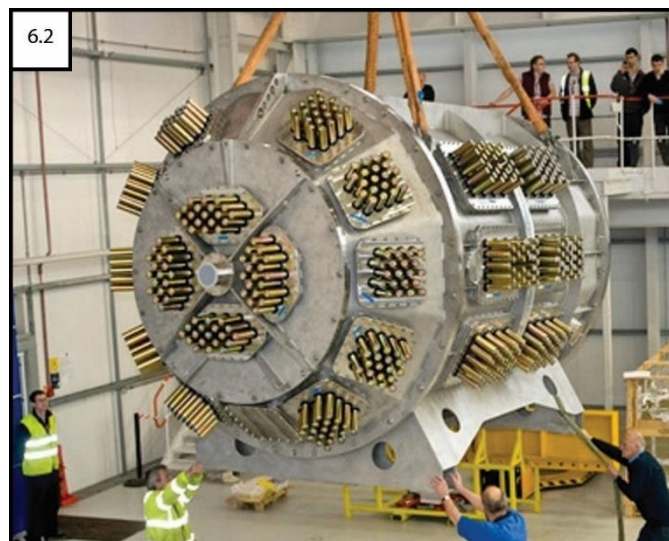


Figure 6.2: Polaris detector tank as seen during installation in target station 1[209]

The resolution of Bragg reflections is best at higher 2θ angles and inversely proportional to d -spacing. Each detector bank collects diffracted neutrons over a specific angular range; the design of the Polaris-SMC reactor incorporates boron nitride shields to exclude interference from thicker sections of the aluminium waveguide. As discussed in section 5.3.7, this limits the data collection only to angles in the range of the bank 4 detectors. The secondary flight path (L_2) refers to the distance between the sample position and the respective detector; the primary flight path is the distance (14 m) between the sample position and the moderator[181].

Table 6.1: Polaris detector bank technical information[181], [210], [211]

Detector bank	Very low angle (1)	Low angle (2)	Low angle (3)	Orthogonal angle (4)	Back scattering (5)
No. modules	4	10	6	6	12
No. elements	55	88	99	110	40–70
2 θ range (°)	6.7–14.0	19.5–34.1	40.4–66.4	75.2–112.9	134.6–167.4
Resolution ($\Delta d/d$)	2.7×10^{-2}	1.5×10^{-2}	8.5×10^{-3}	5×10^{-3}	3×10^{-3}
L ₂ (m)	2.25	2.36–1.31	1.57–0.925	1.08–0.71	1.54–0.795
<i>d</i> -spacing range (Å)	0.5–40	0.5–13.5	0.3–5.9	0.2–3.7	0.2–2.7

6.3 Bespoke SMC microwave reactor components

Most commercial MW systems are constructed around a magnetron (powered by a transformer) for generating the desired waves, a waveguide for transporting the waves and a cavity/applicator where the MWs interact with a target load. The cavity in a common household DMO is the multi mode variety, a metal box with a windowed door that allows the MWs to reflect from all surfaces to create several heating modes. The bespoke SMC reactor discussed in this chapter is built from modular components to produce a single standing wave heating mode.

6.3.1 Gerling GA4015 1.2 kW laboratory magnetron head

This magnetron head is designed specifically to operate in conjunction with the Gerling GA4104A power supply as an integrated MW power generation system. Control potentiometers for the level of MW power are located on the front panels of both the magnetron head and power supply along with a toggle switch on the front panel of the magnetron head to select the source of power control between “Mag Head”, “Power Supply” and “Remote”. In this setup the “Power Supply” position was selected to make the power supply potentiometer the primary controller that overrides the settings of other controllers, unless set to zero. The magnetron has a maximum output power of 1.2 kW and $f = 2450 \pm 30$ MHz. Further information on the physics by which a magnetron produces MW radiation from a current is available in appendix section A–6.1. The stainless steel chassis contains safety interlocks for the waveguide flange, access cover and over-temperature. These interlocks will cut power or prevent operation in the event that the connections are not secure or the component begins to overheat. An internal fan provides cooling airflow with inlet and exhaust vents located at opposite ends of the chassis; at least 5 cm of clearance should be

maintained from each vent for adequate cooling. The magnetron head is positioned first in sequence, for obvious reasons, and should be connected directly to an isolator to protect it from reflected power. When all interlocks are engaged and the system is in “standby” or “operate” mode the relay engages. The +24 V DC high voltage “enable” signal is delivered to the power supply when the green start button is pressed as shown below in figure 6.3. The signal is cut and MW power generation ceased when the red stop button is pressed (below the start button). The power supply controls the MW output power level by adjusting the magnetron anode current which is proportional to the analogue 0–10 V DC control voltage output.



Figure 6.3: Gerling GA4015 1.2 kW laboratory magnetron head when connected in benchtop SMC reactor configuration

All connections for remote control of the MW power system using analogue signals are made to the magnetron head at the 9-pin male D-sub output connector (J4). When additional remote control circuitry is not used, as in the benchtop SMC MW reactor application, a simple female mating connector with jumpers must be connected for the system to function.

6.3.2 Gerling GA1107 2-port isolator

The isolator is ideally connected directly adjacent the magnetron head in order to protect it from reflected MW power which can damage the magnetron. This model was designed for a maximum of 6 kW of continuous forward power and to withstand a full reflection. The isolator is a directional component with port 1 connected to the magnetron and port 2 oriented towards the sample applicator. A black arrow can be seen printed on the top face of the isolator in figure 6.4 that is used to identify the directionality of the component.

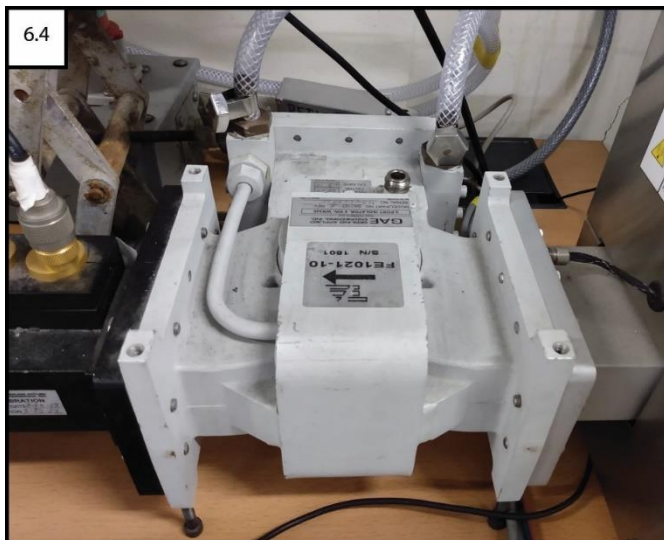


Figure 6.4: Gerling GA1107 2-port isolator when connected in benchtop SMC reactor configuration

The reflected MW power is directed with a strong magnet into a continuously cooled termination plate with water flowing through internal quartz tubes. The water source must be externally set to flow at an adequate rate (minimum of 0.5 gpm) such that the outlet water temperature does not exceed 50°C.

6.3.3 Gerling GA3106 directional waveguide coupler

The directional waveguide coupler is used to measure the level of MW power flowing in the waveguide in both the forward and reflected directions. The information is used to monitor and optimise the MW absorption of a sample by adjusting the short circuit (see section 6.3.8) to maximise the forward power while minimising the reflected power. Each probe consists of a loop antenna mounted above a short section of waveguide and coupled to the waveguide through a round iris. One end of the loop terminates in a 50 Ω RF resistor while the other transmits the attenuated output signal to a female N-type BNC connector port. The MW input and output ports are directional since the coupler probe positions must be maintained. The directional arrow is not visible in figure 6.5, but the ports are labelled on the side of the probe mounting block with “F” for forward power on the right-hand (magnetron) side and “R” for reflected power on the left-hand (applicator) side.

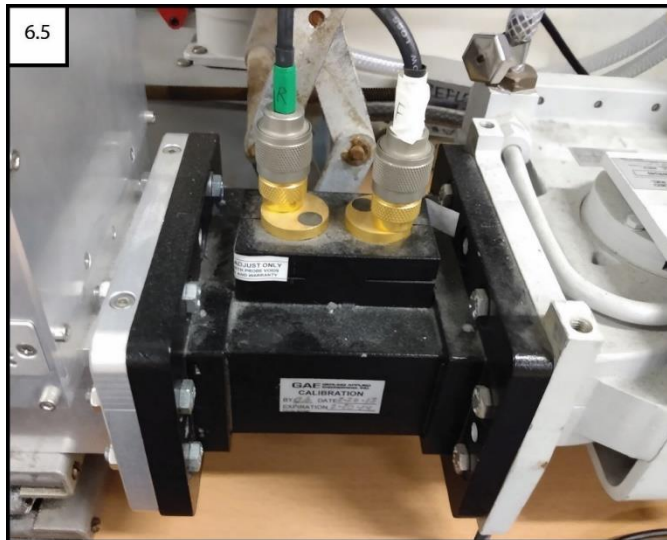


Figure 6.5: Gerling GA3106 directional waveguide coupler when connected in benchtop SMC reactor configuration

The coupler is rated for a frequency of 2.45 ± 0.05 GHz and a nominal coupling factor of 60 ± 0.1 dB which limits the output signal to 3 mW. For detecting the power to and from the process load, the coupler should not be fitted between the auto tuner and the sample applicator. The performance of directional couplers is defined by the coupling factor and directivity. The coupling factor is the attenuation between waveguide power and output signal:

$$\text{Coupling factor} = 10 \log \frac{\text{waveguide power}}{\text{probe output power}} \quad (\text{Equation 6-1})$$

Directivity is the attenuation between output signals from sampling the same waveguide power in opposite directions:

$$\text{Directivity} = 10 \log \frac{\text{probe output sensing in forward direction}}{\text{probe output sensing in reflected direction}} \quad (\text{Equation 6-2})$$

Measurement errors occur when power is propagating in both directions with the error being greater with larger values of reflected power.

6.3.4 Gerling GA3301 coupler power interface (CPI) modules

The coupler power interface (CPI) is a means of converting the MW signal level at the output port of the waveguide coupler to a DC voltage proportional to the power in the waveguide. The components are simple, grey electronic converters as shown in figure 6.6 attached directly to the BNC coupler ports on the Polaris-SMC reactor.



Figure 6.6: Gerling GA3301 coupler power interface (CPI) modules when connected to the waveguide coupler in Polaris-SMC reactor configuration

The output signal can be calibrated for a full-scale operating range of up to 10 mW input power, equivalent to 10 kW waveguide power for -60 dB coupling factor. The output signal from the CPI is a measure of the MW signal level present at the input connector which is usually much lower than the actual waveguide power level. The output signal is determined by the coupling factor of the waveguide coupler and so the waveguide power (P_w) is calculated from:

$$P_w = \frac{V_0 \text{Scale}}{10000} 10^{(CF/10)} \quad \text{(Equation 6-3)}$$

V_0 = CPI output signal voltage

Scale = CPI full scale calibration range

CF = Coupling factor of waveguide coupler probe (positive value)

6.3.5 Gerling GA1022 STHT V 1.5 Auto Tuner

The distribution of \mathbf{E} and \mathbf{H} fields are influenced by the size and shape of the waveguide in which they are being propagated. An auto tuner such as that shown in figure 6.7 is an automatic method of adjusting the impedance between the magnetron and the sample applicator to match variable loads to $Z_G = 50 \Omega$. The auto tuner is a directional component with labels for the flange to be directed towards the generator (GEN) and towards the device under test (DUT). Optimal power coupling between the Z_G and Z_L should be complex conjugates of each other, however where this is not the case the auto tuner supplies a third impedance to be inserted between them to compensate.

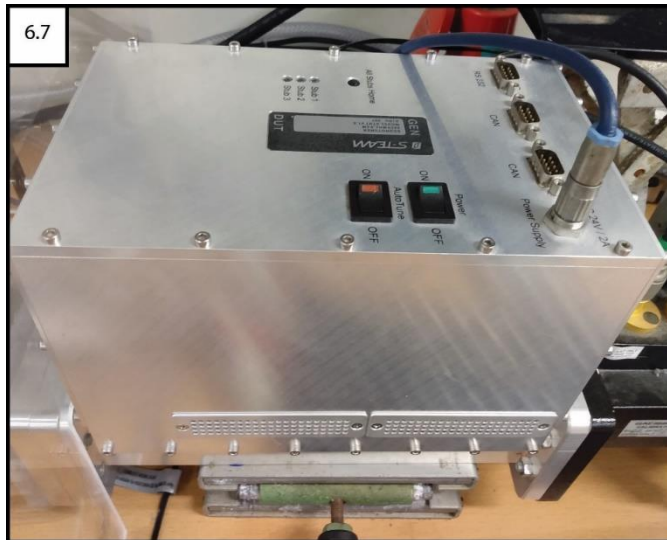


Figure 6.7: Gerling GA1022 STHT V 1.5 Auto Tuner when connected in benchtop SMC reactor configuration

The analyser component can be used to measure both magnitude and phase of the incident and reflection coefficient, the reflected and absorbed power as well as the frequency. The motorised tuner contains three electric stepping motor driven tuning stubs spaced $\frac{1}{4}\lambda_g$ apart that can be introduced or recessed from the attached waveguide section. The device uses data measured by the analyser to move the stubs in and out of the MW path to rapidly and automatically adjust impedance matching of time varying loads, including plasma. The tuner is designed to operate at $f = 2450 \pm 25$ MHz and a working power range of 1–6 kW. It is possible for the system to experience impedance mismatch severe enough that the auto tuning will fail entirely, which will be apparent in the chattering sound of the stubs continuously searching for the optimum position. This level of mismatch can be resolved extending the length of the waveguide sections.

6.3.6 Gerling GA2605 pressure/vacuum quartz window

A fused quartz silica plate held in an aluminium frame with two silicone o-rings. An optional external O-ring can be set in one face of the frame for external pressure/vacuum sealing however this feature was not required for this project. The window is rated for a $f = 2.45 \pm 0.05$ GHz and a maximum input VSWR = 1.2. When attached between components with the same Z_0 the window eliminates the need for a tuner component however, the internal load of a sample in the applicator has a combined impedance value that differs from the waveguide and so it is best located between the tuner and applicator. The window aperture operates in conjunction with the short circuit to create a standing wave in the sample applicator where the MWs reflected from the short circuit constructively interfere with the incident waves.

6.3.7 Gerling GA6004A universal waveguide applicator (UWA)

The universal waveguide applicator (UWA) is a standard section of WR340 waveguide with adapter ports on opposing broad walls which can be fitted with several adapter options depending on the application requirements. For the benchtop application, a simple cylindrical extension was used, as shown in figure 6.8, which allowed easy access for samples and provides an extended choke to prevent MW leakage.

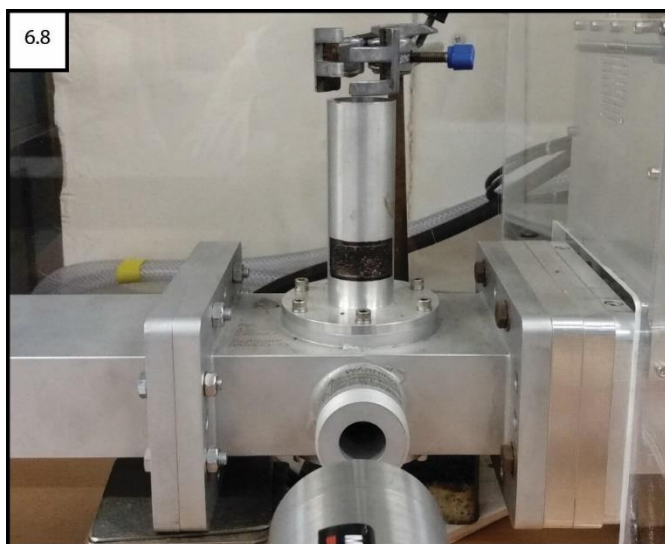


Figure 6.8: Gerling GA6004A universal waveguide applicator when connected in benchtop SMC reactor configuration

TE₁₀ mode orients E perpendicular to the direction of MW propagation in a rectangular waveguide and therefore perpendicular to the vertical adapter ports. The E field varies symmetrically in a sinusoidal manner from a maximum in the centre to zero at the waveguide walls and so heating is relatively uniform with respect to sample height but variable for wide loads. A thread boss aperture is attached to the front narrow face of the UWA for mounting a compatible IR sensor or camera although a suitable bracket was not available for the Iacon Modline IR thermometer and so it was aligned manually with the aperture.

6.3.8 Gerling GA1206A precision sliding short circuit (SSC)

The sliding short circuit (SSC) is the terminal component in the SMC reactor configuration. The SSC contains a sliding metallic plate in the waveguide attached to a plunger with non-metallic contacting surfaces (to reduce wear) that is adjusted on the benchtop configuration with a manually operated precision screw drive mechanism, i.e., the black dial visible in figure 6.9a. On the Polaris-SMC reactor the SSC is adjusted with a motorised track attached to the extended plunger via a bespoke bracket as shown in figure 6.9b.

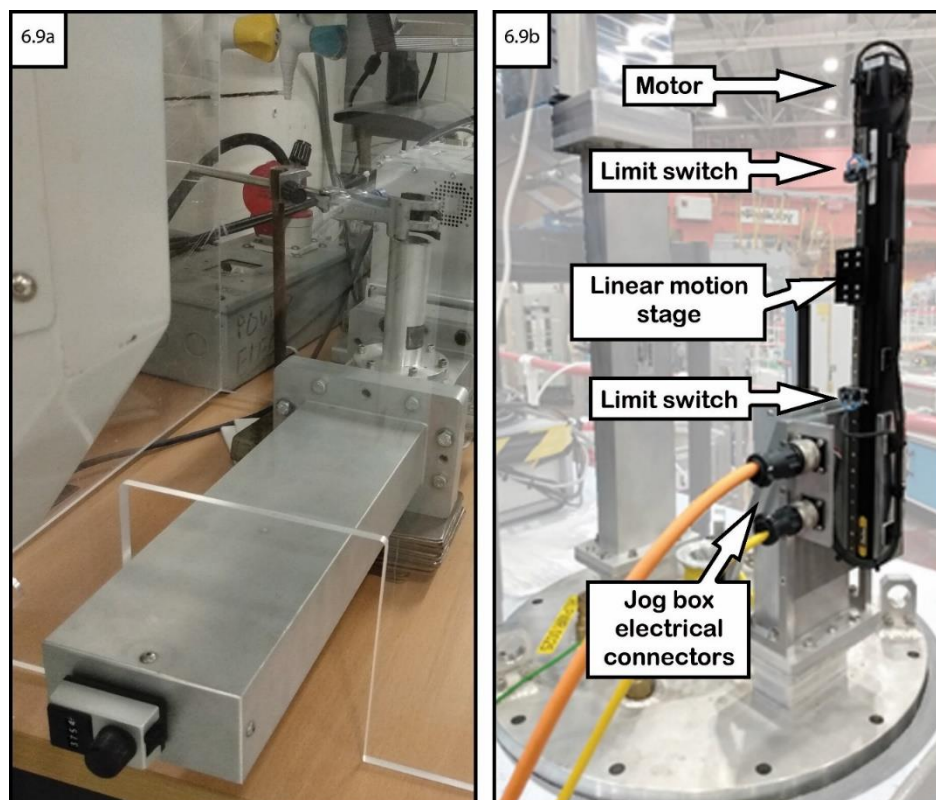


Figure 6.9: Gerling GA1206A precision sliding short circuit with a) screw drive mechanism b) motor controlled linear motion stage

The motorised track features limiter switches at either end to prevent over extension of the plunger at each extreme. The SSC works in conjunction with the fused quartz silica window to establish a standing wave with a very high VSWR and to adjust the heating mode position within the applicator. As with the auto tuner, adjusting the dimensions of the waveguide shape helps attain closer impedance matching with the sample and thus better coupling with the MWs. The SSC is designed for the full range of the plunger to be equivalent to $\frac{1}{2}\lambda_g$, which is the minimum useful range of travel for a standing wave.

6.3.9 Calibrating the electronic sliding short circuit

The bespoke electronic short circuit adjuster had been previously commissioned for use with the Polaris-SMC reactor, operated with the electronic jog box shown in figure 6.10. The jog box was provided by the ISIS workshop to control the short circuit positioning remotely. The DAQ was used to monitor the MW power in the waveguide in real time while the effectiveness and safety of the electronic short circuit was tested. The system was approved with the site safety supervisor James Taylor for manual operation during the initial round of commissioning experiments.



Figure 6.10: Electronic “jog box” control for remote adjustment of the short circuit.

6.3.10 Gerling GA4104A 1.2 kW magnetron power supply

The 1.2 kW magnetron power supply is designed to work in conjunction with the Gerling GA4015 1.2 kW laboratory magnetron head to operate as a complete MW power generation system. The power supply is capable of supplying 180–265 V AC (50/60 Hz) single phase line voltage and is cooled via a forced air external fan. The main power circuit breaker is a two-position rotary switch on the front panel, which when switched on will turn on the magnetron filament for a 10 s warm-up. Following the warm-up and once all interlocks are engaged, the green “System Ready” LED on the magnetron head will turn on. The control potentiometer located on the front panel was used to control the level of forward power generated. The toggle switch on the front panel of the magnetron head must be set to the “Power Supply” position to ensure both the magnetron head potentiometer and remote analogue signal are disabled. The MW power output is approximately linear with the anode current, represented by a series of orange LED indicators on the power supply front panel activating from left to right. The LEDs give a general representation of the magnetron power however, the actual MW power output can vary depending on the operating conditions.

6.3.11 Gerling GA3210 dual digital microwave power meter

The 0–10 V (DC) waveguide power signals output from the CPI modules are transmitted via 9-pin female D-sub output connectors (J3 = forward, J2 = reflected) to the power meter. The digital meters on the front panel are capable of displaying within a range of 0.01–1.00 kW by default. There is an additional 9-pin male D-sub output connector (J4) for the use of external data acquisition and control. The J4 output connector comprises a pair of 0–10 V analogue signals

that scale in proportion to the forward/reflected power. The first four pins give the output voltages from the forward (pins 1 and 2) and reflected (pins 3 and 4) power probes. Pins 5 and 6 operate as an internal short circuit through the CPI modules when both are connected; disconnecting either module opens the interlock loop circuit. Pins 7–9 operate an internal single-pole double-throw (SPDT) relay which activates the warning alarm when the reflected power signal reaches a user-adjustable set-point. The relay latches will be released after activation when the set-point (reset) button is pressed or the main power switch is turned off. The power meter was placed, along with the power supply, on a solid flat table in the benchtop configuration from where it was easily monitored. The chassis of both control panels were standard 1U high rack mount enclosures and so were installed in a standard 19 inch NEMA style rack cabinet along with a key operated remote control interlock for the Polaris-SMC configuration (Figure 6.11).

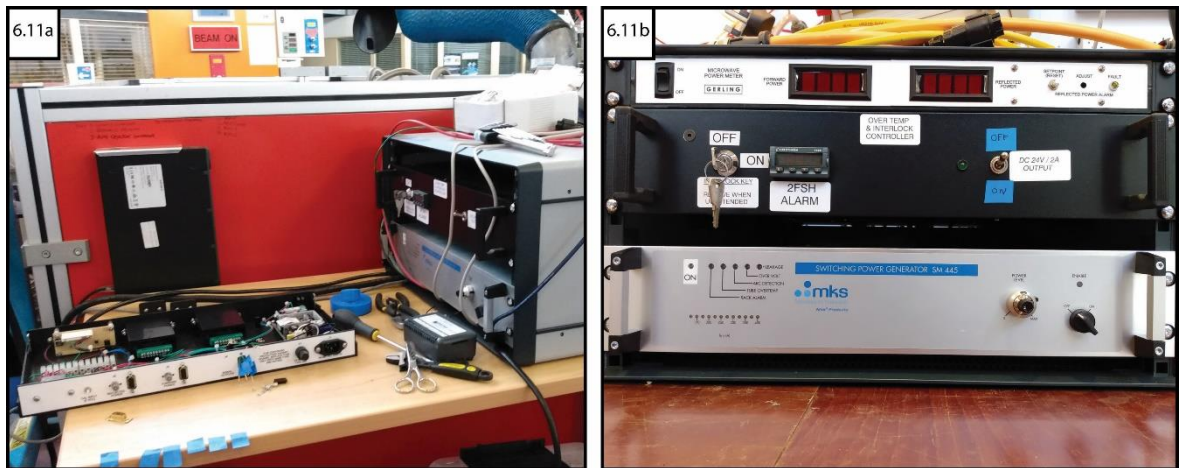


Figure 6.11: a) Power meter d-type signal output port J4 was dismantled to allow individual pins 1–4 to be connected to DAQ b) power supply, high temperature/interlock and power meter control units mounted securely in a rackmount case

The waveguide coupler probe coupling factor is applied to the 0–10 V (DC) input signal to give the waveguide power:

$$P_w = V_{in} \times SF_{in} \times \frac{10^{CF/10}}{1000} \quad \text{(Equation 6-4)}$$

V_{in} = Input signal from coupler power interface module

SF_{in} = Scale factor of input signal

The factory default setting is set to display MW power levels up to 1 kW when the input signal is 10 V (DC). For a maximum power level >1 kW, the display can include a decimal point allowing power levels up to 10.00 kW to be shown.

6.3.12 Dataq Instruments DI-1100 data acquisition (DAQ) module

From the power meter J4 pinout diagram (Figure 6.12a), the first four pins were identified as the source of output voltages from the forward and reflected power probes. A Dataq Instruments DI-1100 4-channel USB Data Acquisition (DAQ) Starter Kit was the most suitable and cost effective method of interpreting these voltages. The 9-pin J4 output port was opened up and the first four pins connected directly to the first four channels of the DAQ module as shown in figures 6.12b and 6.12c.

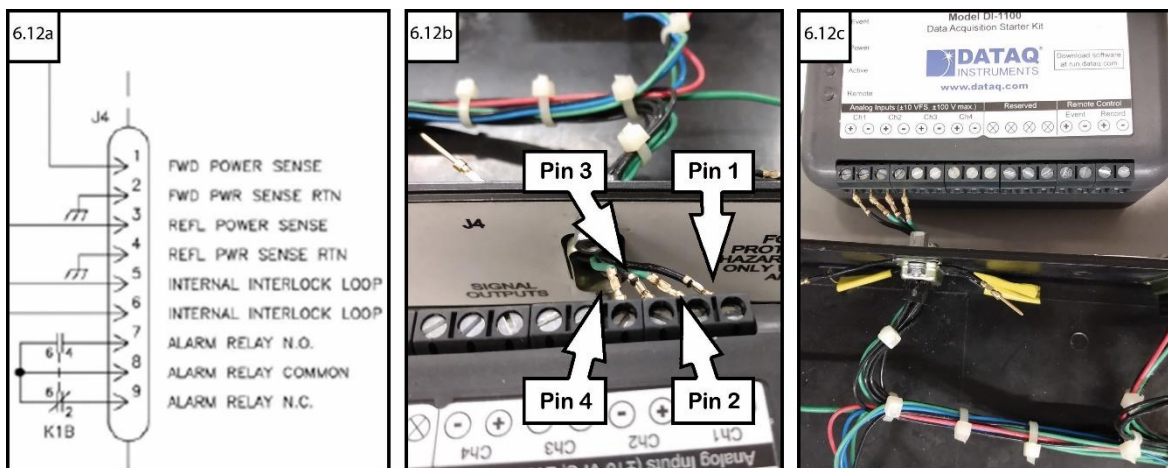


Figure 6.12: Process of connecting digital power meter to DAQ a) dual digital power meter pinout diagram for the J4 9-pin male D-sub output connector port b) pins 1-4 separated out and connected to the DAQ module c) pins connected to positive and negative ports of channels 1 and 2 of DAQ module

The associated WinDAQ software interpreted the difference between the respective pins to display the forward and reflected power in real time. The engineering units were configured to convert the output voltage from the power meter to those of power with a precision of ~ 1 W for both forward and reflected values. The engineering units were calibrated as precisely as possible by specifying the values observed from the power meter when adjusted to heat a sample of graphite in the sample applicator. Once a set of experiment power data was recorded, the approximate amount of power absorbed by the sample over time was calculated by taking the difference between forward and reflected power. ISIS instrument and user support section leader, Jamie Nutter manufactured two dedicated 9 pin d-type connector to 4 pin output adapter cables as a safe, reliable method of connecting the DAQ module to the power meter of both benchtop and Polaris-SMC reactors. The power data obtained using the DAQ module can potentially be used as input at a later date for a simple program to operate the electronic short circuit automatically, adjusting for the optimal position based on real-time feedback.

6.4 Adjusting the SMC reactor configuration and peripherals

During the course of carrying out benchtop *ex-situ* reactions and preparing for the Polaris-SMC *in-situ* experiments, certain challenges with operating the equipment were identified and adjustments were made to the design of certain pieces of equipment.

6.4.1 Redesigning the protective Perspex® box

The benchtop SMC reactor components were connected linearly on a lab desk at the University of Glasgow. This system setup allowed for easy access to the sample applicator and all controls on the power supply and magnetron head. A bespoke Perspex® box was fitted around the applicator to act as a shield in the event that sustained plasma or hotspot formation within the sample compromised the integrity of the quartz ampoule. The original Perspex® box was taller than necessary and positioned where it could be accidentally nudged to press the emergency shutdown button for the bank of fume hoods. This along with the incorporation of the Ircon Modline IR thermometer necessitated a new box design with more appropriate dimensions for the setup along with additional holes for cable management. The new Perspex® box based on my design specs was manufactured by Andrew Hood in the University of Glasgow physics department workshop as shown in figure 6.13.

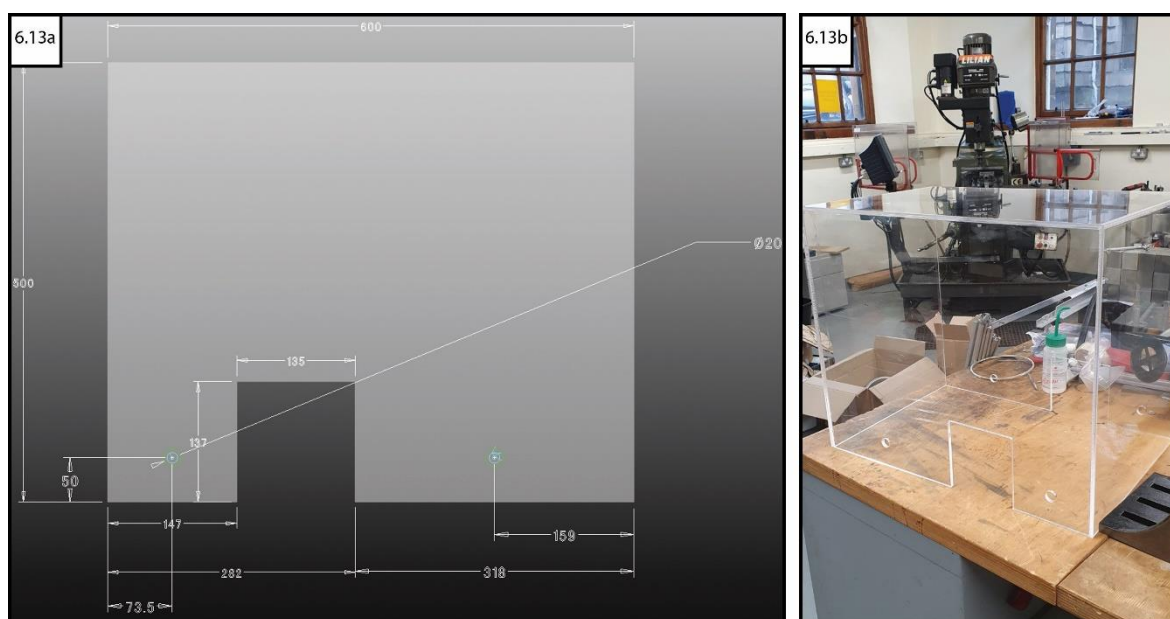


Figure 6.13: a) Schematic CAD diagram generated by John Marshall based on my design specs b) Perspex® box assembly in Physics department workshop prior to hinged door attachment

6.4.2 Redesigning the quick release sample stick and ampoule block

The original conception of accessing the sample applicator within the Polaris tank was to load the starting materials into 8 bore, 10 mm OD quartz glass tubes

and suspend them at a consistent height from the bottom face of the waveguide by securing them in a metal support block as shown in figure 6.14a. The machined Al metal block is a holder designed with a tapered bottom face, for a secure fit with the funnel shaped aperture of the sample applicator ensuring the quartz tube and its contents are aligned in the centre of the waveguide, away from the walls for maximum coupling. The support block design also features external channels to allow ventilation of hot air from the waveguide as a result of radiated heat from the MW-heated samples. A simple ring-shaped ceramic (Macor®) insulator is placed into the support block insulator to protect against unexpected heat transfer from the quartz support tube during a reaction. The quartz tube was inserted through the aperture of both of these with its flared orifice lip designed to be held within the insulator. Finally, a threaded brass adaptor lid was screwed in place and connected to the quick release stick (Figures 6.14b & 6.14c).

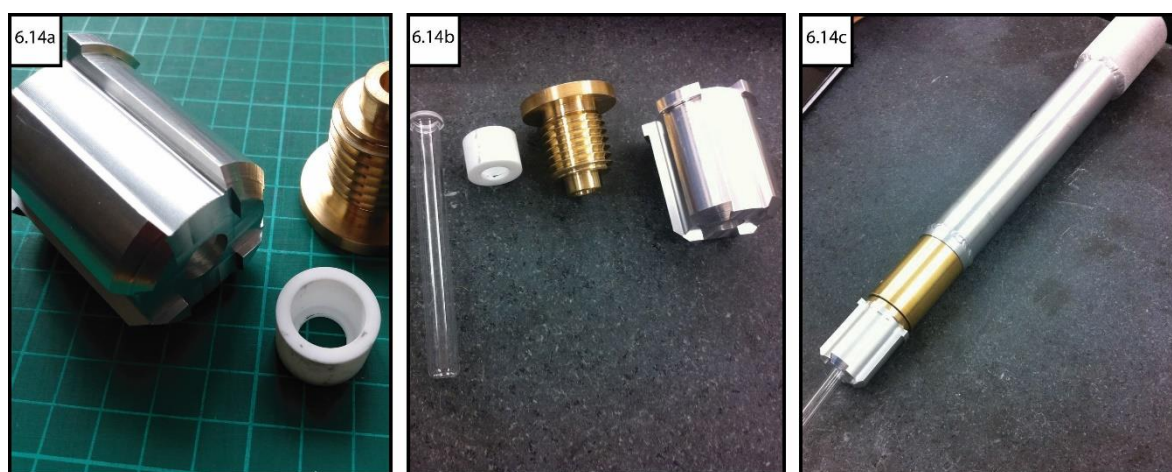


Figure 6.14: a) Original Al support block, brass adaptor lid and Macor® ceramic insulator b) original support block components designed to accommodate 8 bore, 10 mm OD quartz tube c) quick release sample stick connected to support block assembly

The quick release stick is held vertically when transporting a sample, with a release catch operated with a push button located above the grip that secures or releases the brass adaptor lid. The push button location is ergonomically positioned to be activated by a thumb press with minimal effort. During preparation for Polaris-SMC *in-situ* experiments the proposed sample tube and delivery device dimensions were found to be inadequate, due to the unique synthesis conditions of the different chemical systems, such as sealing samples under vacuum or the use of a MW susceptor. Therefore, a redesign of the ampoule block components was proposed to accommodate a larger quartz support tube to make the system more flexible for future *in-situ* experiments. The new quartz support tube was proposed to be at least large enough to contain

samples sealed inside 8 bore, 12 mm OD quartz ampoules with sufficient space for the ampoule to be settled in a small quantity of graphite susceptor if required. The larger quartz tube design necessitated changes to the other support block components, not only to accommodate the increased tube diameter but also the increased diameter of the lip of the tube orifice which would rest within the ceramic insulator. The specific changes were discussed with ISIS supervisor Dr Ron Smith and Colin Offer from the ISIS design division and manufacturing facilities group; the component schematics are included in appendix section A–6.2. The redesigned components were manufactured at ISIS and the assembly tested with the prepared samples at the University of Glasgow. All 52 sealed quartz ampoules were checked to securely fit within the redesigned ampoule support block prior to being sent to ISIS ahead of the *in-situ* Polaris-SMC microwave commissioning experiments.

6.4.3 Polaris-SMC microwave reactor design considerations

To operate the Polaris-SMC reactor at ISIS such that the sample could be heated while in the beamline required the waveguide and components to be connected in a non-linear fashion. The centre of the incident neutron beam is 300 mm below the top of the Polaris sample tank and so the sample applicator waveguide is extended down in a U-bend shape. A cylindrical shaft is extended from the applicator up to the top of the tank to allow insertion and retrieval of experiment samples with the use of the quick release sample stick. As shown in figure 6.15, the U-bend section of waveguide on one side of the sample applicator is thinned to reduce interference with the incident neutron beam.

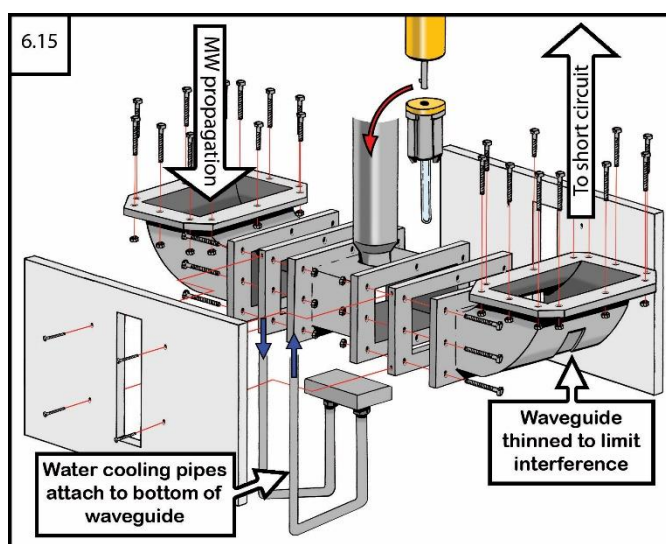


Figure 6.15: Exploded diagram of sample applicator U-bend showing thinned section of waveguide, BN shield apertures and water cooling pipes

The thinned section of waveguide has a width large enough for the neutron beam and a height corresponding to the inner cavity of the waveguide. To limit neutron scattering from the waveguide walls, boron nitride shields are affixed to each side of the sample applicator. A rectangular aperture in the BN shields allow sample-scattered neutrons to pass only through the waveguide walls perpendicular to the sample, which are then collected by bank 4 detectors as illustrated in figure 6.16.

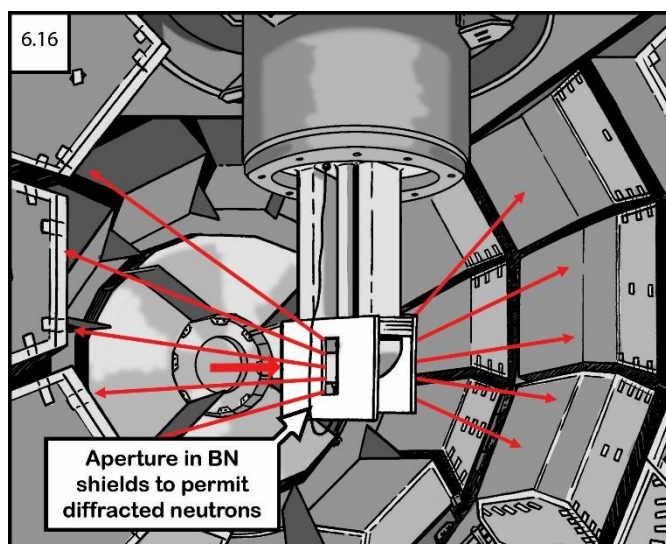


Figure 6.16: Illustration of interior of Polaris collection tank showing incident neutron path through sample applicator aligned with beamline and diffracted neutron paths through BN shield aperture to bank 4 detectors

The detectors in bank 4 of the Polaris instrument have a 2θ range of 75.2° – 112.9° and a d -spacing range of 0.2 \AA – 3.7 \AA , which limits the scattering angles that can be detected but also prohibits signals from the thicker sections of the Al applicator, e.g., flanges from appearing in the diffraction pattern[181]. Each end of the U-bend terminates with standard WR340 flanges for connecting the other MW components. The waveguides are affixed to a 490 mm diameter Tomkinson flange which is designed to fit with the 400 mm Polaris tank access port as shown in figure 6.17. The Tomkinson flange is named for John Tomkinson, an instrument scientist who contributed to the standardisation of instrument services during the design and construction phase ISIS (then referred to as SNS) in the mid-1980s. The standardisation of flange diameter to 400 mm and distance from the neutron beam of 300 mm allows for sample environment equipment to be mostly interchangeable[212].

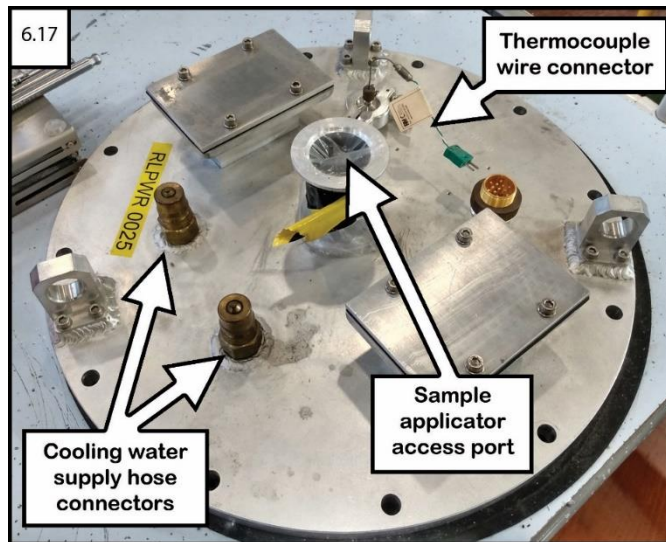


Figure 6.17: Overhead view of Tomkinson flange showing each capped end of the sample applicator waveguide, sample block insertion tube, cooling water supply connectors and thermocouple wire connector

The waveguide geometry and cable placement were planned by comparing the proposed configuration against measurements of the Polaris access well. The Polaris access port is recessed into the floor (Figure 6.18) and so an additional waveguide extension and a 90 ° curved section were required to accommodate the bulky components.

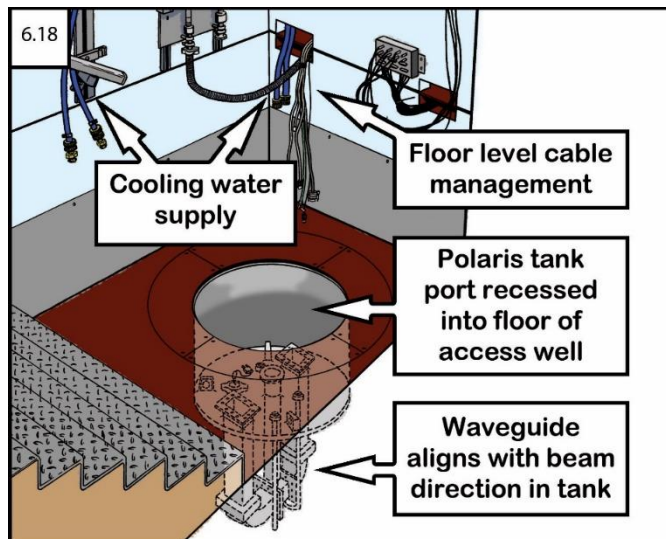


Figure 6.18: Cutaway diagram of Polaris access well showing sample applicator/Tomkinson flange in operational configuration within the recessed floor aperture

The reactor components were unpacked and a test assembly of all the components was carried out on a furnace stand adjacent to the instrument (Figures 6.19a and 6.19b) before any attempt to install within the confined working space of the Polaris well. Several measurements of the Polaris access well and waveguides were made to determine the best configuration of the reactor components to fit within the limited space while allowing user access to all necessary controls and the sample applicator itself. As shown in figure 6.19c, one additional straight section of waveguide was used to allow the reactor

components to be assembled on the Polaris well floor. The auto tuner was connected at 180° rotation to the benchtop configuration, to prevent the bulky component from inhibiting user access to the sample applicator port.

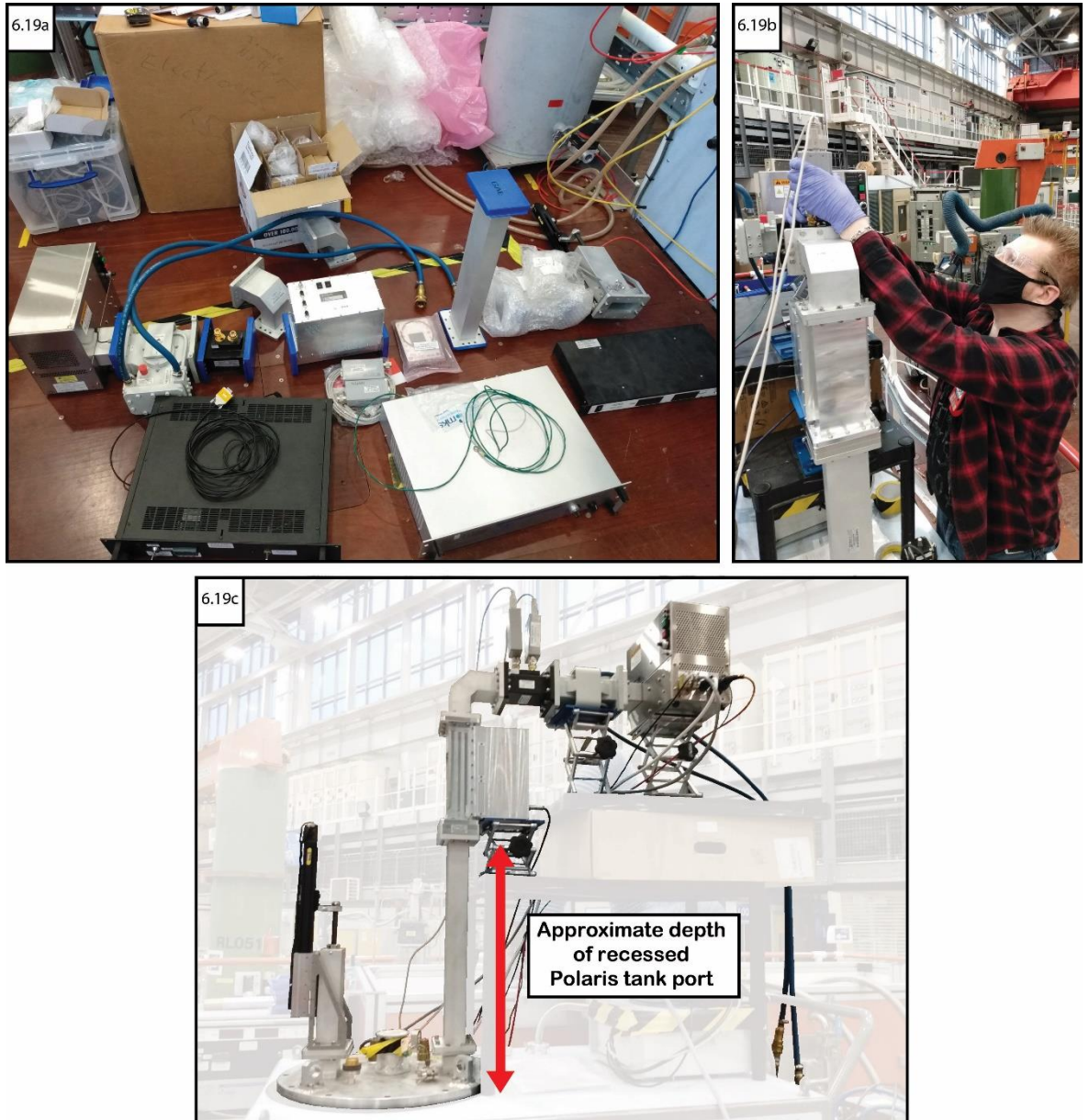


Figure 6.19: a) Polaris-SMC reactor components unpacked from storage and inspected b) configuring the *in-situ* geometry c) waveguide configuration measured and approved

The Tomkinson flange/U-bend was moved into position by Dr Ron Smith via crane and secured with bolts to the top of the tank access port. An additional cement support block and adjustable lab jacks (Figure 6.2a) were used to support the weight of both the magnetron and isolator components which would otherwise put strain on the waveguide flanges. A constant water supply to the isolator was maintained through hoses adjacent to the Polaris access platform, with power cables carefully managed using the floor level apertures as shown in figure 6.20b and secured with electrical tape to minimise any trip hazard with the temporary setup.

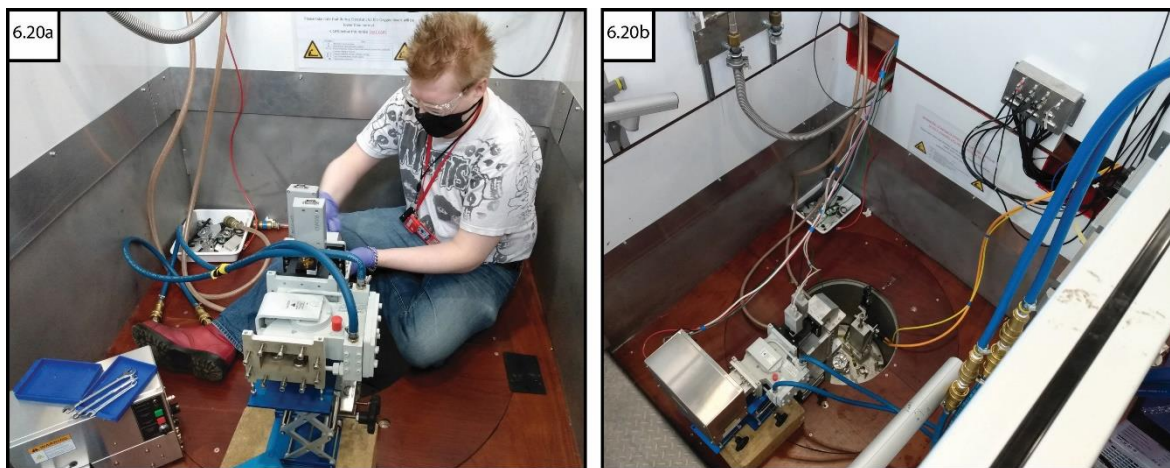


Figure 6.20: a) Installing the microwave components b) Polaris-SMC reactor fully connected and ready for operation with the Polaris access well

The applicator on the benchtop SMC reactor setup was noted to heat up considerably so as to be uncomfortable to the touch after long samples heating durations or if successive experiments were conducted without a sufficient cooldown period. The benchtop applicator featured open ports on the front and rear faces and was located in a well ventilated area. Mitigating the heating of the waveguide allows the sample to be cooled more rapidly through radiative loss once the magnetron is switched off. It also prevents additional radiative heat transfer to subsequent samples from the applicator which could prematurely initiate a reaction where the purpose of the *in-situ* studies is to analyse MW heating alone as much as possible.

The Polaris-SMC applicator was intended to reside for extended periods within the sample tank during operation with only the cylindrical sample insertion tube available for ventilation. The temperature of the waveguide was monitored using a thermocouple attached to the bottom of the applicator and cooled by a continuous flow of temperature controlled water through narrow pipes that conduct excess heat away from the bottom of the waveguide as shown in figure 6.21a. The cooling pipes and thermocouple wire are accessible from the user access side of the Tomkinson flange to monitor and prevent excessive heat build-up in the waveguide during operation. The flow of the water supply to the isolator was controlled using a Julabo FP50-HE refrigerated/heating circulator with the temperature regulated at a constant 20 °C (Figure 6.21b).



Figure 6.21: a) U-bend sample applicator with rectangular, white BN shielding and cooling water supply pipes b) Julabo FP50-HE refrigerated/heating circulator used to supply cooling water to the underside of the sample applicator

The key operated remote control interlock for the Polaris-SMC reactor is designed to cut power to the magnetron as a safety precaution. The interlock will interrupt magnetron power if the key is switched off manually or the thermocouple sensor attached to the bottom face of the sample applicator waveguide reports an increase in temperature past a programable setpoint. The interlock control key must be switched off and removed by the user prior to entering the Polaris access well to prevent the magnetron being activated during sample exchanges or adjustments to the reactor configuration.

Once the system power and auto tuner were switched on all necessary power and cooling water required by the Polaris-SMC reactor was able to be accessed and controlled from outside the Polaris instrument well. The key-switch controlled interlock was incorporated into the control panel shown in figure 6.22, and was used in place of the dummy load manually inserted into the benchtop magnetron head. The electronic jog box for adjusting the short circuit can also be seen beside the rack cabinet, connected via orange and yellow power cables.

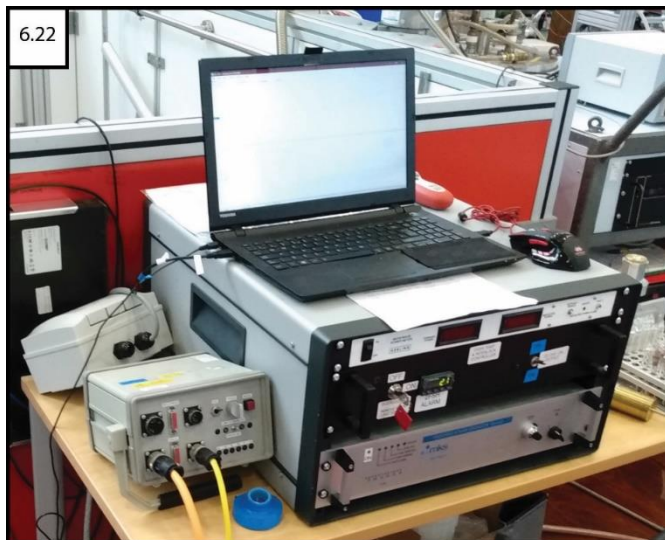
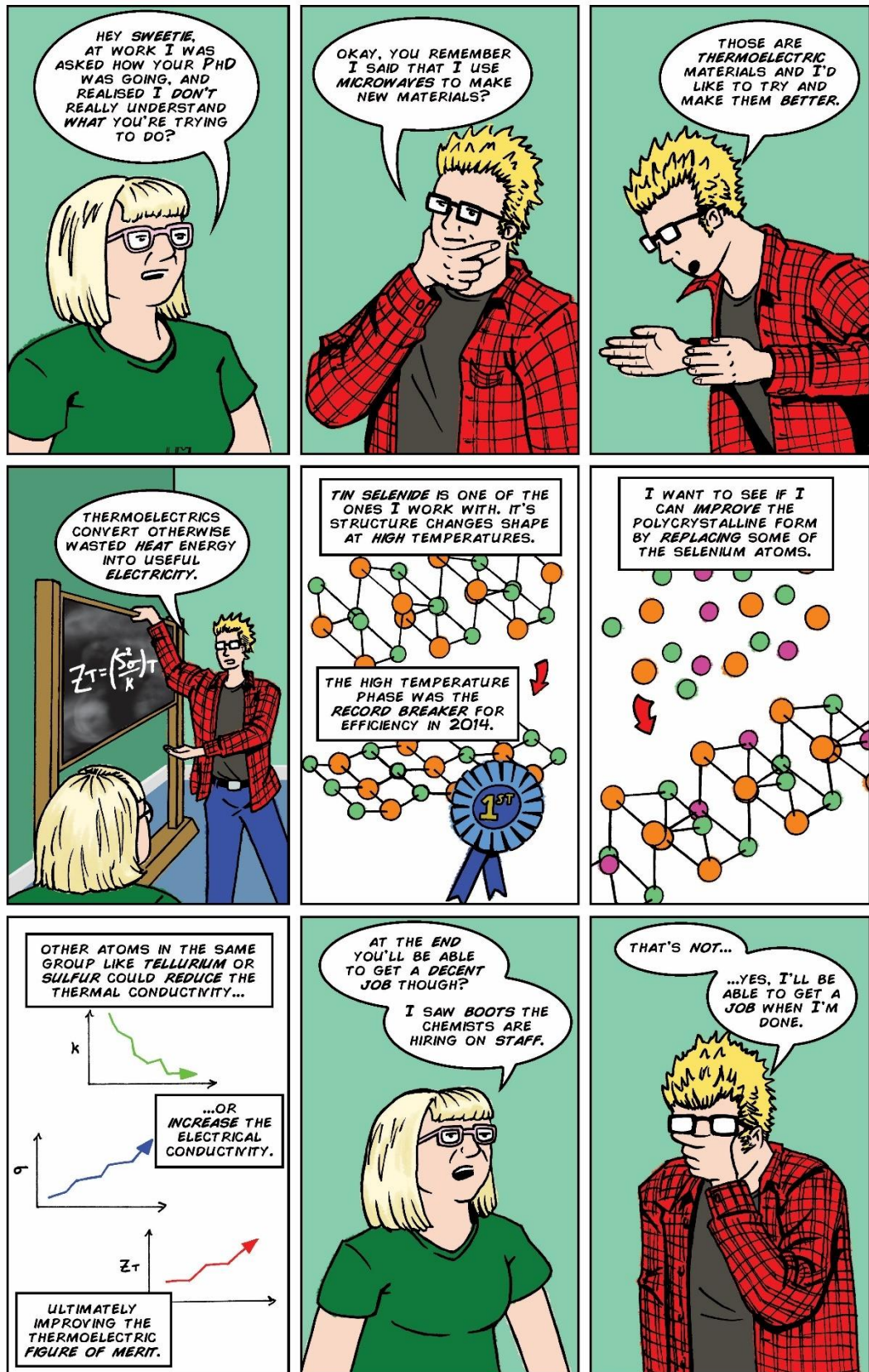


Figure 6.22: Polaris-SMC reactor control panel and motorised sliding short circuit jog-box

Once the beam shutters are opened for the *in-situ* experiments, access to the Polaris well was prohibited by a key operated gate that functions as an interlock for the beam shutter. Likewise, an interlock in the beam shutter control box will not allow it to function unless the access well gate is locked and the key replaced in the control box. Therefore, the beam shutter must be closed before a user can enter the Polaris access well and all interlocks must be engaged before the beam shutter can be opened and data collection initiated. The switches on the magnetron head had to be activated using a long pole maneuvered by the user from outside the Polaris well. This method of switching on the magnetron was deemed acceptable however, a less low-tech solution should probably be pursued in any future work with this equipment.

7 Tuning tin selenide thermoelectric efficiency

7.1 Explaining the thesis to my mum



7.2 Introduction

The impressive reported performance of SnSe single crystals as a TEM (sections 3.3.1–3.3.3) was the main reason for investigating this system as the first material in the project. The indirect band gap semiconductor is also desirable in other applications such as photovoltaic solar cells and memory-switching devices while the anisotropic properties make the material useful in Li-intercalation batteries[93]. Conventional methods of producing SnSe tend to be time consuming and energy intensive, so faster, cheaper methods such as direct MW-heating would be a major commercialisation advantage. SnSe has been produced via MW-heating processes previously in small quantities and usually accompanied by impurities; it is therefore highly desirable to find a way to maximise control of the synthesis process to enable the production of larger quantities in the single phase[104], [213]. Although typically less impressive, there have been promising results in improving the performance of other tin chalcogenides such as SnTe and SnS through partial substitution of both the Sn site along with chalcogen substitution as discussed in section 3.3.4. From this it was decided to focus on preparing a range of samples for chalcogen doping only; in the hope that this would allow for tuning of the thermal and electrical properties to improve TE performance compared to undoped samples.

7.3 Sample preparation and experimental design

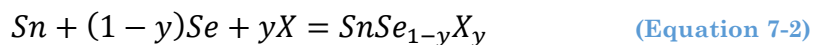
7.3.1 Stoichiometric calculations

The stoichiometric quantities were initially calculated for SnSe_x to be produced from a 1:1 or 1:2 ratio with no excess elemental reactants based on the simplest reaction scheme:



However, an error was accidentally introduced into the calculations (carried out using Excel) which resulted in either 10 % or 30% excess Se being used for a large portion of early experiments. Any data discussed has been interpreted and labelled based on the correct amounts of materials actually prepared. The majority of the affected experiments were intended to compare the effects of varying synthesis time at set MW power levels rather than sample composition. Therefore, comparing these data gave some insights into the MW synthesis process with very little improvement to main phase. The calculation error was discovered and corrected for when transitioning to use of the benchtop SMC

reactor and prompted comparison between the early samples and new stoichiometric preparations. From those observations, samples containing up to 10 % excess Sn were also prepared in an attempt to further improve the main phase purity. Accurate reaction stoichiometry for chalcogen substituted SnSe_{1-y}X_y (X = Te, S) samples without any reactant excesses was calculated based on:



7.3.2 Synthesis parameters

Experiments conducted using the modified DMO were performed using elemental powders as described in section 4.2.2 with no additional changes to the experimental design. 25 samples with target weights of either 0.5 or 5 g were heated for times ranging from 10 to 120 s; the synthesis duration was taken as the total heating time in the active DMO. Products were retrieved as solid deposits/ingots from the bottom of the quartz ampoule depending on sample size and had an easily cut, chalk like consistency with a lustrous metallic appearance as shown in figure 7.1.



Figure 7.1: Example of rough metallic appearance of a ~5 g ingot of SnSe measuring ~20 mm in length that was separated in two following retrieval from quartz ampoule

Experiments conducted using the benchtop SMC reactor were performed as described in section 4.2.3. Early experiments with this instrument were performed without the use of the DAQ for recording the MW power profile or the Iacon Modline IR thermometer. Details of varying the synthesis parameters are discussed in the relevant sections of this chapter.

7.4 Effect of synthesis duration on samples in a modified DMO

A series of 13 SnSe samples prepared with 10 % excess Se each resulted in a multi-phase mixture of SnSe and SnSe₂. For heating duration (t) < 30 s no

reaction occurred, between $30 < t < 40$ s any reaction progression was inconsistent and for $t > 40$ s all syntheses progressed to completion. The calculated phase fraction of the SnSe main phase was not observed to improve with increasing synthesis time as shown in figure 7.2a. Four samples prepared with the correct stoichiometric ratio showed the same multi-phase mixture for $t > 30$ s however, the SnSe phase was calculated to be just over half of the composition (Figure 7.2b). The implication was that SnSe₂ may be more thermodynamically stable and the reaction pathway may require transitioning through a SnSe₂ phase before further heating produces the desired SnSe.

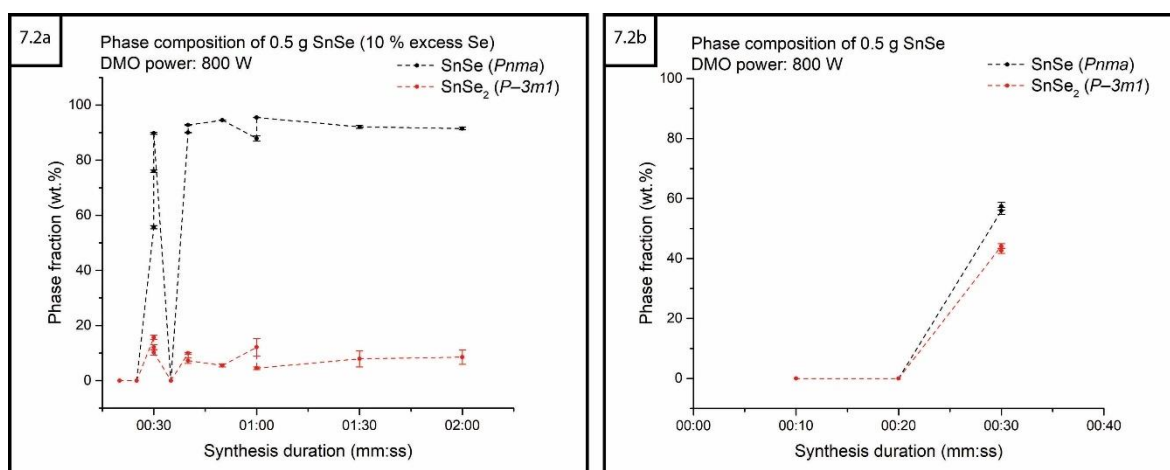


Figure 7.2: Plots of phase fractions (wt.%) against synthesis duration for 0.5 g SnSe samples produced in a modified DMO using 800 W power a) with 10 % excess Se b) with stoichiometric starting materials

The rapid synthesis duration is the result of efficient heating of the Sn powder in the reactant mixture, which experiences Ohmic loss resulting from eddy currents generated by the magnetic component of MWs. Four additional samples were prepared to more carefully examine the synthesis duration period of 30–60 s, with only the 30 s sample data showing signs of unreacted Sn alongside the SnSe and SnSe₂ phases. The fraction of the SnSe phase can be seen in the three other samples (Figure 7.3) to approach a maximum with no unreacted starting materials remaining. The refined crystallography data for the SnSe phase of these samples are available in appendix section A–7.1.

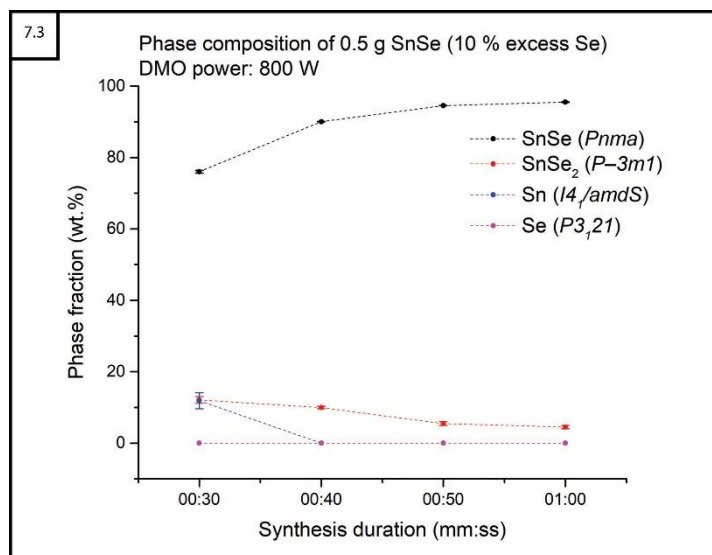


Figure 7.3: Plot of phase fraction (wt.%) against synthesis duration for 0.5 g SnSe samples (with 10 % excess Se) produced in a modified DMO using 800 W power

7.4.1 Scanning electron microscopy (SEM) analysis of early samples

Five of the early samples were imaged using SEM and the chemical composition analysed using EDX as described in sections 5.53–5.54. Two of the samples heated for 10 and 20 s had remained unreacted, with a corresponding distribution of well mixed starting materials, so those results have been excluded.

SnSe has a layered orthorhombic structure which is likely the reason for the striated areas visible in the first sample imaged (Figures 7.4 and 7.5). The first two SnSe samples analysed were synthesised with 10 % excess Se and were characterised in GSAS[187], [188] with a SnSe main phase fraction of 98(1) and 90(3) wt.% respectively. The second identifiable phase was attributed to SnSe₂.

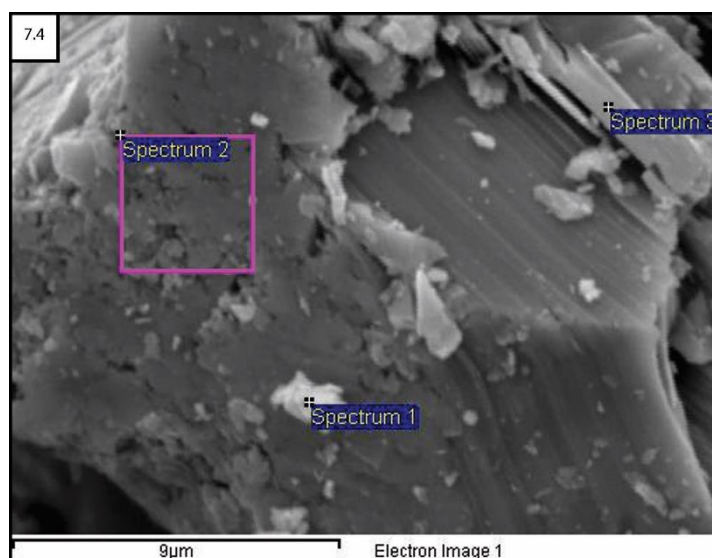


Figure 7.4: 6000x magnification SEM image of SnSe sample 1 made with 10% excess Se (site 1) showing the locations of three EDX spectra

The first spectrum point analysis of one of the lighter structures of sample 1 showed the expected stoichiometric Sn:Se ratio of 1:1. An area analysis and second point analysis location indicated an uneven distribution of Sn and Se, favouring excess Sn by 2:1. This was unexpected and probably indicates isolated areas of unreacted starting material, whereas the striated section is a likely candidate for the structure of the identified SnSe phase.

Table 7.1: Elemental analysis of SnSe sample 1 (site 1) EDX spectra locations

Spectrum location	Element	Weight%	Atomic%
1	Se	40.72	50.80
	Sn	59.28	49.20
2	Se	26.61	35.27
	Sn	73.39	64.73
3	Se	26.78	35.48
	Sn	73.22	64.52

A second site of the same sample was chosen to compare to, with EDX spectra taken from what appeared to be more ordered structures.

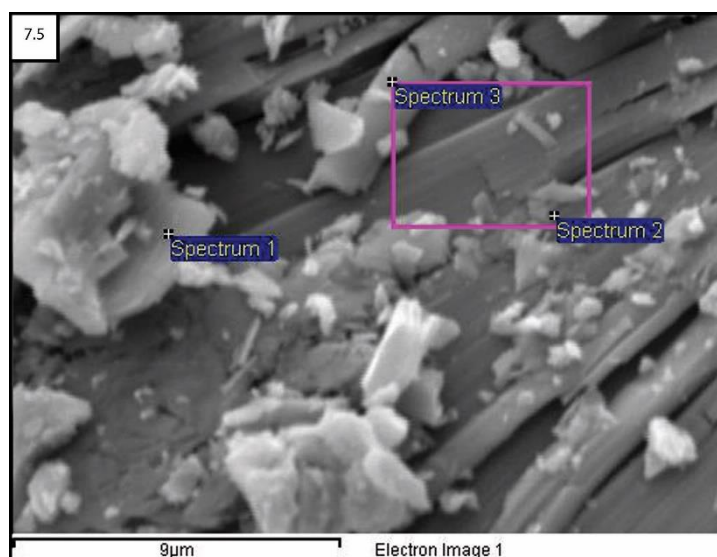


Figure 7.5: 6000x magnification SEM image of SnSe sample 1 made with 10% excess Se (site 2) showing the locations of EDX spectra

All spectrum point and area analyses of the second site focused on the more ordered structures and showed much closer ratio of at.% to the expected composition of SnSe. Although the spectra show a slight deviation from the ideal 1:1 ratio, particularly at location 1, the difference is not enough to indicate the presence of SnSe₂ and may instead point to slight Sn deficiency in the SnSe phase.

Table 7.2: Elemental analysis of SnSe sample 1 (site 2) EDX spectra locations

Spectrum location	Element	Weight%	Atomic%
1	Se	46.32	56.47
	Sn	53.68	43.53
2	Se	41.85	51.96
	Sn	58.15	48.04
3	Se	40.98	51.07
	Sn	59.02	48.93

The second sample imaged had less clear surface detail than the first sample, and generally more granular in appearance as shown in figure 7.6.

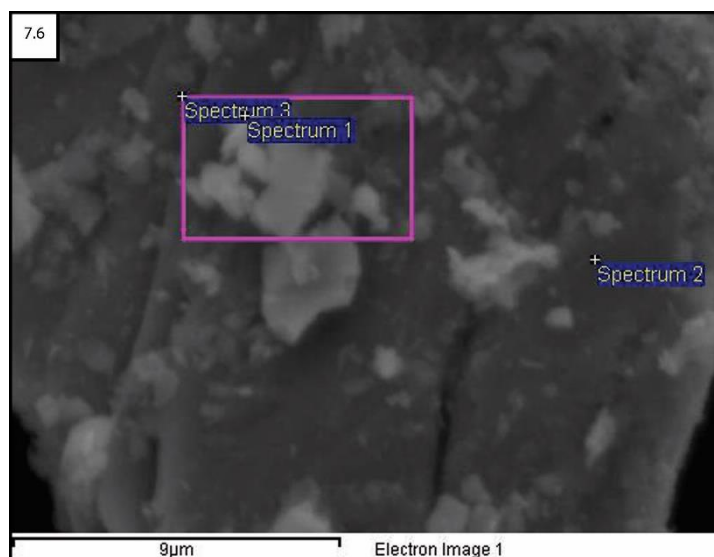


Figure 7.6: 6000x magnification SEM image of SnSe sample 2 made with 10% excess Se showing the locations of three EDX spectra

This sample was characterised with a SnSe main phase fraction of 60(1) wt.% with SnSe₂ making up the remainder. The two spectrum point analyses and area analysis once more showed the same approximately stoichiometric Sn:Se ratio of 1:1 with slight Sn deficiency as noted in the previous sample.

Table 7.3: Elemental analysis of SnSe sample 2 EDX spectra locations

Spectrum location	Element	Weight%	Atomic%
1	Se	48.69	58.79
	Sn	51.31	41.21
2	Se	48.69	58.79
	Sn	51.31	41.21
3	Se	43.63	53.78
	Sn	56.37	46.22

The first imaging site of the third sample shown in figure 7.7 appears to have much more plate-like character than the granular or striated pattern seen previously.

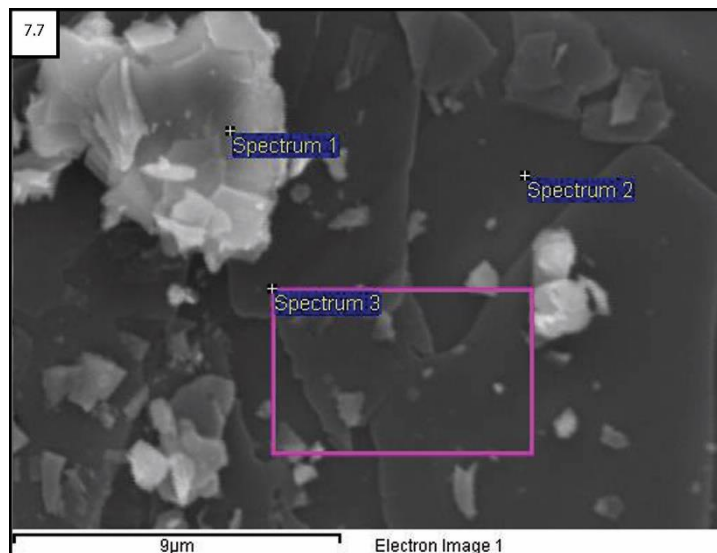


Figure 7.7: 6000x magnification SEM image of SnSe sample 3 made with 1:1 stoichiometric ratio (site 1) showing the locations of three EDX spectra

Both spectrum point analyses of this site showed a consistent Sn:Se ratio around 1:2, which correlates with the secondary SnSe₂ phase. The area analysis however disproportionally contains mostly Se, likely from a large region of unreacted starting material.

Table 7.4: Elemental analysis of SnSe sample 3 (site 1) EDX spectra locations

Spectrum location	Element	Weight%	Atomic%
1	Se	55.29	65.02
	Sn	44.71	34.98
2	Se	54.42	64.22
	Sn	45.58	35.78
3	Se	75.08	81.91
	Sn	24.92	18.09

The second site of sample 3 (Figure 7.8) appears to be mostly granular with slight indication of a striated structure. The two area analyses were performed over what appears to be a grain boundary in the sample.

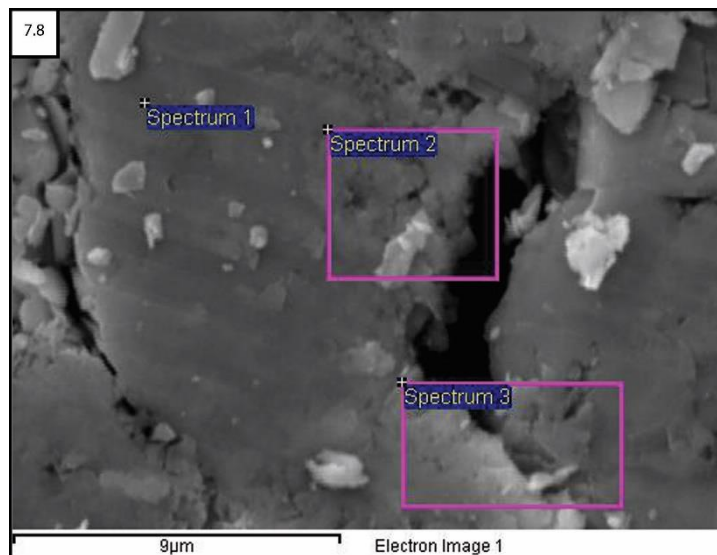


Figure 7.8: 6000x magnification SEM image of SnSe sample 3 made with 1:1 stoichiometric ratio (site 2) showing the location of three EDX spectra

The spectrum point analysis showed an overwhelming majority of Se, strongly indicating a large area of unreacted starting material. Both area analyses showed a distribution of Sn:Se that is inconsistent with either of the two identified phases individually, and possibly the selection areas incorporate examples of both in the region of a grain boundary between crystallites.

Table 7.5: Elemental analysis of SnSe sample 3 (site 2) EDX spectra locations

Spectrum location	Element	Weight%	Atomic%
1	Se	97.42	98.27
	Sn	2.58	1.73
2	Se	65.56	74.10
	Sn	34.44	25.90
3	Se	75.08	81.91
	Sn	24.92	18.09

7.4.2 Gram-scale synthesis and single crystal X-ray diffraction

Four samples with a scaled-up target weight of 5 g were heated for 30–60 s using the modified DMO. All of the samples progressed to completion with no unreacted starting material able to be identified. The larger sample volume within the heating mode enabled greater coupling and a so likely reached the thermal runaway critical temperature faster. The excess Se used in these experiments continued to favour the formation of the stable SnSe₂ phase; and so, increasing the synthesis duration resulted in no improvement in SnSe phase purity as can be seen in figure 7.9. The refined crystallography data for the main SnSe phase of these samples are available in appendix section A–7.2.

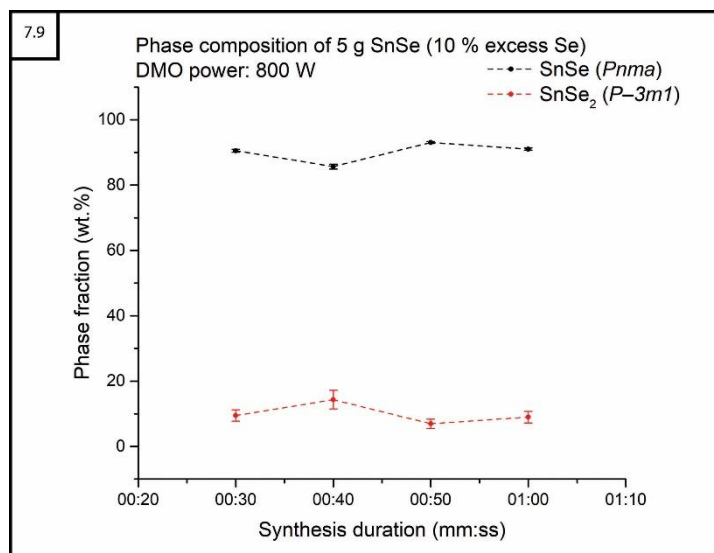


Figure 7.9: Plots of phase fractions (wt.%) against synthesis duration for 5 g SnSe samples produced in a DMO at 800 W

Small shavings in the order of 0.1 mm were cut from the ingot of the 40 s sample (Figure 7.10a and 7.10b) and scanned for 30 s using a Bruker D8 Venture single crystal diffractometer. The crystal sample alignment within the instrument was carried out using a fixed position camera (Figure 7.10c).

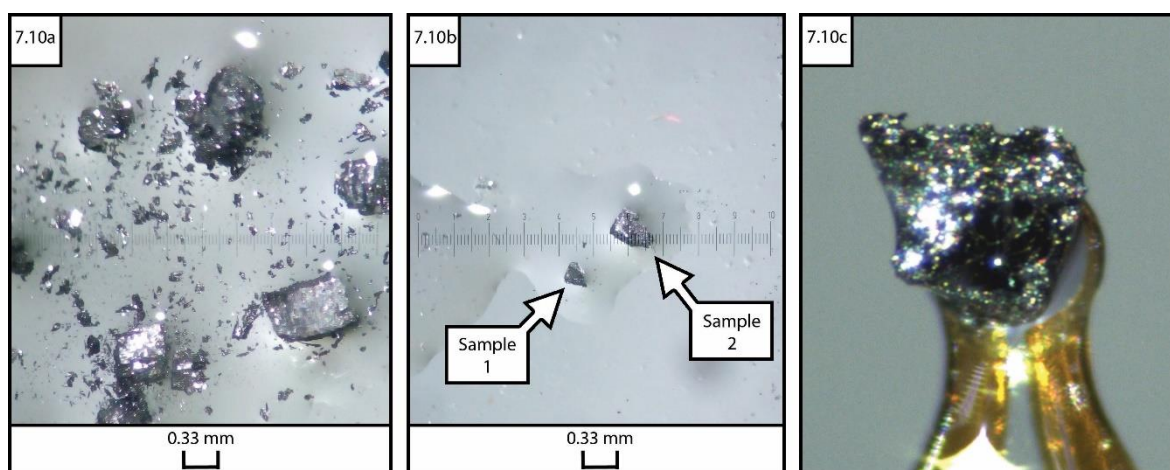


Figure 7.10: Magnified images of a) SnSe sample shavings later characterised with a main phase fraction of 86(7) wt.% b) ingot shavings chosen to be tested c) potential single crystal sample 1 with approximate dimensions: 0.25×0.22×0.15 mm

The analysis of the 5 g SnSe sample was carried out for ~30 s as it was only necessary to determine if the synthesis process was producing large single crystals or a material that was highly disordered. The first sample taken from the ingot showed clear Debye-Scherrer rings and low intensity spots (Figure 7.11) which indicated no preferred orientation and so was most likely a compacted powder.

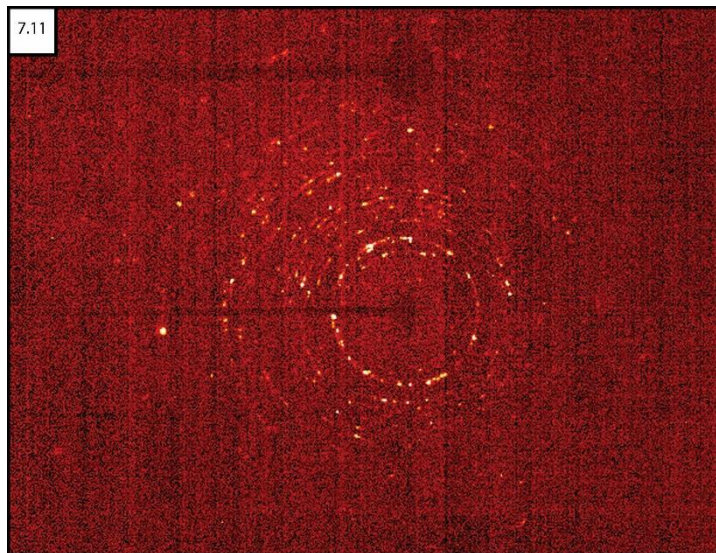


Figure 7.11: Diffraction pattern for SnSe sample 1 which shows prominent Debye-Scherrer ring patterns, indicating that the sample is polycrystalline and not a single crystal as suspected

A second sample measured to approximate dimensions of $0.29 \times 0.26 \times 0.42$ mm (Figure 7.12a and 5.12b) showed less ring-like patterns and more intense diffraction spots as shown in figure 7.12c.

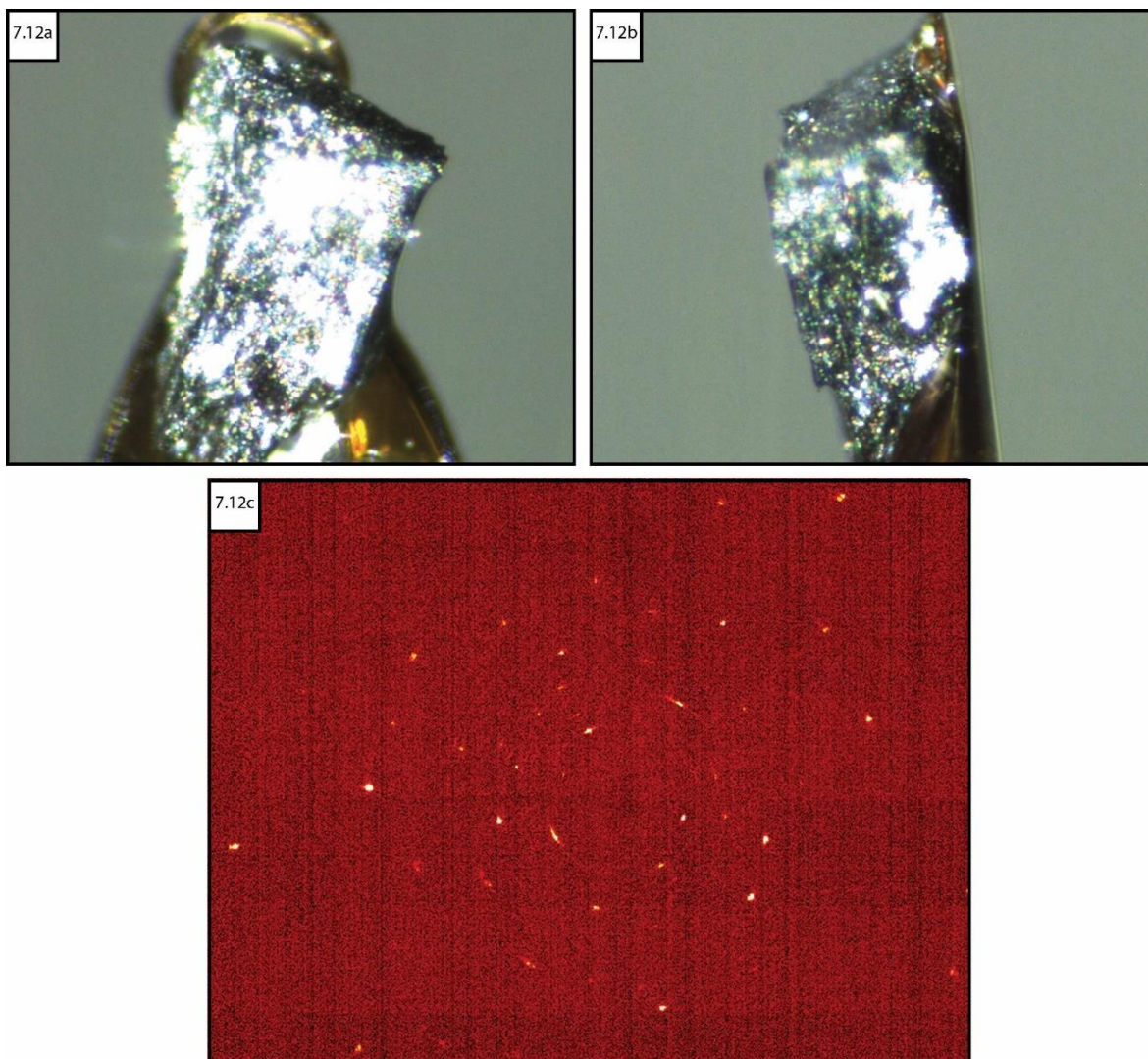


Figure 7.12: Magnified images of potential SnSe single crystal sample 2 from two different angles (a and b) with approximate dimensions: $0.29 \times 0.26 \times 0.42$ mm c) diffraction pattern for SnSe sample 2 which shows intense diffraction spots

The more ordered pattern indicated that the second sample taken from the same ingot was a single crystal, so the data was confirmed by interpretation using the reciprocal lattice (RLATT) viewer software, which shows more clearly in figure 7.13 the ordered diffraction points indicative of a single crystal.

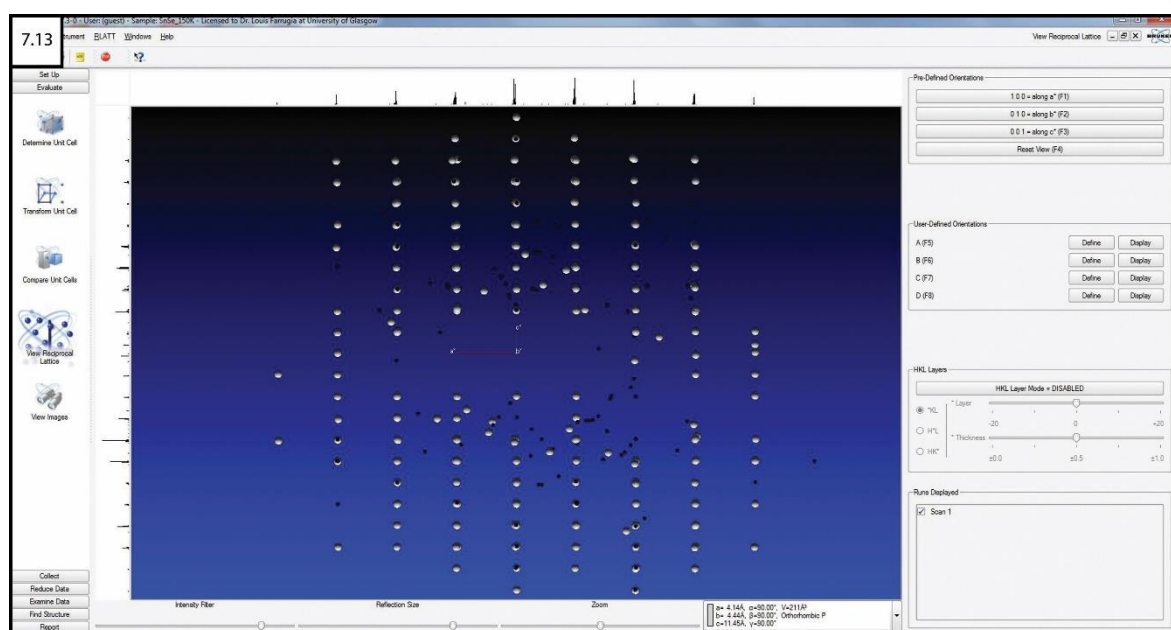


Figure 7.13: Using the reciprocal lattice viewer (RLATT) the highly ordered points resolve to strongly indicate a single crystal.

From these results it was concluded that at least for gram scale samples synthesised using the direct MW-heating method in a modified DMO, small scale single crystals embedded within a larger polycrystalline matrix are produced.

7.4.3 Rapid synthesis of single phase SnSe_2 using a modified DMO

Nine experiments were carried out to check the viability of producing trigonal ($P\bar{3}m1$) SnSe_2 as a single phase product since earlier experiments appeared to demonstrate that it is a more stable phase than SnSe . Samples with a target weight of 0.5 g and 30 % excess Se were heated for 20–70 s. For short synthesis times between 20–40 s, a mixed phase of SnSe_2 and SnSe was produced with the phase fraction of SnSe_2 gradually increasing to become the main phase as shown in figure 7.14. At $t > 40$ s SnSe_2 was reliably produced in the single phase each time; the refined crystallography data for the SnSe_2 phase of these samples are available in appendix section A–7.3.

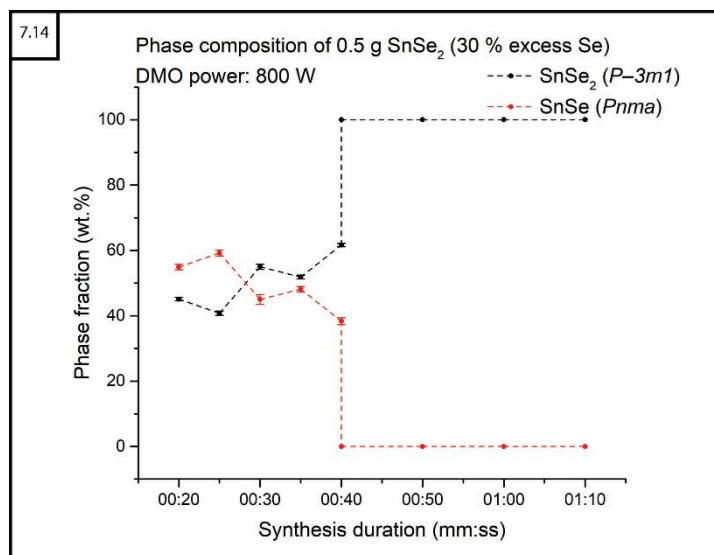


Figure 7.14: Plot of phase fractions (wt.%) against heating duration for 0.5 g SnSe₂ samples (with 30 % excess Se) produced in a modified DMO at 800 W

This trend indicates that in a Se-rich environment the reaction pathway produces both SnSe and SnSe₂ initially before preferentially selecting for the SnSe₂, breaking down any SnSe that has already been produced. This result led to the discovery of the stoichiometric calculation error and explained the difficulty in achieving any improvement of the SnSe phase fraction.

7.5 Practice syntheses using benchtop SMC reactor

While samples were still being prepared with 10 % excess Se, experiments were begun using the benchtop SMC reactor. The Se-rich environment stymied any attempt to improve the phase fraction of SnSe by adjusting the power or synthesis duration. These experiments were also being carried out to develop an understanding of the SMC reactor and its functions; of particular note was the limited accuracy of the power meter digital display and a desire to more precisely record the synthesis duration for these rapid reactions.

7.5.1 Synthesis duration calculated from power absorption profiles

The first attempt to resolve these issues involved setting up two cameras; one to record the material in the sample applicator and the other for forward and reflected power displays of the SMC power meter. The footage was synced up and the forward and reflected power manually recorded as a function of time from the frame-by-frame footage. The experiments were performed using a variety of sample sizes and forward MW power while attempting to limit the reaction period for each sample to 10 s. The power absorption profile of each sample was calculated by subtracting the reflected from the forward power and plotting against relative time as shown in figure 7.15.

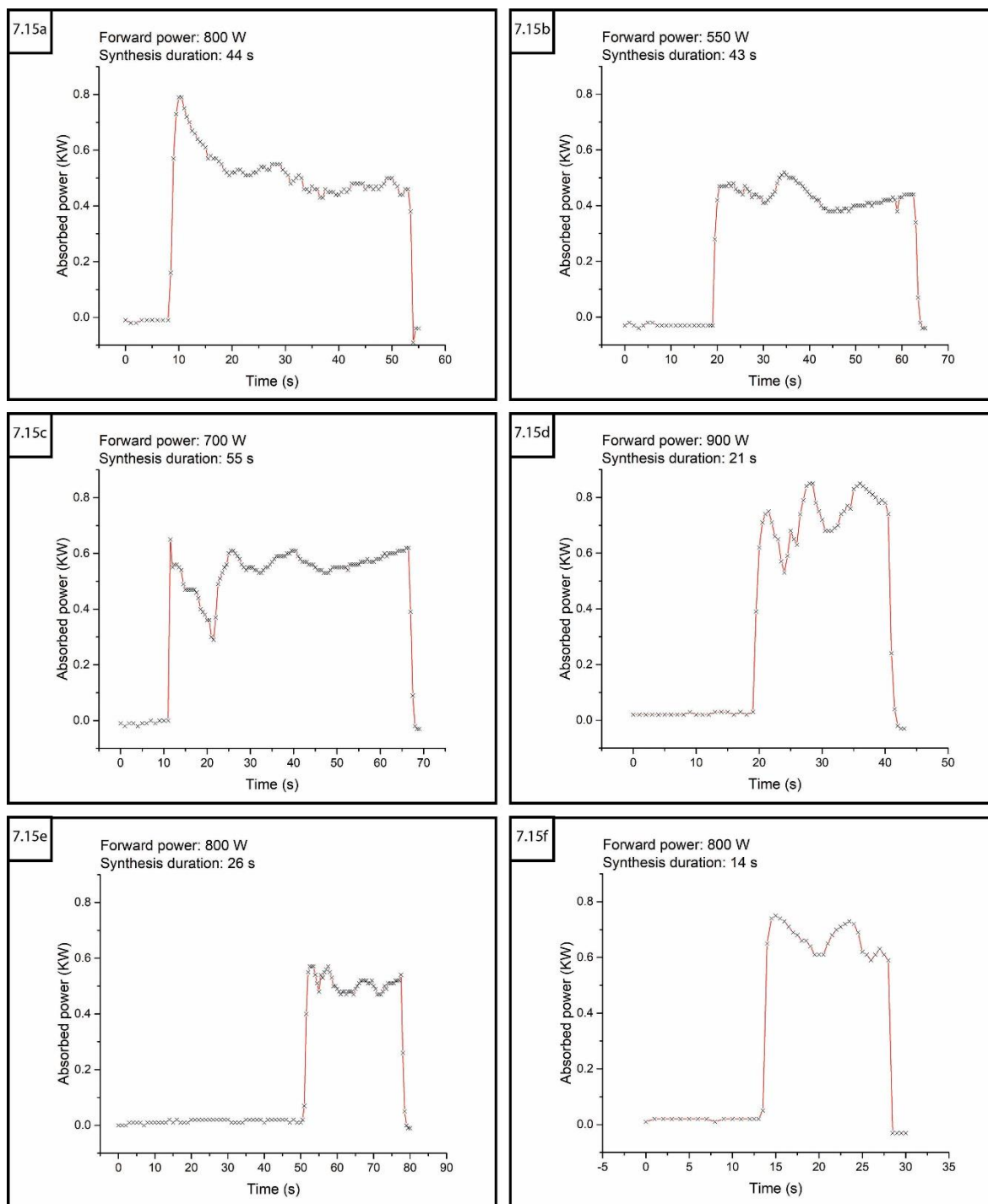


Figure 7.15: Plots of absorbed power against synthesis duration as calculated from manual transcription of digital power meter forward and reflected power displays recorded using a digital camera

When reviewing the recordings post reaction, the appearance of arcing/plasma within the ampoule was concurrent with a reduction in the reflected power attributed to thermal runaway. Calculating the actual synthesis duration from the MW absorption profiles showed that reactions lasted much longer than intended, ranging between 11–55 s. Therefore, attempting to accurately record synthesis duration based upon observations of light emitted from the sample applicator was impractical. Based on the successful production of mixed phase SnSe and SnSe₂ samples for each experiment, the actual reaction duration was

found to be $\ll 30$ s as assumed by the modified DMO experiments. Observation of power could be used as a method of tracking reaction progress and allow better control over synthesis duration, provided that the forward and reflected MW power was easier to follow and could be recorded for verification. The solution was a Dataq Instruments DI-1100 4-channel data acquisition (DAQ) module as described in section 4.4.1, which displays the forward and reflected power as a dynamic rolling chart to a precision of ~ 1 W. The calculated absorbed power profiles are presented with corresponding temperature profiles obtained using the Ircon Modline IR thermometer.

To test the DAQ and IR thermometer, a 1 g sample prepared with 10 % excess Sn was heated using 400 W forward power. As shown in figure 7.16a, the temperature profile follows the standard MW-heating pattern discussed in section 2.2.9. The sample was held above the phase change temperature of $\sim 480^\circ\text{C}$ for the majority of the synthesis duration, with a $T_{\text{max}} \sim 900^\circ\text{C}$. After 152 s the quartz ampoule had softened enough for a hole to melt in the side (Figure 7.16b), exposing the contents to the air. Once the ampoule was no longer under vacuum, the absorption of MWs ceased immediately and the experiment was ended.

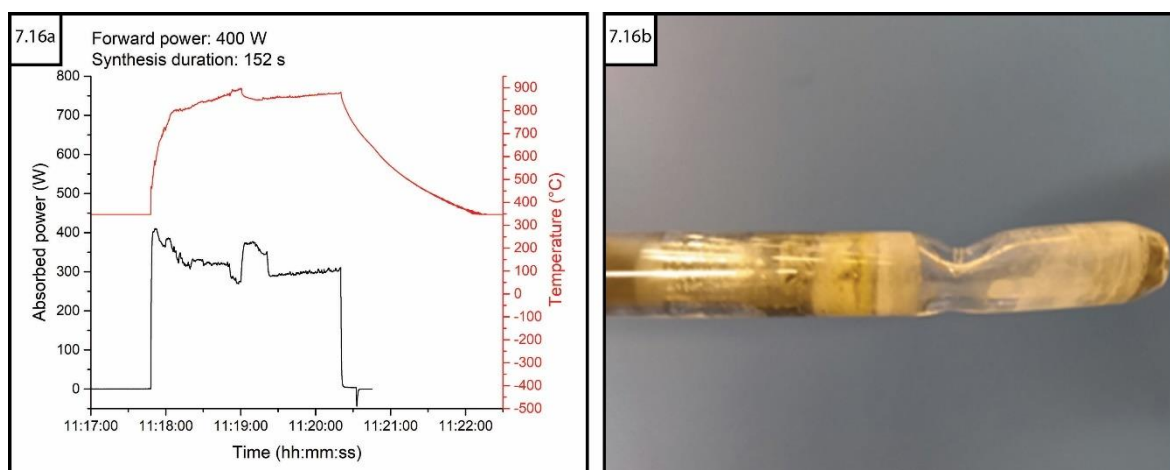


Figure 7.16: a) Plot of refined PXRD data for SnSe sample synthesised in the benchtop SMC microwave reactor using 400 W forward power for 152 s b) quartz ampoule deformation after 152 s of sample heating

The sample was split to determine if there was significant difference between the ingot formed at the bottom of the ampoule compared to the deposits on the interior wall. PXRD analysis of the ingot (Figure 7.17a) showed SnSe as the main phase at a phase fraction of 99.3(1) wt.%, along with some unreacted Sn. Analysis of the material deposits (Figure 7.17b) showed no significant difference

in the phase composition with the SnSe phase fraction at a comparable 99.7(1) wt.%, the refined crystallography data are available in appendix section A–7.4.

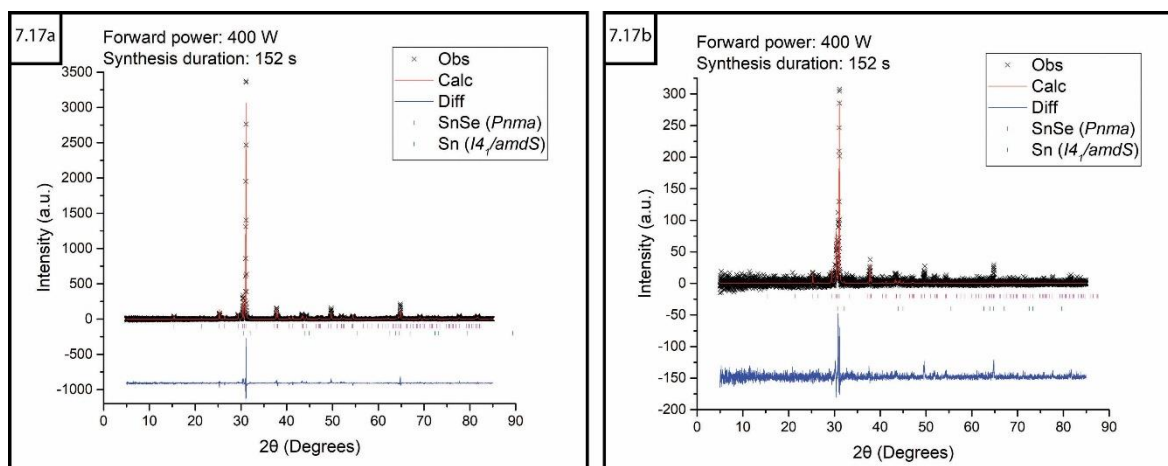


Figure 7.17: Plots of refined PXRD data for SnSe sample synthesised in the benchtop SMC microwave reactor using 400 W forward power for 152 s a) sample ingot b) sample deposits retrieved from quartz ampoule walls

7.5.2 Improvement of SnSe phase fraction with excess Sn

Once the stoichiometric calculation error was corrected, 2×0.5 g and 2×1 g samples were prepared to directly compare the effect of a stoichiometric (1:1) ratio of starting material with a mixture containing 10 % excess Sn. The samples were allowed to react for 5–10 s in the benchtop SMC reactor, with the 1 g samples heated using 400 W and the 0.5 g samples heated using 600 W forward power.

An excess amount of Sn resulted in the phase fraction of SnSe being increased from 91 wt.% to 93 wt.% with a slight reduction of the SnSe₂ from 8 wt.% to 6 wt.% and a corresponding increase in unreacted Sn content from 1 wt.% to 2 wt.% when heated using 600 W forward power. However, when heated using 400 W, the excess Sn reduced the phase fraction of SnSe from 92 wt.% to 85 wt.% with an apparent increase of the SnSe₂ phase from 8 wt.% to 14 wt.% and no change in unreacted Sn. This change is observable in the refined PXRD plots shown in figure 7.18, where the SnSe₂ peaks that are clearly seen in the stoichiometric sample data almost entirely disappear for both samples with excess Sn.

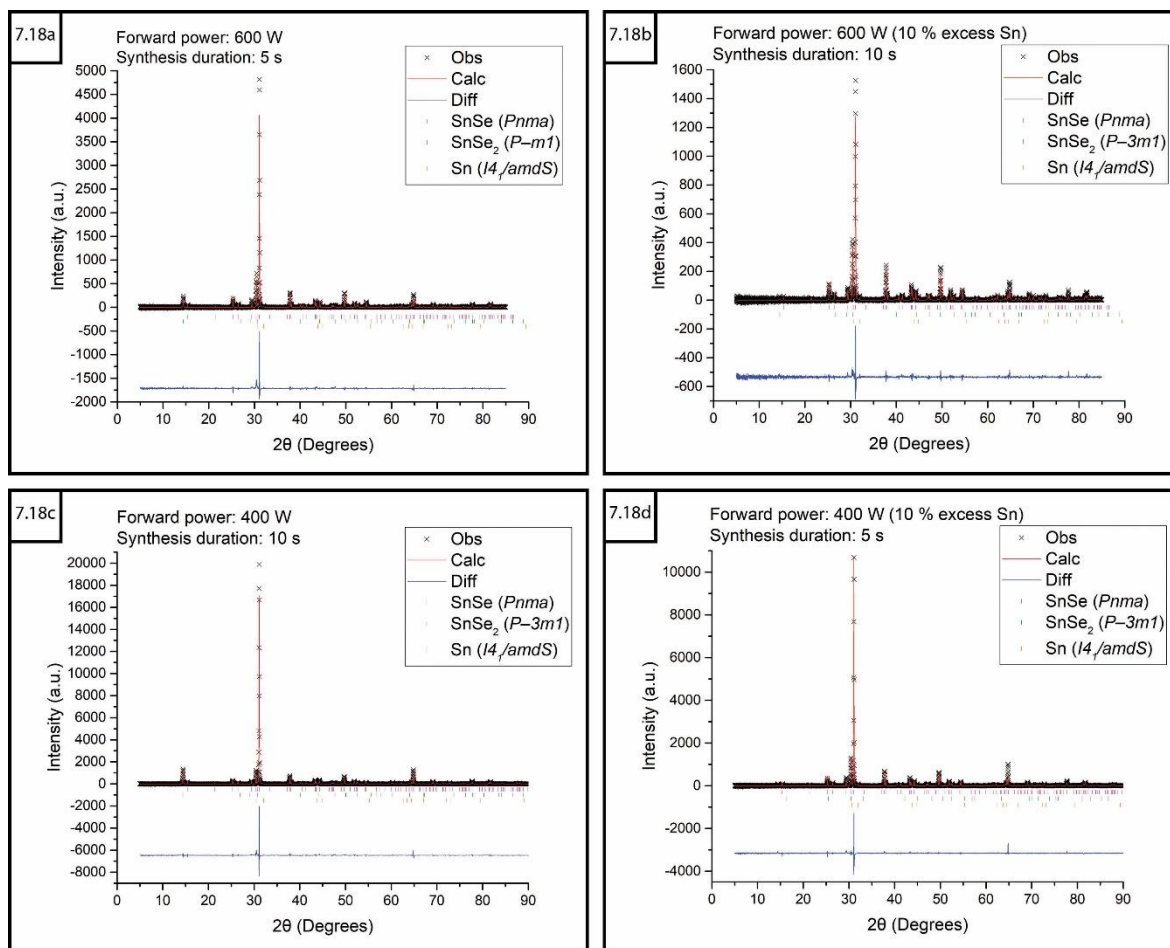


Figure 7.18: Plots of refined PXRD data for SnSe samples synthesised in the benchtop SMC reactor with conditions of a) 0.5 g stoichiometric mixture for 5 s using 600 W b) 0.5 g with 10 % excess Sn for 10 s using 600 W c) 1 g stoichiometric mixture for 10 s using 400 W d) 1 g with 10 % excess Sn for 5 s using 400 W

The reduced SnSe fraction in the 1 g samples is likely due to the slightly shorter synthesis duration compared to the 0.5 g sample, indicating that the trade-off between MW power and shorter synthesis duration for producing single phase samples is more pronounced for larger quantities of material. The refined crystallography data for the SnSe and SnSe₂ phases of the samples presented in figure 7.18 are available in appendix section A–7.5.

7.5.3 Solid state microwave synthesis under various atmospheres

The preparation of solid state samples for MW synthesis is often reported with the mixture being sealed under vacuum. To determine if the evacuation step was necessary or significantly impactful in the synthesis process, four samples were prepared (with either 1:1 stoichiometry or 10 % excess Sn) and sealed under normal atmospheric pressure. One of each sample stoichiometry was sealed under air while the other two were sealed under argon. Neither of the preparations that were sealed in air or the sample with 10 % excess Sn under argon underwent a reaction after >10 mins heating at 450 W forward power using the benchtop SMC reactor.

After heating for 10 mins using 450 W forward power the stoichiometric sample sealed under argon was found to have reacted, although the exact duration of MW absorption is unknown as no visual indicator from the sample applicator or significant reduction in reflected power was observed during the experiment. The sample was characterised as a mixed phase of SnSe and SnSe₂ with no unreacted starting material as shown in figure 7.19, with the crystallographic parameters (available in appendix section A-7.5) showing a SnSe phase fraction of 93.7(1) wt.%.

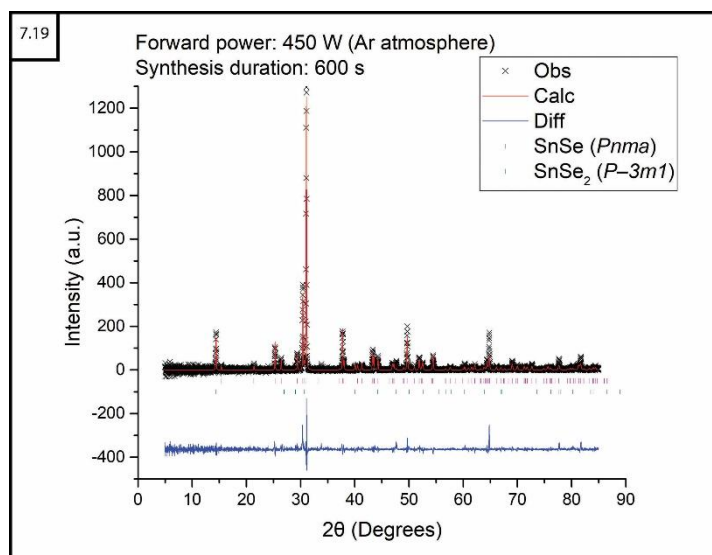


Figure 7.19: Plot of refined PXRD data for SnSe sample synthesised under an argon atmosphere in the benchtop SMC microwave reactor using 450 W forward power for 600 s

The sample prepared under argon atmosphere had no significant impact on the main phase fraction of SnSe compared to one prepared under air then evacuated; leaving a Sn-rich environment as the most optimal synthesis approach. The evacuation step of the direct MW-heating experimental design is an essential one to greatly reduce the induction period by reducing the radiative loss to a surrounding gas, thereby making thermal runaway easier to achieve.

7.6 Partial substitution of chalcogen site (SnSe_{1-y}X_y)

While planning the experiment list for the Polaris-SMC *in-situ* commissioning experiments, a series of samples were prepared to determine if the Se site in SnSe could be gradually substituted with Te or S using the direct MW-heating method. This method has not been reported in the literature for these materials and so it was imperative to have an understanding of the necessary synthesis parameters prior to conducting experiments on limited beamtime. Samples were prepared for a range of each substitution, SnSe_{1-x}Te_x and SnSe_{1-x}S_x (x = 0.2, 0.4,

0.5, 0.6, 0.8, 1), with the aim of synthesising ~1 g of material with the respective product in the main phase.

7.6.1 Direct microwave-heating synthesis parameters for $\text{SnSe}_{1-x}\text{Te}_x$

Six Te-substituted samples were prepared and heated using 500 W forward power for 30 s each. The temperature profiles for each sample showed the expected MW-heating curve correlated with excellent absorption of most of the forward power. By visually comparing the powder diffraction patterns in a waterfall plot (Figure 7.20), it is clear that the orthorhombic ($Pnma$) peaks become less prominent with slight shifting to lower 2θ as the inclusion of more Te expands the structure. The appearance of distinct cubic ($Fm\bar{3}m$) peaks in the data for samples with $x > 0.4$ quickly becoming the dominant phase.

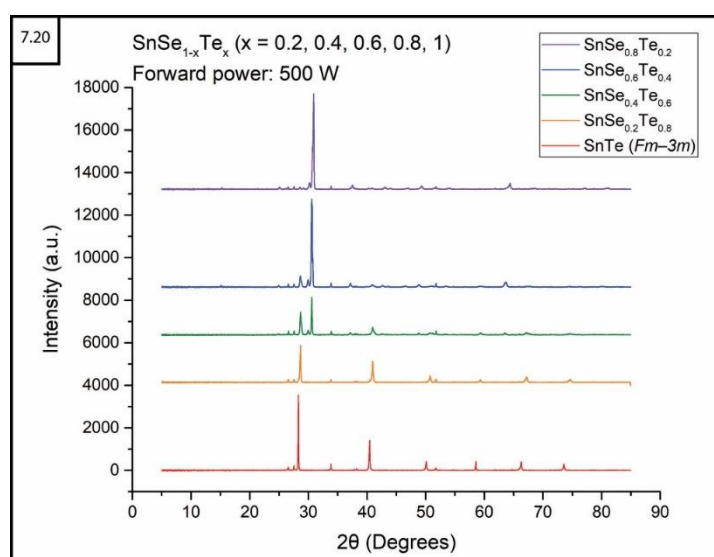


Figure 7.20: Waterfall plot comparing observed PXRD data of $\text{SnSe}_{1-x}\text{Te}_x$ experiments

The refined PXRD data for the $\text{SnSe}_{0.8}\text{Te}_{0.2}$ sample showed that $Pnma$ $\text{SnSe}_{0.6}\text{Te}_{0.4}$ was present as the main phase with a phase fraction of 92.8(2) wt.% along with peaks that were attributed to SnO_2 and unreacted Te (Figure 7.21b). For the other samples in the series, the two main phases were a mixture of $Pnma$ and $Fm\bar{3}m$ $\text{SnSe}_{1-x}\text{Te}_x$ structures as well as small fractions of SnO_2 and unreacted Te.

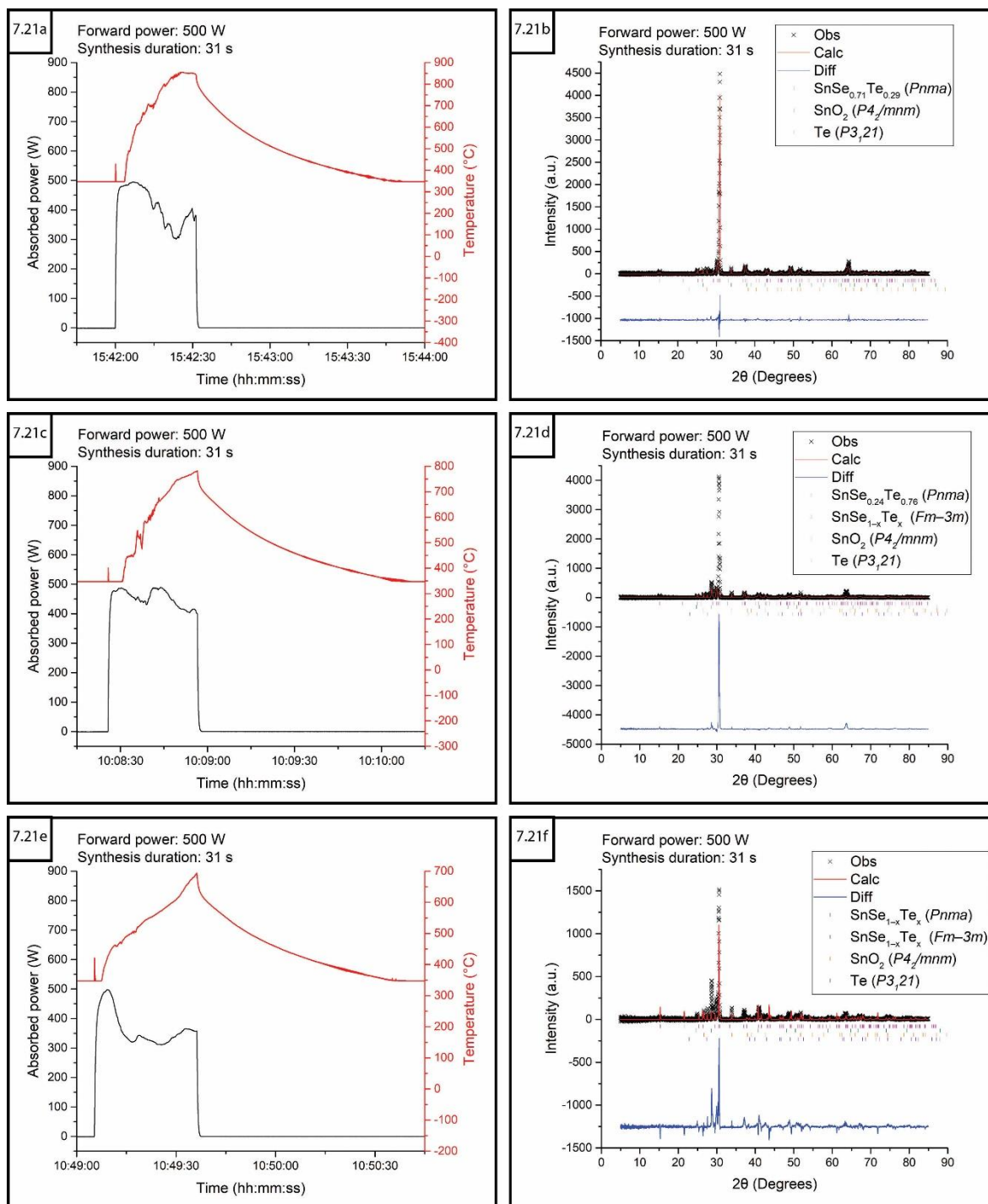


Figure 7.21: Plots of absorbed power and temperature profiles against time (a, c and e) and associated plots of refined PXRD data (b, d and f) of $\text{SnSe}_{1-x}\text{Te}_x$ samples ($x = 0.2, 0.4$ and 0.6 respectively) synthesised using 500 W forward power for 31 s

As the $Fm\bar{3}m$ structure becomes more prominent in the mixed phase system, refinement of both phases became difficult to converge and so the exact level of chalcogen substitution remains unclear. In the final sample, unsubstituted SnTe ($Fm\bar{3}m$) was produced with a phase fraction of 77.8(2) wt.% along with peaks also attributed to SnO_2 and unreacted Te as shown in figure 7.22f.

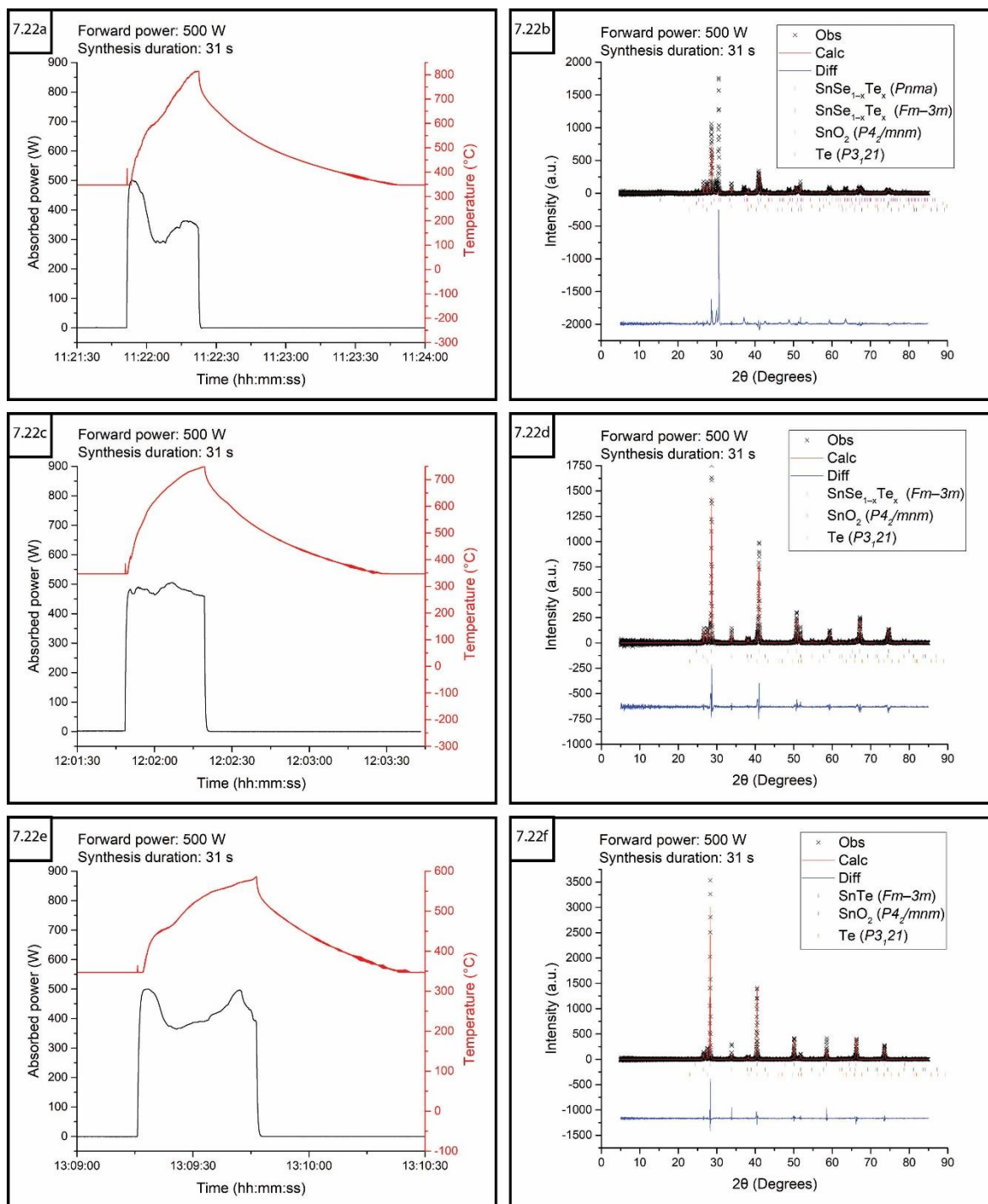


Figure 7.22: Plots of absorbed power and temperature profiles against time (a and c) and associated plots of refined PXRd data (b and d) of $\text{SnSe}_{1-x}\text{Te}_x$ samples ($x = 0.8$ and 1 respectively) synthesised using 500 W forward power for 31 s

From these results it can be concluded that synthesis of the full range of partially substituted $\text{SnSe}_{1-x}\text{Te}_x$ samples was successful using the direct MW-heating method for ~ 30 s of MW absorption. The inclusion of larger Te atoms into the structures is evident with the peak shift to lower 2θ . The refined crystallography data are available in appendix section A-7.7.

7.6.2 Direct microwave-heating synthesis parameters for $\text{SnSe}_{1-x}\text{S}_x$

Six S-substituted samples were prepared and heated for 30, 60 or 90 s, with the resulting PXRd data easier to characterise than the $\text{SnSe}_{1-x}\text{Te}_x$ samples. These

reactions were found to require the aid of a susceptor with 100 W forward power; so, the power and temperature profiles primarily reflect the interaction of the MWs with the graphite. As such, monitoring the reaction progress in real time was hindered and the synthesis duration is instead taken as the entire length of heating time.

Since SnSe and SnS both occupy an orthorhombic space group (*Pnma* and *Pbma* respectively), the Bragg peaks do not change much when comparing the powder diffraction patterns in figure 7.23. There is clear indication of peak shifts to higher 2θ which indicates gradual substitution of heavier Se with S and the associated reduction of the lattice parameters. The trend of peak intensity being increased up to a limit where $x = 0.5$ indicates the structure has more long range order, possibly packing together well at this composition, since Bragg peak intensity is proportional to the square of scattering points.

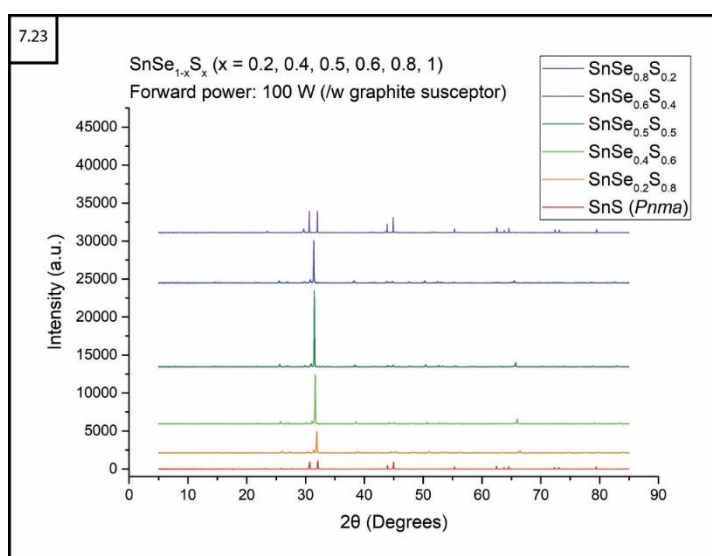


Figure 7.23: Waterfall plot comparing observed PXRD data of $\text{SnSe}_{1-x}\text{S}_x$ experiments

The $\text{SnSe}_{0.8}\text{S}_{0.2}$ sample absorbed ~ 55 W for 31 s however, the temperature did not exceed 347 °C as shown in figure 7.24a and only unreacted Sn and Se peaks were identified (Figure 7.24b). The $\text{SnSe}_{1-x}\text{S}_x$ ($x = 0.4$ and 0.5) samples produced orthorhombic (*Pnma*) $\text{SnSe}_{0.77}\text{S}_{0.23}$ and $\text{SnSe}_{0.52}\text{S}_{0.48}$ with phase fractions of 96.1(5) and 98.4(2) wt.% respectively. Additional peaks were attributed to either unreacted Sn or minimal amounts (~ 1 %) of SnSe_2 .

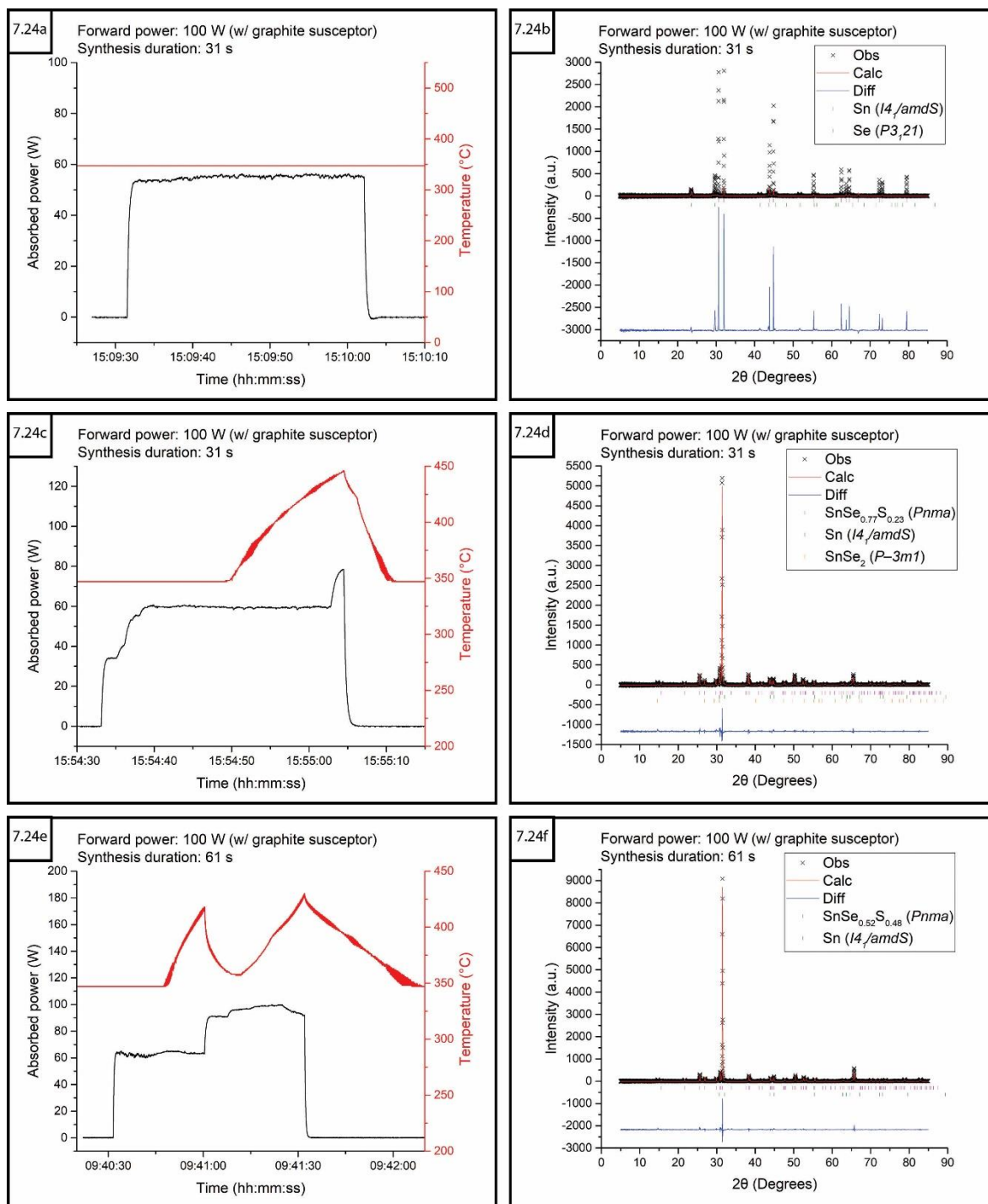


Figure 7.24: Plots of absorbed power and temperature profiles against time (a, c and e) and associated plots of refined PXRD data (b, d and f) of $\text{SnSe}_{1-x}\text{S}_x$ samples ($x = 0.2, 0.4$ and 0.5 respectively) synthesised using 100 W forward power (with a graphite susceptor) for 31 s or 61 s

The $\text{SnSe}_{0.4}\text{S}_{0.6}$ sample also resulted in orthorhombic (*Pnma*) main phase with phase fraction of 96.8(7) wt.% and an actual chalcogen substitution of $\text{SnSe}_{0.6}\text{S}_{0.4}$ (Figure 7.25b). The remaining $\text{SnSe}_{0.2}\text{S}_{0.8}$ sample actually produced $\text{SnSe}_{0.46}\text{S}_{0.54}$ in the orthorhombic (*Pbnm*) main phase with a phase fraction of 89.6(2) wt.% (Figure 7.25d). The SnS sample did absorb ~20–35 W for 91 s however, the temperature did not exceed 347 °C as shown in figure 7.25e and so the mixture did not react (Figure 7.25f). the refined crystallography data are available in appendix section A–7.8.

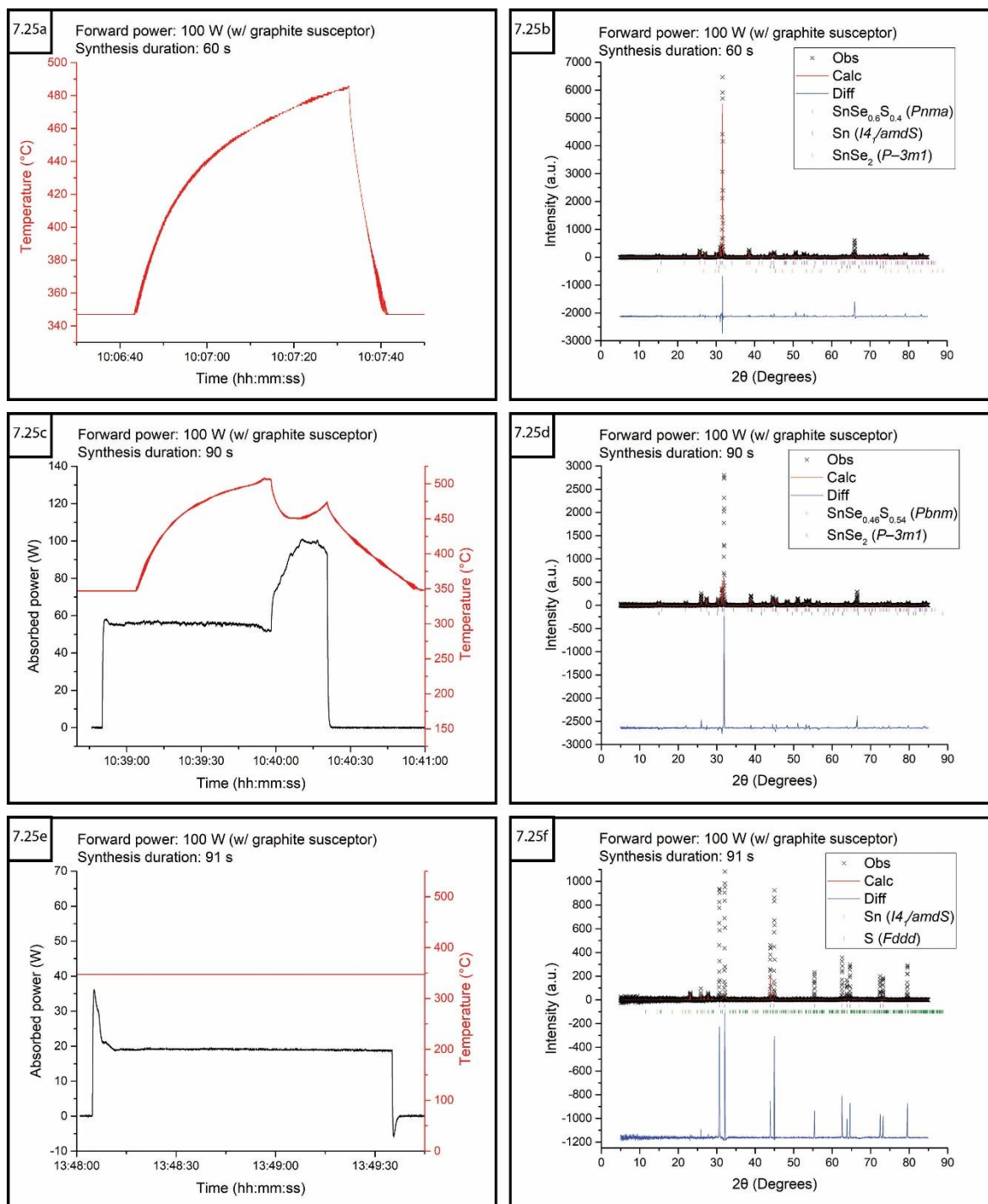


Figure 7.25: Plots of absorbed power and temperature profiles against time (a, c and e) and associated plots of refined PXRD data (b, d and f) of $\text{SnSe}_{1-x}\text{S}_x$ samples ($x = 0.6, 0.8$ and 1 respectively) synthesised using 100 W forward power (with a graphite susceptor) for 60 s , 90 s and 91 s

All of the $\text{SnSe}_{1-x}\text{S}_x$ samples show less S inclusion that calculated for in each sample, possibly owing to the volatility of sulfur when heated and which may need to be present in excess to ensure to achieve the desired level of doping. Figures 7.24e and 7.25c both show interesting features in the temperature profile, namely a second heating curve that corresponds to a step up in MW power absorption. These could relate to the formation of products with a greater $\tan\delta$ resulting from improved dielectric constant and leading to better MW absorption.

7.7 Thermoelectric properties

As described in chapter 5, the dimensionless figure of merit (zT) is defined by the thermal and electrical properties of the material and is a good metric for the effectiveness of a TEM:

$$zT = \left(\frac{PF}{\kappa_T}\right)T = \left(\frac{S^2\sigma}{\kappa_l + \kappa_e}\right)T \quad \text{(Equation 7-3)}$$

As described in section 5.5.2, the band gap of semiconductors relates directly to charge carrier formation and therefore the TE properties. Generally, materials with smaller E_g means less energy is required for electron transition between valance and conduction bands, i.e., greater charge mobility and larger σ .

7.7.1 Optical band gap calculated from UV-vis spectroscopy

Four of the earliest samples that were prepared in the DMO with 10 % excess Se were analysed using a Shimadzu UV-2600 UV-vis Spectrophotometer as described in section 5.5.1 (Figure 7.26).

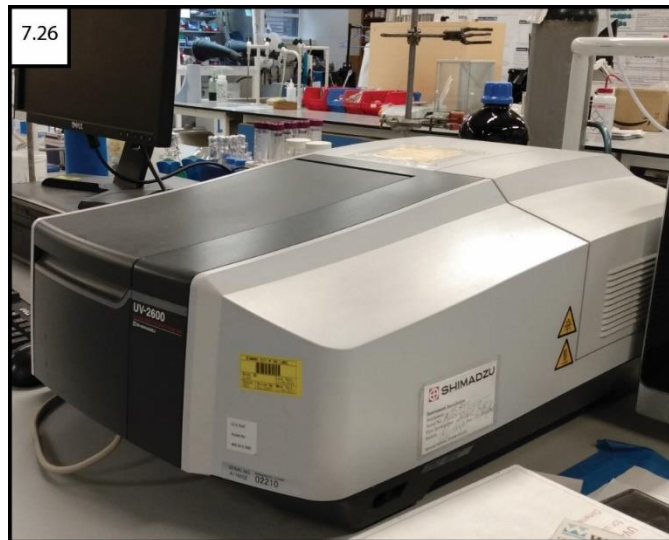


Figure 7.26: Shimadzu UV-2600 UV-vis Spectrophotometer

The first two samples tested had SnSe phase fractions of 92(5) and 92(6) wt.% respectively. As shown in figure 7.27, the direct band gap values were much lower than expected for a bulk sample (1.27–1.3 eV), while the indirect band gap was much closer (0.90(7) and 0.96(3) eV respectively) to the bulk sample value of 0.9 eV listed in Table 7.6.

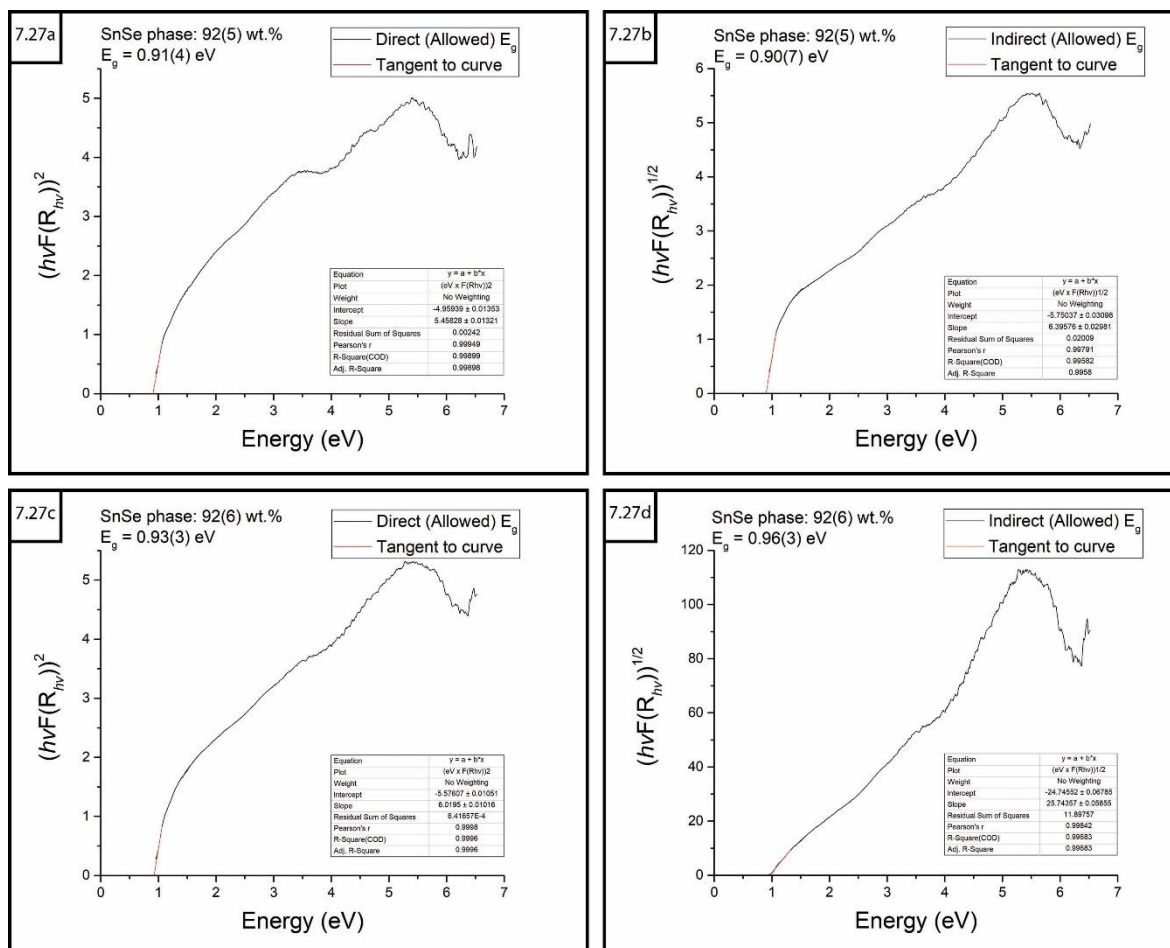


Figure 7.27: Tauc plots of Kubelka-Munk function $(F(R_{hv})^n)$ against photon energy (hv) with tangent to the first inflection indicating band gap (E_g) for a) SnSe sample 1 direct band gap b) SnSe sample 1 indirect band gap c) SnSe sample 2 direct band gap d) SnSe sample 2 indirect band gap

For SnSe, the tight-binding and experimental values of both the direct and indirect band gap (E_g) for a variety of material morphologies have been reported in literature.

Table 7.6: Tight-binding and experimental values for direct and indirect band gap for various SnSe material morphologies as reported in literature [54], [96], [214]

Morphology	Direct (eV)	Indirect (eV)
Bulk (tight-binding)	1.3	0.9
Bulk (experimental)	1.27	0.86–0.89
Single layer	1.66	1.63
Double layer	1.62	1.47
Nanocolumns	–	0.93
Nanosheets	1.1	0.86
Nanoflowers	1.05	0.95
Nanocrystals	1.71	–
Nanoplates	–	0.96
Nanowires	1.12	1.55

The second pair of SnSe samples tested had much lower primary phase fractions of 88(9) and 90(3) wt.% respectively. As shown in figure 7.28, the direct (0.90(4)

and 0.91(4) eV) and indirect (0.98(1) and 0.92(1) eV) band gap values were similar to the previous samples.

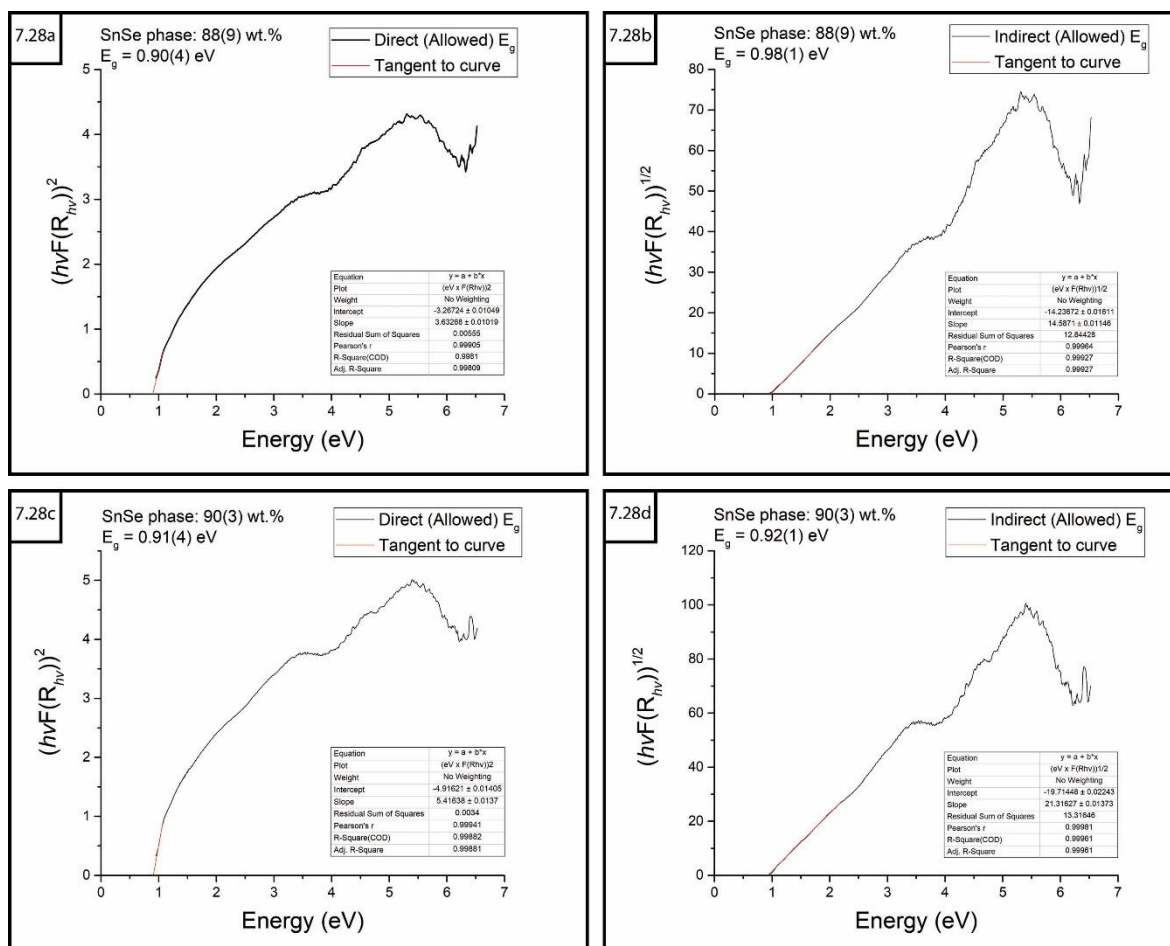


Figure 7.28: Tauc plots of Kubelka-Munk function ($F(R_{hv})^n$) against photon energy ($h\nu$) with tangent to the first inflection indicating band gap (E_g) for a) SnSe sample 3 direct band gap b) SnSe sample 3 indirect band gap c) SnSe sample 4 direct band gap d) SnSe sample 4 indirect band gap

The resulting calculated direct and indirect band gaps (Table 7.7) were not consistent with the reported values for p-type SnSe.

Table 7.7: Experimental values for direct and indirect band gap calculated for SnSe samples with the calculated phase fraction of the SnSe main phase.

SnSe phase fraction (wt.%)	Direct band gap (eV)	Indirect band gap (eV)
92(5)	0.91(4)	0.90(7)
93(3)	0.93(3)	0.96(4)
90(4)	0.90(4)	0.98(1)
91(4)	0.91(4)	0.92(1)

The variation between sample measurements falls within the standard deviation of the direct and indirect values and so are in agreement with one another, which indicates that the deviation from the expected value is not the result of experimental error. The lower measured E_g value may be due to the presence of n-type SnSe₂ resulting from the excess Se used during preparation

allowing the formation of a p-n junction to shift the direct band gap of the sample. Another contributing factor is the presence of defects in the structure. Particularly atom deficiencies, such as with the Sn indicated by the EDX analysis in section 7.4.1, greater numbers of defects will lead to further diminishing E_g . Carrying out new measurements on SnSe samples produced later in the PhD project that were characterised as being more phase pure would probably eliminate the effect of SnSe₂ impurities. However, it was decided that a more comprehensive approach would be to measure the thermoelectric properties directly using instruments capable of recording the Seebeck coefficient (S), electrical conductivity (σ) and total thermal conductivity (κT) of some of those better quality samples.

7.7.2 *Sample densification using hot pressing*

The measurement of thermal and electrical properties of several samples was arranged as a collaboration with the research group of Dr. Jan-Willem Bos at Heriot-Watt University. The samples tested were produced using the Polaris-SMC reactor and so details of their characterisation can be found in section 9.6. The ~5 g ingots were easily cracked with a chalk consistency as discussed previously, and so to carry out testing the samples were required to be pressed into pellets to increase the density and enable them to be shaped for the instruments. At first ~1 g of each sample was cold-pressed using a Specac 13 mm pellet die and compressed using ~1 ton pressure in a Specac hydraulic press. A second set of 13 mm pellets with thickness between 1.40–2.03 mm was prepared in the same way, then sintered in a tube furnace for 6–8 hours in an attempt to further densify the samples. Dr. Bos and Blair Kennedy advised that although the measured densities of the cold pressed and sintered samples were reasonably high (see appendix section A–7.9), they could potentially crack or crumble when impinged upon by the high energy laser of the LFA instrument due to poor relaxation within the polycrystalline structure.

Another ~1 g of material from each of five SnSe_{1-y}X_y samples were hot-pressed using an applied force of 10 bar and temperature of 500 °C for 20 mins. The pellet formation was carried out in a chamber filled with argon at a pressure of 2 bar, shown before the lid was secured in figure 7.29b.

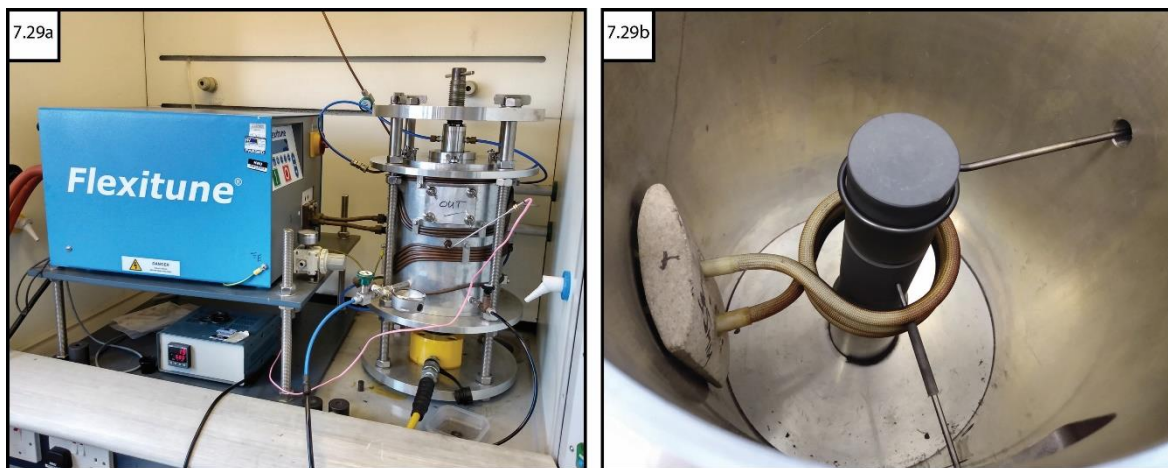


Figure 7.29: Hot press apparatus a) Flexitune induction power supply controlling temperature b) interior configuration of hot press showing graphite pellet die held in place within heating element coils

The density of each pellet was measured using an Ohaus Pioneer Analytical Balance and Density Measurement Kit; the results for the hot-pressed pellets are presented in table 7.8. The percentage density was calculated from the reported density values for SnSe, SnTe and SnS, taken to be 6.18, 6.48 and 5.22 gcm^{-3} respectively.

Table 7.8: Density measurements of hot-pressed pellets performed using an Ohaus Pioneer analytical balance and density measurement kit

Sample	Density measurement (gcm^{-3})				Average density (gcm^{-3})	Percentage density (%)
	1	2	3	4		
SnSe	5.8811	–	–	–	5.8811	95.16
SnSe _{0.8} Te _{0.2}	6.0624	5.9036	5.8667	5.8765	5.9273	–
SnTe	6.2095	–	–	–	6.2095	95.83
SnSe _{0.5} S _{0.5}	5.2401	5.2303	5.2436	–	5.2380	–
SnS	5.0790	5.0886	5.2161	–	5.1279	98.24

The densities of the 13 mm hot-pressed pellets were slightly improved from the cold-pressed and sintered samples and these were determined to least likely result in damage to the LFA instrument. The samples being less than fully dense however, required a numerical correction to be applied to certain calculations to exclude the effect of porosity.

7.7.3 Thermal conductivity measurements

The samples were first analysed using a Linseis LFA 1000 laser flash analysis instrument (Figure 7.30) to record the thermal diffusivity (α) as described in section 5.6.1.



Figure 7.30: Linseis LFA 1000 laser flash analysis instrument

The theoretical density values, accounting for porosity, and heat capacity calculated from the Dulong-Petit estimate were used to determine κT over the temperature range 300–700 °C.

7.7.4 Seebeck coefficient and electrical conductivity measurements

Once analysis using the LFA was complete, the 13 mm pellets were cut into $\sim 2 \times 2 \times 12$ mm bars using a SYJ-150 precision low speed diamond saw as shown in figure 7.31.



Figure 7.31: SYJ-150 precision low speed diamond saw

The bars, once cut, were securely clamped in a Linseis LSR Seebeck and electrical resistivity instrument (Figure 7.32) and the Seebeck coefficient determined as described in section 5.6.2.

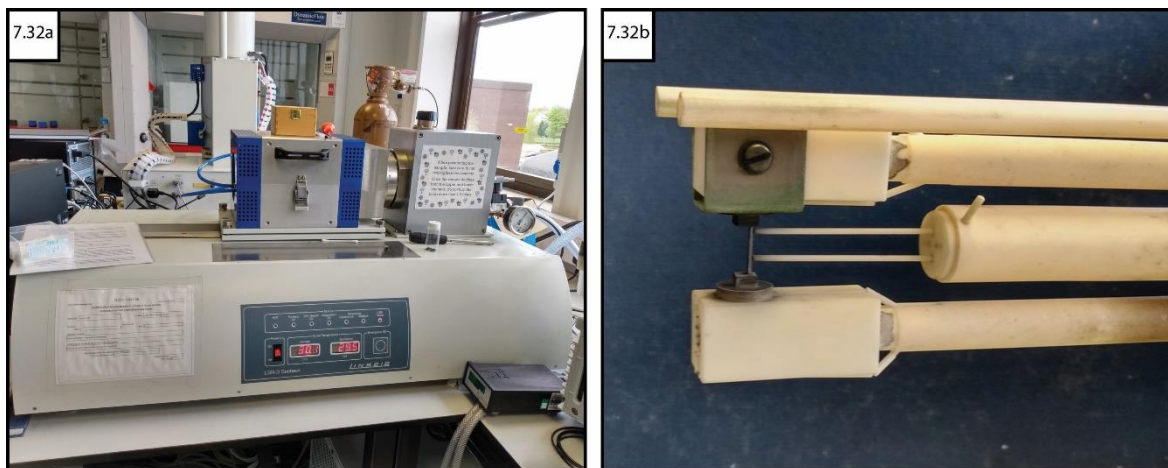


Figure 7.32: a) Linseis LSR Seebeck and electrical resistivity instrument. b) $\sim 2 \times 2 \times 12$ mm bar-shaped sample clamped by Linseis LSR electrodes with thermocouple probes positioned to contact the sample

Electrical conductivity was calculated as the inverse of the recorded electrical resistivity value.

7.7.5 Thermoelectric properties analysis of $\text{SnSe}_{1-y}\text{X}_y$ samples

The SnSe sample, characterised as Sn deficient $\text{Sn}_{0.95}\text{Se}$, performed reasonably well for polycrystalline material measured over the temperature range of the $Pnma$ phase. As shown in figure 7.33b, κT decreases steadily with increasing temperature. The calculated κ_l likewise decreases with increasing temperature and shows very little deviation between cycles. Since the most trustworthy measurements are represented by slow trends, both thermal conductivity values look to be the most reliable for this sample.

Both the S and σ generally increase with increasing temperature (figure 7.33a and 7.33c) leading to improvement of PF as shown in figure 7.33e. The variation of S and σ between different temperature cycles are possibly an indication of further relaxation of the grain structure when heated to ~ 680 K. The calculated zT values for this polycrystalline sample fairly low although the performance improves with increasing temperature as can be seen in figure 7.33f, reaching a maximum $zT = 0.037$ at 671 K.

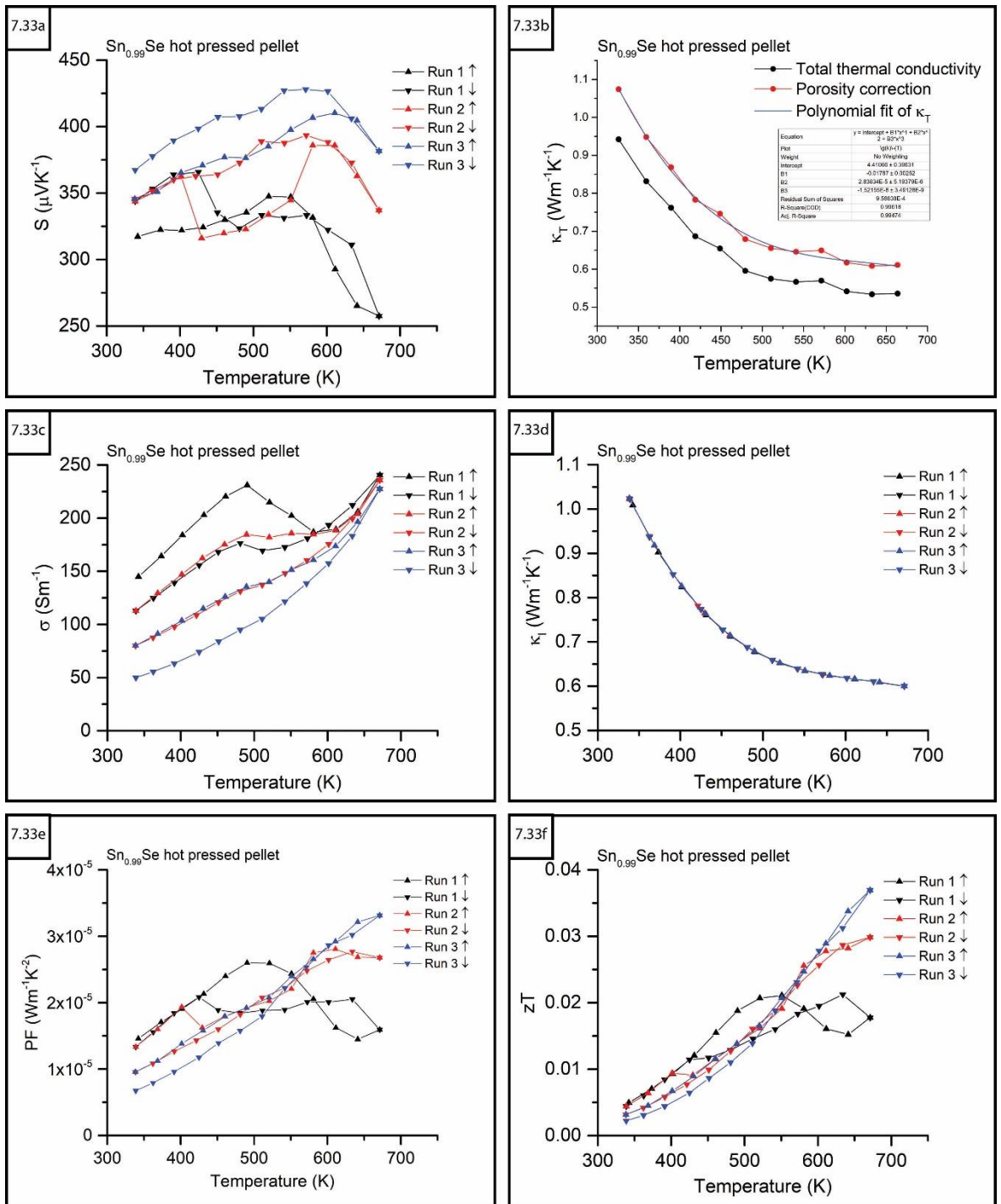


Figure 7.33: Plots of SnSe thermoelectric properties against temperature a) Seebeck coefficient b) total thermal conductivity with a polynomial fit applied to the porosity corrected data c) electrical conductivity d) lattice thermal conductivity e) power factor f) figure of merit

The sample characterised as Sn_{0.99}Se_{0.6}Te_{0.4} showed much more consistent, slow changing results across all thermoelectric parameters. The Seebeck coefficient (Figure 7.34a) demonstrated the most variation between cycles, with general improvement at low temperatures in later runs.

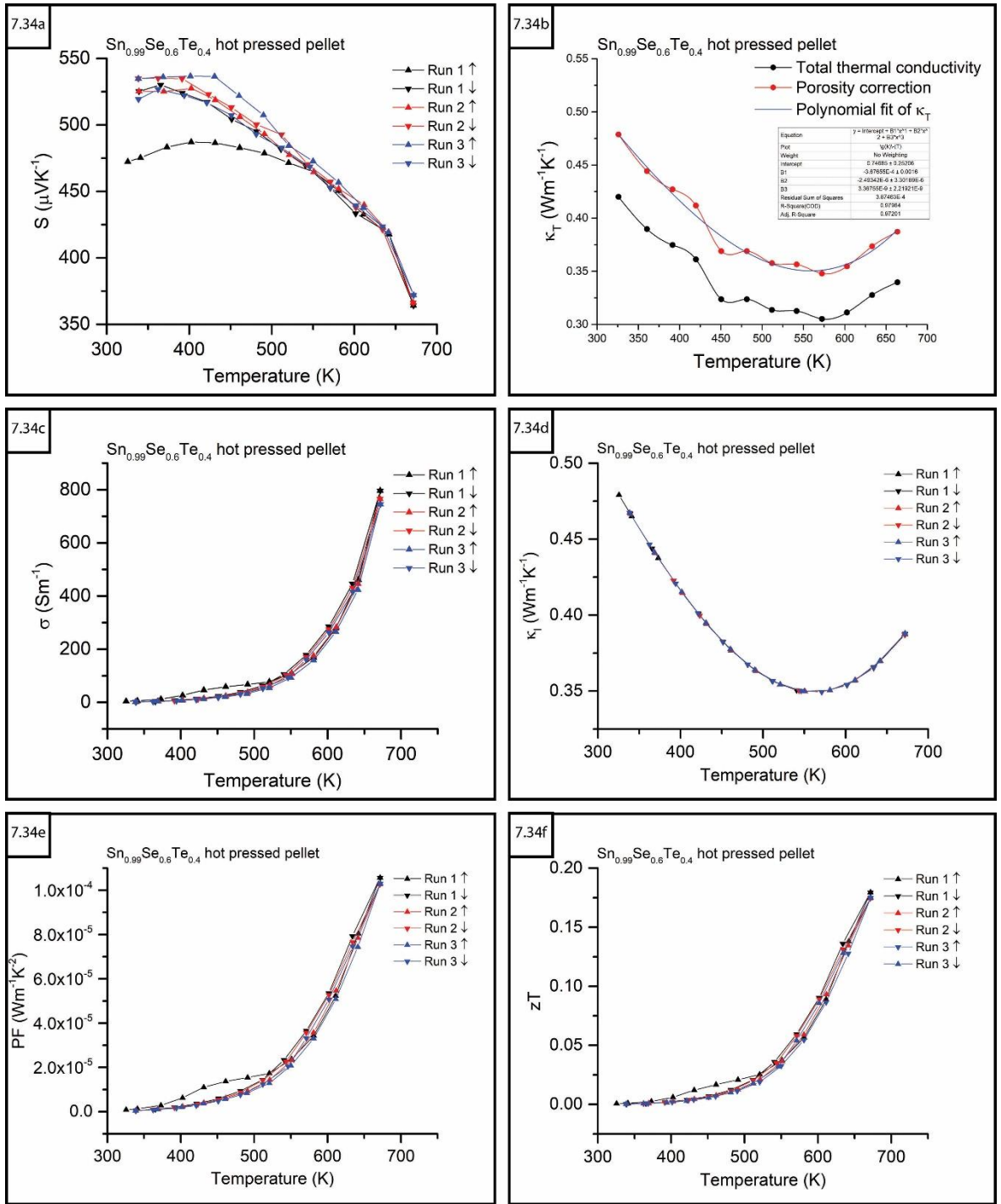


Figure 7.34: Plots of $\text{SnSe}_{0.6}\text{Te}_{0.2}$ thermoelectric properties against temperature a) Seebeck coefficient b) total thermal conductivity with a polynomial fit applied to the porosity corrected data c) electrical conductivity d) lattice thermal conductivity e) power factor f) figure of merit

The uptick seen in both thermal conductivity plots (Figures 7.34b and 7.34d) may be attributed to bipolar recombination reducing the charge carriers through mutual elimination of free electrons and holes. Hall measurements could be used to verify this; the measured Hall voltage (V_H) relates to the charge carrier density (n) from an applied current (I) and magnetic flux density (B) from an applied magnetic field[215]:

$$n = \frac{IB}{e|V_H|} \quad \text{(Equation 7-4)}$$

There was limited time and no ready access to Hall effect instruments to make such measurements of these samples however, as part of any future work with more promising samples, such investigation would be recommended.

Both the PF and zT trends increase smoothly along with temperature, to a maximum $zT = 0.175$ at 672 K, a significant improvement over the unsubstituted SnSe sample. Extrapolating to ~ 900 K, a maximum $zT \sim 0.5$ may be possible for the polycrystalline form of this TEM, although still too low to be considered competitive.

The Linseis LSR instrument developed issues with the machine cooler during the analysis of the $\text{SnSe}_{0.46}\text{S}_{0.54}$ sample, causing the measurement cycles to prematurely shut down. Blair, Stephen and Robert attempted six times to obtain data for the $\text{SnSe}_{0.5}\text{S}_{0.5}$ sample. The best data set obtained was limited to one temperature cycle which was cut short part way through the cooling section of the first run as shown in figure 7.35. Despite the limitation of a single cycle for the data showed consistent, slow changing results across all thermoelectric parameters. Compared to SnSe, S , σ and κT showed steady improvement with increasing temperature (Figures 7.35a–7.35c). The maximum figure of merit was recorded as $zT = 0.069$ at 702 K, a slight improvement over the unsubstituted SnSe sample although lower than $\text{Sn}_{0.99}\text{Se}_{0.6}\text{Te}_{0.4}$.

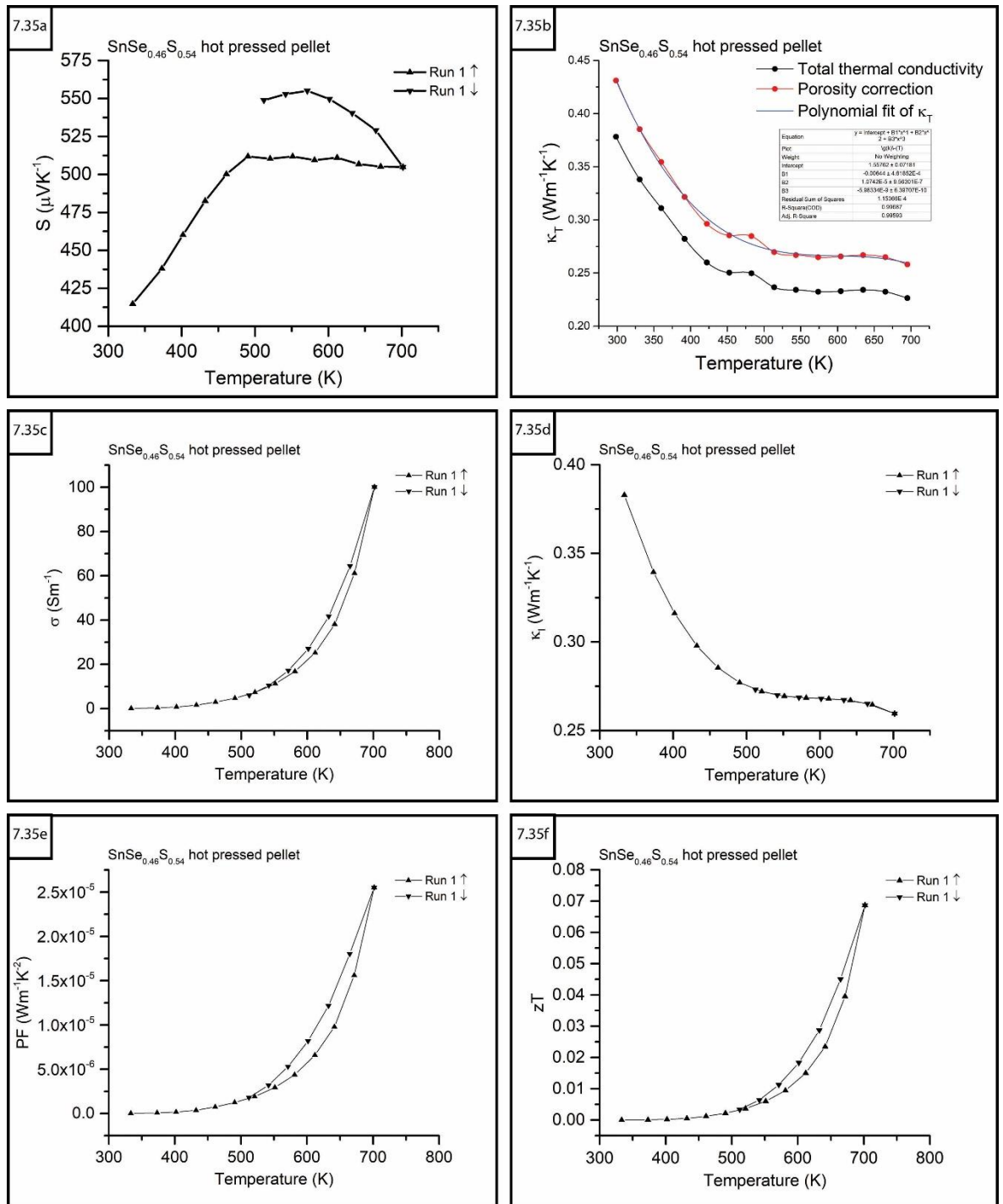


Figure 7.35: Plots of $\text{SnSe}_{0.5}\text{S}_{0.5}$ thermoelectric properties against temperature a) Seebeck coefficient b) total thermal conductivity with a polynomial fit applied to the porosity corrected data c) electrical conductivity d) lattice thermal conductivity e) power factor f) figure of merit

The unsubstituted SnS sample data showed similar variation of S between different temperature cycles as the SnSe sample while all other thermoelectric parameter measurements trended consistently well with increasing temperature as shown in figure 7.36. Both σ and κT data sets showed steady improvement with increasing temperature, leading to similarly promising improvement with the calculated PF . The maximum figure of merit was recorded as $zT = 0.016$ at 701 K, which was the least favourable result from all of the $\text{SnSe}_{1-y}\text{X}_y$ samples analysed.

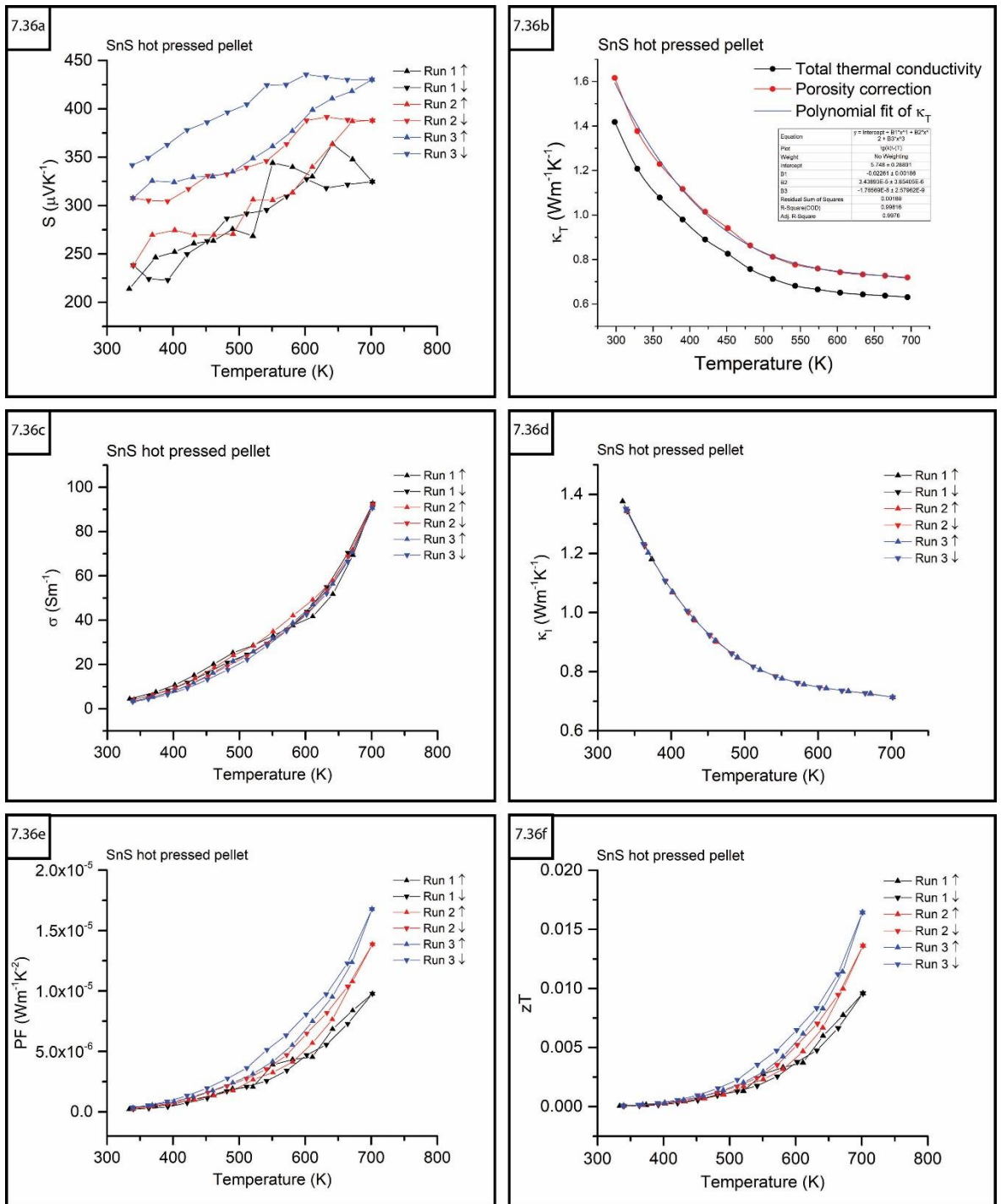


Figure 7.36: Plots of SnS thermoelectric properties against temperature a) Seebeck coefficient b) total thermal conductivity with a polynomial fit applied to the porosity corrected data c) electrical conductivity d) lattice thermal conductivity e) power factor f) figure of merit

The overall low zT values obtained from each of these samples may be reflective of intrinsic defects in the structure that hinder the TE properties of the material. Although it should be noted that the samples were pressed and the measurements made in one direction relative to the axes of compression as shown in figure 7.37a.

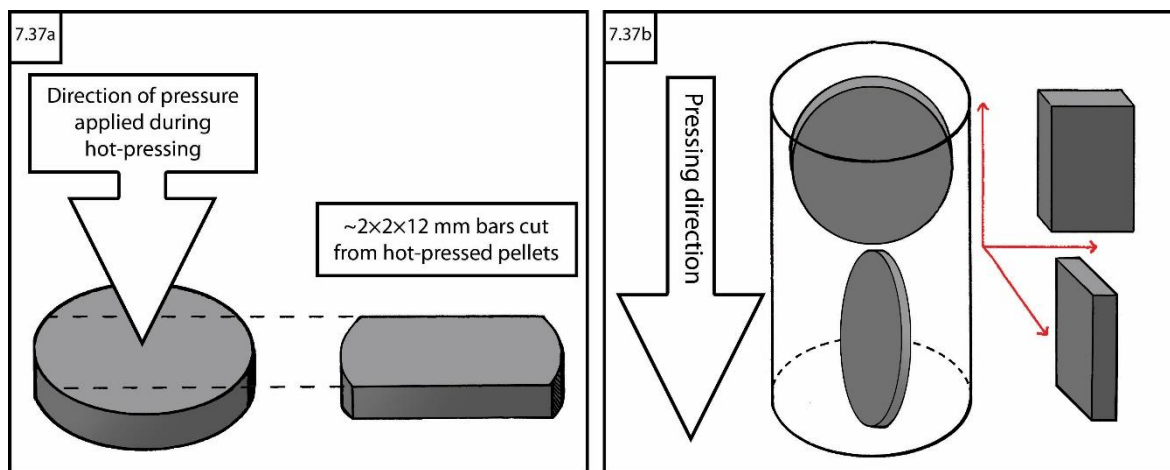


Figure 7.37: Illustration of sample pellet relative to pressing direction a) ~1 mm depth hot-pressed pellet b) ideal comparison of pellets cut relative to different planes

Due to the anisotropy of these structures, it would be preferable to compare pellets/bars cut from larger hot-pressed pellets at different angles relative the direction of compression.

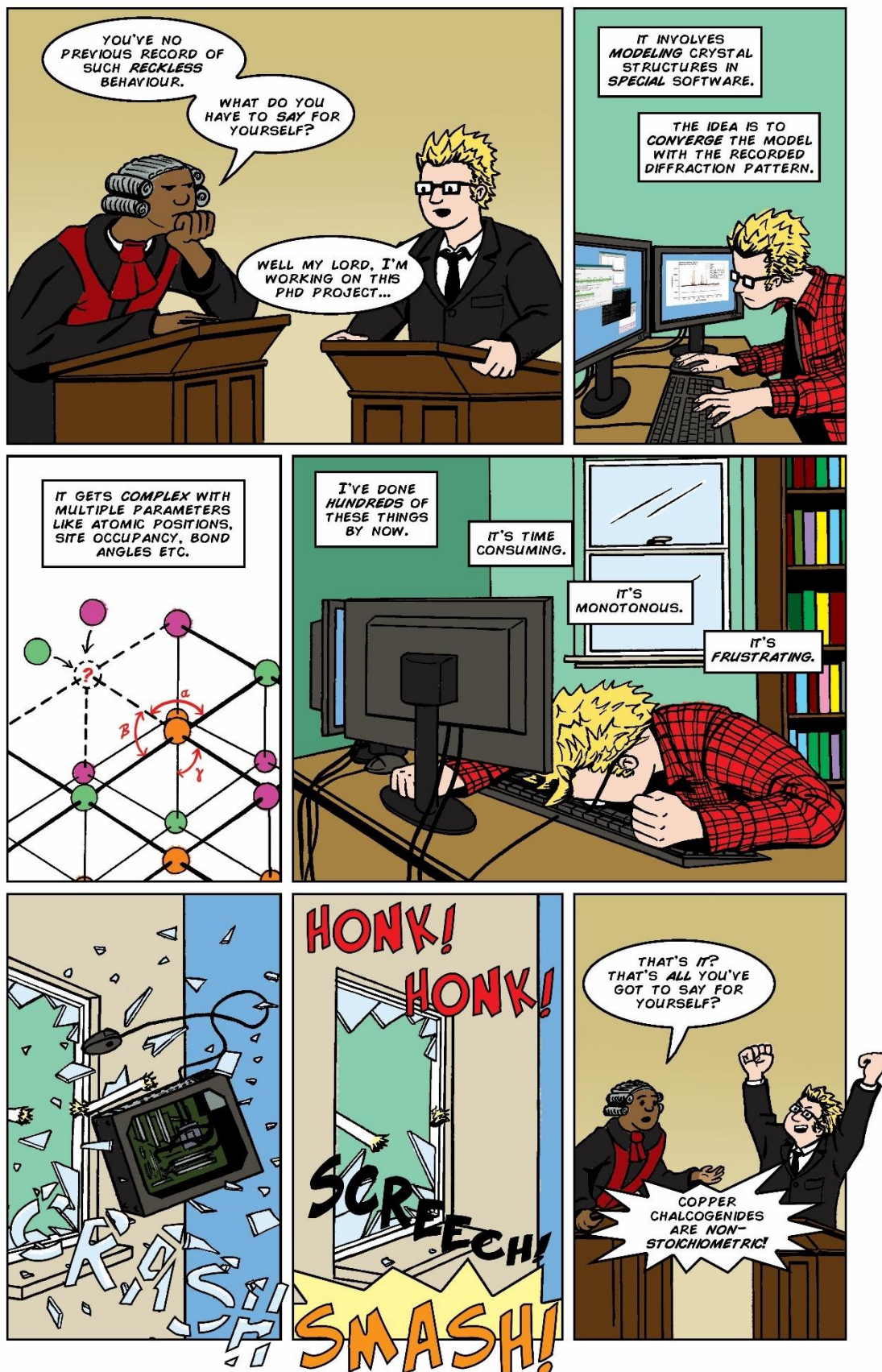
7.8 Summary

It was possible to achieve very high purity polycrystalline SnSe through the use of 10 % excess Sn in the reactant mixture. The reaction parameters for all Te-doped samples using the benchtop SMC reactor were determined to be optimal for 30 s of heating using 500 W forward power, while the S-doped samples should be carried out using 100 W forward power with the aid of a graphite susceptor. From this, a full range of both systems were successfully synthesised however, accurate characterisation of certain structural parameters (particularly for $\text{SnSe}_{1-x}\text{Te}_x$ samples) such as atom substitution or deficiency was very difficult.

These promising synthesis results were carried over to the *in-situ* experiments using the Polaris-SMC reactor where a range of ~5 g $\text{SnSe}_{1-x}\text{Te}_x$ and $\text{SnSe}_{1-x}\text{S}_x$ samples were prepared. The restrictions of time resulted in a limited selection of the most successful samples being hot-pressed into pellets for their TE properties to be measured in collaboration with Dr Bos' research group at Heriot Watt University. The zT values were determined through direct measurement of the thermal and electrical properties, which were lower than desirable however, the materials may perform better along different axes that were not tested. Comparing the results show promising improvement in performance through partial chalcogen substitution, with the best result obtained for $\text{SnSe}_{0.46}\text{S}_{0.54}$ with a maximum $zT = 0.069$ at 702 K.

8 Bismuth, antimony and copper chalcogenides

8.1 Explaining the thesis to a judge

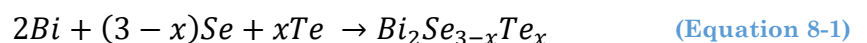


8.2 Microwave synthesis of bismuth chalcogenides ($\text{Bi}_2\text{Se}_{3-x}\text{Te}_x$)

Bismuth chalcogenides have been some of the most consistently well performing TEMs in the literature. As discussed in section 3.3.6, several $\text{Bi}_2\text{Se}_{3-x}\text{Te}_x$ samples have been produced using the direct MW-heating method although a closer analysis of the MW interactions and synthesis process could allow for better control when tuning the structure. Bi and Te are both considered low in abundance within the Earth's crust with Te classed as particularly rare as well as toxic. Since Bi_2Te_3 can be adjusted between n-type and p-type with deviations from stoichiometry, the TE efficiency can most likely be improved through careful control of the development of the crystal microstructure through doping. Producing equivalent or better performing TEMs through partial substitution with more readily available and less toxic elements such as Se would be commercially advantageous. The primary aim was first to synthesise Bi_2Se_3 and Bi_2Te_3 to determine the optimal parameters for repeating the experiments in the Polaris-SMC reactor. Secondly, a range of partially substituted samples were to be prepared in which the chalcogen site was doped with either Se or Te depending on the favoured structure stoichiometry. These samples were used to investigate the ease of tuning the composition using the same MW-heating method.

8.2.1 Stoichiometric calculations and experimental design

The materials for the initial experiments to produce Bi_2Se_3 and Bi_2Te_3 were all weighed out and prepared concurrently using the same procedure as described in chapter 3 with the goal of producing ~1 g stoichiometric samples using the benchtop SMC reactor:



As discussed in section 3.3.3, Mastrovito et al reported that phase pure Bi_2Se_3 requires preparation in an inert atmosphere with 60 % excess Se[3]. This particular paper had not been read prior to the experimental design stage for this subproject and so stoichiometric amounts were used and samples initially prepared in air rather than a glovebox. It became apparent that the air sensitivity of Bi required adjusting all further sample preparations to be carried out inside an MBraun LABstar pro glovebox under nitrogen atmosphere with oxygen levels <2 ppm. Once temporarily held under N_2 atmosphere using the Young's tap the ampoules were evacuated and sealed as usual.

8.3 Optimisation of reaction parameters

The first experiment for each Bi_2Se_3 and Bi_2Te_3 sample batch was heated for 10 minutes using 600 W forward power, during which only a small amount of MW absorption was noted and no physical change, plasma or arcing was observed during the heating process. PXRD analysis confirmed no reaction had occurred, so all further ampoules were placed inside a larger quartz tube (20 bore, 22 mm OD) containing ~5 mm depth of graphite powder and using 100 W forward power. Due to the almost total absorption of MW power by the graphite, it was not possible to identify the exact synthesis duration from minor changes in reflected MW power and so the total heating time is given where appropriate.

8.3.1 Adjusting experimental design to eliminate oxide formation

Certain bismuth oxide impurities were identified in the products of each of these initial samples prepared outside the glovebox, including monoclinic ($P12_1/c1$) Bi_2O_3 and tetragonal ($I4/mmm$) $\text{Bi}_2\text{O}_2(\text{CO}_3)$. Tetragonal ($I4/mmm$) Bi_2SeO_2 , tetragonal ($P4_12_12$) TeO_2 and orthorhombic ($Abm2$) Bi_2TeO_5 phases were also evident where the respective chalcogen was present. The implication was that the Bi powder used was heavily oxidised; which was confirmed by PXRD characterisation of the Bi starting material, showing the presence of $P12_1/c1$ Bi_2O_3 and $I4/mmm$ $\text{Bi}_2\text{O}_2(\text{CO}_3)$. A more in-depth accounting of these initial experiments conducted outside the glovebox is given in appendix sections A–8.1 and A–8.2.

The experimental procedure was adjusted for all subsequent samples to be weighed out and prepared using Bi stored inside the glovebox under N_2 atmosphere; which had been indexed and verified as containing no oxide impurities. Three such Bi_2Se_3 and three Bi_2Te_3 samples were heated using 100 W forward power with the aid of a graphite susceptor for either 60, 90 or 120 s. Visual inspection of the samples after heating (Figure 8.1) showed red deposits on the quartz above the Bi_2Se_3 ingots, while the Bi_2Te_3 samples had none. The Bi_2Te_3 samples had a dull grey colour at the centre with a higher metallic lustre at the edges. It was not possible to cleanly separate the different regions of the Bi_2Te_3 ingots for separate PXRD analysis and so each ingot was prepared as a single powder sample. These samples were retrieved but had to be stored outside of a glovebox in the laboratory during the initial Covid-19 lockdown before they could undergo PXRD analysis.

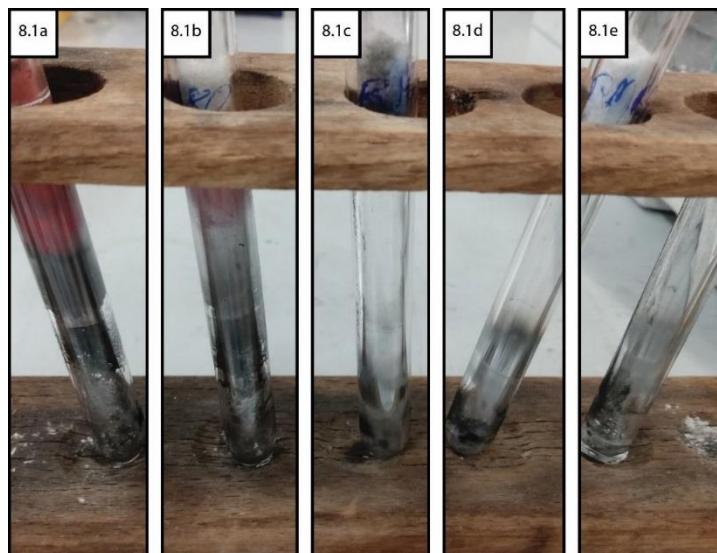


Figure 8.1: Comparison of bismuth chalcogenides synthesised using 100 W forward power with the aid of a graphite susceptor to produce Bi_2Se_3 (a and b) and Bi_2Te_3 (c, d and e) heated for a) 91 s b) 120 s c) 60 s d) 90 s e) 123 s

Use of the glovebox during preparation produced selenide samples with greater proportions of trigonal ($R\bar{3}m$) Bi_2Se_3 as the main phase along with smaller trigonal ($P\bar{3}m1$) BiSe peaks becoming visible after heating for 120 s as shown in figure 8.2. The refined crystallography data for the main Bi_2Se_3 phase of these samples are available in appendix section A–8.3.

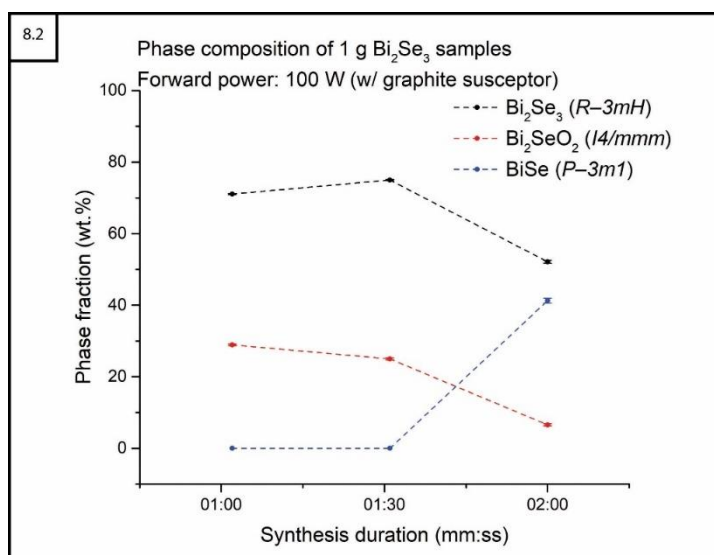


Figure 8.2: Plot of relative phase fractions against synthesis duration for Bi_2Se_3 syntheses

Tetragonal ($I4/mmm$) Bi_2SeO_2 was still identified in each sample despite steps taken to control for the presence of oxidised Bi in the starting mixture. It is a reasonable expectation that the delay between synthesis and analysis would allow a mildly air sensitive sample left on the bench to become oxidised. It is also possible that the process of heating the starting materials in direct contact with the quartz ampoule could lead to a reaction with the oxygen contained in the SiO_2 of the quartz.

The additional BiSe phase in the sample heated for 120 s, may limit the amount of oxidation of Bi_2Se_3 to Bi_2SeO_2 when stored outside of a glovebox post reaction. Alternatively, Bi_2SeO_2 may be formed in the earlier stages of heating and only limited by the surface area contact between the reactants and ampoule wall. As such, with longer synthesis duration, both Bi_2Se_3 and Bi_2SeO_2 phases are decomposed in the process of producing BiSe which liberates the O_2 . The latter explanation would account for the difference in Bi_2SeO_2 phase fraction between the samples despite all being stored under the same conditions. In either scheme, the production of BiSe with longer synthesis duration results in a drastic reduction in the intended Bi_2Se_3 phase fraction therefore, limiting synthesis duration to ≤ 90 s should maximise Bi_2Se_3 production.

PXRD analysis of the telluride samples showed that orthorhombic (*Abm2*) Bi_2TeO_5 comprised a significant portion of the phase composition regardless of synthesis duration as shown in figure 8.3. Like the selenides, the preparations using the glovebox resulted in $R\bar{3}m$ Bi_2Te_3 remaining as the main phase component however, the maximum phase fraction achieved was only 57(4) wt.% after 120 s heating.

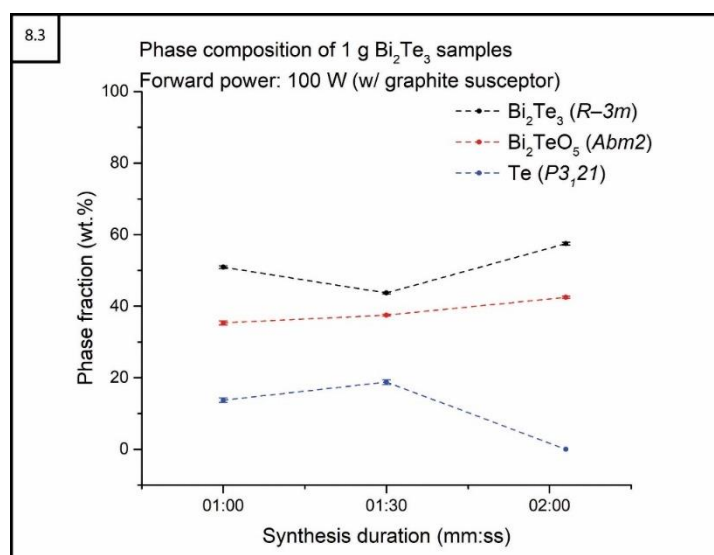


Figure 8.3: Plot of relative phase fractions against synthesis duration for Bi_2Te_3 syntheses

The increasing phase fraction of the Bi_2TeO_5 impurity with increasing synthesis duration indicate that the unwanted oxide is being produced by interaction with the quartz ampoule, with a portion of unreacted Te being consumed with longer heating time. The refined crystallography data for the main Bi_2Te_3 phase of these samples are available in appendix section A–8.3.

If further work were to be conducted on this system, it would be worth increasing the range of heating times to observe if the Bi_2Te_3 and Bi_2TeO_5 mixed phase system remains stable or if one structure were to be decomposed in favour of the other. A revised experimental design specifically to improve the phase purity of the target Bi_2Te_3 material would involve the inclusion of a barrier between the reactants and quartz ampoule.

8.3.2 Bismuth chalcogenide solid solution ($\text{Bi}_2\text{Se}_{3-x}\text{Te}_x$) syntheses

A range of doped samples intended to gradually replace Se with Te in the common $R\bar{3}m$ space group were prepared and all samples heated using 100 W forward power with a graphite susceptor for 90 s. PXRD analysis of the samples showed the continued presence of both tetragonal ($I4/mmm$) Bi_2SeO_2 and orthorhombic ($Abm2$) Bi_2TeO_5 phases throughout the series however, the $R\bar{3}m$ $\text{Bi}_2\text{Se}_{3-x}\text{Te}_x$ remained as the main phase in each case.

The recorded temperature and absorbed MW power data follow the expected progression profile for a good dielectric (Figure 8.4a, 8.4c and 8.4e) as expected with the use of a graphite susceptor. The appearance of short spikes of greater MW absorption, or a slight transition to lower absorption limit by a few Watts could be indicative of the formation of the product phases with lower $\tan\delta$, reducing the overall coupling. The actual necessary synthesis duration is likely much shorter and the restriction of impurity phases could therefore be more precisely controlled if they are truly the result of longer heating time.

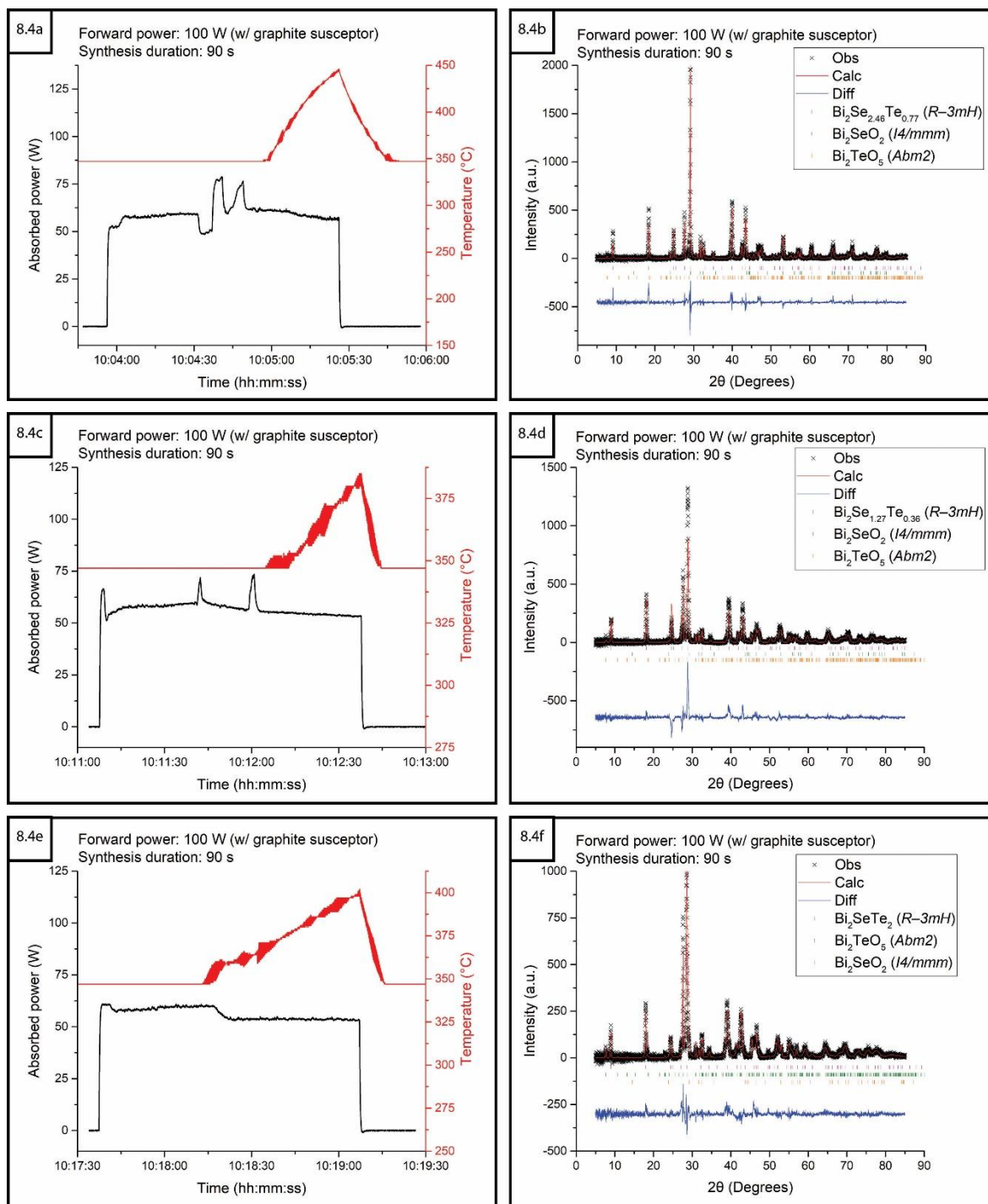


Figure 8.4: Plots of absorbed power and temperature profiles against time (a, c and e) and associated plots of refined PXRD data (b, d and f) for $\text{Bi}_2\text{Se}_{2.5}\text{Te}_{0.5}$, $\text{Bi}_2\text{Se}_2\text{Te}$ and $\text{Bi}_2\text{Se}_{1.5}\text{Te}_{1.5}$ respectively, synthesised using 100 W forward power with the aid of a graphite susceptor for 90 s

The refined crystallographic data given here in table 8.1, shows that the fractional occupancy of the chalcogen site tended to be slightly more heavily Te-doped than calculated for. If a significant proportion of the reactants becomes locked up in the formation of the oxide phases Bi_2SeO_2 and Bi_2TeO_5 through side reactions with the quartz ampoule early on during heating then the remaining material would in effect have an excess of Te.

Table 8.1: Crystallographic cell parameters from Rietveld refinement of $\text{Bi}_2\text{Se}_{3-x}\text{Te}_x$ PXRD data

Sample	$\text{Bi}_2\text{Se}_{2.5}\text{Te}_{0.5}$	$\text{Bi}_2\text{Se}_2\text{Te}$	$\text{Bi}_2\text{Se}_{1.5}\text{Te}_{1.5}$	Bi_2SeTe_2
Refined site occupancy (Te)	0.77(1)	0.36(1)	Te1 = 0.46(3) Te2 = 0.77(2)	Te1 = 0.19(9) Te2 = 0.95(7)
Crystal system	Trigonal	Trigonal	Trigonal	Trigonal
Space group	$R\bar{3}m$	$R\bar{3}m$	$R\bar{3}m$	$R\bar{3}m$
a (Å)	4.164(2)	4.198(3)	4.238(3)	4.27(1)
b (Å)	4.164(2)	4.198(3)	4.238(3)	4.27(1)
c (Å)	28.91(2)	29.29(4)	29.60(5)	29.9(1)
α (°)	90	90	90	90
β (°)	90	90	90	90
γ (°)	120	120	120	120
Volume (Å ³)	534.1(4)	446.9(8)	460.3(8)	471(2)
Phase fraction (wt.%)	85(1)	81(1)	80(2)	72(5)
Observations	4786	4786	4786	4786
Variables	39	38	37	49
R_{wp}	0.2113	0.2451	0.1953	0.2006
R_p	0.1581	0.1813	0.1423	0.1454
χ^2	2.6150	3.6260	2.2630	2.1100

The unit cell parameters a , b and c show a steady increase with the inclusion of greater amounts of larger Te in the chalcogen sites. The calculated atomic distances between Bi and Se/Te given in table 8.2 generally increase as expected with greater Te inclusion within the structure. The associated bond angles change slightly between samples, indicating an increase in lattice distortions that can reduce electron-phonon scattering, potentially improving charge carrier mobility.

Table 8.2: List of atomic distances and angles obtained from the refined $\text{Bi}_2\text{Se}_{3-x}\text{Te}_x$ PXRD data

Sample	$\text{Bi}_2\text{Se}_{2.5}\text{Te}_{0.5}$	$\text{Bi}_2\text{Se}_2\text{Te}$	$\text{Bi}_2\text{Se}_{1.5}\text{Te}_{1.5}$	Bi_2SeTe_2
Bi–Se distance	2.868(4)	2.907(6)	2.72719(17)	3.031(5)
Bi–Te distance	3.0898(23)	3.1265(27)	3.14539(23)	3.097(4)
$\angle\text{Bi1SeBi2}$	93.09(18)	92.44(24)	93.317(6)	89.53(20)
$\angle\text{Bi1SeBi3}$	93.09(18)	92.44(24)	93.317(6)	89.53(20)
$\angle\text{Bi2SeBi3}$	93.09(18)	92.44(24)	93.317(6)	89.53(20)
$\angle\text{Bi1TeBi2}$	84.73(8)	84.33(9)	84.693(7)	87.11(15)
$\angle\text{Bi1TeBi3}$	95.27(8)	95.67(9)	95.307(7)	92.89(15)
$\angle\text{Bi2TeBi3}$	180.000(0)	180.000(0)	180.000(0)	180.000(0)

The calculated phase fraction of the $R\bar{3}m$ $\text{Bi}_2\text{Se}_{3-x}\text{Te}_x$ phase was observed to decrease with the increasing proportion of Te within the structure as shown in figure 8.5. The orthorhombic ($Abm2$) Bi_2TeO_5 phase increases proportionally to

the decline in the $\text{Bi}_2\text{Se}_{3-x}\text{Te}_x$ phase; implying that Bi_2TeO_5 is particularly stable and preferential given sufficient Te for the side reaction to proceed.

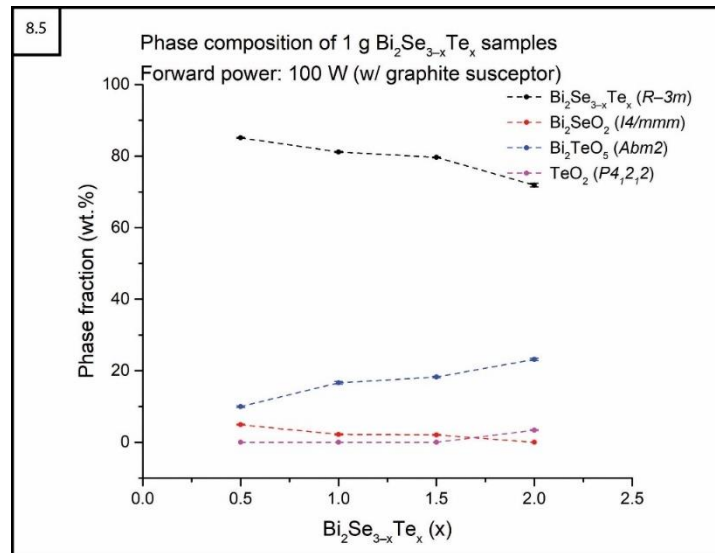


Figure 8.5: Plot of relative phase fractions against chalcogen site fractional occupancy of $\text{Bi}_2\text{Se}_{3-x}\text{Te}_x$ samples.

Due to the constraints of time and lab access during the Covid-19 pandemic, a similar series of 5 g samples to be synthesised in the Polaris-SMC reactor were prepared prior to the characterisation of this set of samples. Therefore, the commissioning experiments reported in chapter 9 were prepared using the same procedures as described here without further accommodations to the experimental design to achieve phase purity. The rapid collection of *in-situ* neutron data should allow for different reaction pathways to be identified with respect to synthesis duration and test these hypotheses further.

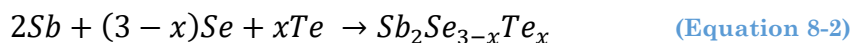
8.4 Antimony chalcogenide solid solutions ($\text{Sb}_2\text{Se}_{3-x}\text{Te}_x$)

Antimony chalcogenides are TEMs with already favourable zT values much like bismuth chalcogenides that could be improved upon. Since Sb is more abundant than Bi, bringing the performance up to the same level as the best performing bismuth chalcogenides would position these materials as some of the most secure TEMs for commercial application. As discussed in section 3.3.8, both Sb_2Se_3 and Sb_2Te_3 samples have been produced using the direct MW-heating method.

The primary aim was first to determine the optimal parameters for performing syntheses of a range of partially substituted $\text{Sb}_2\text{Se}_{3-x}\text{Te}_x$ samples that could be replicated using the *in-situ* Polaris-SMC reactor. Secondly, by successful doping the chalcogen site these samples were used to investigate the ease of tuning the solid solution composition using the direct MW-heating method.

8.4.1 Stoichiometric calculations and experimental design

The materials for the all experiments to produce the full range of $\text{Sb}_2\text{Se}_{3-x}\text{Te}_x$ samples were weighed out and prepared using the procedure described in chapter 3 with the aim of producing ~ 1 g stoichiometric samples using the benchtop SMC reactor:



The first experiment for each Sb_2Se_3 and Sb_2Te_3 sample batch was heated using 600 W forward power and produced inconsistent results for successful synthesis of 1 g samples; and so all further samples were heated using 100 W forward power with the aid of a graphite susceptor.

8.5 Optimisation of reaction parameters

8.5.1 Initial antimony selenide (Sb_2Se_3) synthesis experiments

One Sb_2Se_3 experiment was progressed to completion using 600 W forward power without the aid of a graphite susceptor. The synthesis duration was marked by the observation of a blue glow from the sample applicator and allowed to progress for 20 s. Following PXRD analysis, the data was fit well for orthorhombic ($Pnma$) Sb_2Se_3 with a phase fraction of 96.4(1) wt.% and any additional peaks attributed to unreacted Sb as shown in figure 8.6.

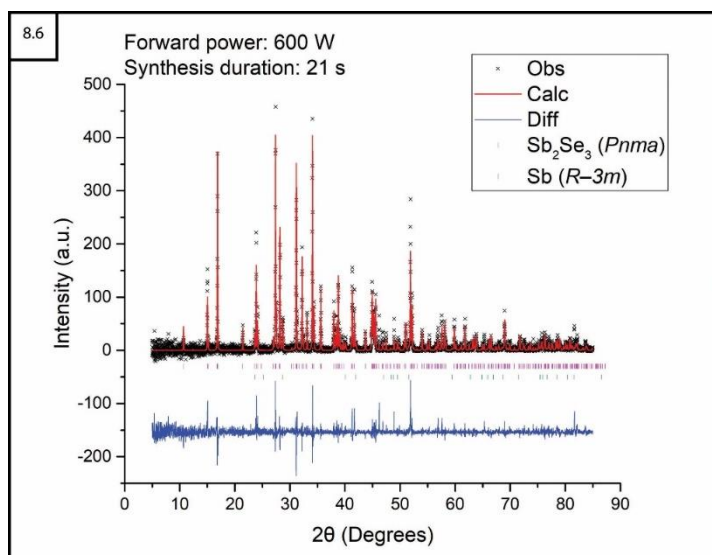


Figure 8.6: Plot of refined PXRD data for Sb_2Se_3 sample synthesised using 600 W forward power for 21 s

All further Sb_2Se_3 experiments required 100 W forward power with the aid of a graphite susceptor to enable reliable synthesis within a reasonable induction period. Under these conditions, synthesis times < 60 s were not enough for a reaction to occur; while for synthesis times ≥ 60 s reactions progressed to

completion, typically with a high phase fraction of $Pnma$ Sb_2Se_3 as shown in figure 8.7.

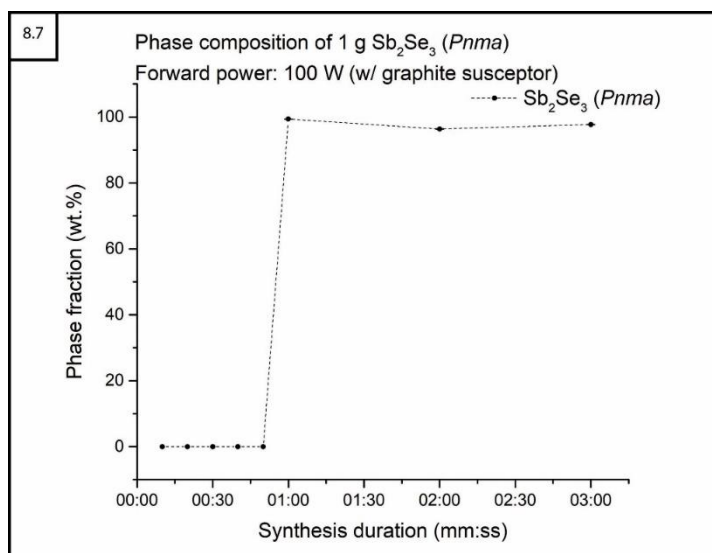


Figure 8.7: Plot of relative phase fractions against synthesis duration for initial Sb_2Se_3 experiments synthesised using 100 W forward power with the aid of a graphite susceptor

It is evident that once a minimum heating duration has been met, no significant improvement in phase purity is obtained by further increasing the heating time. The refined crystallography data for the main Sb_2Se_3 phase of each of these samples are available in appendix section A–8.4.

8.5.2 Initial antimony telluride (Sb_2Te_3) synthesis experiments

All successful Sb_2Te_3 experiments were carried out in the benchtop SMC reactor were done so using 100 W forward power with the aid of a graphite susceptor. As with the Sb_2Se_3 samples, synthesis duration <50 s resulted in no reaction however, for heating times ≥ 50 s, the $R\bar{3}m$ Sb_2Te_3 phase fraction can be seen (Figure 8.8) to be greatly increased with longer synthesis duration up to 73(7) wt.% at a heating time of 180 s. The refined crystallography data for the main Sb_2Te_3 phase of these samples are available in appendix section A–8.5.

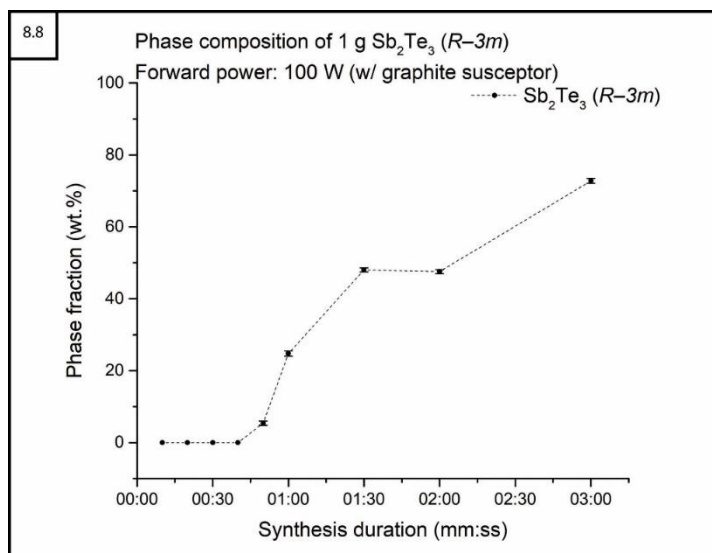


Figure 8.8: Plot of relative phase fractions against synthesis duration for initial Sb_2Te_3 experiments synthesised using 100 W forward power with the aid of a graphite susceptor

8.6 The effect of synthesis duration on $\text{Sb}_2\text{Se}_{3-x}\text{Te}_x$ solid solutions

Three samples were prepared for each $\text{Sb}_2\text{Se}_{3-x}\text{Te}_x$ ($x = 0.5, 1, 1.5, 2, 2.5$) target stoichiometry and heated in the benchtop SMC reactor using 100 W forward power with the aid of a graphite susceptor for either 60, 90 or 120 s to directly compare heating duration on phase fractions and cell parameters.

The 60 s synthesis time did not appear to be sufficient for each sample to consistently initiate a reaction, with $\text{Sb}_2\text{Se}_{2.5}\text{Te}_{0.5}$, $\text{Sb}_2\text{Se}_2\text{Te}$ and $\text{Sb}_2\text{Se}_{1.5}\text{Te}_{1.5}$ remaining unreacted. The Sb_2SeTe_2 and $\text{Sb}_2\text{Se}_{0.5}\text{Te}_{2.5}$ samples produced relatively low phase fractions of a Se-doped $R\bar{3}m$ structure along with secondary phases of orthorhombic ($Pccn$) Sb_2O_3 and unreacted Se and Te. The actual chalcogen site occupancy of the Sb_2SeTe_2 sample was calculated to be $\text{Sb}_2\text{Se}_{2.4}\text{Te}_{0.63}$ while the $\text{Sb}_2\text{Se}_{0.5}\text{Te}_{2.5}$ was much closer to the intended stoichiometry at $\text{Sb}_2\text{Se}_{1.54}\text{Te}_{2.56}$. The oxide phase identified in both samples indicates that the starting material oxidises when heated in contact with the quartz ampoule just as the bismuth chalcogenides were seen to do.

Comparing the calculated cell parameters of the $R\bar{3}m$ $\text{Sb}_2\text{Se}_{3-x}\text{Te}_x$ phase with the Sb_2Te_3 produced under the same conditions showed a trend of expansion in each axis corresponding to increasing Te in the structure (Figure 8.9) as expected.

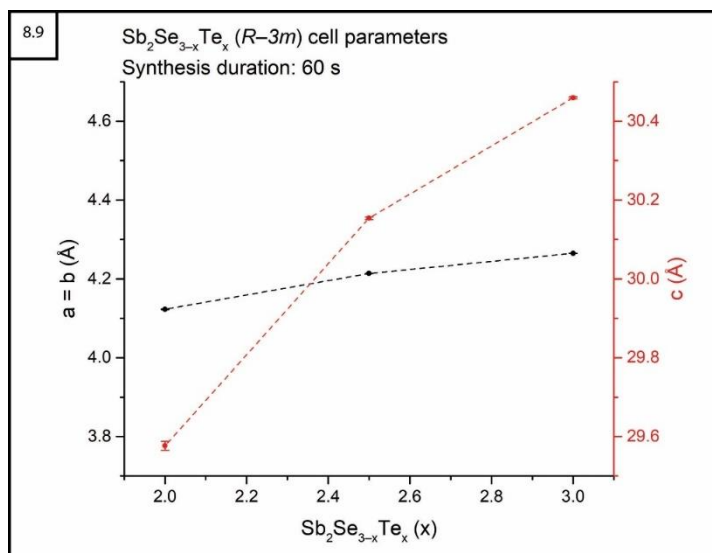


Figure 8.9: Plot of lattice parameters a/b and c for all $Sb_2Se_{3-x}Te_x$ samples successfully synthesised using 100 W forward power with the aid of a graphite susceptor for 60 s

The refined crystallography data for the $R\bar{3}m$ $Sb_2Se_{3-x}Te_x$ phase of these 60 s samples are available in appendix section A–8.6.

The 90 s syntheses were much more successful, with each reaction proceeding to conclusion within the allotted heating time. The data for $Sb_2Se_{2.5}Te_{0.5}$ and Sb_2Se_2Te samples showed a mixed phase system of $Pnma$ and $R\bar{3}m$ structures. The $Pnma$ phase was seen to quickly be diminished until no longer present with Te-doping $x \geq 1.5$ as shown in figure 8.10.

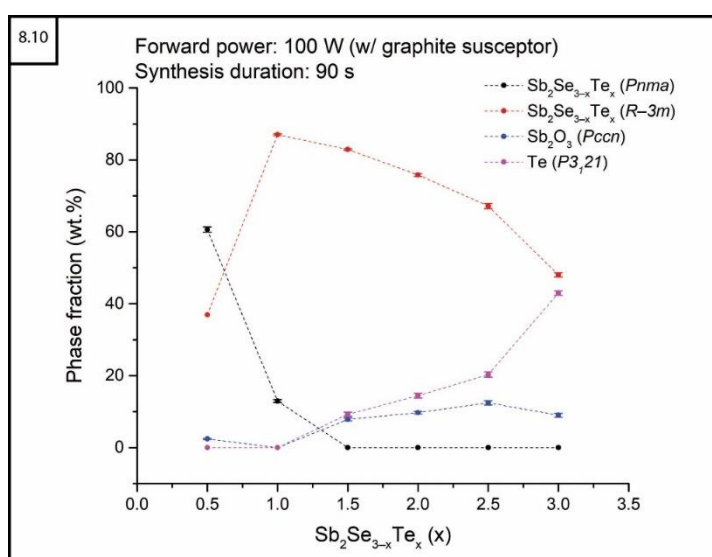


Figure 8.10: Plot of relative phase fractions against intended Te content for $Sb_2Se_{3-x}Te_x$ samples synthesised using 100 W forward power with the aid of a graphite susceptor for 90 s

The Sb_2O_3 phase was also present although the phase fraction of this impurity was not greatly increased with 30 s longer synthesis duration. More apparent was the reduction of the $R\bar{3}m$ $Sb_2Se_{3-x}Te_x$ structure in favour of elemental Te as a secondary phase. This may indicate either that there is a limit to the Te-doping of this structure or that Sb becomes locked up in a favourable oxide phase and

reduces the target phase fraction. Comparing the calculated cell parameters for each $R\bar{3}m$ $Sb_2Se_{3-x}Te_x$ phase (Figure 8.11) shows a clear trend in which expanding lattice constant values were correlated to the increasing Te-doping of the chalcogen site, particularly affecting the c-axis. This seems to confirm the latter interpretation of the phase fractions, in that a stable Sb_2O_3 phase is produced early that limits the formation of the $R\bar{3}m$ $Sb_2Se_{3-x}Te_x$ structure.

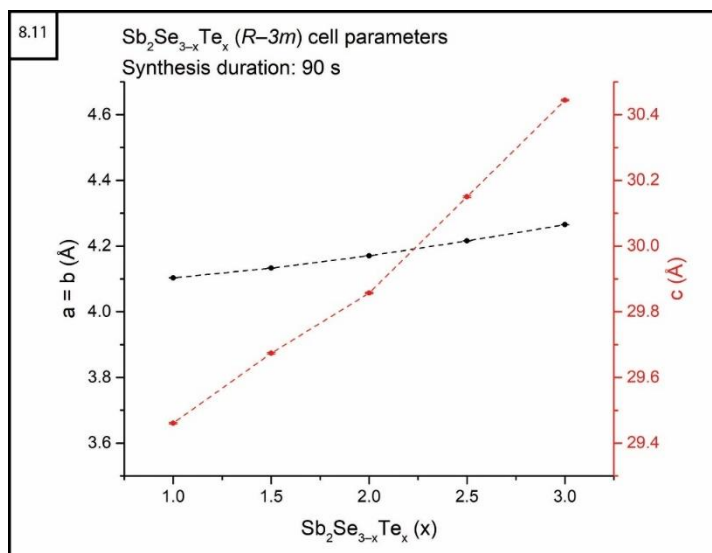


Figure 8.11: Plot of lattice parameters a/b and c for all $Sb_2Se_{3-x}Te_x$ samples synthesised using 100 W forward power with the aid of a graphite susceptor for 90 s

The samples produced after 120 s of direct MW-heating demonstrated the same trend of the $Pnma$ structure present and quickly replaced with the $R\bar{3}m$ structure with increasing Te in the starting mixture as shown in figure 8.12.

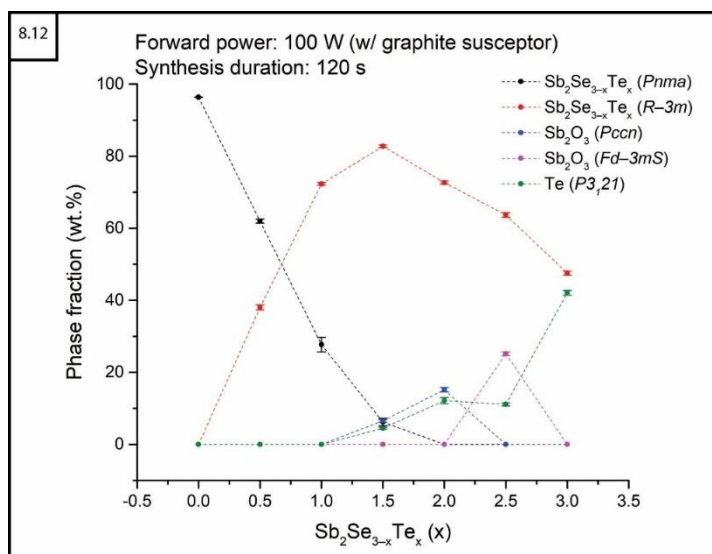


Figure 8.12: Plot of relative phase fractions against intended Te content for $Sb_2Se_{3-x}Te_x$ samples synthesised using 100 W forward power with the aid of a graphite susceptor for 120 s

Two polymorphs of Sb_2O_3 were likewise identified in a majority of the samples with only slightly greater phase fraction than the samples heated for 90 s. The same trend of expanding cell parameters of the $R\bar{3}m$ $Sb_2Se_{3-x}Te_x$ phases (Figure

8.13) correlated to the increasing Te-doping of the chalcogen site gave further evidence that a limited amount of stable Sb_2O_3 is produced in the early stages of synthesis.

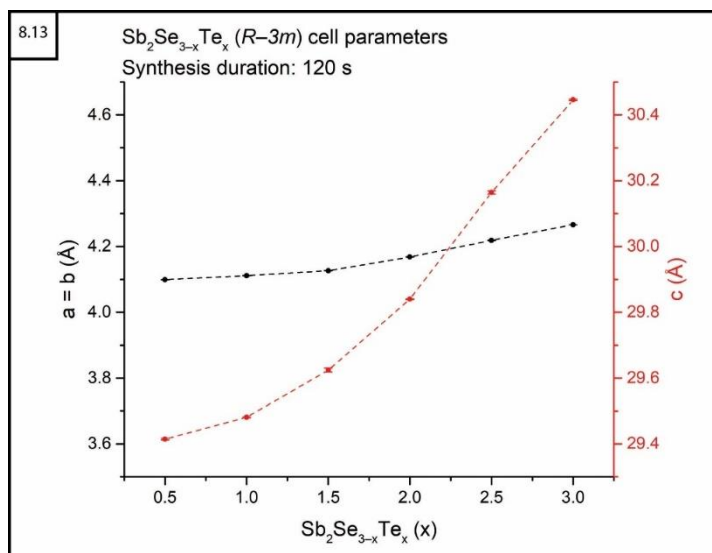


Figure 8.13: Plot of lattice parameters a/b and c for all $\text{Sb}_2\text{Se}_{3-x}\text{Te}_x$ samples synthesised using 100 W forward power with the aid of a graphite susceptor for 120 s

The result of varying heating duration on synthesis of $\text{Sb}_2\text{Se}_{3-x}\text{Te}_x$ solid solutions showed that heating times >60 s are required when using a susceptor and that increasing the time to 120 s did not significantly improve the main phase fraction of the target product. The refined crystallography data for the $Pnma$ and $R\bar{3}m$ $\text{Sb}_2\text{Se}_{3-x}\text{Te}_x$ phases of the 90 and 120 s samples are available in appendix section A–8.6.

8.6.1 *Ex-situ* neutron diffraction of $\text{Sb}_2\text{Se}_{3-x}\text{Te}_x$ solid solution samples

Samples of $\text{Sb}_2\text{Se}_{2.5}\text{Te}_{0.5}$ and $\text{Sb}_2\text{Se}_{0.5}\text{Te}_{2.5}$ synthesised for 90 and 120 s were sent to ISIS for *ex-situ* neutron diffraction analysis through the Xpress access data collection cycle in order to confirm the phase compositions and chalcogen site occupancies. The samples were sealed in vanadium cans and neutron data collected for 180 μAh using the Polaris neutron diffractometer.

Refinement of the neutron data which enables greater distinction between atoms, verified the presence of $Pnma$ and $R\bar{3}m$ structures for the $\text{Sb}_2\text{Se}_{2.5}\text{Te}_{0.5}$ samples with greater Te-doping than previously calculated using PXRD as shown in figure 8.14. The presence of orthorhombic ($Pccn$) Sb_2O_3 only in the sample heated for 90 s illustrates that the oxide phase is intermittently formed rather than encouraged by longer synthesis duration.

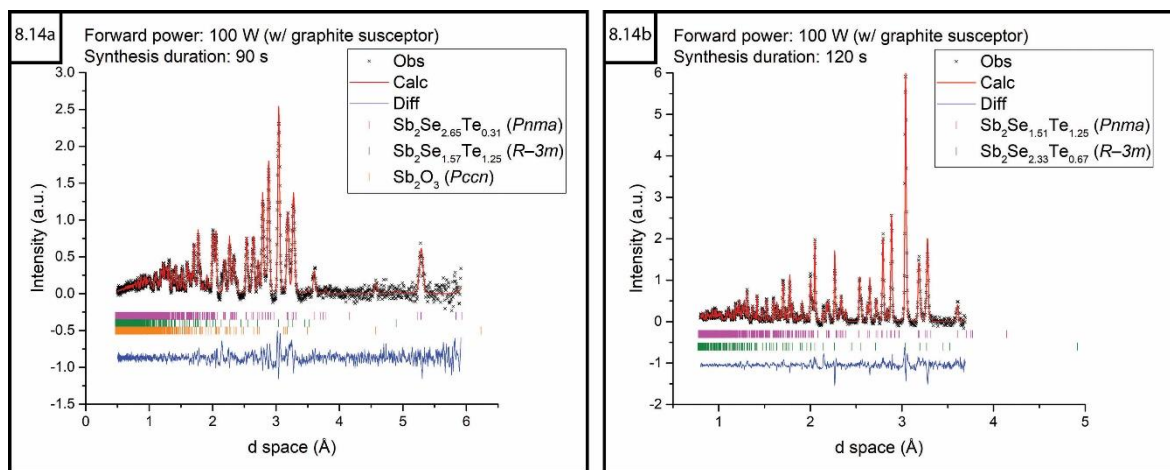


Figure 8.14: Plots of refined PND data for $\text{Sb}_2\text{Se}_{2.5}\text{Te}_{0.5}$ samples synthesised using 100 W forward power with the aid of a graphite susceptor for a) 90 s b) 120 s

The comparison of the crystallographic cell parameters in table 8.3 show that the relative cell dimensions for both space groups that were identified are consistent regardless of synthesis duration.

Table 8.3: Crystallographic cell parameters from Rietveld refinement of PND data for $\text{Sb}_2\text{Se}_{2.5}\text{Te}_{0.5}$ samples (90 and 120 s)

Synthesis duration (s)	90		120	
Refined site occupancy (Te)	Te2 = 0.16(6) Te3 = 0.16(7)	1.25(4)	Te1 = 0.1(2) Te2 = 0.2(1) Te3 = 0.3(1)	1.25(7)
Crystal system	Orthorhombic	Trigonal	Orthorhombic	Trigonal
Space group	$Pnma$	$R\bar{3}m$	$Pnma$	$R\bar{3}m$
a (Å)	11.8551(5)	4.0989(2)	11.8752(8)	4.0960(2)
b (Å)	3.9931(2)	4.0989(2)	3.9984(3)	4.0960(2)
c (Å)	11.6732(6)	29.367(2)	11.688(1)	29.411(2)
α (°)	90	90	90	90
β (°)	90	90	90	90
γ (°)	90	120	90	120
Volume (Å ³)	552.59(3)	427.30(3)	554.98(5)	427.33(3)
Phase fraction (wt.%)	63.9(5)	32.2(9)	56.4(1)	44(1)
Observations	6429		1529	
Variables	144		61	
R_{wp}	0.0317		0.0267	
R_p	0.0490		0.0388	
χ^2	2.418		3.166	

8.6.2 Investigation of $\text{Sb}_2\text{Se}_{3-x}\text{Te}_x$ solid solution between $0 \leq x \leq 1$

The confirmation of a mixed phase solid solution at low levels of Te-doping prompted further investigation to attempt more precise control of the chalcogen substitution. A set of six samples were prepared for $\text{Sb}_2\text{Se}_{3-x}\text{Te}_x$ solid solutions over the range of Te-doped compositions between $0 \leq x \leq 1$. Based on the comparison of synthesis duration, each sample was heated as before for 90 s. At

this stage in the project, the DAQ module for monitoring/recording forward and reflected power had been set up to more precisely determination the reaction duration. When reviewing the power data afterwards, a significant increase in absorbed power was observed for the Sb_2Se_3 and $\text{Sb}_2\text{Se}_{2.5}\text{Te}_{0.5}$ experiments (Figure 8.15) which was likely the result of increased coupling due to thermal runaway and so the actual synthesis times were recorded as 21 and 47 s respectively. The remaining samples were all observed to absorb between 65–75 % of MW power consistently across the 90 s heating cycle.

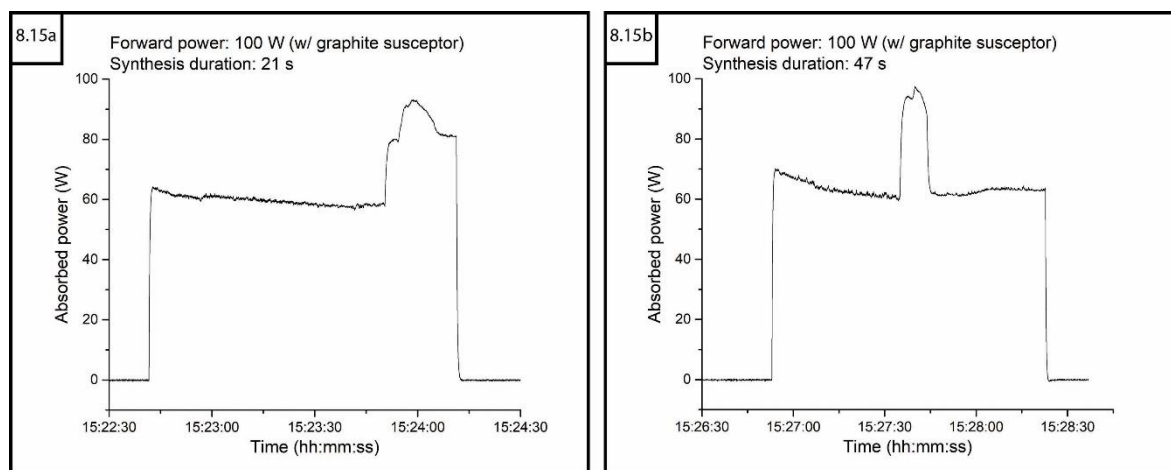


Figure 8.15: Plots of absorbed power against time for $\text{Sb}_2\text{Se}_{3-x}\text{Te}_x$ samples synthesised using 100 W forward power with the aid of a graphite susceptor a) Sb_2Se_3 b) $\text{Sb}_2\text{Se}_{2.5}\text{Te}_{0.5}$

All samples when refined, indicated a mixed phase system containing $Pnma$ and $R\bar{3}m$ $\text{Sb}_2\text{Se}_{3-x}\text{Te}_x$ phases. An error occurred during the preparation of the $\text{Sb}_2\text{Se}_{2.5}\text{Te}_{0.5}$ and $\text{Sb}_2\text{Se}_{2.6}\text{Te}_{0.4}$ samples resulting in a slight Se deficiency and excess in the respective starting materials. This error is the likely cause of the trend deviation observed for site occupancy and phase distribution. When comparing the calculated phase fractions overall (Figure 8.16) the $Pnma$ phase is shown to be steadily replaced in favour of the $R\bar{3}m$ phase. This confirms the previous observation of shifting solid solution balance with greater Te by the incorporation of the new Te-doped samples within the trend as expected.

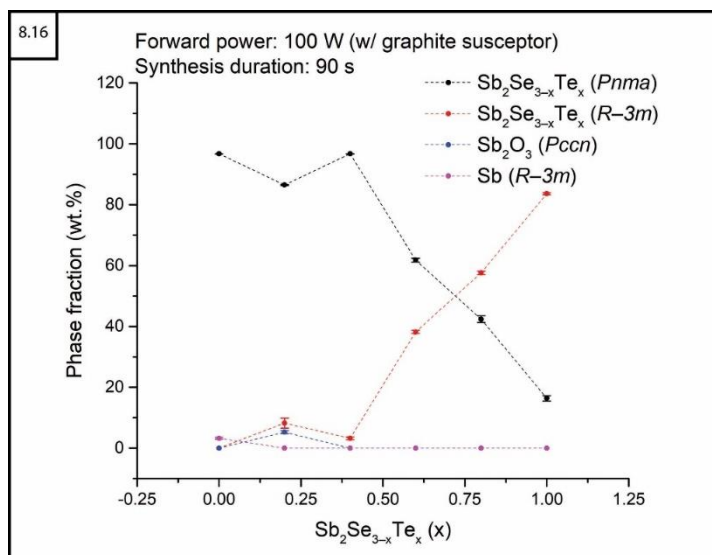


Figure 8.16: Plot of relative phase fractions against intended Te content for $\text{Sb}_2\text{Se}_{3-x}\text{Te}_x$ samples synthesised using 100 W forward power with the aid of a graphite susceptor for 90 s

The cell parameters of the $Pnma$ $\text{Sb}_2\text{Se}_{3-x}\text{Te}_x$ phases showed a clear trend of expanding lattice constant values correlated with the increasing Te-doping of the chalcogen site up to a limit of $x = 0.6$. For samples where $x > 0.6$, a maximum amount of Te-doping seems to be reached as reflected in the cell parameters plotted in figure 8.17a. The $R\bar{3}m$ phase chalcogen site occupancy and associated cell parameters did not demonstrate a correlated trend.

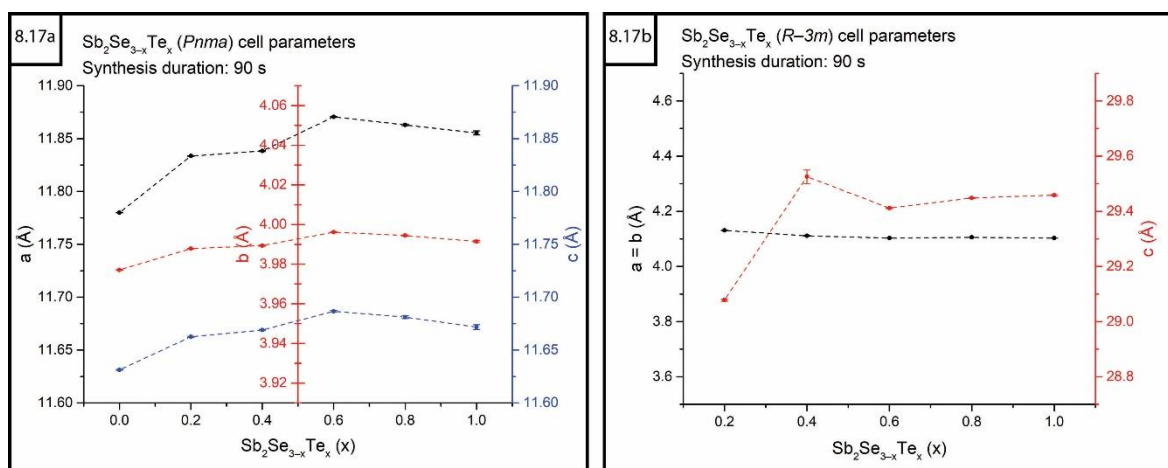


Figure 8.17: Plots of lattice parameters a , b and c for $\text{Sb}_2\text{Se}_{3-x}\text{Te}_x$ ($0 \leq x \leq 1$) samples synthesised using 100 W forward power with the aid of a graphite susceptor for 90 s a) $Pnma$ phase b) $R\bar{3}m$ phase

The refined crystallography data for the $Pnma$ and $R\bar{3}m$ $\text{Sb}_2\text{Se}_{3-x}\text{Te}_x$ phases of these samples are available in appendix section A–8.7.

8.6.3 $\text{Sb}_2\text{Se}_{3-x}\text{Te}_x$ multi phase transition between $0.4 \leq x \leq 0.8$

Three new $\text{Sb}_2\text{Se}_{3-x}\text{Te}_x$ samples were prepared for $x = 0.4, 0.6$ and 0.8 to confirm the transition from $Pnma$ to $R\bar{3}m$ as the preferred phase structure after heating for 120 s. The PXRD data were refined during the first Covid-19 quarantine period, and the calculated chalcogen site occupancy and relative phase fractions

were consistent with the results obtained from the samples heated for 90 s. The two phases were shown to approach equilibrium at a Te inclusion level of $x = 0.7$ as shown in figure 8.18.

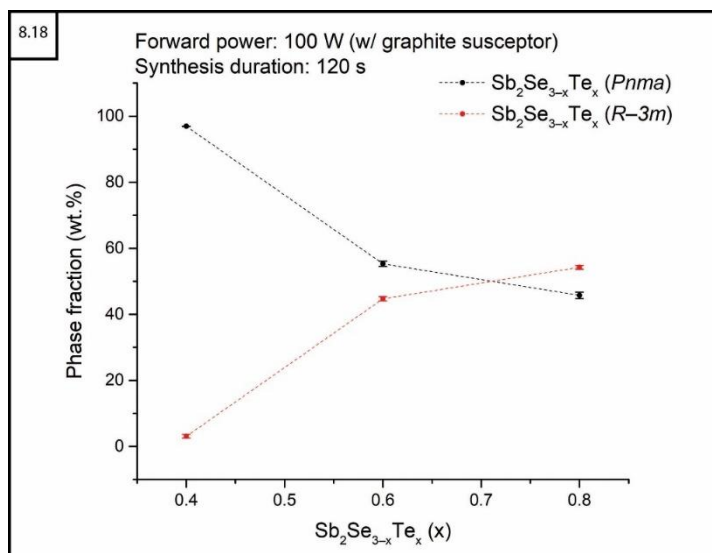


Figure 8.18: Plot of relative phase fractions against intended Te content for $\text{Sb}_2\text{Se}_{3-x}\text{Te}_x$ samples synthesised using 100 W forward power with the aid of a graphite susceptor for 120 s

The refined crystallography data for the $Pnma$ and $R\bar{3}m$ $\text{Sb}_2\text{Se}_{3-x}\text{Te}_x$ phases of these samples are available in appendix section A–8.8.

8.6.4 Scaling-up 5 g $\text{Sb}_2\text{Se}_{3-x}\text{Te}_x$ syntheses (between $0 \leq x \leq 1$)

Seven new samples of $\text{Sb}_2\text{Se}_{3-x}\text{Te}_x$ were prepared ($x = 0, 0.2, 0.4, 0.5, 0.6, 0.8, 1$) based on stoichiometric calculations to produce scaled up ~ 5 g samples as previously described and heated using 100 W forward power with the aid of a graphite susceptor for 90 s. An error occurred during the preparation of the $\text{Sb}_2\text{Se}_{2.8}\text{Te}_{0.2}$ and $\text{Sb}_2\text{Se}_{2.6}\text{Te}_{0.4}$ samples resulting in a slight Se deficiency and excess in the respective starting materials. This error is the likely cause of the trend deviation observed for site occupancy and phase distribution in figure 8.19.

Un-doped Sb_2Se_3 was successfully produced as a single phase $Pnma$ structure while all other $\text{Sb}_2\text{Se}_{3-x}\text{Te}_x$ experiments produced a mixed phase solid solution containing both $Pnma$ and $R\bar{3}m$ phases along with smaller quantities of unreacted starting material. The $\text{Sb}_2\text{Se}_{2.5}\text{Te}_{0.5}$ sample was the only one that contained orthorhombic ($Pccn$) Sb_2O_3 as an impurity. When comparing all of the calculated phase fractions (Figure 8.19), the trend of the $R\bar{3}m$ phase supplanting the $Pnma$ phase with increasing Te-doping was consistent with the previous 1 g samples. However, the crossover point is with a Te inclusion level of $x > 0.8$

which indicates that the phase preference is not explicitly dependent on the amount of Te in the starting mixture.

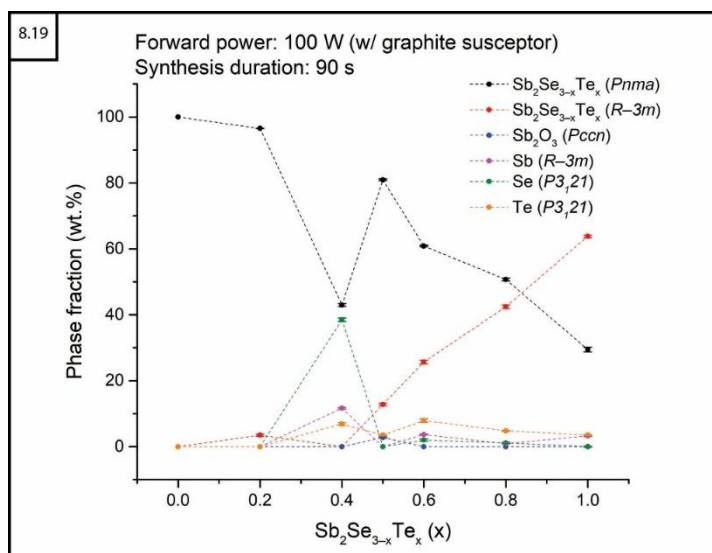


Figure 8.19: Plot of relative phase fractions against intended Te content for $Sb_2Se_{3-x}Te_x$ samples synthesised using 100 W forward power with the aid of a graphite susceptor for 90 s

At this point in the project the IR thermometer was set up to record temperature in conjunction with the DAQ module and these experiments were used to become familiar with the equipment and software. As with the $Bi_2Se_{3-x}Te_x$ reactions described in section 8.3.2, the heating profiles for each of these samples have two standard temperature progression peaks that appear to correspond with slight transition to a lower or higher MW absorption limit by a few Watts.

As can be seen in the selected examples in figure 8.20 the initial heating curve that corresponds to the ~ 80 W absorption is the graphite susceptor coupling alone, while the second is likely indicative of the formation of the product phases with differing $\tan\delta$. The actual necessary synthesis duration is likely much shorter and could therefore be more precisely controlled with careful monitoring of such data.

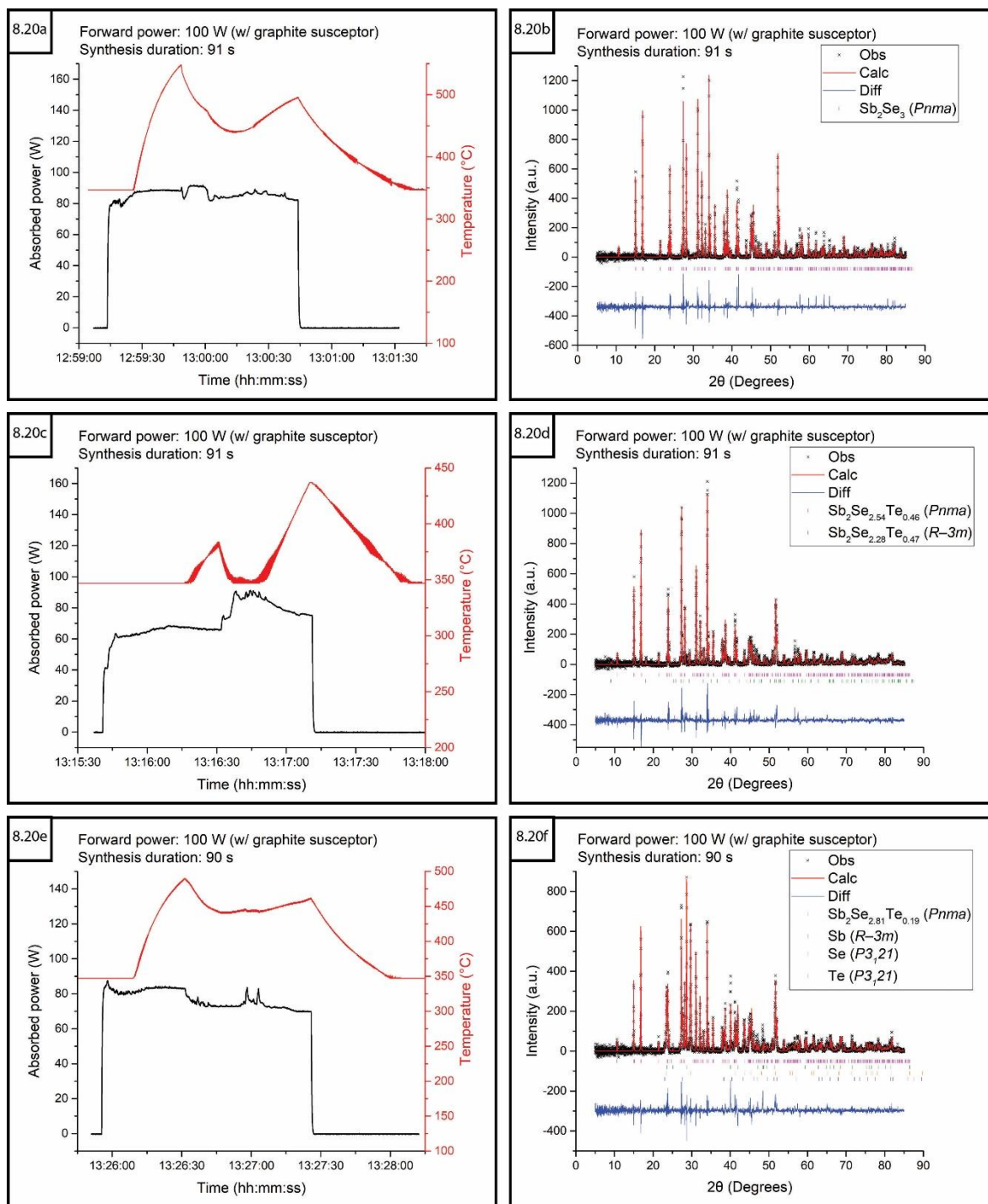


Figure 8.20: Plots of absorbed power and temperature profiles against time (a, c and e) and associated plots of refined PXRD data (b, d and f) of $Sb_2Se_{3-x}Te_x$ samples ($x = 0, 0.2$ and 0.4 respectively) synthesised using 100 W forward power (with a graphite susceptor) for ~ 90 s

As can be seen in figure 8.21, slight difficulty with achieving a satisfying convergence for samples with Te-doping of $x > 0.5$ required the *Pnma* peaks to be attributed to undoped Sb_2Se_3 and so the refined cell parameters show the same trend of lattice expansion to a limit as with the 1 g samples. The refined crystallography data for the *Pnma* and $R\bar{3}m$ $Sb_2Se_{3-x}Te_x$ phases of these samples are available in appendix section A–8.9.

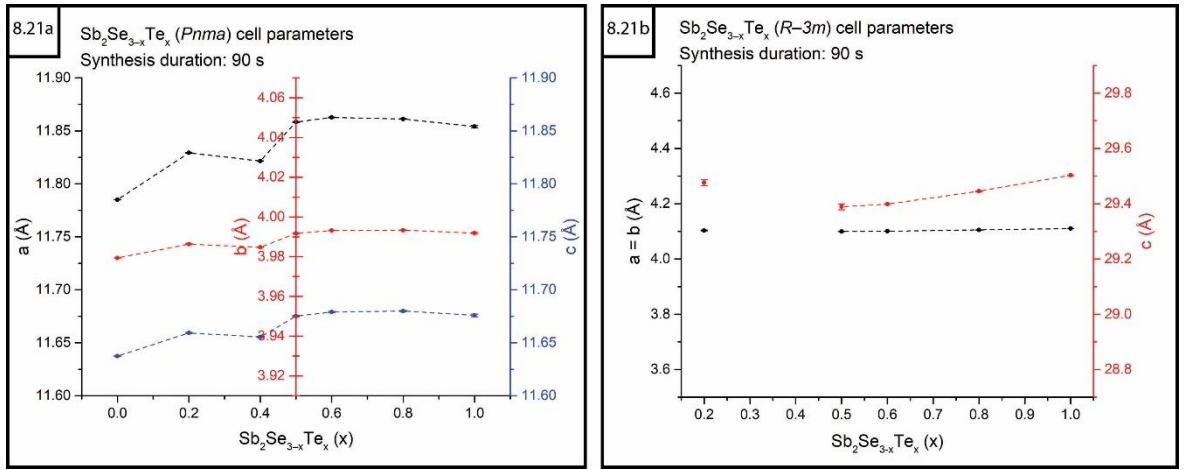


Figure 8.21: Plots of lattice parameters a , b and c for 5 g $\text{Sb}_2\text{Se}_{3-x}\text{Te}_x$ ($0 \leq x \leq 1$) samples synthesised using 100 W forward power with the aid of a graphite susceptor for 90 s a) $Pnma$ phase b) $R\bar{3}m$ phase

As a result of the cumulative benchtop experiments it was decided that the *in-situ* neutron experiments planned for the Polaris-SMC reactor would be carried out for $\text{Sb}_2\text{Se}_{3-x}\text{Te}_x$ samples prepared over a Te-doping range between $0 \leq x \leq 1$.

8.7 Microwave synthesis of copper chalcogenides

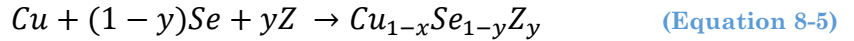
Investigations of copper chalcogenides are less frequent in the literature compared to the other systems studied in this project due to the challenging nature of the non-stoichiometric Cu_{1-x}Se and Cu_{2-x}Se structures. The relatively high abundance and low cost of the starting materials makes them very desirable as TEM candidates provided the product phases can be stably tuned and produced in reliable quantities. Synthesis through direct MW-heating appears to be previously unreported for these systems; so, with the success of producing high purity SnSe and $\text{Sb}_2\text{Se}_{3-x}\text{Te}_x$ solid solutions, this subproject is the first attempt at obtaining both undoped and a range of partially substituted copper chalcogenides with this method.

8.7.1 Stoichiometric calculations and experimental design

Reactant mixtures were weighed out and prepared using the procedure described in chapter 3 with the aim of producing ~ 1 g samples of Cu_{1-x}Se or Cu_{2-x}Se using the benchtop SMC reactor:



Four samples were prepared with either 0, 10, 15 or 20 % excess Se; all other experiments were prepared for intended partial substitution based on the following reaction scheme:



Z = Te or S

The $\text{Cu}_{1-x}\text{Se}_{1-y}\text{Te}_y$ samples were not sealed as ampoules as described in chapter 3 as the glassblowing equipment was removed from use pending safety upgrades to the setup. These samples were instead held under static vacuum of at least 1×10^{-6} mbar using the Young's tap alone. A portable propane/air glassblowing rig was made available from the school glassblower for use with the $\text{Cu}_{1-x}\text{Se}_{1-y}\text{S}_y$ experiments and were carefully sealed at a height of ~90 mm to maximise the number of experiments from a limited number of quartz tubes available due to Covid-19 supply disruptions. The limitation also afforded an opportunity to practice consistently sealing the ampoules at the shorter length, which would be required for later experiments loaded into in the Polaris-SMC reactor sample applicator.

8.8 Optimisation of $\text{Cu}_{1-x}\text{Se}_{1-y}\text{Z}_y$ synthesis parameters

Copper has a particularly high $\sigma = 6.481 \times 10^7 \text{ Sm}^{-1}$ at room temperature meaning that eddy currents induced by the \mathbf{H} field of MWs will cause dramatic heating through Ohmic loss. The copper chalcogenide samples were therefore expected to have short induction periods like the SnSe and $\text{SnSe}_{1-x}\text{Te}_x$ experiments described in chapter 7, and so were initially heated in the benchtop SMC reactor using 300 W of forward power.

8.8.1 Initial Cu_{1-x}Se synthesis experiments

As copper selenides are non-stoichiometric, the initial experiments were designed to vary the Se content to investigate if the main phase composition and phase fraction could be controlled. Four Cu_{1-x}Se samples were each heated for several minutes during which time limited MW absorption was observed. The sudden but brief spikes of MW absorption, seen in figures 8.22 and 8.23, were difficult to detect in real time and so the reaction period was determined afterwards upon inspection of the recorded power profiles.

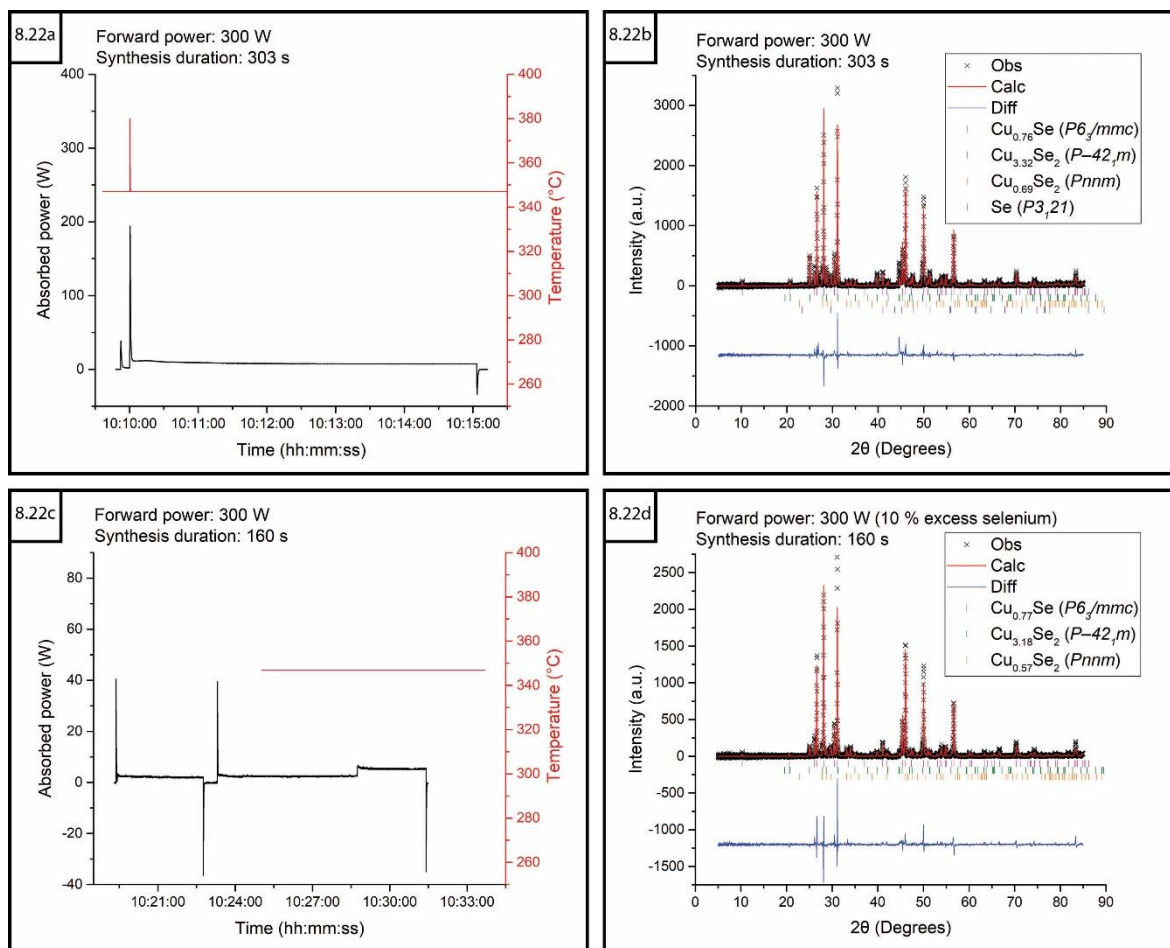


Figure 8.22: Plots of absorbed power and temperature profiles against time (a and c) and associated plots of refined PXRD data (b and d) of Cu_{1-x}Se samples (stoichiometric and 10 % excess Se respectively) synthesised using 300 W forward power for 303 s and 180 s

The low level of MW power absorption indicates a poor level of coupling with the reactants however, since each sample was found to react to completion this minimal amount of interaction still allowed the copper to heat up sufficiently to initiate thermal runaway.

The poor coupling prompted a zoomed in view of the y-axis scale which makes the negative power spikes present in almost all of the DAQ data appear more prominent. The negative power is brief and usually in the order of a few tens of Watts, occurring primarily when the magnetron was switched off but sometimes also at the end of the induction period. These events were attributed to fluctuations in the power meter circuitry associated with the rapid changes in power being administered in the waveguide which the DAQ was sensitive enough to detect.

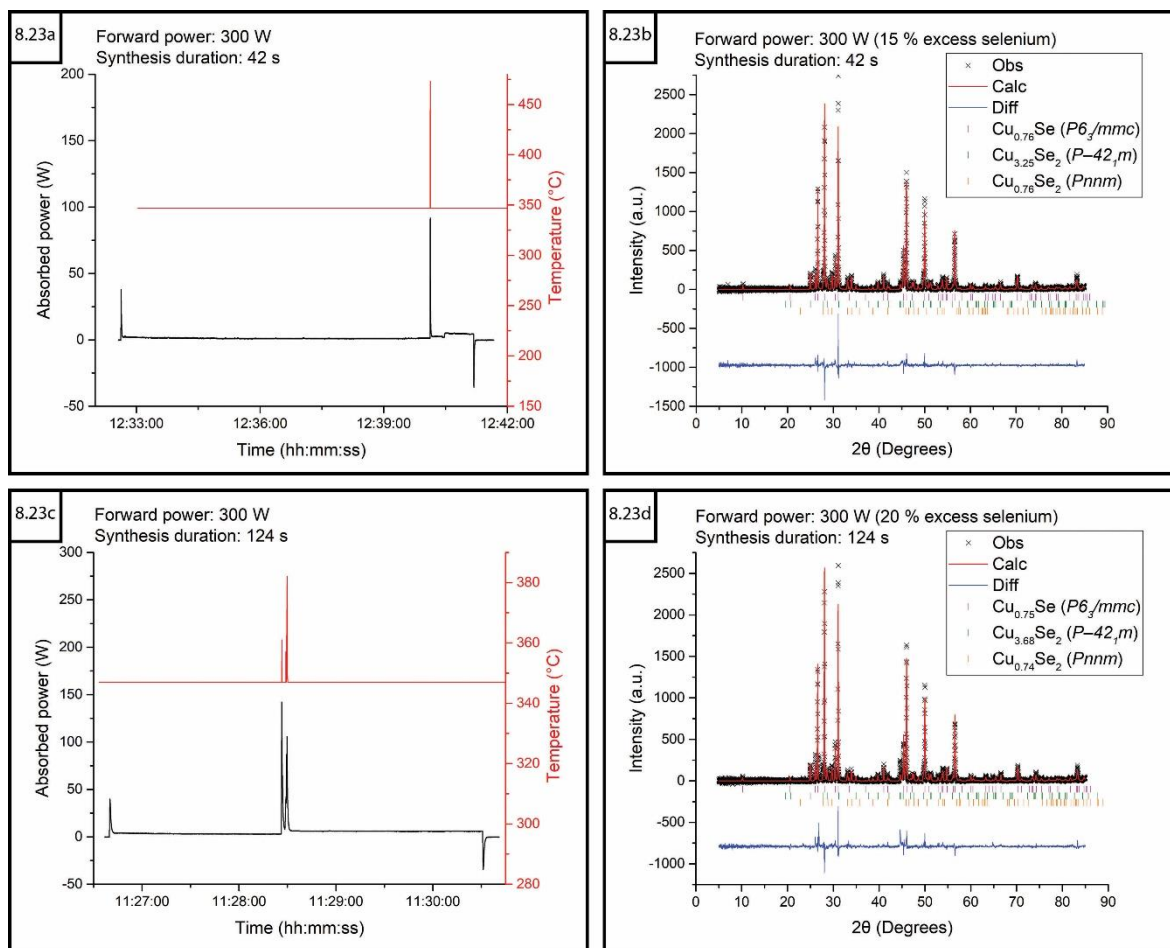


Figure 8.23: Plots of absorbed power and temperature profiles against time (a and c) and associated plots of refined PXRD data (b and d) of Cu_{1-x}Se samples (15 and 20 % excess Se respectively) synthesised using 300 W forward power for 42 s and 124 s

The IR thermometer recorded brief spikes in temperature which corresponded to flashes of light sustained for no more than a second or two in some experiments. These flashes were likely the result of electrical arcing induced in the highly conductive copper at the point of thermal runaway. When video recording the SnSe reactions, arcing was apparent before the brighter sustained blue glow of plasma was observed. It is possible that in the copper selenide experiments, the flashes were the result of microplasma formation that was unable to be sustained by an extremely fast reaction between Cu and Se; however, no video recordings were made to confirm this hypothesis.

When the PXRD data was refined, each Cu_{1-x}Se sample showed the presence of at least three distinct copper selenide phases (Figure 8.24) in the form of hexagonal ($P6_3/mmc$) Cu_{1-x}Se , tetragonal ($P\bar{4}2_1m$) $\text{Cu}_{2-x}\text{Se}_3$ and orthorhombic ($Pnmm$) $\text{Cu}_{1-x}\text{Se}_2$.

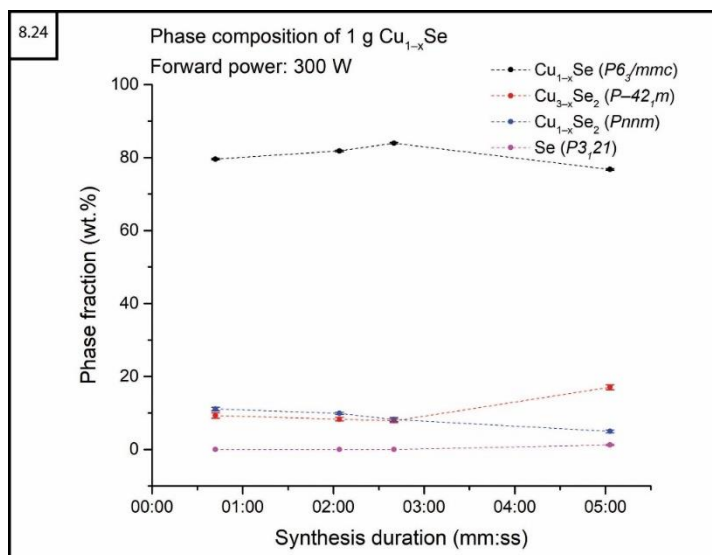


Figure 8.24: Plot of relative phase fractions against synthesis duration for initial 1 g Cu_{1-x}Se samples synthesised using 300 W forward power

The main phase in each sample was $P6_3/mmc$ Cu_{1-x}Se , with relative phase fractions remaining consistent regardless of synthesis duration or amount of excess Se. The refined crystallography data for the Cu_{1-x}Se phase of these samples are available in appendix section A–8.10.

8.8.2 Initial Cu_{2-x}Se synthesis experiments

With the information obtained from the previous experiments, the four Cu_{2-x}Se samples were heated at 300 W forward power and more closely monitored to attempt to control the synthesis duration as close to 60 s as possible. The reaction start point was assumed as beginning from the appearance of a bright flash in the sample applicator or a sudden drop in reflected power indicating a rapid absorption of approximately 100–200 W.

The first sample with no excess Se demonstrated a more volatile temperature and absorption profile than other experiments in this series (Figure 8.25). The resulting material was analysed using PXRD however proved extremely difficult to refine. The X'Pert Highscore refinement software suggested several possible matches for the peaks however the recommended .cif files were not found through a search of the Inorganic Crystal Structure Database (ICSD)[192].

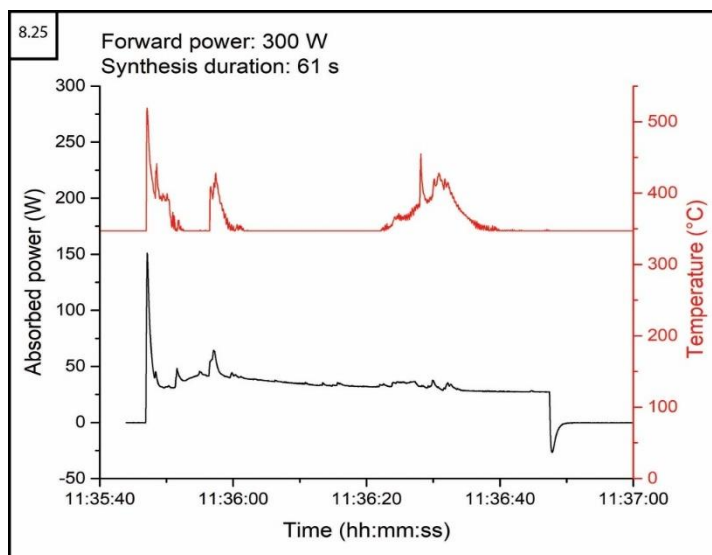


Figure 8.25: Plot of absorbed power and temperature profiles against time for the first Cu_{2-x}Se experiment, showing the volatile temperature and MW power absorption profile

Careful monitoring of the MW power during heating enabled much more control over the heating duration as shown in figure 8.26. The brief MW absorption indicates that the reaction progresses extremely rapidly once the critical temperature for thermal runaway has been reached, and that Cu_{2-x}Se does not couple well with MWs once formed.

The rapid reaction produces a temperature profile much different than the typical progression that would be expected; where at the point of thermal runaway, a maximum temperature between 440–550 °C is reached instantaneously before quickly returning below 347 °C. The accuracy of the temperatures recorded with the IR thermometer should be considered with scepticism in these experiments, as over the short reaction period it may be interpreting the arcing (brief flashes) as radiated heat in the IR spectrum.

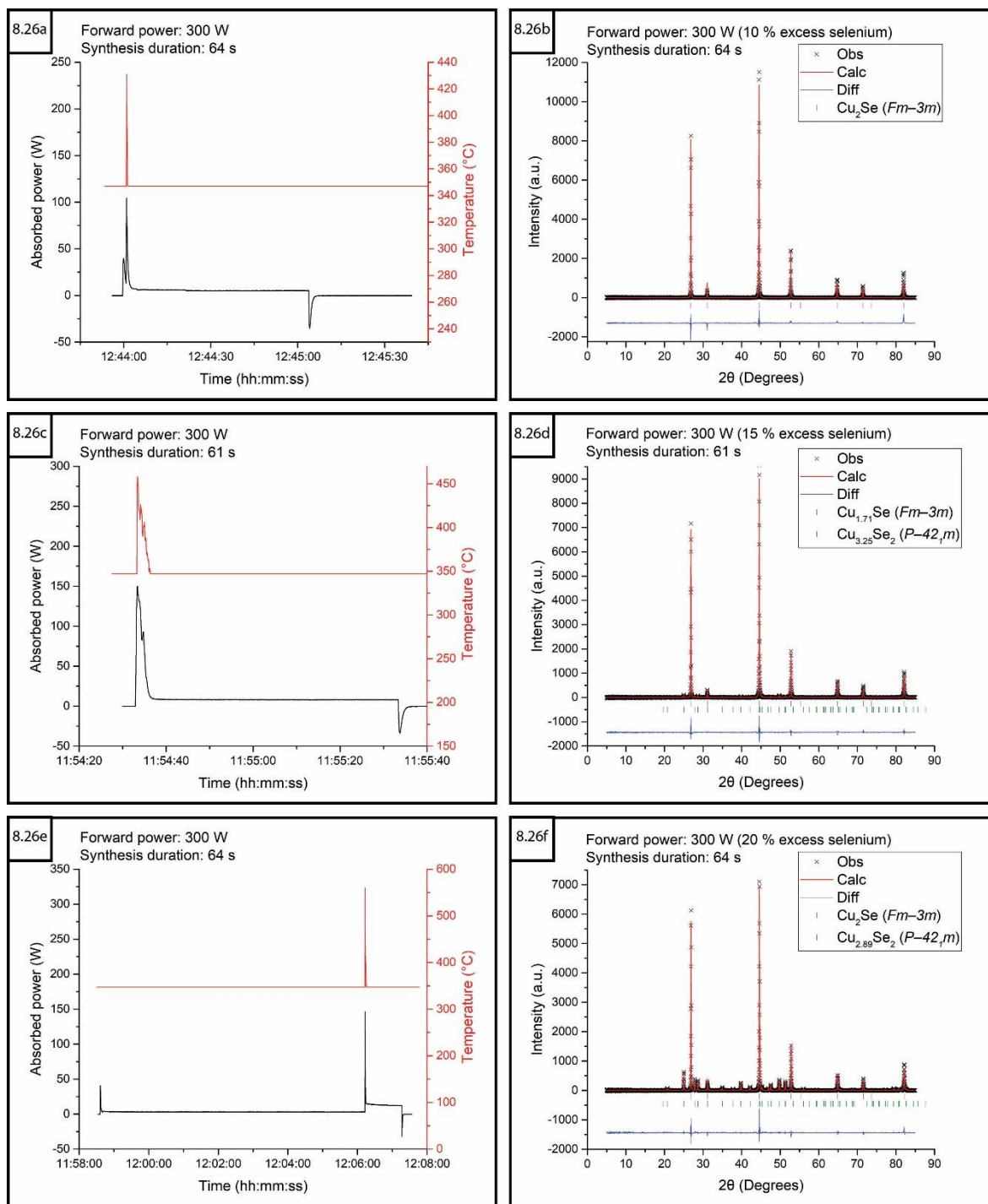


Figure 8.26: Plots of absorbed power and temperature profiles against time (a, c and e) and associated plots of refined PXRD data (b, d and f) of Cu_{2-x}Se samples (10, 15 and 20 % excess Se respectively) synthesised using 300 W forward power for 64 s, 61 s and 64 s

The other three samples with 10, 15 and 20 % excess Se produced cubic ($Fm\bar{3}m$) Cu_{2-x}Se at very high phase purity. Increasing the amount of excess Se in the reactant mixture encouraged the formation of tetragonal ($P\bar{4}2_1m$) $\text{Cu}_{3-x}\text{Se}_2$ as a secondary phase, reducing the $Fm\bar{3}m$ Cu_{2-x}Se phase from 100 wt.% to 84.5(1) wt.%, as shown in figure 8.27. Therefore, all further samples were prepared for the correct target stoichiometry, only adjusting MW power and heating duration.

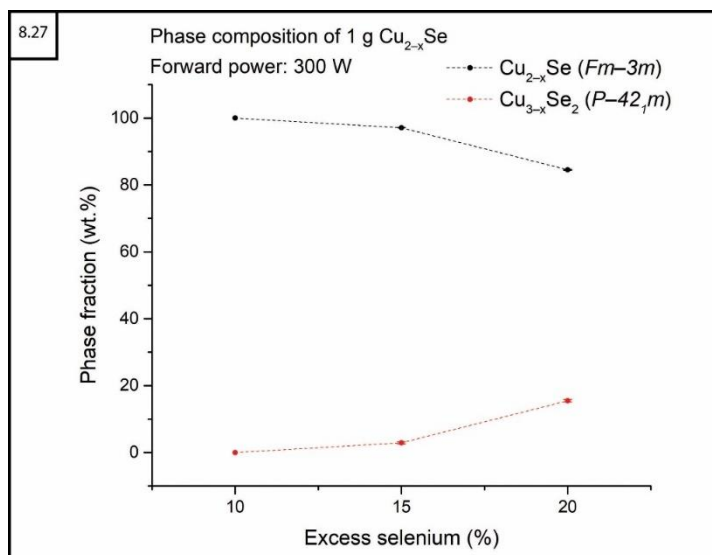


Figure 8.27: Plot of relative phase fractions against excess Se amount for initial 1 g Cu_{1-x}Se samples synthesised using 300 W forward power

The refined crystallography data for the Cu_{2-x}Se phase of these samples are available in appendix section A–8.11.

8.8.3 Copper chalcogenide solid solution ($\text{Cu}_{1-x}\text{Se}_{1-y}\text{Te}_y$) syntheses

Limitations on available ISIS beamtime along with restricted sample preparation time due to the Covid-19 pandemic meant only one copper chalcogenide system with which to attempt partial chalcogenide substitution was chosen. Refinements of initial sample data were ongoing and so a range of Te- and S-doped samples were prepared for the $\text{Cu}_{1-x}\text{Se}_{1-y}\text{Z}_y$ ($y = 0 \leq x \leq 1$) system. A set of six Te-doped samples were prepared to determine the necessary synthesis conditions to inform the preparation of larger samples for the Polaris-SMC reactor *in-situ* commissioning experiments discussed in chapter 9.

The samples were each heated in the benchtop SMC reactor using 500 W forward power for either 30, 60 or 90 s; and as shown in figure 8.28, the Te-doped samples had much more typical temperature curves and MW absorption profiles than the copper selenides. The sustained thermal runaway is the result of better coupling with the telluride phases and made identification of the synthesis duration much easier.

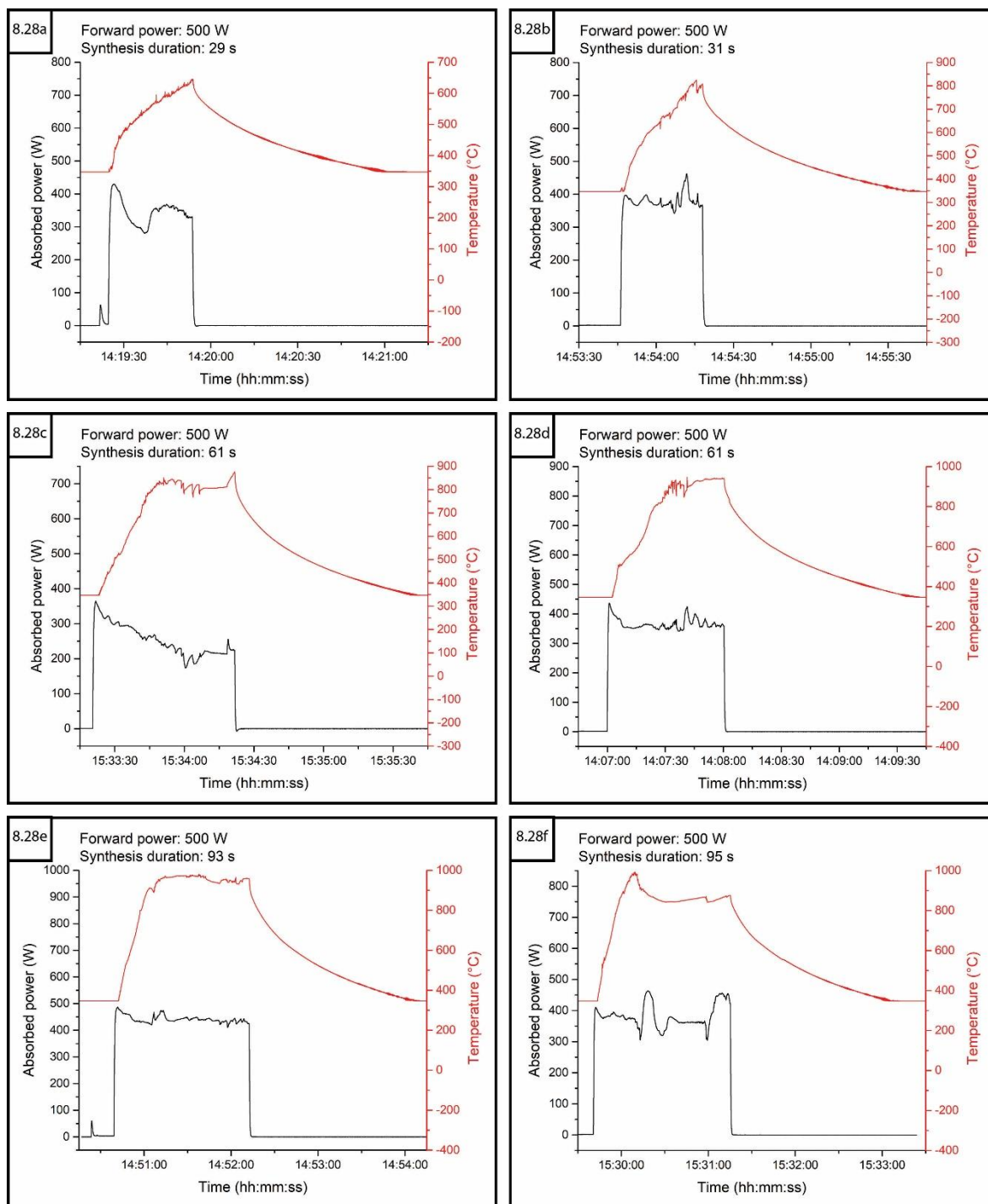


Figure 8.28: Plots of absorbed power and temperature profiles against time for $\text{Cu}_{1-x}\text{Se}_{1-y}\text{Te}_z$ samples synthesised using 500 W forward power for a duration of a) 29 s b) 31 s c) 61 s d) 61 s e) 93 s f) 95 s

The PXRD data were difficult to refine due to Bragg peaks that were unable to be attributed to any expected phase, particularly those with Te content $X > 0.4$. The diffraction data for the $\text{Cu}_{1-x}\text{Se}_{0.6}\text{Te}_{0.4}$ sample shown in figure 8.29b was one of the best fit however, a satisfactory site occupancy could not be made to converge.

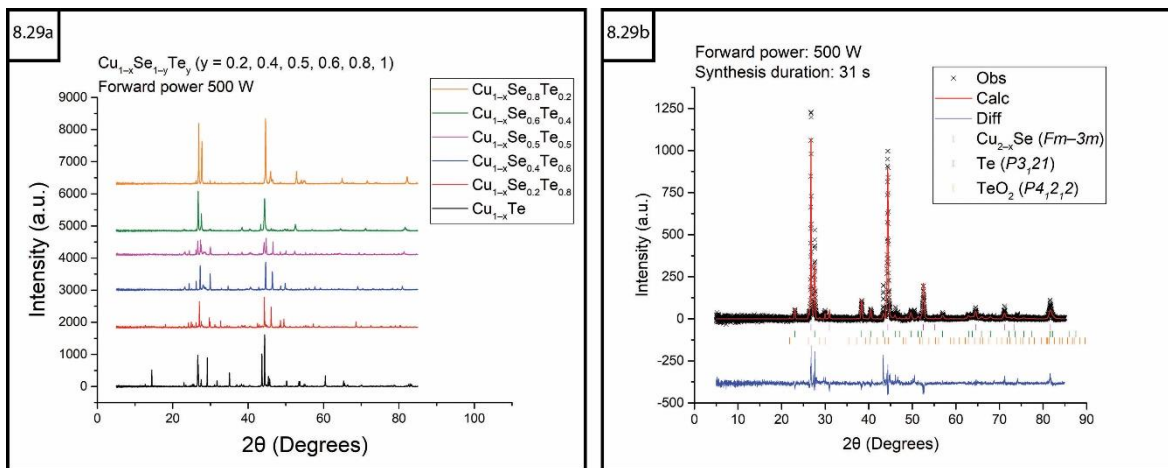


Figure 8.29: a) waterfall plot comparing observed PXRD data of $\text{Cu}_{1-x}\text{Se}_{1-y}\text{Te}_z$ experiments b) refined PXRD data of $\text{Cu}_{1-x}\text{Se}_{0.6}\text{Te}_{0.4}$ sample synthesised using 500 W forward power for 31 s

Comparing the observed powder patterns, the $Fm\bar{3}m$ Cu_{2-x}Se phase forms preferentially in samples with low amounts of Te-doping as shown in figure 8.30. With increasing Te content, tetragonal ($P4_12_12$) TeO_2 becomes prevalent as a secondary phase. The presence of the oxide may indicate that the Young's tap did not provide an effective enough seal against exposure to air.

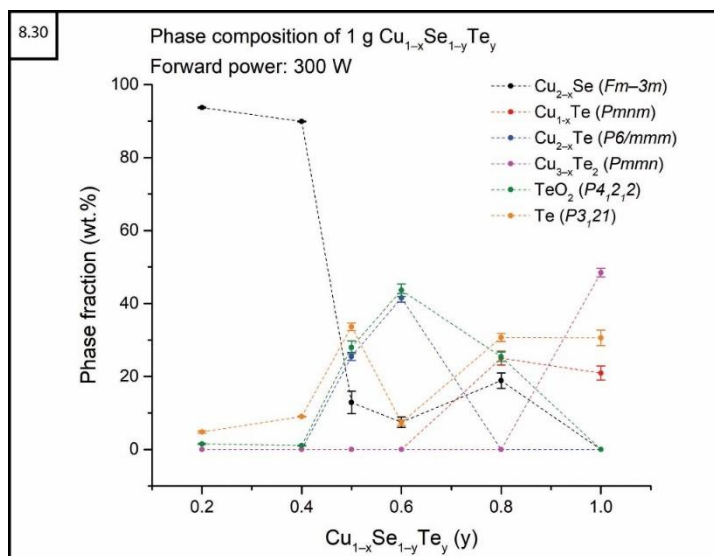


Figure 8.30: Plot of relative phase fractions against chalcogen site fractional occupancy for 1 g $\text{Cu}_{2-x}\text{Se}_{1-y}\text{Te}_z$ samples synthesised using 300 W forward power for durations of either 30 s, 60 s or 90 s

At the highest Te-doping levels, peaks attributed to three distinct copper telluride phases became more prominent; hexagonal ($P6/mmm$) Cu_{2-x}Te , orthorhombic ($Pmnm$) Cu_{1-x}Te and orthorhombic ($Pmnm$) $\text{Cu}_{3-x}\text{Te}_2$. The refined crystallography data for the main $\text{Cu}_{1-x}\text{Se}_{1-y}\text{Te}_z$ phases of these samples are available in appendix section A-8.12.

It was noted that due to larger grain size or poor packing ability of the reactant mixtures, less powder (~ 3 g target product mass) would be required to reach the

~40 mm sample depth necessary for full neutron beam exposure in the Polaris-SMC experiments discussed in chapter 9.

8.8.4 Rapid reaction of $\text{Cu}_{1-x}\text{Se}_{1-y}\text{S}_y$ at low pressure

While preparing the S-doped samples, the first two were observed to react spontaneously while evacuating the quartz tubes using the vacuum pump (Figure 8.31).

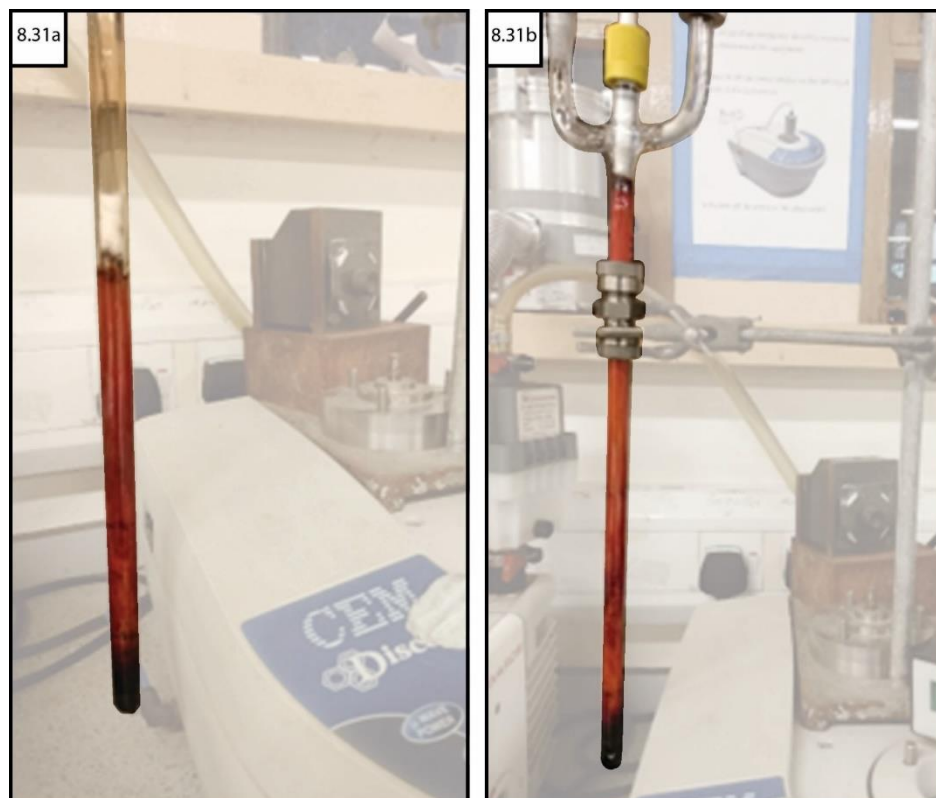


Figure 8.31: Starting material mixtures observed to spontaneously react while under vacuum with no additional heat source applied, depositing material along the interior walls of the quartz tube a) $\text{Cu}_{1-x}\text{Se}_{0.8}\text{S}_{0.2}$ b) $\text{Cu}_{1-x}\text{Se}_{0.6}\text{S}_{0.4}$

One of the samples was immediately retrieved for analysis using PXRD, and was indexed for a mixed phase system composed of $P6_3/mmc$ $\text{Cu}_{1.06}\text{Se}$ and $Fm\bar{3}m$ $\text{Cu}_{1.09}\text{S}$ as shown in figure 8.32.

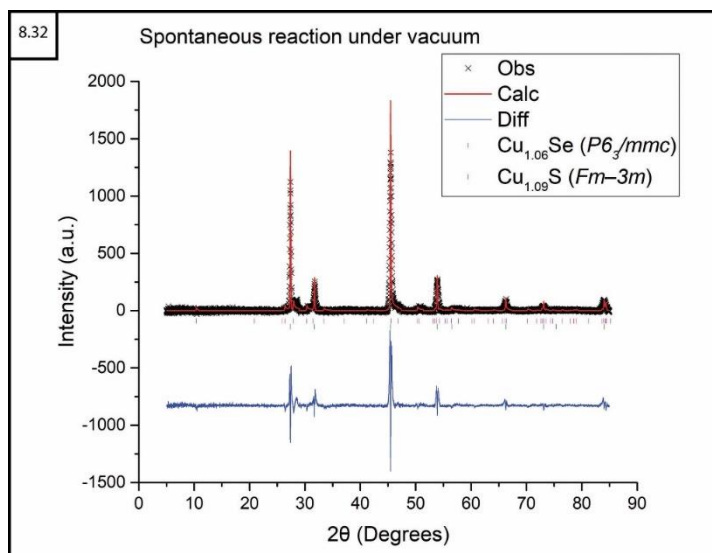


Figure 8.32: Plot of refined PXRD data of $\text{Cu}_{1-x}\text{Se}_{0.6}\text{S}_{0.4}$ sample that underwent a spontaneous reaction while under vacuum with no additional MW heating

The refined crystallography data for the main phases of this sample are available in appendix section A–8.13. Since the spontaneous ignition was consistent while under dynamic vacuum, the remaining experiments were first cold-pressed into 5 mm diameter pellets using a Specac pellet die.

8.8.5 Copper chalcogenide ($\text{Cu}_{1-x}\text{Se}_{1-y}\text{S}_y$) syntheses from pellets

A set of six new S-doped samples of $\text{Cu}_{1-x}\text{Se}_{1-y}\text{S}_y$ ($y = 0.2, 0.4, 0.5, 0.6, 0.8, 1$) were prepared as pellets in sealed ampoules to determine if direct MW-heating was a viable synthesis method, and subsequently the optimal reaction parameters if that were so.

The first two samples were heated in the benchtop SMC reactor using 500 W forward power for ~30 s. The $\text{Cu}_{1-x}\text{Se}_{0.8}\text{S}_{0.2}$ sample was able to be refined as a mixed phase system composed of cubic ($F\bar{4}3m$) $\text{Cu}_{2.06}\text{S}$ and hexagonal ($P6_3/mmc$) $\text{Cu}_{1.07}\text{Se}$. Significant peak broadening indicates significant defects in the structure as shown in figure 8.33b. The second sample proved difficult to satisfactorily refine although the same peak broadening was noted.

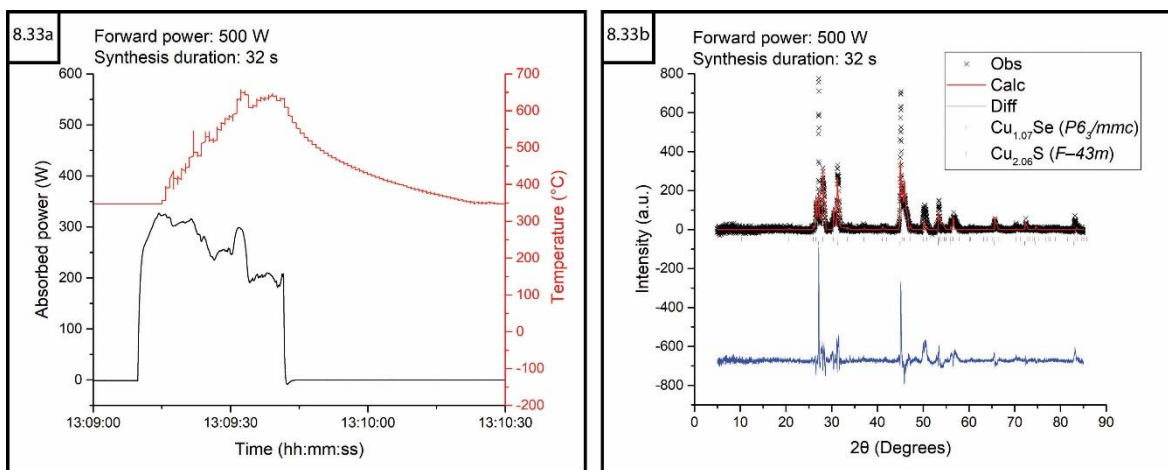


Figure 8.33: Plots of a) absorbed power and temperature against time b) refined PXRD data of $\text{Cu}_{1-x}\text{Se}_{0.8}\text{S}_{0.2}$ sample synthesised using 500 W forward power for a duration of 32 s

All other pellet samples fully reflected MWs without any indication of reaction progress and so were re-heated using 100 W forward power with the aid of a graphite susceptor for 120, 180, 240 or 300 s. Sulfur was deposited on the surface of the pellets and the interior of the quartz ampoules, with the samples heated longer showing a colour change from yellow to red of on the quartz as shown in figure 8.34.

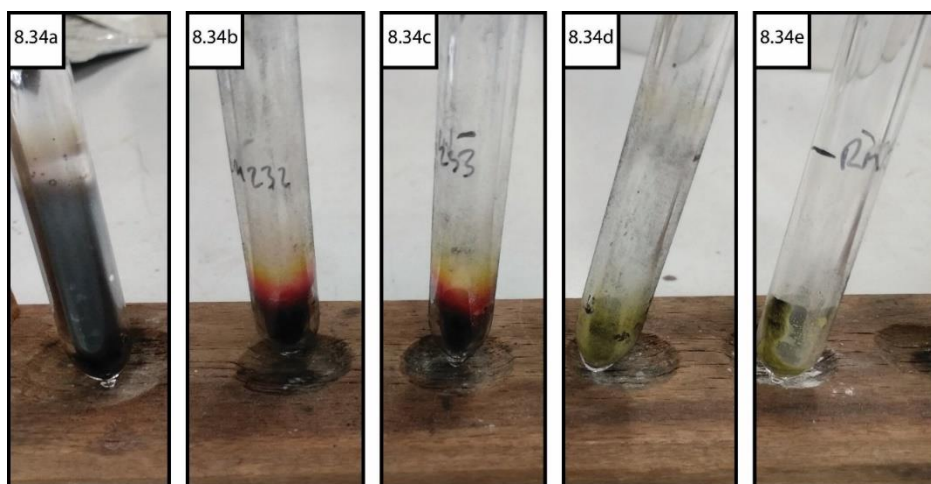


Figure 8.34: Comparison of $\text{Cu}_{1-x}\text{Se}_{1-y}\text{S}_y$ samples synthesised using 100 W forward power with the aid of a graphite susceptor to produce a) $\text{Cu}_{1-x}\text{Se}_{0.6}\text{S}_{0.4}$ b) $\text{Cu}_{1-x}\text{Se}_{0.5}\text{S}_{0.5}$ c) $\text{Cu}_{1-x}\text{Se}_{0.4}\text{S}_{0.6}$ d) $\text{Cu}_{1-x}\text{Se}_{0.8}\text{S}_{0.2}$ e) Cu_{1-x}S heated for 33 s, 301 s, 240 s, 180 s and 125 s respectively

No IR thermometer data was recorded since the temperature did not rise above the minimum detection level of 347 °C as shown in figure 8.35.

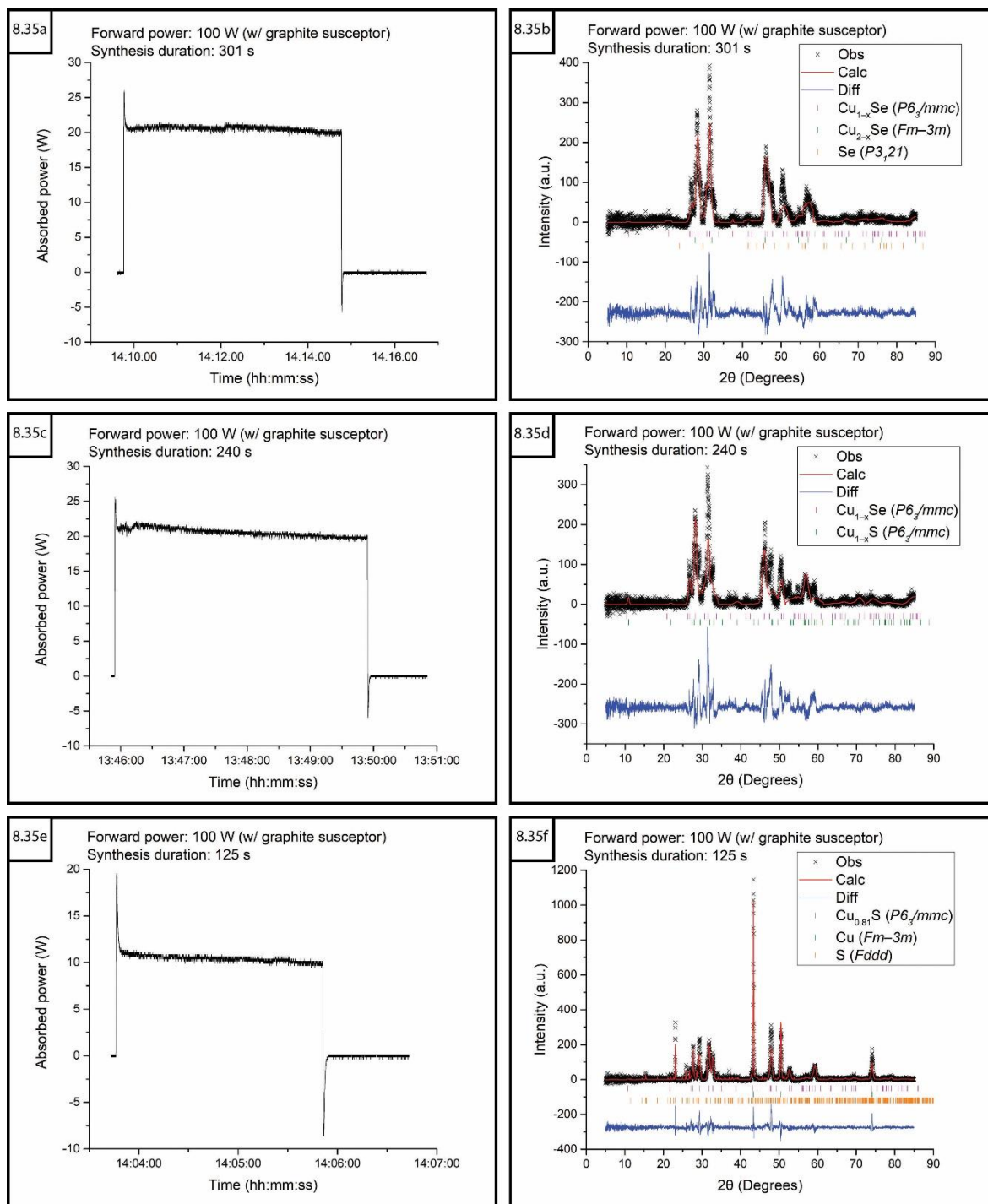


Figure 8.35: Plots of absorbed power and temperature profiles against time (a, c and e) and associated plots of refined PXRD data (b, d and f) of $\text{Cu}_{1-x}\text{Se}_{1-y}\text{S}_y$ samples synthesised using 100 W forward power with the aid of a graphite susceptor for a) 301 s b) 240 s c) 125 s

Refinement of the sample PXRD data continued to be difficult, in particular for the site occupancies of the various phases. The preferential structure in each case however was attributed to $P6_3/mmc$ Cu_{1-x}Z ($Z = \text{Se}$ or S), with the sulfide phase supplanting the selenide phase at S-doping of $y > 0.6$ as shown in figure 8.36.

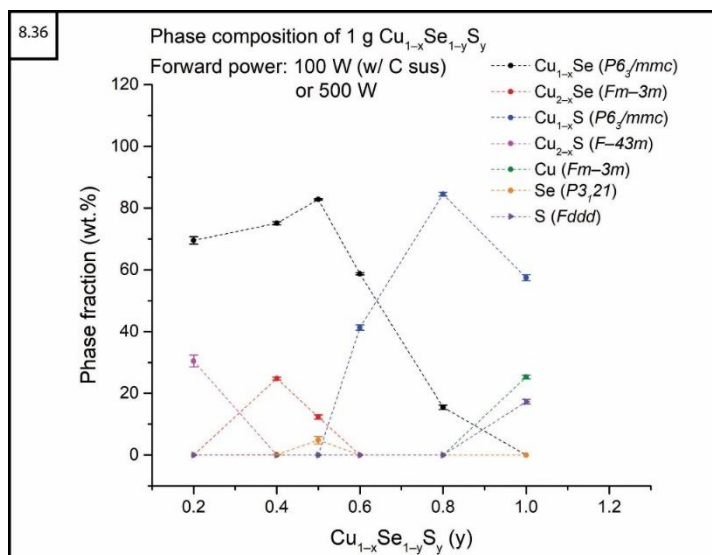


Figure 8.36: Plot of relative phase fractions against chalcogen site fractional occupancy for 1 g $\text{Cu}_{1-x}\text{Se}_{1-y}\text{S}_y$ samples

Additional Bragg peaks were attributed to several possible phases over the series however, no consistent trend in species formation could be identified. The refined crystallography data for the main $\text{Cu}_{1-x}\text{Se}_{1-y}\text{S}_y$ phases of these samples are available in appendix section A-8.5.

It was noted that the average height of the 5 mm $\text{Cu}_{1-x}\text{Se}_{1-y}\text{S}_y$ pellets would require three pellets to be stacked to reach the ~40 mm sample depth necessary for full neutron beam exposure in the Polaris-SMC experiments discussed in chapter 9.

8.9 Summary

Bismuth chalcogenides have been produced using the direct MW-heating method previously and it was thought that a closer analysis of the MW interactions and synthesis process could allow for better control when tuning the structure. Despite the limitations of the experimental design which led to the samples being contaminated with various bismuth oxides, optimal synthesis times were discerned. Undoped Bi_2Se_3 was shown to degrade with heating times >90 s while undoped Bi_2Te_3 showed little change in phase fraction distribution regardless of heating duration after 60 s. The partially substituted $\text{Bi}_2\text{Se}_{3-x}\text{Te}_x$ samples were all successfully synthesised (with oxide impurities) when heated using 100 W forward power with the aid of a graphite susceptor. If the impurity formation in these samples can be eliminated, it should be possible to have very precise control over chalcogen doping in the structure using the direct MW-heating method. Disruption due to the Covid-19 pandemic hindered the process of finding viable solutions to this problem.

Antimony chalcogenides have been investigated in the past as strong TEM candidates almost as much as the bismuth chalcogenides. Previously reported direct MW-heating processes used to synthesise undoped Sb_2Se_3 and Sb_2Te_3 showed promise for a tuneable method of producing a range of partially substituted $\text{Sb}_2\text{Se}_{3-x}\text{Te}_x$ samples. As chalcogens are substituted, the crystal lattice becomes distorted and so the extent to which $Pnma$ and $R\bar{3}m$ phases can be strained was investigated. It was found that the $\text{Sb}_2\text{Se}_{3-x}\text{Te}_x$ produces a consistent mixed phase solid solution that transitions from $Pnma$ to $R\bar{3}m$ structures with a greater Te:Se ratio in the chalcogen sites. The refined cell parameter data showed that the $Pnma$ phase has a greater capacity for structural distortion than the $R\bar{3}m$ phase with increasing Te-doping of the chalcogen site up to a limit of $x = 0.6$; which prevents further reduction of the associated electron-phonon scattering to improve charge carrier mobility. Any future attempts to improve the TE performance of the $\text{Sb}_2\text{Se}_{3-x}\text{Te}_x$ system through doping of the chalcogen site should be focussed on tuning the $Pnma$ phase.

Copper chalcogenides are temperamental and difficult systems to work with due to the non-stoichiometric nature of the Cu atoms in the structures. No previous direct MW-heating methods have been reported for synthesising these systems and so this subproject confirms that both Cu_{1-x}Se and Cu_{2-x}Se can be successfully produced in this way. The Cu_{2-x}Se samples were shown to be more stable as a single phase product while Cu_{1-x}Se tended to form as a mixed phase of polymorphs. Full characterisation of the site occupancies and cell parameters was hindered by the non-stoichiometric nature of the copper chalcogenides and disruption due to the Covid-19 pandemic limited the number of experiments able to be carried out to achieve more phase pure samples. It was possible to identify the synthesis parameters necessary to initiate the full series of reactions for $\text{Cu}_{1-x}\text{Se}_{1-y}\text{Te}_y$ and $\text{Cu}_{1-x}\text{Se}_{1-y}\text{S}_y$ systems, in particular the latter series was found to be particularly volatile during preparation. The S-doped $\text{Cu}_{1-x}\text{Se}_{1-y}\text{S}_y$ samples necessitated the reactants being cold-pressed into pellet form prior to sealing in the quartz ampoules for heating.

9 Polaris-SMC in-situ neutron experiments

9.1 Explaining the thesis in iambic pentameter



9.2 Introduction

The outcomes of the subprojects to investigate the viability of direct MW-heating of various binary chalcogenide TEMs (Chapters 7 and 8), were utilised to create a list of experiments with known optimal synthesis parameters that could be reliably replicated as a means of commissioning the Polaris-SMC *in-situ* microwave reactor. All preparations for the commissioning experiments were carried out in the continually changing environment of the Covid-19 pandemic (discussed in appendix section A–9.1).

In this chapter, the impedance measurements of the various chemical systems will be briefly discussed along with notable performance differences between the benchtop and *in-situ* reactors. The bulk of the discussion however, will be around the collected *in-situ* neutron data through a set of representative samples from each TEM system that was studied. Correlations between MW events and reaction pathways are highlighted using colourmap plots of the event mode TOF data, with additional context regarding reaction progression provided where necessary from comparisons against refined histogram data. Therefore, the aim is to comprehensively demonstrate the depth and scope of information that can be obtained from this analysis technique, as well as any limitations that present themselves. Colourmap plots for all event mode data were generated however, due to time constraints with the project compared to the wealth of data obtained from the experiments, only a representative selection of samples from each of the chemical systems were investigated in detail. The remaining colourmap plots not discussed in this chapter can be found at the end of the appendix, sections A–9.12 to A–9.20.

9.3 Impedance measurements of reactant mixtures

As described in section 4.4.3, a PocketVNA vector network analyser was connected via bespoke waveguide adaptors to the spare sample applicator section of waveguide as shown in figure 9.1. All of the Polaris-SMC reactor experiment samples were analysed prior to being sent to ISIS to investigate any correlation between load impedance (Z_L) and MW absorption. As with the measurements of the empty waveguide and quartz tubes, the PocketVNA was calibrated for coaxial rather than waveguide impedance. This means that all measured impedances should be considered only with respect to the characteristic impedance (Z_0) of the system which was measured as 66 Ω . The

data are plotted on Smith charts with the generator impedance (Z_G) of the VNA, a standard of 50Ω , normalised to 1 in the centre of the plot.

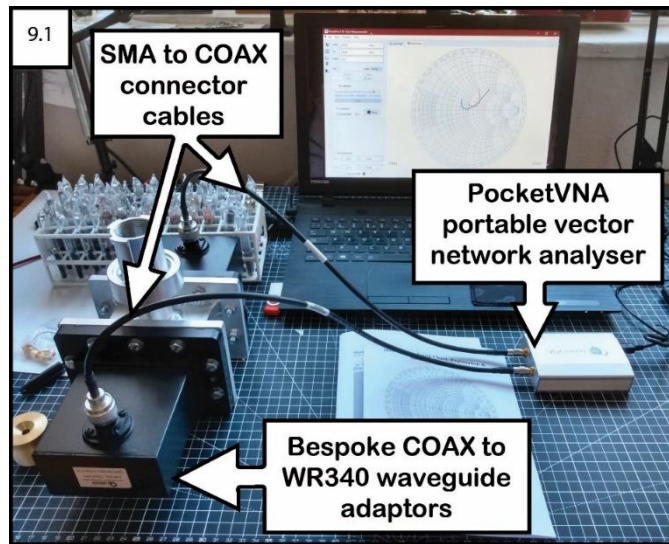


Figure 9.1: Spare sample applicator section of waveguide connected at each end via BNC-SMA waveguide adaptors to the Pocket VNA device

The impedance measurements were made on the ~ 90 mm sealed quartz ampoules containing the powder or pellet starting material preparations. Each data set was performed over the output frequency (f) range of the magnetron (2450 ± 30 Hz) and accumulated for ten repetitions to obtain average values.

9.3.1 $\text{SnSe}_{1-x}\text{Te}_x$ impedance measurements

From previous subproject experiments, all Sn-Se-Te preparations were known to absorb MWs reasonably well and so very little variation was expected in the Z_L for each sample. As shown in figure 9.2, the impedance curves for each Sn-Se-Te mixture did in fact tend towards a path close to the intrinsic load of the system implying very little power reflection from the sample as expected.

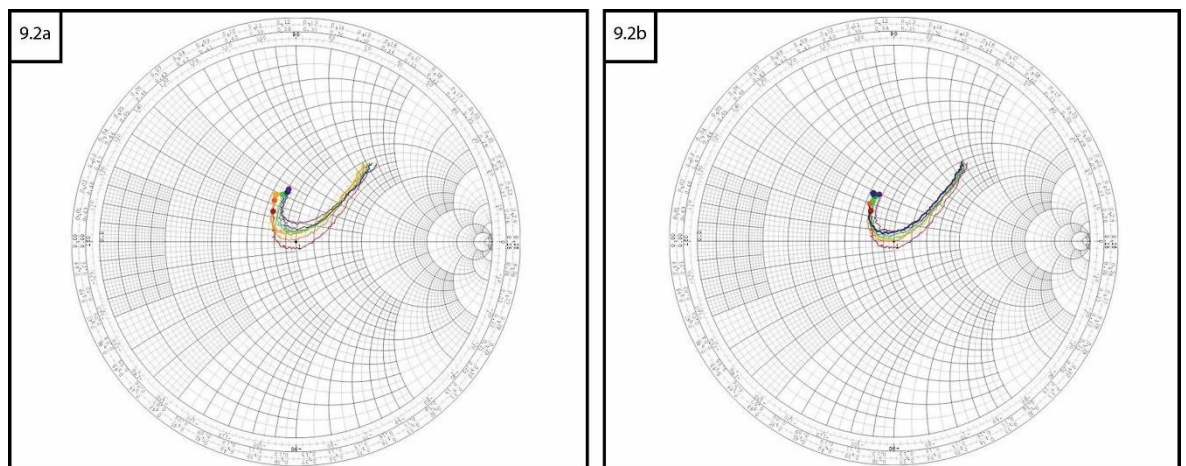


Figure 9.2: Smith chart of complex curves of S_{11} parameter for $\text{SnSe}_{1-x}\text{Te}_x$ ($x = 0, 0.2, 0.4, 0.5, 0.6, 0.8, 1$) a) stoichiometric starting materials b) 10 % excess Sn

The Z_L of most samples at $f = 2.45$ GHz are consistent with each other, $\sim 10 \Omega$ greater than Z_G ; with Z_L only slightly less than Z_0 indicating very little

reflection. The Z_L for samples with 10 % excess Sn was slightly closer to Z_0 than the stoichiometric mixtures. For the stoichiometric SnTe sample $Z_L \ll Z_0$ with a value of 13.234 Ω as shown in table 9.1; indicating that most of the MWs will be transmitted without dissociating the power as heat. This behaviour was observed when using the benchtop SMC reactor, with SnTe syntheses occasionally having longer induction periods than others in the tin chalcogenide series. The Z_L of the SnTe sample with 10 % excess Sn was much closer to the other Sn-Se-Te samples in the set, implying that the excess Sn in the mixture leads to better coupling with the MWs.

Table 9.1: Impedance measurements of $\text{SnSe}_{1-x}\text{Te}_x$ prepared with stoichiometric starting materials and 10 % excess Sn

Sample	Impedance (Ω)	
	S_{11}	S_{22}
SnSe _{0.8} Te _{0.2}	59.722	20.646
SnSe _{0.6} Te _{0.4}	57.578	76.530
SnSe _{0.5} Te _{0.5}	60.405	74.158
SnSe _{0.4} Te _{0.6}	60.238	74.439
SnSe _{0.2} Te _{0.8}	60.553	74.396
SnTe	13.234	15.291
SnSe (+ 10 % Sn)	64.451	68.158
SnSe _{0.8} Te _{0.2} (+ 10 % Sn)	59.496	72.611
SnSe _{0.6} Te _{0.4} (+ 10 % Sn)	60.953	72.284
SnSe _{0.5} Te _{0.5} (+ 10 % Sn)	60.136	72.090
SnSe _{0.4} Te _{0.6} (+ 10 % Sn)	59.415	73.018
SnSe _{0.2} Te _{0.8} (+ 10 % Sn)	57.906	75.559
SnTe (+ 10 % Sn)	60.335	72.934

9.3.2 $\text{SnSe}_{1-x}\text{S}_x$ impedance measurements

As with the $\text{SnSe}_{1-x}\text{Te}_x$ series, the $\text{SnSe}_{1-x}\text{S}_x$ samples synthesised in the subproject were known to absorb MWs well and so very little variation was expected in the Z_L of each sample. As shown in figure 9.3, the impedance curves for each Sn-Se-S mixture showed similar values as the Te-doped samples; with all the impedance curves tracing a consistent path close to the intrinsic load.

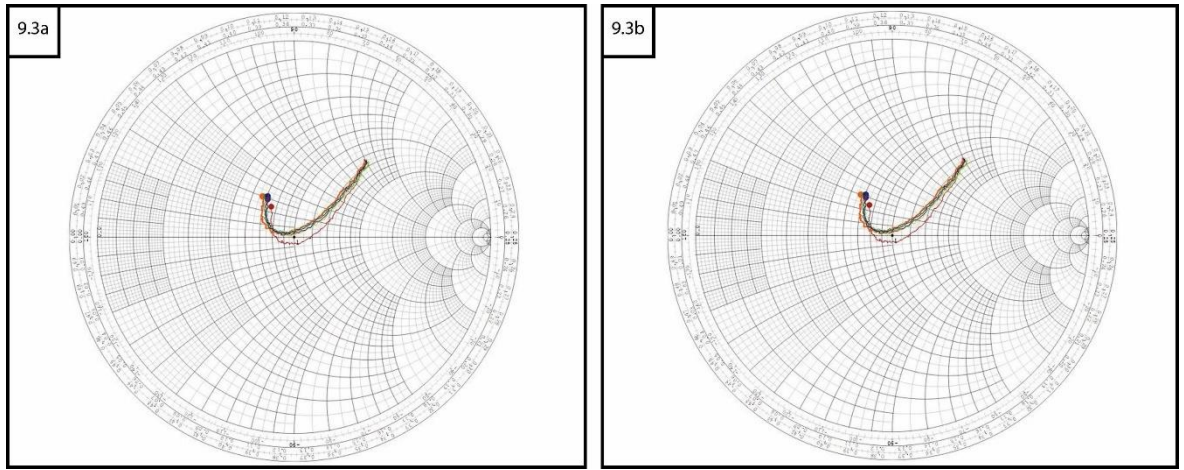


Figure 9.3: Smith chart of complex curves of S_{11} parameter for $\text{SnSe}_{1-x}\text{S}_x$ ($x = 0, 0.2, 0.4, 0.5, 0.6, 0.8, 1$) a) stoichiometric starting materials b) 10 % excess Sn

The Z_L of all samples at $f = 2.45$ GHz were consistent with each other, $\sim 10 \Omega$ greater than Z_G ; with Z_L only slightly less than Z_0 indicating very little reflection as shown in table 9.2.

Table 9.2: Impedance measurements at a frequency of 2.45 GHz for $\text{SnSe}_{1-x}\text{S}_x$ samples prepared with stoichiometric starting materials and 10 % excess Sn

Sample	Impedance (Ω)	
	S_{11}	S_{22}
$\text{SnSe}_{0.8}\text{S}_{0.2}$	60.808	70.181
$\text{SnSe}_{0.6}\text{S}_{0.4}$	57.324	72.849
$\text{SnSe}_{0.5}\text{S}_{0.5}$	57.817	73.067
$\text{SnSe}_{0.4}\text{S}_{0.6}$	60.633	69.571
$\text{SnSe}_{0.2}\text{S}_{0.8}$	57.446	72.906
SnS	60.044	71.474
$\text{SnSe}_{0.8}\text{S}_{0.2}$ (+ 10 % Sn)	57.255	72.550
$\text{SnSe}_{0.6}\text{S}_{0.4}$ (+ 10 % Sn)	60.540	69.109
$\text{SnSe}_{0.5}\text{S}_{0.5}$ (+ 10 % Sn)	61.120	70.125
$\text{SnSe}_{0.4}\text{S}_{0.6}$ (+ 10 % Sn)	58.218	72.846
$\text{SnSe}_{0.2}\text{S}_{0.8}$ (+ 10 % Sn)	58.681	71.328
SnS (+ 10 % Sn)	60.104	70.790

The powdered Sn used for these samples is the likely reason for the consistent trend close to the intrinsic load of the system. The loss tangent, i.e., the ability of a material to absorb MWs, is directly proportional to its Ohmic conductivity (σ) as given by equation 2.79 in section 2.4.4. Metals tend to be exceptional electric and thermal conductors when in bulk form and susceptible to the formation of eddy currents by H fields when finely ground; an important contributing factor to the favourable impedance of the sample as a whole.

9.3.3 $\text{Bi}_2\text{Se}_{3-x}\text{Te}_x$ impedance measurements

Previous subproject experiments indicated that Z_L for all Bi-Se-Te samples would tend away from the intrinsic load at the centre of the Smith chart.

However, the impedance curves for each Bi-Se-Te mixture showed a tendency towards the intrinsic load across the applied frequency (Figure 9.4).

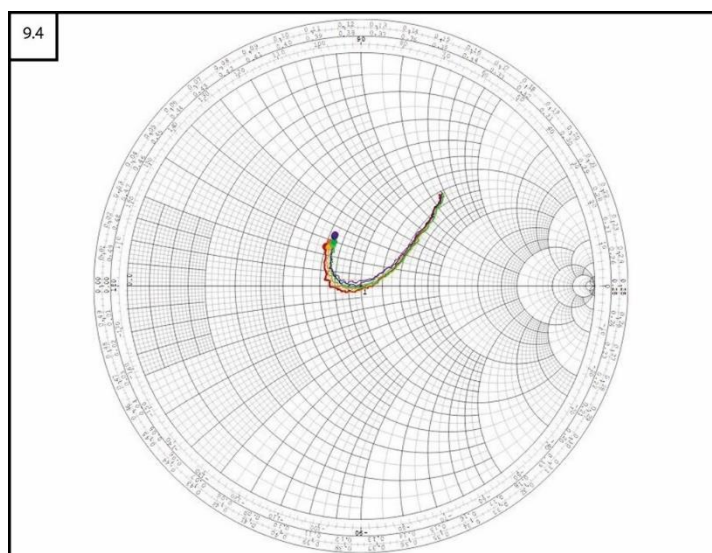


Figure 9.4: Smith chart of complex curves of S_{11} parameter for $\text{Bi}_2\text{Se}_{3-x}\text{Te}_x$ ($x = 0, 0.5, 1, 1.5, 2, 2.5, 3$) starting materials

The Z_L of all samples at $f = 2.45$ GHz were measured to be consistent with the tin-chalcogen mixtures at $\sim 10 \Omega$ greater than Z_G ; with Z_L only slightly less than Z_0 as shown in table 9.3:

Table 9.3: Impedance measurements at a frequency of 2.45 GHz for $\text{Bi}_2\text{Se}_{3-x}\text{Te}_x$ samples

Sample	Impedance (Ω)	
	S_{11}	S_{22}
Bi_2Se_3	58.899	71.856
$\text{Bi}_2\text{Se}_{2.5}\text{Te}_{0.5}$	59.534	72.515
$\text{Bi}_2\text{Se}_2\text{Te}$	60.126	71.531
$\text{Bi}_2\text{Se}_{1.5}\text{Te}_{1.5}$	61.585	70.752
Bi_2SeTe_2	60.935	71.734
$\text{Bi}_2\text{Se}_{0.5}\text{Te}_{2.5}$	58.714	73.064
Bi_2Te_3	59.252	73.966

These data indicated that despite the previous subproject experiments, bismuth-chalcogen mixtures should be expected to absorb MWs just as well as tin-chalcogen mixtures. The favourable impedance is supported by the high $\sigma = 9.346 \times 10^5 \text{ Sm}^{-1}$ for Bi, which is only one order of magnitude lower than Sn at $\sigma = 8.696 \times 10^6 \text{ Sm}^{-1}$ [12]. The slightly lower σ may have led to the longer induction period of the Bi reaction pathway observed during the subproject (>10 mins), meaning that by increasing the sample volume from ~ 1 g to ~ 5 g and increasing the forward power of the MW reactor should reduce the induction period without the need for a graphite susceptor.

9.3.4 $Sb_2Se_{3-x}Te_x$ impedance measurements

The Sb-Se-Te samples were also expected to tend away from the intrinsic load of the Smith chart based on the need for a graphite susceptor in the subproject experiments like the bismuth chalcogenides. However, like the Bi-Se-Te samples, the impedance curves for each starting material mixture (Figure 9.5) indicate that all the samples in the series should be just as susceptible to MWs as the other systems measured so far.

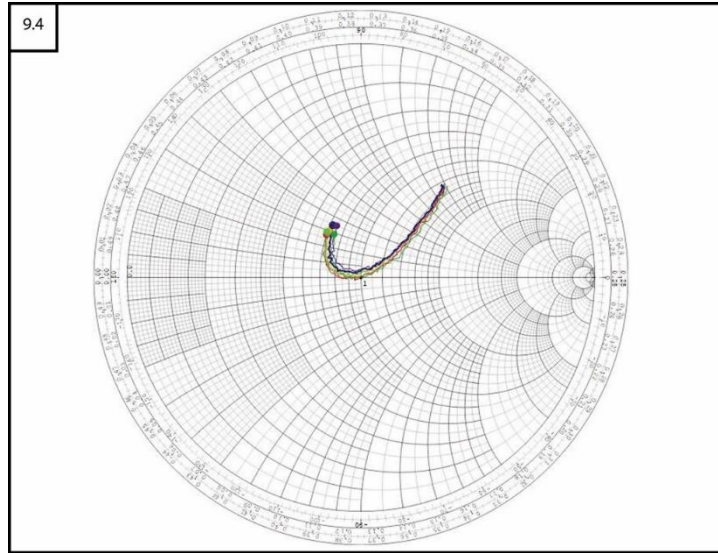


Figure 9.5: Smith chart of complex curves of S_{11} parameter for $Sb_2Se_{3-x}Te_x$ ($x = 0, 0.2, 0.4, 0.5, 0.6, 0.8, 1$) starting materials

The Z_L of all samples at $f = 2.45$ GHz seemed to add weight to this hypothesis, with Z_L only slightly less than Z_0 as shown in table 9.4:

Table 9.4: Impedance measurements at a frequency of 2.45 GHz for $Sb_2Se_{3-x}Te_x$ samples

Sample	Impedance (Ω)	
	S_{11}	S_{22}
Sb_2Se_3	59.075	71.666
$Sb_2Se_{2.4}Te_{0.2}$	59.315	72.489
$Sb_2Se_{2.6}Te_{0.4}$	58.696	73.709
$Sb_2Se_{2.5}Te_{0.5}$	57.894	73.168
$Sb_2Se_{2.4}Te_{0.6}$	61.934	69.959
$Sb_2Se_{2.2}Te_{0.8}$	58.347	73.747
Sb_2Se_2Te	59.050	73.200

During the subproject, the ~ 5 g samples were all synthesised using a graphite susceptor because the earlier experiments with ~ 1 g samples indicated this would be a requirement. The greater sample volume of ~ 5 g samples should in fact allow for reasonable MW absorption and a reduced induction period.

9.3.5 $Cu_{1-x}Se_{1-y}Te_y$ impedance measurements

Previous subproject experiments indicated that MW absorption was low but consistent until the point of thermal runaway for the Cu-Se-Te system. This was expected from the high electrical conductivity of Cu at $6.461 \times 10^7 \text{ Sm}^{-1}$ which is greater than both Bi and Sn[12]. As shown in figure 9.6, the impedance curves closely matched the paths plotted for the previous systems.

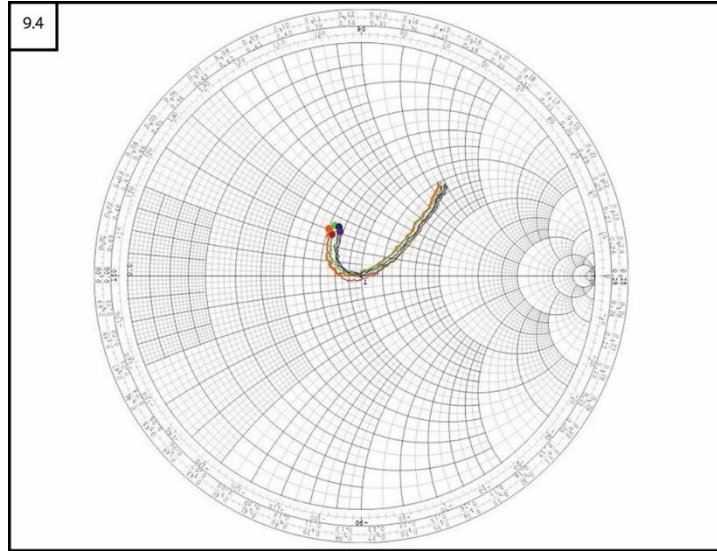


Figure 9.6: Smith chart of complex curves of S_{11} parameter for $Cu_{1-x}Se_{1-y}Te_y$ ($x = 0, 0.2, 0.4, 0.5, 0.6, 0.8, 1$) starting materials

The Z_L of all samples at $f = 2.45 \text{ GHz}$ were as good as, and occasionally better than, the other measured samples as shown in table 9.5:

Table 9.5: Impedance measurements at a frequency of 2.45 GHz for $Cu_{1-x}Se_{1-x}Te_x$ samples

Sample	Impedance (Ω)	
	S_{11}	S_{22}
$Cu_{1-x}Se$	60.676	72.096
$Cu_{1-x}Se_{0.8}Te_{0.2}$	57.424	75.404
$Cu_{1-x}Se_{0.6}Te_{0.4}$	61.012	71.053
$Cu_{1-x}Se_{0.5}Te_{0.5}$	58.596	75.373
$Cu_{1-x}Se_{0.4}Te_{0.6}$	61.909	71.392
$Cu_{1-x}Se_{0.2}Te_{0.8}$	61.462	72.582
$Cu_{1-x}Te$	62.409	70.595

9.3.6 $Cu_{1-x}Se_{1-y}S_y$ impedance measurements

Since the Cu-Se-S mixture was found to be highly reactive under dynamic vacuum during preparation, these were the only samples that were cold-pressed into 5 mm diameter, ~10 mm tall pellets; with three pellets stacked in each quartz ampoule. Previous subproject experiments indicated that the MW absorption of the Cu-Se-S pellets was low, requiring the use of a graphite susceptor to reach thermal runaway. Therefore, the Z_L of all samples was expected to tend away from the intrinsic load of the Smith chart. As shown in

figure 9.7, the impedance curves for each Cu-Se-S mixture only tended further from the centre with increasing quantities of sulfur in the sample stoichiometry.

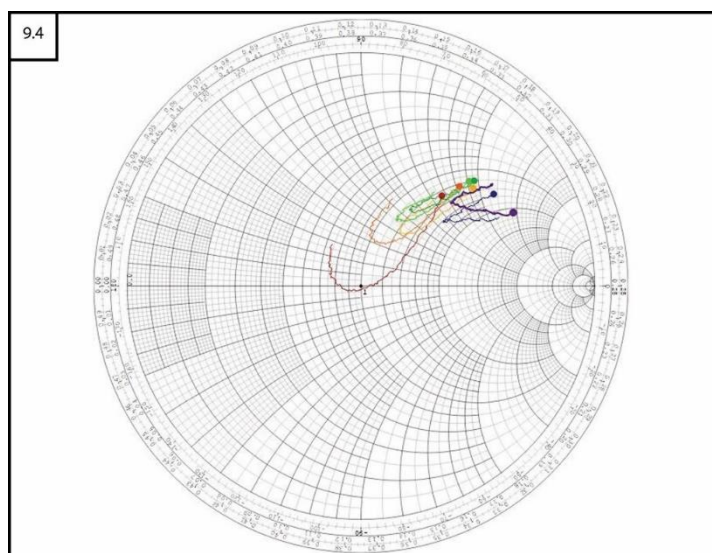


Figure 9.7: Smith chart of complex curves of S_{11} parameter for $Cu_{1-x}Se_{1-y}S_x$ ($x = 0, 0.2, 0.4, 0.5, 0.6, 0.8, 1$) starting materials

The Z_L at $f = 2.45$ GHz likewise showed a divergence from Z_0 , with increasing Z_L that correlates to greater S content in the sample mixture. The Z_L measurements were all $\gg Z_0$ in the range of ~ 65 – 102Ω across the series. The largest step change in Z_L was for stoichiometries between 60–80 % S-doping as shown in table 9.6:

Table 9.6: Impedance measurements at a frequency of 2.45 GHz for $Cu_{1-x}Se_{1-y}S_x$ samples

Sample	Impedance (Ω)	
	S_{11}	S_{22}
$Cu_{1-x}Se_{0.8}S_{0.2}$	64.760	81.858
$Cu_{1-x}Se_{0.6}S_{0.4}$	75.247	86.561
$Cu_{1-x}Se_{0.5}S_{0.5}$	70.440	96.520
$Cu_{1-x}Se_{0.4}S_{0.6}$	75.537	102.759
$Cu_{1-x}Se_{0.2}S_{0.8}$	98.688	102.518
$Cu_{1-x}S$	101.731	133.764

Cu has an electrical conductivity of $6.481 \times 10^7 \text{ Sm}^{-1}$, greater than that of tin by an order of magnitude while S is a non-metal insulator with the lowest known value (of the elements studied in this project) at $5 \times 10^{-16} \text{ Sm}^{-1}$ [12], [13]. From these results then, it is strongly indicated that the contribution of Cu to the MW susceptibility of the mixture becomes superseded by the increasing quantity of S that can insulate against eddy currents. These samples should be expected to absorb MWs well at low S-doping concentrations, followed by more heavily substituted samples requiring the aid of a graphite suscepter.

9.4 Polaris-SMC reactor operation and performance

Drawing on experience with carrying out syntheses on the benchtop SMC reactor, the samples' stoichiometries and optimal reaction parameters were planned out for each system as shown in table 9.7. Each set of parameters was chosen with the intent to allow each sample to undergo a synthesis duration of ~60 s while using the optimal MW power to minimise the induction period and make the most of the available beam time.

Table 9.7: Planned experimental parameters for all *in-situ* Polaris-SMC experiments

TEM system	Target mass (g)	Forward power (W)	Notes
$\text{SnSe}_{1-x}\text{Te}_x$	5	500	Stoichiometric and 10% excess Sn
$\text{SnSe}_{1-x}\text{S}_x$	5	100 w/ graphite susceptor	Stoichiometric and 10% excess Sn
$\text{Sb}_2\text{Se}_{3-x}\text{Te}_x$	5	100 w/ graphite susceptor	–
$\text{Bi}_2\text{Se}_{3-x}\text{Te}_x$	5	100 w/ graphite susceptor	Prepared in glovebox
$\text{Cu}_{1-x}\text{Se}_{1-y}\text{Te}_y$	3	500	–
$\text{Cu}_{1-x}\text{Se}_{1-y}\text{S}_y$	3	100 w/ graphite susceptor	Pellet (×3)

Once the *in-situ* experiments were begun, the materials were found to heat faster, with shorter induction periods and often without the need for a graphite susceptor. The rapid heating was assumed to be due a combination of larger sample size providing a better coupling target for the MWs as well as the magnetron being in better condition through lack of use. The short induction period prompted the reduction of the forward power for all the remaining experiments. Regardless, the experiment parameters were adjusted on the fly for each chemical system, typically by reducing the forward power or heating without the aid of a susceptor. Specific changes are rationalised in the appropriate sections of this chapter.

It was also noted that the forward and reflected power showed fluctuations that were not consistent with the benchtop reactor. In particular, at the point of thermal runaway, the forward power measurement would rise to values much greater than the actual setting of the power meter. An example is shown in figure 9.8 where the actual 500 W forward power used for the initial SnSe reaction was recorded at a maximum value >800 W. When the absorbed power of the reaction was calculated however, the maximum absorbed power was within the actual range of power administered by the power supply.

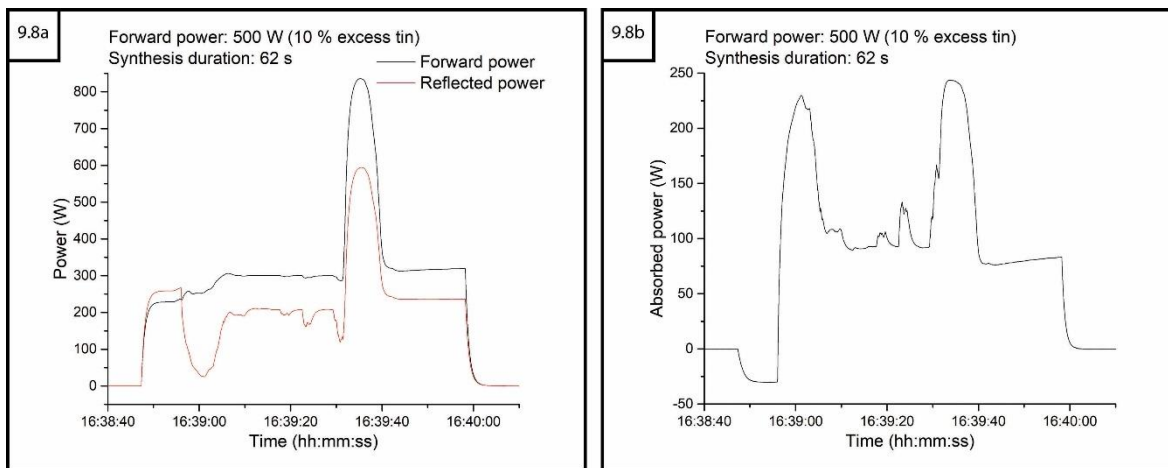


Figure 9.8: Power profile plots for initial SnSe synthesis a) forward and reflected power showing a maximum forward power >800 W b) absorbed power showing a maximum absorbed power value <250 W (within physical limits)

This does indicate that the accuracy of the individual directional MW power measurements is questionable during the turbulent period of synthesis. The Gerling CPI modules that connect to the coupler probes via standard BNC connectors were attached via an extension cable on the benchtop configuration, while the Polaris-SMC CPIs were connected directly. The modules do not weigh much and so any mechanical strain on the BNC connectors was not considered enough to affect the power measurements. The use of male to female BNC extensions to relieve any such mechanical strain on the coupler probes would be a simple and inexpensive way to verify this possibility during any future work carried out with the Polaris-SMC reactor.

9.5 Tin chalcogenide *in-situ* neutron diffraction studies

The starting materials for both 5 g SnSe_{1-x}Te_x and SnSe_{1-x}S_x series (x = 0.2, 0.4, 0.5, 0.6, 0.8, 1) were weighed out and prepared for stoichiometric and 10 % excess Sn sample sets. A single sample of SnSe was prepared using 10 % excess Sn as this was determined to be the optimal stoichiometry for greater phase purity. The SnSe sample was heated using the planned forward power of 500 W however, the induction period was observed to be much shorter than had been expected as discussed previously. The forward power for the next samples was adjusted to 300 W although the induction period for the SnSe_{0.8}Te_{0.2}, SnSe_{0.6}Te_{0.4} and SnSe_{0.5}Te_{0.5} samples (with 10 % excess Sn) was still very short and so the forward power was lowered further to 100 W for the remaining experiments in the SnSe_{1-x}Te_x series. Comparison waterfall plots of the post reaction histogram data for each sample set (Figure 9.9) show clear trends of Bragg peaks representative of the *Pnma* space group being shifted to higher *d*-spacing; the

lattice constants increase with the inclusion of larger Te atoms in the Se sites of the crystal lattice. The $Fm\bar{3}m$ structure associated with SnTe appears as a secondary phase in the samples containing >50 % Te-doping.

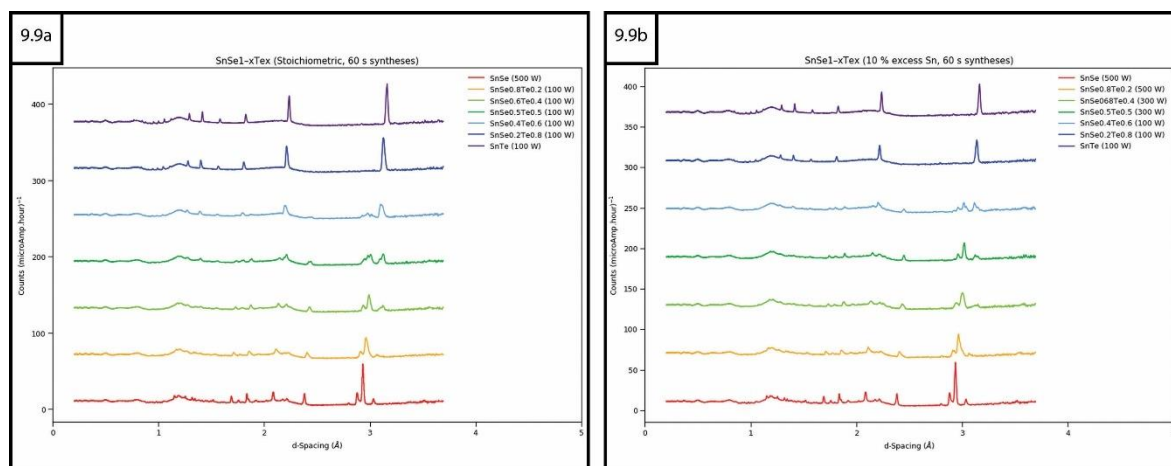


Figure 9.9: Comparison waterfall plot of SnSe_{1-x}Te_x synthesised using 100–500 W forward power for 60 s post reaction histogram TOF data a) 10 % excess Sn b) stoichiometric ratio of starting material

There was no significant improvement on the phase composition between the sample sets with ideal stoichiometry or 10 % excess Sn in terms of secondary phase peaks belonging to unreacted starting material or additional impurities. The samples discussed in this section are limited to those produced from a stoichiometric ratio unless otherwise stated.

9.5.1 SnSe (10 % excess Sn) in-situ TOF data

The undoped SnSe sample data file was split into 20 s and 5 s sections in which the transition from reactants to final product appears to be completed within the first 20 s. This rapid reaction correlates with the large MW absorption peak observed in the first 10 s as shown in figure 9.10.

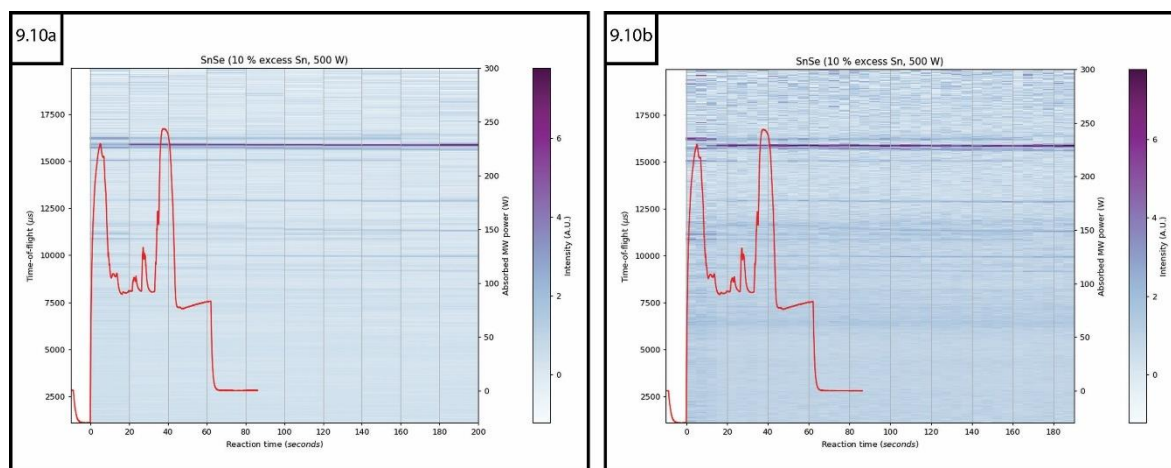


Figure 9.10: Colourmap plots of sliced event mode TOF data with absorbed MW power overlaid for SnSe heated using 500 W forward power for 62 s a) data processed as 20 s sections b) data processed as 5 s sections

The second absorption peak around 35 s into the reaction does not coincide with any significant change in the observed powder patterns. Such MW events can manifest as a result of arcing or sustained plasma formation causing the material to shift around inside the ampoule affecting the coupling.

When the data for the first four 20 s sections were refined, they showed three phases in each belonging to *Pnma* SnSe along with unreacted Sn and Se. The fraction of the SnSe phase increased up to 75(1) wt.% at 20 s from the end of heating while the reactant peaks remained visible in the colourmap plots until 100 s after heating was ceased. Comparing with the refined crystallographic data for the post reaction histogram of this sample (appendix section A–9.1) the reaction pathway appears to continue during the cooling process, ultimately reaching a final SnSe phase fraction of 98.1(2) wt.%. Since the peaks for the SnSe phase can be clearly seen appearing within the first 20 s in the 5 s colourmap plot (Figure 9.11a), these data were refined in an attempt to determine the exact timeframe of the initial reaction progress.

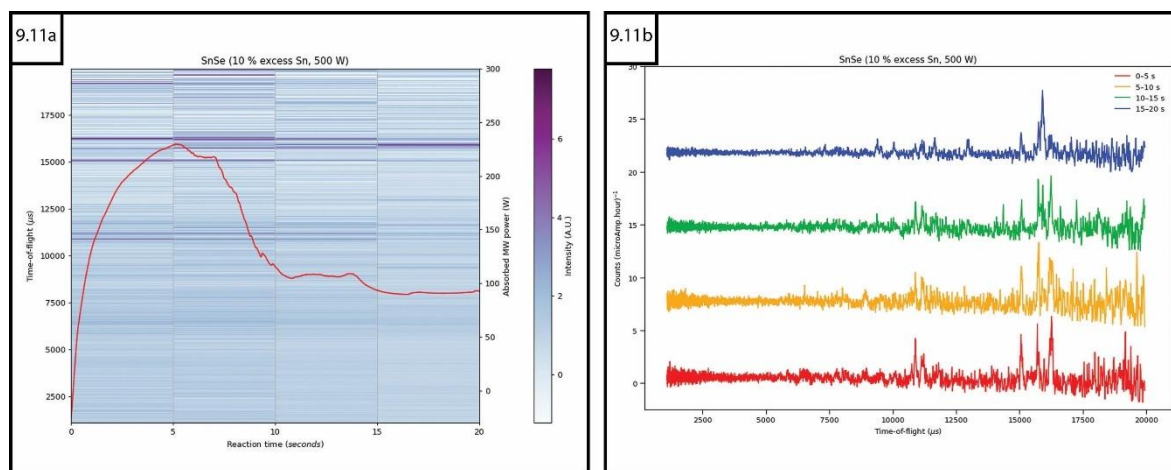


Figure 9.11: Sliced event mode TOF data with absorbed MW power overlaid for SnSe (prepared with 10 % excess Sn) heated using 500 W forward power for 62 s a) colourmap plot b) waterfall plot of initial 0–20 s of synthesis processed as 5 s sections

Despite the lower signal to noise ratio, the peaks were able to be indexed in the 5 s slices as can be seen in figure 9.12. There is enough information in the data sections to confirm that SnSe appears only after 10 s of thermal runaway.

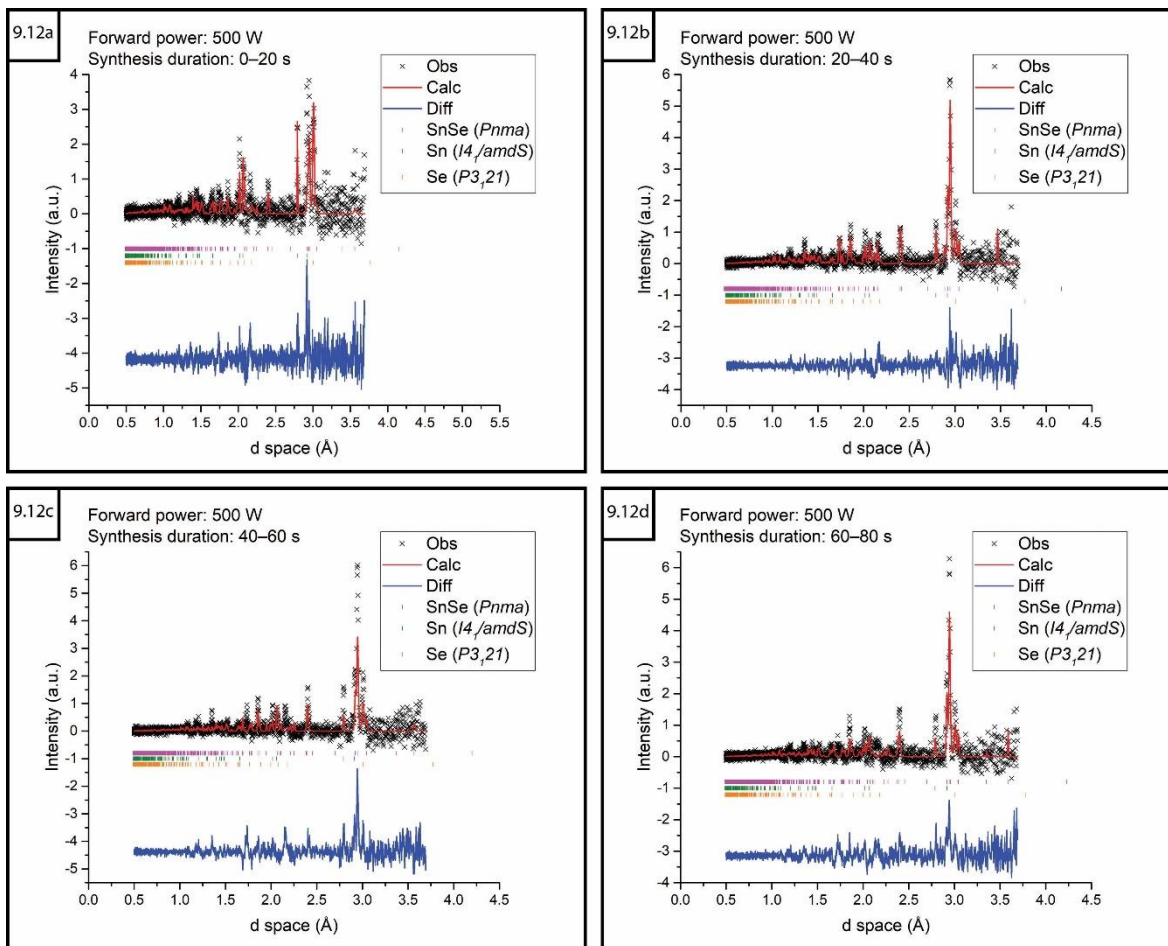


Figure 9.12: Plots of refined event mode TOF data for SnSe split into 5 s slices of the synthesis duration a) 0–5 s b) 5–10 s c) 10–15 s d) 15–20 s

The intensities of the crystal peaks were prominent enough to calculate the phase fractions for each section as shown in figure 9.13, and as previously noted with the 20 s sliced data, the SnSe phase fraction has not reached the maximum identified in the post reaction histogram.

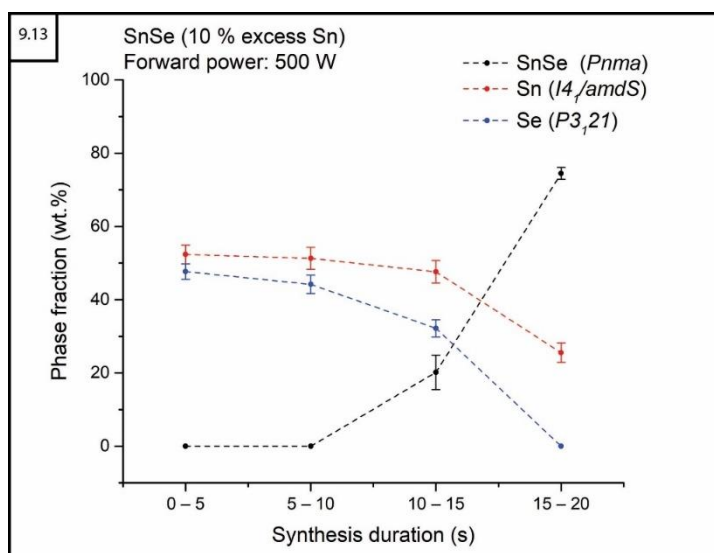


Figure 9.13: Plot of relative phase fractions against synthesis duration calculated from SnSe Rietveld refinement of sliced event mode TOF data

The Se phase has already been shown to still be present past the 15–20 s section, however the poorer resolution of the 5 s sections made converging the powder

pattern while including Se phase impossible. The refined crystallography data for the SnSe phase of these 20 s and 5 s sliced event mode data are available in appendix section A–9.1.

9.5.2 $\text{SnSe}_{1-x}\text{Te}_x$ in-situ TOF data

The partially substituted samples were difficult to refine however an attempt was made to characterise early reaction progression of $\text{SnSe}_{0.6}\text{Te}_{0.4}$ from the 20 s sliced data shown in figure 9.14. Unlike the SnSe sample, no starting material peaks appear after ~ 40 s of the reaction start point.

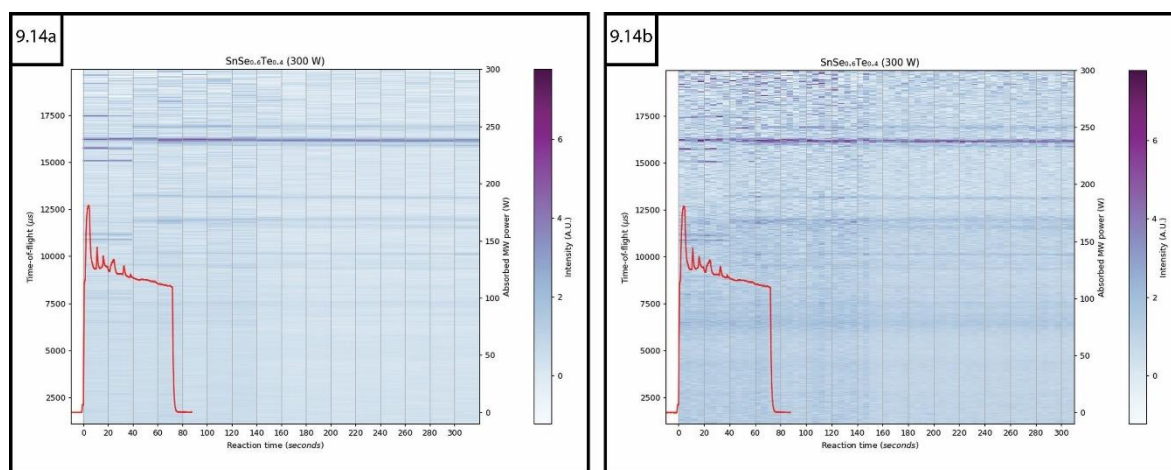


Figure 9.14: Colourmap plots of sliced event mode TOF data with absorbed MW power overlaid for stoichiometric $\text{SnSe}_{0.6}\text{Te}_{0.4}$ heated using 300 W forward power for 72 s a) data processed as 20 s sections b) data processed as 5 s sections

A more successful characterisation of the 20 s sliced data for $\text{SnSe}_{0.4}\text{Te}_{0.6}$ was carried out. As can be seen from figure 9.15, the reaction progression time continues to extend with increasing Te-doping. The mixed phase products only begin to appear after ~ 60 s from the start of the reaction, with the signal to noise ratio of the crystal peak intensities being greatly improved during cooling.

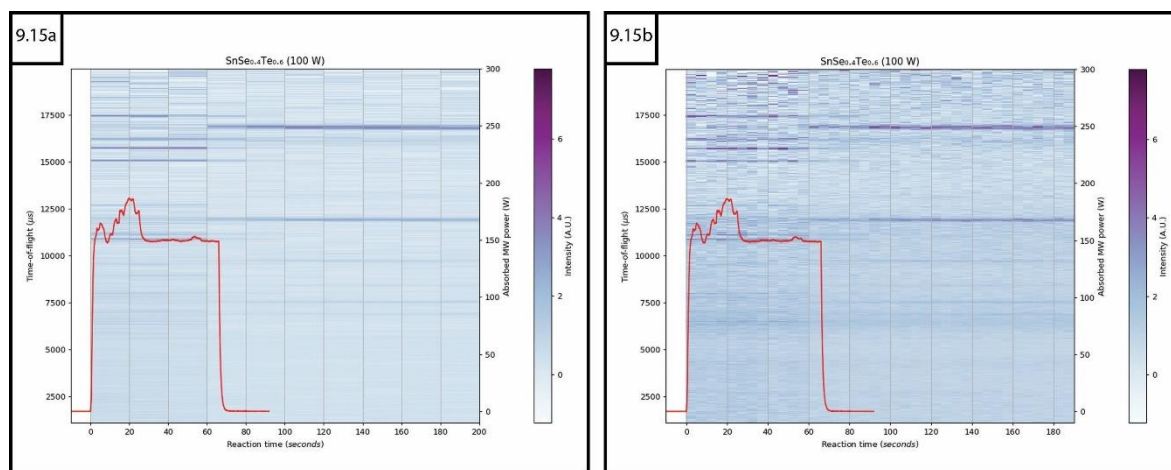


Figure 9.15: Colourmap plots of sliced event mode TOF data with absorbed MW power overlaid for $\text{SnSe}_{0.4}\text{Te}_{0.6}$ heated using 100 W forward power for 66 s a) data processed as 20 s sections b) data processed as 5 s sections

Although the site occupancies were unable to be refined, the main phases were able to be characterised showing the formation of the preferred $Fm\bar{3}m$ phase as shown in table 9.8. The peaks attributed to the starting materials were once more only seen to significantly reduce during cooling (80–100 s section).

Table 9.8: Crystallographic cell parameters from Rietveld refinement of sliced $\text{SnSe}_{0.4}\text{Te}_{0.6}$ event mode TOF data (40–100 s)

Data time-slices (s)	40–60	60–80	80–100
Crystal system	Orthorhombic	Cubic	Cubic
Space group	$Pnma$	$Fm\bar{3}m$	$Fm\bar{3}m$
Phase fraction (wt.%)	19(3)	52(3)	73(1)
Observations	1998	1999	1998
Variables	58	54	51
R_{wp}	0.1145	0.0796	0.0750
R_p	0.2083	0.1408	0.1364
χ^2	0.9273	0.8809	0.7845

Looking closer at the 60–80 s section with the 5 s sliced data (Figure 9.16), the $Fm\bar{3}m$ phase was confirmed in each section with the relevant peak intensities becoming more prominent as the sample began to cool.

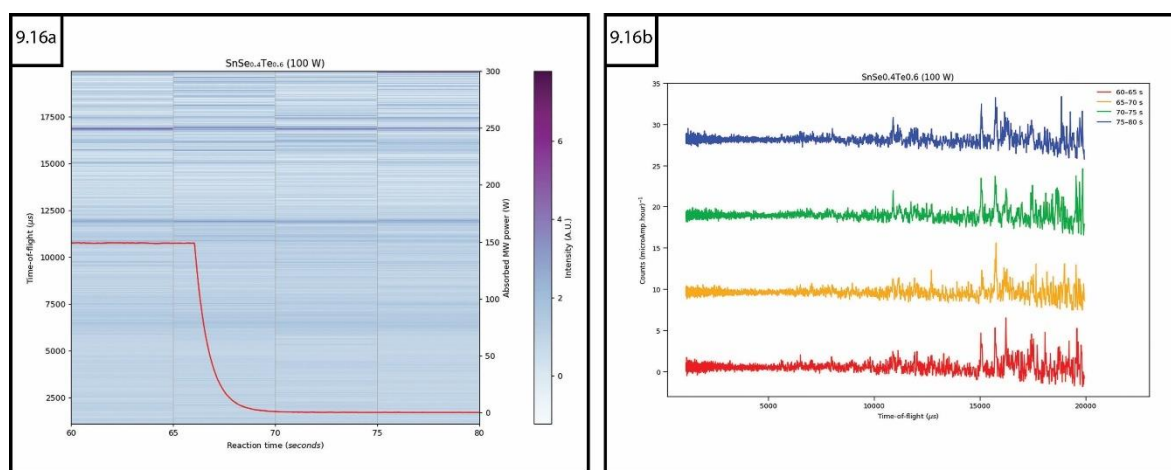


Figure 9.16: Sliced event mode TOF data with absorbed MW power overlaid for $\text{SnSe}_{0.4}\text{Te}_{0.6}$ (prepared with 10 % excess Sn) heated using 100 W forward power for 62 s a) colourmap plot b) waterfall plot 60–80 s section of synthesis processed as 5 s slices

The fraction of the $\text{SnSe}_{0.4}\text{Te}_{0.6}$ phase across the whole 20 s period is largely determined to be consistent, shown in figure 9.17 to be in the range of ~50 wt.%.

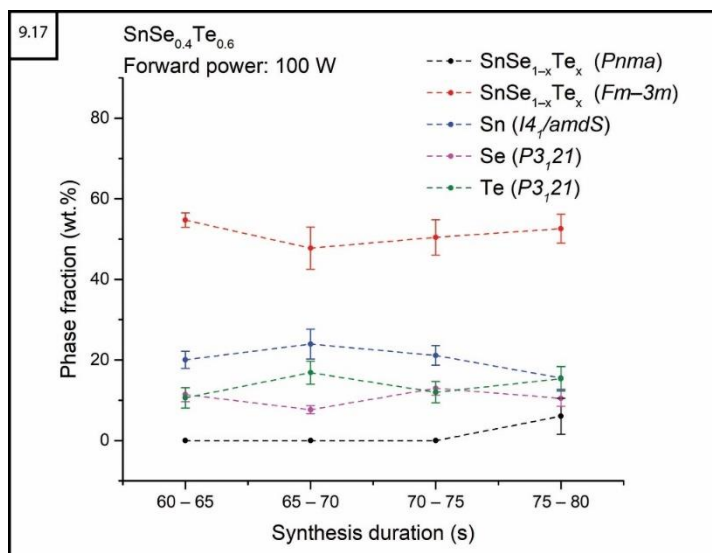


Figure 9.17: Plot of relative phase fractions against synthesis duration calculated from $\text{SnSe}_{0.4}\text{Te}_{0.6}$ Rietveld refinement of 5 s sliced event mode TOF data

The refined crystallography data for the $Fm\bar{3}m$ phase of these 5 s sliced event mode TOF data are available in appendix section A–9.2.

The SnTe colourmaps (Figure 9.18) show that Bragg peaks become difficult to identify as heating progresses and only during the cooling period does the crystal peak resolution become more easily distinguished from the background.

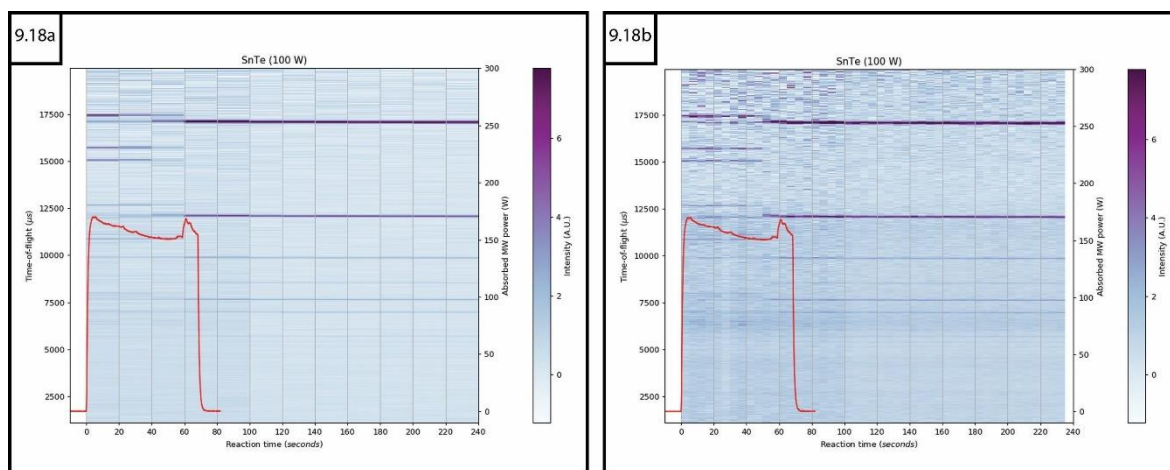


Figure 9.18: Colourmap plots of sliced event mode TOF data with absorbed MW power overlaid for SnTe heated using 100 W forward power for 68 s a) data processed as 20 s sections b) data processed as 5 s sections

The reaction pathway was very direct and fast, with $Fm\bar{3}m$ SnTe peaks appearing faintly within the first 20 s of the reaction, confirmed by the refined crystallographic data (Table 9.9). The SnTe was produced with a phase fraction of 20(2) wt.% in the first 20 s that increase to single phase at the end of the ~60 s synthesis.

Table 9.9: Crystallographic cell parameters from Rietveld refinement of sliced SnTe event mode TOF data (0–80 s)

Data time-slice (s)	0–20	20–40	40–60	60–80
Crystal system	Cubic	Cubic	Cubic	Cubic
Space group	$Fm\bar{3}m$	$Fm\bar{3}m$	$Fm\bar{3}m$	$Fm\bar{3}m$
Phase fraction (wt.%)	20(2)	21(1)	47(3)	100
Observations	1991	1995	1995	1995
Variables	49	52	49	41
R_{wp}	0.1197	0.1222	0.1107	0.1059
R_p	0.2074	0.2168	0.1971	0.1820
χ^2	0.9439	0.9001	0.8270	0.7707

9.5.3 $\text{SnSe}_{1-x}\text{S}_x$ *in-situ* TOF data

Based on the efficiency observed with the previous *in-situ* experiments, heating of the $\text{SnSe}_{1-x}\text{S}_x$ series was attempted at 300 W forward power without the use of a graphite susceptor as initially planned. As can be seen with the comparison waterfall plots in figure 9.19, there are clear trends of crystallographic peak shifts to shorter d -spacing as expected with the amount of S-doping being increased. The peak shifts are less drastic than the $\text{SnSe}_{1-x}\text{Te}_x$ samples and so Rietveld refinement of each was easier to converge.

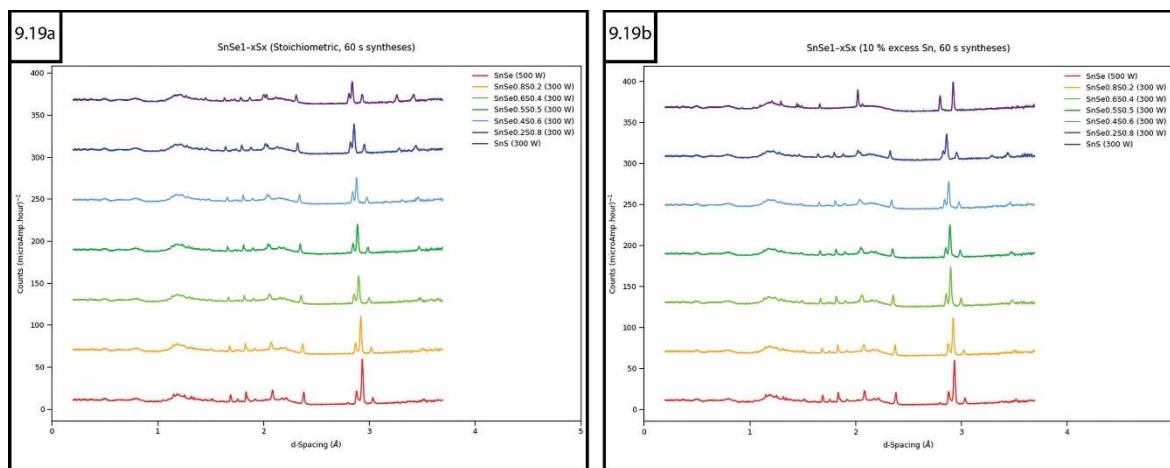


Figure 9.19: Comparison waterfall plot of $\text{SnSe}_{1-x}\text{S}_x$ synthesised using 300 W forward power for 60 s post reaction histogram TOF data a) 10 % excess Sn b) stoichiometric ratio of starting material

Both sample sets of post reaction histogram data were fully characterised as single phase products. There were no obvious secondary phase peaks belonging to unreacted Sn or additional impurities.

Looking at the $\text{SnSe}_{0.6}\text{S}_{0.4}$ colourmap plots (Figure 9.20), despite the dramatic absorption peak at the beginning of the reaction, the sample required heating for ~60 s until significant phase changes were able to be identified compared to

the Te-doped system. The starting material peak intensities are faint but still visible up to 40 s after the magnetron was switched off.

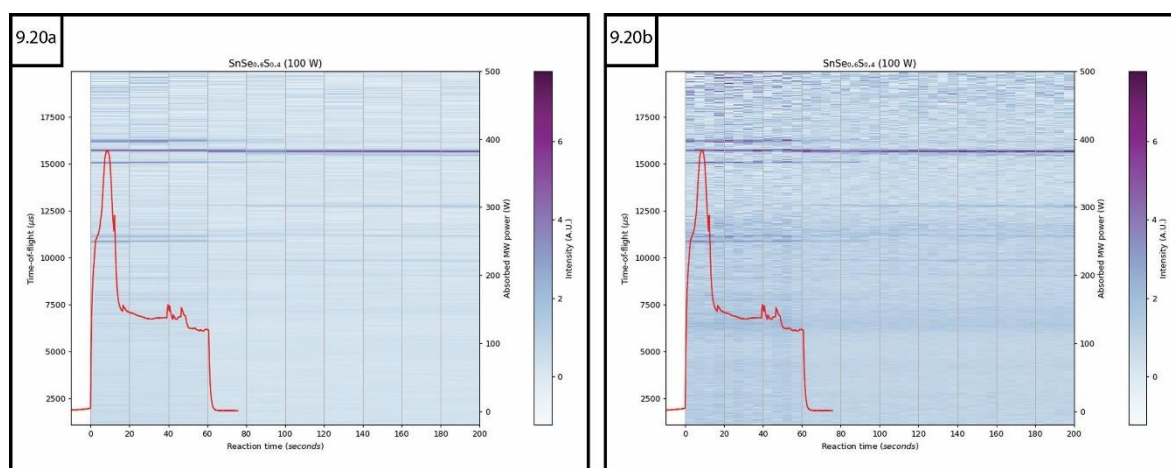


Figure 9.20: Colourmap plots of sliced event mode TOF data with absorbed MW power overlaid for SnSe_{0.6}S_{0.4} heated using 300 W forward power for 61 s a) data processed as 20 s sections b) data processed as 5 s sections

The *Pnma* SnSe_{1-x}S_x phase was identified at 27(3) wt. % in the 40–60 s section, quickly becoming the most prominent component as the sample cooled, which is reflected in the refined crystallographic data shown in table 9.10.

Table 9.10: Crystallographic cell parameters for Rietveld refinement of the SnSe_{0.6}S_{0.4} main phase sliced event mode TOF data (40–100 s)

Data time-slice (s)	40–60	60–80	80–100
Crystal system	Orthorhombic	Orthorhombic	Orthorhombic
Space group	<i>Pnma</i>	<i>Pnma</i>	<i>Pnma</i>
Phase fraction (wt.%)	27(3)	67(1)	83(2)
Observations	1994	1997	1998
Variables	53	50	57
<i>R</i>_{wp}	0.1122	0.0852	0.0780
<i>R</i>_p	0.1990	0.1494	0.1333
<i>χ</i>²	0.9412	0.9849	0.8084

The peak intensities for the latter section were prominent enough to attempt atomic parameter characterisation of the main phase, with chalcogen site occupancy calculated to be SnSe_{0.27}S_{0.73}. Closer inspection of the 80–100 s section, where the starting material peaks become indistinguishable from the background, was carried out on 5 s sliced event mode data as shown in figure 9.21.

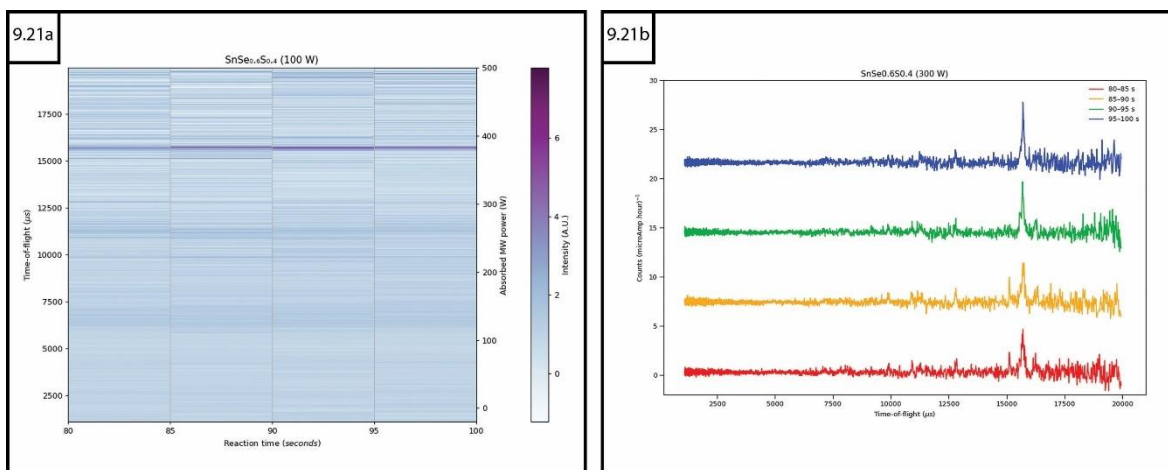


Figure 9.21: Sliced event mode TOF data with absorbed MW power overlaid for $\text{SnSe}_{0.6}\text{S}_{0.4}$ (prepared with 10 % excess Sn) heated using 300 W forward power for 62 s a) colourmap plot b) waterfall plot of 80–100 s section of synthesis processed as 5 s slices

Only starting material peaks were indexed between 80–85 s; $Pnma$ $\text{SnSe}_{1-x}\text{S}_x$ forms as the main phase at 43(5) wt. % in the 85–90 s section (Figure 9.22b).

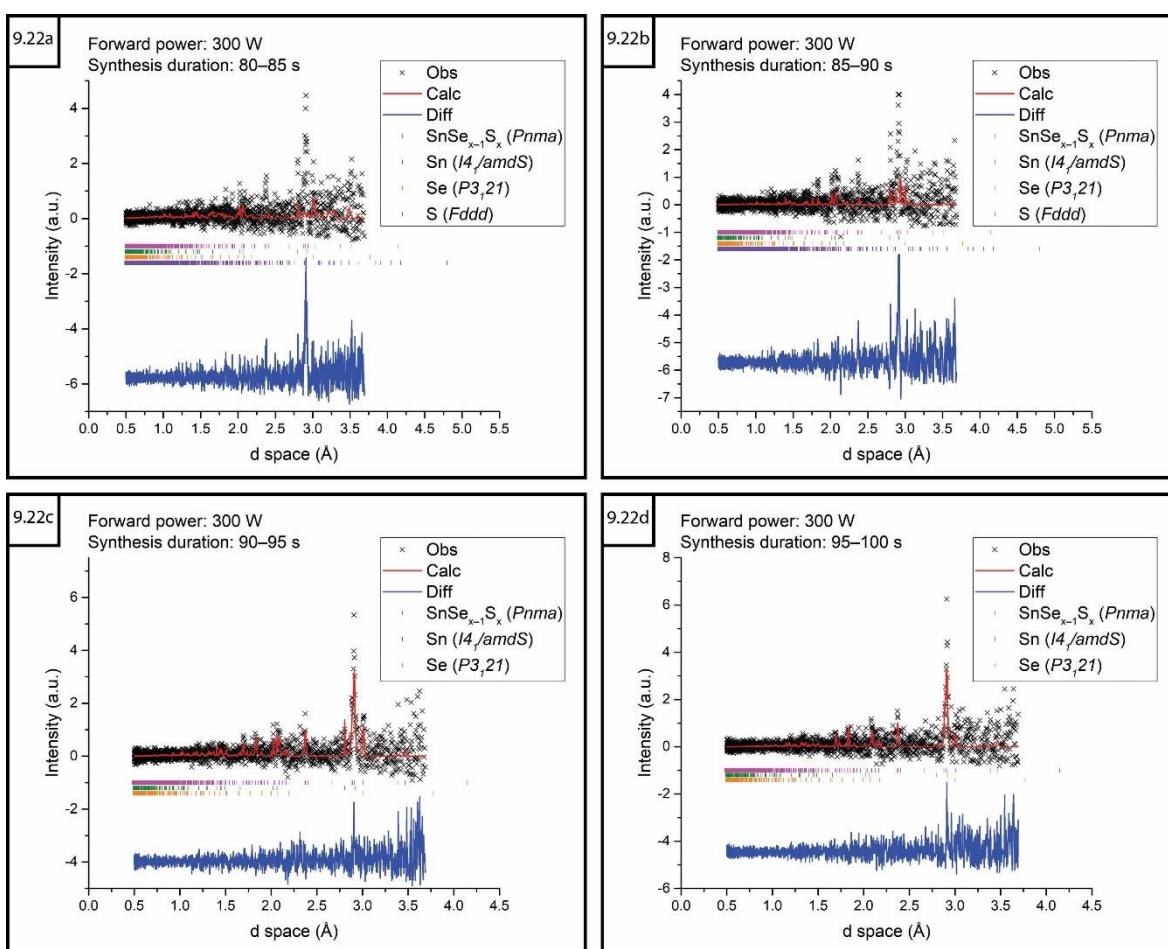


Figure 9.22: Plots of refined event mode TOF data for $\text{SnSe}_{0.6}\text{S}_{0.4}$ split into 5 s slices of the synthesis duration a) 80–85 s b) 85–90 s c) 90–95 s d) 95–100 s

Sulfur was unable to be indexed in sections >90 s, and Se was similarly reduced until no longer able to be identified after 95 s. The final 95–100 s section showed $\text{SnSe}_{1-x}\text{S}_x$ approaching a single phase state with a calculated phase fraction of 93(1) wt.%. The refined crystallography data for the $Pnma$ phase of these 5 s sliced event mode TOF data are available in appendix section A–9.3.

Both the $\text{SnSe}_{0.4}\text{S}_{0.6}$ and SnS colourmap plots (Figure 9.23) showed a similar reaction progression in terms of MW power profile and a reaction pathway lasting the extent of the synthesis duration. The powder pattern peak intensities of the SnS sample become almost indistinguishable from the background immediately after heating is ceased before the $Pnma$ phase becomes identifiable in the single phase.

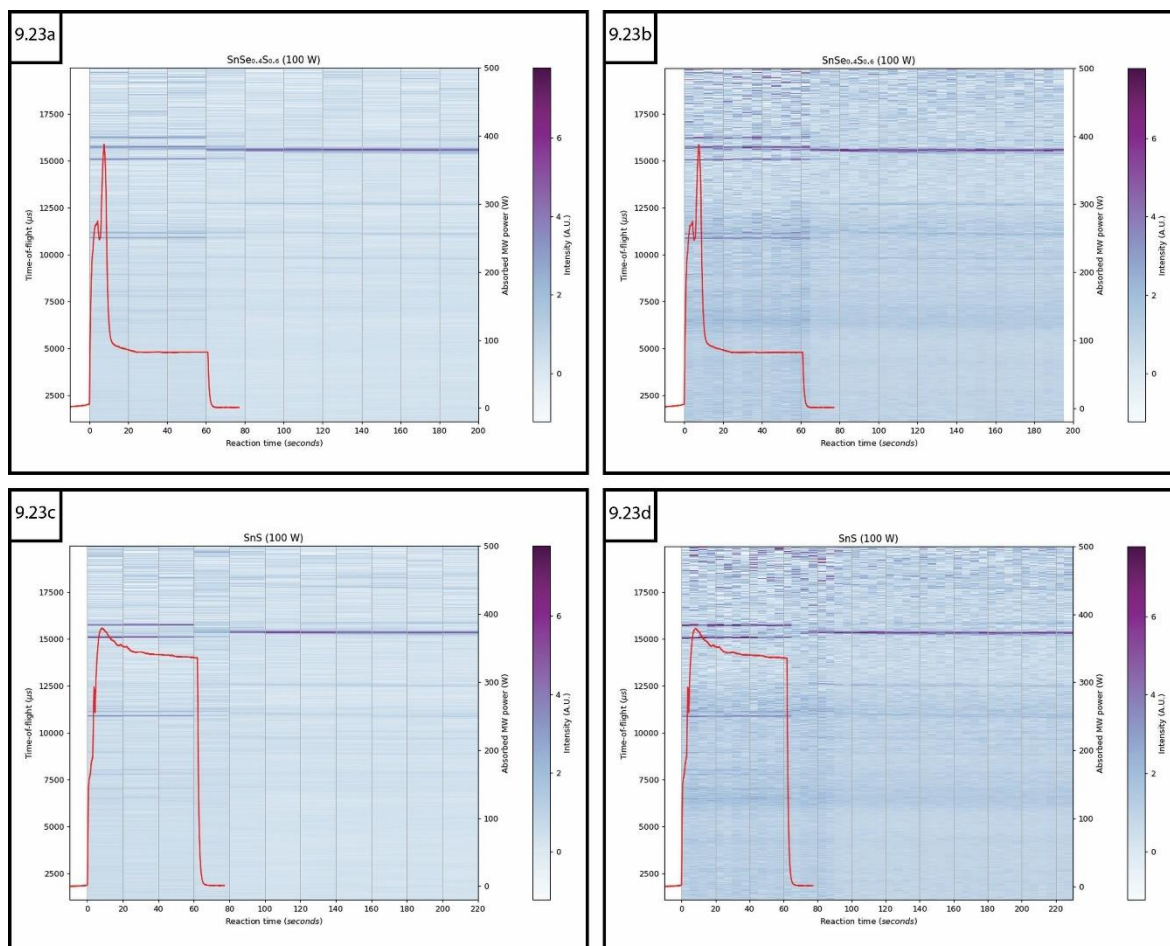


Figure 9.23: Colourmap plots of sliced event mode TOF data with absorbed MW power overlaid for $\text{SnSe}_{1-x}\text{S}_x$ samples heated using 300 W forward power for a) 61 s synthesis of $\text{SnSe}_{0.4}\text{S}_{0.6}$ processed as 20 s sections and b) 5 s sections c) 62 s synthesis of SnS processed as 20 s sections and d) 5 s sections

The post reaction histogram data for all of the $\text{SnSe}_{1-x}\text{S}_x$ samples were characterised as single phase, which confirms that the actual reaction pathway seems to progress instantaneously after ~ 60 s synthesis duration. For each of the samples in the $\text{SnSe}_{1-x}\text{S}_x$ series, the site occupancy was able to be calculated as a closer reflection of the target stoichiometry as shown in the selection of refinement plots in figure 9.24.

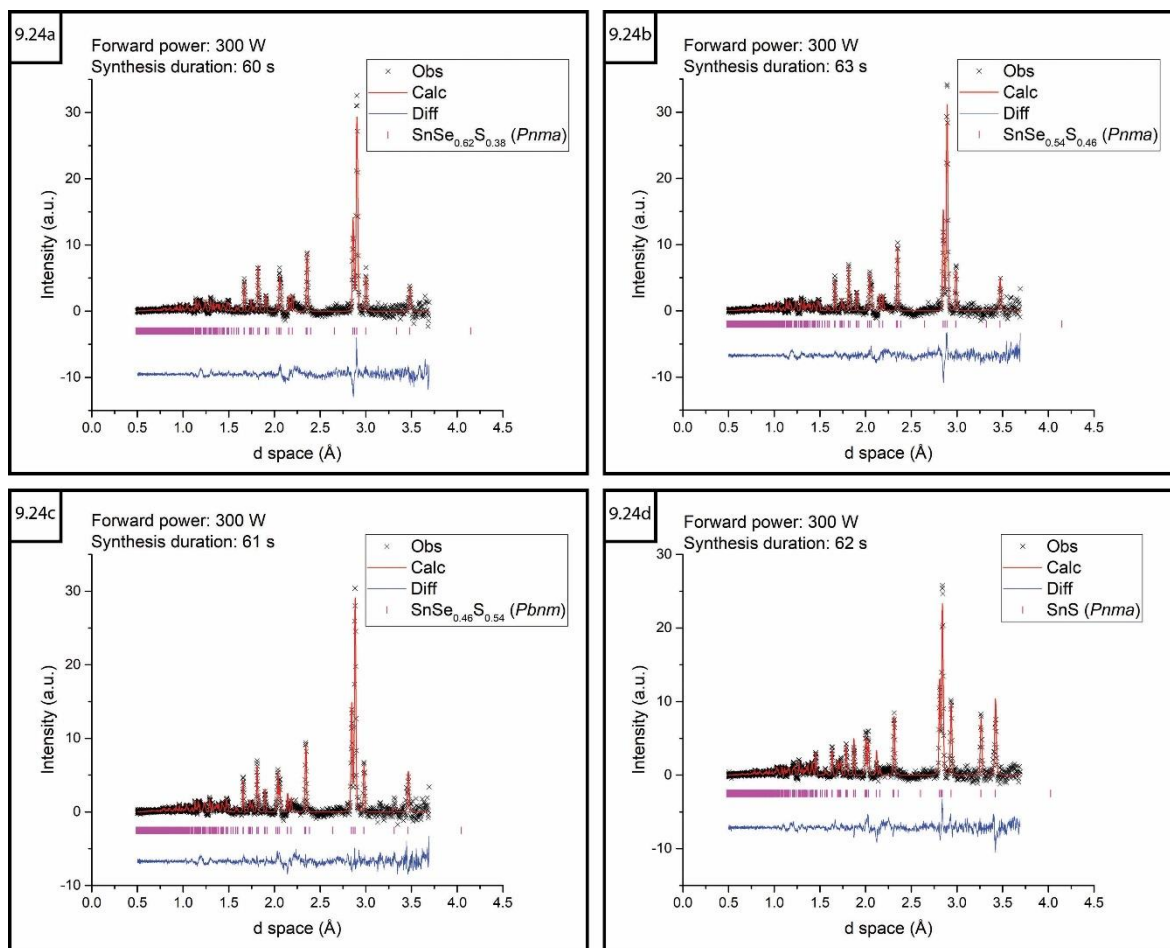


Figure 9.24: Plots of refined post reaction histogram TOF data for a) $\text{SnSe}_{0.6}\text{S}_{0.4}$ b) $\text{SnSe}_{0.5}\text{S}_{0.5}$ c) $\text{SnSe}_{0.4}\text{S}_{0.6}$ d) SnS

The refined crystallography data of these histogram TOF data that show the decreasing lattice parameters of the orthorhombic phase with increased S-doping are available in appendix section A–9.3.

9.6 Bismuth chalcogenide *in-situ* neutron diffraction studies

Each of the 5 g $\text{Bi}_2\text{Se}_{3-x}\text{Te}_x$ ($x = 0, 0.5, 1, 1.5, 2, 2.5, 3$) samples was heated using 500 W forward power without the aid of a graphite suscepter as originally planned, with the exception of Bi_2Te_3 . The waterfall plot comparing the post reaction histogram data (Figure 9.25) indicates that the main $R\bar{3}m$ phase peaks clearly visible in the Bi_2Se_3 sample are shifted to higher d -spacing as expected with greater Te-doping. The peak broadening further points to defects within the partially substituted structure.

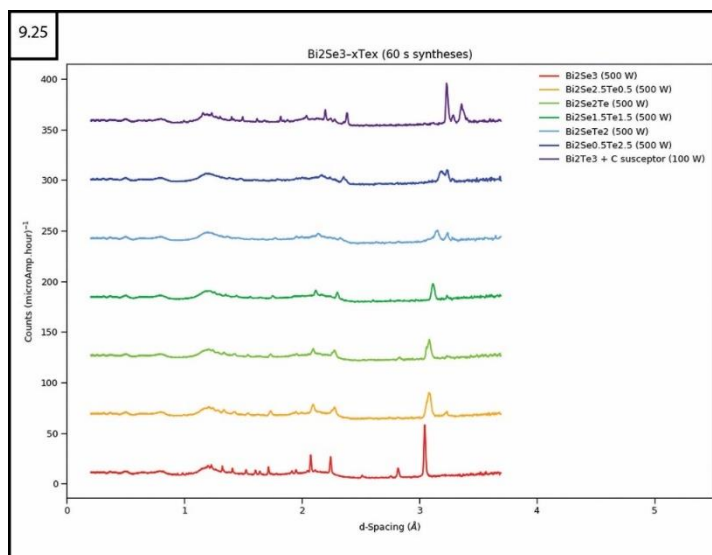


Figure 9.25: Comparison waterfall plot of $\text{Bi}_2\text{Se}_{3-x}\text{Te}_x$ synthesised using 500 W forward power for 60 s, except for Bi_2Te_3 which was heated at 100 W using a graphite susceptor post reaction histogram TOF data

The targeted $R\bar{3}m$ $\text{Bi}_2\text{Se}_{3-x}\text{Te}_x$ phases were confirmed in each sample to be the main component of the final composition. However, as with the benchtop experiments $I4/mmm$ Bi_2SeO_2 was identified in the first few samples, quickly being replaced with the seemingly preferential $Abm2$ Bi_2TeO_5 and $P4_12_12$ TeO_2 impurities where greater Te content would allow. The refined crystallography data for a selection of post reaction histogram data that shows the increasing lattice parameters of the $R\bar{3}m$ phase with increased Te-doping are available in appendix section A–9.4.

9.6.1 $\text{Bi}_2\text{Se}_{3-x}\text{Te}_x$ in-situ TOF data (60 s syntheses)

Without the masking effect of the MW susceptor, these power absorption profiles give novel insights into the reaction pathways of the system. As shown for the first two samples (Figure 9.26), the rapid absorption of ~60 % of MW power at the point of thermal runaway lasts for only 5–10 s before falling to a consistent plateau of ~100 W with the formation of the product phase. This verifies the observations of the subproject experiments using the benchtop SMC reactor.

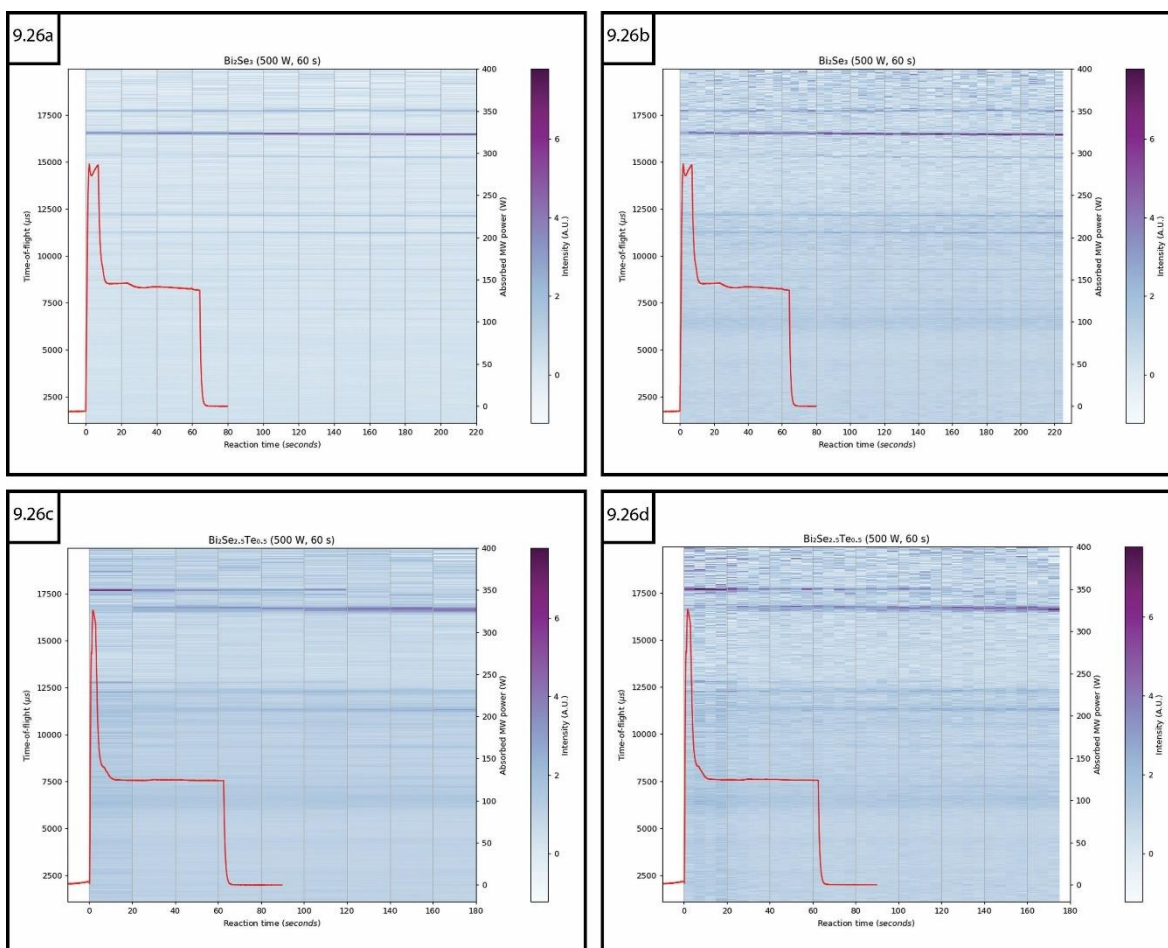


Figure 9.26: Colourmap plots of sliced event mode TOF data with absorbed MW power overlaid for $\text{Bi}_2\text{Se}_{3-x}\text{Te}_x$ samples heated using 500 W forward power for a) 64 s synthesis of Bi_2Se_3 processed as 20 s sections and b) 5 s sections c) 63 s synthesis of $\text{Bi}_2\text{Se}_{2.5}\text{Te}_{0.5}$ processed as 20 s sections and d) 5 s sections

What is more clearly seen in the $\text{Bi}_2\text{Se}_{2.5}\text{Te}_{0.5}$ colourmap is the formation of the $R\bar{3}m$ peaks at ~ 20 s with low intensity, which gradually grow past the heating period and as the sample cools. Conversely, the starting material peaks gradually decrease until ~ 60 s after heating was ceased. The event mode data for each Te-doped $\text{Bi}_2\text{Se}_{3-x}\text{Te}_x$ sample was difficult to satisfactorily refine for each of the multiple phases as the peak intensities of the powder patterns were found to be particularly poor. As can be seen in the $\text{Bi}_2\text{Se}_2\text{Te}$ and $\text{Bi}_2\text{Se}_{1.5}\text{Te}_{1.5}$ colourmaps (Figure 9.27), patterns in the shorter 5 s sections of data were even harder to distinguish although generally show the same gradual reaction over the sample cooling period.

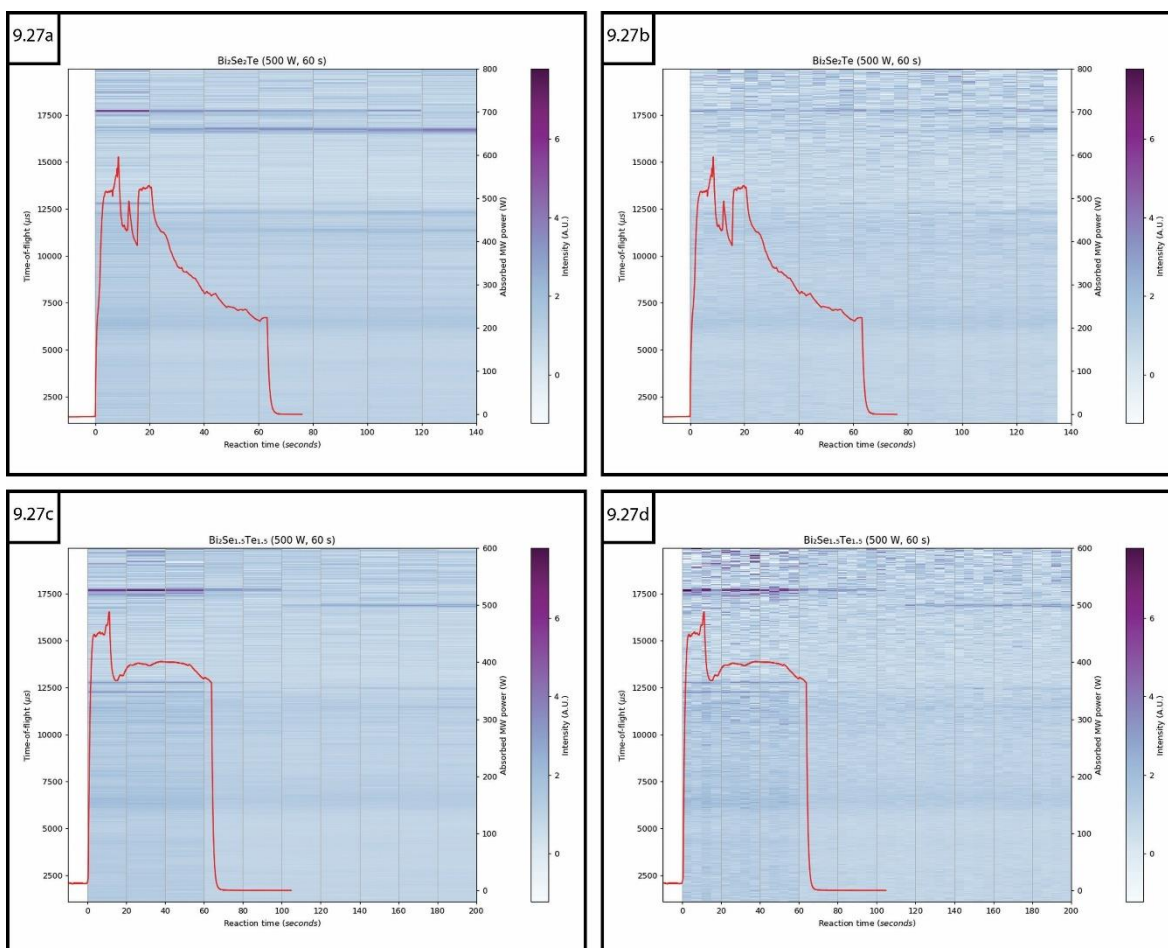


Figure 9.27: Colourmap plots of sliced event mode TOF data with absorbed MW power overlaid for $\text{Bi}_2\text{Se}_{3-x}\text{Te}_x$ samples heated using 500 W forward power for a) 63 s synthesis of $\text{Bi}_2\text{Se}_2\text{Te}$ processed as 20 s sections and b) 5 s sections c) 64 s synthesis of $\text{Bi}_2\text{Se}_{1.5}\text{Te}_{1.5}$ processed as 20 s sections and d) 5 s sections

As the Bi_2Te_3 sample was the only experiment in the series to be carried out with the aid of a graphite susceptor, a separate background histogram file was created by recording an empty quartz ampoule set in ~ 5 mm depth of graphite powder in the quartz support tube to normalise the data. The background file appears to overcorrect in the region of $18,000 \mu\text{s}$ with a trough appearing in the neutron counts as shown in figure 9.28.

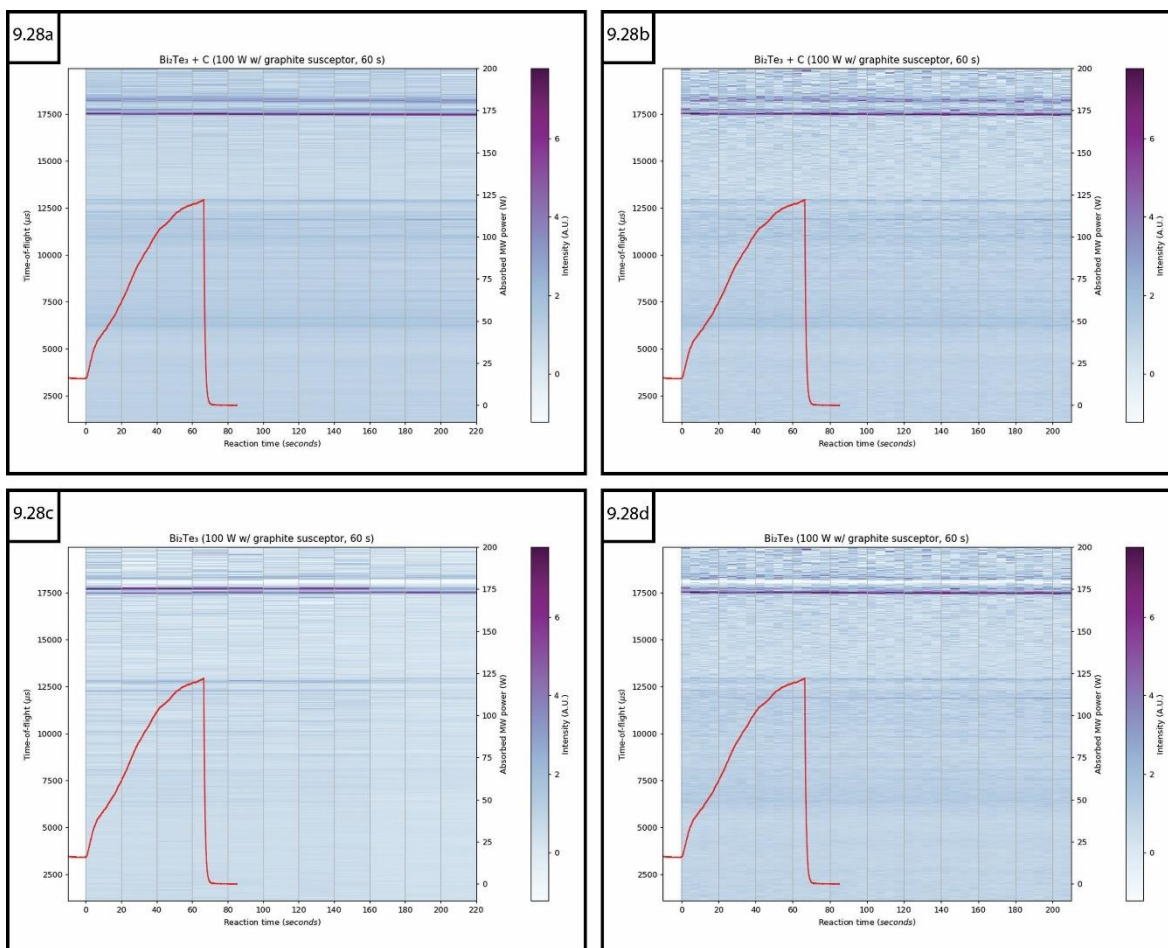


Figure 9.28: Colourmap plots of sliced event mode TOF data with absorbed MW power overlaid for Bi_2Te_3 heated using 100 W forward power with the aid of a graphite susceptor for 66 s a) processed as 20 s sections b) processed as 5 s sections c) processed with graphite peaks subtracted from background as 20 s sections and d) 5 s sections

Despite the removal of some peaks with the graphite correction, the rest of the pattern was able to be indexed with a particular focus on the first 20 s section of heating. The reaction appears to be almost instantaneous, with $R\bar{3}m$ Bi_2Te_3 clearly identified with a phase fraction of 65(2) wt.%. A comparison table of the Bi_2Te_3 crystallography data refined with and without normalisation for the graphite susceptor peaks is available in appendix section A–9.4.

Looking closer at the initial 20 s after the start of synthesis by slicing the data down to 5 s sections (Figure 9.29), the diffraction peaks became more difficult to refine against the background even when accounting for graphite peaks. Although $R\bar{3}m$ Bi_2Te_3 can be identified visually based on peak positions, attempts to converge the phase composition failed.

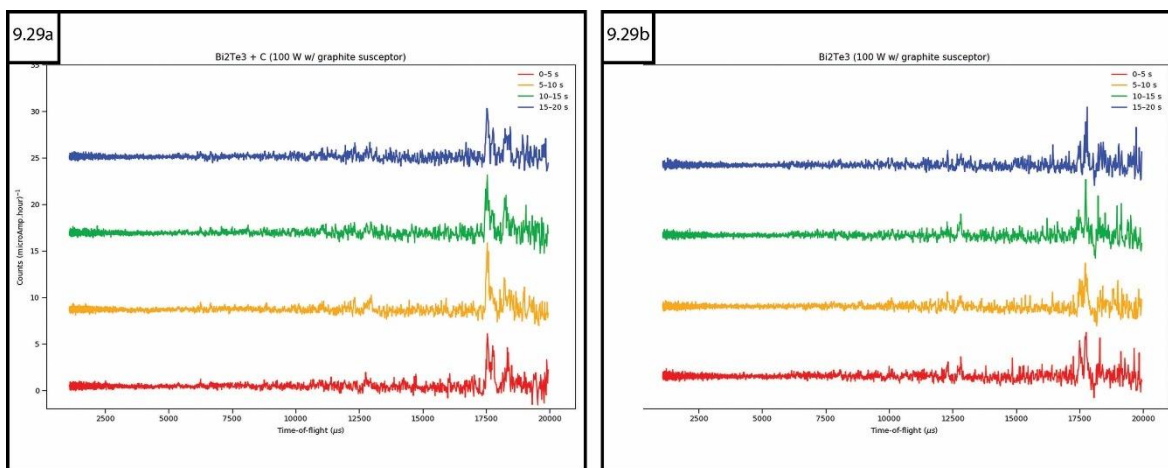


Figure 9.29: Waterfall plots of 20–40 s section of Bi_2Te_3 synthesis event mode TOF data processed as 5 s slices a) without normalising for graphite susceptor b) graphite susceptor peaks removed from background

9.6.2 Analysis of elemental powders during second ISIS beamtime

In the middle of the allotted beamtime, the synchrotron current of the neutron beamline dropped to 0 μA and remained inoperative for more than 24 hours; luckily, no event mode data was lost. Further information is given in appendix section A–9.5. The interruption meant that a handful of syntheses could not be completed without an additional visit at a later date. Based on the successful heating of samples without a susceptor (prior to the event mode data being processed), it was thought that repeating some experiments with longer synthesis durations would potentially give more insight into those reactions. Therefore, during the intervening month between site visits a duplicate set of $\text{Bi}_2\text{Se}_{3-x}\text{Te}_x$ and $\text{Sb}_2\text{Se}_{3-x}\text{Te}_x$ samples were prepared. Additionally, samples of individual reactant powders (Table 9.11) were sealed in quartz ampoules at $\sim 1 \times 10^{-6}$ mbar to investigate their MW susceptibility and any change in structure with heating if there was sufficient beamtime available.

Table 9.11: Experimental parameters for elemental powder samples heated in the Polaris-SMC reactor

Elemental powder	Forward power (W)	Heating duration (s)	Sample depth (mm)
Tin	300	60	37.8
Antimony	500	60	34.9
Bismuth	500	60	37.6
Selenium	300	60	28.3
Tellurium	300	60	26.8
Sulfur	300	60	30.8

For each sample, a $\sim 15 \mu\text{A}$ histogram scan was collected, followed by an event mode scan while the samples were heated for ~ 60 s. Unfortunately, an error was encountered while processing the Sn event mode data that indicates “The proton

charge found in the input workspace (POLARIS130512) run information is zero”; making it unreadable.

The pre-heated histogram data for Bi was found to contain ~25 % *P121/c1* Bi₂O₃ impurity which confirms that the formation of the various bismuth oxides and oxychalcogenide phases in each experiment were the sole result of contamination in the starting mixture. Since the Bi powder used for the sample preparation had previously been confirmed as phase pure (see section 8.3.1), the contamination could have occurred due to either an operational failure of the glovebox over the lockdown period or during the process of transferring the samples from the glovebox to the glassblowing station to be sealed. The Bi and Sb powders were heated using 500 W forward power; Bi demonstrated a steady absorption profile of ~110 W while Sb showed immediate absorption of > 200 W for ~5 s followed by a reduction to a lower range between 150–175 W. The forward power for the Se heating experiment was initially set too low and so the forward power was raised from 100 W to 300 W during the first 37 s and then the sample was heated for a further 67 s, absorbing a consistent ~40 W. The Te and S samples were heated using 300 W forward power and likewise showed consistent MW absorption of ~40 W, confirming that the primary interaction with MWs in the synthesis of each binary metal chalcogenide is the formation of eddy currents in the metal powders by the *H* field component. Some slight peak broadening or shifts to higher *d*-spacing was visible in each samples’ powder pattern as the lattices were expanded during heating. The pattern resolution for S was too low to observe its peaks. The changes were not significant enough to justify further analysis refinement of the crystallographic parameters within the limited time; the colourmap plots are available in appendix section A–9.6.

9.6.3 Extending Bi₂Se_{3-x}Te_x heating duration (120 s syntheses)

The duplicate batch of Bi₂Se_{3-x}Te_x samples were heated using 500 W forward power and with synthesis time extended to 120 s. As with the original set, the Bi₂Te₃ sample was the only one heated using 100 W forward power with the aid of a graphite susceptor. The resultant histogram scans of the samples heated for 120 s showed the same peak shifts and low signal to noise ratio observed in those heated for 60 s (Figure 9.30) that made their refinement difficult. The refined phase fractions of the histogram data confirmed that extending the heating

duration did not improve upon the $R\bar{3}m$ $\text{Bi}_2\text{Se}_{3-x}\text{Te}_x$ phase (Appendix section A–9.4). It is possible that adjusting the synthesis duration of samples without a competing oxide phase present in future work could improve the tuneability of these materials.

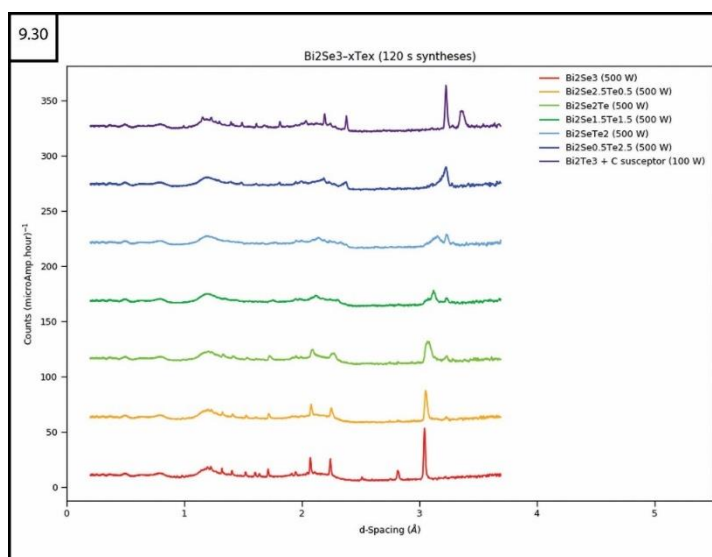


Figure 9.30: Comparison waterfall plot of $\text{Bi}_2\text{Se}_{3-x}\text{Te}_x$ synthesised using 500 W forward power for 120 s, except for Bi_2Te_3 which was heated at 100 W using a graphite susceptor post reaction histogram TOF data

As noted with the samples heated for ~ 60 s, the same trend of rapid synthesis within 5–10 s of thermal runaway followed by a sudden reduction in MW absorption to a lower plateau was evident for most of the 120 s synthesis experiments (Figure 9.31). Peaks attributed to the $R\bar{3}m$ $\text{Bi}_2\text{Se}_{3-x}\text{Te}_x$ phase steadily become more prominent over the same timeframe as with the samples heated for only 60 s.

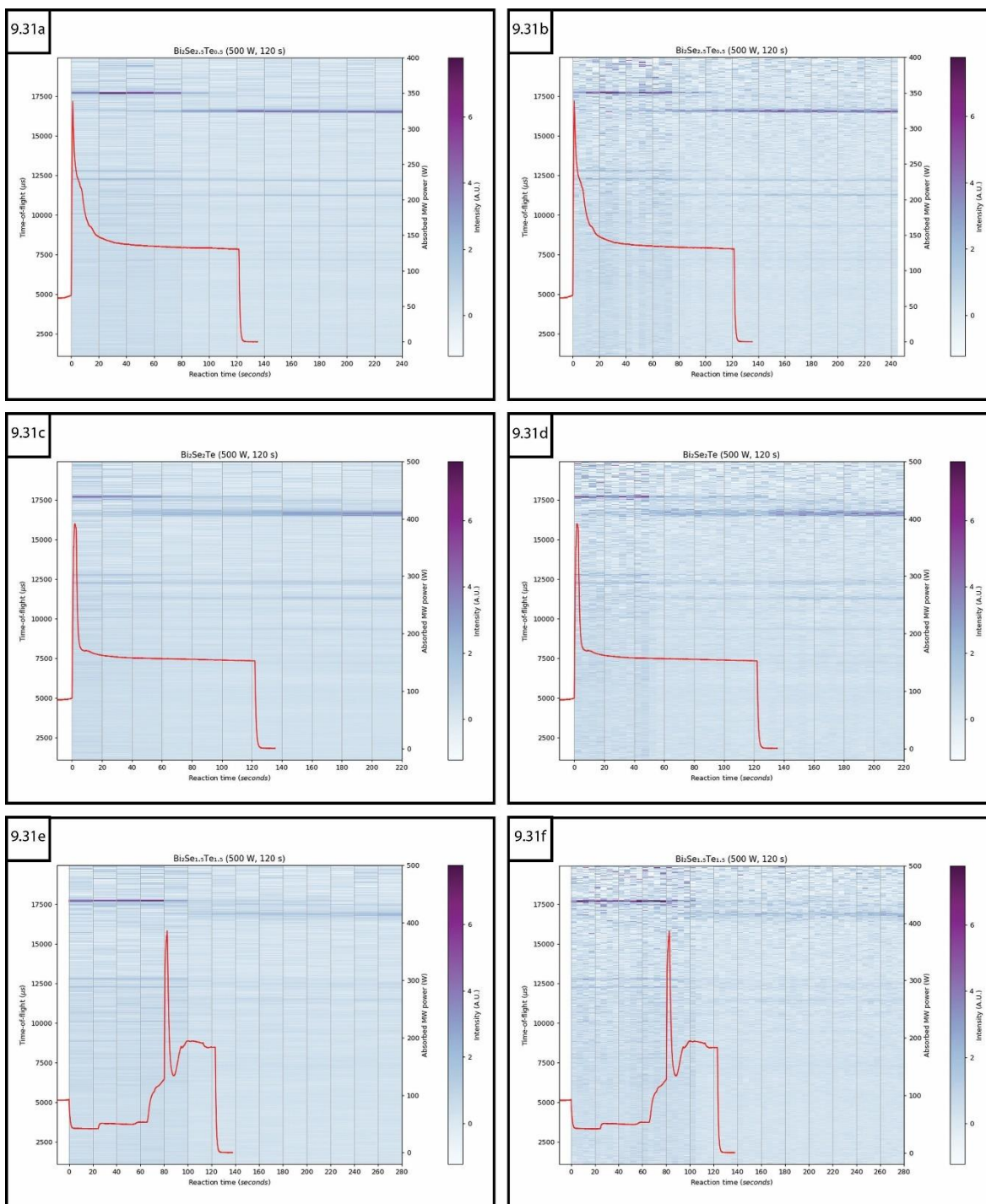


Figure 9.31: Colourmap plots of sliced event mode TOF data with absorbed MW power overlaid for $\text{Bi}_2\text{Se}_{3-x}\text{Te}_x$ samples heated using 500 W forward power for a) 122 s synthesis of $\text{Bi}_2\text{Se}_{2.5}\text{Te}_{0.5}$ processed as 20 s sections and b) 5 s sections c) 122 s synthesis of $\text{Bi}_2\text{Se}_2\text{Te}$ processed as 20 s sections and d) 5 s sections e) 40 s synthesis of $\text{Bi}_2\text{Se}_{1.5}\text{Te}_{1.5}$ processed as 20 s sections and f) 5 s sections

A decreasing MW absorption event was incorrectly used as the starting point of the $\text{Bi}_2\text{Se}_{1.5}\text{Te}_{1.5}$ synthesis duration; later calculated to actually be 40 s. It is worth noting from this result that no changes in the starting materials are evident before thermal runaway. These results indicate strongly that the main thrust of the reaction is contained within this significant MW absorption event and is not affected by direct MW-heating beyond this point.

The interesting result of these *in-situ* neutron studies is the discovery that all product phases for this system are generated together in the early stages of heating, with the reaction path progressing at a consistent rate regardless of heating duration. The interference of bismuth oxides in these particular samples obscures a closer examination of the synthesis pathways and how they might otherwise be affected by adjusting the parameters. It is intriguing enough to warrant further exploration in future work by limiting heating to the ~10–20 s where the greatest amount of MW absorption is consistently observed and tracking the development during cooling. This along with ensuring the use of pristine Bi starting material should enable the production of single phase $R\bar{3}m$ $\text{Bi}_2\text{Se}_{3-x}\text{Te}_x$ samples that can be reliably tuned in a fraction of the time of conventional methods.

9.7 Antimony chalcogenide *in-situ* neutron diffraction studies

All of the 5 g $\text{Sb}_2\text{Se}_{3-x}\text{Te}_x$ ($x = 0, 0.2, 0.4, 0.5, 0.6, 0.8, 1$) samples were successfully heated using 500 W forward power without the need for a graphite susceptor just as with the bismuth chalcogenides. Two sets were prepared due to the beamtime interruption to compare any effects of synthesis duration between 60 s and 120 s on phase composition or site occupancy. Both sets of comparison waterfall plots (Figure 9.32) show that all syntheses proceeded to completion by the expected transition from identified $Pnma$ to $R\bar{3}m$ phases and the associated peak shifts with increased Te-doping.

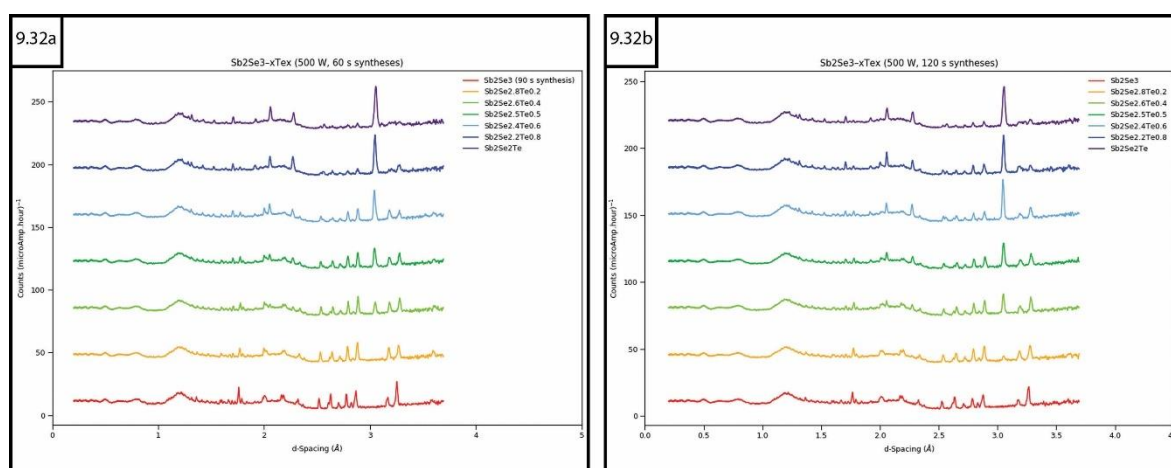


Figure 9.32: Comparison waterfall plot of $\text{Sb}_2\text{Se}_{3-x}\text{Te}_x$ synthesised using 500 W forward power post reaction histogram TOF data a) 60 s syntheses except for Sb_2Se_3 which was heated for ~90 s b) 120 s syntheses

9.7.1 Effect of synthesis duration on $\text{Sb}_2\text{Se}_{3-x}\text{Te}_x$ solid solutions

The post reaction histogram data for all of the samples in the $\text{Sb}_2\text{Se}_{3-x}\text{Te}_x$ system were fully characterised as dual phase solid solutions comprised of both $Pnma$

and $R\bar{3}m$ crystal structures as expected from the subproject benchtop experiments. No oxide or oxychalcogen peaks were identified in either of the sample sets which strongly indicates that the use of a graphite susceptor to reduce the induction period of this system encourages side oxidation reactions between the quartz vessel and its contents when heated past a critical point. By selectively heating the sample materials without a susceptor, the unwanted impurities appear to have been avoided. The refined unit cell parameters of both $Pnma$ and $R\bar{3}m$ phases for each heating scheme are shown in figure 9.33 to follow the same pattern of lattice expansion with increasing Te-doping as in the benchtop experiments.

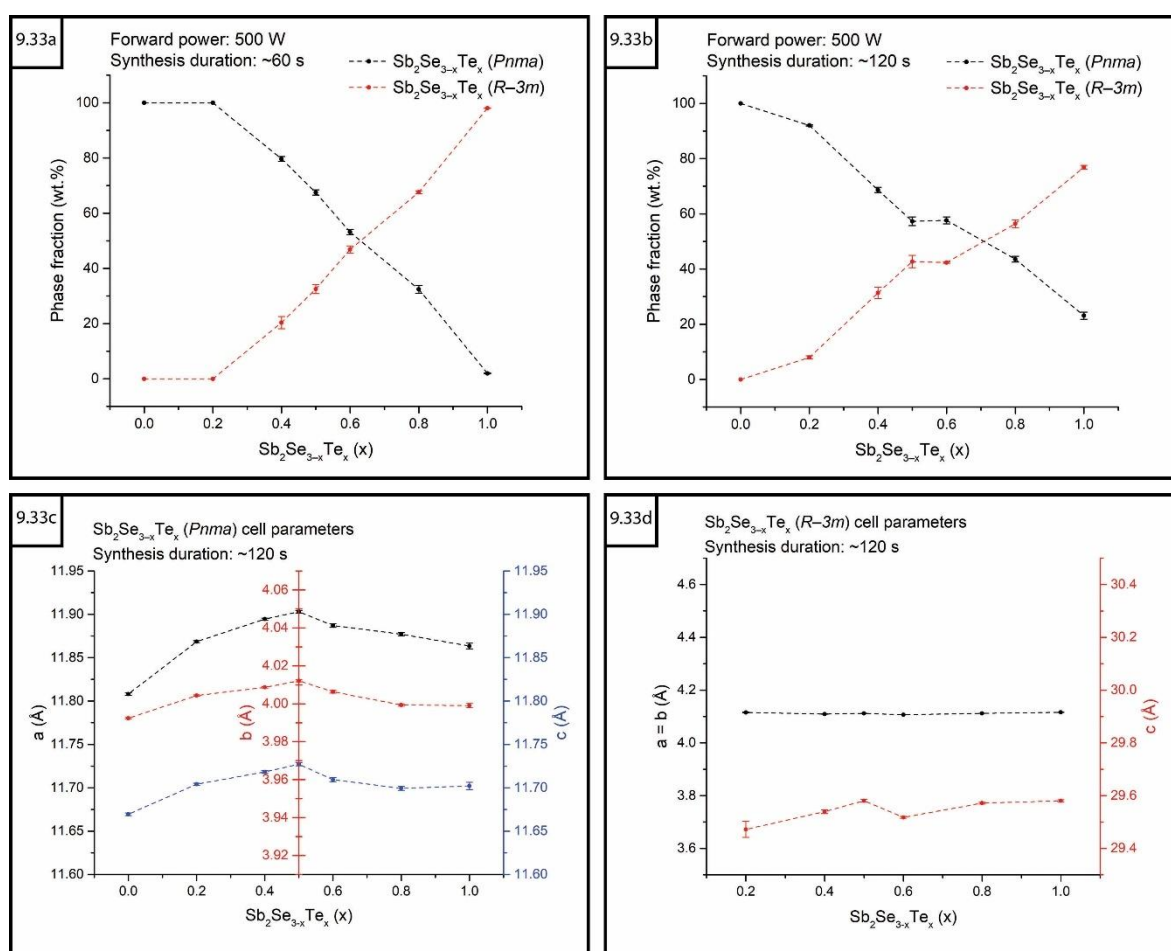


Figure 9.33: Plots of lattice parameters a , b and c for $Sb_2Se_{3-x}Te_x$ samples synthesised using 500 W forward power a) 60 s syntheses, $Pnma$ phase b) 60 s syntheses, $R\bar{3}m$ phase c) 120 s syntheses, $Pnma$ phase d) 120 s syntheses, $R\bar{3}m$ phase

The extent to which the cell is distorted is noticeably greater in the samples synthesised for 120 s as the longer heating allows for the atoms in the structure to move around more, making Te easier to incorporate into the chalcogen sites in place of the smaller Se atoms. The changing relative phase fraction of the dual phase solid solution against increasing Te-doping for each sample set is shown in figure 9.34. It is clear that by increasing the heating duration to 120

s, the $R\bar{3}m$ phase is encouraged to appear as a greater phase fraction with Te-doping amounts of $x < 0.8$. Conversely with longer synthesis duration, the $Pnma$ phase fraction does not get supplanted as much at levels of Te substitution for $x > 0.8$. This means that the balance between phases in the final solid solution matrix can be tuned by adjusting the direct MW-heating duration, possibly above Te-doping of 30 %.

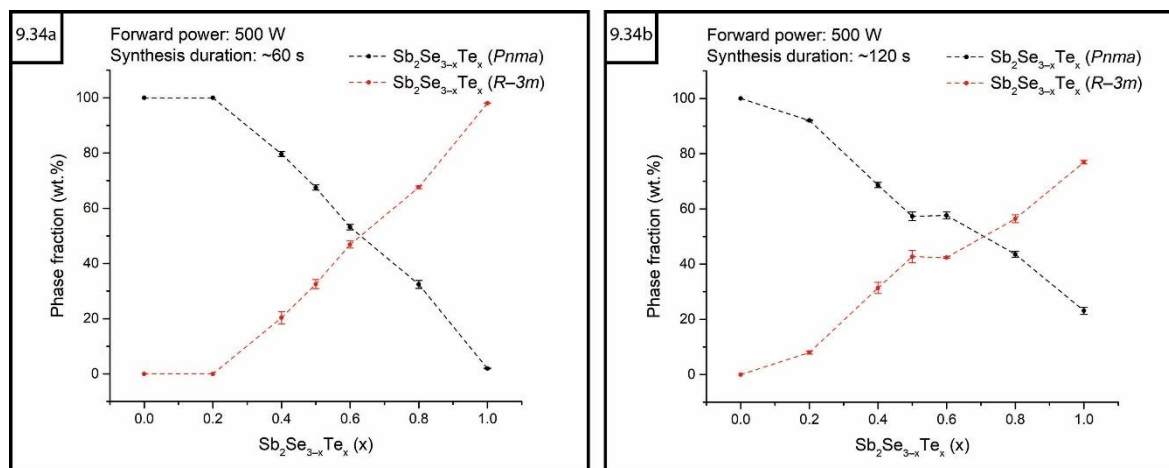


Figure 9.34: Plots of relative phase fractions against intended Te content for $Sb_2Se_{3-x}Te_x$ samples heated using 500 W forward power a) 60 s syntheses, except for Sb_2Se_3 which was heated for ~90 s b) 120 s syntheses

The refined crystallography data and well fit plots of a selection of post reaction histogram data used to calculate the phase fractions, chalcogen site occupancies and increasing lattice parameters are available in appendix section A–9.4.

9.7.2 Comparing $Sb_2Se_{3-x}Te_x$ (60 s and 120 s) *in-situ* TOF data

As with the bismuth chalcogenides, it was expected that the successful synthesis of all $Sb_2Se_{3-x}Te_x$ samples without the aid of a graphite susceptor would allow the power profiles obtained from the *in-situ* experiments to be more closely correlated with events in the powder profiles. The prominent and easily identifiable powder patterns obtained from the post reaction histograms were not reflective of the quality of the event mode data. The poor resolution of the powder peaks in the samples with Te-doping of $x < 0.6$ made any attempts at structure characterisation impossible for samples heated for 60–120 s. The step change of the recorded powder profile between high and low plateaus of MW absorption are strongly indicative of new phase formation, unfortunately for most of the experiments, this could not be correlated with any events in the neutron data. Faint peaks can be distinguished in the colourmap plots (Figure 9.35) usually 20–40 s after heating has ceased. The $Sb_2Se_{2.6}Te_{0.4}$ sample begins

to show product phase formation after ~ 80 s from the start of thermal runaway regardless of the duration of heating.

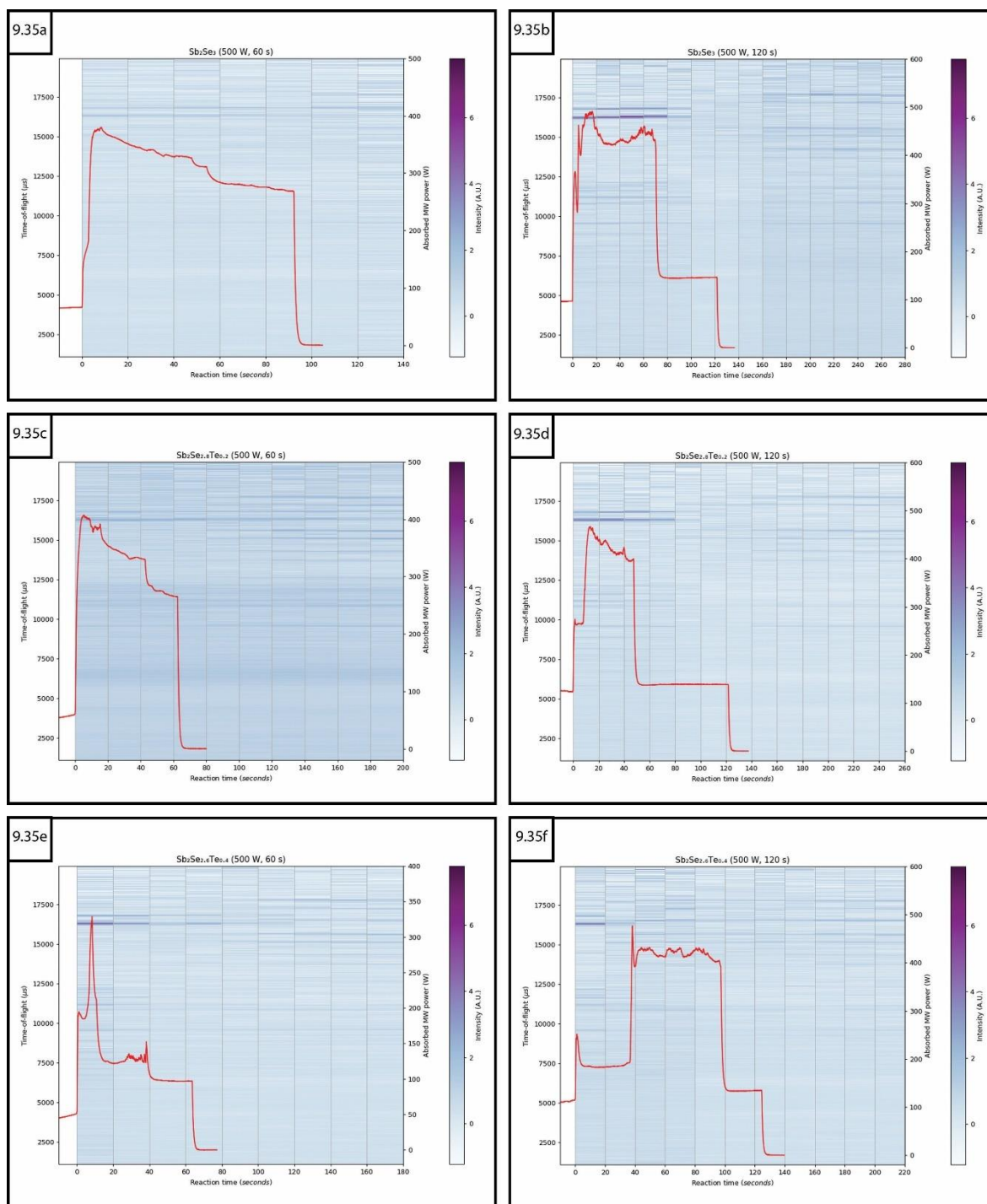


Figure 9.35: Colourmap plots of sliced event mode TOF data processed as 20 s sections with absorbed MW power overlaid for $Sb_2Se_{3-x}Te_x$ samples heated using 500 W forward power for a) 92 s synthesis of Sb_2Se_3 b) 122 s synthesis of Sb_2Se_3 c) 62 s synthesis of $Sb_2Se_{2.8}Te_{0.2}$ d) 122 s synthesis of $Sb_2Se_{2.8}Te_{0.2}$ e) 64 s synthesis of $Sb_2Se_{2.6}Te_{0.4}$ f) 125 s synthesis of $Sb_2Se_{2.6}Te_{0.4}$

Since each of the elemental powders and the post reaction histogram data were easily characterised, the poor TOF resolution is not due to the structures being invisible to neutrons. The reaction *in-situ* may be more volatile, with the powder being churned up during heating or may have completely melted, resulting in

the neutron beam interacting with an amorphous phase that only begins to crystallise once the sample began cooling.

At Te-doping of $x \geq 0.5$, the $R\bar{3}m$ structure that has been established to form preferentially appears to crystallise faster than the $Pnma$ phase, due to the apparently more stable structure. The peak intensities, particularly for the $Pnma$ phase, are still relatively low against the background (Figure 9.36) until later in the cooling period.

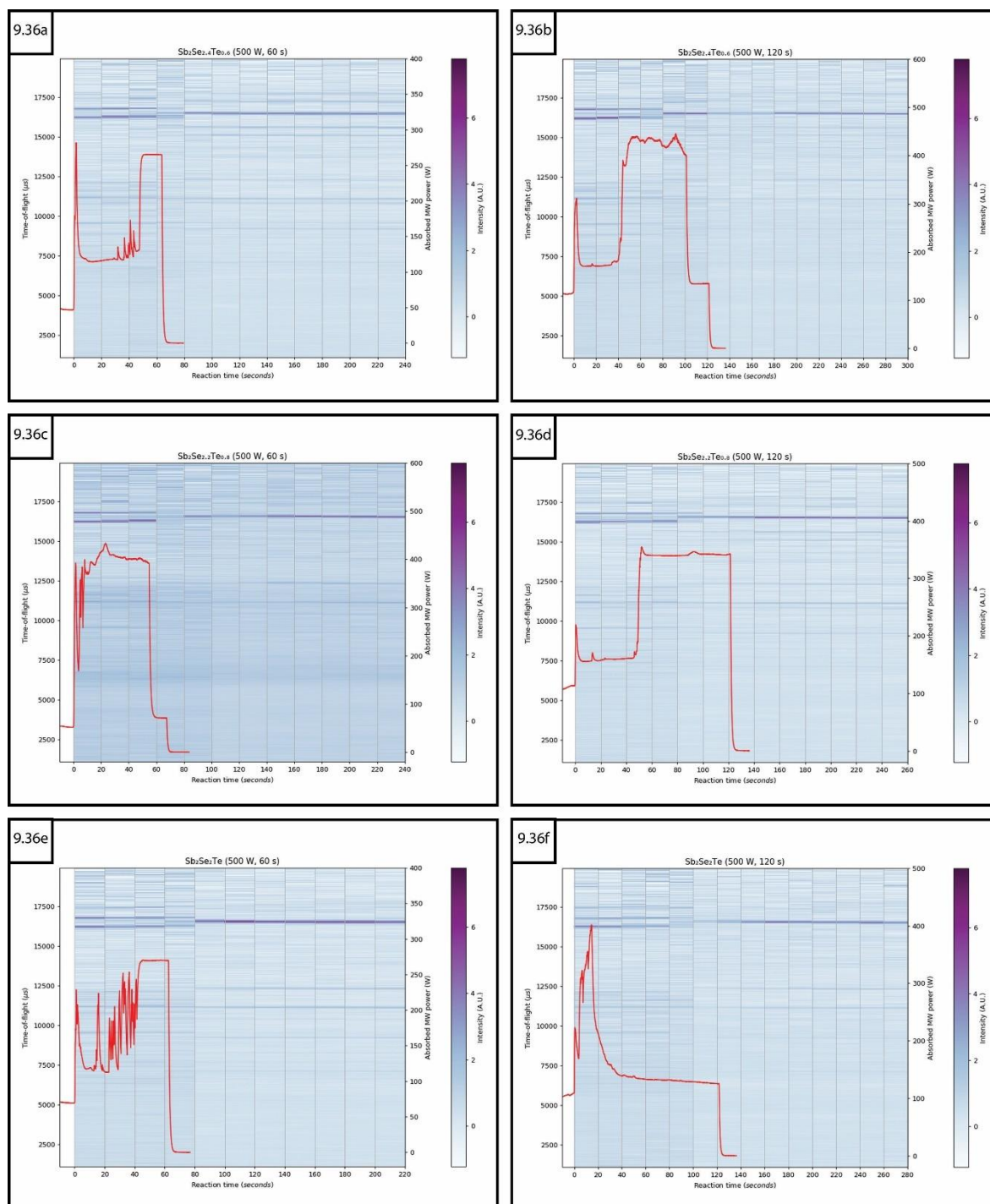


Figure 9.36: Colourmap plots of sliced event mode TOF data processed as 20 s sections with absorbed MW power overlaid for $Sb_2Se_{3-x}Te_x$ samples heated using 500 W forward power for a) 64 s synthesis of $Sb_2Se_{2.4}Te_{0.6}$ b) 122 s synthesis of $Sb_2Se_{2.4}Te_{0.6}$ c) 67 s synthesis of $Sb_2Se_{2.2}Te_{0.8}$ d) 121 s synthesis of $Sb_2Se_{2.2}Te_{0.8}$ e) 63 s synthesis of Sb_2Se_2Te f) 121 s synthesis of Sb_2Se_2Te

The reaction progression for these samples at least confirms the observation from the $\text{Sb}_2\text{Se}_{2.6}\text{Te}_{0.4}$ sample that powder peaks associated with the starting mixture remain unchanged during the first ~60–80 s of thermal runaway regardless of heating duration. The pattern resolution then becomes significantly worse (temporary amorphous behaviour) before the solid solution phases begin to manifest throughout the cooling period. The poor quality of the event mode neutron data obtained for the antimony chalcogenide system establish that unique chemical reaction dynamics will exclude or restrict certain materials from being effectively investigated using the Polaris-SMC reactor system. Future work with this system could be carried out by repeating the *in-situ* reactions using much a lower forward power of ~200–300 W. More gentle heating would drastically extend the induction times but may allow the reaction pathway to be more closely examined.

9.8 Copper chalcogenide *in-situ* neutron diffraction studies

The 3 g $\text{Cu}_{1-x}\text{Se}_{1-y}\text{Te}_y$ and $\text{Cu}_{1-x}\text{Se}_{1-y}\text{S}_y$ ($y = 0, 0.2, 0.4, 0.5, 0.6, 0.8, 1$) series were successfully synthesised without the need for a graphite susceptor. The first Cu_{1-x}Se experiment was heated using the planned 500 W forward power however, as shown in figure 9.37, although the induction period was very short the maximum amount of absorbed power was <200 W.

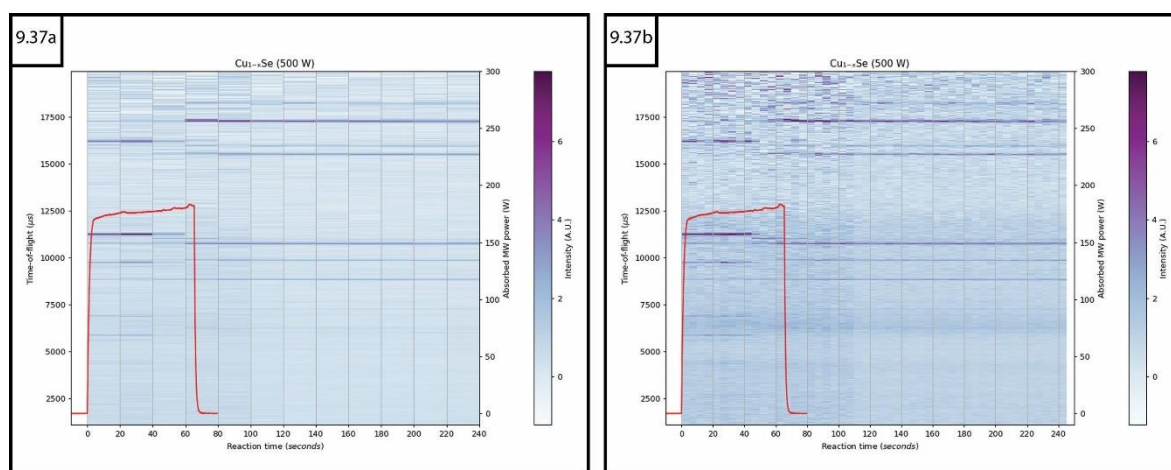


Figure 9.37: Colourmap plots of sliced event mode TOF data with absorbed MW power overlaid for Cu_{1-x}Se heated using 500 W forward power for 65 s a) data processed as 20 s sections b) data processed as 5 s sections

The favourable MW absorption compared to the benchtop experiments is more in line with the expected behaviour of samples containing Cu powder as indicated by the impedance measurements discussed in sections 9.3.5–9.3.6. Based on the results of the first experiment, all further $\text{Cu}_{1-x}\text{Se}_{1-y}\text{Z}_y$ samples were heated using 300 W forward power.

9.8.1 $Cu_{1-x}Se_{1-y}Te_y$ *in-situ* TOF data

The non-stoichiometric nature of copper selenides makes accurate characterisation of sample phases difficult as established in chapter 8. However, the event mode data obtained present with a reasonably high signal to noise ratio in the powder patterns.

Refinement of the 20 s sliced $Cu_{1-x}Se$ data confirm the observations from the colourmap that the reaction pathway runs to completion in the 40–60 s section following thermal runaway. A mixed phase material is produced with peaks attributed to hexagonal ($P6_3/mmc$) $Cu_{1-x}Se$ and cubic ($Fm\bar{3}m$) $Cu_{2-x}Se$. The post reaction histogram data showed that the final composition was for a dual phase mixture of $P6_3/mmc$ $Cu_{1-x}Se$ (81(6) wt.%) and orthorhombic ($Pnmm$) $Cu_{1-x}Se_2$. The refined crystallography data for the $P6_3/mmc$ $Cu_{1-x}Se$ phase of these 20 s sliced event mode TOF data are available in appendix section A–9.9.

The second sample ampoule containing the starting material for the $Cu_{1-x}Se_{0.8}Te_{0.2}$ synthesis was accidentally dropped, spilling the contents while preparing for the experiment and so no *in-situ* data was collected for it. A comparison plot of the remaining $Cu_{1-x}Se_{1-y}Te_y$ post reaction histogram data is shown in figure 9.38. The structure peaks for $Pnmm$ $Cu_{1-x}Se_2$ seen in the $Cu_{1-x}Se$ data are not present in any of the Te-doped samples, indicating a suppression of certain phases in the presence of Te. The $P6_3/mmc$ phase peaks are no longer present in samples where for Te-doping $x \geq 0.4$, being supplanted when the $Fm\bar{3}m$ structure became the primary phase.

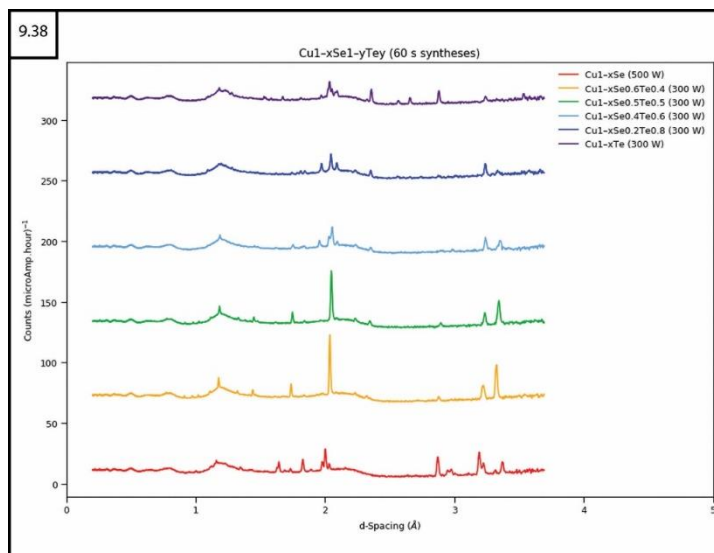


Figure 9.38: Comparison waterfall plot of $Cu_{1-x}Se_{1-y}Te_y$ synthesised using 300 W forward power for 60s post reaction histogram TOF data

Each of the $\text{Cu}_{1-x}\text{Se}_{1-y}\text{Te}_y$ sample data proved difficult to successfully converge adjustments to the site occupancies, with the most successful fits being achieved by leaving the Cu and Se site occupancies unchanged. The crystallographic parameters that were able to be refined demonstrate the preferential formation of the $Fm\bar{3}m$ phase with increasing Te-doping up to $x = 0.5$, as shown in figure 9.39. The Cu_{1-x}Te sample formed in the orthorhombic ($Pm\bar{m}nS$) phase, leaving almost half the starting material unreacted as with most of the other highly Te-doped samples.

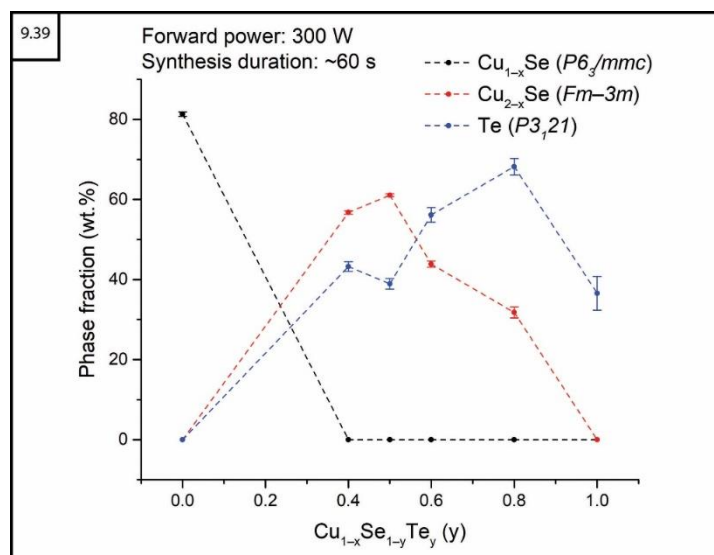


Figure 9.39: Plot of relative phase fractions against intended Te content for $\text{Cu}_{1-x}\text{Se}_{1-y}\text{Te}_y$

The refined crystallography data of these $\text{Cu}_{1-x}\text{Se}_{1-y}\text{Te}_y$ post reaction histogram data are available in appendix section A-9.10.

Each of the samples showed a consistent reaction timing where the product phases begin to appear ~ 40 s after the start of thermal runaway. As can be seen in figure 9.40, the resolution of the data processed into 5 s sections was very poor and noisy until ~ 40 s after heating was ceased. In fact, with Te-doping for $x > 0.5$, the structure patterns were extremely faint even for data processed as 20 s sections until after a couple of minutes cooling. The Te-doped phases require longer to crystallise and so any future studies using the Polaris-SMC reactor should extend the event mode collection further into the cooling period to build a more robust picture of the reaction pathways.

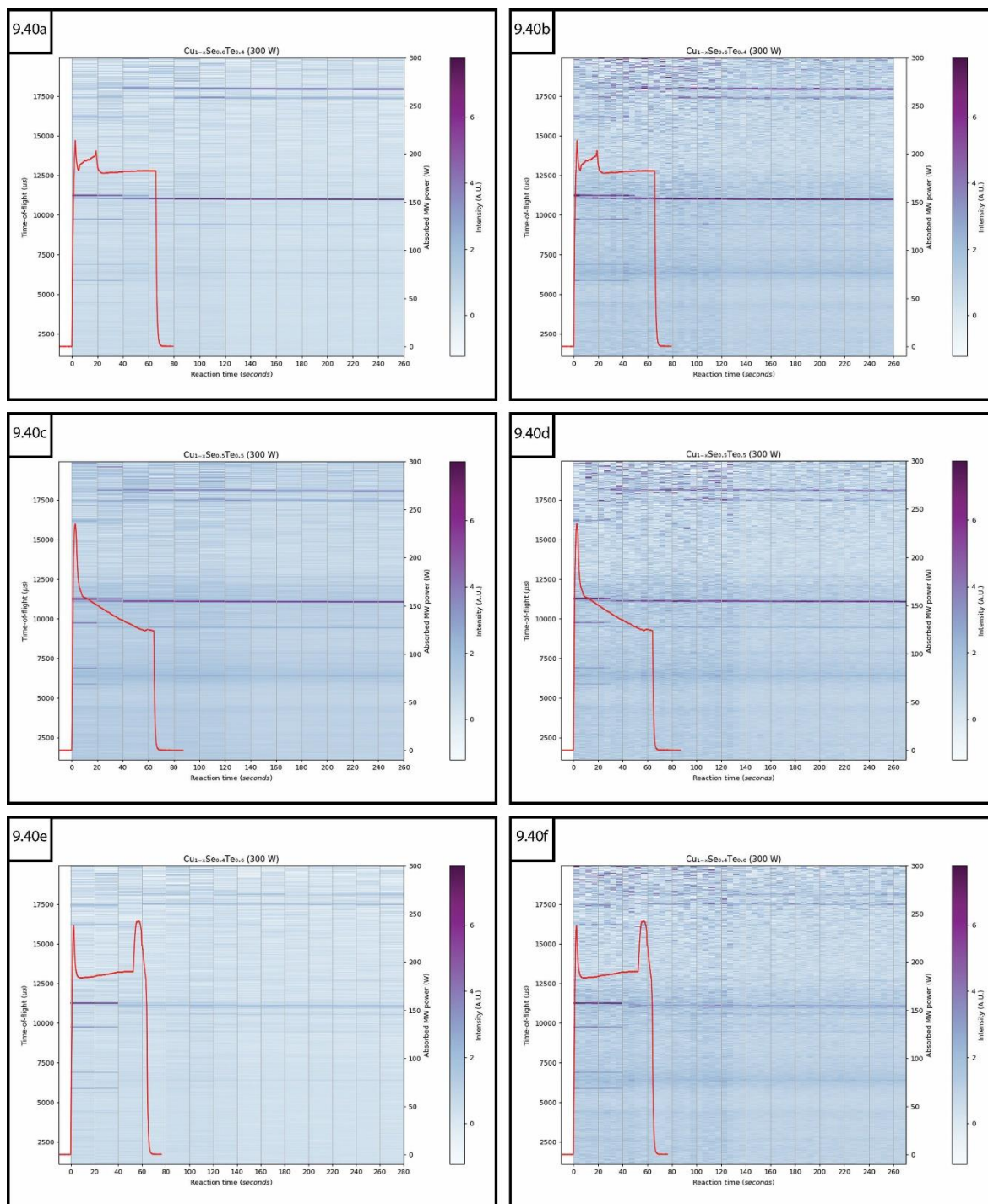


Figure 9.40: Colourmap plots of sliced event mode TOF data with absorbed MW power overlaid for $\text{Cu}_{1-x}\text{Se}_x\text{Te}_{1-y}$ samples heated using 300 W forward power for a) 66 s synthesis of $\text{Cu}_{1-x}\text{Se}_{0.6}\text{Te}_{0.4}$ processed as 20 s sections and b) 5 s sections c) 64 s synthesis of $\text{Cu}_{1-x}\text{Se}_{0.5}\text{Te}_{0.5}$ processed as 20 s sections and d) 5 s sections e) 64 s synthesis of $\text{Cu}_{1-x}\text{Se}_{0.4}\text{Te}_{0.6}$ processed as 20 s sections and f) 5 s sections

The improved resolution of the event mode data in the sample cooling period allowed for easier refinement when processed into 5 s sections. The event mode data for $\text{Cu}_{1-x}\text{Se}_{0.6}\text{Te}_{0.4}$ in the 80–100 s section (Figure 9.41) was characterised; table 9.12 shows the fluctuating phase fraction of the preferred $Fm\bar{3}m$ Cu_{2-x}Se crystal structure. The second most prominent phase identified was unreacted Te, indicating that Te-doping of the chalcogen site of this system is not favourable.

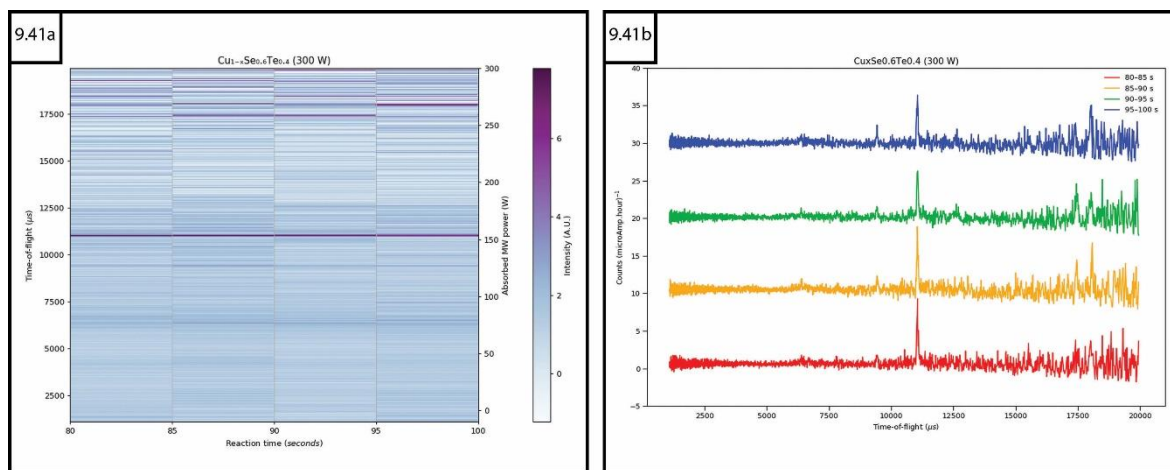


Figure 9.41: Sliced event mode TOF data processed as 5 s sections with absorbed MW power overlaid for $\text{Cu}_{1-x}\text{Se}_x\text{Te}_{0.4}$ heated using 300 W forward power for 66 s a) colourmap plot and b) waterfall plot of 80–100 s section of synthesis

The fluctuations in the calculated phase fraction of the $Fm\bar{3}m$ Cu_{2-x}Se phase are most likely the result of the noisy background rather than a true reflection of the synthesis route and should be considered with scepticism.

Table 9.12: Crystallographic cell parameters from Rietveld refinement of sliced $\text{Cu}_x\text{Se}_{0.6}\text{Te}_{0.4}$ event mode TOF data (80–100 s)

Data time-slices (s)	80–85	85–90	90–95	95–100
Main phase	$\text{Cu}_{1.8}\text{Se}_{1-y}\text{Te}_y$	$\text{Cu}_{1.8}\text{Se}_{1-y}\text{Te}_y$	$\text{Cu}_{1.8}\text{Se}_{1-y}\text{Te}_y$	$\text{Cu}_{1.8}\text{Se}_{1-y}\text{Te}_y$
Crystal system	Cubic	Cubic	Cubic	Cubic
Space group	$Fm\bar{3}m$	$Fm\bar{3}m$	$Fm\bar{3}m$	$Fm\bar{3}m$
Phase fraction (wt.%)	97(2)	55(1)	58(2)	68(1)
Observations	1949	1952	1953	1942
Variables	42	45	47	46
R_{wp}	0.1886	0.1894	0.1840	0.1912
R_p	0.3072	0.3097	0.2972	0.2976
χ^2	0.6272	0.6773	0.6647	0.6455

The 40–60 s section of the $\text{Cu}_{1-x}\text{Se}_{0.4}\text{Te}_{0.6}$ sample event mode data when processed as 5 s sections confirmed the generation of the $Fm\bar{3}m$ structure as the main phase over this period, despite the extremely low resolution of the powder pattern peaks seen in figure 9.42.

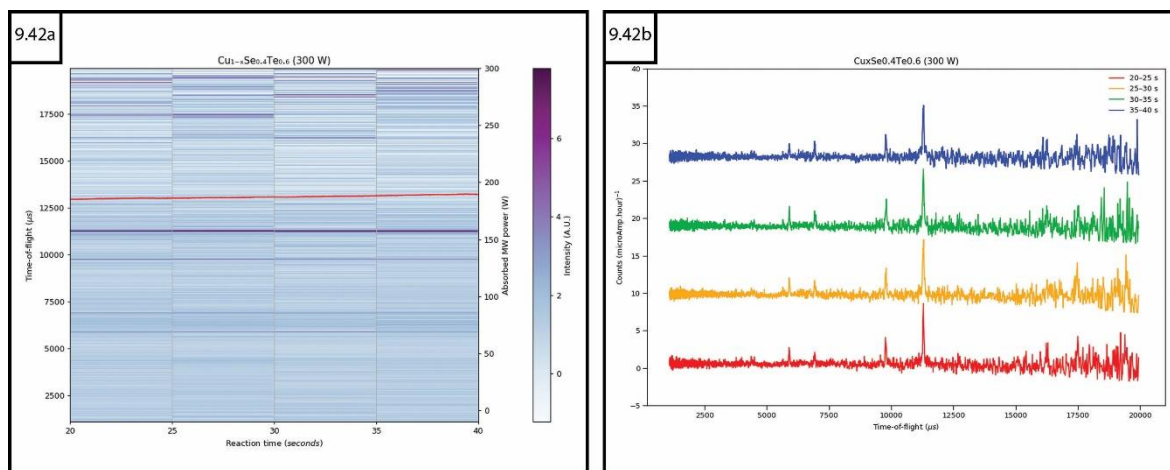


Figure 9.42: Sliced event mode TOF data processed as 5 s sections with absorbed MW power overlaid for $\text{Cu}_{1-x}\text{Se}_x\text{Te}_{0.6}$ heated using 300 W forward power for 64 s a) colourmap plot and b) waterfall plot of 40–60 s section of synthesis

Refinement of the chalcogen site fractional occupancy for Te-doping was only able to be converged for the 55–60 s section as shown in table 9.13 however, the calculated Te inclusion was very low.

Table 9.13: Crystallographic cell parameters from Rietveld refinement of sliced $\text{Cu}_x\text{Se}_{0.4}\text{Te}_{0.6}$ event mode TOF data (40–60 s)

Data time-slices (s)	40–45	45–50	50–55	55–60
Refined site occupancy (Te)	—	—	—	0.1(9)
Main phase	$\text{Cu}_{1-x}\text{Se}_{1-y}\text{Te}_y$	$\text{Cu}_{1.8}\text{Se}_{1-y}\text{Te}_y$	$\text{Cu}_{1.8}\text{Se}_{1-y}\text{Te}_y$	$\text{Cu}_{1.8}\text{Se}_{0.96}\text{Te}_{0.04}$
Crystal system	Hexagonal	Cubic	Cubic	Cubic
Space group	$P6_3/mmc$	$Fm\bar{3}m$	$Fm\bar{3}m$	$Fm\bar{3}m$
Phase fraction (wt.%)	28(5)	37(6)	78(4)	50(1)
Observations	1946	1959	1954	1945
Variables	43	45	39	45
R_{wp}	0.1891	0.1928	0.1798	0.1980
R_p	0.3071	0.3300	0.3066	0.3191
χ^2	0.6497	0.6984	0.6891	0.6704

9.8.2 $\text{Cu}_{1-x}\text{Se}_{1-y}\text{S}_y$ in-situ TOF data

Based on the results of the first Cu_xSe experiment and the success of the antimony and bismuth chalcogenide syntheses, the $\text{Cu}_{1-x}\text{Se}_{1-y}\text{S}_y$ pellet samples were heated using 300 W forward power and reacted to completion without the need for a graphite susceptor. A comparison waterfall plot of the post reaction histogram data (Figure 9.43) shows significant peak broadening and gradual shifting to lower d -spacing with increased S-doping as expected. The extreme peak broadening indicates the effect of severe defects in the structure, most likely deficiencies in the Cu site along with chalcogen substitution; however, as a result, satisfactory convergence of the site occupancies was difficult.

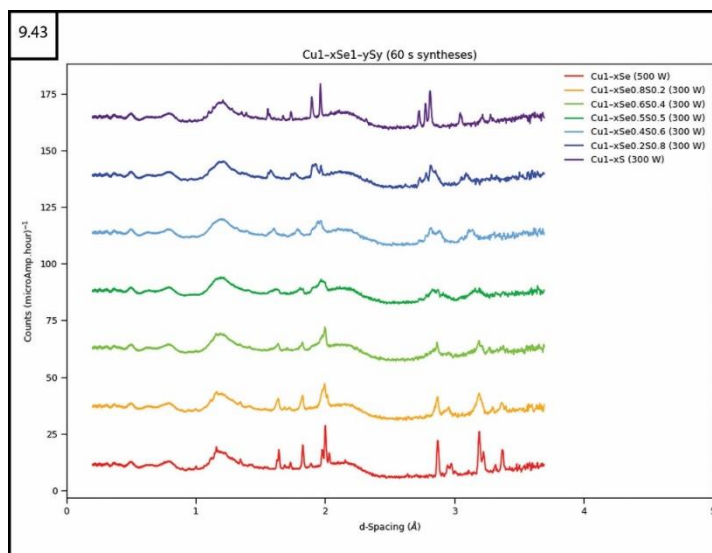


Figure 9.43: Comparison waterfall plot of $\text{Cu}_{1-x}\text{Se}_{1-y}\text{S}_y$ synthesised using 300 W forward power for 60 s post reaction histogram TOF data

The main phase obtained at the end of each synthesis was attributed to hexagonal ($P6_3/mmc$) $\text{Cu}_{1-x}\text{Se}_{1-y}\text{S}_y$ with additional prominent peaks that were unable to be indexed against any of the expected crystal structures. The $P6_3/mmc$ structure is one shared by both the selenide and sulfide, and so the increasing S content of the starting mixture likely drives the reaction towards this configuration rather than competing structures as with the $\text{Cu}_{1-x}\text{Se}_{1-y}\text{Te}_y$ series. The refined crystallography data of these $\text{Cu}_{1-x}\text{Se}_{1-y}\text{S}_y$ post reaction histogram data are available in appendix section A–9.11.

The initial $\text{Cu}_{1-x}\text{Se}_{1-y}\text{S}_y$ experiments produced event mode data with much less defined powder pattern peaks across the whole range of samples compared to the $\text{Cu}_{1-x}\text{Se}_{1-y}\text{Te}_y$ data (Figure 9.44). The low resolution of the event mode data means that full characterisation of the reaction progression was impossible, with the only concrete conclusion being that the product phases only become identifiable suddenly in >20 s after heating has ceased.

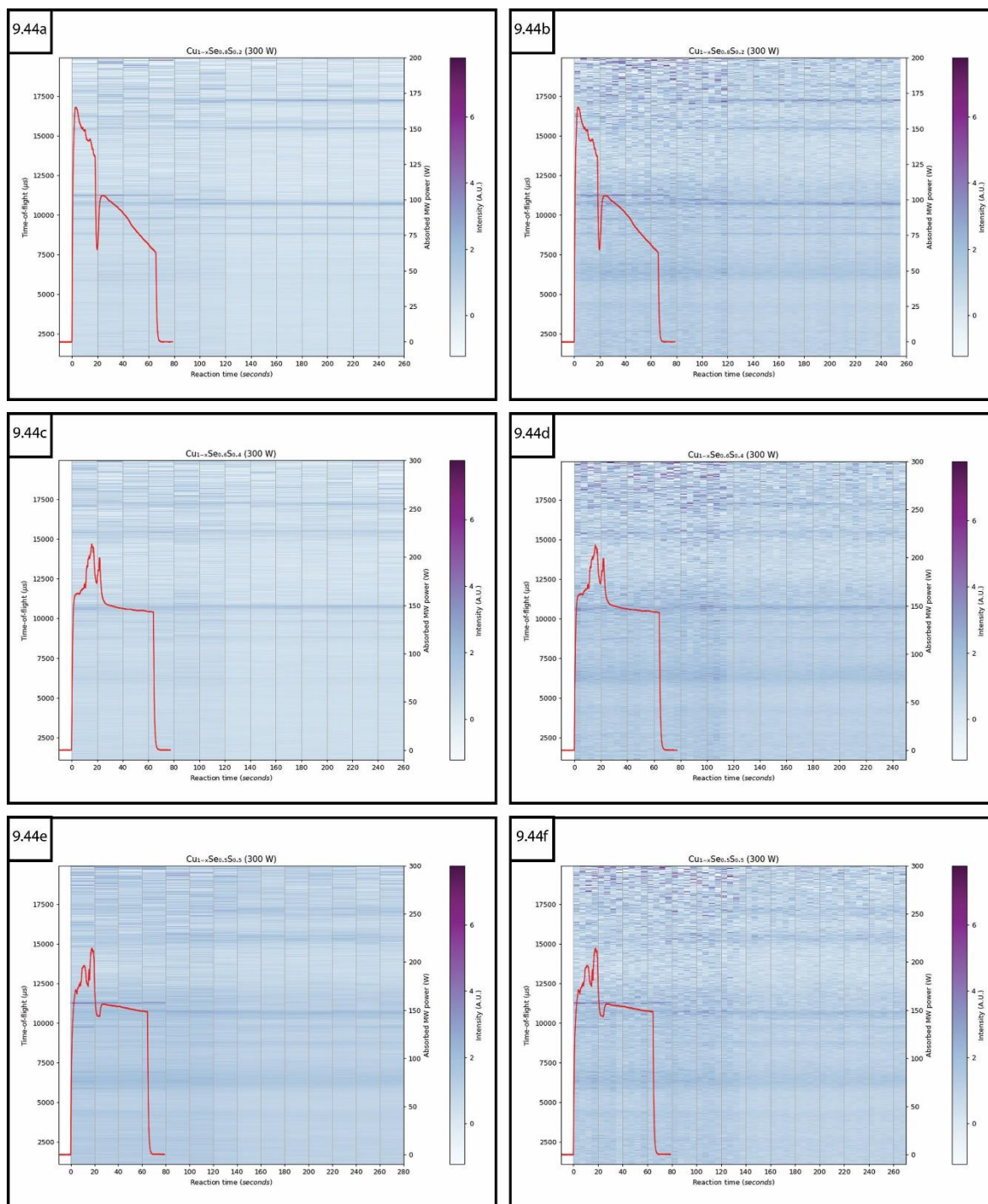


Figure 9.44: Colourmap plots of sliced event mode TOF data with absorbed MW power overlaid for $\text{Cu}_{1-x}\text{Se}_{1-y}\text{S}_y$ samples heated using 300 W forward power for a) 66 s synthesis of $\text{Cu}_{1-x}\text{Se}_{0.8}\text{S}_{0.2}$ processed as 20 s sections and b) 5 s sections c) 64 s synthesis of $\text{Cu}_{1-x}\text{Se}_{0.6}\text{S}_{0.4}$ processed as 20 s sections and d) 5 s sections e) 65 s synthesis of $\text{Cu}_{1-x}\text{Se}_{0.5}\text{S}_{0.5}$ processed as 20 s sections and f) 5 s sections

The powder pattern resolution was seen to improve in each $\text{Cu}_{1-x}\text{Se}_{1-y}\text{S}_y$ sample late in the cooling period, as the final $P6_3/mmc$ structure crystallises. It would therefore be recommended that future investigations with copper chalcogenides extend the event mode neutron collection window further into the cooling period and compare the effect of a range of synthesis durations from 20 s to 120 s on final composition. The subproject results also indicated that the $\text{Cu}_{2-x}\text{Se}_{1-y}\text{Z}_y$

structure is more stable as a single phase product and so the reaction stoichiometry should be adjusted to favour increased Cu occupancy.

9.9 Summary

The precise synthesis duration of Te-doped $\text{SnSe}_{1-x}\text{Te}_x$ increases from ~ 20 s to ~ 60 s when the forward power used was reduced from 500 W to 100 W. Reactions were shown to continue during the sample cooling period, with final phase pure compositions only appearing 20–40 s after MW heating had ceased. In contrast, the S-doped $\text{SnSe}_{1-x}\text{S}_x$ samples required a longer synthesis duration of consistently ~ 60 s before the single phase orthorhombic products were produced.

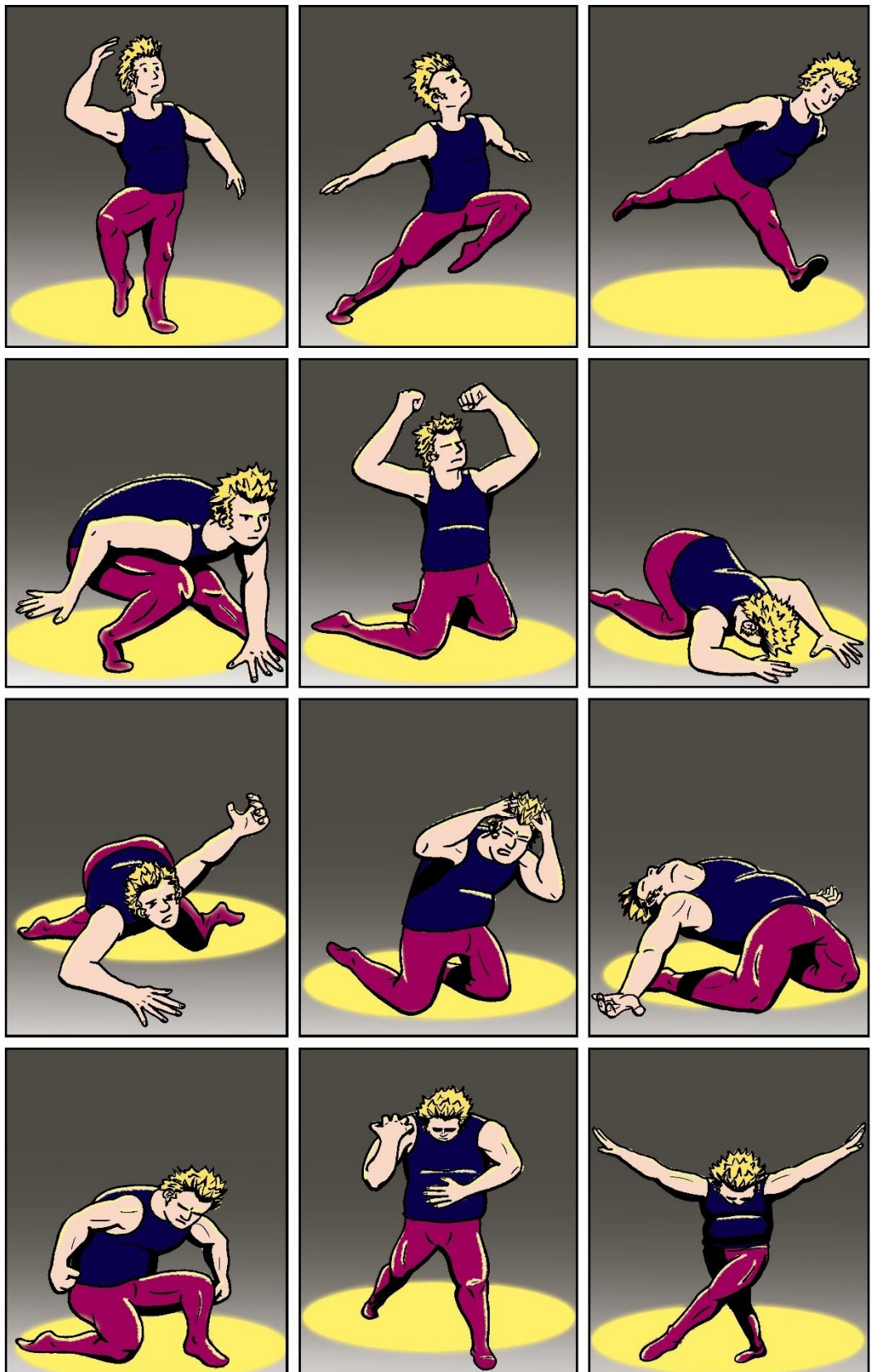
To ensure successful synthesis of $\text{Bi}_2\text{Se}_{3-x}\text{Te}_x$ solid solutions, stricter measures are required to prevent the starting Bi powder from becoming oxidised prior to direct MW-heating. The colourmap/power profile correlations indicated that extending the heating duration does not improve the phase purity of the target materials which mostly form during the sample cooling stage. Adjusting synthesis duration for samples without oxide impurities may affect the extent of Te-doping however, future work should focus on limiting heating to 10–20 s where the greatest amount of MW absorption is consistently observed. The extreme step change in MW absorption of most samples would be an ideal input to automate heating duration based on real time MW power data from the DAQ.

The ratio of $Pnma$ to $R\bar{3}m$ structures in the $\text{Sb}_2\text{Se}_{3-x}\text{Te}_x$ solid solutions was shown to be tuneable by lengthening synthesis duration. The solid solution matrix tends to favour the $R\bar{3}m$ phase at higher Te-doping however, the $Pnma$ phase was sustained up to Te-doping of $x = 1$ by increasing the heating time from 60 s to 120 s. Further work to investigate the extent of heating times >120 s may facilitate control of the solid solution composition beyond 30 % Te-doping.

As with the antimony chalcogenides the resolution of the *in-situ* neutron data for the $\text{Cu}_{1-x}\text{Se}_{1-y}\text{Z}_y$ series was very low, preventing detailed investigation of the reaction progression or correlation with the clear step changes in MW absorption. Future work with both of these systems could attempt to follow the reaction pathway and tune the solid solution composition by gently heating the samples (lower MW power) over a wider range of times and extending the event mode neutron collection window further into the cooling period.

10 Summary and suggested future work

10.1 Explaining the thesis with interpretative dance



10.2 Summary of novel project outcomes

The experimental design of the direct MW-heating method for solid state inorganic reactions is based on established procedures from the literature. Conducting MW-induced syntheses within a neutron diffractometer to obtain time resolved *in-situ* data however, is a new approach to investigating these processes. By carefully recording the MW power in the waveguide using a DAQ module, time dependent events such as phase transitions have been correlated with MW absorption in the samples. In some instances, it was possible to confirm the effect of extending heating duration on final product composition and control the level of doping in mixed phase structures.

The Polaris-SMC reactor system was designed to make the most out of the rapid data collection capabilities of the Polaris neutron diffractometer. The sample insertion apparatus, used to lower sealed ampoules of starting material into the centre of the waveguide and hold it in the path of the neutron beam, was redesigned to accommodate larger quartz ampoules. This maximised the sample volume to achieve better coupling with the MW standing wave mode and provided more coverage for the incident neutron beam cross section to interact with. The optimal sample parameters to successfully synthesise each of the binary metal chalcogenides was determined through individual subprojects.

10.2.1 Chapter 7: tin chalcogenide subproject

Undoped SnSe was already known from the literature to be a high performance TEM in both single crystal and polycrystalline form. The conventional synthesis approaches, e.g., Bridgman method of producing high quality single crystals is both time and energy intensive. No direct MW-heating in the solid state has been reported for tin chalcogenides in the past, so efforts to achieve phase pure samples in this way would offer an economical manufacturing alternative for this material. As a result, very high purity polycrystalline SnSe was achieved through the use of 10 % excess Sn in the reactant mixture, with a total heating time of ~1–5 mins (accounting for induction period) using only 400–500 W of incident MW power.

The reaction parameters necessary for a range of Te-doped $\text{SnSe}_{1-x}\text{Te}_x$ samples were determined to be optimal for only 30 s of heating following thermal runaway when using 500 W forward power. The S-doped $\text{SnSe}_{1-x}\text{S}_x$ samples had

longer induction periods due to the insulating nature of sulfur powder reducing the heating rate. The full range of samples was able to be produced in a reasonable timeframe of 30–90 s when using 100 W forward power with the aid of a graphite susceptor. A small selection of samples from each set of solid solutions was able to be hot-pressed into pellets to directly measure the TE properties (thermal conductivity, electrical conductivity and electrical resistivity) in collaboration with Dr Bos' research group at Heriot Watt University. The TE figure of merit in each was disappointingly calculated to be less than unity however, the material is anisotropic and analysis was only performed along a single axis. The TE efficiency did improve through chalcogen doping; and the best result was obtained for $\text{SnSe}_{0.46}\text{S}_{0.54}$ with a maximum $zT = 0.069$ at 702 K.

10.2.2 Chapter 8: other binary metal chalcogenides

Synthesis of bismuth chalcogenides was known to be possible using the direct MW-heating method from literature and so the goal of this subproject was to enhance Te-doping of the $\text{Bi}_2\text{Se}_{3-x}\text{Te}_x$ solid solution by controlling the synthesis parameters. Failures in the experimental design led to all the samples being contaminated with oxide or oxychalcogenide phases. The solid solutions were therefore unable to be tuned however, it was shown that undoped Bi_2Se_3 would degrade when heated using 100 W forward power with the aid of a graphite susceptor for >90 s. Conversely, undoped Bi_2Te_3 showed little change in phase fraction distribution regardless of heating duration >60 s.

Antimony chalcogenides (Sb_2Se_3 and Sb_2Te_3) have been previously synthesised using the same direct MW-heating method. A series of $\text{Sb}_2\text{Se}_{3-x}\text{Te}_x$ samples were successfully produced using 100 W forward power with the aid of a graphite susceptor for 60–120 s. The samples produced a consistent mixed phase solid solution that transitions from $Pnma$ to $R\bar{3}m$ structures with increasing Te-doping of the chalcogen sites. The $Pnma$ phase showed greater structural distortion by incorporating a greater amount of Te than the $R\bar{3}m$ structure up to a limit of $x = 0.6$.

Copper chalcogenides are non-stoichiometric in nature due to the liquid-like behaviour of Cu atoms forming deficiency defects in the possible crystal structures. No previous direct MW-heating of solid state samples were reported and so both Cu_{1-x}Se and Cu_{2-x}Se polymorphs were verified to be produced using

this method. The Cu_{2-x}Se samples were shown to be more stable as in a single phase while Cu_{1-x}Se tended to contain hexagonal ($P6_3/mmc$) Cu_{1-x}Se , tetragonal ($P\bar{4}2_1m$) $\text{Cu}_{2-x}\text{Se}_3$ and orthorhombic ($Pnmm$) $\text{Cu}_{1-x}\text{Se}_2$ phases. Control of the $\text{Cu}_{1-x}\text{Se}_{1-y}\text{Te}_y$ system phase composition was unsuccessful due to the non-stoichiometric effect of multiple potential space groups however, the $\text{Cu}_{1-x}\text{Se}_{1-y}\text{S}_y$ samples were produced with higher phase fractions of the target products in a mostly binary solid solution composition. For direct MW-heating, the S-doped $\text{Cu}_{1-x}\text{Se}_{1-y}\text{S}_y$ samples were particularly volatile and prone to fast spontaneous reactions during preparation unless first cold-pressed into pellet form.

10.2.3 Chapter 9: *in-situ* neutron diffraction studies

The Polaris-SMC *in-situ* reactor commissioning experiments provided a large number of datasets within a very short period of time. The nature of the chemical reaction pathways had a strong influence on the quality of the data obtained from the Polaris detector banks; more so than the rapidity of the MW-induced reactions. Even at extremely low powder pattern resolutions, it was possible in most cases to confirm basic phase changes in the time resolved neutron data when correlated with the MW absorption profiles. These in turn gave precise synthesis duration parameters otherwise unavailable in *ex-situ* or PXRD studies. Generally, MW absorption during thermal runaway was more prone to fluctuations at high levels of forward power (500 W) compared to steadier absorption with less power. The minimum synthesis duration necessary for 5 g Te-doped $\text{SnSe}_{1-x}\text{Te}_x$ samples increases from ~20 s to ~60 s when the forward MW power used was reduced. This conclusion is backed up by the consistent ~60 s synthesis duration required for the single phase orthorhombic products to appear in the S-doped $\text{SnSe}_{1-x}\text{S}_x$ *in-situ* powder patterns.

The colourmap/power profile correlations of the $\text{Bi}_2\text{Se}_{3-x}\text{Te}_x$ solid solution samples demonstrated that all product phases for this system are formed more or less simultaneously (within a ~20 s window) in the early stages of heating. The reaction path appears to progress at a consistent rate and so extending the heating duration does not improve the phase purity of the target materials; which mostly form during the sample cooling stage regardless. Interference of bismuth oxide and oxychalcogenide phases prohibited a closer examination of the reaction pathways and how they might otherwise be affected by adjusting the synthesis parameters.

The *in-situ* neutron data showed that some systems require a longer cooling period after the initial heating before the target product crystallises, such as for the antimony chalcogenides. The incredible reduction of Bragg peak intensity during the heating period made full characterisation and inferring detailed information about the reaction schemes extremely difficult. The phase composition of the solid solution system that crystallised out from the reactions during sample cooling demonstrated that adjusting the heating duration provides more control over the end product than would otherwise be assumed. The mixed phase solid solution, heated without the use of a graphite susceptor and identified in the subproject as a ratio of $Pnma$ and $R\bar{3}m$ crystal structures, was able to be tuned by increasing the synthesis duration. Extending the heating from 60 s to 120 s increased the fraction of the $R\bar{3}m$ phase at low levels of Te-doping but also maintained a larger fraction of the $Pnma$ phase up to $x = 1$. Performing these syntheses without the need for a graphite susceptor eliminated the oxide impurities noted from the benchtop experiments.

The resolution of the *in-situ* neutron data for the $\text{Cu}_{1-x}\text{Se}_{1-y}\text{Z}_y$ series was extremely low for several minutes during and after heating, which prevented detailed characterisation of any intermediary reaction steps or correlation of phase changes with the clear step changes in MW absorption. Reaction progression was inferred to continue during the sample cooling period, with final phase compositions only appearing 20–40 s after MW heating had ceased.

The Polaris-SMC reactor has been successfully demonstrated to be a powerful tool for interrogating the rapid and volatile nature of solid state, MW-induced synthesis reactions. Were this information to be applied for commercial applications, a database of performance information for a variety of chemical systems would be invaluable. A single production line could be automated based on simple adjustments to reactant stoichiometry, incident MW power and synthesis duration in order to selectively tune the properties and performance of a desired TEM (or other inorganic material of interest).

10.3 Suggested future work

The TE figure of merit values for the $\text{SnSe}_{1-x}\text{Te}_x$ and $\text{SnSe}_{1-x}\text{S}_x$ samples that were tested were much lower than the typically acceptable level at unity. The anisotropic nature of these structures however, means that future experiments

using direct MW-heating should focus on hot pressing larger pellets of gram scale material. From these densified samples smaller pellets and bars can be cut along different axial planes relative to the pressing direction, allowing any preferred packing orientation in the polycrystalline sample to be accounted for.

Stricter control method should be used during all of the preparation steps for $\text{Bi}_2\text{Se}_{3-x}\text{Te}_x$ samples in order to eliminate sample contamination with oxide impurities. By doing so, it should be possible to investigate the extent of tuning the Te-doping that can be achieved through adjusting the synthesis parameters. In particular based on the MW absorption profiles that show discrete step changes over the course of heating, synthesis duration should be limited to the ~10–20 s period of thermal runaway where MW absorption is greatest.

The extent to which $\text{Sb}_2\text{Se}_{3-x}\text{Te}_x$ solid solution composition can be tuned beyond 30 % Te-doping by further extending synthesis duration is an area that could easily be explored. This knowledge would be invaluable for designing industrial scale MW reactor processes for synthesising bulk TEMs such as this, where tuning of the structure parameters can have a significant effect on their performance. Additional work on structure doping should be focussed on the *Pnma* phase which was shown to be more easily distorted with greater substitution of Te into the Se sites.

The Polaris-SMC reactor has shown it is capable of heating certain samples well enough that the powder pattern resolution is detrimentally affected by the material becoming amorphous. The use of a parametric Rietveld refinement method, such as has been proposed by Graham Stinton and John Evans may overcome this challenge. The method was developed specifically for diffraction data collected as a function of an independent variable, such as time, to enable the fitting to an evolving structural model[216]. Additionally, the experimental design should be adjusted to try heating more gently (reducing the forward power) at the expense of extending the induction period, varying the actual synthesis duration from the point of thermal runaway and extending the neutron collection window by several minutes into the sample cooling period. The extreme step change in MW absorption observed in many sample data should be looked at as opportunities to attempt automation of the heating duration based on real time monitoring of MW power data.

Appendix

A–1 Managing disruption as a result of the Covid-19 pandemic

Access to the Gregory group laboratory was restricted from Tuesday 17th March 2020, prior to the first mandatory lockdown enforced by the University of Glasgow chemistry department. All non-essential operations were shut down and made safe before the Joseph Black building was closed to staff and students on Wednesday 25th March 2020. It was necessary to pivot efforts on this project as much as practically possible from focussing on experimental work to data analysis, preparations for writing up and literature research. The university remained closed to researchers not actively working on the Covid-19 problem between phase one in March 2020 and the start of phase three on Wednesday 1st July 2020. Due to my reliance on public transport to commute for ~2 hr per day, Prof Gregory supported my concern for extra caution by continuing to work from home for an additional period of two weeks, returning in August 2020.

Upon returning to on-site working, safeguards were implemented across campus such as restrictions to the total number of people per room, mandatory face coverings while working indoors, strategically placed hand sanitisation stations and staggered working shifts for carrying out research work. Prof Gregory carried out a risk assessment for the safe return of researchers to the group laboratory, with specific measures identified for the C3-13 laboratory. Laboratory work was reinitiated over a rotating shift pattern of 2.5 days per week from Wednesday 17th July with Covid-19 COSHH amendments carried out for all experimental procedures to include sanitisation of equipment and workstations before and after use. This shift pattern remained in effect until January 2021 when a new lockdown was enforced within Scotland, resulting in several group members choosing to work from home full time. Prof Gregory approved my request to adjust the laboratory rota to enable my full time access every day of the week in order to finish subproject practical work and sample preparations for the planned Polaris-SMC reactor commissioning experiments prior to the rescheduled ISIS beamtime deadline in March 2021.

A–1.1 Equipment breakdowns and supply chain delays

The PANalytical X'Pert Pro MPD Diffractometer was out of commission for several weeks after staff were able to return to work due to a faulty X-ray tube.

Limited availability of technicians and supply chain problems delayed repair of the instrument until August 2020, after which booking slots were limited to a single person nominated to operate the instrument either in the mornings or afternoons. Shorter two-hour booking slots were only implemented from September 2020.

In September 2020 an inspection of the Gregory Group glassblowing workstation was carried out by John Liddell, Phil Rodger, Billy Russell and Ross Slavin. The review highlighted several recommendations for upgrades to improve safety and so operation of the glassblowing equipment was forbidden until the improvements had been implemented. John Liddell temporarily loaned the group a portable propane/oxygen blowtorch rig to allow experiments involving sealing quartz tubes to continue from January 2021 while awaiting the workstation upgrades. Several delays with obtaining/approving quotes, delivery of parts and availability of University of Glasgow Estates and Services staff impeded the completion of the minimum required safety upgrades to the glassblowing workstation until April 2021.

A-1.2 ISIS shutdown and user cycle postponement

The Polaris-SMC reactor commissioning experiments were initially planned to be carried out as part of the final user cycle prior to the anticipated long shutdown of the ISIS beamline for extensive upgrades (target station 1 and linac refurbishment project) in the final quarter of 2020. After the first national lockdown period was established, Dr Ron Smith confirmed that the planned ISIS shutdown window had been postponed. Once the ISIS user programme was resumed, approved experiments would be limited to simple operations without a complicated setup or technical support to allow for social distancing and safe operation by instrument scientists. External users were not allowed on site for the first round of initial experiment slots. Since this project necessitated significant setup of equipment with Dr Smith in attendance, access to beamtime allocation was postponed until a later batch of experimental slots. Dr Smith maintained regular contact regarding the continually changing ISIS deadlines and confirmed with Prof Gregory and I that the start of the ISIS long shutdown would be delayed from the proposed date of January to April 2021. ISIS operations confirmed in January 2021 that the planned user run cycle was to be held from the end of April through mid-June 2021 with the start of the long

shutdown postponed once more to June 2021. A site access request was finally approved to attend and setup/test the Polaris-SMC reactor configuration between Monday 22nd February and Friday 26th February 2021. A beamtime request was approved to attend and carry out the *in-situ* experiments between Monday 17th May and Sunday 23rd May 2021. These experiments were interrupted due to a component failure of the synchrotron resulting in lost beamtime as discussed in section A-9.1. A final week-long visit was approved to complete the series of *in-situ* experiments between Monday 7th June and Friday 11th June 2021.

A-1.3 Managing the effects of the Covid-19 pandemic on mental health

Depression has affected my mental health throughout my adult life however, it was manageable prior to the Covid-19 pandemic without pharmaceutical or therapeutic intervention. Management of symptoms was largely achieved through maintaining a regular schedule, in particular a consistent sleep pattern, regular home cooked meals, moderate regular exercise and a strict work-life balance. These management strategies were severely disrupted due to the stress and anxiety caused by the escalating Covid-19 pandemic, associated uncertainty with the scope of the PhD project, a heavier financial burden and a breakdown of the work-life relationship due to the shift to working from home. This led to increasing difficulties with focus and motivation when attempting to continue working on the project as well as disruption to normal means of relaxation and destressing. Additional anxiety was caused when adjusting to a resumed commute using public transport after months of isolation.

My mental health status was disclosed to Prof Gregory in July 2020 when my anxiety about returning to the laboratory was high, who advised contacting the University of Glasgow disability service and informing them about my situation. The student counselling service advised that when applying for an extension and completing a good cause form, a diagnosis by my general practitioner (GP) or NHS surgery would possibly be necessary for evidence. I was given a phone consultation with my GP in September 2020, who confirmed that the symptoms I described indicated mild to moderate depression and information about the options available for treatment were discussed. I was only able to begin weekly talking therapy phone sessions through an external, self-referred service (Lifelink) from December 2020 until April 2021. The University of Glasgow

disability service required a signed letter from my GP that provided evidence of disability. After several hurdles, the evidence was sent in December 2020 and the disability service needs assessment was carried out in February 2021. The University of Glasgow Counselling and Psychological Services (CaPS) provided talking therapy phone sessions on a weekly basis from that point until the completion of the PhD project.

A-1.4 Financial burdens and request for funded extension to project

The instigation of lockdown caused job losses and economic stagnation around the globe. My partner was searching for a new job in March 2020 when the process was interrupted by the pandemic, which resulted in my PhD stipend becoming the sole source of income for the household. The monthly amount was slightly more than the eligible limit for hardship loans from either the University of Glasgow or Royal Society of Chemistry. Once I returned to the laboratory in August 2020, the restricted shift pattern negated the cost saving benefits of my student discount for travel. The commute distance, being several miles, was significant enough that alternative options such as walking were not feasible.

The unavoidable delays that led to the postponement of beamtime access made a significant extension to the PhD project a necessity. Dr Smith and Martin Owen Jones confirmed in May 2020 that ISIS would support an extension to the PhD for up to six months provided the host university would provide half of the financial support. Applications to the University for funded extensions in response to Covid-19 disruptions were staggered based on the original expected end date of the projects. This project was only considered within the final round of funded extension applications, announced in March 2021, with a six-month extension finally being approved in May 2021. The extent of the data analysis required, following the Polaris-SMC reactor commissioning experiments along testing the thermal and electrical properties of selected samples, necessitated a further non-funded extension period of six months during which time I was supported only by limited personal savings.

A-4 Chapter 4 supplementary material

A-4.1 *Sample heating using a bespoke single mode cavity (SMC) reactor*

The order of operations for using the benchtop SMC microwave reactor:

1. Water supply to isolator switched on
2. Mains switch for power cable extension and Windows 10 workstation switched on
3. WinDAQ software for power monitoring and Modline software for IR thermometer monitoring initialised
4. Power meter and power supply (power level set to 0) switched on
5. Both switches on auto tuner (power and auto tune) switched on
6. Sample inserted into applicator
7. Forward power level chosen on power meter (dial)
8. Testmate MW-100 microwave leak detector switched on
9. Dummy interlock inserted into magnetron head
10. Start recording forward and reflected power using WinDAQ software
11. Microwave start button on magnetron switched on
12. Once heating finished, magnetron switched off with microwave stop button
13. Stop recording forward and reflected power using WinDAQ software
14. Save temperature data from Modline software
15. Sample allowed to cool to room temperature before retrieval of contents

A-4.2 *Collecting pre reaction, in-situ and post reaction neutron data*

Once the Polaris-SMC reactor has been assembled in the Polaris access well and the orientation of directional components are confirmed, the order of operations for preparing the initial experiment is:

1. Water pump switched on and checked for leaks
2. Auto tuner power supply and power meter switched on at control panel
3. Laptop switched on and WinDAQ software for power monitoring opened
4. Switch off and remove interlock key from control panel
5. Disconnect orange and yellow cables from jog box before entering Polaris well
6. Insert graphite sample into quartz support tube and secure in ampoule block
7. Enter Polaris access well
8. Both switches on auto tuner (power and auto tune) switched on

9. Ensure magnetron head dial is set to “0” and switch is set to “power supply”
10. Insert graphite sample into sample applicator using quick release stick
11. Exit the Polaris well and secure gate, then reconnect jog box cables
12. Switch on power supply at control panel
13. Ensure power supply dial is set to “0”
14. Switch on Testmate MW100 microwave leak detector
15. Insert interlock key in control panel and switch on
16. Switch on magnetron head (green button) from outside the access well
17. Increase power supply dial to desired forward power
18. Adjust short circuit until display on power meter matches the dial value
19. Adjust the WinDAQ software engineering units and recalibrate if necessary
20. Switch off magnetron head (red button) from outside the access well

The order of operations for safely exchanging samples in the Polaris-SMC reactor is:

1. Switch off and remove interlock key from control panel
2. Disconnect orange and yellow cables from jog box before entering Polaris well
3. Replace previous ampoule in sample applicator with new experiment sample
4. Exit the Polaris well and secure gate

The order of operations for recording *in-situ* experiments in the Polaris-SMC reactor is:

1. Insert interlock key in control panel and switch on
2. Begin recording power interface data using WinDAQ software
3. Open Polaris shutter from control box
4. Record pre-reaction TOF histogram data for $\sim 15 \mu\text{A}$
5. Change neutron scan type to event mode and begin recording
6. Switch on magnetron head (green button) from outside the well using pole
7. Monitor forward and reflected power using WinDAQ software
8. Adjust forward power, if necessary, using power supply dial
9. Switch off magnetron head (red button) from outside the access well
10. Stop and save recorded power data using WinDAQ software
11. Allow event mode data to accumulate for an additional minute or two
12. Change neutron scan type back to histogram mode and begin recording
13. Record post-reaction TOF histogram data for $\sim 15 \mu\text{A}$

14. Close Polaris shutter from control box
15. Secure next experiment sample in second ampoule block
16. Switch off and remove interlock key from control panel
17. Enter Polaris access well and exchange ampoule in sample applicator
18. Exit the Polaris access well and secure gate
19. Check the radioactivity level of the removed sample using Geiger counter
20. Allow sample to cool to room temperature before handling
21. Label and store sample in active samples cabinet until activity level is safe

A-4.3 Calibration of a vector network analyser (VNA) for a waveguide

Specialised adaptors are used to calibrate a VNA for a waveguide system, including a flush short, i.e., a blank plate attached to a waveguide flange that causes total reflection in the waveguide and waveguide loads. Leaving an open waveguide will cause it to radiate like an antenna with an associated return loss. Instead, a $\frac{1}{4}\lambda$ spacer with a flush end (known as an offset short) causes the wave to pass through the spacer twice during reflection resulting in a 180° delay to meet the requirements of an open circuit[13]. These waveguide calibration adaptors were not available or known to be necessary at the time they were being used, hampered also by Covid-19 disruptions.

A-4.4 Covid-19 precautions at Rutherford Appleton Laboratories (RAL)

Provisions for external users to carry out work on site at Rutherford Appleton Laboratories (RAL) were put in place in the final quarter of 2020. Additional online training was required prior to building access being approved and to ensure new on-site restrictions and operational procedures were understood. Movement between site buildings was restricted to only the areas agreed with building supervisors and group leaders. Occupancy of all buildings was restricted significantly and corridors and access points signposted to facilitate a one-way traffic system. Toilets and certain small shared facilities were designated as single occupancy spaces. Physical distancing of 2 m was to be maintained at all times. Hand washing for at least 20 s using soap was encouraged regularly as well as using hand sanitiser provide at entrances and exits. A face covering was required when two or more people were working on the same task, where 2 m distancing was not possible and in all indoor communal areas. Contact time with others was minimised as much as possible

to limit the potential exposure. A limited number of rooms were made available at the site-adjacent Ridgeway hotel when external users were once more allowed to travel to site. Bedding and towels were not changed in the duration of the stay and morning and evening meals were delivered to the rooms rather than served in the communal dining room.

A-5 Chapter 5 supplementary material

A-5.1 Unit mesh tessellation

Tessellation limits the number of possible unit mesh shapes to 3-, 4- or 6-sided polygons as illustrated in figure A-5.1.

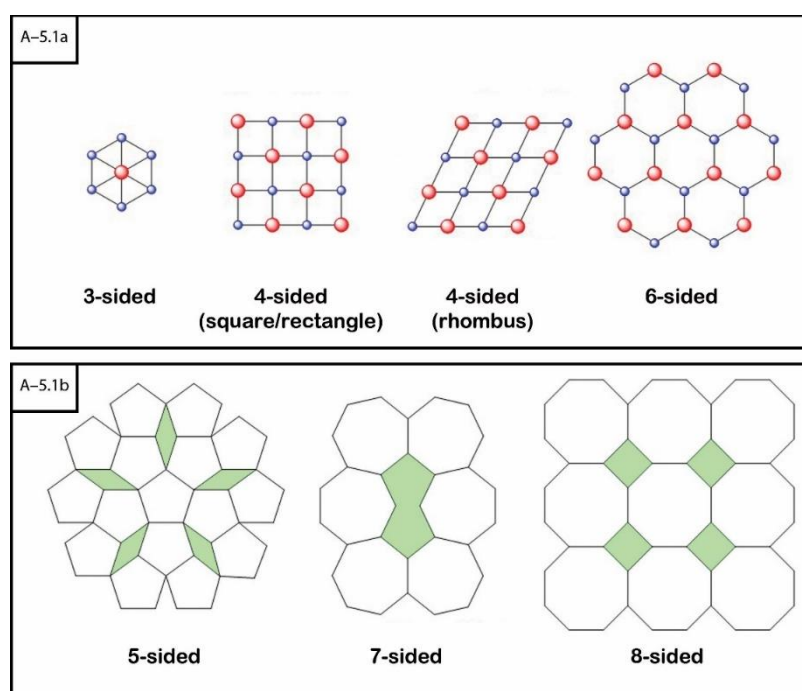


Figure A-5.1: a) Tessellated patterns formed from 3-, 4- and 6-sided unit mesh polygons b) 5-, 7- and 8-sided unit mesh polygons with empty untessellated space represented by green shading

A-5.2 Compound symmetry operations

Table A-5.1: Compound symmetry operations resulting from sequential simple operations [2]

	Rotation	Reflection	Inversion	Translation
Rotation	–	Roto-reflection	Roto-inversion	Screw rotation
Reflection	Roto-reflection	–	2-fold rotation	Glide reflection
Inversion	Roto-inversion	2-fold rotation	–	Inversion
Translation	Screw rotation	Glide reflection	Inversion	–

Roto-inversion axes (\bar{X}) are expressed as an integer representing one of the five possible rotation axes. Roto-reflection symmetry (S_x) implies the compound

operations occur in a plane normal to the axis and are already represented by other symmetry operations ($S_1 = m$, $S_2 = \bar{1}$, $S_3 = \bar{6}$, $S_4 = \bar{4}$ and $S_6 = \bar{3}$). Screw rotation features a handedness that does not apply to rotation or roto-inversion and is apparent only with both rotation and translation in the direction of rotation axes[2].

A-5.3 Unit cells and Bravais lattices

Primitive (*P*) unit cells are defined by lattice points solely occupying each vertex of the unit cell.

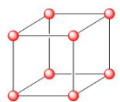
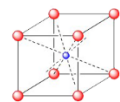
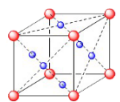
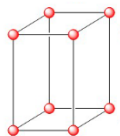
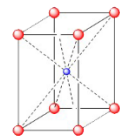
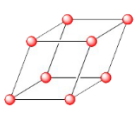
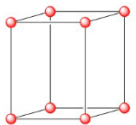
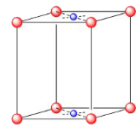
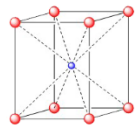
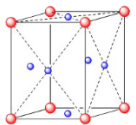
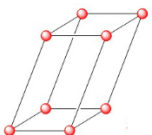
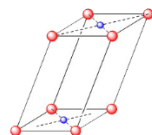
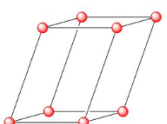
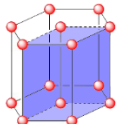
Base-centred (*A*, *B* or *C*) unit cells have lattice point occupation at every vertex, along with one pair of lattice points on the centre of opposing faces.

Body-centred (*I*) unit cells have lattice point occupation at every vertex, along with a single lattice point at the centre of the unit cell.

Face-centred (*F*) unit cells have lattice point occupation at every vertex, along with a single lattice point on the centre of each face.

Rhombohedral (*R*) unit cells are a type of primitive unit cell which have a 3-fold rotation axis diagonally across the body of the shape.

Table A-5.2: The 14 Bravais lattice structures and associated lattice parameters [2], [3]

Lattice	Lattice parameters	Primitive (P)	Base-centred (A, B or C)	Body-centred (I)	Face-centred (F)
Cubic	$a_0 = b_0 = c_0$ $\alpha = \beta = \gamma = 90^\circ$				
Tetragonal	$a_0 = b_0 \neq c_0$ $\alpha = \beta = \gamma = 90^\circ$				
Rhombohedral	$a_0 = b_0 = c_0$ $\alpha = \beta = \gamma \neq 90^\circ$				
Orthorhombic	$a_0 \neq b_0 \neq c_0$ $\alpha = \beta = \gamma = 90^\circ$				
Monoclinic	$a_0 \neq b_0 \neq c_0$ $\alpha = \gamma = 90^\circ$ $\beta \neq 90^\circ$				
Triclinic	$a_0 \neq b_0 \neq c_0$ $\alpha \neq \beta \neq \gamma \neq 90^\circ$				
Hexagonal	$a_0 = b_0 \neq c_0$ $\alpha = \beta = 90^\circ$ $\gamma = 120^\circ$				

The set of 14 Bravais lattices can be considered as resulting from translational symmetry operations of the unit cell.

A-5.4 Miller indices

Lattice planes which intersect the axes have intercept coordinates of m , n and p , which define the plane position; convention dictates the use of the smallest reciprocal of these coordinates, referred to as the Miller indices [2]:

$$h \sim \frac{1}{m} \quad k \sim \frac{1}{n} \quad l \sim \frac{1}{p}$$

The integer coordinates (uvw) and Miller indices (hkl) are related by sets of lines and planes that lie parallel to each other. The equation of any plane or set of

parallel lattice planes into which the Miller indices can be substituted to define their orientation with respect to the origin is given by[2]:

$$\frac{X}{m} + \frac{Y}{n} + \frac{Z}{p} = 1 \quad \text{(Equation A-5-1)}$$

$$hX + kY + lZ = C \quad \text{(Equation A-5-2)}$$

X, Y and Z = coordinates of points lying on the plane

Positive Miller indices ($C = +1$) describe the set of planes in positive axes directions while negative Miller indices ($C = -1$) describe planes in negative axes directions. Neutral Miller indices ($C = 0$) intersect through the origin[2].

A-5.5 $K\alpha$ and $K\beta$ electron transitions in X-ray tubes

Characteristic peaks in X-ray tube diffraction patterns correspond to the transition of electrons in the atomic core (ejected by the impact of electrons accelerated by the tube) to lower energy levels. The transitions occur from shells L to K or M to K, with the transitions being referred to as $K\alpha$ and $K\beta$ respectively. The $K\alpha$ transition consists of two characteristic wavelengths referred to as $K\alpha_1$ and $K\alpha_2$ radiation. The $K\beta$ transition is typically filtered out and consists of multiple discrete spectral lines close enough together so as to be typically indistinguishable[7].

The energy gap between levels is unique to different elements and therefore different anode materials will produce peaks at likewise unique wavelengths as shown in table A-5.3.

Table A-5.3: Characteristic wavelengths of five common anode materials[7]

Anode material	Wavelength (Å)			Suitable $K\beta$ filter
	$K\alpha_1$	$K\alpha_2$	$K\beta$	
Cr	2.28975(3)	2.293652(2)	2.08491(3)	V
Fe	1.93608(1)	1.94002(1)	1.75664(3)	Mn
Co	1.78900(1)	1.79289(1)	1.62082(3)	Fe
Cu	1.5405929(5)	1.54441(2)	1.39225(1)	Ni/Nb
Mo	0.7093171(4)	0.71361(1)	0.63230(1)	Zr

Copper is typically used as the anode material in powder diffraction instruments, while molybdenum is the preferred material for the anode in single crystal diffractometers. Single intense wavelengths are preferable for most diffraction applications and since the $K\alpha_1$ spectral line is double the intensity of $K\alpha_2$ and typically five times more than $K\beta$, it is usually selected for through the use of a monochromator device. Other anode materials can be utilised with the

understanding that there will be a trade off between increased range of observable Bragg peaks at the expense of decreased pattern resolution from reduced distance between individual peaks[7].

A-5.6 Polaris event mode data processing using Mantid Workbench

Each neutron experiment produces .raw (Raw) and .nxs (Nexus) data files that are named sequentially by the instrument run number in the form of POLARIS00#####. Once processed/normalised, new Nexus files are generated with a similar naming format: POLARIS#####.nxs. The recorded histogram data are processed with a simple script from the Raw and Nexus files to give the normalised diffraction patterns against TOF in three different file formats in the designated output file location. All five detector bank data sets are processed as a new Nexus file generated that can be read by the Mantid to plot the Raw data along with a .gsas file for later refinement and characterisation. A three-column x, y, sigma(y) .dat file is produced for each bank separately that can be read by most plotting software. Since the boron nitride shields attached to the Polaris-SMC reactor limit the diffraction angle, only data collected from bank four were of interest.

The Python script used to extract and process the Polaris-SMC reactor event mode data was written by Mantid developer Danny Hindson for operation with the Mantid Workbench software. In developing the script, Danny was able to identify a bug with the Mantid software that prevented the extraction and processing of event mode data recorded against time. A large selection of neutron counts were erroneously allocated to the final second of the list of events. Processing the data was delayed until an updated version of Mantid Workbench was released to address this issue.

The event mode Python script splits the neutron counts recorded in Nexus file format into discrete diffraction patterns against d -spacing that correspond to user-defined time intervals. The data are output as a series of .gsas, Nexus and .dat files, the maximum number of which are dependent on the specified duration of the sliced sections. The three user-defined parameters for processing the event mode data require identification of the reaction start time, calculating the duration of the induction period and determining the number of possible slices that can be obtained given a specified slice duration. The spreadsheet

shown in figure A-5.2 in which columns A–E and I were obtained from ISIS records of the Polaris instrument runs and used to determine all of these parameters.

A	B	C	D	E	F	G	H	I	J	K	L	M	N	O	P
Run No.	Title	µA	Start Date	Polaris Start (hh:mm:ss)	SMC Start (hh:mm:ss)	Microwave Absorption (hh:mm:ss)	SMC Finish (hh:mm:ss)	Polaris Finish (hh:mm:ss)	interesting_start (hh:mm:ss)	interesting_start (s)	Synthesis Time (hh:mm:ss)	Polaris Run - interesting_start	Polaris Run - interesting_start (s)	chunk_size (s)	number_chunks
129537	Glasgow ISIS microwave cell - empty - beam 20k x 15w	45.3953	Wed 19 May 2021	11:42:15				11:57:34							
129538	Glasgow ISIS microwave cell - empty - beam 30k x 15w	40.7678	Wed 19 May 2021	12:06:29				12:20:01							
129539	Glasgow ISIS microwave cell - empty - beam 35k x 15w	36.7362	Wed 19 May 2021	12:26:08				12:38:19							
129540	Glasgow ISIS microwave cell - empty - beam 32k x 15w	164.8199	Wed 19 May 2021	12:41:30				13:36:10							
129541	Glasgow ISIS microwave cell - empty - beam 25k x 10w (h offset +2.5)	73.7860	Wed 19 May 2021	13:47:12				14:11:56							
129542	Glasgow ISIS microwave cell - empty outer SiO2 tube	55.6078	Wed 19 May 2021	14:30:27				14:49:13							
129543	Glasgow ISIS microwave cell - 5mm depth graphite in outer SiO2 tube	132.6686	Wed 19 May 2021	14:57:11				15:41:19							
129544	Glasgow ISIS microwave cell - RMPOL1_Sn5e	29.0229	Wed 19 May 2021	16:16:02				16:26:01							
129545	Glasgow ISIS microwave cell - RMPOL1_Sn5e_500W_60s_Event_Mode	20.1519	Wed 19 May 2021	16:35:26	16:38:47	16:38:56	16:39:58	16:42:08	00:03:30	210	00:01:02	00:03:12	192	20	10
129546	Glasgow ISIS microwave cell - RMPOL1_Sn5e_Post_Reaction_Histogram	22.7521	Wed 19 May 2021	16:43:45				16:51:20							
129547	Glasgow ISIS microwave cell - RMPOL2b_Sn5e+Te_Histogram	14.9500	Wed 19 May 2021	17:12:13				17:17:12							
129548	Glasgow ISIS microwave cell - RMPOL2b_Sn5e6.4Te0.2_300W_60s_Event_Mode	12.7045	Wed 19 May 2021	17:20:36				17:24:50	00:00:00	0	00:04:14	00:04:14	254	20	13
129549	Glasgow ISIS microwave cell - RMPOL2b_Sn5e6.8Te0.2_Post_Reaction_Histogram	14.9756	Wed 19 May 2021	17:25:32				17:30:30							
129550	Glasgow ISIS microwave cell - RMPOL3b_Sn5e+Te_Histogram	14.9919	Wed 19 May 2021	17:41:43				17:46:42							
129551	Glasgow ISIS microwave cell - RMPOL3b_Sn5e6.4Te0.4_300W_60s_Event_Mode	18.0232	Wed 19 May 2021	17:50:36	17:51:23	17:51:23	17:52:37	17:56:35	00:00:47	47	00:01:34	00:05:12	312	20	16
129552	Glasgow ISIS microwave cell - RMPOL3b_Sn5e6.4Te0.4_Post_Reaction_Histogram	14.9396	Wed 19 May 2021	17:57:14				18:02:12							
129553	Glasgow ISIS microwave cell - RMPOL4b_Sn5e+Te_Histogram	15.3767	Wed 19 May 2021	18:10:43				18:15:50							
129554	Glasgow ISIS microwave cell - RMPOL4b_Sn5e6.3Te0.5_300W_60s_Event_Mode	16.5606	Wed 19 May 2021	18:18:27	18:21:16	18:21:16	18:22:12	18:26:06	00:02:49	169	00:00:56	00:04:50	290	20	15
129555	Glasgow ISIS microwave cell - RMPOL4b_Sn5e6.3Te0.5_Post_Reaction_Histogram	15.0609	Wed 19 May 2021	18:26:43				18:31:43							
129556	Glasgow ISIS microwave cell - RMPOL5b_Sn5e+Te_Histogram	15.0720	Thu 20 May 2021	09:06:13				09:11:14							
129557	Glasgow ISIS microwave cell - RMPOL5b_Sn5e6.4Te0.6_100W_60s_Event_Mode	15.3858	Thu 20 May 2021	09:14:04	09:15:54	09:15:54	09:17:01	09:19:09	00:01:50	110	00:01:07	00:03:15	195	20	10
129558	Glasgow ISIS microwave cell - RMPOL5b_Sn5e6.4Te0.6_Post_Reaction_Histogram	15.0913	Thu 20 May 2021	09:19:53				09:24:52							
129559	Glasgow ISIS microwave cell - RMPOL6b_Sn5e+Te_Histogram	15.0833	Thu 20 May 2021	09:31:23				09:36:22							
129560	Glasgow ISIS microwave cell - RMPOL6b_Sn5e6.3Te0.8_100W_60s_Event_Mode	15.5651	Thu 20 May 2021	09:37:16	09:38:09	09:38:09	09:39:15	09:42:25	00:00:53	53	00:01:06	00:04:16	256	20	13

Figure A-5.2: Microsoft Excel spreadsheet containing Polaris instrument run data along with calculated sliced section parameters for use with the Python script in Mantid Workbench

The WinDAQ software was checked while on site to be approximately in sync with the Polaris instrument absolute time to within one second. The precise times for magnetron on, reaction start and magnetron off events could therefore be taken directly from the power profile of each experiment and was entered in columns F–H. The induction period to be ignored was simply calculated by subtracting the MW absorption time (column G) from Polaris start time (column E). The induction period was then converted to seconds for use in the Python script (column K). The reaction period was calculated by subtracting the induction period (column J) from the total Polaris run time, i.e., the difference between column E and I. The slice size can be user-specified (column O) and is used to divide the remaining event mode duration to calculate the maximum number of discrete slices the file can be processed into (column P).

For Mantid Workbench to run the script several important files were required for the data to be properly processed:

- focus_event_mode.py: the Python script necessary for slicing up the event mode data
- cycle_21_1_silicon_all_spectra.cal: used while putting neutron counts onto a d -spacing scale

- `Master_copy_of_grouping_file_with_essential_masks.cal`: used when grouping detector elements into the five detector banks
- `VanSplined_129462_cycle_21_1_silicon_all_spectra.cal.nxs`: pre-processed vanadium file used in data normalisation
- `POLARIS00129463.nxs`: Histogram scan of empty diffractometer background data set which is subtracted from the experimental data. This file was replaced with alternative background datasets recorded when on site to further flatten out the structured background from the quartz tubes and graphite.

The `focus_event_mode.py` script is opened in Mantid Workbench and adjustments to certain lines made before being run; but any changes must be intentionally saved if they are to be maintained for later use. The following lines of codes should be checked/adjusted as necessary:

- Line 17: directs to the folder location of the unprocessed Nexus data on the user's computer workstation.
- Line 19: directs to desired file output location
- Type `Ctrl + F` then use the "Replace ALL" function to change the Polaris experiment run number throughout the script
- Line 117 (`interesting_start = #`): input number of seconds to be ignored from start of run (spreadsheet column K)
- Line 118 (`chunk_size = #`): specify the size of individual sections the data should be sliced into (spreadsheet column O)
- Line 119 (`number_chunks = #`): specify the number of sections to be processed and output up to a maximum value from spreadsheet column P

Once these lines of script have been checked and updated, the Python script can be run by clicking the green play button at the top of the window. It is possible to adjust `chunk_size` and `number_chunks` to obtain a compromise between short slices with good time resolution and more counting statistics to better visualise reaction pathways.

Processed Nexus files have the naming format of `POLARIS#####.nxs` and for sliced event mode files, an additional suffix identifies the start time and finish time of that section as `POLARIS#####_##_##_nxs`. When importing processed Nexus files back into Mantid Workbench, the workspace group can be expanded

into individual workspaces, labelled with a suffix between _1 and _5 to indicate the detector bank. Loading multiple Nexus files to compare sections, the workspaces are labelled with an additional “_#” suffix to identify the section number however, they are labelled in the order in which the Nexus files were loaded into Mantid so care must be taken to make a selection of files in the correct order that can then be drag and dropped into Mantid Workbench.

A-5.7 Rietveld refinement functions

The corrected observed intensity at step i ($y_{o,i}$) is given by the overall scale factor (c') and the summation taken over all reflections (F_k)[18]:

$$y_{o,i} = c' \sum_k w_i^k F_k^2 \quad \text{(Equation A-5-3)}$$

$$c' = \frac{2c}{\sqrt{\pi \ln 2}} \quad \text{(Equation A-5-4)}$$

w_i^k is a measure of the contribution of structure factor (F_k) at position $2\theta_k$ to the intensity measured at position $2\theta_i$ which for well resolved peaks can be replaced by a δ peak whereby all the observed intensities are made zero except for a single value that is made equal to the area of the Gaussian peak[18]:

$$w_i^k = \delta_{i,0,k} \frac{0.709667}{\sin 2\theta_{0,k} \sin \theta_{0,k}} \quad \text{(Equation A-5-5)}$$

This eliminates the need to introduce an uncertainty associated with assuming an idealised Gaussian peak shape. Most Rietveld refinement algorithms now incorporate the March-Dollase function to account for small degrees of preferred orientation[24]:

$$P_K = \frac{1}{\left(\sqrt{G_1^2 \cos^2 \alpha + \frac{\sin^2 \alpha}{G_1}} \right)^3} \quad \text{(Equation A-5-6)}$$

G_1 = Preferred orientation factor

α = Polar angle between preferred orientation direction and specimen direction

Certain crystallites, particularly plate-shaped structures tend to align when samples are loaded into cylindrical holders for transmission diffractometry or in flat plates for Bragg-Brentano geometry. An intensity correction factor can be applied, particularly effective in patterns where the effect is not overwhelming such as with neutron data. The correction (I_c) is taken by multiplying the

observed intensity (I_o) by the exponential of preferred orientation parameter (G) and the angle between the scattering vector and the normal to the crystallites (α)[25]:

$$I_c = I_o \exp(-G\alpha^2) \quad \text{(Equation A-5-7)}$$

For overlapping peaks, the profile intensity is simply the sum of Bragg peak contributions and structure factor (S_k)[19]:

$$y_i = \sum_k w_{i,k} S_k^2 \quad \text{(Equation A-5-8)}$$

The structure factor is determined by the Miller indices and the positional parameters (x , y and z) at the j^{th} atom of the unit cell[24]:

$$S_k = \sum_j N_j f_j \exp(2\pi i(hx_j + ky_j + lz_j)) \exp(-M_j) \quad \text{(Equation A-5-9)}$$

$$M_j = \frac{8\pi^2 u_s^2 \sin^2 \theta}{\lambda^2} \quad \text{(Equation A-5-10)}$$

N_j = Site occupancy multiplier for j^{th} atom site

f_j = Scattering factor

u_s^2 = Root mean square displacement of j^{th} atom parallel to diffraction vector

The observed structure factor ($S_{o,k}^2$), nuclear ($F_{o,k}^2$) and magnetic ($J_{o,k}^2$) contributions define their respective R-factors[19]:

$$R_T = 100 \times \sum_i \frac{\left| S_{o,i}^2 - \frac{1}{c} \times S_{c,i}^2 \right|}{\sum_i S_{o,i}^2} \quad \text{(Equation A-5-11)}$$

$$R_{nuclear} = 100 \times \sum_i \frac{\left| F_{o,i}^2 - \frac{1}{c} \times F_{c,i}^2 \right|}{\sum_i F_{o,i}^2} \quad \text{(Equation A-5-12)}$$

$$R_{magnetic} = 100 \times \sum_i \frac{\left| J_{o,i}^2 - \frac{1}{c} \times J_{c,i}^2 \right|}{\sum_i J_{o,i}^2} \quad \text{(Equation A-5-13)}$$

A-5.8 Diffuse reflectance and UV-vis spectroscopy

During diffuse reflectance measurements, two reference plates are fixed onto positions 1 and 2 using screws, as shown in figure A-5.3a, to obtain a baseline correction measurement. The barium sulfate standard was compacted tightly and smoothed onto a reference stage at position 1 while a cut rectangle of filter paper was attached to the sample stage at position 2. The reference plate in

position 1 is then replaced with the sample to be measured as shown in figure A–5.3b. The specular light is reflected directly back and out of the integrating sphere through the incident beam aperture and is therefore not recorded [28].

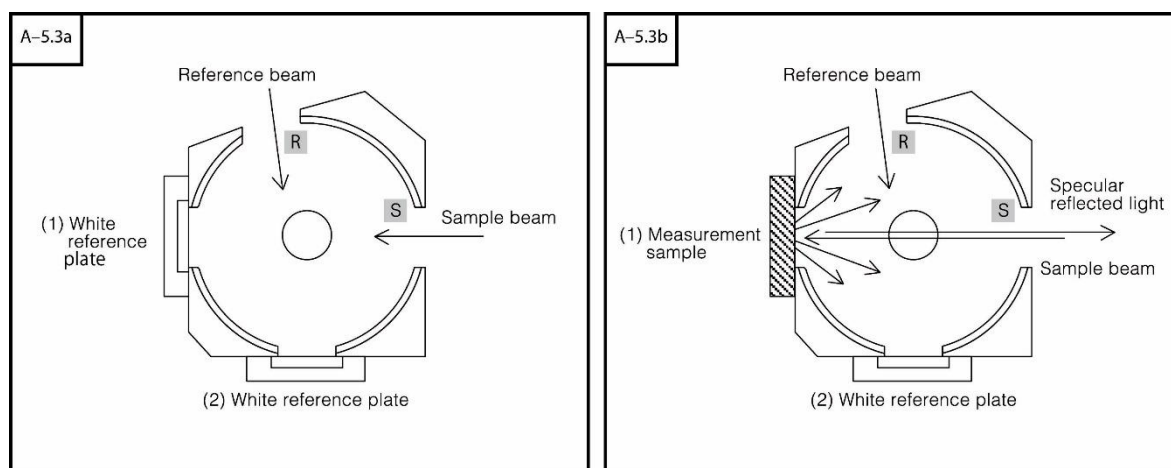


Figure A–5.3: Schematic diagrams of integrating sphere, with detector represented as circle in the centre a) during baseline correction with reference plate in position 1 b) during sample measurement with sample plate in position 1 [28]. Diagrams reproduced courtesy of Shimadzu Corporation

A–5.9 Preparing pellets for thermoelectric properties measurement

Thermal conductivity measurements in a LFA instrument requires powder samples to be pressed into 13 mm diameter pellets. Cold-pressed pellets involve compressing the powder sample in a pellet die with the use of a pneumatic press at ambient temperature. Cold-pressed pellets can crack or break during heating due to strain in the material and so sintering the pellet in a furnace for several hours can help densify the material and relax the strain. The alternative hot-pressing method applies heat and pressure simultaneously in a controlled manner. The pellet die is placed in a furnace chamber containing heating elements that are electrically controlled, the furnace is sealed under a known pressure and the sample is compressed while a uniform temperature in the chamber is maintained. Hot-pressing usually requires longer holding time to achieve uniform heating of the sample as well as a lower heating rate compared to other densification methods such as spark plasma sintering (SPS) [36].

Taking measurements of a pressed pellet has limitations in terms of crystal structures that are anisotropic since the measurements are only valid for a specific axis determined by the direction of pressure application. If sample volume allows, multiple pellets can be cut to allow measurement both parallel and normal to the direction of pressure application during preparation.

A–6 Chapter 6 supplementary material

A–6.1 How magnetrons generate microwaves

Microwaves are produced from a resonant cavity magnetron comprised of a cathode surrounded by a copper anode block as illustrated in figure A–6.1. The MW generating components are typically surrounded by metal fins which draw heat from the anode block by acting as a heatsink. A high voltage transformer generates a current that flows through the central cathode where a coiled filament heats up and emits electrons into the central cavity. The emitted electrons are accelerated radially towards the positively charged anode vanes; with the acceleration of moving charges resulting in EM radiation production. Circular permanent magnets affixed to the top and bottom of the resonant cavity produce an orthogonal H field that deflects the electrons into an expanding spiral path towards the anode. This elongated path increases the time for the electrons to reach the anode, generating more MWs[6], [7].

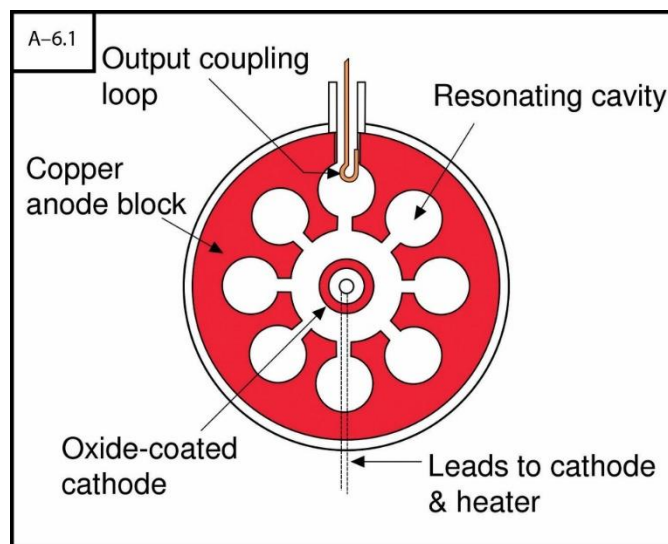


Figure A–6.1: Cross sectional diagram of resonant cavity magnetron[8]. Image by Ian Dunster and Vanessa Ezekowitz, CC BY-SA 3.0 via Wikimedia Commons

The efficiency of EM wave production is improved by the inclusion of resonating cavities within the anode block which enables LC oscillation to occur. LC oscillation is a phenomenon that occurs when a charged capacitor is connected to an inductor which instigates back and forth electron motion. The inductor develops an EMF (V_L) across it based on the change in current flow:

$$V_L = -L \frac{dt}{dt} \quad \text{(Equation A–6-1)}$$

L = Inductance

When an antenna with an inductor attached is placed alongside an LC circuit the antenna radiates EM waves. So as electrons pass near the surface of the anode block, it repels other electrons within the material. When the electrons pass a cavity, it causes charges to build up across the cavity surfaces much like capacitor plates. The curved outer surface of the anode acts as an inductor across the cavity surface and allows the charges to start oscillating. A metal loop attached to an antenna interacts with the oscillation as it would within an LC circuit and converts it into EM waves. The antenna need only be connected to a single cavity since all cavities are linked, a phenomenon known as mutual coupling.

Overall, magnetrons have an efficiency range of 60–85 % for converting electrical power to MW output power in the range of 0.4–100 kW for commercial or industrial applications. The power output of a magnetron is controlled by either the tube current or the strength of H , with a limit usually enforced by the temperature of the anode which must remain below its melting point; typically, in the range of 1.5 kW and 25 kW for air or water cooled anodes respectively[6], [9].

A–6.2 Redesign of quick release sample stick and ampoule block

The four main components of the ampoule support block were redesigned and new parts manufactured in collaboration with ISIS supervisor Dr Ron Smith and Colin Offer from the ISIS design division and manufacturing facilities group. The ISIS design schematics were adjusted to allow for 15 bore quartz tubes to be securely held and transported by the ampoule support block and sample stick mechanism as shown figure A–6.1. These diagrams were used to demonstrate the required changes effectively to the manufacturing team.

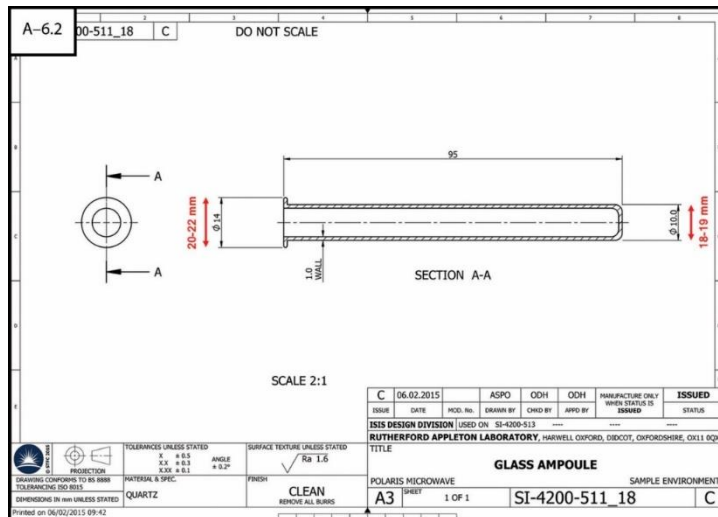


Figure A-6.2: ISIS design schematic and redesign notes for a larger 18-19 mm OD quartz support tube with ~2 mm width lipped opening

The orifices of the ceramic insulator (Figure A-6.2) and Al ampoule block (Figure A-6.3) were increased in line with the requirements of the quartz tube.

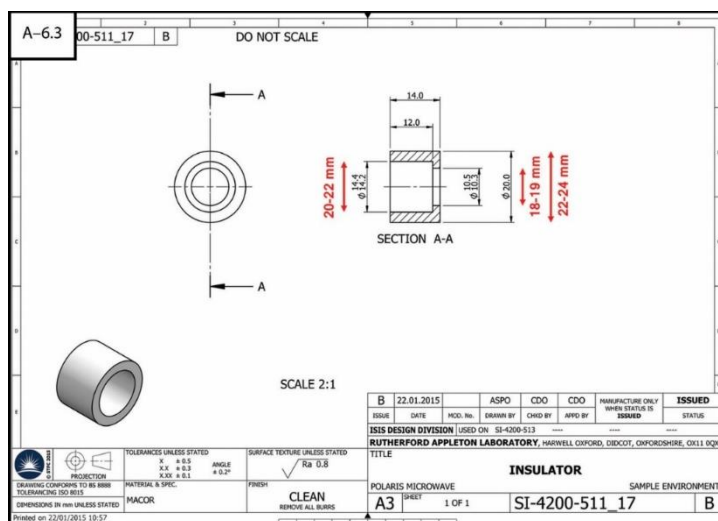


Figure A-6.3: ISIS design schematic and redesign notes for a larger Macor[®] ceramic insulator to accommodate the 18 mm OD quartz support tube

The additional space required in the ampoule block for the ceramic spacer would result in shallower external grooves used for venting excess heated air from the waveguide during a reaction. The threading to attach the adaptor lid would also need to be made wider in order to accommodate the larger ceramic spacer.

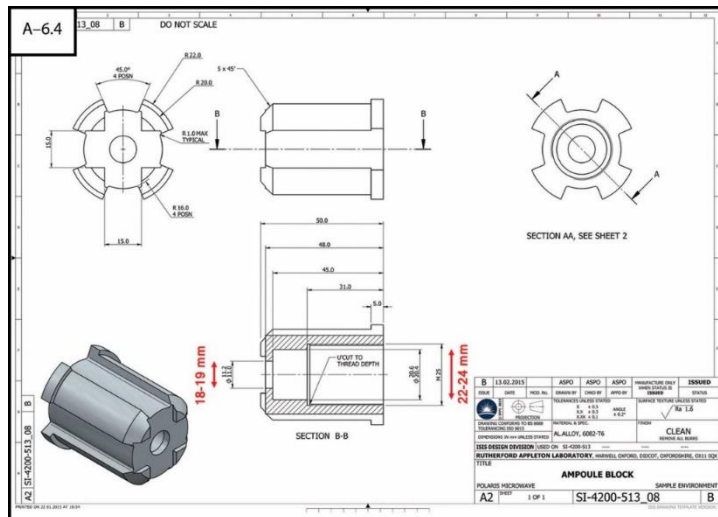


Figure A-6.4: ISIS design schematic and redesign notes for an ampoule block with larger orifices to accommodate the quartz support tube and 20–22 mm OD ceramic insulator

The brass threaded lid adaptor required a larger thread depth to correspond to the adjusted ampoule block; it was however, possible to maintain the same quick release sample stick attachment dimensions and so the existing stick design was sufficient. When discussing the design changes, the excess 6 mm protuberance of the lid adaptor into the space of the ampoule block was requested to be eliminated from the new component. The removal of this original design feature would allow for an increased margin of error when sealing the experiment sample ampoules to ~90 mm height.

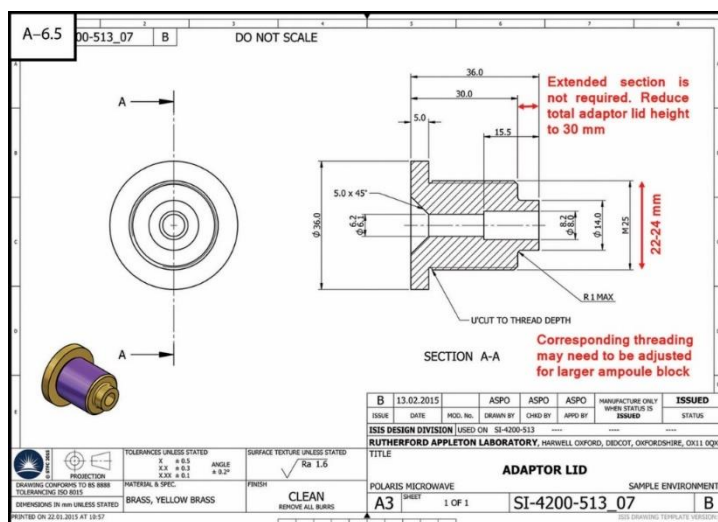


Figure A-6.5: ISIS design schematic and redesign notes for a brass adaptor lid with removal of the 6 mm protuberance and larger thread depth to fit within the redesigned ampoule block

A-7 Chapter 7 supplementary material

A-7.1 Effect of synthesis duration on SnSe using a modified DMO

The refined PXRD crystallographic data for 0.5 g SnSe samples heated in the modified DMO with 10 % excess Se, appearing in figure 7.2a:

Table A-7.1: Crystallographic cell parameters from Rietveld refinement of PXRD data (30–40 s syntheses) for *Pnma* SnSe phase

Synthesis duration (s)	30	30	30	40	40
Phase fraction (wt.%)	55.7(6)	76.0(4)	89.8(3)	90.0(1)	92.8(1)
Observations	4832	4832	4832	4786	4832
Variables	37	28	32	30	25
R_{wp}	0.1159	0.1283	0.2182	0.2653	0.1338
R_p	0.0882	0.0993	0.1665	0.1975	0.1011
χ^2	1.294	1.132	1.116	2.435	1.291

Table A-7.2: Crystallographic cell parameters from Rietveld refinement of PXRD data (50–120 s syntheses) for *Pnma* SnSe phase

Synthesis duration (s)	50	60	60	90	120
Phase fraction (wt.%)	94.5(1)	87.9(9)	95.5(1)	92.1(6)	91.5(5)
Observations	4786	4653	4775	4692	4746
Variables	30	19	26	19	21
R_{wp}	0.2856	0.4795	0.3517	0.4775	0.4796
R_p	0.2111	0.3895	0.2482	0.3867	0.3888
χ^2	2.520	0.954	2.805	1.008	1.054

The refined PXRD crystallographic data for 0.5 g SnSe samples heated in the modified DMO with stoichiometric starting materials, appearing in figure 7.2b:

Table A-7.3: Crystallographic cell parameters from Rietveld refinement of PXRD data (30 s syntheses) for *Pnma* SnSe phase

Synthesis duration (s)	30	30
Phase fraction (wt.%)	57(1)	56(1)
Observations	4832	4832
Variables	34	26
R_{wp}	0.2227	0.2308
R_p	0.1702	0.1775
χ^2	1.142	1.210

The refined PXRD crystallographic data for 0.5 g SnSe samples heated in the modified DMO with 10 % excess Se, appearing in figure 7.3:

Table A-7.4: Crystallographic cell parameters from Rietveld refinement of PXRD data (30–60 s syntheses) for *Pnma* SnSe phase

Synthesis duration (s)	30	40	50	60
Phase fraction (wt.%)	76.0(4)	90.0(1)	94.5(1)	95.5(1)
Observations	4832	4786	4786	4775
Variables	28	30	30	26
R_{wp}	0.1283	0.2653	0.2856	0.3517
R_p	0.0993	0.1975	0.2111	0.2482
χ^2	1.132	2.435	2.520	2.805

A-7.2 Gram-scale samples prepared using modified DMO

The refined PXRD crystallographic data for 5 g SnSe samples heated in the modified DMO with 10 % excess Se, appearing in figure 7.9:

Table A-7.5: Crystallographic cell parameters from Rietveld refinement of PXRD data (30–60 s syntheses) for *Pnma* SnSe phase

Synthesis duration (s)	30	40	50	60
Phase fraction (wt.%)	90.5(4)	85.7(7)	93.1(3)	91.0(4)
Observations	4813	4814	4678	4719
Variables	27	29	26	26
R_{wp}	0.3925	0.3852	0.4340	0.4453
R_p	0.3034	0.2942	0.3479	0.3524
χ^2	1.179	1.151	0.9831	1.095

A-7.3 Rapid synthesis of single phase SnSe₂ using a modified DMO

The refined PXRD crystallographic data for 0.5 g SnSe₂ samples heated in the modified DMO with 30 % excess Se, appearing in figure 7.14:

Table A-7.6: Crystallographic cell parameters from Rietveld refinement of PXRD data (20–40 s syntheses) for *P3m1* SnSe₂ phase

Synthesis duration (s)	20	25	30	35	40
Phase fraction (wt.%)	45.1(5)	40.8(7)	55.0(8)	51.9(6)	61.7(5)
Observations	4832	4832	4832	4832	4832
Variables	26	27	26	26	25
R_{wp}	0.1209	0.1145	0.1300	0.1224	0.1382
R_p	0.0911	0.0872	0.0989	0.0931	0.1055
χ^2	1.255	1.156	1.269	1.280	1.374

Table A-7.7: Crystallographic cell parameters from Rietveld refinement of PXRD data (40–70 s syntheses) for $P3m1$ SnSe₂ phase

Synthesis duration (s)	40	50	60	70
Phase fraction (wt.%)	Single phase	Single phase	Single phase	Single phase
Observations	4830	4832	4831	4832
Variables	19	18	19	19
R_{wp}	0.3307	0.2949	0.2904	0.2711
R_p	0.2542	0.2265	0.2246	0.2067
χ^2	1.338	1.356	1.323	1.288

A-7.4 Implementation of power and temperature data acquisition devices

The refined PXRD crystallographic data for the 1 g SnSe sample with 10 % excess Sn heated in the benchtop SMC reactor using 400 W forward power, appearing in figure 7.17:

Table A-7.8: Crystallographic cell parameters from Rietveld refinement of PXRD data for $Pnma$ SnSe phase

Portion of sample	Ingot	Deposits
Phase fraction (wt.%)	99.4(1)	99.7(1)
Observations	4734	4770
Variables	32	25
R_{wp}	0.3080	0.3662
R_p	0.2260	0.2741
χ^2	1.824	1.525

A-7.5 Improving SnSe phase fraction with excess Sn

The refined PXRD crystallographic data for SnSe samples heated in the benchtop SMC reactor using 400 or 600 W forward power, appearing in figure 7.18:

Table A-7.9: Crystallographic cell parameters from Rietveld refinement of PXRD data (0.5 g samples, 600 W forward power)

Stoichiometry	1:1		10 % excess Sn	
Phase	SnSe	SnSe ₂	SnSe	SnSe ₂
Phase fraction (wt.%)	91.4(1)	7.5(3)	92.5(1)	6.0(5)
Observations	4783		4765	
Variables	32		31	
R_{wp}	0.2618		0.2621	
R_p	0.1909		0.1871	
χ^2	2.105		1.661	

Table A-7.10: Crystallographic cell parameters from Rietveld refinement of PXRD data (1 g samples, 400 W forward power)

Stoichiometry	1:1		10 % excess Sn	
Phase	SnSe	SnSe ₂	SnSe	SnSe ₂
Phase fraction (wt.%)	91.5(1)	7.8(3)	84.5(1)	14.2(9)
Observations	6282		6282	
Variables	35		32	
<i>R_{wp}</i>	0.2263		0.2107	
<i>R_p</i>	0.1680		0.1506	
<i>χ²</i>	3.724		2.610	

A-7.6 Solid state MW synthesis under varied atmospheric conditions

The refined PXRD crystallographic data for the 1 g SnSe sample heated in the benchtop SMC reactor using 450 W forward power under Ar atmosphere, appearing in figure 7.19:

Table A-7.11: Crystallographic cell parameters from Rietveld refinement of PXRD data

Phase	SnSe	SnSe ₂
Crystal system	Orthorhombic	Trigonal
Space group	<i>Pnma</i>	<i>P$\bar{3}m1$</i>
<i>a</i> (Å)	11.5067(2)	3.8144(9)
<i>b</i> (Å)	4.1557(2)	3.8144(9)
<i>c</i> (Å)	4.4489(3)	6.1387(9)
<i>a</i> (°)	90	90
<i>β</i> (°)	90	90
<i>γ</i> (°)	90	120
Volume (Å³)	212.74(1)	77.35(3)
Phase fraction (wt.%)	93.7(1)	6.3(3)
Observations	4777	
Variables	29	
<i>R_{wp}</i>	0.2629	
<i>R_p</i>	0.1797	
<i>χ²</i>	1.751	

A-7.7 Direct MW-heating parameters for $\text{SnSe}_{1-x}\text{Te}_x$

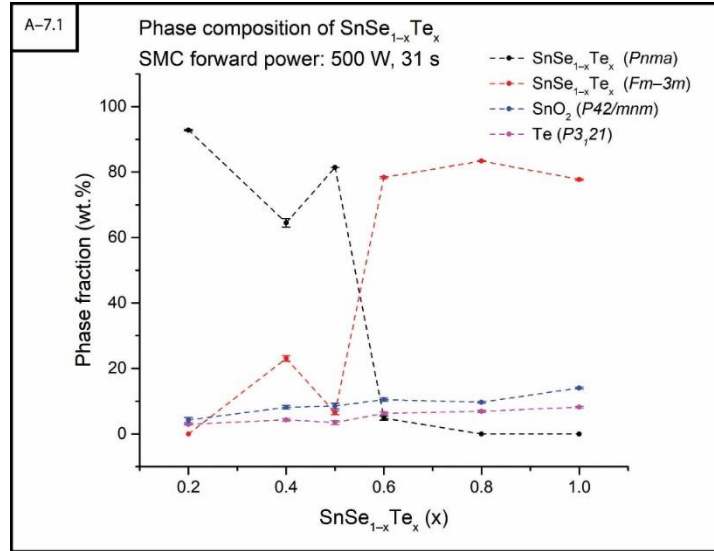


Figure A-7.1: Plot of phase fractions (wt.%) against Te content for 1 g $\text{SnSe}_{1-x}\text{Te}_x$ samples produced in the benchtop SMC reactor at 500 W

The refined PXRD crystallographic data for 1 g $\text{SnSe}_{1-x}\text{Te}_x$ samples heated in the benchtop SMC reactor using 500 W forward power, appearing in figures 7.21 and A-7.1:

Table A-7.12: Crystallographic cell parameters from Rietveld refinement of PXRD data for main $\text{SnSe}_{1-x}\text{Te}_x$ ($x = 0.2, 0.4, 0.5$) phase

Sample	$\text{SnSe}_{0.8}\text{Te}_{0.2}$	$\text{SnSe}_{0.6}\text{Te}_{0.4}$	$\text{SnSe}_{0.5}\text{Te}_{0.5}$
Refined site occupancy (Te)	0.40(6)	0.8(1)	–
Crystal system	Orthorhombic	Orthorhombic	Orthorhombic
Space group	<i>Pnma</i>	<i>Pnma</i>	<i>Pnma</i>
Phase fraction (wt.%)	92.8(2)	65(1)	81.4(1)
Observations	4786	4786	4786
Variables	40	36	31
R_{wp}	0.2768	0.5428	0.5849
R_p	0.2057	0.4047	0.3715
χ^2	3.792	15.46	14.24

The refined PXRD crystallographic data for 1 g $\text{SnSe}_{1-x}\text{Te}_x$ samples heated in the benchtop SMC reactor using 500 W forward power, appearing in figures 7.22 and A-7.1:

Table A-7.13: Crystallographic cell parameters from Rietveld refinement of PXRD data for main $\text{SnSe}_{1-x}\text{Te}_x$ ($x = 0.6, 0.8, 1$) phase

Sample	$\text{SnSe}_{0.4}\text{Te}_{0.6}$	$\text{SnSe}_{0.2}\text{Te}_{0.8}$	SnTe
Refined site occupancy (Te)	–	–	1
Crystal system	Orthorhombic	Cubic	Cubic
Space group	$Pnma$	$Fm\bar{3}m$	$Fm\bar{3}m$
Phase fraction (wt.%)	4.8(6)	83.4(1)	77.8(2)
Observations	4786	4784	4786
Variables	31	32	35
R_{wp}	0.4114	0.2380	0.2216
R_p	0.02834	0.1700	0.1565
χ^2	7.310	2.175	1.936

A-7.8 Direct MW-heating parameters for $\text{SnSe}_{1-x}\text{S}_x$

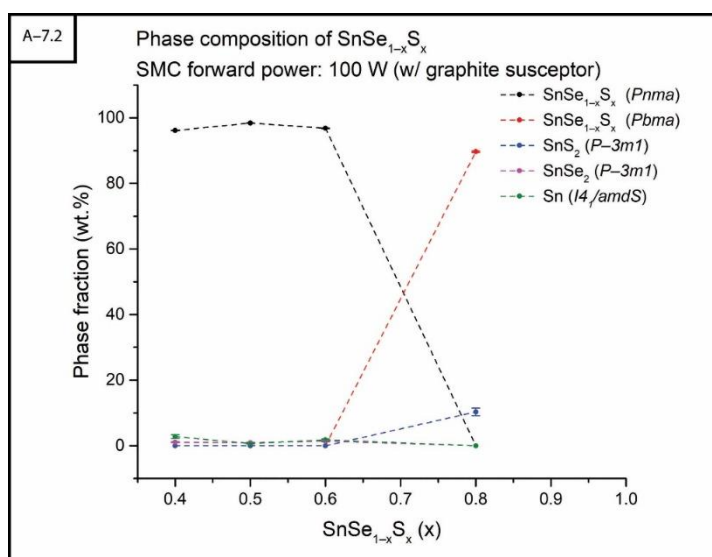


Figure A-7.2: Plot of phase fractions (wt.%) against Te content for 1 g $\text{SnSe}_{1-x}\text{S}_x$ samples produced in the benchtop SMC reactor at 100 W with the aid of a graphite susceptor

The refined PXRD crystallographic data for 1 g $\text{SnSe}_{1-x}\text{Te}_x$ samples heated in the benchtop SMC reactor using 100 W forward power with the aid of a graphite susceptor, appearing in figures 7.24, 7.25 and A-7.2:

Table A-7.14: Crystallographic cell parameters from Rietveld refinement of PXRD data for main $\text{SnSe}_{1-x}\text{Te}_x$ ($x = 0.4, 0.5, 0.6, 0.8$) phase

Sample	$\text{SnSe}_{0.6}\text{S}_{0.4}$	$\text{SnSe}_{0.5}\text{S}_{0.5}$	$\text{SnSe}_{0.4}\text{S}_{0.6}$	$\text{SnSe}_{0.2}\text{S}_{0.8}$
Refined site occupancy (S)	0.23(3)	0.48(3)	0.40(6)	0.55(3)
Crystal system	Orthorhombic	Orthorhombic	Orthorhombic	Orthorhombic
Space group	<i>Pnma</i>	<i>Pnma</i>	<i>Pnma</i>	<i>Pbma</i>
Phase fraction (wt.%)	96.1(1)	98.4(1)	96.8(1)	89.7(2)
Observations	4786	4786	4786	4785
Variables	34	38	37	28
R_{wp}	0.2246	0.2287	0.3109	0.4328
R_p	0.1587	0.1638	0.2203	0.3102
χ^2	2.131	2.398	4.117	6.817

A-7.9 Sample densification by cold pressing and sintering

Density measurements of $\text{SnSe}_{1-y}\text{X}_y$ samples following cold-pressing process measured using an Ohaus Pioneer Analytical Balance and Density Measurement Kit:

Table A-7.15: Density measurements of cold-pressed pellets performed using an Ohaus Pioneer analytical balance and density measurement kit

Sample	Density measurement (gcm^{-3})				Average density (gcm^{-3})	Percentage density (%)
	1	2	3	4		
$\text{Sn}_{0.95}\text{Se}$	6.0877	6.0274	5.9172	5.8282	5.9651	96.52
$\text{Sn}_{0.99}\text{Se}_{0.6}\text{Te}_{0.4}$	6.0895	6.1581	5.9924	6.1254	6.0914	–
$\text{Sn}_{0.99}\text{Te}$	6.2383	6.0810	6.0413	–	6.1202	94.45
$\text{SnSe}_{0.46}\text{S}_{0.54}$	5.3427	5.3319	5.3169	5.3427	5.3305	–
SnS	4.8646	4.9297	4.7502	4.8646	4.8482	92.88

Density measurements of $\text{SnSe}_{1-y}\text{X}_y$ samples following cold-pressing and sintering process measured using an Ohaus Pioneer Analytical Balance and Density Measurement Kit:

Table A–7.16: Density measurements of sintered pellets performed using an Ohaus Pioneer analytical balance and density measurement kit

Sample	Density measurement (gcm^{-3})				Average density (gcm^{-3})	Percentage density (%)
	1	2	3	4		
Sn _{0.95} Se	6.0495	5.6119	5.5915	5.5856	5.7096	92.39
Sn _{0.99} Se _{0.6} Te _{0.4}	5.9059	5.4974	5.3752	5.4458	5.5561	–
Sn _{0.99} Te	5.5886	5.4649	5.5167	–	5.5234	85.24
SnSe _{0.46} S _{0.54}	4.9545	4.9670	4.9391	–	4.9535	–
SnS	4.7188	4.7296	4.7026	–	4.7170	90.36

A hot-pressed SnTe pellet was prepared however, when the graphite spacer was sanded off the pellet it was seen to be cracked and unsuitable for analysis. Blair was unable to help prepare further hot-pressed pellets or carry out additional analyses as he requested time off due to a family bereavement.

A–8 Chapter 8 supplementary material

A–8.1 Initial bismuth selenide (Bi_2Se_3) synthesis experiments

As described in section 8.3.1 the initial samples were prepared with oxidised Bi powder, which produced several oxide species in the mixed phase product. The samples synthesised with the aid of a graphite susceptor at 100 W forward power were each heated for a duration of 1–4 mins.

Increasing heating time >90 s reduced the trigonal ($R\bar{3}m$) Bi_2Se_3 phase in favour of tetragonal ($I4/mmm$) Bi_2SeO_2 (Figure A–8.1). Tetragonal ($I4/mmm$) $\text{Bi}_2\text{O}_2(\text{CO}_3)$, present in the starting mixture, was also reduced then eliminated with longer heating durations.

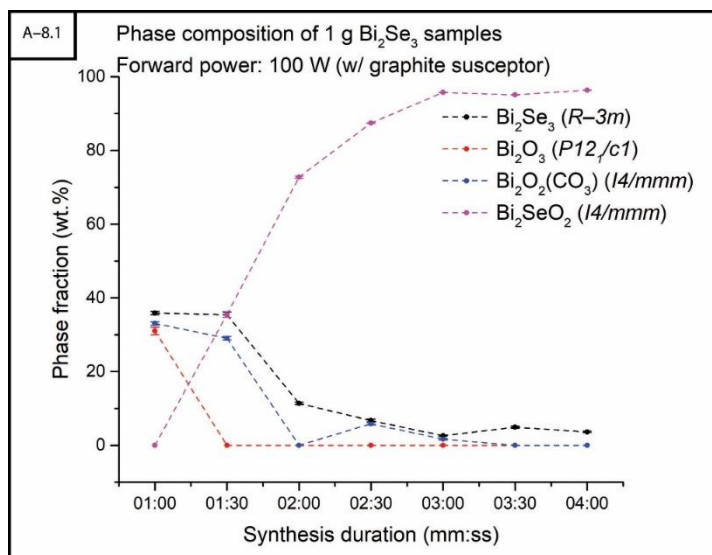


Figure A–8.1: Plot of relative phase fractions against synthesis duration for initial Bi₂Se₃ synthesis attempts

The results from these experiments prompted a redesign of the experimental parameters in order to eliminate the presence of oxygen within the starting material mixture. The crystallographic data for these Bi₂Se₃ PXRD refinements is presented in table A–8.1:

Table A–8.1: Crystallographic cell parameters from Rietveld refinement of PXRD data for main Bi₂Se₃ phase (60–240 s)

Synthesis duration (s)	60	90	120	150	180	210	240
Phase fraction (wt.%)	35.9(4)	35.4(7)	11.4(3)	6.7(4)	2.6(2)	4.9(3)	3.7(2)
Observations	4785	4785	4779	4778	4774	4774	4752
Variables	42	38	41	39	36	29	31
R_{wp}	0.3158	0.3094	0.2577	0.2396	0.2353	0.2735	0.2387
R_p	0.2305	0.2237	0.1810	0.1688	0.1625	0.2030	0.1640
χ^2	2.606	2.454	1.555	1.404	1.376	1.809	1.299

A–8.2 Initial bismuth telluride (Bi₂Te₃) synthesis experiments

The initial Bi₂Te₃ experiments were prepared and carried out alongside the Bi₂Se₃ experiments and likewise, required the aid of a graphite susceptor. The samples were shown to produce *R* $\bar{3}$ *m* Bi₂Te₃ along with the previously described bismuth oxide species. As shown in figure A–8.2, the Bi₂Te₃ was reduced in favour of orthorhombic (*Abm2*) Bi₂TeO₅.

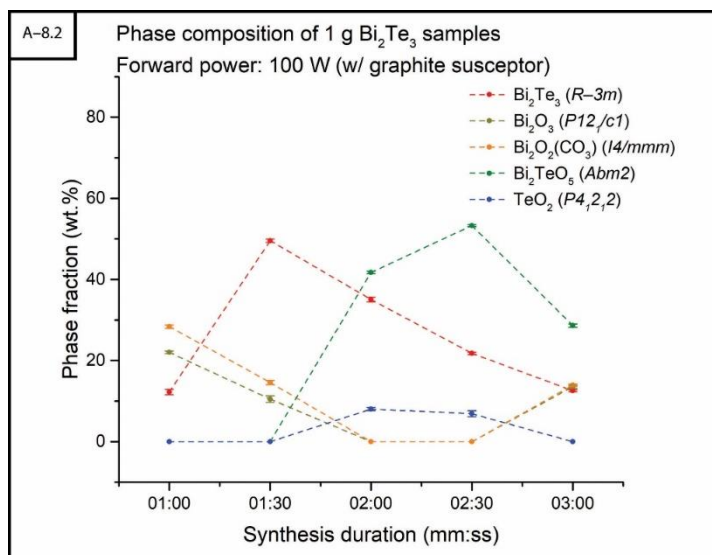


Figure A–8.2: Plot of relative phase fractions against synthesis duration for initial Bi₂Te₃ synthesis attempts

Tetragonal (*P4₁2₁2*) TeO₂ was identified in samples produced from heating durations >120 s; the crystallographic data for these Bi₂Te₃ PXRD refinements is presented in table A–8.2:

Table A–8.2: Crystallographic cell parameters from Rietveld refinement of PXRD data for main Bi₂Te₃ phase (60–120 s)

Synthesis duration (s)	60	90	120	150	210
Phase fraction (wt.%)	12.2(7)	49.5(4)	35.1(6)	21.8(3)	12.6(3)
Observations	4785	4784	4775	4770	4785
Variables	53	41	48	47	60
<i>R_{wp}</i>	0.2706	0.3714	0.2575	0.2566	0.2585
<i>R_p</i>	0.1967	0.2805	0.1832	0.1794	0.1834
χ^2	1.845	3.513	1.513	1.533	1.607

A–8.3 Adjusting experimental design to eliminate oxide formation

The refined PXRD crystallographic data for 1 g Bi₂Se₃ samples heated in the benchtop SMC reactor using 100 W forward power with the aid of a graphite susceptor appearing in figure 8.2:

Table A–8.3: Crystallographic cell parameters from Rietveld refinement of PXRD data for main Bi₂Se₃ phase (62–120 s)

Synthesis duration (s)	62	91	120
Phase fraction (wt.%)	71.1(2)	75.0(2)	52.1(4)
Observations	4786	4786	4786
Variables	32	33	39
<i>R_{wp}</i>	0.2379	0.2387	0.2614
<i>R_p</i>	0.1738	0.1768	0.1881
χ^2	3.973	3.352	5.038

The refined PXRD crystallographic data for 1 g Bi₂Te₃ samples heated in the benchtop SMC reactor using 100 W forward power with the aid of a graphite susceptor appearing in figure 8.3:

Table A-8.4: Crystallographic cell parameters from Rietveld refinement of PXRD data for main Bi₂Te₃ phase (60–123 s)

Synthesis duration (s)	60	90	123
Phase fraction (wt.%)	50.9(4)	43.7(2)	57.5(4)
Observations	4786	4786	4786
Variables	48	37	42
<i>R_{wp}</i>	0.2070	0.2202	0.2263
<i>R_p</i>	0.1462	0.1612	0.1636
<i>χ²</i>	2.422	3.166	3.131

A-8.4 Initial antimony selenide (Sb₂Se₃) synthesis experiments

The refined PXRD crystallographic data for 1 g Sb₂Se₃ samples heated in the benchtop SMC reactor appearing in figures 8.6 and 8.7:

Table A-8.5: Crystallographic cell parameters from Rietveld refinement of PXRD data for main Sb₂Se₃ phase (20–180 s)

Synthesis duration (s)	20	60	120	180
MW power (W)	600	100 (w/ C susceptor)	100 (w/ C susceptor)	100 (w/ C susceptor)
Phase fraction (wt.%)	96.4(1)	99.4(1)	96.4(1)	97.7(1)
Observations	4770	4776	4774	4764
Variables	48	39	46	47
<i>R_{wp}</i>	0.2748	0.2827	0.2725	0.2779
<i>R_p</i>	0.2009	0.2093	0.2042	0.2025
<i>χ²</i>	1.538	1.705	1.607	1.574

A-8.5 Initial antimony telluride (Sb_2Te_3) synthesis experiments

The refined PXRD crystallographic data for 1 g Sb_2Te_3 samples heated in the benchtop SMC reactor using 100 W forward power with the aid of a graphite susceptor appearing in figure 8.8:

Table A-8.6: Crystallographic cell parameters from Rietveld refinement of PXRD data for main Sb_2Te_3 phase (50–180 s)

Synthesis duration (s)	50	60	90	120	180
Phase fraction (wt.%)	5.4(6)	24.8(7)	48.0(6)	47.5(6)	72.8(7)
Observations	4696	4733	4764	4768	4747
Variables	37	46	42	39	34
R_{wp}	0.3012	0.2843	0.2702	0.2742	0.3706
R_p	0.2160	0.2001	0.1918	0.1947	0.2672
χ^2	1.602	1.470	1.389	1.467	2.510

A-8.6 The effect of synthesis duration on $Sb_2Se_{3-x}Te_x$ solid solutions

The refined PXRD crystallographic data for $Sb_2Se_{3-x}Te_x$ heated for 60 s in the benchtop SMC reactor using 100 W forward power with the aid of a graphite susceptor appearing in figure 8.9:

Table A-8.7: Crystallographic cell parameters from Rietveld refinement of PXRD data for main $Sb_2Se_{3-x}Te_x$ (x = 2, 2.5) phase

Sample	Sb_2SeTe_2	$Sb_2Se_{0.5}Te_{2.5}$
Refined site occupancy (Te)	0.63(5)	1.28(3)
a (Å)	4.123(1)	4.2137(3)
b (Å)	4.123(1)	4.2137(3)
c (Å)	29.58(1)	30.154(3)
α (°)	90	90
β (°)	90	90
γ (°)	90	120
Volume (Å³)	435.4(2)	463.67(6)
Phase fraction (wt.%)	37(1)	70(1)
Observations	4770	4774
Variables	40	43
R_{wp}	0.3113	0.2830
R_p	0.2219	0.1969
χ^2	1.809	1.585

The refined PXRD crystallographic data for 1 g $Sb_2Se_{3-x}Te_x$ samples heated for 90 s in the benchtop SMC reactor using 100 W forward power with the aid of a graphite susceptor appearing in figure 8.10 and 8.11:

Table A–8.8: Crystallographic cell parameters from Rietveld refinement of PXRD data for main $\text{Sb}_2\text{Se}_{3-x}\text{Te}_x$ ($x = 0.5, 1$) phases

Sample	$\text{Sb}_2\text{Se}_{2.5}\text{Te}_{0.5}$		$\text{Sb}_2\text{Se}_2\text{Te}$	
Refined site occupancy (Te)	Te2 = 0.11(6)	0.73(3)	0	1.10(2)
Crystal system	Orthorhombic	Trigonal	Orthorhombic	Trigonal
Space group	$Pnma$	$R\bar{3}m$	$Pnma$	$R\bar{3}m$
a (Å)	11.859(1)	4.1007(4)	11.848(2)	4.1033(3)
b (Å)	3.9912(4)	4.1007(4)	3.9918(6)	4.1033(3)
c (Å)	11.677(1)	29.372(5)	11.673(2)	29.461(2)
α (°)	90	90	90	90
β (°)	90	90	90	90
γ (°)	90	120	90	120
Volume (Å ³)	552.73(9)	427.75(7)	552.1(1)	429.58(6)
Phase fraction (wt.%)	60.6(7)	36.9(1)	13.0(4)	87.0(3)
Observations	4787		4782	
Variables	58		46	
R_{wp}	0.2741		0.2777	
R_p	0.2016		0.1949	
χ^2	1.779		1.834	

Table A–8.9: Crystallographic cell parameters from Rietveld refinement of PXRD data for main $\text{Sb}_2\text{Se}_{3-x}\text{Te}_x$ ($x = 1.5, 2, 2.5$) phase

Sample	$\text{Sb}_2\text{Se}_{1.5}\text{Te}_{1.5}$	Sb_2SeTe_2	$\text{Sb}_2\text{Se}_{0.5}\text{Te}_{2.5}$
Refined site occupancy (Te)	0.71(1)	1.10(1)	1.10(2)
Crystal system	Trigonal	Trigonal	Trigonal
Space group	$R\bar{3}m$	$R\bar{3}m$	$R\bar{3}m$
a (Å)	4.1329(3)	4.1704(2)	4.2154(3)
b (Å)	4.1329(3)	4.1704(2)	4.2154(3)
c (Å)	29.673(2)	29.857(2)	30.150(3)
α (°)	90	90	90
β (°)	90	90	90
γ (°)	120	120	120
Volume (Å ³)	438.9(1)	449.72(4)	463.98(7)
Phase fraction (wt.%)	82.9(3)	75.8(4)	67.2(7)
Observations	4780	4770	4749
Variables	45	48	46
R_{wp}	0.2742	0.2573	0.2824
R_p	0.1941	0.1824	0.1979
χ^2	1.549	1.355	1.446

The refined PXRD crystallographic data for 1 g $\text{Sb}_2\text{Se}_{3-x}\text{Te}_x$ samples heated for 120 s in the benchtop SMC reactor using 100 W forward power with the aid of a graphite susceptor appearing in figure 8.12 and 8.13:

Table A-8.10: Crystallographic cell parameters from Rietveld refinement of PXRD data for main $\text{Sb}_2\text{Se}_{3-x}\text{Te}_x$ ($x = 0.5, 1$) phase

Sample	$\text{Sb}_2\text{Se}_{2.5}\text{Te}_{0.5}$		$\text{Sb}_2\text{Se}_2\text{Te}$	
Refined site occupancy (Te)	0.77(3)	Te1 = 0.37(6) Te2 = 0.22(6)	0.74(1)	Te2 = 0.1(2)
Crystal system	Orthorhombic	Trigonal	Orthorhombic	Trigonal
Space group	$Pnma$	$R\bar{3}m$	$Pnma$	$R\bar{3}m$
a (Å)	4.0990(3)	11.8887(5)	4.1113(3)	11.850(2)
b (Å)	4.0990(3)	4.0015(4)	4.1113(3)	3.9900(5)
c (Å)	29.415(2)	11.6949(9)	29.481(2)	11.673(2)
α (°)	90	90	90	90
β (°)	90	90	90	90
γ (°)	90	120	90	120
Volume (Å ³)	428.0(1)	556.35(6)	431.54(6)	551.9(1)
Phase fraction (wt.%)	62.0(6)	38.0(7)	28(2)	72.3(4)
Observations	4785		4779	
Variables	51		41	
R_{wp}	0.2695		0.2983	
R_p	0.1984		0.2173	
χ^2	1.719		1.744	

Table A-8.11: Crystallographic cell parameters from Rietveld refinement of PXRD data for main $\text{Sb}_2\text{Se}_{3-x}\text{Te}_x$ ($x = 1.5, 2, 2.5$) phase

Sample	$\text{Sb}_2\text{Se}_{1.5}\text{Te}_{1.5}$		Sb_2SeTe_2	$\text{Sb}_2\text{Se}_{0.5}\text{Te}_{2.5}$
Refined site occupancy (Te)	–	1.03(2)	1.06(2)	0.90(3)
Crystal system	Orthorhombic	Trigonal	Trigonal	Trigonal
Space group	$Pnma$	$R\bar{3}m$	$R\bar{3}m$	$R\bar{3}m$
a (Å)	11.31(2)	4.1264(6)	4.1682(2)	4.2186(3)
b (Å)	3.830(6)	4.1264(6)	4.1682(2)	4.2186(3)
c (Å)	12.11(2)	29.625(6)	29.840(1)	30.167(5)
α (°)	90	90	90	90
β (°)	90	90	90	90
γ (°)	120	90	120	120
Volume (Å ³)	524.4(9)	436.8(1)	448.97(4)	464.90(9)
Phase fraction (wt.%)	6(1)	82.8(4)	72.7(4)	63.7(6)
Observations	4780		4762	4746
Variables	38		48	46
R_{wp}	0.3584		0.2740	0.2937
R_p	0.2565		0.1969	0.2072
χ^2	2.532		1.471	1.554

A-8.7 Investigation of $Sb_2Se_{3-x}Te_x$ phase transition between $0 \leq x \leq 1$

The refined PXRD crystallographic data for 1 g $Sb_2Se_{3-x}Te_x$ samples heated for 90 s in the benchtop SMC reactor using 100 W forward power with the aid of a graphite susceptor appearing in figures 8.16 and 8.17:

Table A-8.12: Crystallographic cell parameters from Rietveld refinement of PXRD data for main $Sb_2Se_{3-x}Te_x$ ($x = 0, 0.2$) phases

Sample	Sb_2Se_3	$Sb_2Se_{2.8}Te_{0.2}$	
Refined site occupancy (Te)	–	Te1 = 0.11(4)	
		Te2 = 0.17(4)	0.9(3)
		Te3 = 0.27(5)	
Crystal system	Orthorhombic	Orthorhombic	Trigonal
Space group	$Pnma$	$Pnma$	$R\bar{3}m$
a (Å)	11.7800(2)	11.8335(3)	4.1309(3)
b (Å)	3.9771(1)	3.9878(2)	4.1309(3)
c (Å)	11.6313(4)	11.6625(5)	29.078(4)
α (°)	90	90	90
β (°)	90	90	90
γ (°)	90	90	120
Volume (Å ³)	544.92(2)	550.35(3)	429.72(5)
Phase fraction (wt.%)	96.75(4)	86.5(2)	8(2)
Observations	4784	4783	
Variables	48	55	
R_{wp}	0.2606	0.2675	
R_p	0.1937	0.1932	
χ^2	1.709	1.644	

Table A-8.13: Crystallographic cell parameters from Rietveld refinement of PXRD data for $Sb_2Se_{3-x}Te_x$ ($x = 0.4, 0.6$) phases

Sample	$Sb_2Se_{2.6}Te_{0.4}$		$Sb_2Se_{2.4}Te_{0.6}$	
Refined site occupancy (Te)	Te1 = 0.09(4)		Te2 = 0.05(5)	
	Te2 = 0.04(3)	0.4(1)	Te3 = 0.28(6)	0.82(2)
	Te3 = 0.06(4)			
Crystal system	Orthorhombic	Trigonal	Orthorhombic	Trigonal
Space group	$Pnma$	$R\bar{3}m$	$Pnma$	$R\bar{3}m$
a (Å)	11.8383(5)	4.111(2)	11.8706(5)	4.1028(3)
b (Å)	3.9893(2)	4.111(2)	3.9962(3)	4.1028(3)
c (Å)	11.6690(6)	29.53(2)	11.6867(8)	29.412(1)
α (°)	90	90	90	90
β (°)	90	90	90	90
γ (°)	90	120	90	120
Volume (Å ³)	551.09(6)	432.2(5)	554.38(5)	428.76(5)
Phase fraction (wt.%)	96.74(6)	3.3(5)	61.8(6)	38.2(5)
Observations	4780		4785	
Variables	51		55	
R_{wp}	0.2667		0.2822	
R_p	0.1876		0.2073	
χ^2	1.610		2.031	

Table A-8.14: Crystallographic cell parameters from Rietveld refinement of PXRD data for $\text{Sb}_2\text{Se}_{3-x}\text{Te}_x$ ($x = 0.8, 1$) phases

Sample	$\text{Sb}_2\text{Se}_{2.2}\text{Te}_{0.8}$		$\text{Sb}_2\text{Se}_2\text{Te}$	
Refined site occupancy (Te)	Te1 = 0.09(9)			
	Te2 = 0.09(9)	0.77(2)	–	0.78(2)
	Te3 = 0.10(9)			
Crystal system	Orthorhombic	Trigonal	Orthorhombic	Trigonal
Space group	$Pnma$	$R\bar{3}m$	$Pnma$	$R\bar{3}m$
a (Å)	11.8629(8)	4.1054(2)	11.855(2)	4.1030(3)
b (Å)	3.9944(3)	4.1054(2)	3.9914(6)	4.1030(3)
c (Å)	11.681(1)	29.449(2)	11.672(2)	29.459(2)
α (°)	90	90	90	90
β (°)	90	90	90	90
γ (°)	90	120	90	120
Volume (Å ³)	553.52(7)	429.85(4)	552.3(2)	429.48(5)
Phase fraction (wt.%)	42(1)	57.6(6)	16.4(9)	83.6(3)
Observations	4784		4782	
Variables	59		51	
R_{wp}	0.2698		0.2719	
R_p	0.1917		0.1942	
χ^2	1.643		1.631	

A-8.8 $\text{Sb}_2\text{Se}_{3-x}\text{Te}_x$ multi phase transition between $0.4 \leq x \leq 0.8$

The refined PXRD crystallographic data for 1 g $\text{Sb}_2\text{Se}_{3-x}\text{Te}_x$ samples heated for 120 s in the benchtop SMC reactor using 100 W forward power with the aid of a graphite susceptor appearing in figure 8.18:

Table A-8.15: Crystallographic cell parameters from Rietveld refinement of PXRD data for main $\text{Sb}_2\text{Se}_{3-x}\text{Te}_x$ ($x = 0.4, 0.6$) phases

Sample	$\text{Sb}_2\text{Se}_{2.6}\text{Te}_{0.4}$		$\text{Sb}_2\text{Se}_{2.4}\text{Te}_{0.6}$	
Refined site occupancy (Te)	Te1 = 0.07(4)		Te1 = 0.10(6)	
	Te2 = 0.02(4)	1.3(2)	Te2 = 0.08(6)	0.49(2)
	Te3 = 0.08(5)		Te3 = 0.09(7)	
Crystal system	Orthorhombic	Trigonal	Orthorhombic	Trigonal
Space group	$Pnma$	$R\bar{3}m$	$Pnma$	$R\bar{3}m$
a (Å)	11.8433(4)	4.117(1)	11.8722(6)	4.0986(5)
b (Å)	3.9903(2)	4.117(1)	3.9960(3)	4.0986(5)
c (Å)	11.6700(7)	29.502(9)	11.686(1)	29.393(4)
α (°)	90	90	90	90
β (°)	90	90	90	90
γ (°)	90	120	90	120
Volume (Å ³)	551.51(4)	433.1(3)	554.40(5)	427.6(1)
Phase fraction (wt.%)	96.92(7)	3.1(6)	55.3(8)	44.7(7)
Observations	4757		4785	
Variables	56		40	
R_{wp}	0.3064		0.2937	
R_p	0.2248		0.2179	
χ^2	1.605		1.692	

Table A–8.16: Crystallographic cell parameters from Rietveld refinement of PXRD data for main $\text{Sb}_2\text{Se}_{2.2}\text{Te}_{0.8}$ phases

Sample	$\text{Sb}_2\text{Se}_{2.2}\text{Te}_{0.8}$	
Refined site occupancy (Te)	Te1 = 0.13(8)	0.75(2)
Crystal system	Orthorhombic	Trigonal
Space group	$Pnma$	$R\bar{3}m$
a (Å)	11.8619(7)	4.1069(3)
b (Å)	3.9943(3)	4.1069(3)
c (Å)	11.679(1)	29.461(2)
α (°)	90	90
β (°)	90	90
γ (°)	90	120
Volume (Å ³)	553.37(7)	430.34(6)
Phase fraction (wt.%)	46(1)	54.2(6)
Observations	4779	
Variables	55	
R_{wp}	0.2942	
R_p	0.2161	
χ^2	1.495	

A–8.9 Scaling-up 5 g $\text{Sb}_2\text{Se}_{3-x}\text{Te}_x$ syntheses (between $0 \leq x \leq 1$)

The refined PXRD crystallographic data for 5 g $\text{Sb}_2\text{Se}_{3-x}\text{Te}_x$ samples heated for 90 s in the benchtop SMC reactor using 100 W forward power with the aid of a graphite susceptor appearing in figures 8.19–8.21:

Table A–8.17: Crystallographic cell parameters from Rietveld refinement of PXRD data for main $\text{Sb}_2\text{Se}_{3-x}\text{Te}_x$ ($x = 0.2, 0.4$) phases

Sample	$\text{Sb}_2\text{Se}_{2.8}\text{Te}_{0.2}$		$\text{Sb}_2\text{Se}_{2.6}\text{Te}_{0.4}$
Refined site occupancy (Te)	Te1 = 0.10(3)	Te2 = 0.10(3)	Te3 = 0.19(4)
		0.47(8)	
	Te3 = 0.26(3)		
Crystal system	Orthorhombic	Trigonal	Orthorhombic
Space group	$Pnma$	$R\bar{3}m$	$Pnma$
a (Å)	11.8292(3)	4.103(1)	11.8216(3)
b (Å)	3.9864(2)	4.103(1)	3.9847(1)
c (Å)	11.6593(5)	29.48(1)	11.6555(4)
α (°)	90	90	90
β (°)	90	90	90
γ (°)	90	120	90
Volume (Å ³)	549.80(3)	429.8(3)	549.04(2)
Phase fraction (wt.%)	96.53(3)	3.5(4)	43.0(4)
Observations	4786		4786
Variables	53		68
R_{wp}	0.1982		0.1783
R_p	0.1442		0.1307
χ^2	2.332		1.866

Table A–8.18: Crystallographic cell parameters from Rietveld refinement of PXRD data for main $\text{Sb}_2\text{Se}_{3-x}\text{Te}_x$ ($x = 0.5, 0.6$) phases

Sample	$\text{Sb}_2\text{Se}_{2.5}\text{Te}_{0.5}$		$\text{Sb}_2\text{Se}_{2.4}\text{Te}_{0.6}$	
Refined site occupancy (Te)	Te1 = 0.09(5) Te3 = 0.31(6)	Unrefined	–	0.619(6)
Crystal system	Orthorhombic	Trigonal	Orthorhombic	Trigonal
Space group	$Pnma$	$R\bar{3}m$	$Pnma$	$R\bar{3}m$
a (Å)	11.8584(4)	4.0999(7)	11.8628(4)	4.1010(2)
b (Å)	3.9917(2)		3.9932(1)	4.1010(2)
c (Å)	11.6752(7)	29.39(1)	11.6790(5)	29.399(1)
α (°)	90	90	90	90
β (°)	90	90	90	90
γ (°)	90	120	90	120
Volume (Å ³)	552.65(4)	427.8(1)	553.24(3)	428.19(4)
Phase fraction (wt.%)	80.9(3)	12.8(4)	60.8(3)	25.7(5)
Observations	4786		4786	
Variables	54		60	
R_{wp}	0.2903		0.1805	
R_p	0.2044		0.1332	
χ^2	5.220		1.853	

Table A–8.19: Crystallographic cell parameters from Rietveld refinement of PXRD data for main $\text{Sb}_2\text{Se}_{3-x}\text{Te}_x$ ($x = 0.8, 1$) phases

Sample	$\text{Sb}_2\text{Se}_{2.2}\text{Te}_{0.8}$		$\text{Sb}_2\text{Se}_2\text{Te}$	
Refined site occupancy (Te)	–	0.612(4)	–	0.622(6)
Crystal system	Orthorhombic	Trigonal	Orthorhombic	Trigonal
Space group	$Pnma$	$R\bar{3}m$	$Pnma$	$R\bar{3}m$
a (Å)	11.8613(4)	4.1052(2)	11.854(1)	4.1103(2)
b (Å)	3.9933(2)	4.1052(2)	3.9919(3)	4.1103(2)
c (Å)	11.6799(6)	29.445(1)	11.676(1)	29.503(2)
α (°)	90	90	90	90
β (°)	90	90	90	90
γ (°)	90	120	90	120
Volume (Å ³)	553.23(4)	429.76(4)	552.51(9)	431.67(5)
Phase fraction (wt.%)	50.7(4)	42.4(5)	29.4(7)	63.8(4)
Observations	4786		4786	
Variables	54		59	
R_{wp}	0.2008		0.1950	
R_p	0.1460		0.1370	
χ^2	2.268		2.104	

A–8.10 *Initial Cu_{1-x}Se synthesis experiments*

The refined PXRD crystallographic data for 1 g Cu_{1-x}Se samples heated in the benchtop SMC reactor using 300 W forward power, appearing in figures 8.22–8.24:

Table A–8.20: Crystallographic cell parameters from Rietveld refinement of PXRD data for main Cu_{1-x}Se (42–303 s) phase

Synthesis duration (s)	42	124	160	303
Phase fraction (wt.%)	79.6(2)	81.8(2)	84.0(2)	76.7(2)
Observations	4786	4786	4786	4786
Variables	58	56	54	66
R_{wp}	0.1595	0.1854	0.1940	0.1855
R_p	0.1211	0.1353	0.1474	0.1357
χ^2	1.978	2.646	2.783	2.844

A–8.11 *Initial Cu_{2-x}Se synthesis experiments*

The refined PXRD crystallographic data for 1 g Cu_{2-x}Se samples heated in the benchtop SMC reactor using 300 W forward power, appearing in figures 8.25–8.27:

Table A–8.21: Crystallographic cell parameters from Rietveld refinement of PXRD data for main Cu_{2-x}Se phases with excess Se (10–20 %)

Excess Se (%)	10	15		20	
Phase	Cu _{2-x} Se	Cu _{2-x} Se	Cu _{3-x} Se ₂	Cu _{2-x} Se	Cu _{3-x} Se ₂
Crystal system	Cubic	Cubic	Tetragonal	Cubic	Tetragonal
Space group	$Fm\bar{3}m$	$Fm\bar{3}m$	$P\bar{4}2_1m$	$Fm\bar{3}m$	$P42\bar{4}2_1m$
a (Å)	5.75266(4)	5.74530(4)	6.4058(7)	5.74303(4)	6.4035(2)
b (Å)	5.75266(4)	5.74530(4)	6.4058(7)	5.74303(4)	6.4035(2)
c (Å)	5.75266(4)	5.74530(4)	4.2825(9)	5.74303(4)	4.2808(2)
α (°)	90	90	90	90	90
β (°)	90	90	90	90	90
γ (°)	90	90	90	90	90
Volume (Å ³)	190.374(4)	189.644(4)	175.73(5)	189.419(4)	175.54(1)
Phase fraction (wt.%)	100	97.11(2)	2.9(3)	84.5(1)	15.5(3)
Observations	4786	4786		4786	
Variables	20	40		38	
R_{wp}	0.1628	0.1393		0.1398	
R_p	0.1139	0.1036		0.1056	
χ^2	2.328	1.688		1.624	

The refined PXRD crystallographic data for 1 g $\text{Cu}_{1-x}\text{Se}_{1-y}\text{Te}_y$ samples heated in the benchtop SMC reactor using 500 W forward power, appearing in figures 8.29 and 8.30:

Table A-8.22: Crystallographic cell parameters from Rietveld refinement of PXRD data for main $\text{Cu}_{1-x}\text{Se}_{1-y}\text{Te}_y$ ($y = 0.2, 0.4, 0.5$) phases

Sample	$\text{Cu}_{1-x}\text{Se}_{0.8}\text{Te}_{0.2}$	$\text{Cu}_{1-x}\text{Se}_{0.6}\text{Te}_{0.4}$	$\text{Cu}_{1-x}\text{Se}_{0.5}\text{Te}_{0.5}$	
Crystal system	Cubic	Cubic	Cubic	Hexagonal
Space group	$Fm\bar{3}m$	$Fm\bar{3}m$	$Fm\bar{3}m$	$P6/mmm$
<i>a</i> (Å)	5.7419(2)	5.7718(3)	4.454(2)	4.2066(7)
<i>b</i> (Å)	5.7419(2)	5.7718(3)	4.454(2)	4.2066(7)
<i>c</i> (Å)	5.7419(2)	5.7718(3)	4.454(2)	7.287(3)
<i>a</i> (°)	90	90	90	90
<i>β</i> (°)	90	90	90	90
<i>γ</i> (°)	90	90	90	120
Volume (Å³)	189.31(2)	192.28(3)	101.49(7)	111.67(7)
Phase fraction (wt.%)	93.7(2)	89.89(9)	13(3)	25(1)
Observations	4786	4785	4786	
Variables	36	33	40	
<i>R_{wp}</i>	0.3510	0.2220	0.3966	
<i>R_p</i>	0.2322	0.1599	0.2851	
<i>χ</i>²	6.246	2.129	6.426	

Table A-8.23: Crystallographic cell parameters from Rietveld refinement of PXRD data for main $\text{Cu}_{1-x}\text{Se}_{1-y}\text{Te}_y$ ($y = 0.6, 0.8$) phases

Sample	$\text{Cu}_{1-x}\text{Se}_{0.4}\text{Te}_{0.6}$		$\text{Cu}_{1-x}\text{Se}_{0.2}\text{Te}_{0.8}$	
Crystal system	Cubic	Hexagonal	Cubic	Orthorhombic
Space group	$Fm\bar{3}m$	$P6/mmm$	$Fm\bar{3}m$	$Pmnm$
<i>a</i> (Å)	–	4.2227(3)	5.698(1)	3.137(2)
<i>b</i> (Å)	–	4.2227(3)	5.698(1)	4.082(2)
<i>c</i> (Å)	–	7.308(1)	5.698(1)	6.945(2)
<i>a</i> (°)	90	90	90	90
<i>β</i> (°)	90	90	90	90
<i>γ</i> (°)	90	120	90	90
Volume (Å³)	–	112.85(2)	185.0(1)	88.95(7)
Phase fraction (wt.%)	7(1)	42(1)	19(2)	25(2)
Observations	4786		4786	
Variables	25		37	
<i>R_{wp}</i>	0.4181		0.4258	
<i>R_p</i>	0.3024		0.3044	
<i>χ</i>²	6.753		6.656	

Table A-8.24: Crystallographic cell parameters from Rietveld refinement of PXRD data for main Cu_{1-x}Te phases

Sample	Cu_{1-x}Te	
Crystal system	Orthorhombic	Orthorhombic
Space group	$Pmnm$	$Pmmn$
a (Å)	3.156(1)	3.9951(3)
b (Å)	3.156(1)	3.9951(3)
c (Å)	6.959(4)	6.1180(6)
α (°)	90	90
β (°)	90	90
γ (°)	90	90
Volume (Å ³)	89.63(8)	96.92(2)
Phase fraction (wt.%)	21(2)	48(1)
Observations	4785	
Variables	41	
R_{wp}	0.4962	
R_p	0.3625	
χ^2	9.055	

A-8.13 *Rapid reaction of $\text{Cu}_{1-x}\text{Se}_{1-y}\text{S}_y$ at low pressure*

The refined PXRD crystallographic data for 1 g $\text{Cu}_{1-x}\text{Se}_{0.6}\text{S}_{0.4}$ sample that underwent spontaneous reaction under dynamic vacuum, appearing in figure 8.32:

Table A-8.25: Crystallographic cell parameters from Rietveld refinement of PXRD data for main $\text{Cu}_{1-x}\text{Se}_{0.6}\text{S}_{0.4}$ phases

Sample	$\text{Cu}_{1-x}\text{Se}_{0.6}\text{S}_{0.4}$	
Crystal system	Hexagonal	Cubic
Space group	$P6_3/mmc$	$Fm\bar{3}m$
a (Å)	3.9758(7)	5.6364(1)
b (Å)	3.9758(7)	5.6364(1)
c (Å)	17.018(6)	5.6364(1)
α (°)	90	90
β (°)	90	90
γ (°)	120	90
Volume (Å ³)	232.96(8)	179.06(1)
Phase fraction (wt.%)	12(1)	87.8(3)
Observations	4786	
Variables	27	
R_{wp}	0.3066	
R_p	0.2254	
χ^2	5.346	

The refined PXRD crystallographic data for 1 g $\text{Cu}_{1-x}\text{Se}_{1-y}\text{S}_y$ samples heated in the benchtop SMC reactor, appearing in figures 8.33 and 8.35:

Table A-8.26: Crystallographic cell parameters from Rietveld refinement of PXRD data for main $\text{Cu}_{1-x}\text{Se}_{1-y}\text{S}_y$ ($y = 0.2, 0.4$) phases

Sample	$\text{Cu}_{1-x}\text{Se}_{0.8}\text{S}_{0.2}$		$\text{Cu}_{1-x}\text{Se}_{0.6}\text{S}_{0.4}$	
Crystal system	Hexagonal	Cubic	Hexagonal	Cubic
Space group	$P6_3/mmc$	$F\bar{4}3m$	$P6_3/mmc$	$Fm\bar{3}m$
a (Å)	3.9544(4)	5.6975(5)	–	–
b (Å)	3.9544(4)	5.6975(5)	–	–
c (Å)	17.192(2)	5.6975(5)	–	–
α (°)	90	90	90	90
β (°)	90	90	90	90
γ (°)	120	90	120	90
Volume (Å³)	232.81(5)	184.95(5)	–	–
Phase fraction (wt.%)	70(1)	30(2)	75.1(5)	24.8(5)
Observations	4787		4787	
Variables	28		24	
R_{wp}	0.3063		0.3058	
R_p	0.2318		0.2371	
χ^2	4.543		4.057	

The refined PXRD crystallographic data for 1 g $\text{Cu}_{1-x}\text{Se}_{1-y}\text{S}_y$ samples heated in the benchtop SMC reactor using 100 W forward power with the aid of a graphite susceptor, appearing in figures 8.35 and 8.36:

Table A-8.27: Crystallographic cell parameters from Rietveld refinement of PXRD data for main $\text{Cu}_{1-x}\text{Se}_{1-y}\text{S}_y$ ($y = 0.5, 0.6$) phases

Sample	$\text{Cu}_{1-x}\text{Se}_{0.5}\text{S}_{0.5}$		$\text{Cu}_{1-x}\text{Se}_{0.4}\text{S}_{0.6}$	
Crystal system	Hexagonal	Cubic	Hexagonal	Hexagonal
Space group	$P6_3/mmc$	$Fm\bar{3}m$	$P6_3/mmc$	$P6_3/mmc$
a (Å)	3.901(1)	–	3.931(1)	–
b (Å)	3.901(1)	–	3.931(1)	–
c (Å)	17.025(4)	–	17.028(8)	–
α (°)	90	90	90	90
β (°)	90	90	90	90
γ (°)	120	90	120	90
Volume (Å³)	224.3(1)	–	227.9(2)	–
Phase fraction (wt.%)	82.8(2)	12.3(7)	58.7(4)	41.3(9)
Observations	4787		4787	
Variables	25		23	
R_{wp}	0.2769		0.3103	
R_p	0.2086		0.2362	
χ^2	3.438		4.016	

Table A-8.28: Crystallographic cell parameters from Rietveld refinement of PXRD data for main $\text{Sb}_2\text{Se}_{3-x}\text{Te}_x$ ($x = 0.8, 1$) phase

Sample	$\text{Cu}_{1-x}\text{Se}_{0.2}\text{S}_{0.8}$		Cu_{1-x}S
Crystal system	Hexagonal	Hexagonal	Hexagonal
Space group	$P6_3/mmc$	$P6_3/mmc$	$P6_3/mmc$
a (Å)	3.9336(7)	3.7977(6)	3.7908(5)
b (Å)	3.9336(7)	3.7977(6)	3.7908(5)
c (Å)	17.229(5)	16.410(4)	16.377(3)
α (°)	90	90	90
β (°)	90	90	90
γ (°)	90	120	90
Volume (Å³)	230.87(9)	204.97(8)	203.81(6)
Phase fraction (wt.%)	15.5(7)	84.5(6)	57(1)
Observations		4786	4787
Variables		38	53
R_{wp}		0.2415	0.2235
R_p		0.1837	0.1695
χ^2		2.271	2.009

A-9 Chapter 9 supplementary material

A-9.1 SnSe (10 % excess Sn) in-situ TOF data

The refined PND crystallographic data for 20 s and 5 s sliced SnSe event mode TOF data, appearing in figures 9.12 and 9.13:

Table A-9.1: Crystallographic cell parameters from Rietveld refinement of sliced SnSe event mode TOF data (0-80 s)

Data time-slice (s)	0-20	20-40	40-60	60-80
Crystal system	Orthorhombic	Orthorhombic	Orthorhombic	Orthorhombic
Space group	$Pnma$	$Pnma$	$Pnma$	$Pnma$
Phase fraction (wt.%)	41(2)	72(1)	68(1)	75(1)
Observations	1994	1998	1999	1999
Variables	51	52	49	50
R_{wp}	0.1079	0.0838	0.1012	0.0969
R_p	0.1878	0.1484	0.1732	0.1681
χ^2	1.0060	0.9294	1.3710	1.2380

Table A-9.2: Crystallographic cell parameters from Rietveld refinement of sliced SnSe event mode TOF data (10–20 s)

Data time-slice (s)	10–15		15–20	
Phase	SnSe	Sn	SnSe	Sn
Crystal system	Orthorhombic	Tetragonal	Orthorhombic	Tetragonal
Space group	<i>Pnma</i>	<i>I4₁/amdS</i>	<i>Pnma</i>	<i>I4₁/amdS</i>
Phase fraction (wt.%)	20(5)	48(3)	74(2)	26(3)
Observations	1959		1976	
Variables	46		44	
R_{wp}	0.1907		0.1613	
R_p	0.3151		0.2753	
χ^2	0.7484		0.8844	

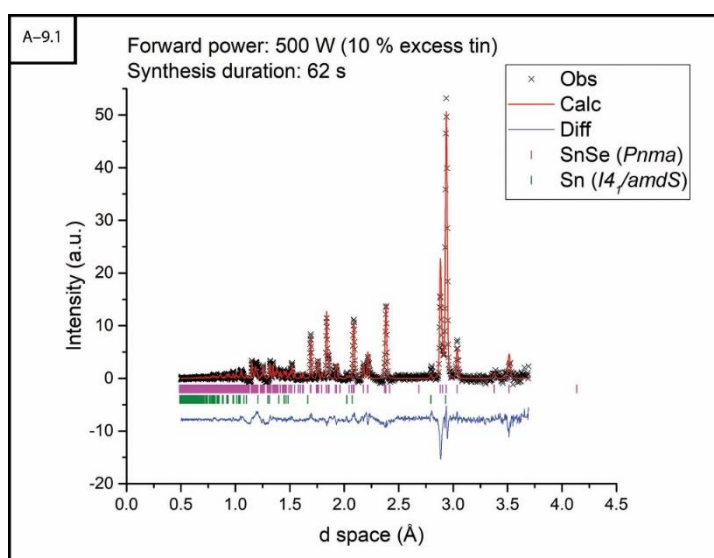


Figure A-9.1: Plot of refined post reaction TOF histogram data for SnSe (10 % excess Sn) heated using 500 W forward power for 62 s

The refined PND crystallographic data for SnSe heated using 500 W forward power for ~62 s post reaction TOF histogram data, appearing in figure A-9.1:

Table A-9.3: Crystallographic cell parameters from Rietveld refinement of SnSe post reaction TOF histogram data

Sample	SnSe
Crystal system	Orthorhombic
Space group	<i>Pnma</i>
<i>a</i> (Å)	11.524(8)
<i>b</i> (Å)	4.167(4)
<i>c</i> (Å)	4.429(5)
<i>a</i> (°)	90
<i>β</i> (°)	90
<i>γ</i> (°)	90
Volume (Å ³)	212.7(2)
Phase fraction (wt.%)	98.1(2)
Observations	1999
Variables	40
<i>R_{wp}</i>	0.0281
<i>R_p</i>	0.0405
<i>χ</i> ²	5.584

A-9.2 SnSe_{1-x}Te_x in-situ TOF data

The refined PND crystallographic data for 5 s sliced SnSe_{0.4}Te_{0.6} event mode TOF data, appearing in figure 9.17:

Table A-9.4: Crystallographic cell parameters from Rietveld refinement of sliced SnSe_{0.4}Te_{0.6} event mode TOF data (60–80 s)

Data time-slice (s)	60–65	65–70	70–75	75–80
Crystal system	Cubic	Cubic	Cubic	Cubic
Space group	<i>Fm$\bar{3}$m</i>	<i>Fm$\bar{3}$m</i>	<i>Fm$\bar{3}$m</i>	<i>Fm$\bar{3}$m</i>
Phase fraction (wt.%)	55(2)	48(5)	50(4)	53(4)
Observations	1989	1980	1982	1983
Variables	52	52	53	51
<i>R_{wp}</i>	0.1424	0.1464	0.1376	0.1515
<i>R_p</i>	0.2324	0.2480	0.2365	0.2683
<i>χ</i> ²	0.7263	0.7522	0.7013	0.7621

A-9.3 SnSe_{1-x}S_x in-situ TOF data

The refined PND crystallographic data for 5 s sliced SnSe_{0.6}S_{0.4} event mode TOF data, appearing in figure 9.22:

Table A-9.5: Crystallographic cell parameters from Rietveld refinement of sliced SnSe_{0.6}S_{0.4} event mode TOF data (80–100 s)

Data time-slice (s)	80–85	85–90	90–95	95–100
Crystal system	Orthorhombic	Orthorhombic	Orthorhombic	Orthorhombic
Space group	<i>Pnma</i>	<i>Pnma</i>	<i>Pnma</i>	<i>Pnma</i>
Phase fraction (wt.%)	–	43(5)	76(2)	93.0(7)
Observations	1984	1979	1991	1988
Variables	48	44	50	44
R_{wp}	0.1563	0.1596	0.1409	0.1494
R_p	0.2712	0.2742	0.2289	0.2561
χ^2	0.8297	0.8526	0.6707	0.7350

The refined PND crystallographic data for SnSe_{1-x}S_x samples heated using 300 W forward power for ~60 s post reaction TOF histogram data, appearing in figure 9.24:

Table A-9.6: Crystallographic cell parameters from Rietveld refinement of SnSe_{1-x}S_x (x = 0.6, 0.8, 1) post reaction TOF histogram data

Sample	SnSe _{0.6} S _{0.4}	SnSe _{0.5} S _{0.5}	SnSe _{0.4} S _{0.6}	SnS
Refined site occupancy (S)	0.38(4)	0.46(4)	0.54(3)	–
Crystal system	Orthorhombic	Orthorhombic	Orthorhombic	Orthorhombic
Space group	<i>Pnma</i>	<i>Pnma</i>	<i>Pbnm</i>	<i>Pnma</i>
a (Å)	11.432(8)	11.392(8)	4.365(5)	11.236(9)
b (Å)	4.107(4)	4.086(4)	11.372(8)	4.006(4)
c (Å)	4.389(5)	4.377(5)	4.072(4)	4.310(4)
α (°)	90	90	90	90
β (°)	90	90	90	90
γ (°)	90	90	90	90
Volume (Å ³)	206.0(2)	203.7(2)	202.2(2)	194.0(2)
Observations	1999	1999	1999	1999
Variables	50	50	50	49
R_{wp}	0.0182	0.0182	0.018	0.0192
R_p	0.0322	0.0316	0.0308	0.0333
χ^2	1.551	1.595	1.524	1.727

A-9.4 $\text{Bi}_2\text{Se}_{3-x}\text{Te}_x$ in-situ TOF data (60 s syntheses)

The refined PND crystallographic data for the $R\bar{3}m$ phase of $\text{Bi}_2\text{Se}_{3-x}\text{Te}_x$ samples heated using 300 W forward power (except for Bi_2Te_3 which was heated using 100 W forward power with the aid of a graphite susceptor) for ~60 s post reaction TOF histogram data:

Table A-9.7: Crystallographic cell parameters from Rietveld refinement of $\text{Bi}_2\text{Se}_{3-x}\text{Te}_x$ ($x = 0, 1.5, 2, 3$) post reaction TOF histogram data

Sample	Bi_2Se_3	$\text{Bi}_2\text{Se}_{1.5}\text{Te}_{1.5}$	Bi_2SeTe_2	Bi_2Te_3
Refined site occupancy (Te)	–	Te2 = 0.4(3)	0.7(1)	–
a (Å)	4.1473(1)	4.2334(5)	4.277(1)	4.3970(3)
b (Å)	4.1473(1)	4.2334(5)	4.277(1)	4.3970(3)
c (Å)	28.720(2)	29.563(7)	29.90(2)	30.574(4)
α (°)	90	90	90	90
β (°)	90	90	90	90
γ (°)	120	120	120	120
Volume (Å³)	427.82(2)	458.8(1)	473.8(2)	511.91(6)
Phase fraction (wt.%)	77.6(2)	91.4(6)	75(2)	74.5(6)
Observations	1999	1999	1999	1999
Variables	58	52	61	61
R_{wp}	0.0156	0.0177	0.0181	0.0209
R_p	0.0281	0.0304	0.0345	0.0402
χ^2	1.219	1.461	1.533	2.168

The refined PND crystallographic data for 20 s sliced Bi_2Te_3 event mode TOF data:

Table A–9.8: Crystallographic cell parameters from Rietveld refinement of sliced Bi₂Te₃ event mode TOF data (0–20 s)

PND background	Standard background			Graphite peaks removed	
Phase	Bi ₂ Te ₃	Bi	C	Bi ₂ Te ₃	Bi
Crystal system	Trigonal	Trigonal	Hexagonal	Trigonal	Trigonal
Space group	$R\bar{3}m$	$R\bar{3}m$	$P6_3/mmc$	$R\bar{3}m$	$R\bar{3}m$
<i>a</i> (Å)	4.419(1)	4.561(2)	2.463(1)	4.419(1)	4.559(2)
<i>b</i> (Å)	4.419(1)	4.561(2)	2.463(1)	4.419(1)	4.559(2)
<i>c</i> (Å)	30.75(1)	11.83(1)	6.780(4)	30.74(2)	11.814(8)
<i>a</i> (°)	90	90	90	90	90
<i>β</i> (°)	90	90	90	90	90
<i>γ</i> (°)	120	120	120	120	120
Volume (Å ³)	520.0(2)	213.1(2)	35.63(3)	519.8(2)	212.6(1)
Phase fraction (wt.%)	50(1)	46(2)	3.8(3)	65(2)	35(2)
Observations	1999			1989	
Variables	52			46	
<i>R</i> _{wp}	0.0738			0.0860	
<i>R</i> _p	0.1261			0.1499	
<i>χ</i> ²	0.8341			0.9340	

A–9.5 Interruption of neutron beam during first batch of experiments

The synchrotron current of the neutron beamline dropped to 0 μA immediately after beginning the post reaction TOF histogram scan of the Sb₂Se₃ sample on Thursday afternoon (Figure A–9.2). The beamline failure was later attributed to a vacuum leak in injector tank 3 for which the window was replaced and conditioning procedure started on the Friday morning.

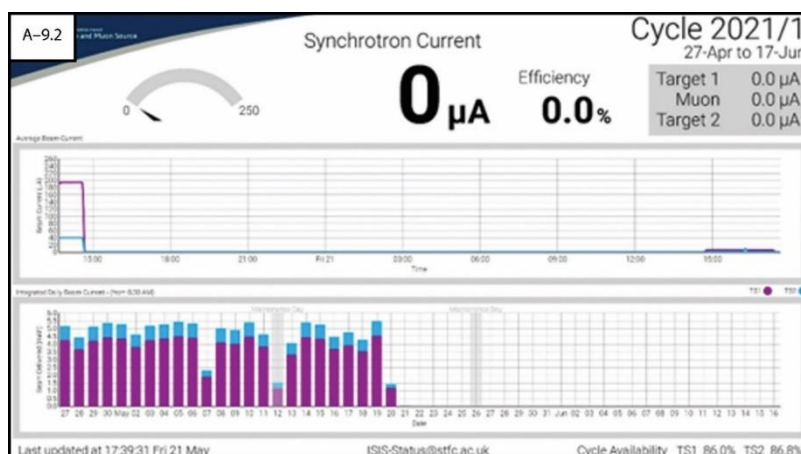


Figure A–9.2: Synchrotron current display showing duration of neutron beam downtime between Thursday afternoon until Friday evening due to a fault with injector tank 3 window

The base rate beam of ~7 μA was established at 1500 on the Friday afternoon which allowed the post reaction TOF histogram collection for the Sb₂Se₃ sample to resume. Dr Smith advised that the lower beam energy would extend the

histogram collection window by a factor of hours in order to obtain an equivalent resolution to the usual ~5 min scan time. The pre reaction TOF histogram scan of $\text{Sb}_2\text{Se}_{2.8}\text{Te}_{0.2}$ sample was started at 1724 on the Friday however the synchrotron current was turned off again at 1725 due to an issue with synchrotron diagnostics. The typical synchrotron current of ~180 μA for target station 1 was restored at ~2200 on Friday evening (Figure A–9.3) which allowed a some of the remaining experiments to be completed. The synchrotron diagnostics issue was rectified and a typical consistent total synchrotron current of ~230 μA was restored in the early hours of Saturday morning.

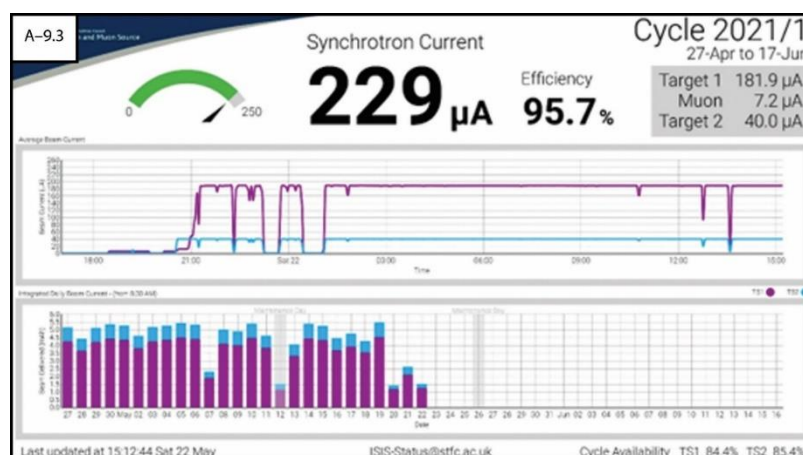


Figure A–9.3: Synchrotron current display showing base rate beam of 7 μA re-established at ~1500 on Friday following conditioning of replacement injector tank 3 window

The remaining experiment samples were left on site and a second visit was arranged one month later as an extension of the same beamtime application.

A–9.6 Elemental reactant powders' event mode TOF data

Colourmap plots for 20 s and 5 s sliced elemental powder (Bi, Sb, Se, Te, S) event mode TOF data against reaction time with absorbed MW power overlaid:

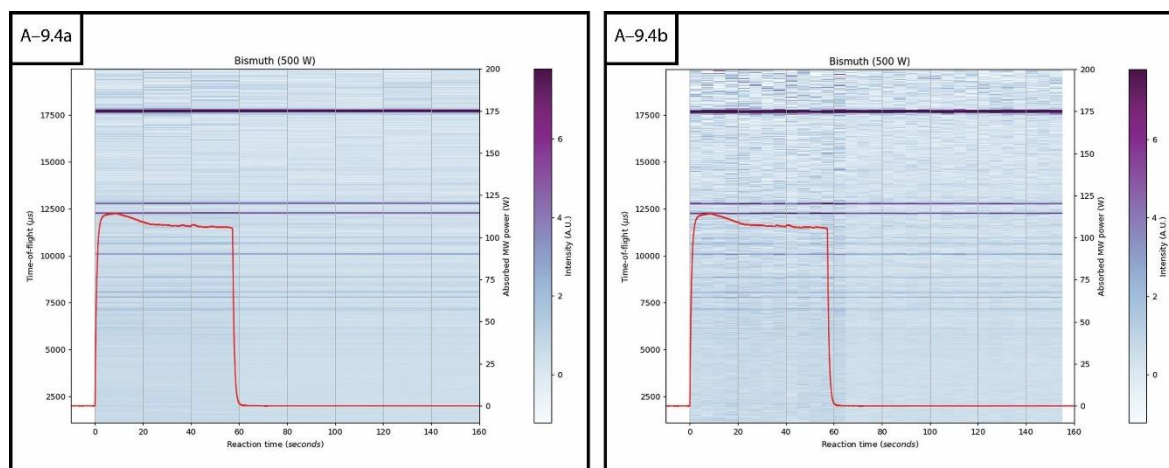


Figure A–9.4: Colourmap plots of sliced event mode TOF data with absorbed MW power overlaid for Bi powder heated using 500 W forward power for 57 s a) data processed as 20 s sections and b) 5 s sections

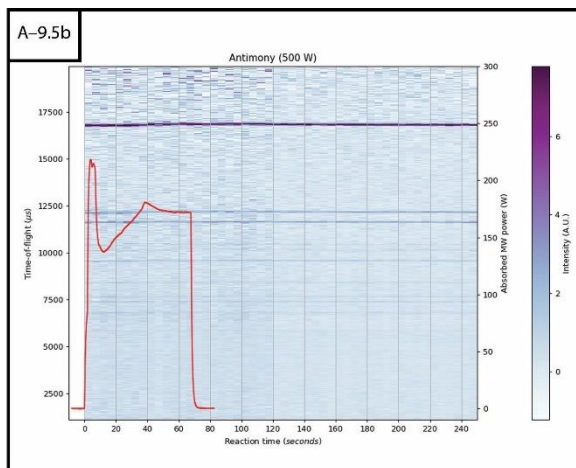
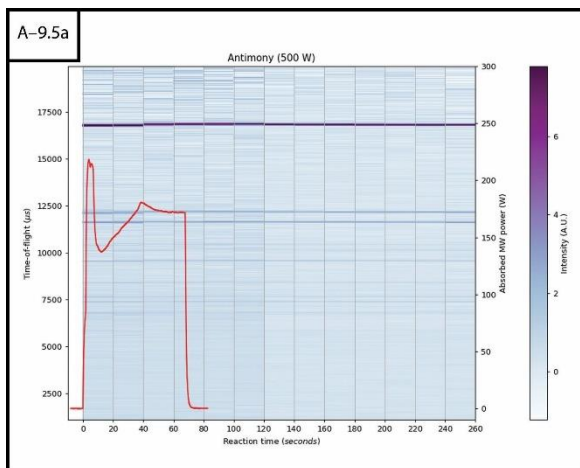


Figure A-9.5: Colourmap plots of sliced event mode TOF data with absorbed MW power overlaid for Sb powder heated using 500 W forward power for 67 s a) data processed as 20 s sections and b) 5 s sections

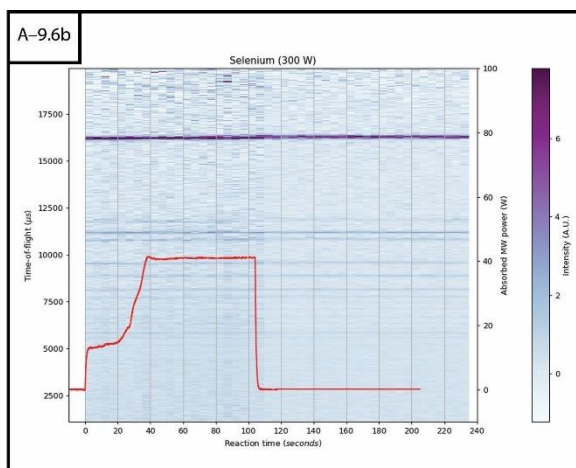
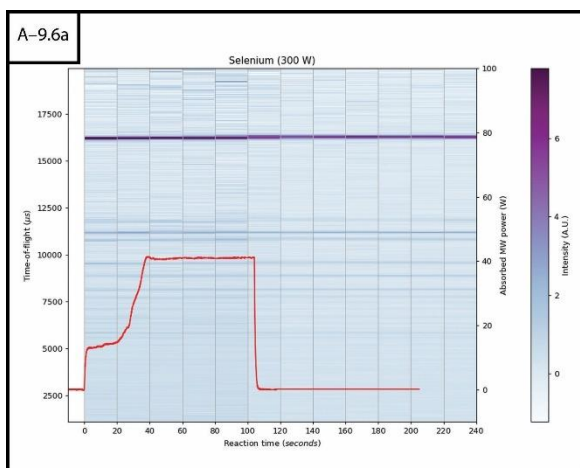


Figure A-9.6: Colourmap plots of sliced event mode TOF data with absorbed MW power overlaid for Se powder heated using 300 W forward power for 104 s a) data processed as 20 s sections and b) 5 s sections

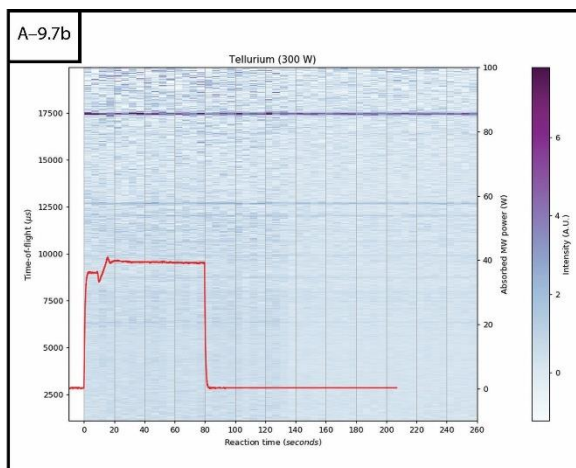
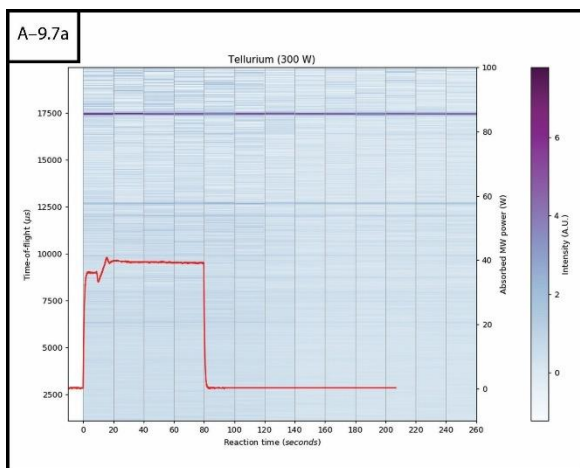


Figure A-9.7: Colourmap plots of sliced event mode TOF data with absorbed MW power overlaid for Te powder heated using 300 W forward power for 80 s a) data processed as 20 s sections and b) 5 s sections

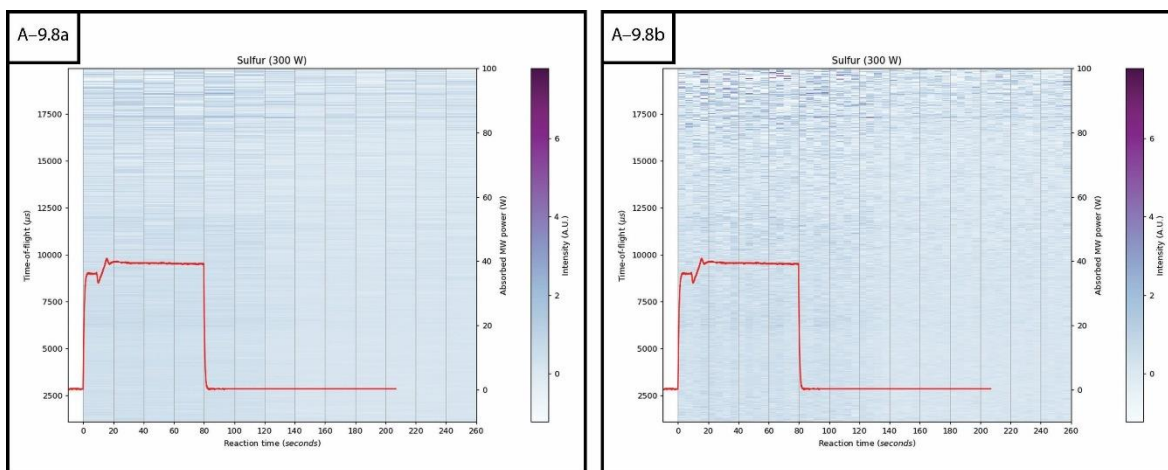


Figure A-9.8: Colourmap plots of sliced event mode TOF data with absorbed MW power overlaid for S powder heated using 300 W forward power for 75 s a) data processed as 20 s sections and b) 5 s sections

A-9.7 Extending $\text{Bi}_2\text{Se}_{3-x}\text{Te}_x$ heating duration (120 s syntheses)

The refined PND crystallographic data for the $R\bar{3}m$ phase of $\text{Bi}_2\text{Se}_{3-x}\text{Te}_x$ samples heated using 300 W forward power (except for Bi_2Te_3 which was heated using 100 W forward power with the aid of a graphite susceptor) for ~120 s post reaction TOF histogram data:

Table A-9.9: Crystallographic cell parameters from Rietveld refinement of $\text{Bi}_2\text{Se}_{3-x}\text{Te}_x$ ($x = 0, 0.5, 1, 1.5, 3$) post reaction TOF histogram data

Sample	Bi_2Se_3	$\text{Bi}_2\text{Se}_{2.5}\text{Te}_{0.5}$	$\text{Bi}_2\text{Se}_2\text{Te}$	$\text{Bi}_2\text{Se}_{1.5}\text{Te}_{1.5}$	Bi_2Te_3
Refined site occupancy (Te)	–	–	1.8(2)	–	–
Crystal system	Trigonal	Trigonal	Trigonal	Trigonal	Trigonal
Space group	$R\bar{3}m$	$R\bar{3}m$	$R\bar{3}m$	$R\bar{3}m$	$R\bar{3}m$
a (Å)	4.1476(2)	4.1613(3)	4.1839(6)	4.234(2)	4.3903(3)
b (Å)	4.1476(2)	4.1613(3)	4.1839(6)	4.234(2)	4.3903(3)
c (Å)	28.715(3)	28.857(4)	29.106(9)	29.60(3)	30.538(3)
α (°)	90	90	90	90	90
β (°)	90	90	90	90	90
γ (°)	120	120	120	120	120
Volume (Å³)	427.79(4)	432.76(5)	441.2(1)	459.5(3)	509.8(5)
Phase fraction (wt.%)	63.5(5)	89.7(7)	83(1)	87.7(3)	91.5(2)
Observations	1999	1999	1999	1999	1999
Variables	60	60	60	47	58
R_{wp}	0.0223	0.0174	0.0189	0.0189	0.0203
R_p	0.0362	0.0332	0.0368	0.0374	0.0375
χ^2	2.357	1.430	1.749	1.698	2.031

The refined PND crystallographic data for 20 s sliced $\text{Bi}_2\text{Se}_2\text{Te}$ ($R\bar{3}m$ phase) event mode TOF data:

Table A-9.10: Crystallographic cell parameters from Rietveld refinement of sliced $\text{Bi}_2\text{Se}_2\text{Te}$ event mode TOF data (40–120 s)

Data time-slices (s)	40–60	60–80	80–100	100–120
Refined site occupancy (Te)	–	2.4(5)	2.0(4)	–
Crystal system	Trigonal	Trigonal	Trigonal	Trigonal
Space group	$R\bar{3}m$	$R\bar{3}m$	$R\bar{3}m$	$R\bar{3}m$
Phase fraction (wt.%)	–	75(4)	69(3)	75(1)
Observations	1935	1942	1938	1945
Variables	45	57	51	52
R_{wp}	0.2119	0.1817	0.1927	0.2007
R_p	0.3234	0.2582	0.2727	0.2829
χ^2	0.8173	0.6794	0.7334	0.7059

A-9.8 Effect of synthesis duration on $\text{Sb}_2\text{Se}_{3-x}\text{Te}_x$ solid solutions

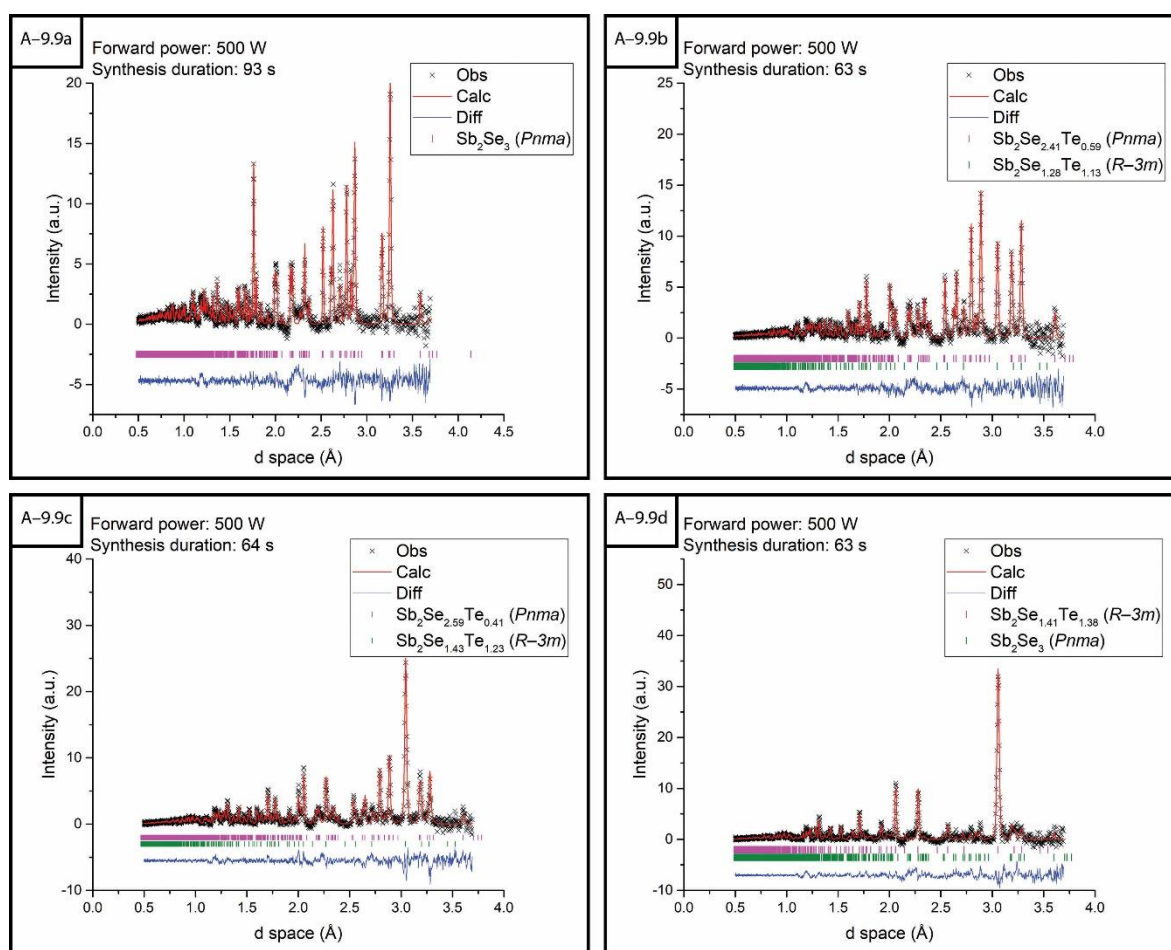


Figure A-9.9: Plots of refined post reaction histogram TOF data for a) Sb_2Se_3 synthesised for 93 s b) $\text{Sb}_2\text{Se}_{2.6}\text{Te}_{0.4}$ synthesised for 63 s c) $\text{Sb}_2\text{Se}_{2.4}\text{Te}_{0.6}$ synthesised for 64 s d) $\text{Sb}_2\text{Se}_2\text{Te}$ synthesised for 63 s

The refined PND crystallographic data for $\text{Sb}_2\text{Se}_{3-x}\text{Te}_x$ synthesised in 60 s post reaction TOF histogram data, appearing in figures 9.33, 9.34 and A-9.9:

Table A-9.11: Crystallographic parameters from Rietveld refinement of $\text{Sb}_2\text{Se}_{3-x}\text{Te}_x$ ($x = 0, 0.2, 0.4$) post reaction TOF histogram

Sample	Sb_2Se_3	$\text{Sb}_2\text{Se}_{2.8}\text{Te}_{0.2}$	$\text{Sb}_2\text{Se}_{2.6}\text{Te}_{0.4}$	
Refined site		Te1 = 0.3(1)	Te1 = 0.1(2)	
occupancy (Te)	–	Te2 = 0.3(1) Te3 = 0.3(1)	Te2 = 0.4(1)	1.1(1)
Crystal system	Orthorhombic	Orthorhombic	Orthorhombic	Trigonal
Space group	<i>Pnma</i>	<i>Pnma</i>	<i>Pnma</i>	$R\bar{3}m$
<i>a</i> (Å)	11.777(5)	11.847(8)	11.89(1)	4.110(6)
<i>b</i> (Å)	3.977(2)	3.995(3)	4.003(3)	4.110(6)
<i>c</i> (Å)	11.632(7)	11.69(1)	11.71(1)	29.53(1)
α (°)	90	90	90	90
β (°)	90	90	90	90
γ (°)	120	120	120	120
Phase fraction (wt.%)	100	100	80(1)	20(2)
Observations	1999	1999	1999	
Variables	61	61	71	
R_{wp}	0.0168	0.0158	0.0152	
R_p	0.0288	0.0297	0.0281	
χ^2	1.396	1.210	1.129	

Table A-9.12: Crystallographic parameters from Rietveld refinement of $\text{Sb}_2\text{Se}_{3-x}\text{Te}_x$ ($x = 0.5, 0.6$) post reaction TOF histogram data

Sample	$\text{Sb}_2\text{Se}_{2.5}\text{Te}_{0.5}$		$\text{Sb}_2\text{Se}_{2.4}\text{Te}_{0.6}$	
Refined site	Te1 = 0.1(1)		Te2 = 0.4(1)	
occupancy (Te)	Te2 = 0.2(1)	1.19(8)		1.23(5)
Crystal system	Orthorhombic	Trigonal	Orthorhombic	Trigonal
Space group	<i>Pnma</i>	$R\bar{3}m$	<i>Pnma</i>	$R\bar{3}m$
<i>a</i> (Å)	11.88(1)	4.103(4)	11.88(1)	4.102(3)
<i>b</i> (Å)	3.999(4)	4.103(4)	3.999(5)	4.102(3)
<i>c</i> (Å)	11.69(1)	29.49(6)	11.69(2)	29.45(4)
α (°)	90	90	90	90
β (°)	90	90	90	90
γ (°)	120	120	120	120
Phase fraction (wt.%)	67(1)	33(2)	53(1)	47(1)
Observations	1999		1999	
Variables	71		68	
R_{wp}	0.0150		0.0174	
R_p	0.0261		0.0312	
χ^2	1.154		1.486	

Table A-9.13: Crystallographic parameters from Rietveld refinement of $\text{Sb}_2\text{Se}_{3-x}\text{Te}_x$ ($x = 0.8, 1$) post reaction TOF histogram data

Sample	$\text{Sb}_2\text{Se}_{2.2}\text{Te}_{0.8}$		$\text{Sb}_2\text{Se}_2\text{Te}$	
Refined site occupancy (Te)	–	–	–	1.38(5)
Crystal system	Orthorhombic	Trigonal	Orthorhombic	Trigonal
Space group	$Pnma$	$R\bar{3}m$	$Pnma$	$R\bar{3}m$
a (Å)	11.86(4)	4.110(3)	11.85(8)	4.117(3)
b (Å)	4.00(1)	4.110(3)	3.99(2)	4.117(3)
c (Å)	11.69(5)	29.48(4)	11.70(7)	29.59(4)
α (°)	90	90	90	90
β (°)	90	90	90	90
γ (°)	120	120	120	120
Phase fraction (wt.%)	32(1)	68(1)	1.9(1)	98.1(1)
Observations	1999		1999	
Variables	56		54	
R_{wp}	0.0196		0.0191	
R_p	0.0358		0.0349	
χ^2	1.878		1.750	

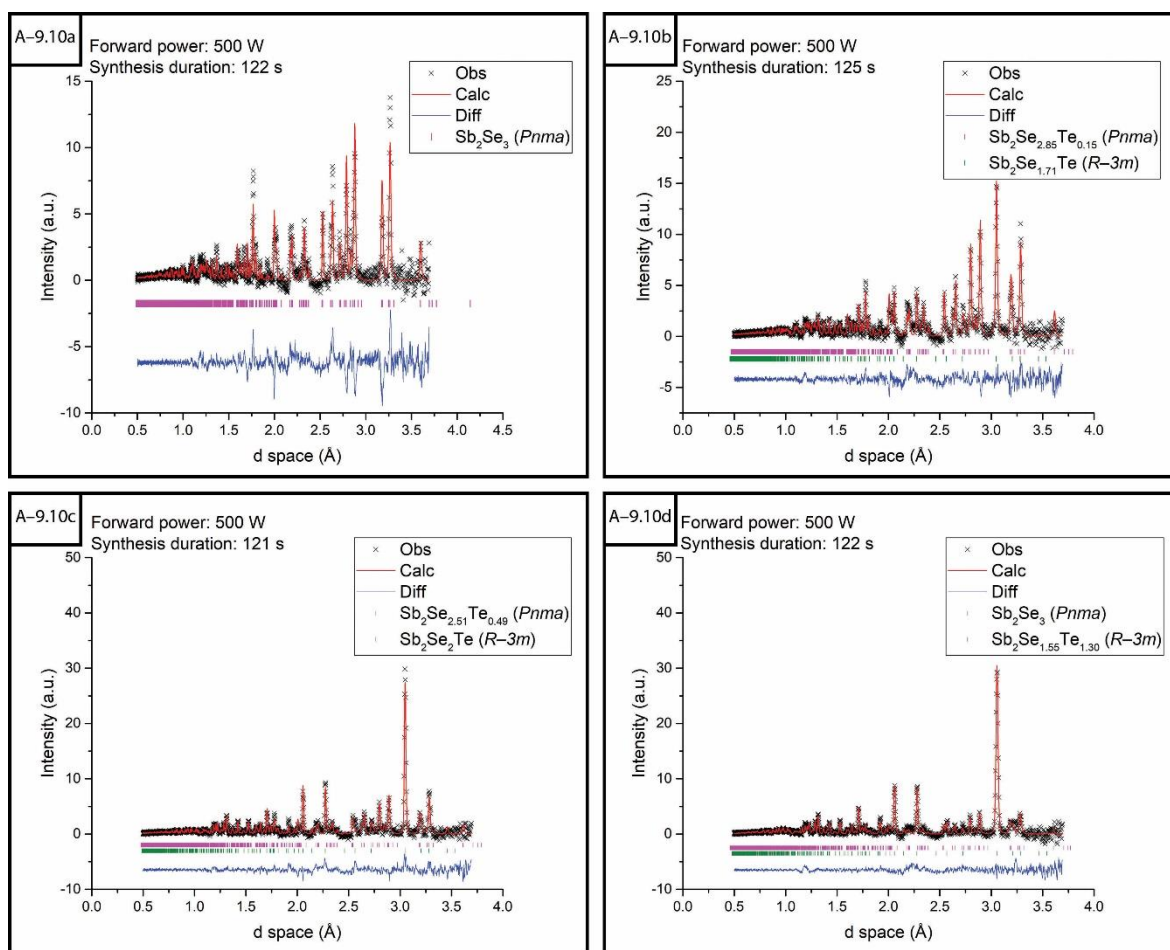


Figure A-9.10: Plots of refined post reaction histogram data for a) Sb_2Se_3 synthesised for 122 s b) $\text{Sb}_2\text{Se}_{2.6}\text{Te}_{0.4}$ synthesised for 125 s c) $\text{Sb}_2\text{Se}_{2.4}\text{Te}_{0.6}$ synthesised for 121 s d) $\text{Sb}_2\text{Se}_2\text{Te}$ synthesised for 122 s

The refined PND crystallographic data for $\text{Sb}_2\text{Se}_{3-x}\text{Te}_x$ synthesised in 120 s post reaction TOF histogram data, appearing in figures 9.33, 9.34 and A-9.10:

Table A-9.14: Crystallographic parameters from Rietveld refinement of $\text{Sb}_2\text{Se}_{3-x}\text{Te}_x$ ($x = 0, 0.2, 0.4$) post reaction TOF histogram data

Sample	Sb_2Se_3	$\text{Sb}_2\text{Se}_{2.8}\text{Te}_{0.2}$	
Refined site occupancy (Te)	–	Te1 = 0.1(1)	–
Crystal system	Orthorhombic	Orthorhombic	Trigonal
Space group	$Pnma$	$Pnma$	$R\bar{3}m$
a (Å)	11.81(1)	11.87(1)	4.12(2)
b (Å)	3.992(4)	4.004(4)	4.12(2)
c (Å)	11.67(2)	11.704(1)	29.5(3)
α (°)	90	90	90
β (°)	90	90	90
γ (°)	120	120	120
Phase fraction (wt.%)	100	92(2)	8(21)
Observations	1999	1999	
Variables	58	64	
R_{wp}	0.0223	0.0175	
R_p	0.0404	0.0322	
χ^2	2.394	1.440	

Table A-9.15: Crystallographic parameters from Rietveld refinement of $\text{Sb}_2\text{Se}_{3-x}\text{Te}_x$ ($x = 0.5, 6$) post reaction TOF histogram data

Sample	$\text{Sb}_2\text{Se}_{2.6}\text{Te}_{0.4}$		$\text{Sb}_2\text{Se}_{2.5}\text{Te}_{0.5}$	
Refined site occupancy (Te)	Te1 = 0.1(1)	1.00(9)	Te1 = 0.1(2) Te2 = 0.1(2)	1.3(1)
Crystal system	Orthorhombic	Trigonal	Orthorhombic	Trigonal
Space group	$Pnma$	$R\bar{3}m$	$Pnma$	$R\bar{3}m$
a (Å)	11.89(1)	4.109(4)	11.90(2)	4.112(3)
b (Å)	4.009(4)	4.109(4)	4.012(5)	4.112(3)
c (Å)	11.72(2)	29.54(7)	11.73(2)	29.58(5)
α (°)	90	90	90	90
β (°)	90	90	90	90
γ (°)	120	120	120	120
Phase fraction (wt.%)	69(1)	31(2)	57(2)	43(2)
Observations	1999		1999	
Variables	70		73	
R_{wp}	0.0165		0.0150	
R_p	0.0295		0.0276	
χ^2	1.317		1.066	

Table A-9.16: Crystallographic parameters from Rietveld refinement of $\text{Sb}_2\text{Se}_{3-x}\text{Te}_x$ ($x = 0.6, 0.8$) post reaction TOF histogram data

Sample	$\text{Sb}_2\text{Se}_{2.4}\text{Te}_{0.6}$		$\text{Sb}_2\text{Se}_{2.2}\text{Te}_{0.8}$	
Refined site occupancy (Te)	Te1 = 0.5(2)	–	–	1.40(7)
Crystal system	Orthorhombic	Trigonal	Orthorhombic	Trigonal
Space group	$Pnma$	$R\bar{3}m$	$Pnma$	$R\bar{3}m$
a (Å)	11.89(2)	4.107(2)	11.88(2)	4.112(2)
b (Å)	4.006(7)	4.107(2)	3.999(6)	4.112(2)
c (Å)	11.71(3)	29.52(3)	11.70(2)	29.57(3)
α (°)	90	90	90	90
β (°)	90	90	90	90
γ (°)	120	120	120	120
Phase fraction (wt.%)	58(1)	42(1)	44(1)	56(1)
Observations	1999		1999	
Variables	63		71	
R_{wp}	0.0180		0.0169	
R_p	0.0316		0.0321	
χ^2	1.579		1.378	

Table A-9.17: Crystallographic parameters from Rietveld refinement of $\text{Sb}_2\text{Se}_2\text{Te}$ post reaction TOF histogram data

Sample	$\text{Sb}_2\text{Se}_2\text{Te}$	
Refined site occupancy (Te)	–	1.30(4)
Crystal system	Orthorhombic	Trigonal
Space group	$Pnma$	$R\bar{3}m$
a (Å)	11.86(3)	4.116(2)
b (Å)	4.00(1)	4.116(2)
c (Å)	11.70(4)	29.58(4)
α (°)	90	90
β (°)	90	90
γ (°)	120	120
Phase fraction (wt.%)	23(1)	77(1)
Observations	1999	
Variables	53	
R_{wp}	0.0163	
R_p	0.0284	
χ^2	1.554	

A-9.9 $Cu_{1-x}Se_{1-y}Te_y$ in-situ TOF data

The refined PND crystallographic data for 20 s sliced $Cu_{1-x}Se$ event mode TOF data, appearing in figure 9.39:

Table A-9.18: Crystallographic cell parameters from Rietveld refinement of sliced $Cu_{1-x}Se$ event mode TOF data (20–80 s)

Data time-slices (s)	20–40	40–60	60–80
Main phase	Cu	$Cu_{1-x}Se$	$Cu_{1-x}Se$
Crystal system	Cubic	Hexagonal	Hexagonal
Space group	$Fm\bar{3}m$	$P6_3/mmc$	$P6_3/mmc$
a (Å)	3.6165(2)	3.990(1)	–
b (Å)	3.6165(2)	3.990(1)	–
c (Å)	3.6165(2)	17.282(9)	–
α (°)	90	90	–
β (°)	90	90	–
γ (°)	90	120	–
Volume (Å ³)	47.30(1)	238.3(1)	–
Phase fraction (wt.%)	49.5(5)	43(3)	–
Observations	1994	1986	1995
Variables	45	50	37
R_{wp}	0.1086	0.1072	0.1333
R_p	0.1965	0.1857	0.2339
χ^2	0.7991	0.7737	1.161

A-9.10 $Cu_{1-x}Se_{1-y}Te_y$ post reaction TOF histogram data

The refined PND crystallographic data for $Cu_{1-x}Se_{1-y}Te_y$ samples heated using 300 W forward power for ~60 s post reaction TOF histogram data:

Table A-9.19: Crystallographic cell parameters from Rietveld refinement of $Cu_{1-x}Se_{1-y}Te_y$ ($x = 0, 0.4, 0.5$) post reaction TOF histogram data

Sample	$Cu_{1-x}Se$	$Cu_{1-x}Se_{0.6}Te_{0.4}$	$Cu_{1-x}Se_{0.5}Te_{0.5}$
Crystal system	Hexagonal	Cubic	Cubic
Space group	$P6_3/mmc$	$Fm\bar{3}m$	$Fm\bar{3}m$
a (Å)	3.9923(6)	5.7569(1)	5.7902(1)
b (Å)	3.9923(6)	5.7569(1)	5.7902(1)
c (Å)	17.216(5)	5.7569(1)	5.7902(1)
α (°)	90	90	90
β (°)	90	90	90
γ (°)	120	90	90
Volume (Å ³)	237.63(6)	190.79(1)	194.13(1)
Phase fraction (wt.%)	81.3(6)	56.8(4)	61.1(3)
Observations	1999	1999	1999
Variables	51	52	52
R_{wp}	0.0334	0.0169	0.0161
R_p	0.0594	0.0290	0.0291
χ^2	5.429	1.533	1.273

Table A-9.20: Crystallographic cell parameters from Rietveld refinement of $\text{Cu}_{1-x}\text{Se}_{1-y}\text{Te}_y$ ($x = 0.6, 0.8, 1$) post reaction TOF histogram data

Sample	$\text{Cu}_{1-x}\text{Se}_{0.4}\text{Te}_{0.6}$	$\text{Cu}_{1-x}\text{Se}_{0.2}\text{Te}_{0.8}$	Cu_{1-x}Te
Crystal system	Cubic	Cubic	Orthorhombic
Space group	$Fm\bar{3}m$	$Fm\bar{3}m$	$Pmmn$
<i>a</i> (Å)	5.7973(7)	5.7794(7)	3.153(2)
<i>b</i> (Å)	5.7973(7)	5.7794(7)	4.067(2)
<i>c</i> (Å)	5.7973(7)	5.7794(7)	7.060(7)
<i>a</i> (°)	90	90	90
<i>β</i> (°)	90	90	90
<i>γ</i> (°)	90	90	120
Volume (Å³)	194.84(7)	193.04(8)	90.5(1)
Phase fraction (wt.%)	43.8(8)	32(1)	54(3)
Observations	1999	1999	1999
Variables	50	50	51
<i>R</i>_{wp}	0.0258	0.0289	0.0374
<i>R</i>_p	0.0388	0.0406	0.0545
χ^2	3.215	4.010	6.954

A-9.11 $\text{Cu}_{1-x}\text{Se}_{1-y}\text{S}_y$ post reaction TOF histogram data

The refined PND crystallographic data for $\text{Cu}_{1-x}\text{Se}_{1-y}\text{S}_y$ samples heated using 300 W forward power for ~60 s post reaction TOF histogram data:

Table A-9.21: Crystallographic cell parameters from Rietveld refinement of $\text{Cu}_{1-x}\text{Se}_{1-y}\text{S}_y$ ($x = 0.2, 0.4, 0.5, 0.6, 1$) post reaction TOF histogram data

Sample	$\text{Cu}_{1-x}\text{Se}_{1-y}\text{S}_y$				
	0.2	0.4	0.5	0.6	1
Refined site occupancy (S)	S1 = 0.51(6)	0.92(4)	–	S1 = 0.2(2)	–
Crystal system	Hexagonal	Hexagonal	Hexagonal	Hexagonal	Hexagonal
Space group	$P6_3/mmc$	$P6_3/mmc$	$P6_3/mmc$	$P6_3/mmc$	$P6_3/mmc$
<i>a</i> (Å)	3.9695(6)	3.972(1)	3.926(2)	3.885(1)	3.7895(4)
<i>b</i> (Å)	3.9695(6)	3.972(1)	3.926(2)	3.885(1)	3.7895(4)
<i>c</i> (Å)	17.176(4)	17.08(1)	16.96(2)	16.87(1)	16.348(3)
<i>a</i> (°)	90	90	90	90	90
<i>β</i> (°)	90	90	90	90	90
<i>γ</i> (°)	120	120	120	120	120
Volume (Å³)	234.39(6)	233.4(1)	226.4(2)	220.5(1)	203.31(4)
Observations	1999	1999	1999	1999	1999
Variables	50	46	43	48	41
<i>R</i>_{wp}	0.0199	0.0204	0.0213	0.0202	0.0321
<i>R</i>_p	0.0380	0.0396	0.0388	0.0372	0.0419
χ^2	1.957	2.124	2.225	2.027	5.091

A-9.12 $\text{SnSe}_{1-x}\text{Te}_x$ (stoichiometric) event mode TOF data

Colourmap plots for 20 s and 5 s sliced $\text{SnSe}_{1-x}\text{Te}_x$ event mode TOF data against reaction time with absorbed MW power overlaid. The MW power data for the $\text{SnSe}_{0.8}\text{Te}_{0.2}$ sample was not recorded:

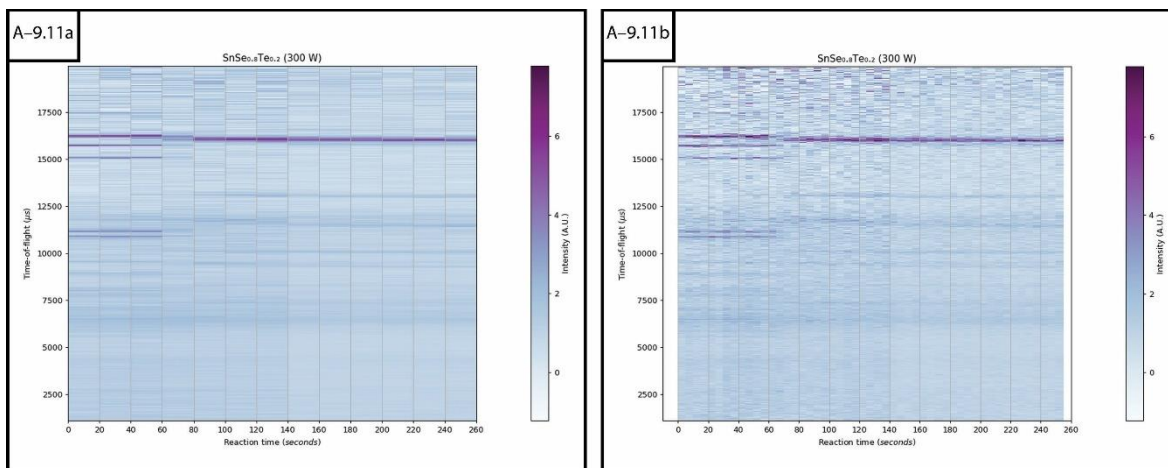


Figure A-9.11: Colourmap plots of sliced event mode TOF data for $\text{SnSe}_{0.8}\text{Te}_{0.2}$ heated using 300 W forward power a) data processed as 20 s sections and b) 5 s sections

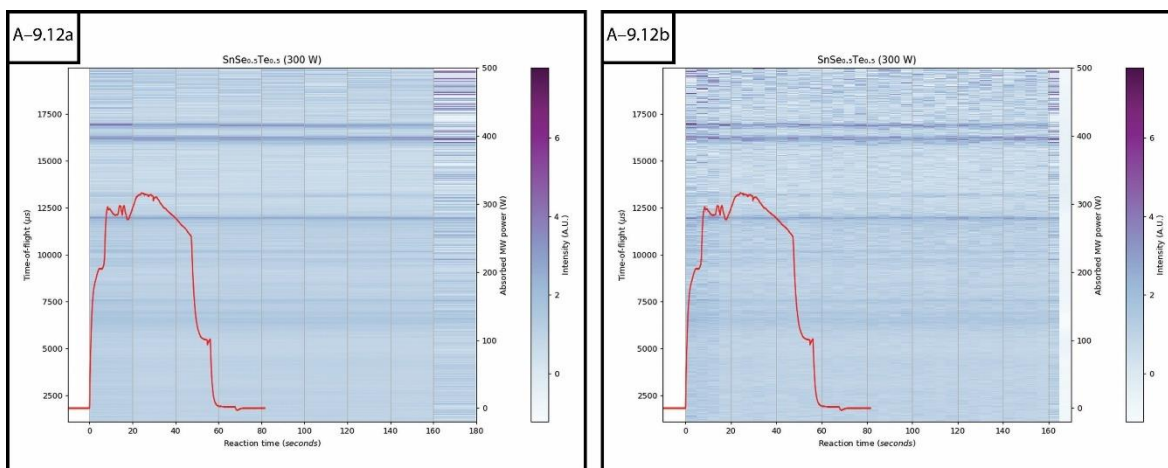


Figure A-9.12: Colourmap plots of sliced event mode TOF data with absorbed MW power overlaid for $\text{SnSe}_{0.5}\text{Te}_{0.5}$ heated using 300 W forward power for 68 s a) data processed as 20 s sections and b) 5 s sections

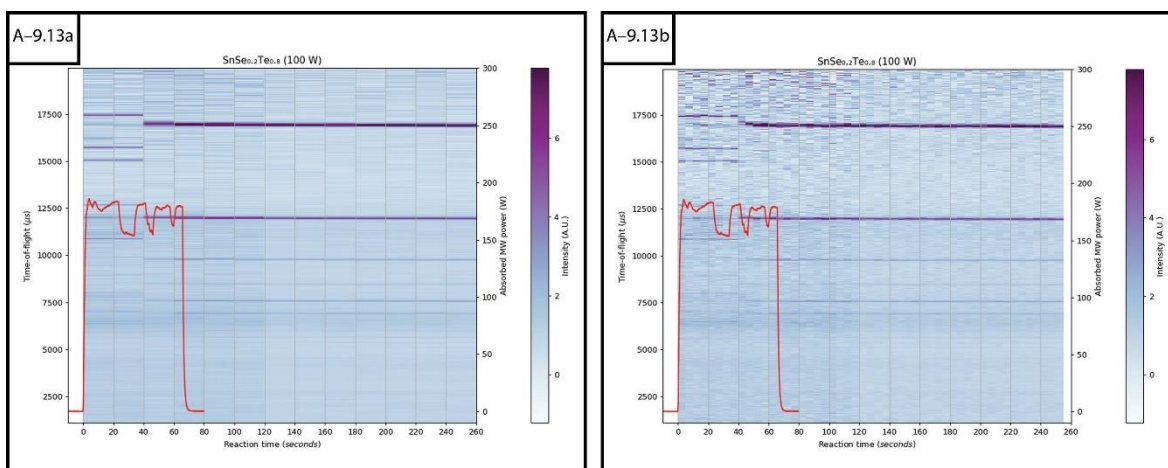


Figure A-9.13: Colourmap plots of sliced event mode TOF data with absorbed MW power overlaid for $\text{SnSe}_{0.2}\text{Te}_{0.8}$ heated using 300 W forward power for 66 s a) data processed as 20 s sections and b) 5 s sections

A-9.13 $\text{SnSe}_{1-x}\text{Te}_x$ (10 % excess Sn) event mode TOF data

Colourmap plots for 20 s and 5 s sliced $\text{SnSe}_{1-x}\text{Te}_x$ (with 10 % excess Sn) event mode TOF data against reaction time with absorbed MW power overlaid:

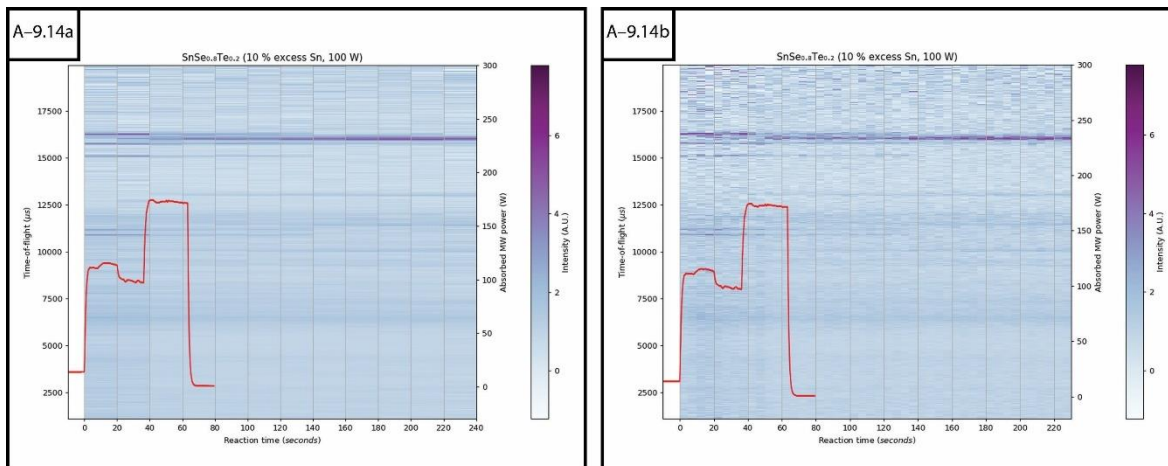


Figure A-9.14: Colourmap plots of sliced event mode TOF data with absorbed MW power overlaid for $\text{SnSe}_{0.8}\text{Te}_{0.2}$ heated using 100 W forward power for 63 s a) data processed as 20 s sections and b) 5 s sections

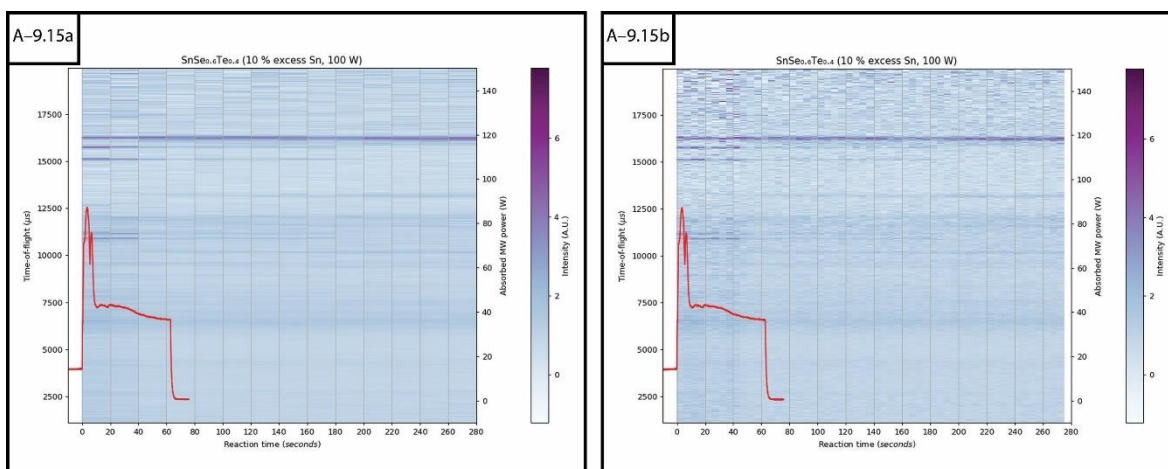


Figure A-9.15: Colourmap plots of sliced event mode TOF data with absorbed MW power overlaid for $\text{SnSe}_{0.6}\text{Te}_{0.4}$ heated using 100 W forward power for 63 s a) data processed as 20 s sections and b) 5 s sections

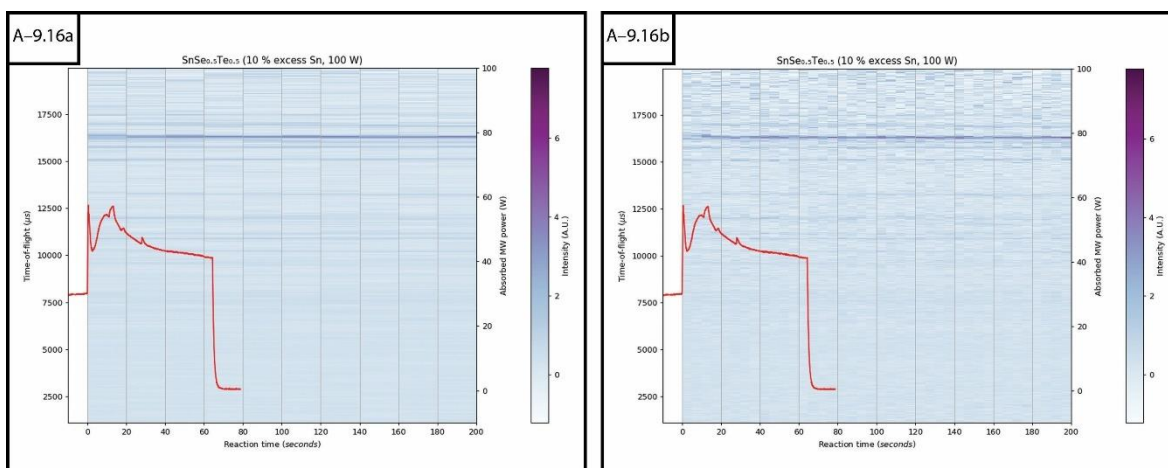


Figure A-9.16: Colourmap plots of sliced event mode TOF data with absorbed MW power overlaid for $\text{SnSe}_{0.5}\text{Te}_{0.5}$ heated using 100 W forward power for 64 s a) data processed as 20 s sections and b) 5 s sections

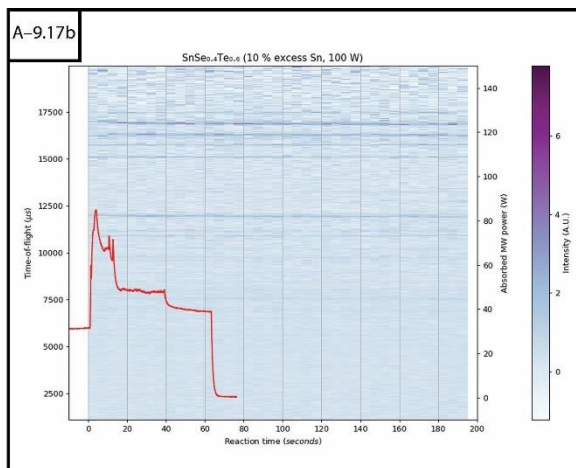
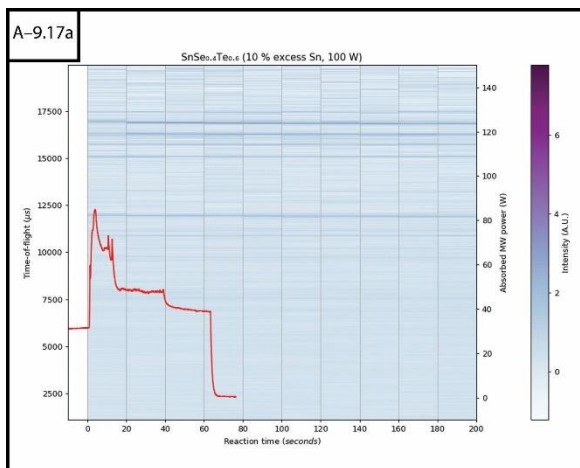


Figure A-9.17: Colourmap plots of sliced event mode TOF data with absorbed MW power overlaid for $\text{SnSe}_{0.4}\text{Te}_{0.6}$ heated using 100 W forward power for 62 s a) data processed as 20 s sections and b) 5 s sections

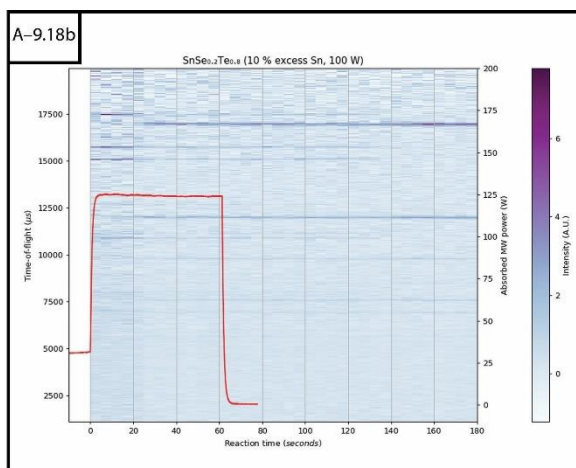
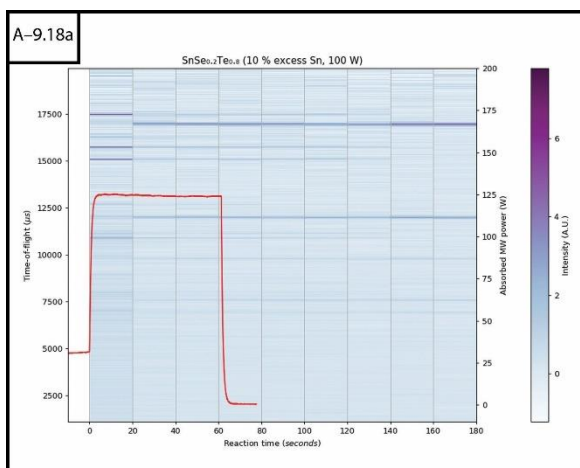


Figure A-9.18: Colourmap plots of sliced event mode TOF data with absorbed MW power overlaid for $\text{SnSe}_{0.2}\text{Te}_{0.8}$ heated using 100 W forward power for 61 s a) data processed as 20 s sections and b) 5 s sections

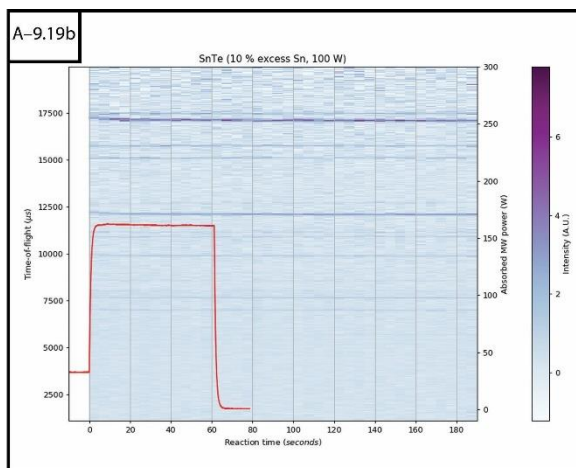
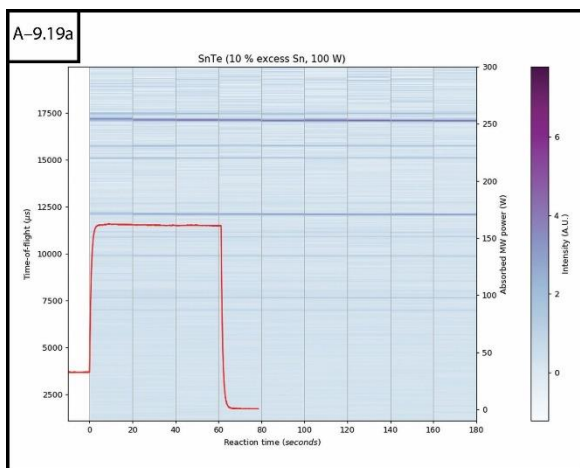


Figure A-9.19: Colourmap plots of sliced event mode TOF data with absorbed MW power overlaid for SnTe heated using 100 W forward power for 61 s a) data processed as 20 s sections and b) 5 s sections

A-9.14 $\text{SnSe}_{1-x}\text{S}_x$ (stoichiometric) event mode TOF data

Colourmap plots for 20 s and 5 s sliced $\text{SnSe}_{1-x}\text{S}_x$ event mode TOF data against reaction time with absorbed MW power overlaid:

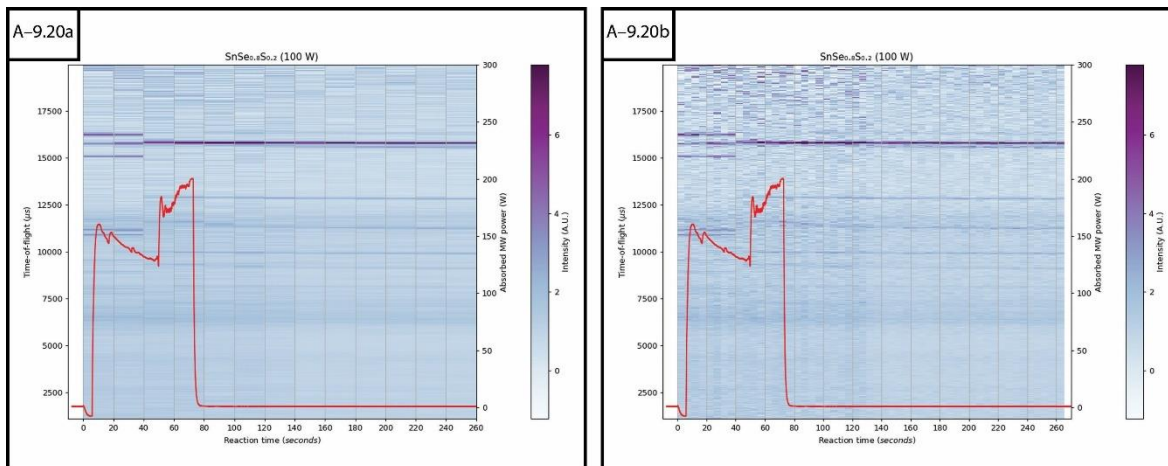


Figure A-9.20: Colourmap plots of sliced event mode TOF data with absorbed MW power overlaid for $\text{SnSe}_{0.8}\text{S}_{0.2}$ heated using 300 W forward power for 73 s a) data processed as 20 s sections and b) 5 s sections

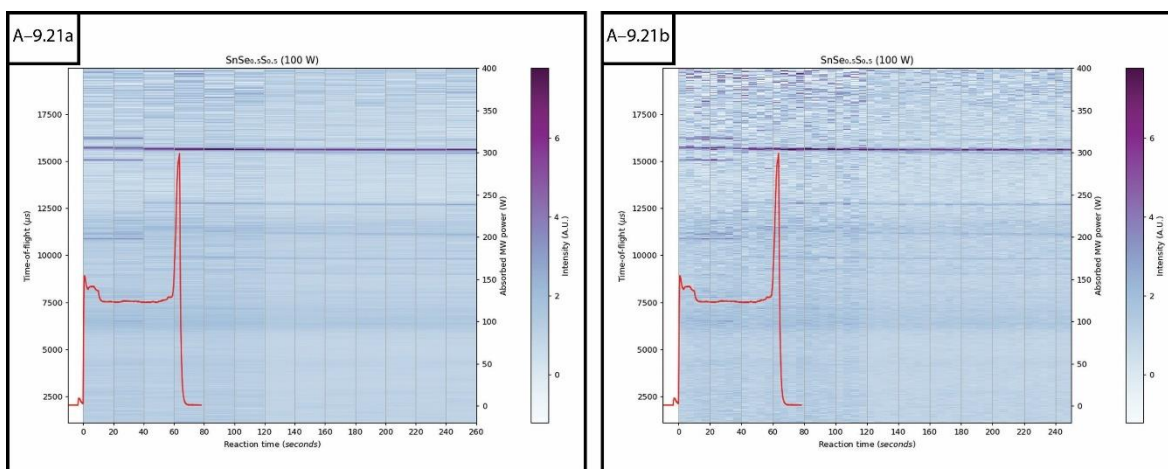


Figure A-9.21: Colourmap plots of sliced event mode TOF data with absorbed MW power overlaid for $\text{SnSe}_{0.5}\text{S}_{0.5}$ heated using 300 W forward power for 64 s a) data processed as 20 s sections and b) 5 s sections

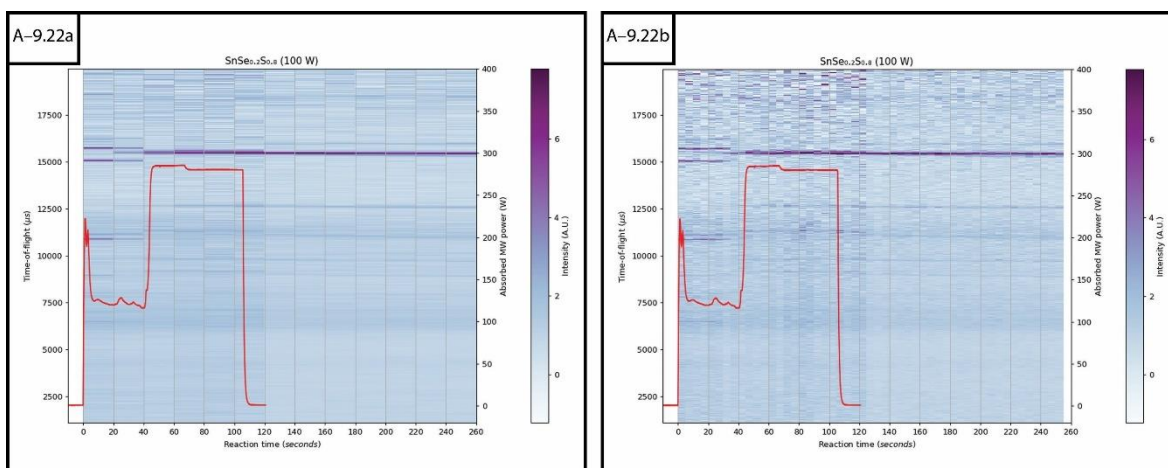


Figure A-9.22: Colourmap plots of sliced event mode TOF data with absorbed MW power overlaid for $\text{SnSe}_{0.2}\text{S}_{0.8}$ heated using 300 W forward power for 106 s a) data processed as 20 s sections and b) 5 s sections

A-9.15 $\text{SnSe}_{1-x}\text{S}_x$ (10 % excess Sn) event mode TOF data

Colourmap plots for 20 s and 5 s sliced $\text{SnSe}_{1-x}\text{S}_x$ (with 10 % excess Sn) event mode TOF data against reaction time with absorbed MW power overlaid:

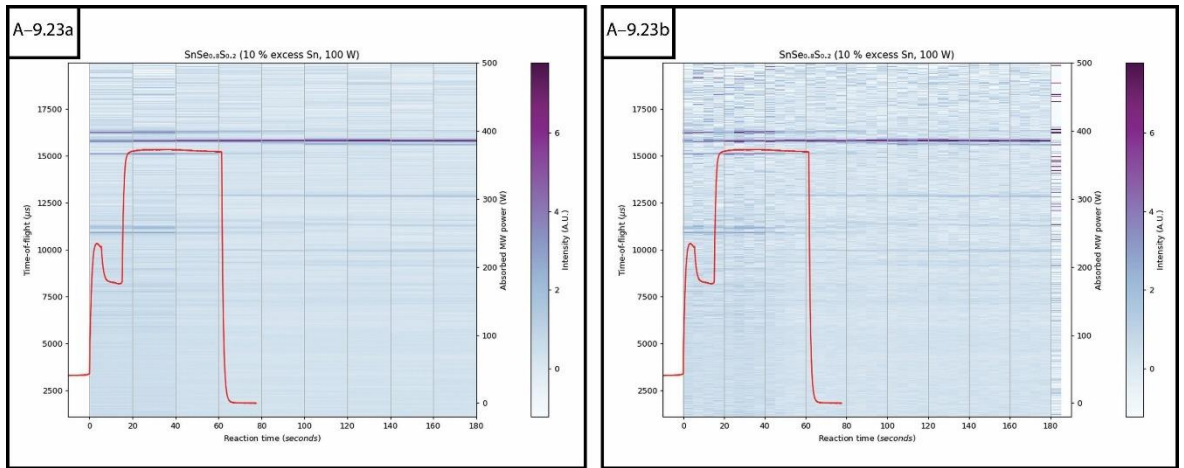


Figure A-9.23: Colourmap plots of sliced event mode TOF data with absorbed MW power overlaid for $\text{SnSe}_{0.8}\text{S}_{0.2}$ heated using 300 W forward power for 62 s a) data processed as 20 s sections and b) 5 s sections

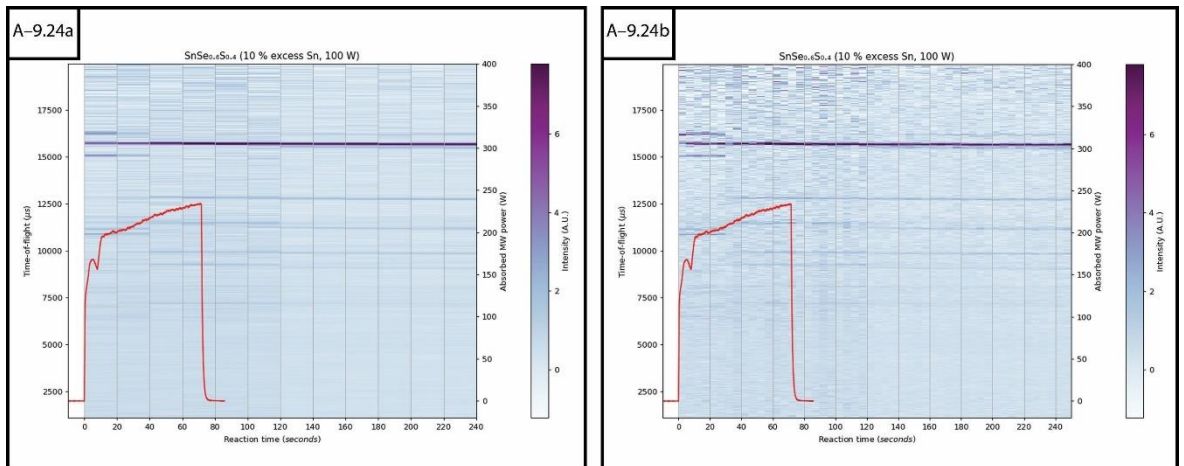


Figure A-9.24: Colourmap plots of sliced event mode TOF data with absorbed MW power overlaid for $\text{SnSe}_{0.6}\text{S}_{0.4}$ heated using 300 W forward power for 72 s a) data processed as 20 s sections and b) 5 s sections

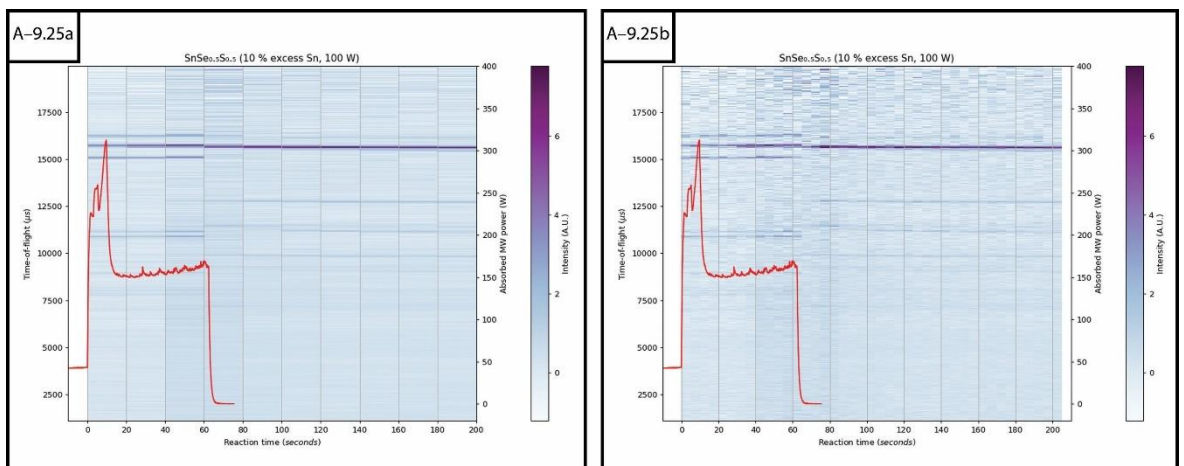


Figure A-9.25: Colourmap plots of sliced event mode TOF data with absorbed MW power overlaid for $\text{SnSe}_{0.5}\text{S}_{0.5}$ heated using 300 W forward power for 62 s a) data processed as 20 s sections and b) 5 s sections

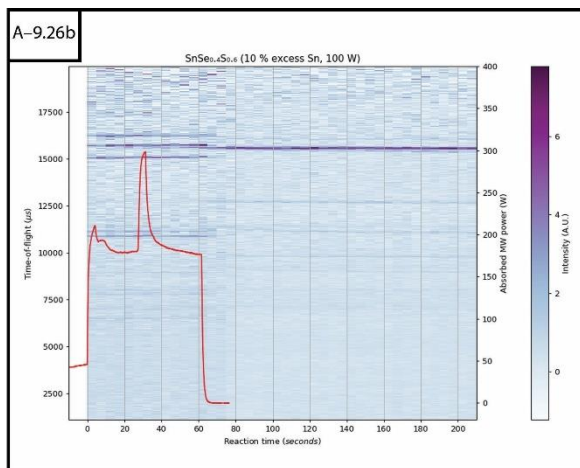
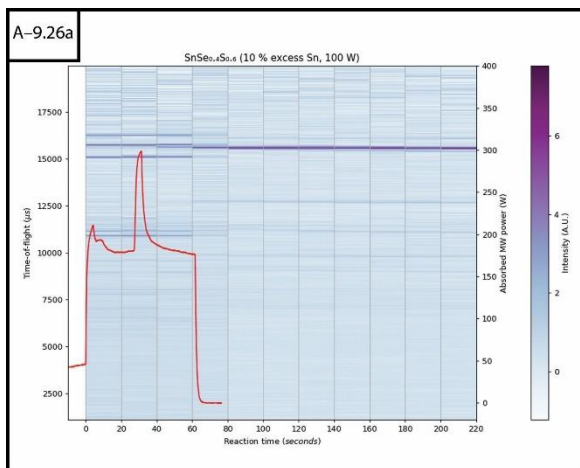


Figure A-9.26: Colourmap plots of sliced event mode TOF data with absorbed MW power overlaid for $\text{SnSe}_{0.4}\text{S}_{0.6}$ heated using 300 W forward power for 62 s a) data processed as 20 s sections and b) 5 s sections

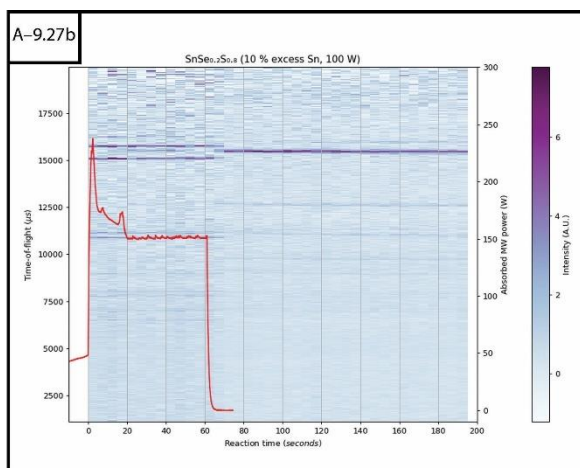
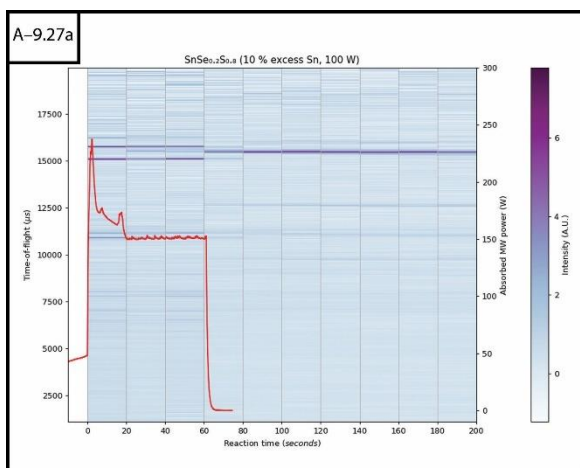


Figure A-9.27: Colourmap plots of sliced event mode TOF data with absorbed MW power overlaid for $\text{SnSe}_{0.2}\text{S}_{0.8}$ heated using 300 W forward power for 61 s a) data processed as 20 s sections and b) 5 s sections

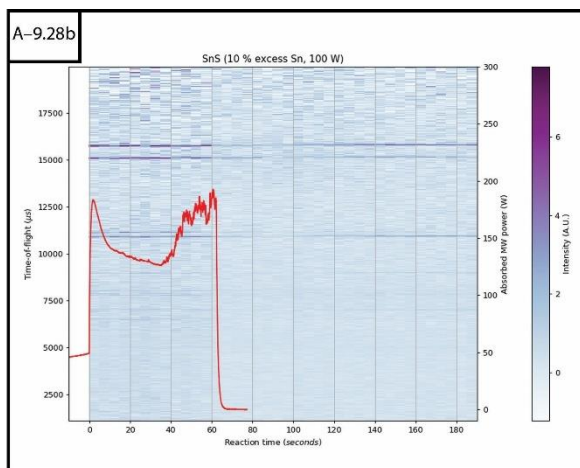
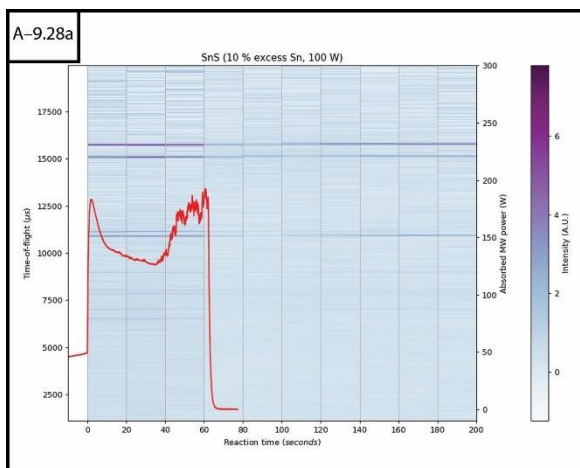


Figure A-9.28: Colourmap plots of sliced event mode TOF data with absorbed MW power overlaid for SnS heated using 300 W forward power for 62 s a) data processed as 20 s sections and b) 5 s sections

A-9.16 $\text{Bi}_2\text{Se}_{3-x}\text{Te}_x$ event mode TOF data (60 s syntheses)

Colourmap plots for 20 s and 5 s sliced $\text{Bi}_2\text{Se}_{3-x}\text{Te}_x$ (60 s) event mode TOF data against reaction time with absorbed MW power overlaid:

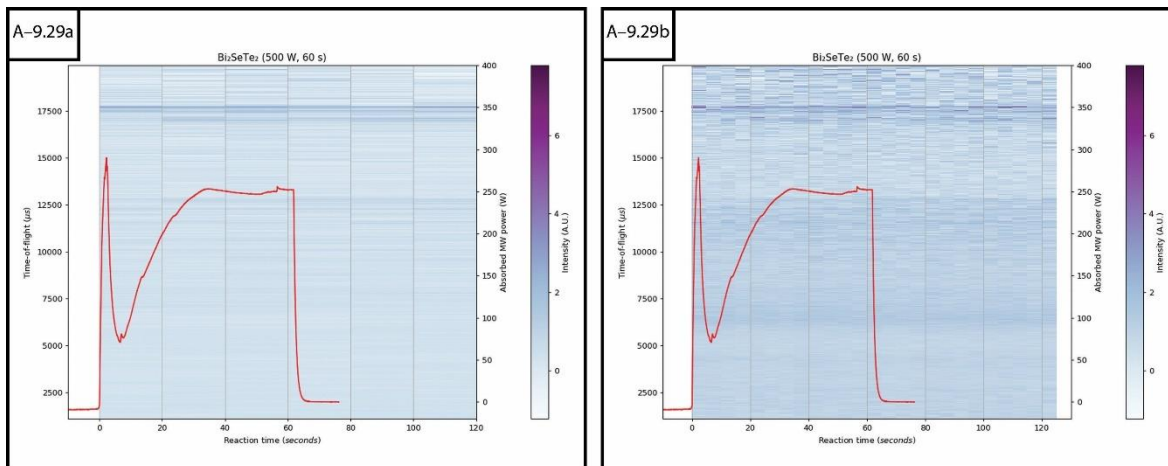


Figure A-9.29: Colourmap plots of sliced event mode TOF data with absorbed MW power overlaid for Bi_2SeTe_2 heated using 500 W forward power for 62 s a) data processed as 20 s sections and b) 5 s sections

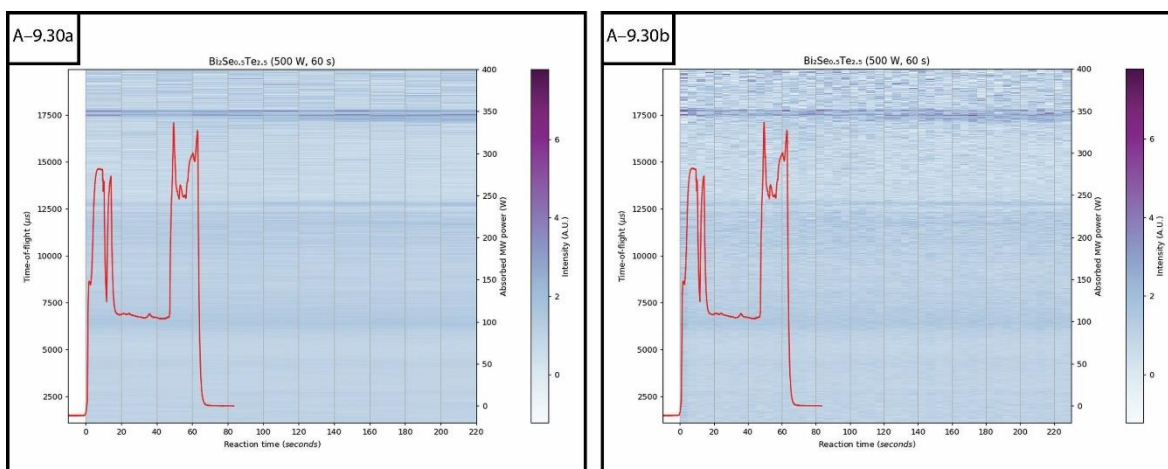


Figure A-9.30: Colourmap plots of sliced event mode TOF data with absorbed MW power overlaid for $\text{Bi}_2\text{Se}_{0.5}\text{Te}_{2.5}$ heated using 500 W forward power for 63 s a) data processed as 20 s sections and b) 5 s sections

A-9.17 $\text{Bi}_2\text{Se}_{3-x}\text{Te}_x$ event mode TOF data (120 s syntheses)

Colourmap plots for 20 s and 5 s sliced $\text{Bi}_2\text{Se}_{3-x}\text{Te}_x$ (120 s) event mode TOF data against reaction time with absorbed MW power overlaid:

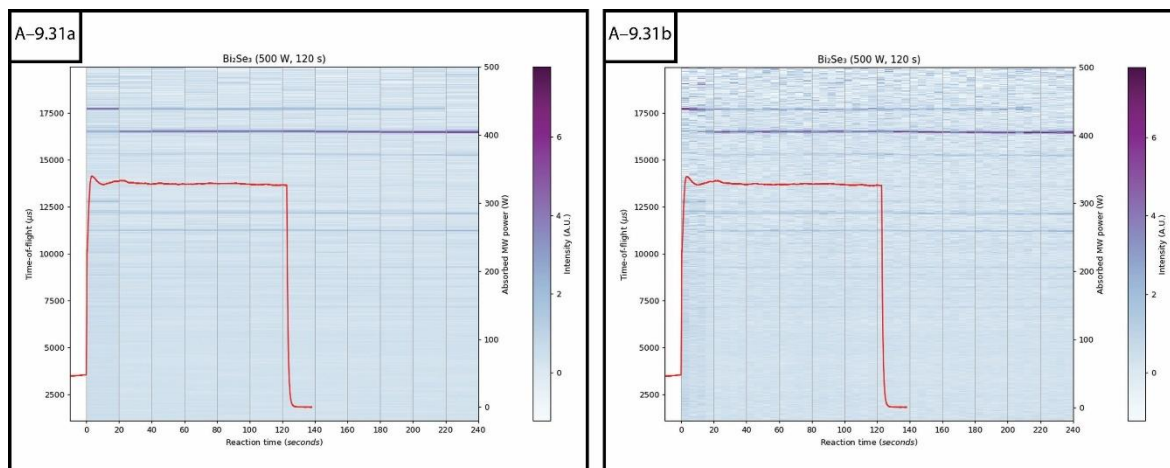


Figure A-9.31: Colourmap plots of sliced event mode TOF data with absorbed MW power overlaid for Bi_2Se_3 heated using 500 W forward power for 123 s a) data processed as 20 s sections and b) 5 s sections

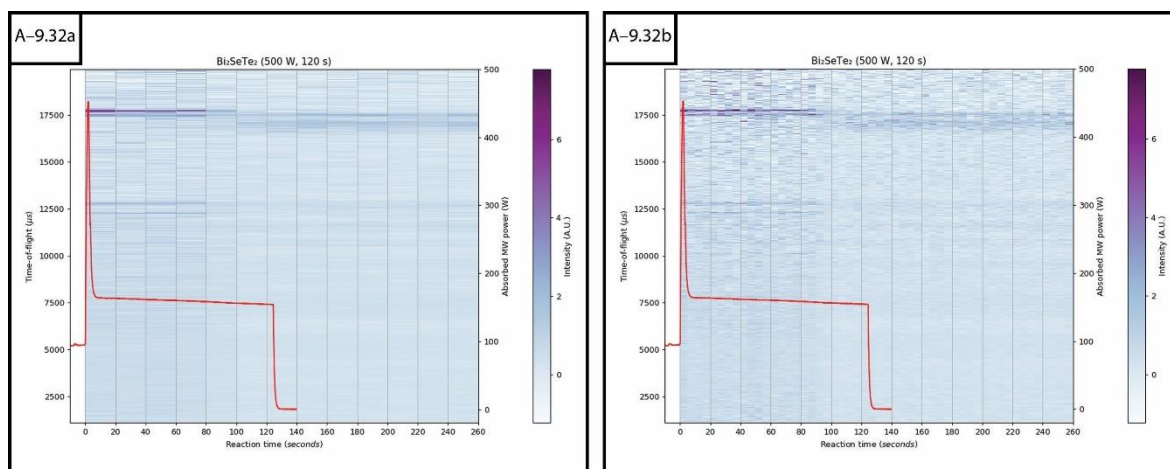


Figure A-9.32: Colourmap plots of sliced event mode TOF data with absorbed MW power overlaid for Bi_2SeTe_2 heated using 500 W forward power for 122 s a) data processed as 20 s sections and b) 5 s sections

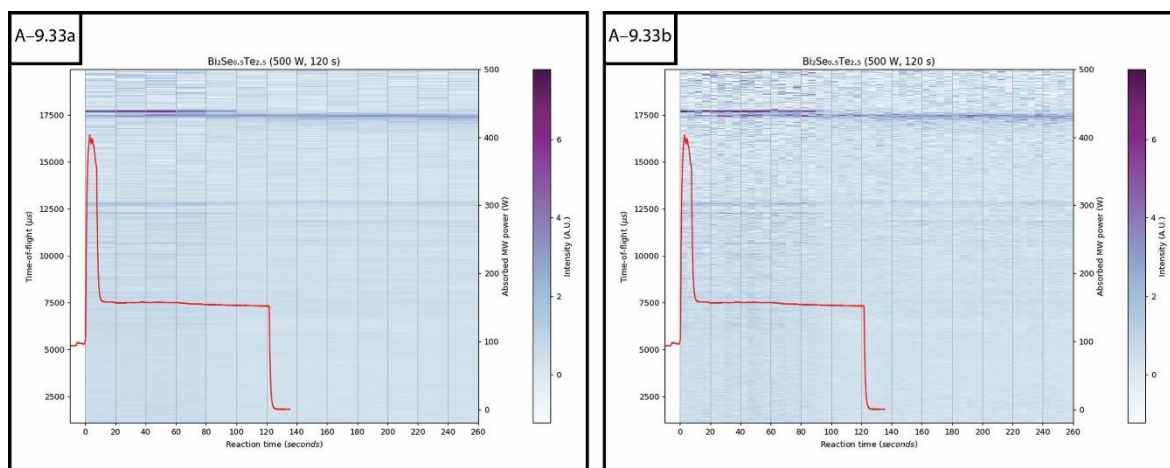


Figure A-9.33: Colourmap plots of sliced event mode TOF data with absorbed MW power overlaid for $\text{Bi}_2\text{Se}_{0.5}\text{Te}_{2.5}$ heated using 500 W forward power for 124 s a) data processed as 20 s sections and b) 5 s sections

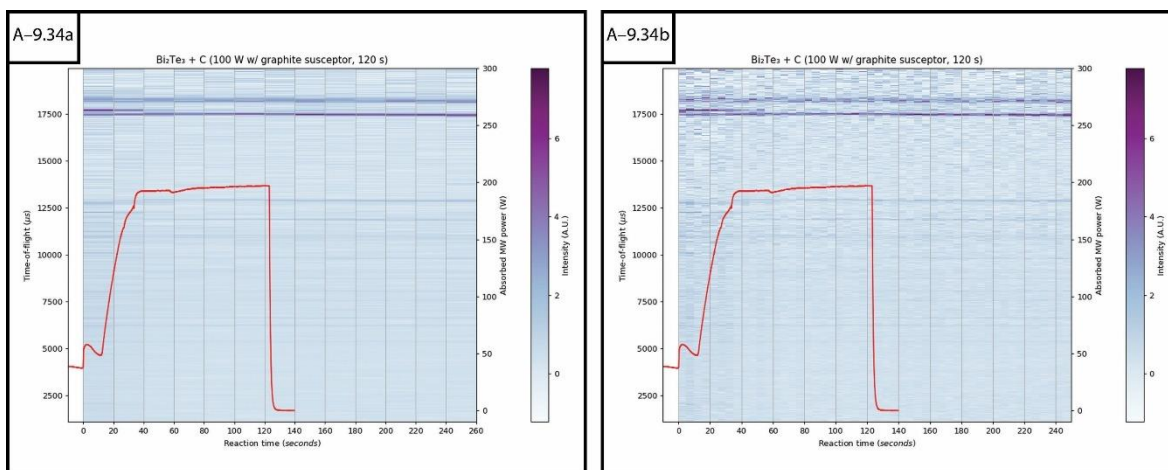


Figure A-9.34: Colourmap plots of sliced event mode TOF data with absorbed MW power overlaid for Bi_2Te_3 heated using 100 W forward power with the aid of a graphite susceptor for 123 s a) data processed as 20 s sections and b) 5 s sections

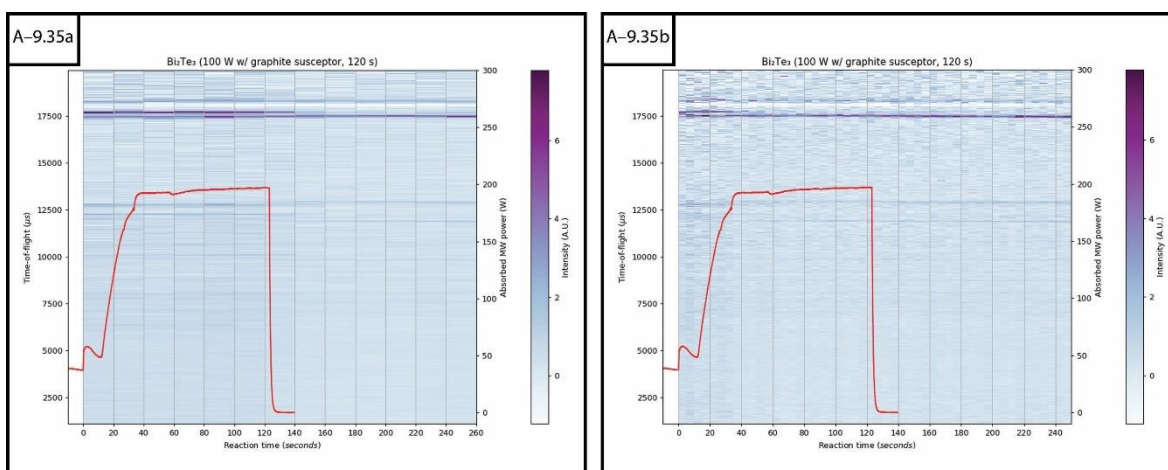


Figure A-9.35: Colourmap plots of sliced event mode TOF data with absorbed MW power overlaid for Bi_2Te_3 heated using 100 W forward power with the aid of a graphite susceptor for 123 s a) data processed with graphite peaks subtracted from background as 20 s sections and b) 5 s sections

A-9.18 Comparing $\text{Sb}_2\text{Se}_{3-x}\text{Te}_x$ (60 s and 120 s) event mode TOF data

Colourmap plots for 20 s and 5 s sliced $\text{Sb}_2\text{Se}_{2.5}\text{Te}_{0.5}$ (60 s and 120 s) event mode TOF data against reaction time with absorbed MW power overlaid:

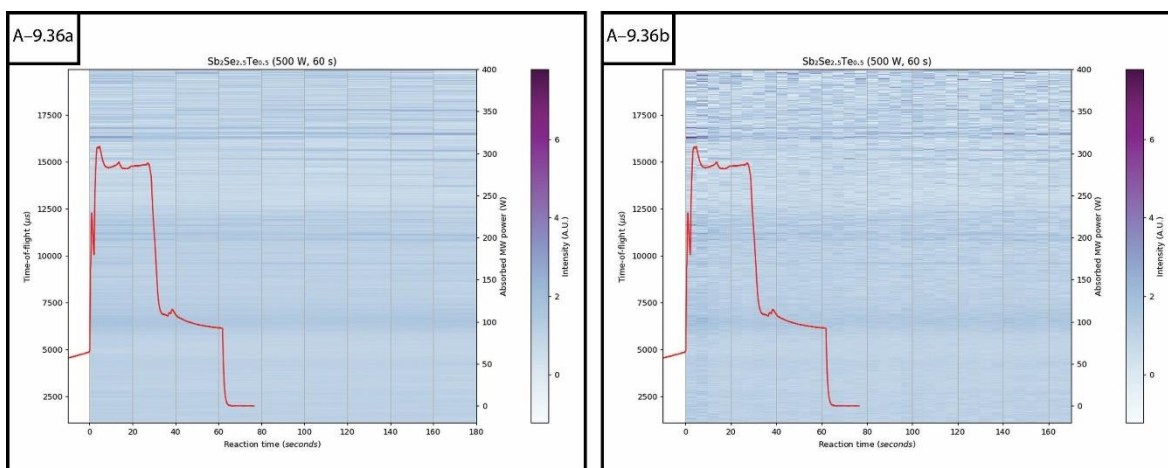


Figure A-9.36: Colourmap plots of sliced event mode TOF data with absorbed MW power overlaid for $\text{Sb}_2\text{Se}_{2.5}\text{Te}_{0.5}$ heated using 500 W forward power for 62 s a) data processed as 20 s sections and b) 5 s sections

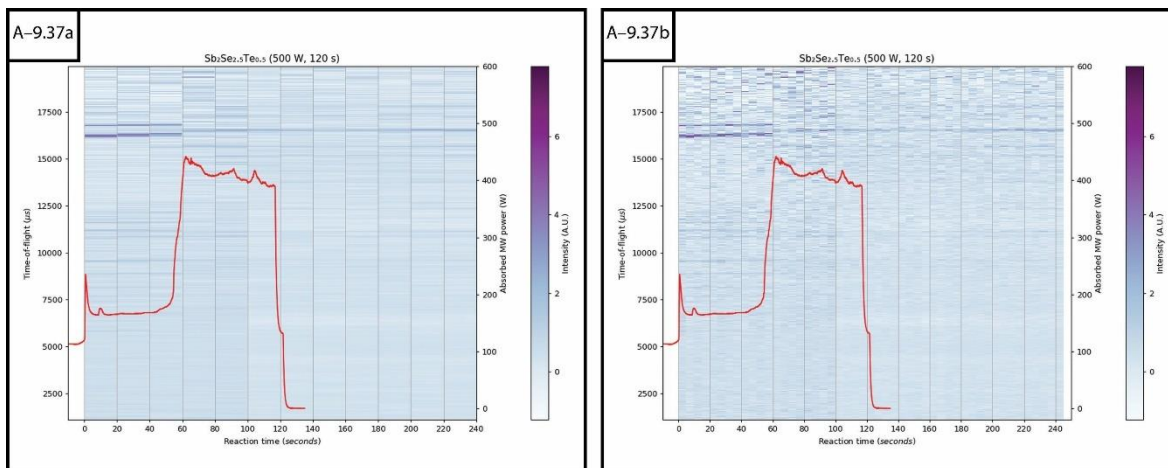


Figure A-9.37: Colourmap plots of sliced event mode TOF data with absorbed MW power overlaid for $\text{Sb}_2\text{Se}_{2.5}\text{Te}_{0.5}$ heated using 500 W forward power for 122 s a) data processed as 20 s sections and b) 5 s sections

A-9.19 $\text{Cu}_{1-x}\text{Se}_{1-y}\text{Te}_y$ event mode TOF data

Colourmap plots for 20 s and 5 s sliced $\text{Cu}_{1-x}\text{Se}_{1-y}\text{Te}_y$ event mode TOF data against reaction time with absorbed MW power overlaid:

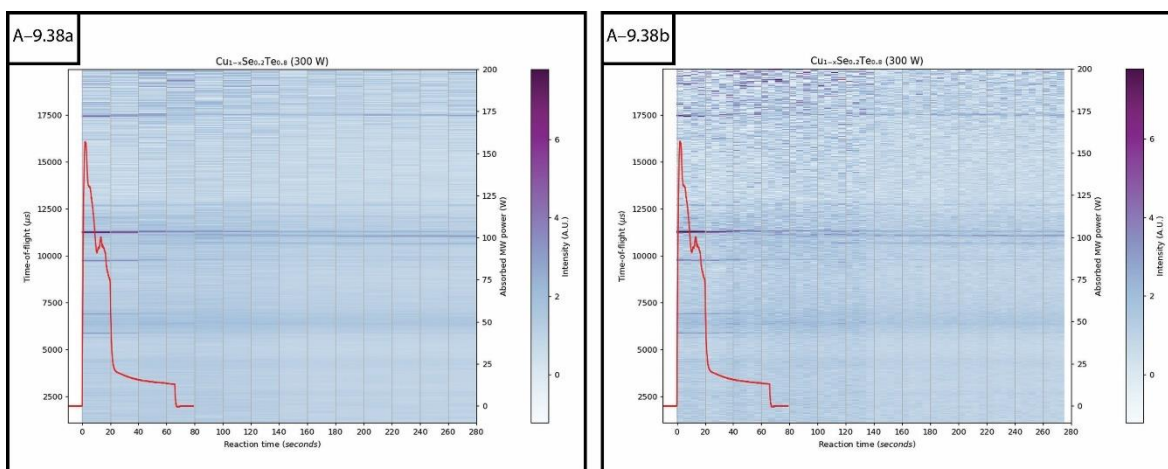


Figure A-9.38: Colourmap plots of sliced event mode TOF data with absorbed MW power overlaid for $\text{Cu}_{1-x}\text{Se}_{0.2}\text{Te}_{0.8}$ heated using 300 W forward power for 66 s a) data processed as 20 s sections and b) 5 s sections

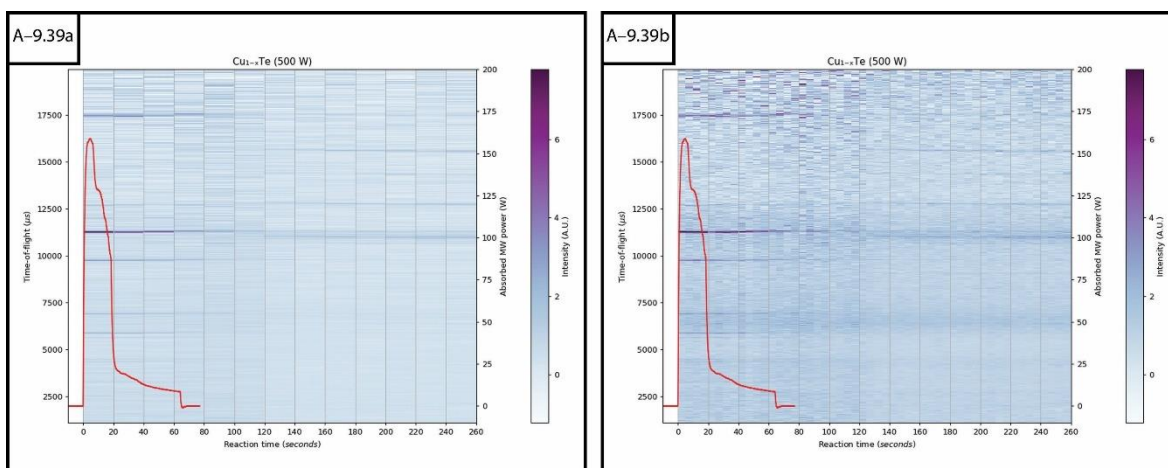


Figure A-9.39: Colourmap plots of sliced event mode TOF data with absorbed MW power overlaid for Cu_{1-x}Te heated using 300 W forward power for 64 s a) data processed as 20 s sections and b) 5 s sections

A-9.20 $Cu_{1-x}Se_{1-y}S_y$ event mode TOF data

Colourmap plots for 20 s and 5 s sliced $Cu_{1-x}Se_{1-y}S_y$ event mode TOF data against reaction time with absorbed MW power overlaid:

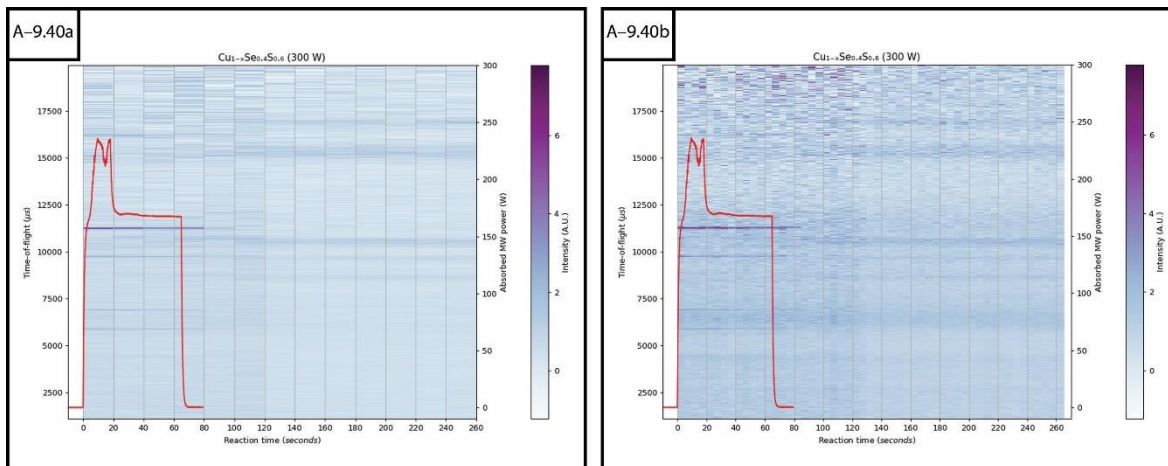


Figure A-9.40: Colourmap plots of sliced event mode TOF data with absorbed MW power overlaid for $Cu_{1-x}Se_{0.4}S_{0.6}$ heated using 300 W forward power for 65 s a) data processed as 20 s sections and b) 5 s sections

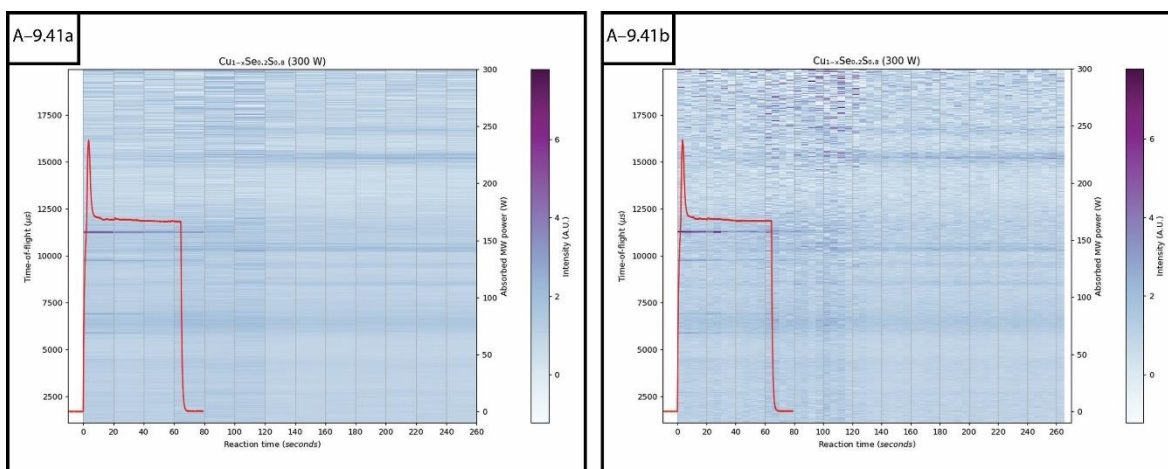


Figure A-9.41: Colourmap plots of sliced event mode TOF data with absorbed MW power overlaid for $Cu_{1-x}Se_{0.2}S_{0.8}$ heated using 300 W forward power for 65 s a) data processed as 20 s sections and b) 5 s sections

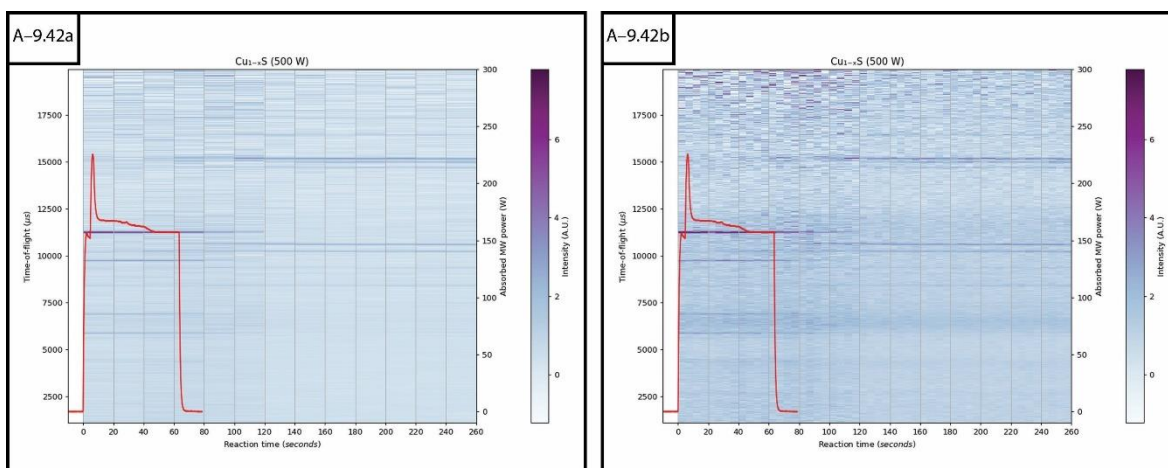


Figure A-9.42: Colourmap plots of sliced event mode TOF data with absorbed MW power overlaid for $Cu_{1-x}S$ heated using 300 W forward power for 63 s a) data processed as 20 s sections and b) 5 s sections

References

- [1] M. Allowitz, "The Flash S03E22 - Infantino Street," The CW, United States of America, 2017.
- [2] H. J. Kitchen *et al.*, "Modern Microwave Methods in Solid-State Inorganic Materials Chemistry: From Fundamentals to Manufacturing," *Chem Rev*, vol. 114, no. 2, pp. 1170–1206, Jan. 2014, doi: 10.1021/cr4002353.
- [3] C. Mastrovito, J. W. Lekse, and J. A. Aitken, "Rapid solid-state synthesis of binary group 15 chalcogenides using microwave irradiation," *J Solid State Chem*, vol. 180, no. 11, pp. 3262–3270, Nov. 2007, doi: 10.1016/J.JSSC.2007.09.001.
- [4] M. Mehdizadeh, "The impact of fields on materials at microwave and radio frequencies," in *Microwave/RF Applicators and Probes*, M. Mehdizadeh, Ed., Oxford: William Andrew Publishing, 2015, pp. 1–33. doi: 10.1016/B978-0-323-32256-0.00001-4.
- [5] D. Obermayer, B. Gutmann, and C. Oliver Kappe, "Microwave Chemistry in Silicon Carbide Reaction Vials: Separating Thermal from Nonthermal Effects," *Angewandte Chemie International Edition*, vol. 48, no. 44, pp. 8321–8324, Oct. 2009, doi: 10.1002/ANIE.200904185.
- [6] A. Harrison *et al.*, "In situ neutron diffraction studies of single crystals and powders during microwave irradiation," *Faraday Discuss*, vol. 122, no. 0, pp. 363–379, Oct. 2003, doi: 10.1039/B203379H.
- [7] A. C. Metaxas, "Microwave heating," *Power Engineering Journal*, vol. 5, no. 5, pp. 237–247, 1991, doi: 10.1049/PE:19910047.
- [8] J. W. Makepeace, H. M. A. Hunter, T. J. Wood, R. I. Smith, C. A. Murray, and W. I. F. David, "Ammonia decomposition catalysis using lithium–calcium imide," *Faraday Discuss*, vol. 188, no. 0, pp. 525–544, Jul. 2016, doi: 10.1039/C5FD00179J.
- [9] J. W. Makepeace, T. J. Wood, H. M. A. Hunter, M. O. Jones, and W. I. F. David, "Ammonia decomposition catalysis using non-stoichiometric lithium imide," *Chem Sci*, vol. 6, no. 7, pp. 3805–3815, Jun. 2015, doi: 10.1039/C5SC00205B.
- [10] J. W. Makepeace, T. J. Wood, P. L. Marks, R. I. Smith, C. A. Murray, and W. I. F. David, "Bulk phase behavior of lithium imide–metal nitride ammonia decomposition catalysts," *Physical Chemistry Chemical Physics*, vol. 20, no. 35, pp. 22689–22697, Sep. 2018, doi: 10.1039/C8CP02824A.
- [11] I. Bilecka and M. Niederberger, "Microwave chemistry for inorganic nanomaterials synthesis," *Nanoscale*, vol. 2, no. 8, p. 1358, Aug. 2010, doi: 10.1039/b9nr00377k.
- [12] Philip Ronan, "EM spectrum.svg," *Wikimedia Commons*, Aug. 06, 2007. https://commons.wikimedia.org/wiki/File:EM_spectrum.svg (accessed Aug. 22, 2022).
- [13] M. Regier, K. Knoerzer, and H. Schubert, "Introducing microwave-assisted processing of food: Fundamentals of the technology," in *The Microwave Processing of Foods*, M. Regier, K. Knoerzer, and H. Schubert, Eds., 2nd ed. Cambridge: Woodhead Publishing, 2017, pp. 1–22. doi: 10.1016/B978-0-08-100528-6.00001-2.
- [14] S. Horikoshi, R. F. Schiffmann, J. Fukushima, and N. Serpone, *Microwave Chemical and Materials Processing: A Tutorial*. Singapore: Springer International Publishing, 2018. doi: 10.1007/978-981-10-6466-1.
- [15] Charles. A. Holt, *Introduction To Electromagnetic Fields And Waves*. John Wiley & Sons, Inc, 1967.
- [16] B. I. Bleaney, *Electricity and Magnetism*. London: Oxford University Press, 1976.
- [17] D. J. Griffiths, *Introduction to Electrodynamics*. Noida, India: Pearson India Education Services, 2015.
- [18] D. R. Corson and P. Lorrain, *Introduction to electromagnetic fields and waves*. San Francisco: W. H. Freeman, 1962.
- [19] R. G. Geyer, *Dielectric Characterization and Reference Materials*, NIST Techn. Boulder: National Institute of Standards and Technology, 1990.
- [20] A. C. Metaxas and R. J. (Roger J.) Meredith, *Industrial Microwave Heating*. London: The Institution of Engineering and Technology, 2008. Accessed: May 16, 2019. [Online]. Available: https://books.google.co.uk/books/about/Industrial_Microwave_Heating.html?id=BLfwWTq76sIC&redir_esc=y
- [21] S. Taghian Dinani, A. Jenn, and U. Kulozik, "Effect of Vertical and Horizontal Sample Orientations on Uniformity of Microwave Heating Produced by Magnetron and Solid-State Generators," *Foods 2021, Vol. 10, Page 1986*, vol. 10, no. 9, p. 1986, Aug. 2021, doi: 10.3390/FOODS10091986.
- [22] W. Klinbun and P. Rattanadecho, "Analysis of microwave induced natural convection in a single mode cavity (Influence of sample volume, placement, and microwave power level)," *Appl Math Model*, vol. 36, no. 2, pp. 813–828, Feb. 2012, doi: 10.1016/J.APM.2011.07.003.
- [23] D. M. Pozar, *Microwave Engineering (4th Edition)*, 4th ed. John Wiley & Sons, Inc., 2012.
- [24] Unknown author, "18.6: Variation of the Dielectric Constant in Alternating Fields," *University of Cambridge*, Nov. 22, 2020. https://eng.libretexts.org/Bookshelves/Materials_Science/TLP_Library_I/18%3A_Dielectric_materials/18.06%3A_Section_6- (accessed Mar. 07, 2023).
- [25] J. Goerth, "Early magnetron development especially in Germany," in *2010 International Conference on the Origins and Evolution of the Cavity Magnetron*, IEEE, Apr. 2010, pp. 17–22. doi: 10.1109/CAVMAG.2010.5565571.

- [26] A. W. Hull, "The magnetron," *Journal of the American Institute of Electrical Engineers*, vol. 40, no. 9, pp. 715–723, Sep. 1921, doi: 10.1109/JoAIEE.1921.6594005.
- [27] E. H. Hans, "Magnetron," US2123728A, Nov. 27, 1936
- [28] J. C. Gallawa, "Microwave Oven," 2015. http://www.smecc.org/microwave_oven.htm (accessed Oct. 23, 2017).
- [29] P. L. Spencer, "Method of treating foodstuffs," US2495429A, Oct. 08, 1945
- [30] S. W. Liu and J. P. Wightman, "Decomposition of simple alcohols, ethers and ketones in a microwave discharge," *Journal of Applied Chemistry and Biotechnology*, vol. 21, no. 6, pp. 168–172, Jun. 1971, doi: 10.1002/jctb.5020210605.
- [31] R. Gedye *et al.*, "The use of microwave ovens for rapid organic synthesis," *Tetrahedron Lett.*, vol. 27, no. 3, pp. 279–282, Jan. 1986, doi: 10.1016/S0040-4039(00)83996-9.
- [32] G. Hargreaves *et al.*, "The importance of ionic conduction in microwave heated polyesterifications," *React Chem Eng*, vol. 5, no. 3, pp. 495–505, Mar. 2020, doi: 10.1039/C9RE00313D.
- [33] A. M. Abioye and F. N. Ani, "Advancement in the production of activated carbon from biomass using microwave heating," *J Teknol*, vol. 79, no. 3, pp. 79–88, Feb. 2017, doi: 10.11113/JT.V79.7249.
- [34] G. A. Tompsett, W. C. Conner, and K. S. Yngvesson, "Microwave Synthesis of Nanoporous Materials," *ChemPhysChem*, vol. 7, no. 2, pp. 296–319, Feb. 2006, doi: 10.1002/cphc.200500449.
- [35] J. P. Siebert, C. M. Hamm, and C. S. Birkel, "Microwave heating and spark plasma sintering as non-conventional synthesis methods to access thermoelectric and magnetic materials," *Appl Phys Rev*, vol. 6, no. 4, p. 041314, Dec. 2019, doi: 10.1063/1.5121442.
- [36] J. Cheng, R. Roy, and D. Agrawal, "Experimental proof of major role of magnetic field losses in microwave heating of metal and metallic composites," *J Mater Sci Lett*, vol. 20, no. 17, pp. 1561–1563, Sep. 2001, doi: 10.1023/A:1017900214477/METRICS.
- [37] M. Baghbanzadeh, L. Carbone, P. D. Cozzoli, and C. O. Kappe, "Microwave-Assisted Synthesis of Colloidal Inorganic Nanocrystals," *Angewandte Chemie International Edition*, vol. 50, no. 48, pp. 11312–11359, Nov. 2011, doi: 10.1002/anie.201101274.
- [38] Archimerged, "Dielectric responses.svg," *Wikimedia Commons*, Sep. 01, 2010. https://commons.wikimedia.org/wiki/File:Dielectric_responses.svg (accessed Aug. 22, 2022).
- [39] J.-H. Peng, J. Binner, and S. Bradshaw, "Microwave initiated self-propagating high temperature synthesis of materials," *Materials Science and Technology*, vol. 18, no. 12, pp. 1419–1427, Dec. 2002, doi: 10.1179/026708302225006142.
- [40] Unknown author, "Skin Depth," 2004. <https://www.microwaves101.com/encyclopedias/skin-depth> (accessed Apr. 30, 2019).
- [41] W. M. Haynes, D. R. Lide, and T. J. Bruno, *CRC Handbook of Chemistry and Physics: A Ready-Reference Book of Chemical and Physical Data*, 97th ed. London: CRC Press, 2017.
- [42] J. Tang, "Unlocking Potentials of Microwaves for Food Safety and Quality," *J Food Sci*, vol. 80, no. 8, pp. E1776–E1793, Aug. 2015, doi: 10.1111/1750-3841.12959.
- [43] K. Berdel, J. G. Rivas, P. H. Bolívar, P. De Maagt, and H. Kurz, "Temperature dependence of the permittivity and loss tangent of high-permittivity materials at terahertz frequencies," *IEEE Trans Microw Theory Tech*, vol. 53, no. 4 I, pp. 1266–1271, Apr. 2005, doi: 10.1109/TMTT.2005.845752.
- [44] V. S. Yadav, D. K. Sahu, Y. Singh, M. Kumar, and D. C. Dhukarya, "Frequency and Temperature Dependence of Dielectric Properties of Pure Poly Vinylidene Fluoride (PVDF) Thin Films," *AIP Conf Proc*, vol. 1285, no. 1, p. 267, Oct. 2010, doi: 10.1063/1.3510553.
- [45] Unknown author, "18.8: Effect of Temperature on the Dielectric Constant," *University of Cambridge*, Nov. 26, 2020. https://eng.libretexts.org/Bookshelves/Materials_Science/TLP_Library_I/18%3A_Dielectric_materials/18.8%3A_Effect_of_Temperature_on_the_Dielectric_Constant (accessed Mar. 07, 2023).
- [46] M. Bhattacharya and T. Basak, "A review on the susceptor assisted microwave processing of materials," *Energy*, vol. 97, pp. 306–338, Feb. 2016, doi: 10.1016/J.ENERGY.2015.11.034.
- [47] H.-I. Yoo, "Defect Chemistry in Solid State Ionic Materials," *Encyclopedia of Applied Electrochemistry*, pp. 295–303, 2014, doi: 10.1007/978-1-4419-6996-5_152.
- [48] J. Maier, "Defect Chemistry: Composition, Transport, and Reactions in the Solid State; Part I: Thermodynamics," *Angewandte Chemie International Edition in English*, vol. 32, no. 3, pp. 313–335, Mar. 1993, doi: 10.1002/ANIE.199303133.
- [49] J. Maier, "Doping Strategies in Inorganic and Organic Materials," *Z Anorg Allg Chem*, vol. 643, no. 23, pp. 2083–2087, Dec. 2017, doi: 10.1002/ZAAC.201700317.
- [50] R. Sass, "Defects in Solids," *Encyclopedia of Applied Electrochemistry*, pp. 303–307, 2014, doi: 10.1007/978-1-4419-6996-5_299.
- [51] J. Maier, "Defect Chemistry: Composition, Transport, and Reactions in the Solid State; Part II: Kinetics," *Angewandte Chemie International Edition in English*, vol. 32, no. 4, pp. 528–542, Apr. 1993, doi: 10.1002/ANIE.199305281.
- [52] G. J. Snyder and E. S. Toberer, "Complex thermoelectric materials," *Nat Mater*, vol. 7, no. 2, pp. 105–114, Feb. 2008, doi: 10.1038/nmat2090.
- [53] L. E. Bell, "Cooling, heating, generating power, and recovering waste heat with thermoelectric systems," *Science (1979)*, vol. 321, no. 5895, pp. 1457–1461, Sep. 2008, doi:

- 10.1126/SCIENCE.1158899/ASSET/D6DE4C69-9F6E-4611-A58D-293EA6101F04/ASSETS/GRAPHIC/321_1457_F3.JPEG.
- [54] D. Beretta *et al.*, “Thermoelectrics: From history, a window to the future,” *Materials Science and Engineering: R: Reports*, Nov. 2018, doi: 10.1016/J.MSER.2018.09.001.
- [55] Y. Du, J. Xu, B. Paul, and P. Eklund, “Flexible thermoelectric materials and devices,” *Appl Mater Today*, vol. 12, pp. 366–388, Sep. 2018, doi: 10.1016/J.APMT.2018.07.004.
- [56] J. P. Heremans, “The ugly duckling,” *Nature*, vol. 508, no. 7496, pp. 327–328, Apr. 2014, doi: 10.1038/508327a.
- [57] D. Rowe, “General Principles and Basic Considerations,” in *Thermoelectric handbook: macro to nano*, D. M. Rowe, Ed., Boca Raton: CRC Press, 2006, pp. 1.1-1.10.
- [58] G. J. Snyder and A. H. Snyder, “Figure of merit ZT of a thermoelectric device defined from materials properties,” *Energy Environ Sci*, vol. 10, no. 11, pp. 2280–2283, Nov. 2017, doi: 10.1039/C7EE02007D.
- [59] H. S. Kim, W. Liu, G. Chen, C.-W. Chu, and Z. Ren, “Relationship between thermoelectric figure of merit and energy conversion efficiency.,” *Proc Natl Acad Sci U S A*, vol. 112, no. 27, pp. 8205–10, Jul. 2015, doi: 10.1073/pnas.1510231112.
- [60] C. Goupil, H. Ouerdane, K. Zabrocki, W. Seifert, N. F. Hinsche, and E. Müller, “Thermodynamics and Thermoelectricity,” in *Continuum Theory and Modeling of Thermoelectric Elements*, C. Goupil, Ed., Weinheim: Wiley-VCH Verlag GmbH & Co. KGaA, 2016, pp. 1–59. doi: 10.1002/9783527338405.fmatter.
- [61] C. Goupil, *Continuum theory and modeling of thermoelectric elements*. Weinheim: Wiley-VCH Verlag GmbH & Co. KGaA, 2016.
- [62] D. D. Fan, H. J. Liu, L. Cheng, J. H. Liang, and P. H. Jiang, “A first-principles study of the effects of electron–phonon coupling on the thermoelectric properties: a case study of the SiGe compound,” *J Mater Chem A Mater*, vol. 6, no. 25, pp. 12125–12131, Jun. 2018, doi: 10.1039/C8TA01806E.
- [63] L. Yang, Z.-G. Chen, M. S. Dargusch, and J. Zou, “High Performance Thermoelectric Materials: Progress and Their Applications,” *Adv Energy Mater*, vol. 8, no. 6, p. 1701797, Feb. 2018, doi: 10.1002/aenm.201701797.
- [64] T. M. Tritt and M. A. Subramanian, “Thermoelectric Materials, Phenomena, and Applications: A Bird’s Eye View,” *MRS Bull*, vol. 31, no. 3, pp. 188–198, Mar. 2006, doi: 10.1557/mrs2006.44.
- [65] X. Zhang and L.-D. Zhao, “Thermoelectric materials: Energy conversion between heat and electricity,” *Journal of Materiomics*, vol. 1, no. 2, pp. 92–105, Jun. 2015, doi: 10.1016/J.JMAT.2015.01.001.
- [66] H. S. Kim, Z. M. Gibbs, Y. Tang, H. Wang, and G. J. Snyder, “Characterization of Lorenz number with Seebeck coefficient measurement,” *APL Mater*, vol. 3, no. 4, p. 041506, Feb. 2015, doi: 10.1063/1.4908244.
- [67] D. Emin, “Effects of Charge Carriers’ Interaction on Seebeck Coefficients,” in *Thermoelectric handbook: macro to nano*, D. Rowe, Ed., Boca Raton: CRC Press, 2006, pp. 5.2-5.2.
- [68] L.-D. Zhao *et al.*, “Ultralow thermal conductivity and high thermoelectric figure of merit in SnSe crystals,” *Nature*, vol. 508, no. 7496, pp. 373–377, Apr. 2014, doi: 10.1038/nature13184.
- [69] J. Yang *et al.*, “On the tuning of electrical and thermal transport in thermoelectrics: an integrated theory–experiment perspective,” *NPJ Comput Mater*, vol. 2, no. 1, p. 15015, Nov. 2016, doi: 10.1038/npjcompumats.2015.15.
- [70] X. L. Shi, J. Zou, and Z. G. Chen, “Advanced thermoelectric design: From materials and structures to devices,” *Chem Rev*, vol. 120, no. 15, pp. 7399–7515, Aug. 2020, doi: 10.1021/acs.chemrev.0c00026.
- [71] Y. Sun, Y. Liu, R. Li, Y. Li, and S. Bai, “Strategies to Improve the Thermoelectric Figure of Merit in Thermoelectric Functional Materials,” *Front Chem*, vol. 10, p. 580, May 2022, doi: 10.3389/FCHEM.2022.865281/XML/NLM.
- [72] J. Park, M. Dylla, Y. Xia, M. Wood, G. Jeffrey Snyder, and A. Jain, “When band convergence is not beneficial for thermoelectrics,” *Nat Commun*, vol. 12, 2021, doi: 10.1038/s41467-021-23839-w.
- [73] J. He and T. M. Tritt, “Advances in thermoelectric materials research: Looking back and moving forward.,” *Science*, vol. 357, no. 6358, p. eaak9997, Sep. 2017, doi: 10.1126/science.aak9997.
- [74] C. Fu *et al.*, “Realizing high figure of merit in heavy-band p-type half-Heusler thermoelectric materials,” *Nature Communications 2015 6:1*, vol. 6, no. 1, pp. 1–7, Sep. 2015, doi: 10.1038/ncomms9144.
- [75] B. A. Cook and J. L. Harringa, “Solid-State Synthesis of Thermoelectric Materials,” in *Thermoelectric handbook: macro to nano*, Boca Raton: CRC Press, 2006, pp. 19.13-19.13.
- [76] G. Rogl *et al.*, “New bulk p-type skutterudites DD0.7Fe2.7Co1.3Sb12-xXx (X = Ge, Sn) reaching ZT > 1.3,” *Acta Mater*, vol. 91, pp. 227–238, Jun. 2015, doi: 10.1016/J.ACTAMAT.2015.03.008.
- [77] G. Rogl *et al.*, “In-doped multifilled n-type skutterudites with ZT = 1.8,” *Acta Mater*, vol. 95, pp. 201–211, Aug. 2015, doi: 10.1016/J.ACTAMAT.2015.05.024.
- [78] S. R. Brown, S. M. Kauzlarich, F. Gascoin, and G. Jeffrey Snyder, “Yb14MnSb11: New high efficiency thermoelectric material for power generation,” *Chemistry of Materials*, vol. 18, no. 7, pp. 1873–1877, Apr. 2006, doi: 10.1021/CM060261T/ASSET/IMAGES/LARGE/CM060261TF00005.JPEG.
- [79] J. Zhang, L. Song, S. H. Pedersen, H. Yin, L. T. Hung, and B. B. Iversen, “Discovery of high-performance low-cost n-type Mg3Sb2-based thermoelectric materials with multi-valley conduction

- bands,” *Nature Communications* 2017 8:1, vol. 8, no. 1, pp. 1–8, Jan. 2017, doi: 10.1038/ncomms13901.
- [80] G. S. Nolas, “Structure, Thermal Conductivity, and Thermoelectric Properties of Clathrate Compounds,” in *Thermoelectric handbook: macro to nano*, D. Rowe, Ed., Boca Raton: CRC Press, 2006, pp. 33.2-33.2.
- [81] Y. Saiga, B. Du, S. K. Deng, K. Kajisa, and T. Takabatake, “Thermoelectric properties of type-VIII clathrate Ba₈Ga₁₆Sn₃₀ doped with Cu,” *J Alloys Compd*, vol. 537, pp. 303–307, Oct. 2012, doi: 10.1016/J.JALLCOM.2012.05.049.
- [82] M. I. Fedorov, V. K. Zaitsev, and G. N. Isachenko, “High Effective Thermoelectrics Based on the Mg₂Si-Mg₂Sn Solid Solution,” *Solid State Phenomena*, vol. 170, pp. 286–292, 2011, doi: 10.4028/WWW.SCIENTIFIC.NET/SSP.170.286.
- [83] P. Gao *et al.*, “Transport and mechanical properties of high-ZT Mg_{2.08}Si 0.4-x Sn_{0.6}Sb x thermoelectric materials,” *J Electron Mater*, vol. 43, no. 6, pp. 1790–1803, Jun. 2014, doi: 10.1007/S11664-013-2865-8/METRICS.
- [84] I. Terasaki, Y. Sasago, and K. Uchinokura, “Large thermoelectric power in NaCo₂O₄ single crystals,” *Phys Rev B*, vol. 56, no. 20, p. R12685, Nov. 1997, doi: 10.1103/PhysRevB.56.R12685.
- [85] M. Lee *et al.*, “Large enhancement of the thermopower in Na_xCoO₂ at high Na doping,” *Nature Materials* 2006 5:7, vol. 5, no. 7, pp. 537–540, Jun. 2006, doi: 10.1038/nmat1669.
- [86] H. Lin *et al.*, “Concerted Rattling in CsAg₅Te₃ Leading to Ultralow Thermal Conductivity and High Thermoelectric Performance,” *Angewandte Chemie International Edition*, vol. 55, no. 38, pp. 11431–11436, Sep. 2016, doi: 10.1002/ANIE.201605015.
- [87] Y. Pei *et al.*, “Multiple Converged Conduction Bands in K₂Bi₈Se₁₃: A Promising Thermoelectric Material with Extremely Low Thermal Conductivity,” *J Am Chem Soc*, vol. 138, no. 50, pp. 16364–16371, Dec. 2016, doi: 10.1021/JACS.6B09568/SUPPL_FILE/JA6B09568_SI_001.PDF.
- [88] G. Tan, S. Hao, J. Zhao, C. Wolverton, and M. G. Kanatzidis, “High Thermoelectric Performance in Electron-Doped AgBi₃S₅ with Ultralow Thermal Conductivity,” *J Am Chem Soc*, vol. 139, no. 18, pp. 6467–6473, May 2017, doi: 10.1021/JACS.7B02399/SUPPL_FILE/JA7B02399_SI_007.AVI.
- [89] Y. Shi, C. Sturm, and H. Kleinke, “Chalcogenides as thermoelectric materials,” *J Solid State Chem*, vol. 270, pp. 273–279, Feb. 2019, doi: 10.1016/J.JSSC.2018.10.049.
- [90] T.-R. Wei, C.-F. Wu, F. Li, and J.-F. Li, “Low-cost and environmentally benign selenides as promising thermoelectric materials,” *Journal of Materiomics*, vol. 4, no. 4, pp. 304–320, Dec. 2018, doi: 10.1016/J.JMAT.2018.07.001.
- [91] M. Taniguchi, R. L. Johnson, J. Ghijsen, and M. Cardona, “Core excitons and conduction-band structures in orthorhombic GeS, GeSe, SnS, and SnSe single crystals,” *Phys Rev B*, vol. 42, no. 6, pp. 3634–3643, Aug. 1990, doi: 10.1103/PhysRevB.42.3634.
- [92] Y. Huang *et al.*, “First-principles study on intrinsic defects of SnSe,” *RSC Adv*, vol. 7, no. 44, pp. 27612–27618, May 2017, doi: 10.1039/C7RA03367B.
- [93] C. Julien, M. Eddrief, I. Samaras, and M. Balkanski, “Optical and electrical characterizations of SnSe, SnS₂ and SnSe₂ single crystals,” *Materials Science and Engineering: B*, vol. 15, no. 1, pp. 70–72, Oct. 1992, doi: 10.1016/0921-5107(92)90033-6.
- [94] G. Li, G. Ding, and G. Gao, “Thermoelectric properties of SnSe₂ monolayer,” *Journal of Physics: Condensed Matter*, vol. 29, no. 1, p. 015001, Nov. 2016, doi: 10.1088/0953-8984/29/1/015001.
- [95] J. Rundle and S. Leoni, “Layered Tin Chalcogenides SnS and SnSe: Lattice Thermal Conductivity Benchmarks and Thermoelectric Figure of Merit,” *Journal of Physical Chemistry C*, vol. 126, no. 33, pp. 14036–14046, Aug. 2022, doi: 10.1021/ACS.JPCC.2C02401/ASSET/IMAGES/LARGE/JP2C02401_0011.JPEG.
- [96] W. Shi *et al.*, “Tin Selenide (SnSe): Growth, Properties, and Applications,” *Advanced Science*, vol. 5, no. 4, p. 1700602, Apr. 2018, doi: 10.1002/advs.201700602.
- [97] Y. Li *et al.*, “Investigation of the Anisotropic Thermoelectric Properties of Oriented Polycrystalline SnSe,” *Energies (Basel)*, vol. 8, no. 7, pp. 6275–6285, Jun. 2015, doi: 10.3390/en8076275.
- [98] L. D. Zhao *et al.*, “Ultrahigh power factor and thermoelectric performance in hole-doped single-crystal SnSe,” *Science (1979)*, vol. 351, no. 6269, pp. 141–144, Jan. 2016, doi: 10.1126/SCIENCE.AAD3749/SUPPL_FILE/ZHAO.SM.PDF.
- [99] A. T. Duong *et al.*, “Achieving ZT=2.2 with Bi-doped n-type SnSe single crystals,” *Nature Communications* 2016 7:1, vol. 7, no. 1, pp. 1–6, Dec. 2016, doi: 10.1038/ncomms13713.
- [100] C. Chang *et al.*, “3D charge and 2D phonon transports leading to high out-of-plane ZT in n-type SnSe crystals,” *Science (1979)*, vol. 360, no. 6390, pp. 778–783, May 2018, doi: 10.1126/SCIENCE.AAQ1479/SUPPL_FILE/AAQ1479_CHANG_SM.PDF.
- [101] C. Zhou *et al.*, “Polycrystalline SnSe with a thermoelectric figure of merit greater than the single crystal,” *Nature Materials* 2021 20:10, vol. 20, no. 10, pp. 1378–1384, Aug. 2021, doi: 10.1038/s41563-021-01064-6.
- [102] Y. Li *et al.*, “Enhanced mid-temperature thermoelectric performance of textured SnSe polycrystals made of solvothermally synthesized powders,” *J Mater Chem C Mater*, vol. 4, no. 10, pp. 2047–2055, Mar. 2016, doi: 10.1039/C5TC04202J.
- [103] Q. Tan, C. F. Wu, W. Sun, and J. F. Li, “Solvothermally synthesized SnS nanorods with high carrier mobility leading to thermoelectric enhancement,” *RSC Adv*, vol. 6, no. 50, pp. 43985–43988, May 2016, doi: 10.1039/C6RA06874J.

- [104] D. Ni, Y. Chen, X. Yang, C. Liu, and K. Cai, "Microwave-assisted synthesis method for rapid synthesis of tin selenide electrode material for supercapacitors," *J Alloys Compd*, vol. 737, pp. 623–629, Mar. 2018, doi: 10.1016/J.JALLCOM.2017.12.037.
- [105] R. Moshwan, L. Yang, J. Zou, and Z. G. Chen, "Eco-Friendly SnTe Thermoelectric Materials: Progress and Future Challenges," *Adv Funct Mater*, vol. 27, no. 43, p. 1703278, Nov. 2017, doi: 10.1002/ADFM.201703278.
- [106] Y. X. Chen, F. Li, D. Li, Z. Zheng, J. Luo, and P. Fan, "Thermoelectric Properties of Tin Telluride Quasi Crystal Grown by Vertical Bridgman Method," *Materials 2019, Vol. 12, Page 3001*, vol. 12, no. 18, p. 3001, Sep. 2019, doi: 10.3390/MA12183001.
- [107] A. Banik, B. Vishal, S. Perumal, R. Datta, and K. Biswas, "The origin of low thermal conductivity in Sn_{1-x}Sb_xTe: phonon scattering via layered intergrowth nanostructures," *Energy Environ Sci*, vol. 9, no. 6, pp. 2011–2019, Jun. 2016, doi: 10.1039/C6EE00728G.
- [108] B. D. Malone, A. Gali, and E. Kaxiras, "First principles study of point defects in SnS," *Physical Chemistry Chemical Physics*, vol. 16, no. 47, pp. 26176–26183, Nov. 2014, doi: 10.1039/C4CP03010A.
- [109] Q. Tan and J. F. Li, "Thermoelectric properties of Sn-S bulk materials prepared by mechanical alloying and spark plasma sintering," *J Electron Mater*, vol. 43, no. 6, pp. 2435–2439, Jun. 2014, doi: 10.1007/S11664-014-3127-0/METRICS.
- [110] T.-R. Wei *et al.*, "Thermoelectric transport properties of pristine and Na-doped SnSe_{1-x}Tex polycrystals," *Phys. Chem. Chem. Phys*, vol. 17, p. 30102, 2015, doi: 10.1039/c5cp05510e.
- [111] Q. Zhang *et al.*, "Studies on Thermoelectric Properties of n-type Polycrystalline SnSe_{1-x}S_x by Iodine Doping," *Adv Energy Mater*, vol. 5, no. 12, p. 1500360, Jun. 2015, doi: 10.1002/AENM.201500360.
- [112] Asfandiyar *et al.*, "Thermoelectric SnS and SnS-SnSe solid solutions prepared by mechanical alloying and spark plasma sintering: Anisotropic thermoelectric properties," *Scientific Reports 2017 7:1*, vol. 7, no. 1, pp. 1–7, Feb. 2017, doi: 10.1038/srep43262.
- [113] J. Deng and Z. Y. Zhao, "Electronic structure and optical properties of bismuth chalcogenides Bi₂Q₃ (Q = O, S, Se, Te) by first-principles calculations," *Comput Mater Sci*, vol. 142, pp. 312–319, Feb. 2018, doi: 10.1016/J.COMMATSCI.2017.10.032.
- [114] S. Wang and P. Zhang, "Native point defects in Bi₂Se₃: A first-principles study," *Phys Lett A*, vol. 384, no. 14, p. 126281, May 2020, doi: 10.1016/J.PHYSLETA.2020.126281.
- [115] B. Zhao, B. Zhou, C. Y. Li, N. Qi, and Z. Q. Chen, "First-Principles Calculation of Defect Formation and Positron Annihilation States in Bi₂Te₃," *Defect and Diffusion Forum*, vol. 373, pp. 41–45, 2016, doi: 10.4028/WWW.SCIENTIFIC.NET/DDF.373.41.
- [116] G. J. Snyder, "Thermoelectric Power Generation: Efficiency and Compatibility," in *Thermoelectric handbook: macro to nano*, D. Rowe, Ed., Boca Raton: CRC Press, 2006, pp. 9.14–9.16.
- [117] Y. M. Belov, S. M. Maniakin, and I. V. Morgunov, "Review of Methods of Thermoelectric Materials Mass Production," in *Thermoelectric handbook: macro to nano*, D. Rowe, Ed., Boca Raton: CRC Press, 2006, pp. 20.2–20.4.
- [118] J. Li, Y. Pan, C. Wu, F. Sun, and T. Wei, "Processing of advanced thermoelectric materials," *Sci China Technol Sci*, vol. 60, no. 9, pp. 1347–1364, Sep. 2017, doi: 10.1007/s11431-017-9058-8.
- [119] A. Kadhim, A. Hmood, and H. A. Hassan, "Physical properties of Bi₂ (Te, Se)₃ and Bi₂Se_{1.2}Te_{1.8} prepared using solid-state microwave synthesis," *Mater Lett*, vol. 65, no. 19–20, pp. 3105–3108, Oct. 2011, doi: 10.1016/J.MATLET.2011.06.069.
- [120] A. Kadhim, A. Hmood, and H. Abu Hassan, "Electrical characterization of thermoelectric generators based on p-type Bi_{0.4}Sb_{1.6}Se_{2.4}Te_{0.6} and n-type Bi₂Se_{0.6}Te_{2.4} bulk thermoelectric materials," *Mater Lett*, vol. 97, pp. 24–26, Apr. 2013, doi: 10.1016/J.MATLET.2013.01.108.
- [121] H. J. Goldsmid, "Bismuth Telluride and Its Alloys as Materials for Thermoelectric Generation," *Materials 2014, Vol. 7, Pages 2577-2592*, vol. 7, no. 4, pp. 2577–2592, Mar. 2014, doi: 10.3390/MA7042577.
- [122] J. Cen, I. Pallikara, and J. M. Skelton, "Structural Dynamics and Thermal Transport in Bismuth Chalcogenide Alloys," *Chemistry of Materials*, vol. 33, no. 21, pp. 8404–8417, Nov. 2021, doi: 10.1021/ACS.CHEMMATER.1C02777/ASSET/IMAGES/LARGE/CM1C02777_0012.JPEG.
- [123] S. Wang, W. Xie, H. Li, and X. Tang, "Enhanced performances of melt spun Bi₂(Te,Se)₃ for n-type thermoelectric legs," *Intermetallics (Barking)*, vol. 19, no. 7, pp. 1024–1031, Jul. 2011, doi: 10.1016/J.INTERMET.2011.03.006.
- [124] L. Hu, T. Zhu, X. Liu, and X. Zhao, "Point Defect Engineering of High-Performance Bismuth-Telluride-Based Thermoelectric Materials," *Adv Funct Mater*, vol. 24, no. 33, pp. 5211–5218, Sep. 2014, doi: 10.1002/ADFM.201400474.
- [125] S. Yokoyama *et al.*, "Green synthesis and formation mechanism of nanostructured Bi₂Te₃ using ascorbic acid in aqueous solution," *Advanced Powder Technology*, vol. 26, no. 3, pp. 789–796, May 2015, doi: 10.1016/J.APT.2015.02.002.
- [126] M. Hong *et al.*, "N-Type Bi₂Te₃-xSex Nanoplates with Enhanced Thermoelectric Efficiency Driven by Wide-Frequency Phonon Scatterings and Synergistic Carrier Scatterings," *ACS Nano*, vol. 10, no. 4, pp. 4719–4727, Apr. 2016, doi: 10.1021/ACS.NANO.6B01156/ASSET/IMAGES/LARGE/NN-2016-011156U_0009.JPEG.
- [127] S. il Kim *et al.*, "Dense dislocation arrays embedded in grain boundaries for high-performance bulk thermoelectrics," *Science (1979)*, vol. 348, no. 6230, pp. 109–114, Apr. 2015, doi: 10.1126/SCIENCE.AAA4166/SUPPL_FILE/KIM-SM.PDF.

- [128] F. Hao *et al.*, “High efficiency Bi₂Te₃-based materials and devices for thermoelectric power generation between 100 and 300 °C,” *Energy Environ Sci*, vol. 9, no. 10, pp. 3120–3127, Oct. 2016, doi: 10.1039/C6EE02017H.
- [129] B. Poudel *et al.*, “High-thermoelectric performance of nanostructured bismuth antimony telluride bulk alloys,” *Science (1979)*, vol. 320, no. 5876, pp. 634–638, May 2008, doi: 10.1126/SCIENCE.1156446/ASSET/1A557A61-CF37-427C-BCB3-BD0D868A5ADB/ASSETS/GRAPHIC/320_634_F5.JPEG.
- [130] H. A. Rahnamaye Aliabad and F. Asadi Rad, “Structural, electronic and thermoelectric properties of bulk and monolayer of Sb₂Se₃ under high pressure: By GGA and mBJ approaches,” *Physica B Condens Matter*, vol. 545, pp. 275–284, Sep. 2018, doi: 10.1016/J.PHYSB.2018.06.030.
- [131] L. D. Ivanova, L. I. Petrova, Yu. V. Granatkina, and V. S. Zemskov, “Thermoelectric materials based on Sb₂Te₃-Bi₂Te₃ solid solutions with optimal performance in the range 100–400 K,” *Inorganic Materials*, vol. 43, no. 9, pp. 933–937, Sep. 2007, doi: 10.1134/S002016850709004X.
- [132] L. P. Hu *et al.*, “Enhanced figure of merit in antimony telluride thermoelectric materials by In–Ag co-alloying for mid-temperature power generation,” *Acta Mater*, vol. 85, pp. 270–278, Feb. 2015, doi: 10.1016/J.ACTAMAT.2014.11.023.
- [133] X. Wang, Z. Li, S. R. Kavanagh, A. M. Ganose, and A. Walsh, “Lone pair driven anisotropy in antimony chalcogenide semiconductors,” *Physical Chemistry Chemical Physics*, vol. 24, no. 12, pp. 7195–7202, Mar. 2022, doi: 10.1039/D1CP05373F.
- [134] N. Guijarro, T. Lutz, T. Lana-Villarreal, F. O’Mahony, R. Gómez, and S. A. Haque, “Toward Antimony Selenide Sensitized Solar Cells: Efficient Charge Photogeneration at spiro - OMeTAD/Sb₂Se₃/Metal Oxide Heterojunctions,” *J Phys Chem Lett*, vol. 3, no. 10, pp. 1351–1356, May 2012, doi: 10.1021/jz3004365.
- [135] C. N. Savory and D. O. Scanlon, “The complex defect chemistry of antimony selenide,” *J Mater Chem A Mater*, vol. 7, no. 17, pp. 10739–10744, Apr. 2019, doi: 10.1039/C9TA02022E.
- [136] D. Das, K. Malik, A. K. Deb, S. Dhara, S. Bandyopadhyay, and A. Banerjee, “Defect induced structural and thermoelectric properties of Sb₂Te₃ alloy,” *J Appl Phys*, vol. 118, no. 4, p. 045102, Jul. 2015, doi: 10.1063/1.4927283.
- [137] J. Olivier-Fourcade *et al.*, “Chemical bonding and electronic properties in antimony chalcogenides,” *J Solid State Chem*, vol. 87, no. 2, pp. 366–377, Aug. 1990, doi: 10.1016/0022-4596(90)90039-Z.
- [138] G. H. Dong, Y. J. Zhu, and L. D. Chen, “Microwave-assisted rapid synthesis of Sb₂Te₃ nanosheets and thermoelectric properties of bulk samples prepared by spark plasma sintering,” *J Mater Chem*, vol. 20, no. 10, pp. 1976–1981, Feb. 2010, doi: 10.1039/B915107A.
- [139] X. Y. Wang *et al.*, “Thermoelectric Performance of Sb₂Te₃-Based Alloys is Improved by Introducing PN Junctions,” *ACS Appl Mater Interfaces*, vol. 10, no. 27, pp. 23277–23284, Jul. 2018, doi: 10.1021/ACSAMI.8B01719/ASSET/IMAGES/LARGE/AM-2018-01719G_0007.JPEG.
- [140] S. C. Singh *et al.*, “Structural and compositional control in copper selenide nanocrystals for light-induced self-repairable electrodes,” *Nano Energy*, vol. 51, pp. 774–785, Sep. 2018, doi: 10.1016/J.NANOEN.2018.07.020.
- [141] R. Yousefi, M. Moradi, G. H. Bordbar, and M. A. M. Teridi, “Role of non-stoichiometric defects in optical properties of metal-selenide nanostructures,” *J Lumin*, vol. 223, p. 117211, Jul. 2020, doi: 10.1016/J.JLUMIN.2020.117211.
- [142] Y. He, T. Zhang, X. Shi, S. H. Wei, and L. Chen, “High thermoelectric performance in copper telluride,” *NPG Asia Materials 2015 7:8*, vol. 7, no. 8, pp. e210–e210, Aug. 2015, doi: 10.1038/am.2015.91.
- [143] H. Liu *et al.*, “Copper ion liquid-like thermoelectrics,” *Nat Mater*, vol. 11, no. 5, pp. 422–425, Mar. 2012, doi: 10.1038/nmat3273.
- [144] C. Coughlan, M. Ibáñez, O. Dobrozhan, A. Singh, A. Cabot, and K. M. Ryan, “Compound Copper Chalcogenide Nanocrystals,” *Chemical Review*, vol. 117, no. 9, pp. 5865–6109, Apr. 2017, Accessed: May 01, 2023. [Online]. Available: <https://pubs.acs.org/doi/10.1021/acs.chemrev.6b00376>
- [145] H. Liu *et al.*, “Ultrahigh Thermoelectric Performance by Electron and Phonon Critical Scattering in Cu₂Se_{1-x}I_x,” *Advanced Materials*, vol. 25, no. 45, pp. 6607–6612, Dec. 2013, doi: 10.1002/ADMA.201302660.
- [146] B. Zhong *et al.*, “High superionic conduction arising from aligned large lamellae and large figure of merit in bulk Cu_{1.94}Al_{0.02}Se,” *Appl Phys Lett*, vol. 105, no. 12, Sep. 2014, doi: 10.1063/1.4896520.
- [147] A. A. Olvera *et al.*, “Partial indium solubility induces chemical stability and colossal thermoelectric figure of merit in Cu₂Se †,” *1668 | Energy Environ. Sci*, vol. 10, p. 1668, 2017, doi: 10.1039/c7ee01193h.
- [148] Y. He *et al.*, “High Thermoelectric Performance in Non-Toxic Earth-Abundant Copper Sulfide,” *Advanced Materials*, vol. 26, no. 23, pp. 3974–3978, Jun. 2014, doi: 10.1002/ADMA.201400515.
- [149] L. Zhao *et al.*, “High thermoelectric and mechanical performance in highly dense Cu_{2-x}S bulks prepared by a melt-solidification technique †,” 2015, doi: 10.1039/c5ta01667c.
- [150] K. Zhao *et al.*, “Enhanced Thermoelectric Performance through Tuning Bonding Energy in Cu₂Se_{1-x}S_x Liquid-like Materials,” *Chemistry of Materials*, vol. 29, no. 15, pp. 6367–6377, Aug. 2017, doi: 10.1021/ACS.CHEMMATER.7B01687/ASSET/IMAGES/CM-2017-01687F_M006.GIF.

- [151] Y.-B. Zhu, B.-P. Zhang, and Y. Liu, "Enhancing thermoelectric performance of Cu₂Se by doping Te," *Phys. Chem. Chem. Phys.*, vol. 19, no. 40, pp. 27664–27669, Oct. 2017, doi: 10.1039/C7CP05149B.
- [152] K. Zhao *et al.*, "Thermoelectric properties of Cu₂Se_{1-x}Te_x solid solutions," *J Mater Chem A Mater*, vol. 6, no. 16, pp. 6977–6986, Apr. 2018, doi: 10.1039/C8TA01313F.
- [153] Unknown author, "Periodic Table – Royal Society of Chemistry," *Royal Society of Chemistry*. <https://www.rsc.org/periodic-table/> (accessed Sep. 08, 2022).
- [154] C. Y. Ho, R. W. Powell, and P. E. Liley, "Thermal Conductivity of the Elements," *J Phys Chem Ref Data*, vol. 1, no. 2, p. 279, Oct. 2009, doi: 10.1063/1.3253100.
- [155] K. F. Young and H. P. R. Frederikse, "Compilation of the Static Dielectric Constant of Inorganic Solids," *J Phys Chem Ref Data*, vol. 2, no. 2, p. 313, Oct. 2009, doi: 10.1063/1.3253121.
- [156] A. M. Helmenstine, "Flame Temperatures Table for Different Fuels," *ThoughtCo*, Aug. 27, 2020.
- [157] O. Arnold *et al.*, "Mantid—Data analysis and visualization package for neutron scattering and μ SR experiments," *Nucl Instrum Methods Phys Res A*, vol. 764, pp. 156–166, Nov. 2014, doi: 10.1016/J.NIMA.2014.07.029.
- [158] L. B. Jassie *et al.*, *Introduction to microwave sample preparation: Theory and practice*. American Chemical Society, 1988.
- [159] Unknown author, "Characteristic Impedance," *Microwaves101*. <https://www.microwaves101.com/encyclopedias/characteristic-impedance> (accessed Nov. 25, 2021).
- [160] Unknown author, "Waveguide Primer," *Microwaves101*. <https://www.microwaves101.com/encyclopedias/waveguide-primer> (accessed Sep. 05, 2022).
- [161] Y. Herhil, S. Piltyay, O. Bulashenko, and A. Bulashenko, "Characteristic Impedances of Rectangular and Circular Waveguides for Fundamental Modes," 2021, doi: 10.1109/UKRCON53503.2021.9575359.
- [162] R. B. Marks and D. F. Williams, "A general waveguide circuit theory," *J. Res. Natl. Inst. Stand. Technol*, vol. 97, no. 5, 1992.
- [163] ETH Zurich, "Smith chart bmd.svg," *Wikimedia Commons*, Aug. 06, 1996. https://commons.wikimedia.org/wiki/File:Smith_chart_bmd.svg (accessed Sep. 05, 2022).
- [164] Unknown author, "Macor - Machinable Glass Ceramic," *Precision Ceramics UK*. <https://precision-ceramics.com/uk/materials/macor/> (accessed Jan. 03, 2023).
- [165] Unknown author, "Macor Technical Properties," *Precision Ceramics UK*, 2022. <https://precision-ceramics.com/uk/macor-technical-properties/> (accessed Jan. 03, 2023).
- [166] H. Rauch and W. Waschkowski, "Neutron Scattering Lengths," in *Neutron Data Booklet*, A.-J. Dianoux and G. Lander, Eds., 2nd ed. Grenoble: Institut Laue-Langevin, 2003, pp. 1.1.1-1.1.17.
- [167] Unknown author, "Activation table of elements - ILL Neutrons for Society," *Institut Laue-Langevin (ILL)*. <https://www.ill.eu/users/scientific-groups/spectroscopy/useful-links/activation-table-of-elements> (accessed Aug. 30, 2022).
- [168] Lesley. Smart and E. (Elaine A.) Moore, *Solid state chemistry: an introduction*. Chapman & Hall, 1995.
- [169] W. Borchardt-Ott, *Crystallography: an Introduction (3rd Edition)*, 3rd ed. Berlin, Heidelberg: Springer, 2011.
- [170] Unknown author, "Crystallographic Point Groups," *Birkbeck College, University of London*, 2006. <http://pd.chem.ucl.ac.uk/pdnn/symm2/group32.htm> (accessed Aug. 23, 2022).
- [171] L. E. Smart and E. A. Moore, *Solid State Chemistry: An Introduction (3rd Edition)*, 3rd ed. Boca Raton: Taylor & Francis Group, LLC, 2005.
- [172] J. H. Conway, O. D. Friedrichs, D. H. Huson, and W. P. Thurston, "On Three-Dimensional Space Groups," *Contributions to Algebra and Geometry*, vol. 42, no. 2, pp. 475–507, 2001.
- [173] T. Hahn, H. Klapper, U. Müller, and Aroyo M. I., "Point groups and crystal classes," in *International tables for crystallography*, 2016, pp. 720–737.
- [174] P. Y. Zavalij and V. K. Pecharsky, *Fundamentals of Powder Diffraction and Structural Characterization of Materials (2nd Edition)*. Boston, MA: Springer US, 2009. doi: 10.1007/978-0-387-09579-0.
- [175] C. G. Shull and E. O. Wollan, "X-Ray, Electron, and Neutron Diffraction.," *Science*, vol. 108, no. 2795, pp. 69–75, Jul. 1948, doi: 10.1126/science.108.2795.69.
- [176] G. E. Bacon and K. Lonsdale, *Neutron diffraction*, vol. 16, no. 1. IOP Publishing, 1953. doi: 10.1088/0034-4885/16/1/301.
- [177] R. B. Von Dreele, "X-ray and Neutron Crystallography: A Powerful Combination," *Los Alamos Sci*, vol. 19, pp. 132–157, 1990, [Online]. Available: <https://fas.org/sgp/othergov/doe/lanl/pubs/00326654.pdf>
- [178] M. Font-bardia and X. Alcobé, "X-ray single crystal and powder diffraction: possibilities and applications," in *Handbook of instrumental techniques for materials, chemical and biosciences research*, J. R. Seoane and X. Llovet Ximenes, Eds., Barcelona: CCiTUB, 2012, pp. 1–13.
- [179] N. Kourkoumelis, "PowDLL, a reusable .NET component for interconverting powder diffraction data: Recent developments," in *ICDD Annual Spring Meetings*, L. O'Neill, Ed., Powder Diffraction, 2013, pp. 137–148.
- [180] C. C. Wilson, "Time-Of-Flight Neutron Diffraction," in *Neutron Data Booklet*, A.-J. Dianoux and G. Lander, Eds., 2nd ed. Grenoble: Institut Laue-Langevin, 2003, pp. 2.3.1-2.3.9.

- [181] R. I. Smith *et al.*, “The upgraded Polaris powder diffractometer at the ISIS neutron source,” *Review of Scientific Instruments*, vol. 90, no. 11, p. 115101, Nov. 2019, doi: 10.1063/1.5099568.
- [182] Unknown author, “Characteristics of a pulsed source,” *ISIS Neutron and Muon Source*. <https://www.isis.stfc.ac.uk/Pages/Characteristics-of-a-pulsed-source.aspx> (accessed Aug. 30, 2022).
- [183] C. J. Carlile, “The Production of Neutrons,” in *Neutron Data Booklet*, A.-J. Dianoux and G. Lander, Eds., 2nd ed. Grenoble: Institut Laue-Langevin, 2003, pp. 3.1.1-3.1.19.
- [184] H. M. Rietveld, “Line profiles of neutron powder-diffraction peaks for structure refinement,” *Acta Crystallogr*, vol. 22, no. 1, pp. 151–152, Jan. 1967, doi: 10.1107/S0365110X67000234.
- [185] H. M. Rietveld, “A profile refinement method for nuclear and magnetic structures,” *J Appl Crystallogr*, vol. 2, no. 2, pp. 65–71, Jun. 1969, doi: 10.1107/S0021889869006558.
- [186] E. Prince, “Mathematical aspects of Rietveld refinement,” in *The Rietveld Method*, R. A. Young, Ed., Oxford, UK: Oxford University Press, 2002, p. 43–54.
- [187] B. H. Toby and IUCr, “EXPGUI , a graphical user interface for GSAS,” *J Appl Crystallogr*, vol. 34, no. 2, pp. 210–213, Apr. 2001, doi: 10.1107/S0021889801002242.
- [188] A. C. Larson and R. B. von Dreele, “General Structure Analysis System (GSAS),” Los Alamos National Laboratory Report LAUR, Los Alamos, 2000.
- [189] L. B. McCusker, R. B. von Dreele, D. E. Cox, D. Louër, and P. Scardi, “Rietveld refinement guidelines,” *J Appl Crystallogr*, vol. 32, no. 1, pp. 36–50, Feb. 1999, doi: 10.1107/S0021889898009856.
- [190] R. A. Young, “Introduction to the Rietveld method,” in *The Rietveld Method*, R. A. Young, Ed., Oxford, UK: Oxford University Press, 2002, pp. 1–36.
- [191] R. L. Snyder, “Analytical profile fitting of X-ray powder diffraction profiles in Rietveld analysis,” in *The Rietveld Method*, R. A. Young, Ed., Oxford, UK: Oxford University Press, 2002, pp. 111–130.
- [192] G. Bergerhoff and I. D. Brown, *Crystallographic Databases: information content, software systems, scientific applications*. Cambridge: Data Commission of the International Union of Crystallography, 1987.
- [193] B. H. Toby, “R factors in Rietveld analysis: How good is good enough?,” *Powder Diffr*, vol. 21, no. 01, pp. 67–70, Mar. 2006, doi: 10.1154/1.2179804.
- [194] Unknown author, “Solid Sample Reflectance Measurements,” *Shimadzu Corporation*. https://www.shimadzu.com/an/service-support/technical-support/analysis-basics/fundamentals-uv/reflectance_measurements.html (accessed Sep. 05, 2022).
- [195] A. S. Hassanien and A. A. Akl, “Effect of Se addition on optical and electrical properties of chalcogenide CdSSe thin films,” *Superlattices Microstruct*, vol. 89, pp. 153–169, Jan. 2016, doi: 10.1016/J.SPML.2015.10.044.
- [196] J. Torrent and V. Barrón, “Diffuse Reflectance Spectroscopy,” in *Methods of Soil Analysis (Part 5): Mineralogical Methods*, Madison: Soil Science Society of America, 2008, pp. 367–385.
- [197] Unknown author, “Scanning Electron Microscopy,” *Nanoscience Instruments*. <https://www.nanoscience.com/techniques/scanning-electron-microscopy/> (accessed Sep. 05, 2022).
- [198] Ponor, “Electron-matter interaction volume and various types of signal generated - v1.svg,” *Wikimedia Commons*, Aug. 28, 2020. https://commons.wikimedia.org/wiki/File:Electron-matter_interaction_volume_and_various_types_of_signal_generated_-_v1.svg (accessed Sep. 05, 2022).
- [199] K. C. A. Smith and C. W. Oatley, “The scanning electron microscope and its fields of application,” *British Journal of Applied Physics*, vol. 6, no. 11, pp. 391–399, Nov. 1955, doi: 10.1088/0508-3443/6/11/304.
- [200] P. Sielicki, H. Janik, A. Guzman, A. Reynolds, and J. Namieśnik, “Analysis of airborne metal containing particles with EDX/EDS detectors in electron microscopes,” in *Central European Journal of Chemistry*, 2011, pp. 308–313. doi: 10.2478/s11532-010-0144-6.
- [201] Unknown author, “Linseis LFA 1000 - Laser Flash - measuring thermal conductivity,” *Linseis Messgeraete GmbH*. <https://www.linseis.com/en/products/thermal-conductivity-instruments/lfa-1000/> (accessed Sep. 05, 2022).
- [202] Unknown author, “Pioneer™ Precision,” *OHAUS*. <https://europe.ohaus.com/en-EU/PioneerPrecision-21> (accessed Sep. 05, 2022).
- [203] Unknown author, “Density Determination Kit (Solids),” *OHAUS*. <https://europe.ohaus.com/en-EU/Products/Accessories/Other/Density-Determination-Kits/Density-Kit-Solids> (accessed Sep. 05, 2022).
- [204] Unknown author, “SYJ-150 Digital Low Speed Diamond Saw,” *MTI Corporation*. <https://www.mtixtl.com/diamondsaw-SYJ-150.aspx> (accessed Sep. 05, 2022).
- [205] Unknown author, “Linseis LSR-3: electrical conductivity, Seebeck, Harman & ZT,” *Linseis Messgeraete GmbH*. <https://www.linseis.com/en/products/thermoelektrik/lsr-3/> (accessed Sep. 05, 2022).
- [206] H. J. Goldsmid and J. W. Sharp, “Estimation of the thermal band gap of a semiconductor from seebeck measurements,” *Journal of Electronic Materials* 1999 28:7, vol. 28, no. 7, pp. 869–872, 1999, doi: 10.1007/S11664-999-0211-Y.
- [207] T. R. Wei, M. Guan, J. Yu, T. Zhu, L. Chen, and X. Shi, “How to Measure Thermoelectric Properties Reliably,” *Joule*, vol. 2, no. 11, pp. 2183–2188, Nov. 2018, doi: 10.1016/J.JOULE.2018.10.020.

- [208] S. T. Norberg, I. Ahmed, R. I. Smith, S. G. Eriksson, L. C. Chapon, and S. Hull, “The Polaris Diffractometer at ISIS: Planned Upgrade and New Facilities,” ISIS Neutron and Muon Source, Oxford, 2016. [Online]. Available: <https://www.isis.stfc.ac.uk/Pages/polaris-upgrade-poster.pdf>
- [209] Unknown author, “ISIS Polaris,” *ISIS Neutron and Muon Source*. <https://www.isis.stfc.ac.uk/Pages/polaris.aspx> (accessed Aug. 20, 2022).
- [210] Unknown author, “Polaris Technical Information,” Aug. 14, 2009. <https://www.isis.stfc.ac.uk/Pages/Polaris-technical-information.aspx> (accessed Aug. 20, 2022).
- [211] S. T. Norberg, I. Ahmed, R. I. Smith, S. G. Eriksson, L. C. Chapon, and S. Hull, “The Polaris Diffractometer at ISIS: Planned Upgrade and New Facilities.”
- [212] I. Bailey, J. R. J. Bennett, J. Tomkinson, and R. A. Laboratory, “Sample Environment Equipment for the SNS,” in *Journal of Neutron Research*, Oxford, UK, Jul. 1985, pp. 812–817.
- [213] D. Ni, Y. Chen, X. Yang, C. Liu, and K. Cai, “Microwave-assisted synthesis method for rapid synthesis of tin selenide electrode material for supercapacitors,” *J Alloys Compd*, vol. 737, pp. 623–629, Mar. 2018, doi: 10.1016/J.JALLCOM.2017.12.037.
- [214] H. S. Soliman, D. A. Abdel Hady, K. F. Abdel Rahman, S. B. Youssef, and A. A. El-Shazly, “Optical properties of tin-selenid films,” *Physica A: Statistical Mechanics and its Applications*, vol. 216, no. 1–2, pp. 77–84, Jun. 1995, doi: 10.1016/0378-4371(94)00298-8.
- [215] Unknown author, “The Hall Effect,” *NIST*, Mar. 01, 2023. <https://www.nist.gov/pml/nanoscale-device-characterization-division/popular-links/hall-effect/hall-effect> (accessed May 12, 2023).
- [216] G. W. Stinton, J. S. O. Evans, and IUCr, “Parametric Rietveld refinement,” *J Appl Crystallogr*, vol. 40, no. 1, pp. 87–95, Feb. 2007, doi: 10.1107/S0021889806043275.
- [217] Unknown author, “Waveguide calibration of a vector network analyzer (VNA),” *Kirby Microwave*. <https://www.kirkbymicrowave.co.uk/Support/FAQ/How-do-I-perform-waveguide-calibration/> (accessed Apr. 30, 2023).
- [218] H. M. Rietveld and IUCr, “A profile refinement method for nuclear and magnetic structures,” *J Appl Crystallogr*, vol. 2, pp. 65–71, Jun. 1969, doi: 10.1107/S0021889869006558.
- [219] I. Dunster and V. Ezekowitz, “Resonant Cavity Magnetron Diagram.svg,” *Wikimedia Commons*, Aug. 07, 2008. https://commons.wikimedia.org/wiki/File:Resonant_Cavity_Magnetron_Diagram.svg (accessed Sep. 06, 2022).